LAST ACT OF THE RUSTENBURG LAYERED SUITE, BUSHVELD COMPLEX: FROM THE FINAL MAJOR PULSE OF MAGMA TO MODERN AMBIENT TEMPERATURES

By

JACOB BRAILEY SETERA

A dissertation submitted to the

School of Graduate Studies

Rutgers, The State University of New Jersey

In partial fulfillment of the requirements

For the degree of

Doctor of Philosophy

Graduate Program in Geological Sciences

Written under the direction of

Jill A. VanTongeren

And approved by

_____

_____

_____

_____

New Brunswick, New Jersey

January, 2020

ABSTRACT OF THE DISSERTATION

Last act of the Rustenburg Layered Suite, Bushveld Complex: From the final major pulse of magma to modern ambient temperatures

By

JACOB BRAILEY SETERA

Dissertation Director:

Jill A. VanTongeren

The Bushveld Complex in South Africa is the largest, most studied, and most economically important layered intrusion in the world. The magmatic and thermal evolution of such an igneous body has significant consequences for the formation of ore deposits both within the intrusive body itself, as well as in the rocks it intruded into. Despite being vigorously studied, the thermal evolution of the Bushveld Complex, from magmatic temperatures to the present-day ambient geotherm, remains largely unknown. Within this dissertation, I attempt to elucidate the complete thermal history of the Rustenburg Layered Suite (RLS), the predominately mafic to ultramafic portion of the Bushveld Complex.

I start by first investigating the lateral variation associated with the final major pulse of magma into the RLS magma chamber. The observed lateral compositional

variations produce a general theme which carries on throughout the dissertation. That theme is namely that an awareness of position within the magma chamber is particularly important for all studies of the RLS as considerable variations can occur dependent on location.

The majority of the dissertation is then focused on the sub-solidus thermal history of the RLS. To meet this goal, I produce the first comprehensive dataset of $^{40}Ar/^{39}Ar$ biotite and plagioclase ages throughout the ~7 km RLS stratigraphy. The varying closure temperature between the $^{40}Ar/^{39}Ar$ system in biotite and plagioclase, as well as the U-Pb system in zircon, allows for the calculation of cooling rates at every level of the stratigraphy. Results from $^{40}Ar/^{39}Ar$ biotite combined with published U-Pb zircon chronology, show that the RLS cooled rapidly (~1000°C Ma^{-1}) to ~400°C due to enhanced heat loss from hydrothermal circulation associated with the emplacement of the RLS. Numerical heat loss simulations additionally confirm the need for hydrothermal circulation at high-temperatures in order to produce the observed ages.

With the aid of an improved $^{40}Ar/^{39}Ar$ step-heating method, plagioclase $^{40}Ar/^{39}Ar$ ages and calculated closure temperatures show that hydrothermal circulation stopped within 1 Ma of zircon crystallization, as calculated cooling rates below ~400°C slow substantially (~10°C Ma^{-1}). The initial rapid cooling of the RLS, and cessation of hydrothermal circulation, provides precise age constraints on hydrothermal ore deposits within the host rocks of the RLS, that are thought have formed from fluids related to its emplacement.

ACKNOWLEDGEMENTS

It's hard to describe the journey to a PhD. It is almost as if you've "blacked out" and then you're not really quite sure how you ended up where you are. Once you take a step back, however, you realize all the wonderful connections and people who made the once seemingly impossible, possible.

First and foremost, I need to thank my advisor, Jill VanTongeren. Jill took a chance on me in 2014, which I will forever be indebted to. I was a prospective student without a Masters, two years out of an undergrad degree, and currently working as sedimentologist. However, after finding ourselves in the middle of the Bushveld Complex in South Africa within a few days of meeting each other, it was a perfect fit. Jill was always my toughest scientific critic, but also my greatest supporter. Having a habit of getting too "into the weeds", she always knew how to bring me back to the big picture and remind me how exciting the science really was. I'm also thankful to the entire Earth and Planetary Sciences department at Rutgers. I worked with almost every person within the department during my 5.5 years as a PhD student. These connections and friendships that will last a lifetime, and for that I will be forever grateful.

Finally, but not lastly, I want to thank my family. I'm not the easiest person to keep in touch with or get updates from, but they are always there when I need them, unconditionally. I'm a first-generation graduate student and with that said it’s likely that anything I am working on at any point doesn't register past, "Jake looks at rocks". However, whether it be health issues or significant life changes, my family was my "rock" and supportive through everything. Without that, and the amazing friendships and mentorship I received at Rutgers University, this work would not be written.

PREFACE

Layered mafic intrusions are often considered excellent natural laboratories for observing and understanding the geochemical and lithologic evolution of igneous bodies within the shallow crust. They also contain some of the world's largest known sources of precious metals such as Cu, Ni, PGE (Platinum Group Elements), Cr, V, etc. Given the economic and scientific potential of layered mafic intrusions, they have been studied intensely by researchers for over half a century. The largest of these intrusions, and arguably the most studied, is the Bushveld Complex in South Africa. Despite the amount of research already accomplished on the Bushveld Complex, recent improvements in methodology and analytical techniques have spurred exciting and sometimes controversial new hypotheses that can be tested.

My dissertation investigates, from magmatic temperatures to present day ambient temperatures, the thermal and magmatic history of the Rustenburg Layered Suite (RLS), the predominately mafic to ultramafic portion of the Bushveld Complex. The dissertation first focuses on the last major pulse of magma into the Bushveld Complex magma chamber. This chapter elucidates both magma-mixing and fractional crystallization processes, as well as the lateral homogeneity of magma compositions across the chamber. From there, moving down in temperature, my work provides a comprehensive subsolidus thermal history of the Rustenburg Layered Suite of the Bushveld Complex through the use of $^{40}Ar/^{39}Ar$ thermochronology. The dissertation is broken up into four chapters. Each chapter contains a chapter-specific introduction and geologic background, as well as full analytical methods, results, discussion, conclusions, and references. Below, each chapter is briefly described.

INTRODUCTION TO THE CHAPTERS

Chapter 1

Chapter 1 builds upon the initial work of VanTongeren & Mathez (2013) in the Leolo Mountain and Magnet Heights areas of the Eastern Limb of the Bushveld Complex. The work of VanTongeren & Mathez (2013) calculated the volume and composition of the last major pulse of magma that entered the Bushveld Complex magma chamber. My work was focused on the same stratigraphic interval and magmatic pulse. However, my selected study area was located 75 km South of the work of VanTongeren & Mathez (2013), in the Roossenekal area, which allows us to investigate any lateral variations associated with this final pulse of magma. The samples included in this study were collected during an extensive field campaign in 2014, where I collected twenty-three samples encompassing the entire stratigraphic interval of the Main Zone of the Bushveld Complex.

This chapter first provides a new stratigraphic thickness of the Main Zone in the Roossenekal area based on careful sampling and a detailed reconstruction using existing geological maps. Combining the new stratigraphic thickness with *in situ* mineral major and trace element data, I calculated the volume and incoming magma composition at Roossenekal. The observed differences between the Leolo Mountain traverse (VanTongeren & Mathez, 2013) and the Roossenekal traverse indicate that this last major pulse of magma entered the chamber laterally, moving from North to South. This result serves as a warning that lateral variations need to be considered in studies of large magma chambers, and more importantly layered intrusions. This last point is especially important given the current interest in the layered intrusions community to drill a

reference core of the Bushveld Complex as part of the International Continental Drilling Program.

This work produced one published paper:

Setera, J. B., & VanTongeren, J. A. (2018). Lateral Variability in the Upper Main Zone, Bushveld Complex, owing to Directional Magma Recharge and Emplacement from North to South. **Journal of Petrology**, 59(9), 1763-1786.

Chapter 2

Chapter 2 moves away from magmatic processes and focuses on the thermal history of the RLS, post-crystallization. The thermal evolution of the RLS, and layered intrusions in general, remains enigmatic due to sparse geochronologic constraints. To elucidate the thermal history of the RLS from magmatic temperatures to ~350-450°C, I produced a total of 30 $^{40}Ar/^{39}Ar$ biotite ages throughout ~5.5 km of the RLS stratigraphy. This is the first study that reports $^{40}Ar/^{39}Ar$ biotite ages for the majority of the cumulate rocks of the RLS stratigraphy, thus providing essential age constraints. Careful step-heating procedures and data analysis overcome some of the challenges many other researchers have encountered in attempting to date biotite from the RLS using $^{40}Ar/^{39}Ar$ geochronology.

When comparing the $^{40}Ar/^{39}Ar$ biotite ages with published high-temperature chronology, I show that the RLS cooled rapidly to the closure temperature of the

$^{40}Ar/^{39}Ar$ system in biotite (~350-450°C) , with cooling rates potentially similar to those observed within the oceanic crust. In companion with the geochronology, I also conducted numerical thermal modeling of the RLS. As was a theme in Chapter 1, this thermal modeling makes a point to focus on potential lateral variabilities within the RLS. In this case, the lateral variability comes from samples closer to the edge of the intrusion cooling faster than those at its center. Heat-loss through the sides of the intrusion has not yet been incorporated in thermal models of the RLS until this point. The combined thermal modeling and $^{40}Ar/^{39}Ar$ biotite results indicate that the igneous body must have cooled rapidly due to enhanced heat loss from a hydrothermal system associated with the emplacement of the RLS.

To deduce the thermal history of the RLS at even lower temperatures (<350°C), I set out to use $^{40}Ar/^{39}Ar$ thermochronology of plagioclase. This required the development of a new method of $^{40}Ar/^{39}Ar$ step-heating, which provides precise paired ages and closure temperatures for individual plagioclase grains.

This work produced one published paper:

Setera, J. B., VanTongeren, J. A., Turrin, B. D., & Swisher, C. C. (2019). Rapid Cooling of the Rustenburg Layered Suite of the Bushveld Complex: Insights from biotite $^{40}Ar/^{39}Ar$ geochronology. **Geology**.

Chapter 3

This chapter details the development of a new novel $^{40}Ar/^{39}Ar$ step-heating approach aimed at producing precise age and diffusion parameters for small samples. The method involves placing a sample on a tantalum platform and heating said platform with a CO_2 laser. The temperature calibration procedure, using a two-color pyrometer, ensures that accurate temperatures are being recorded throughout step-heating experiments. The platform design also allows for constant visualization of samples during step-heating, which is specifically vital when the moment of fusion for the sample is reached. The method provides a simple, inexpensive, and reliable means for the heating of samples as small as a few tens of micrograms and is particularly useful to the Ar-geochronology community, as it provides an easy to implement technique for laboratories that do not have a diode laser, with tantalum providing a metal that easily couples to a CO_2 laser.

During the development of the method, I produced ages and diffusion parameters for a variety of samples. First, I produced data for 3 individual plagioclase grains (2 stratigraphic levels) from the RLS. The results from these grains, to be used primarily in chapter 4, matched well with published results on plagioclase feldspars. I also produced new data on a 174 μg mafic clast from the howardite meteorite, MAC 02666. The precise age and diffusion parameters from the mafic clast provided 2 main advancements: (1) they provide inferences and constraints on the impact history of the HED parent body, asteroid 4 Vesta and (2) they demonstrate that extremely small, low K_2O, samples can provide precise and meaningful results using the new step-heating technique.

With the method developed and proven, I expanded the use of the new technique from the 2 initial stratigraphic levels of the RLS, to the entirety of the stratigraphy.

This chapter resulted in one submitted paper:

Setera, J. B., Turrin B. D., Herzog G. F., Delaney J. S., VanTongeren J. A., Lindsay F. N., Boesenberg J F., & Swisher C. C. (2019). $^{40}Ar/^{39}Ar$ thermochronology for sub-milligram samples with illustrations from the Bushveld Complex and howardite, MAC 02666. **Geochemistry, Geophysics, Geosystems**.

Chapter 4

The final chapter of the dissertation aims at elucidating the remaining thermal history of the RLS, namely that below the $^{40}Ar/^{39}Ar$ closure temperature of biotite (see chapter 2). To date, low temperature thermochronology is only available from a single stratigraphic level within the ~7-8 km thick RLS. Using the method described in chapter 3, I report $^{40}Ar/^{39}Ar$ ages and closure temperatures for a total of 20 individual plagioclase grains. The 20 grains represent 12 stratigraphic levels of the RLS and provide essential age/temperature constraints (~150-300°C) that encompass the entire stratigraphy of the RLS in the Eastern Limb of the Bushveld Complex (~7 km).

Plagioclase $^{40}Ar/^{39}Ar$ results are paired with the biotite $^{40}Ar/^{39}Ar$ results from chapter 2 to deduce low-temperature cooling rates of the RLS. The calculated cooling rates indicate a rapid and significant shift to slower cooling rates below the $^{40}Ar/^{39}Ar$ closure temperature of biotite. This shift is result of cessation of the hydrothermal system

associated with the emplacement of the RLS and a transition to primarily conductive-cooling of the RLS. Detailed numerical heat-loss simulations, again paying close attention to the lateral effects of cooling within the intrusion, confirm (1) the need for hydrothermal circulation to produce observed high-temperature cooling rates and (2) a switch to conductive cooling of the RLS to produce observed $^{40}Ar/^{39}Ar$ plagioclase results. As a result, the combined modeling and $^{40}Ar/^{39}Ar$ data also provide important age constraints on RLS-related hydrothermal ore deposits that formed within the host rocks of the intrusion.

As a final ending of the dissertation and chapter 4, I use the results from all chapters to describe a full model of the thermal evolution of the RLS within the Eastern Limb of the Bushveld Complex.

This chapter resulted in one prepared manuscript:

Setera, J. B., VanTongeren J. A., Turrin B. D., & Swisher C. C. (2020). A low-temperature hydrothermal cutoff: Plagioclase $^{40}Ar/^{39}Ar$ thermochronology of the Rustenburg Layered Suite., Bushveld Complex. **Earth & Planetary Science Letters**.

Table of Contents

ABSTRACT OF THE DISSERTATION ii

ACKNOWLEDGMENTS iv

PREFACE v

Table of contents xii

Chapter 1 1

The last major pulse of magma: composition and lateral variability in the Upper & Upper Main Zones 1

1. Introduction 2

2. Geologic and Stratigraphic Setting 4

3. Previous Lateral Variation Studies at the Level of the Pyroxenite Marker 6

4. Analytical Methods 8

5. Results 11

5.1 Roosenekal Results 11

5.2 Comparison of the Leolo Mountain Traverse (N) and Roossenekal Traverse (S) 13

5.2.1 Mineral Major Element Compositions 13

5.2.2 Pyroxene Cr Concentration 14

5.3 Calculation of Mixing Parameters 15

5.3.1 Proportions 15

5.3.2 Calculation of Total Magma Thicknesses at Roossenekal 15

5.3.3 Calculation of Total Stratigraphic Excursion 17

5.3.4 Resident, Incoming, and Mixed Magma Compositions 18

6. Discussion 22

6.1 Lateral variations from trapped liquid? 22

6.2 Lateral variability owing to structural upwarp?: the Cawthorn et al. (2016) model 23

6.3 A new hypothesis for magma recharge and lateral variability in the Eastern Limb 25

6.4 Reliability of the pyroxene record? 28

7. Conclusions 32

8. References 33
Figure Captions 39
Figure 1 46
Figure 2 47
Figure 3 48
Figure 4 49
Figure 5 50
Figure 6 51
Figure 7 52
Figure 8 53
Figure 9 54
Figure 10 55
Figure 11 56
Figure 12 57
Figure 13 58
Figure 14 59
Figure 15 60
Table 1 61
Table 2 62
Table 3 67
Table 4 72
Table 5 77
Table 6 82
Table 7 85
Table 8 88
Table 9 89
Table 10 92
Chapter 2 93
The mid-high temperature subsolidus thermal evolution of the Rustenburg Layered Suite 93
1. Introduction 94
2. Samples and Methods 96
2.1 Samples 96

2.2 Argon Isotope Analyses 96
2.3 Discordant Age Spectra (Chloritization) 98
2.4 Electron Microprobe Analyses 100
3. Results 100
4. Rapid Cooling of the RLS 101
4.1 Geochronology, Cooling Rate, and Closure Temperature 101
4.2 Numerical Heat-loss Modelling 102
4.3 Implications of Modelling and Observed Cooling Rate 105
5. Long-lived, Localized Hydrothermal Activity 106
6. Conclusions 107
7. References 108
Figure Captions 113
Figure 1 116
Figure 2 117
Figure 3 121
Figure 4 125
Figure 5 129
Figure 6 130
Figure 7 131
Figure 8 132
Table 1 133
Table 2 134
Table 3 165
Table 4 166
Table 5 168
Chapter 3 170
A new method for $^{40}Ar/^{39}Ar$ thermochronology for sub-milligram and low K_2O samples 170
1. Introduction 171
2. Experimental Procedures 173
2.1 Samples and Sample Preparation 173
2.1.1 Plagioclase from the Bushveld Complex 173
2.1.2 Mafic Clast - MAC 02666 174

2.2 Electron Microprobe Analyses 175
2.3 Irradiation and Standards 176
2.4 Step-Heating 177
2.4.1 Platform Design 177
2.4.2 Energy 2D Modelling 179
2.4.3 Temperature Measurements 180
2.5 Argon Measurements and Ages 183
2.6 Arrhenius Regression and Closure Temperature Calculation 184
2.6.1 Detailed Calculations for Diffusion Parameters, Closure Temperature, and Diffusive Losses 184
2.6.2 Derivation of Closure Temperature Uncertainty 186
2.7 Accounting for Cosmogenic Ar in Isochron Calculations 190
2.7.1 Lever Rule Calculations 190
2.7.2 The role of Chlorine 191
2.7.3 Calculation of $^{38}Ar_{Tr}$ from the Cosmic-ray Exposure Age 192
2.8 Calculation of Cosmic-ray Exposure Age 193
3. Results 195
3.1 Plagioclase from the Bushveld Complex 195
3.2 Mafic Clast (MC 001) - MAC 02666 196
4. Discussion 199
4.1 Benefits of Ta-Platform Heating 199
4.2 Application to Howardite, MAC 02666 203
4.2.1 Thermal Resetting Events on Vesta 203
4.2.2 Howardite Age Evolution 207
5. Conclusions 209
6. References 210
Figure Captions 218
Figure 1 223
Figure 2 224
Figure 3 225
Figure 4 226
Figure 5 227
Figure 6 228

Figure 7 229
Figure 8 230
Figure 9 231
Figure 10 232
Figure 11 233
Figure 12 234
Figure 13 235
Figure 14 236
Figure 15 237
Table 1 238
Table 2 239
Table 3 240
Table 4 241
Table 5 242
Table 6 244
Table 7 245
Table 8 246
Table 9 248
Table 10 249
Table 11 250
Table 12 251
Table 13 252
Table 14 253
Chapter 4 254
An end to hydrothermal circulation: Low temperature $^{40}Ar/^{39}Ar$ thermochronology of the Rustenburg Layered Suite 254
1. Introduction 255
2. Geologic Setting 258
3. Samples & Methods 259
3.1 Samples & Stratigraphy 259
3.2 Electron Microprobe 261
3.3 Irradiation & Standards 261
3.4 Argon Measurements & Calculations 262

4. Results 262
4.1 Plagioclase $^{40}Ar/^{39}Ar$ Plateau ages 262
4.2 Diffusion Parameters 264
4.3 Calculation of Cooling Rates & Closure Temperature 265
4.4 Early, Young Apparent $^{40}Ar/^{39}Ar$ Ages 266
5. Discussion 268
5.1 Low Temperature Cooling Rates 270
5.2 Numerical Modeling of Heat Loss 270
5.2.1 Confirmation of Hydrothermal Circulation 272
5.2.2 Comparison to 40Ar/39Ar Plagioclase Data 273
5.3 Physical Evidence of Hydrothermal Circulation at High-mid Temperature 275
5.4 Implications for the Timing of Hydrothermal Ore Deposits 277
6. Conclusions 278
7. References 281
Figure Captions 286
Figure 1 290
Figure 2 291
Figure 3 292
Figure 4 293
Figure 5 294
Figure 6 297
Figure 7 302
Figure 8 303
Figure 9 304
Figure 10 305
Figure 11 306
Table 1 307
Table 2 308
Table 3 309
Table 4 310
Table 5 327

Table 6 342
Table 7 343
Table 8 344

Chapter 1

The last major pulse of magma: composition and lateral variability in the Upper & Upper Main Zones.

This chapter resulted in one published paper:

Setera, J. B., & VanTongeren, J. A. (2018). Lateral Variability in the Upper Main Zone, Bushveld Complex, owing to Directional Magma Recharge and Emplacement from North to South. **Journal of Petrology**, 59(9), 1763-1786.

Abstract

Recharge and magma mixing into shallow crustal reservoirs is a critical parameter in understanding magma diversity and predicting volcanic activity and hazards. Direct observation of magma mixing within the crust, however, is impossible. The solidified remnants of large magma chambers in layered mafic intrusions are therefore some of the most important natural laboratories for measuring and understanding past magma chamber dynamics. Here we provide *in situ* major and trace element compositions of all major mineral phases throughout a single stratigraphic section of a well-defined magma recharge interval in the *c.* 2.06 Ga Bushveld Complex layered intrusion of South Africa. This section, the Roossenekal Traverse, is located approximately 75 km south of a previously documented section of the same stratigraphy, the Leolo Mountain Traverse. Despite their distance, the two profiles show remarkably similar thicknesses and

compositional variations, however both resident and incoming magmas recorded in the Roossenekal Traverse are slightly more compositionally evolved. We show that the lateral compositional variability is a direct result of the locus of magma recharge originating in the north, near the Thabazimbi-Murchison Lineament. New primitive magma was emplaced in the north, mixed with more evolved magma towards the south, and fractionated as it filled the magma chamber progressively to the south.

1. Introduction

The solidified remnants of large magma chambers in layered mafic intrusions remain some of the most important natural laboratories for measuring and understanding past magma mixing and recharge events. Evidence in support of magma mixing and recharge in the cumulates of layered intrusions can be identified by major shifts in whole rock isotopic composition as well as reversals to more primitive major and trace element compositions with increasing height in the stratigraphic sequence (e.g. VanTongeren, 2018).

One layered intrusion in particular, the Rustenberg Layered Suite (RLS) of the Bushveld Complex, shows clear evidence of discrete magma mixing and recharge events throughout its stratigraphy. The *c.* 2.06 Ga RLS is approximately 8-9 km thick, spans *c.* 450 km E-W, 150-200 km N-S (SACS, 1980) and occurs in four distinct limbs (Northern, Western, Eastern and the Southern Bethal lobe; Fig. 1). The mafic-ultramafic magmas of the RLS were emplaced in at least four major injections (Eales, 2002). The last of these major injections occurred near the top of the Main Zone of the RLS, below the Pyroxenite Marker (Fig. 2). Evidence for a new magma injection at this level comes from

clear reversals to more primitive major and trace element chemistry as well as distinctly lower whole rock initial $^{87}Sr/^{86}Sr$ compositions (Sharpe, 1985; Kruger *et al.*, 1987; Cawthorn *et al.*, 1991; VanTongeren & Mathez, 2013). The stratigraphic interval, in which compositions become progressively more primitive upwards through the stratigraphy prior to the Pyroxenite Marker, was investigated by VanTongeren & Mathez (2013) in the Eastern Limb near the Leolo Mountains (Fig. 1) and is defined as the 'Zone of Magma Mixing' (Fig. 2).

Many scenarios involving the input of new primitive magma have been described to explain the compositional reversal within cumulus minerals below the Pyroxenite Marker. Based on higher Al_2O_3 contents of pyroxenes immediately above the Pyroxenite Marker in the Western Limb, Cawthorn *et al*. (1991) proposed that the incoming magma was denser than the resident magma and was emplaced into a stratified, poorly mixed, resident magma chamber. However, the uniformity of the whole rock Sr isotopic compositions from the Pyroxenite Marker to the roof (e.g. Kruger *et al*., 1987; Sharpe, 1985), and the clear trends in *in situ* major and trace elements of plagioclase and pyroxenes, led VanTongeren & Mathez (2013) to conclude that the new magma was emplaced in multiple small batches into a homogenous resident magma body. Rapid mixing between incoming and resident magma allowed for homogenization of the two magmas and partial crystallization between each pulse.

With the exception of a recent study looking at lateral changes in plagioclase An content at the Pyroxenite Marker (e.g. Cawthorn *et al*., 2016), the majority of studies attempting to elucidate the nature of this magma recharge event (i.e. compositions and volume of incoming magma), focus on individual boreholes or single stratigraphic

sections and do not investigate potential lateral variation within the magma chamber. Incorporating lateral variations into previous findings regarding magma chamber dynamics is vital, particularly in the case of the RLS due to its immense size.

The goal of this work is to use *in situ* major and trace element analyses to investigate the lateral variation in the magma chamber during the final recharge event into the RLS near the level of the Pyroxenite Marker.

2. Geologic and Stratigraphic Setting

The RLS was intruded around 2.06 Ga (Buick *et al.*, 2001; Scoates & Friedman, 2008; Olsson *et al.*, 2010; Scoates & Wall, 2015; Zeh *et al.*, 2015; Mungall *et al.*, 2016) into the Neoarchean to Paleoproterozoic Transvaal Supergroup sediments (Eriksson & Altermann, 1998) within the central northeast portion of the Kaapvaal craton. The layered sequence crops out in predominately eastern and western limbs that dip gently toward each other and appear to connect at depth (Cawthorn & Webb, 2001; Webb *et al.*, 2004) (Fig. 1). The predominately mafic and ultramafic unit of the Bushveld Complex, the Rustenburg Layered Suite (RLS), is stratigraphically subdivided (SACS, 1980) into the Lower, Critical, Main and Upper Zones based on cumulus mineral assemblages (Fig. 1). It is in the Eastern Limb that the RLS is best exposed.

The estimated thickness of the Main Zone varies considerably from north to south in the Eastern Limb. The Main Zone in the Eastern Limb of the RLS has been described to be *c.* 2,900 m in the north near the Leolo Mountains (Molyneux, 1974) to *c.* 3,940 m (von Gruenewaldt, 1973) or 2,635 m (Fig. 3; this study) at Roossenekal and *c.* 1,100-1,450 m at Stoffberg toward the south (Groeneveld, 1970) (Fig. 1). Some of the

variability in estimates arises from ambiguity in the official boundary between the base of the Main Zone and the top of the Critical Zone (Kruger, 1990; Kruger, 1991; Mitchell & Scoon, 1991). The South African Commission for Stratigraphy (SACS, 1980) positions the boundary above the Merensky Reef on top of a distinct series of anorthositic rocks containing large mottled pyroxene called the Bastard mottled anorthosite (Giant mottled anorthosite). A reexamination of the Main Zone boundaries by Kruger (1990) places the base of the Main Zone at an unconformity immediately below the Merensky Reef, where there is a distinctive change in the whole rock strontium isotopic signature (Kruger, 1994). Above the Merensky Reef, the Main Zone consists of norite, gabbronorite and occasional anorthosite layers. Inverted pigeonite eventually replaces orthopyroxene as the Ca-poor pyroxene upwards through the stratigraphy.

The Main Zone-Upper Zone boundary is officially defined as the first appearance of cumulus magnetite (SACS, 1980). However, it is below the Pyroxenite Marker, a nearly-ubiquitous *c.* 3 m thick orthopyroxenite layer in the upper Main Zone, that the whole rock Sr isotopic composition changes and the major element compositions of the cumulus mineral phases become more primitive (Kruger *et al.*, 1987; Cawthorn *et al.*, 1991; VanTongeren & Mathez, 2013). The change in whole rock Sr isotopes across this boundary led Kruger *et al.* (1987) to define the geochemical boundary between the Upper Zone and Main Zone at the level of the Pyroxenite Marker. In order to avoid confusion with nomenclature, the stratigraphy from the Pyroxenite Marker to the roof of the intrusion, which encompasses the combined Upper Zone and Upper Main Zone, has been termed the UUMZ (Fig. 2c; VanTongeren *et al.*, 2010).

In the Eastern Limb, the Pyroxenite Marker has been traced along strike from N to S before disappearing *c*. 5 km south of Roossenekal. Where the Pyroxenite Marker is absent in the south, it is replaced by magnetite gabbro while still recording compositional reversals similar to those observed in the north (von Gruenewaldt, 1973; Klemm *et al.*, 1985; Cawthorn *et al.*, 2016). Due to poor outcrop availability, the Western Limb is primarily studied via boreholes and only a single representation of the Pyroxenite Marker has been found (Cawthorn *et al.*, 1991), although compositional reversals have been recorded without the presence of the Pyroxenite Marker (Mitchell, 1990). The Pyroxenite Marker is entirely absent from boreholes and exposed outcrop in the Northern Limb. Although there are two pyroxene-rich horizons observed within a borehole from the Northern Limb, Ashwal *et al.* (2005) concluded, based on mineralogical evidence, that these are not correlated to the Pyroxenite Marker.

3. Previous Lateral Variation Studies at the Level of the Pyroxenite Marker

Lateral variation in the RLS magma chamber at the level of the Pyroxenite Marker was previously investigated on a small scale in a study by Klemm *et al.* (1985). Klemm *et al.* (1985) measured three profiles just south of Roossenekal spaced over approximately 10 km along strike. The authors measured bulk plagioclase (measured on a universal stage) and orthopyroxene compositions (measured via X-ray diffraction) and found that the maximum plagioclase An content in their three profiles decreased towards the south from An_{73} (*c*. 5 km south of Roossenekal) to An_{65} and An_{63}. They concluded that lateral variations in bulk plagioclase and orthopyroxene compositions were due to decreasing proportions of incoming magma as well as a change in the oxygen fugacity within the

magma chamber, however there was no attempt at quantifying the proportions or compositions of the magmas involved.

The most laterally extensive investigation into variability at the level of the Pyroxenite Marker of the Eastern Limb of the RLS to date was undertaken by Cawthorn *et al.* (2016). Cawthorn *et al.* (2016) compiled published data on plagioclase anorthite content from eight profiles throughout the Eastern Limb, covering a lateral distance of 110 km. They showed that the maximum average plagioclase An content near the Pyroxenite Marker varies by only *c*. 2 mol % (*c.* An_{75} to An_{73}) from the Leolo Mountain traverse of VanTongeren & Mathez (2013) to the first traverse just south of Roossenekal of Klemm *et al.* (1985) – a lateral distance of *c*. 80 km. However, another 35 km to the south, at Stoffberg, the maximum An content of plagioclase is *c.* 63 (Cawthorn *et al.*, 2016), yielding a decrease of maximum average plagioclase An content of *c.* 12 An mol % over the *c.* 110 km from the Leolo Mountain traverse to Stoffberg. Cawthorn et al. (2016) concluded that changes in the stratigraphic level and the maximum plagioclase An content near the Pyroxenite Marker were controlled by a structural upwarp in the magma chamber basin. As is described in detail below (see discussion section), there is no robust field evidence of a structural upwarp in this region. Thus, a different mechanism must be responsible for the lateral variability observed in maximum An content in the eastern limb by Cawthorn et al. (2016).

Lundgaard et al. (2006), while not focused on the recharge interval at the level of the Pyroxenite Marker, also investigated lateral variations within the mid to lower Main Zone of the Eastern Limb. The location of the three investigated profiles range from Thornhill in the north (analogous to the Leolo Mountain traverse of this study) to

Roossenekal and further south to Stoffberg (Fig. 1). They show that the average An content of plagioclase cores in the mid-lower Main Zone shows no systematic variation from north at Thornhill to south at Stoffberg. Conversely, there is a decrease in the Mg# of orthopyroxene cores ($Mg\#_{67-61}$ – $Mg\#_{59-50}$) as well as in bulk plagioclase An content (An_{67-61} – An_{59-55}), from Thornhill to Stoffberg. This change is coupled with an increase in the whole rock concentration of incompatible elements from north at Thornhill to south at Stoffberg. Lundgaard et al. (2006) suggest these lateral variations are a product of an increased trapped melt from 0-10% in the north at Thornhill to 30-45% in the south at Stoffberg (Fig. 1). The lateral variations from Thornhill to Roossenekal are less pronounced and indicate an only slight increase in trapped melt fraction at Roossenekal compared with Thornhill (Lundgaard et al., 2006).

Apart from the study of Lundgaard et al. (2006), the conclusions deduced by the studies above rely primarily on the anorthite content of plagioclase. As noted above, these changes are sometimes extremely subtle and even within the uncertainties of average plagioclase anorthite content. This manuscript provides a comprehensive dataset of whole rock and *in situ* mineral major element, as well as trace element compositions from a traverse of the Main Zone near Roossenekal (Figs. 4-7). Our data from the Roossenekal traverse, are compared with the data of VanTongeren & Mathez (2013) for the Leolo Mountain traverse, *c.* 75 km to the north. We calculate the proportion and composition of the incoming magma for both profiles using the method of VanTongeren & Mathez (2013). Our results provide a more robust quantification of the lateral variation in both the proportion of incoming versus resident magma and the composition of the incoming magma below the Pyroxenite Marker in the Eastern Limb of the RLS.

4. Analytical Methods

Twenty-three samples of the Main Zone in the eastern RLS were collected along an approximately E-W traverse from Roossenekal (S 25°12.098, E 029°55.907) to Draaikaal (S 25°13.849, E 030°05.374) (Figs. 1, 3). The lack of well-defined layering in the Main Zone makes it difficult to constrain the dip of the rocks along the transect. Each sample was placed in its stratigraphic position by incorporating the elevation at each locality and using a shallow 10° dip as recorded in the lower Main Zone *c*. 5 km north of the transect (Molyneux, 1974, Molyneux, 2008). The total thickness of the Main Zone at Roossenekal, using this dip angle, is *c*. 2,635 m. This is significantly less than the 3,940 m thickness cited at Roossenekal by von Gruenewaldt (1973), which was calculated using a steeper dip angle of *c.* 15°. There is evidence for steeper dip angles to the South at Stoffberg [up to 25°; Groeneveld (1970)], however the scarcely recorded dips in the Roossenekal traverse area are shallow, 10° in the lower Main Zone (Molyneux, 1974), and 10°-12° in the Upper Zone (Scoon & Mitchell, 2012). All stratigraphic depths reported in this study are relative to the Merensky Reef at 0 m. A full list of samples with their stratigraphic height above the Merensky Reef and geographic location is provided in Table 1. The pyroxenite Marker occurs at *c.* 2,133 m above the Merensky Reef in the Roossenekal traverse.

The samples in this study consist of gabbronorites with nearly adcumulate textures and a cumulate mineral assemblage of 50-70% plagioclase, 15-30% low-Ca pyroxene and 5-20% clinopyroxene. Low-Ca pyroxene within the Main Zone is represented by a combination of primary orthopyroxene and inverted pigeonite, with

inverted pigeonite becoming the primary low-Ca pyroxene below the Pyroxenite Marker. Modal abundances were estimated optically by point counting (minimum of 300 points per thin section).

Major element compositions for plagioclase, clinopyroxene and low Ca pyroxene were determined using the JEOL JXA 8200 electron microprobe at Rutgers University and the Cameca SX100 microprobe at the American Museum of Natural History. All analyses used an acceleration potential of 15kV, beam current of 15nA, count time of 30 s on peak and 15 s on background for each element, and a beam diameter of 5 μm and 1 μm for plagioclase and pyroxene, respectively. Standards were analyzed between every *c.* 50 unknowns and consistently yielded results within 2σ of published values (Table 2).

In situ trace element compositions of plagioclase, clinopyroxene, and low-Ca pyroxene were obtained at Rutgers University using the Thermo Scientific iCAP Qc ICP-MS system equipped with a Photon Machines 193 nm laser ablation system. Spot sizes of 65 μm and 40 μm were used for plagioclase and pyroxene, respectively. Approximately 10 seconds of gas backgrounds were collected before 30 seconds of sample ablation. Standards NIST610 and NIST612 were regularly analyzed for continuous calibration and to account for any drift. BCR and BIR were also analyzed regularly as a secondary standard to confirm accuracy (Table 2).

In all samples collected for this study, thin section billets were cut perpendicular to the foliation and, where possible, parallel to the lineation so as to ensure that the thin section plane cuts through the center of alignment of the grains. Additionally, we were careful to only measure the center of cumulus grains (Fig. 8) and did not select grains

with abnormal aspect ratios (possibly indicative of not being at the geometric center of the grain).

Major and trace-element concentrations of bulk rocks were determined using a ThermoARL Advant XP + sequential X-ray fluorescence (XRF) spectrometer at the Peter Hooper GeoAnalytical Lab at Washington State University. Replicate analyses of bulk rocks were run from aliquots of the same crushed and powdered rocks.

Major and trace element compositions for plagioclase, clinopyroxene and low Ca pyroxene are available in Tables 3-5. Whole rock analyses for each sample are available in Table 6.

5. Results

5.1 Roossenekal Results

Abrupt increases in Cr concentration are often interpreted as new fresh pulses of magma (e.g. Cawthorn, 2007; VanTongeren & Mathez, 2013; Tanner et al., 2014). Three such increases occur within the Main Zone at Roossenekal. The first increase in Cr content occurs *c*. 137 m above the Merensky Reef (Fig. 4). This study does not include any samples below this depth, however this elevated Cr concentration in pyroxene is likely a consequence of the pulse(s) of magma responsible for forming the lower Main Zone. A distinctive second new pulse of magma is recorded in our section at approximately 704 m above the Merensky Reef (Fig. 4).

The third and final pulse of new magma into the RLS occurs approximately 270 m below the Pyroxenite Marker in Roossenekal (Fig. 4). From approximately 704 m to 1750 m above the Merensky Reef, pyroxene Cr concentrations remain relatively low and

constant upwards through the stratigraphy. At approximately 1750 m above the Merensky Reef, Cr concentrations begin to gradually increase over *c*. 270 m until they reach a maximum just below the Pyroxenite Marker (Fig. 4). In contrast to the previous two pulses of new magma recorded by the Cr content, this interval of increasing Cr also coincides with reversals in the plagioclase An content (Fig. 5), pyroxene Mg# (Fig. 5), and whole rock Sr isotopic compositions (Kruger et al., 1987; Cawthorn et al., 1991) as well as the formation of the Pyroxenite Marker. Therefore, it is likely that this final pulse of magma introduced a significantly larger volume of new magma into the resident Main Zone magma chamber.

Average plagioclase An content and pyroxene Mg#s throughout the Main Zone of the Roossenekal traverse are shown in Fig. 5a. Variations in measured plagioclase An content are similar to those reported by Cawthorn et al. (2016) at Roossenekal and those reported by VanTongeren & Mathez (2013) for the Leolo Mountain traverse. The average An content of plagioclase decreases with increasing stratigraphic height within the lower Main Zone reaching a minimum value of 55 at approximately 1,843 m. Average plagioclase An values become progressively more primitive from approximately 1,843 m above the Merensky Reef until they reach a maximum value of 73 at approximately 2,252 m, *c.* 119 m above the Pyroxenite Marker. Average low-Ca pyroxene and clinopyroxene Mg# follow the same trend as An content in plagioclase, with the maximum Mg# reaching 72.9 for low-Ca pyroxene and 78.2 for clinopyroxene. The reversal of An content in plagioclase and Mg# in pyroxene occurs at the same stratigraphic height with no evidence of decoupling as was described below the Pyroxenite Marker, within the Main Zone of the Western Limb (Nex *et al.*, 2002). The stratigraphic interval over which

major element compositions of plagioclase and pyroxene become more primitive is hereafter termed the Zone of Magma Mixing following VanTongeren & Mathez (2013). In the Roossenekal traverse, studied here, the Zone of magma mixing occurs from 1,843 m to 2,133 m (Fig. 2, 5).

Figure 6 shows the stratigraphic variation of *in situ* trace element concentrations in plagioclase (Fig. 6a) and low-Ca pyroxene (Fig. 6b) from which equilibrium liquid compositions were calculated (Table 9). While not as pronounced as those observed in major elements, incompatible trace elements measured *in situ* generally record decreases in concentration associated with the onset of magma mixing at approximately 1,843 m above the Merensky Reef, whereas compatible trace elements generally increase (Fig. 6). REE concentrations in all mineral phases decrease within the Zone of Magma Mixing and are lowest in samples above the Pyroxenite Marker (Fig. 7).

Measured concentrations for trace elements to be used in magma mixing calculations are listed in Table 7 for plagioclase, low-Ca pyroxene and clinopyroxene, and full elemental suites for each mineral can be found in Tables 3-5.

5.2 Comparison of the Leolo Mountain Traverse (N) and Roossenekal Traverse (S)

5.2.1 Mineral Major Element Compositions

The level of the Pyroxenite Marker is similar in both traverses, *c*. 2,200 m above the Merensky Reef in the north at Leolo and *c*. 2,133 m above the Merensky Reef in the south at Roossenekal. The maximum plagioclase An content, after the input of new primitive magma, is slightly higher in the north at Leolo than in the south at Roossenekal, with An contents of 76 and 73 respectively (Fig. 9a). Maximum pyroxene Mg# also are

slightly higher in the north at Leolo, than in the south at Roossenekal, with the maximum Mg# of low-Ca pyroxene decreasing from 74 to 73 and clinopyroxene from 80 to 78 (Fig. 9b,c). The level at which the Zone of Magma Mixing begins (i.e. the most evolved plagioclase An content) is almost identical between the two profiles, with the most evolved sample at 1,849 m above the Merensky Reef in the north at Leolo and 1,843 m above the Merensky Reef in the south at Roossenekal. Overall, the major element variations (plagioclase An content and pyroxene Mg#) between the two traverses is small, pointing towards a remarkable consistency near the level of the Pyroxenite Marker over a distance of *c.* 75 km.

Mineral major element differences between the Leolo and Roossenekal traverses are found primarily *below* the Zone of Magma Mixing. In the Leolo traverse to the north, plagioclase An content is slightly higher prior to new magma input than in the south at Roossenekal. The most evolved low-Ca pyroxene Mg# prior to new magma input is approximately 65 at Leolo, whereas is approximately 54 at Roossenekal. Likewise, the clinopyroxene Mg# is 75 at Leolo but 64 in Roossenekal prior to new magma input. Lundgaard et al. (2006) also found a similar offset in pyroxene Mg# between their Thornhill (northern) and Roossenekal traverses throughout the lower Main Zone.

5.2.2 Pyroxene Cr Concentration

There is a significant decrease in the maximum Cr concentration of pyroxenes at the level of the Pyroxenite Marker from north to south. In the north, the Leolo Mountain traverse records a maximum Cr concentration of 1,630 ppm and 2,480 ppm for low-Ca pyroxene and clinopyroxene, respectively (VanTongeren & Mathez, 2013). The maximum Cr

concentration recorded at the same stratigraphic level in the south at Roossenekal is nearly half of that observed at Leolo, *c.* 675 ppm for low-Ca pyroxene and 1,590 ppm for clinopyroxene. Both traverses show pyroxene Cr concentrations within the Zone of Magma Mixing that are variable within a single sample.

5.3 Calculation of Mixing Parameters

5.3.1 Proportions

The proportion of incoming magma (X_{inc}) to resident magma (X_{res}) is inferred according the method outlined in VanTongeren & Mathez (2013), where the total magma thickness is equal to the sum of the resident magma thickness and the incoming magma thickness. The total thickness of the incoming magma is calculated as the stratigraphic excursion from the onset of magma mixing to the point at which the compositions return to their pre-mixing values (Figs. 2, 5). The thicknesses of each unit are based on average plagioclase core An content as it is more resistant to subsolidus re-equilibration than pyroxenes due to the coupled substitution of Ca-Al with Na-Si (Morse, 1984; Cherniak, 2003).

5.3.2 Calculation of Total Magma Thicknesses at Roossenekal

Scoon & Mitchell (2012) collected a full stratigraphic record of the Upper Zone from multiple boreholes near Roossenekal and cited a total thickness of *c*. 2,300 m from the appearance of cumulus magnetite (Main Zone-Upper Zone boundary) to the roof of the intrusion. This thickness is significantly greater than the thickness for the same interval reported to the north near Magnet Heights (Fig. 2) of 1,775 m (Molyneux, 1974). A

detailed comparison of the UUMZ stratigraphy between the combined Leolo Mountain and Magnet Heights area (Molyneux, 1974) and the Roossenekal traverse shows that individual magnetitite seams, as well as the first appearance of cumulus olivine, are traceable to remarkably similar stratigraphic levels over the *c.* 75 km distance between the two traverses (Fig. 10). Stratigraphic thicknesses, however, deviate between the two profiles starting near the base of Subzone D (the appearance of cumulus apatite). It is at this point that the upper portion of the UUMZ becomes significantly thicker at Roossenekal than at Leolo. Within this portion of the stratigraphy, Magnetitite Seam 21 (the uppermost seam) also records varying thicknesses ranging from cm-scale near Magnet Heights (Molyneux, 1974) to >25 m thicknesses with some instances as much as 60 m recorded at Roossenekal (Scoon & Mitchell, 2012). We interpret this lateral continuity of marker layers within the Upper Zone as an indication that both traverses initially had roughly the same thickness during the UUMZ magma recharge event and any subsequent thickening in the uppermost portion of the Roossenekal traverse is likely the result of a new magma pulse or assimilation affecting only the absolute last portions of the stratigraphy there.

Based on the geologic map of Molyneux (2008), the stratigraphic interval from the Pyroxenite Marker to the appearance of cumulus magnetite (start of the Upper Zone) is *c*. 521 m at Roossenekal and thus, assuming an original UZ thickness of 1,775 m as in the Leolo Mountain section of VanTongeren & Mathez (2013), the total magma thickness of the UUMZ from the Pyroxenite Marker to the roof at Roossenekal is 2,296 m. Based on thermodynamic modelling and mineral-melt partition coefficients, VanTongeren *et al.* (2010) estimated that the UUMZ had lost approximately 15-25% of its original volume

due to eruption. Including this missing evolved melt, the total original UUMZ magma layer thickness is between 2,640 – 2,870 m.

In the traverse studied here, at Roossenekal, the Zone of Magma Mixing containing both resident and new incoming magma, has a thickness of *c.* 270 m and is calculated as the thickness from the onset of mixing (i.e. the depth of the most evolved plagioclase An content below the Pyroxenite Marker) to the Pyroxenite Marker (Figs. 2, 5). The total magma thickness, including the Zone of Magma Mixing and the UUMZ in Roossenekal, is calculated to be 2,566 m (assuming 0 % magma loss), and between 2,910 – 3,140 m (assuming 15-25% loss).

5.3.3 Calculation of Total Stratigraphic Excursion

The total stratigraphic excursion caused by the new pulse of magma is calculated as the thickness from the onset of magma mixing below the Pyroxenite Marker to the level at which the An content in plagioclase returns to the composition prior to the onset of magma mixing (e.g. the most evolved sample below the Pyroxenite Marker (An 55)). The samples from this study do not progress into the Upper Zone and consequently the An values of plagioclase in this study do not return to the most evolved value below the Pyroxenite Marker of An 55. An approximation of the thickness of the stratigraphic excursion can be obtained using the average plagioclase An compositions measured by Harney *et al.* (1996) from a single borehole, drilled *c.* 2 km north of Roossenekal at Mapoch's Mine (Fig. 1) covering the lowermost *c.* 200 m of the Upper Zone (above cumulus magnetite) in Roossenekal. Average plagioclase core An compositions return to pre-mixing compositions *c.* 2,824 m above the Merensky Reef (Figs. 2, 5). The total

thickness from the Pyroxenite Marker until the return to pre-mixing compositions is 711 m, which when added to the Zone of Magma Mixing (270 m) yields a total excursion thickness of 981 m for the Roossenekal traverse (Figs. 2, 5). This is less than the 1200 m thick excursion to the north in the Leolo Mountain traverse calculated by VanTongeren & Mathez (2013).

All thicknesses cited above for the Roossenekal Traverse and the Leolo Mountain Traverse are summarized in Table 8. At Roossenekal, the proportion of incoming magma relative to the total is calculated to be between 38, 34 and 31% for the scenarios of 0, 15 and 25% loss of original UUMZ magma thickness (Table 8).

5.3.4 Resident, Incoming, and Mixed Magma Compositions

For a direct comparison of the resident and incoming magma compositions in the Zone of Magma Mixing from north to south, the equilibrium trace element liquid composition is calculated for each mineral phase of each sample. For ease of comparison, the equilibrium liquid compositions for the Roosenekal traverse are calculated using the same partition coefficients as described in VanTongeren & Mathez (2013) for the Leolo Traverse. Sr, Ba, Rb, Pb and LREE liquid compositions are calculated from plagioclase with the partition coefficients of Bindeman *et al.* (1998). REE liquid compositions are calculated from clinopyroxene with the partition coefficients of Wood and Blundy (1997). Sc, Y and HREE liquid compositions are calculated from orthopyroxene using partition coefficients of Bédard (2007). D_{Zr}^{opx} and D_{Cr}^{opx} regressions with measured orthopyroxene Mg# do not show strong correlations (Bédard, 2007). Therefore, as in VanTongeren & Mathez (2013), we use the constant D_{Cr}^{opx} = 11.5 of Barnes (1986)

derived for magmas at QFM and 1150 °C and the constant D_{Zr}^{opx} = 0.021 of Dunn and Sen (1994) calculated for similar orthopyroxene major element compositions. When necessary, a pressure of 200 MPa is assumed. As in VanTongeren & Mathez (2013), the plagioclase and low-Ca pyroxene equilibrium liquid composition is used whenever possible, as they are a more reliable indicator of the equilibrium liquid due to their higher modal abundance in the samples studied here.

Average crystallization temperatures are calculated for each sample using the REE-in-plagioclase-clinopyroxene thermometer developed by Sun & Liang (2017). The REE-in-plagioclase-clinopyroxene thermometer estimates the crystallization temperature of co-existing plagioclase and clinopyroxene. Through numerical simulations, Sun & Liang (2017) showed that the calculated crystallization temperatures are resistant to any artifacts from compositional zoning and diffusive resetting. The REE thermometer is potentially a significant improvement to An-based thermometers due to the variability in An content of plagioclase (Fig. 5b) as well as the large uncertainties of plagioclase crystallization temperatures in previous low-pressure experiments (e.g. Charlier & Grove, 2012). Although it is an improved method for estimating crystallization temperatures, it should also be noted that calculated crystallization temperatures for the Leolo Mountain traverse of VanTongeren & Mathez (2013) using the REE thermometer are in close agreement with the An-based thermometer used in VanTongeren & Mathez (see Fig. 9b in Sun & Liang, 2017).

The calculated equilibrium liquid and crystallization temperature for each sample is listed in Table 9.

Maximum crystallization temperatures near the level of the Pyroxenite Marker decrease from 1,181°C for the Leolo Mountain traverse to 1166°C for the Roossenekal traverse. Prior to the Zone of Magma Mixing, the crystallization temperature of the most evolved sample below the Pyroxenite Marker (analogous to resident magma) decreases from 1,105°C for the Leolo Mountain traverse to 1,075°C (Fig. 11)

The composition of the fully mixed magma (C_{UUMZ}) at Roossenekal is calculated from the average trace element equilibrium liquid composition of samples B14-018 and B14-016. Sample B14-018 (*c*. 35 m below the Pyroxenite Marker) records the highest calculated crystallization temperature (1,166 °C) above the onset of magma mixing as well as the highest Cr concentration in both low-Ca pyroxene and clinopyroxene. Although sample B14-016 is located *c*. 119 m above the Pyroxenite Marker, it also records a similarly high crystallization temperature of 1,162 °C as well as elevated Cr concentrations in low-Ca Pyroxene and clinopyroxene. More importantly, sample B14-016 records the maximum plagioclase An content. The calculated composition of the fully mixed magma (C_{UUMZ}) at Roossenekal (Table 10) is similar to that calculated for the Leolo Mountain traverse of VanTongeren & Mathez (2013) (Table 10).

The composition of the resident magma (C_{res}) is calculated from the most evolved sample (B14-021) below the onset of magma mixing, 270 m below the Pyroxenite Marker. The calculated resident magma compositions, prior to the Zone of Magma Mixing, are shown in Fig. 12a. Compositions of moderately incompatible trace elements, Sc, Sr are indistinguishable between the calculated resident magma compositions at Leolo and Roossenekal. Highly incompatible trace elements (Ba, Zr, LREE, MREE) however, are higher in the south and indicate a slightly more evolved resident magma in

the south. Notably, there are a few exceptions; the incompatible elements of Y, Er, Yb and Lu all show slightly lower concentrations at Roossenekal. The only trace element with a compatible bulk partition coefficient, Cr, is slightly lower in the south.

The composition of the incoming magma below the Pyroxenite Marker is calculated following a two-component mixing equation (VanTongeren & Mathez, 2013)

$$C_{UUMZ} = C_{res}X_{res} + C_{inc}X_{inc} \quad (1)$$

where X_{res} and X_{inc} are the proportions of resident and incoming magma, and C_{UUMZ}, C_{res}, and C_{inc} are the fully mixed UUMZ parent magma composition, and the composition of the resident and incoming magmas.

For Roossenekal, the range of calculated incoming magma compositions, as well as the mineral phase from which each element was calculated, is given in Table 10 along with the range of incoming magma compositions for the Leolo Mountain traverse (VanTongeren & Mathez, 2013), re-calculated using the REE-in-plagioclase-clinopyroxene thermometer described above (Sun & Liang, 2017). Rb is excluded in the calculations at Roossenekal due to high uncertainties in the measurement of low Rb concentrations.

The proportion of incoming magma calculated at Roossenekal is nearly identical to the proportion calculated *c.* 75 km to the north by VanTongeren & Mathez (2013) (Table 8). For the 0% loss of original UUMZ magma thickness scenario, the proportion of incoming magma decreases from 43% in the north at Leolo (VanTongeren & Mathez, 2013) to 38% at Roossenekal (Table 8).

Focusing on the 0% UUMZ magma loss scenario for simplicity, the composition of the incoming magma is similar between the two profiles, although there is a slight

enrichment in incompatible trace elements and depletion in compatible trace elements (e.g. Cr) from north to south (Table 10; Fig. 12b). The incoming magma calculated at Roossenekal also displays a prominent negative Eu (and Sr) anomaly possibly indicating potential fractional crystallization of the incoming magma from north to south, however, there is no significant change in the modal abundance of plagioclase for a given stratigraphic level between the Leolo Mountains and Roossenekal traverses.

6. Discussion

6.1 Lateral variations from trapped liquid?

Lundgaard, *et al*. (2006) investigated the lateral variations within the mid to lower Main Zone (below the injection of new magma) in the Eastern Limb and attributed decreases in pyroxene Mg# and increases in whole rock trace element compositions to be a product of increased trapped melt from north (near Thornhill; ~24°30.320', S 030°59.194' E) to south (near Stoffberg; ~25°31.060' S, 029°54.752' E) (Fig. 1). Our data from the lower Main Zone near Roossenekal and the Leolo Mountain Traverse also support the conclusion that there was a greater fraction of trapped liquid present in the South compared with the North (Fig. 13, a-e).

The trapped liquid shift, however, is not a factor in the lateral changes noted in this study over the Zone of Magma Mixing from Leolo to Roossenekal (Fig. 14, a-e). Within the Zone of Magma Mixing, a plot of whole rock Mg# versus incompatible whole rock trace element concentrations (P, Ba, Zr, Rb) shows no noticeable shift from the Leolo Mountain to Roossenekal traverse (Fig. 14, b-e). Orthopyroxene Mg# and plagioclase An content also appear to follow the same fractional crystallization trend

between the Leolo Mountain and Roossenekal traverses over the Zone of Magma Mixing (Fig. 14a), but are offset from one another in the Lower Main Zone samples (Fig. 13a). Thus, we are confident that all lateral changes observed between the two traverses within the Zone of Magma Mixing are a true representation of a changing incoming magma composition.

6.2 Lateral variability owing to structural upwarp?: the Cawthorn et al. (2016) model

Cawthorn *et al.* (2016) suggest that the vertical and lateral variations in plagioclase An content are controlled by the injection of new magma into a structural basin. In their scenario, the new primitive magma is denser than the resident magma and is injected just south of Magnet Heights, into a structural basin which encompasses the northern portion of the Eastern Limb from the Leolo Mountains to some distance between Magnet Heights and Roossenekal, where the upwarp begins [See Fig. 5 in Cawthorn *et al.* (2016)].

Evidence for a structural upwarp as described by Cawthorn *et al.* (2016) comes from map relationships just south of Roossenekal (Fig. 1) where the Critical Zone wedges out and the Main Zone is in contact with the floor rocks. In their model, the alleged structural upwarp would be controlled by floor rocks becoming ductile and developing into diapiric structures (e.g. Uken & Watkeys (1997)). While there is good evidence for basal diapirs and other structures affecting the lower parts of the intrusion elsewhere in the RLS, no such evidence exists in this area. An example is the pre-Bushveld Complex Schwerin anticlinal fold, located in the northeast portion of the eastern Bushveld Complex. Schwerin fold deformation also occurred during the accumulation of the Lower Zone, forming separate magma compartments, however its development was completed

before the magma addition forming the Critical Zone (Cameron, 1978, Sharpe, 1982; Hartzer, 1995; Uken & Watkeys, 1997; Longridge *et al.*, 2009). It is clear from map relationships that the fold separates the lower portion of the Lower Zone into separate compartments, with the stratigraphy in the area dipping away from the axial center of the fold. Above this part of the stratigraphy in the region, all other markers and contacts are regionally parallel to those above, including the roof contact.

In contrast to the evidence in support of basal diapirs in the Lower Zone in the north, no such evidence exists for the Upper Zone/Main Zone in the area of Roossenekal. Field and map evidence in the southern portion of the Eastern Limb shows remarkably planar layering in the UUMZ cumulates that make up the top of the magma chamber. Detailed mapping by Molyneux (2008) shows that the layering in the UUMZ of the Eastern Limb of the RLS is regionally parallel to the roof contact. In particular, throughout the proposed areas of basinal upwarp of Cawthorn *et al.* (2016) (e.g. profiles just south of Roossenekal and the single profile near Stoffberg), the upper magnetitite seam 21 is parallel to the roof contact. The Main Magnetitite seam is also mapped parallel to the roof contact through the area south of Roossenekal where Cawthorn *et al.* (2016) suggest the structural upwarp reaches its maximum. The Main Magnetitite seam is also mapped parallel to the roof contact when it reappears further south, near Stoffberg. The only observable exception is in a small area north and east of Loskop Dam, where Main Zone rocks directly abut the roof of the intrusion. These observations contradict the idea of having an upwarping basinal structure controlling the lateral variations within the UUMZ and Zone of Magma Mixing.

Instead, the presence of Main Zone rocks onlapping the floor of the intrusion near Stoffberg is more consistent with the gradual inflation and lateral expansion of the RLS magma chamber as a result of new volumetrically significant magma fluxes entering the crust associated with the Main Zone and Upper Zone. This alternative hypothesis is also consistent with the changing lithology of both roof and floor rocks from north to south in the Eastern Limb (e.g. VanTongeren & Mathez, 2015).

Another aspect of the Cawthorn et al. (2016) model is the requirement of a density stratified magma chamber. In their model, density differences constrain the incoming magma to the bottom of the chamber while limiting the mixing between the incoming and resident magma. Limited mixing between the two magmas at the bottom of the chamber would inevitably lead to a rapid increase of crystallization temperature as well as a return to pre-mixing (more radiogenic) initial $^{87}Sr/^{86}Sr$ values of the original resident magma, above the Zone of Magma Mixing. However, recorded crystallization temperatures show a gradual increase up to the Pyroxenite Marker and fully mixed magma (i.e. cessation of input of new primitive magma; Fig. 11) while initial whole rock $^{87}Sr/^{86}Sr$ values above the Pyroxenite Marker are relatively homogenous, both arguing against a density stratified magma chamber.

6.3 A new hypothesis for magma recharge and lateral variability in the Eastern Limb

The data presented here (Figs. 12a,b) show that both the resident and incoming magmas in the Roossenekal Traverse are slightly more evolved than those observed in the north along the Leolo Mountain Traverse of VanTongeren & Mathez (2013). In their study, VanTongeren & Mathez (2013) suggested that the gradual compositional reversal

throughout the Zone of Magma Mixing stratigraphy is due to repeated injection and mixing of small magma batches into a rapidly-mixed homogeneous magma chamber. The repeated injection of small magma batches allowed the magmas to mix while continuing to crystallize. Our data from the Roossenekal traverse support this hypothesis and allow us to additionally determine the directionality of magma emplacement.

We propose that new batches of primitive magma were periodically injected into the magma chamber near the Thabazimbi-Murchison Lineament (TML) as the magma chamber was inflated from north to south (Fig. 1). Our model is based on three observed differences between the Leolo Mountain Traverse in the North and the Roossenekal traverse in the South. (1) The calculated proportions of incoming versus resident magma decrease from 43% in the north for the Leolo Mountain traverse to 38% for the Roossenekal traverse, *c.* 75 km to the south (Table 8). (2) The slightly more evolved trace element composition of the resident magma towards the south at Roossenekal, accompanied by more evolved major element compositions towards the south below the Zone of Magma Mixing (Figs. 9, 12a). (3) The slightly more evolved trace element composition of the calculated incoming magma in the south relative to the north, as well as the shift to a more evolved plagioclase An content from north to south within the Zone of Magma Mixing (Figs. 9, 12b).

In our model (Fig. 15), as in that of VanTongeren & Mathez (2013), pulses of new primitive magma mix with resident magma, up to the immediate roof, while simultaneously crystallizing in between pulses. However, in our model, due to the directed injection of new primitive magma from the TML, the proportion of incoming magma mixing with resident magma decreases slightly towards the south. Each new

pulse of magma fully mixes with the resident magma in the north and gradually inflates the magma chamber by mixing over a progressively wider lateral area. During the initial recharge events, the proportion of new magma is small enough in volume that it remains dominantly in the north. However, as new pulses are added the amount of incoming magma increases and the mixed magma spreads into the resident magma in the south. The resident magma in the south thus has a longer period of time to undergo fractionation and hence the resident magma records slightly more evolved compositions prior to the onset of magma mixing in Roossenekal as compared with Leolo. In both Leolo and Roossenekal, fractional crystallization on the magma chamber floor likely proceeded *in situ* in a small (<4 m) thick mush layer (e.g. Holness *et al*,, 2017), such that mixing between the incoming magma and any previously formed crystals from the resident magma would only occur at a scale smaller than our sampling interval and would not be recorded in our dataset. Thus, the slightly more evolved compositions recorded in the resident magma at Roossenekal are a robust indicator of fractionation of the liquid prior to new magma input, and not simply a greater proportion of mixing with a resident magma.

Our directional recharge scenario is consistent with the muted and/or lack of reversal recorded in plagioclase An content much farther South, at Stoffberg (e.g. Cawthorn *et al*., 2016; Fig. 1), as this is where the proportion of new incoming magma would be predicted to be the least.

This scenario also explains why the incoming magma is slightly more evolved in the south. Incompatible trace element concentrations of the calculated incoming magma (C_{inc}) increase from north to south, while Cr concentrations decrease from 245 ppm to

181 ppm for the Leolo Mountain and Roossenekal traverses respectively. C_{inc} for Roossenekal shows a slightly more negative Eu anomaly (Eu/Eu* = 0.56) than the one recorded from the relatively flat REE profile of C_{inc} for the Leolo Mountain traverse of VanTongeren & Mathez (2013) (Eu/Eu* = 0.76; Fig 12b). Thus, if the incoming magma were a homogeneous composition, it must have experienced some degree of fractional crystallization in the north, prior to entering and mixing with the resident magma in the south.

Numerous authors have also postulated that the locus of magma injection in the Eastern Limb is near the TML [e.g. Kruger (2005); Clarke *et al.* (2009); VanTongeren & Mathez (2015)] (Fig. 1). On the basis of structural and compositional evidence, Clarke *et al.* (2009) concluded that a feeder dike used the existing TML to fill the RLS magma chamber, inflating the chamber away from the TML (i.e. north and south of the TML). Investigating the variability in the immediate roof and floor lithologies of the Bushveld Complex (Fig. 1), VanTongeren & Mathez (2015) presented a model in which the RLS was intruded as an enormous sill occupying varying structural depths (deeper in the north and shallower in the south), consistent with the locus of the magma injection originating in the north near the TML. Kruger (2005) similarly postulated that the Main Zone magmas were input into the magma chamber, just north of the TML, first interacting with the floor rocks to produce the Platreef, locking in higher initial $^{87}Sr/^{86}Sr$ ratios, before spreading south and mixing with the residual Critical Zone magma. In the model of Kruger (2005), incoming Main Zone magma spreads south and mixes with the residual Critical Zone magma, containing a lower initial $^{87}Sr/^{86}Sr$ ratio, to produce the average $^{87}Sr/^{86}Sr$ ratio in the Lower Main Zone of *c.* 0.7086.

6.4 Reliability of the pyroxene record?

As a final note, it is important to consider the reliability of the cumulate record when calculating magma compositions and inferring magma dynamics. For example, in their study, VanTongeren & Mathez (2013) observed the rapid increase in Cr contents of pyroxenes within the Zone of Magma Mixing up to the Pyroxenite Marker, followed by a rapid return to their pre-mixing values. They also noted that the Pyroxenite Marker exhibits a lower whole rock Sr isotopic composition than both the Main Zone and the UUMZ and hypothesized that the pyroxenes within the Zone of Magma Mixing may have been intruded within the incoming magma as crystal cargo. The pyroxene Cr contents within the Zone of Magma Mixing at Roossenekal, although overall lower, agree with the hypothesis of VanTongeren & Mathez (2013) that the pyroxenes were intruded as a crystal cargo.

At Roossenekal, both low-Ca pyroxene and clinopyroxene Cr contents show the same rapid increase to the Pyroxenite Marker and return to pre-mixing values (Fig. 4) as seen within the Leolo Mountain traverse. The calculated equilibrium liquid composition for Cr just below the Pyroxenite Marker is *c.* 59 ppm while just 400 m above, this value returns to *c.* 4 ppm. Simple Rayleigh fractional crystallization modelling indicates that this change in Cr composition would require *c.* 55% crystallization over the 400 m stratigraphic interval. Assuming 0% magma loss from the UUMZ, this 400 m interval only accounts for *c.* 17% of the UUMZ stratigraphy and therefore it is unlikely that fractional crystallization can account for reversal of pyroxene Cr compositions and their rapid return to pre-mixing values.

As mentioned above, below the Zone of Magma Mixing the Mg# of low-Ca pyroxene and clinopyroxene decreases considerably from north to south (Fig. 9). In the lower Main Zone, Lundgaard *et al*. (2006) attributed this decrease to an increased fraction of trapped liquid resetting the relatively fast-diffusive Fe-Mg cations. As shown above, however, this explanation does not apply to the cumulates within the Zone of Magma Mixing, were the two profiles reach similar Mg#s at similar stratigraphic intervals for both low-Ca pyroxene and clinopyroxene. Instead, an alternative explanation for the reversal in major element compositions of pyroxene within the Zone of Magma Mixing incorporates low-Ca pyroxene and clinopyroxene as a crystal cargo within the incoming magma at the level of the Pyroxenite Marker. If the pyroxene major element compositions were a product of incoming magma mixing with resident magma, one would expect a similar offset in pyroxene Mg# between the two profiles throughout the Zone of Magma Mixing. Rather, it is likely that some fraction of the pyroxenes were intruded as crystal cargo within the new incoming magma. This model is supported by the observation by Roelofse & Ashwal (2012) of isotopic disequilibrium between coexisting plagioclase and pyroxene within the lower Main Zone of the Northern Limb.

If a portion of the pyroxenes found in the Zone of Magma Mixing cumulates were entrained as a crystal cargo with the incoming magma, then the proposal of Cawthorn *et al*. (1991) that the incoming magma was denser than the resident magma must also be in question. The high Al_2O_3 of pyroxenes near the Pyroxenite Marker, as discussed in Cawthorn *et al*. (1991) as a signature of high density liquid, would instead be explained by a higher pressure crystallization (e.g. Wood, 1974) as would be likely from a deeper staging chamber.

The intrusion of pyroxenes as a crystal cargo within the Zone of Magma Mixing inevitably leads to a questioning of the REE-in-plagioclase-clinopyroxene thermometer developed by Sun & Liang (2017). A fundamental assumption of the thermometer is that clinopyroxene and plagioclase were co-crystallized from the same parental magma, thus recording accurate crystallization temperatures of plagioclase. Sun & Liang (2017) conducted experiments testing the effectiveness of the thermometer in these types of situations by pairing plagioclase grains with random clinopyroxene grains that crystallized at various portions of a fractional crystallization sequence. Sun & Liang (2017) found that if the mineral pairs were both crystallized within a relative 10% crystallization sequence, this would ensure a discrepancy of <10°C discrepancy between REE-in-plagioclase-clinopyroxene calculated temperatures versus temperatures calculated via plagioclase An content only. Sun & Liang (2017) tested the REE thermometer on 19 samples from the Leolo Mountain traverse and compared the results with the An-based thermometer used by VanTongeren & Mathez (2013). VanTongeren & Mathez (2013) calculated crystallization temperatures assuming plagioclase of An_{75} crystallized at 1150°C and applied a slope of 6.8°C/An from MELTS modelling (Ghiorso & Sack, 1995; VanTongeren *et al.*, 2010). Based on new MELTS modelling, Sun & Liang (2017) updated the liquidus temperature of these samples to 1200°C and re-calculated the crystallization temperatures for the Leolo Mountain traverse using the An-based thermometer. The authors note that there are REE patterns for the RLS gabbros that indicate plagioclase and clinopyroxene may have crystallized at different times, however the REE calculated temperatures match closely with the An-based thermometer,

demonstrating that the REE-in-plagioclase and clinopyroxene thermometer is providing reasonable plagioclase crystallization temperatures for the RLS Main Zone samples.

7. Conclusions

We present new data, using both major and trace element compositions of all mineral phases, investigating the lateral variations associated with the replenishment of the Rustenburg Layered Suite at the level of the Pyroxenite Marker. The proportion of incoming versus resident magma below the Pyroxenite Marker decreases from north (Leolo) to south (Roossenekal). Crystallization temperatures recorded before magma addition, as well as near the Pyroxenite Marker, decrease from north to south. The calculated incoming magma composition at Roossenekal is elevated in incompatible element concentrations and depleted in compatible elements when compared to the incoming magma composition in the northern part of the Eastern Limb at Leolo, while also exhibiting a more prominent negative Eu anomaly. Reconstruction of the stratigraphic profile at Roossenekal using a shallow dip of 10° indicates that the input of new primitive magma as well as the formation of the Pyroxenite Marker occur at approximately the same depth between the two profiles, suggesting that a structural basin [e.g. Cawthorn *et al.* (2016)] is not necessary to explain the lateral variations.

We conclude that new batches of primitive magma were periodically injected into the magma chamber and that the locus of magma injection in the Eastern Limb is near the Thabazimbi-Murchison Lineament. The multiple small batches of new magma contained a pyroxene crystal cargo and mixed rapidly with the resident magma while simultaneously crystallizing between pulses. The lateral variations are caused by a

slightly enriched resident magma from north to south, a decrease in proportion of incoming magma from north to south, and an incoming magma that is undergoing fractional crystallization.

Lateral variations ought to be considered in studies of the RLS and layered mafic intrusions in general. It is conceivable, as demonstrated here, that the directed input during magma recharge events can produce varying geochemical signatures observed over lateral distances at the same stratigraphic interval, potentially obfuscating the real magma chamber processes.

8. References

Ashwal, L. D., Webb, S. J., Knoper, M. W. (2005). Magmatic stratigraphy in the Bushveld Northern Lobe: continuous geophysical and mineralogical data from the 2950 m Bellevue drillcore. *South African Journal of Geology* **108**, 199-232.

Barnes, S. J. (1986). The distribution of chromium among orthopyroxene, spinel and silicate liquid at atmospheric pressure. *Geochimica et Cosmochimica Acta* **50**, 1889-1909.

Bédard, J. (2007). Trace element partitioning coefficients between silicate melts and orthopyroxene: parameterizations of D variations. *Chemical Geology* **244**, 263-303.

Bindeman, I. N., Davis, A. M., Drake, M. J. (1998). Ion microprobe study of plagioclase-basalt partition experiments at natural concentration levels of trace elements. *Geochimica et Cosmochimica Acta* **62**, 1175-1193.

Buick, I. S., Maas, R., Gibson, R. (2001). Precise U–Pb titanite age constraints on the emplacement of the Bushveld Complex, South Africa. *Journal of the Geological Society* **158**, 3-6.

Cameron, E. N. (1978). The lower zone of the eastern Bushveld Complex in the Olifants River trough. *Journal of Petrology* **19**, 437-462.

Cawthorn, R. & Webb, S. (2001). Connectivity between the western and eastern limbs of the Bushveld Complex. *Tectonophysics* **330**, 195-209.

Cawthorn, R. G. (2007). Cr and Sr: Keys to parental magmas and processes in the Bushveld Complex, South Africa. *Lithos* **95**, 381-398.

Cawthorn, R. G., Lundgaard, K. L., Tegner, C., Wilson, J. R. (2016). Lateral variations in plagioclase compositions, Main Zone, Bushveld Complex, South Africa: Evidence for slow mixing of magmas in basinal structures. *Mineralogical Magazine* **80**, 213-225.

Cawthorn, R. G., Meyer, P. S., Kruger, F. J. (1991). Major addition of magma at the Pyroxenite Marker in the western Bushveld Complex, South Africa. *Journal of Petrology* **32**, 739-763.

Cawthorn, R. G. & Walraven, F. (1998). Emplacement and crystallization time for the Bushveld Complex. *Journal of Petrology* **39**, 1669-1687.

Charlier, B. & Grove, T. L. (2012). Experiments on liquid immiscibility along tholeiitic liquid lines of descent. *Contributions to Mineralogy and Petrology*, **164**, 27-44.

Cherniak, D. (2003). Silicon self-diffusion in single-crystal natural quartz and feldspar. *Earth and Planetary Science Letters* **214**, 655-668.

Clarke, B., Uken, R., Reinhardt, J. (2009). Structural and compositional constraints on the emplacement of the Bushveld Complex, South Africa. *Lithos* **111**, 21-36.

Clarke, B. M., Uken, R., Watkeys, M. K., Reinhardt, J. (2005). Folding of the Rustenburg layered suite adjacent to the Steelpoort pericline: implications for syn-Bushveld tectonism in the eastern Bushveld Complex. *South African Journal of Geology* **108**, 397-412.

Coombs, D. (1963). Trends and affinities of basaltic magmas and pyroxenes as illustrated on the diopside-olivine-silica diagram. *Min Soc Am Spec Pap* **1**, 227-250.

Dunn, T. & Sen, C. (1994). Mineral/matrix partition coefficients for orthopyroxene, plagioclase, and olivine in basaltic to andesitic systems: a combined analytical and experimental study. *Geochimica et Cosmochimica Acta* **58**, 717-733.

Eales, H. (2002). Caveats in defining the magmas parental to the mafic rocks of the Bushveld Complex, and the manner of their emplacement: review and commentary. *Mineralogical Magazine* **66**, 815-832.

Eriksson, P. & Altermann, W. (1998). An overview of the geology of the Transvaal Supergroup dolomites (South Africa). *Environmental geology* **36**, 179-188.

Ghiorso, M. S. & Sack, R. O. (1995). Chemical mass transfer in magmatic processes IV. A revised and internally consistent thermodynamic model for the interpolation and extrapolation of liquid-solid equilibria in magmatic systems at elevated

temperatures and pressures. *Contributions to Mineralogy and Petrology* **119**, 197-212.

Groeneveld, D. (1970). The structural features and the petrography of the Bushveld Complex in the vicinity of Stoffberg, Eastern Transvaal. *Special Publication of the Geological Society of South Africa* **1**, 36-45.

Harney, D., Von Gruenewaldt, G., Merkle, R. (1996). The use of plagioclase composition as an indicator of magmatic processes in the Upper Zone of the Bushveld Complex. *Mineralogy and Petrology* **56**, 91-103.

Hartzer, F. (1995). Transvaal Supergroup inliers: geology, tectonic development and relationship with the Bushveld Complex, South Africa. *Journal of African Earth Sciences* **21**, 521-547.

Klemm, D., Ketterer, S., Reichhardt, F., Steindl, J., Weber-Diefenbach, K. (1985). Implication of vertical and lateral compositional variations across the pyroxene marker and its associated rocks in the upper part of the Main Zone in the eastern Bushveld Complex. *Economic Geology* **80**, 1007-1015.

Kruger, F. (1991). Author's reply to discussion on The stratigraphy of the Bushveld Complex; a reappraisal and the relocation of the Main Zone boundaries. *South African Journal of Geology* **94**, 187-190.

Kruger, F. (1994). The Sr-isotopic stratigraphy of the western Bushveld Complex. *South African Journal of Geology* **97**, 393-398.

Kruger, F., Cawthorn, R., Walsh, K. (1987). Strontium isotopic evidence against magma addition in the Upper Zone of the Bushveld Complex. *Earth and Planetary Science Letters* **84**, 51-58.

Kruger, F. J. (1990). The stratigraphy of the Bushveld Complex: a reappraisal and the relocation of the Main Zone boundaries. *South African Journal of Geology* **93**, 376-381.

Kruger, F. J. (2005). Filling the Bushveld Complex magma chamber: lateral expansion, roof and floor interaction, magmatic unconformities, and the formation of giant chromitite, PGE and Ti-V-magnetitite deposits. *Mineralium Deposita* **40**, 451-472.

Longridge, L., Gibson, R. L., Nex, P. A. (2009). Structural controls on melt segregation and migration related to the formation of the diapiric Schwerin Fold in the contact aureole of the Bushveld Complex, South Africa. *Earth and Environmental Science Transactions of the Royal Society of Edinburgh* **100**, 61-76.

Lundgaard, K. L., Tegner, C., Cawthorn, R. G., Kruger, F. J., Wilson, J. R. (2006). Trapped intercumulus liquid in the Main Zone of eastern Bushveld Complex, South Africa. *Contributions to Mineralogy and Petrology* **151**, 352-369.

McDonough, W. F. & Sun, S.-S. (1995). The composition of the Earth. *Chemical Geology* **120**, 223-253.

Mitchell, A. (1990). The stratigraphy, petrography and mineralogy of the Main Zone of the northwestern Bushveld Complex. *South African Journal of Geology* **93**, 818-831.

Mitchell, A. & Scoon, R. (1991). Discussion on The stratigraphy of the Bushveld Complex; a reappraisal and the relocation of the Main Zone boundaries. *South African Journal of Geology* **94**, 183-187.

Molyneux, T. (1974). A geological investigation of the Bushveld Complex in Sekhukhuneland and part of the Steelpoort valley. *South African Journal of Geology* **77**, 329-338.

Molyneux, T. (2008). *Compilation on a scale of 1: 50000 of the geology of the eastern compartment of the Bushveld Complex. Special Publication 1 of the Johannes Willemse Bushveld Intelligence Centre. Pretoria: Department of Geology, University of Pretoria*.

Morse, S. (1984). Cation diffusion in plagioclase feldspar. *Science* **225**, 504-505.

Mungall, J. E., Kamo, S. L., McQuade, S. (2016). U-Pb geochronology documentsout-of-sequence emplacement of ultramafic layers in the Bushveld Igneous Complex of South Africa. *Nature Communications* **7**, 13385.

Nex, P., Cawthorn, R., Kinnaird, J. (2002). Geochemical effects of magma addition: compositional reversals and decoupling of trends in the Main Zone of the western Bushveld Complex. *Mineralogical Magazine* **66**, 833-856.

Nomade, S., Renne, P. R., Merkle, R. K. (2004). 40Ar/39Ar age constraints on ore deposition and cooling of the Bushveld Complex, South Africa. *Journal of the Geological Society* **161**, 411-420.

Olsson, J., Söderlund, U., Klausen, M., Ernst, R. (2010). U–Pb baddeleyite ages linking major Archean dyke swarms to volcanic-rift forming events in the Kaapvaal craton (South Africa), and a precise age for the Bushveld Complex. *Precambrian Research* **183**, 490-500.

Roelofse, F. & Ashwal, L. D. (2012). The Lower Main Zone in the Northern Limb of the Bushveld Complex—a> 1· 3 km thick sequence of intruded and variably contaminated crystal mushes. *Journal of Petrology* **53**, 1449-1476.

SACS. (1980). *Lithostratigraphy of the Republic of South Africa, South West Africa/Namibia and the Republic of Botswana, Transkei, and Venda. South African Geological Survey Handbook* **8**, 690.

Scoates, J. S. & Friedman, R. M. (2008). Precise age of the platiniferous Merensky Reef, Bushveld Complex, South Africa, by the U-Pb zircon chemical abrasion ID-TIMS technique. *Economic Geology* **103**, 465-471.

Scoates, J. S. & Wall, C. J. (2015). Geochronology of layered intrusions. *Layered Intrusions*: Springer, 3-74.

Scoon, R. & Mitchell, A. (2012). The Upper Zone of the Bushveld Complex at Roossenekal, South Africa: geochemical stratigraphy and evidence of multiple episodes of magma replenishment. *South African Journal of Geology* **115**, 515-534.

Sharpe, B. (1982). Structures in Transvaal Sequence rocks within and adjacent to the eastern Bushveld Complex. *South African Journal of Geology* **85**, 29-41.

Sharpe, M. R. (1985). Strontium isotope evidence for preserved density stratification in the main zone of the Bushveld Complex, South Africa. *Nature* **316**, 119-126.

Sun, C. & Liang, Y. (2017). A REE-in-plagioclase–clinopyroxene thermometer for crustal rocks. *Contributions to Mineralogy and Petrology* **172**, 24.

Sun, S.-S. & McDonough, W.-s. (1989). Chemical and isotopic systematics of oceanic basalts: implications for mantle composition and processes. *Geological Society, London, Special Publications* **42**, 313-345.

Tanner, D., Mavrogenes, J. A., Arculus, R. J., Jenner, F. E. (2014). Trace element stratigraphy of the Bellevue Core, Northern Bushveld: multiple magma injections obscured by diffusive processes. *Journal of Petrology* **55**, 859-882.

Uken, R. & Watkeys, M. K. (1997). Diapirism initiated by the Bushveld complex, South Africa. *Geology* **25**, 723-726.

VanTongeren, J. A. (2018). Mixing and Unmixing in the Bushveld Complex Magma Chamber. *Processes and Ore Deposits of Ultramafic-Mafic Magmas through Space and Time*, 113-138.

VanTongeren, J. & Mathez, E. (2013). Incoming magma composition and style of recharge below the pyroxenite marker, eastern Bushveld complex, South Africa. *Journal of Petrology* **54**, 1585-1605.

VanTongeren, J. & Mathez, E. (2015). On the relationship between the Bushveld Complex and its felsic roof rocks, part 2: the immediate roof. *Contributions to Mineralogy and Petrology* **170**, 56.

VanTongeren, J. A., Mathez, E. A., Kelemen, P. B. (2010). A felsic end to Bushveld differentiation. *Journal of Petrology* **51**, 1891-1912.

von Gruenewaldt, G. (1973). The main and upper zones of the Bushveld Complex in the Roossenekal area, eastern Transvaal. *Transactions of the Geological Society of South Africa* **76**, 207-227.

Webb, S. J., Cawthorn, R. G., Nguuri, T., James, D. (2004). Gravity modeling of Bushveld Complex connectivity supported by Southern African seismic experiment results. *South African Journal of Geology* **107**, 207-218.

Wood, B. J. & Blundy, J. D. (1997). A predictive model for rare earth element partitioning between clinopyroxene and anhydrous silicate melt. *Contributions to Mineralogy and Petrology* **129**, 166-181.

Zeh, A., Ovtcharova, M., Wilson, A. H., Schaltegger, U. (2015). The Bushveld Complex was emplaced and cooled in less than one million years–results of zirconology, and geotectonic implications. *Earth and Planetary Science Letters* **418**, 103-114.

Figure Captions

Figure 1

(a) Generalized map of the Bushveld Complex and the predominately mafic and ultramafic Rustenburg Layered Suite (RLS) showing the approximate location of the Thabazimbi Murchison Lineament (TLM), the likely locus point for magma injection below the Pyroxenite Marker. (b) Geologic map of the eastern Bushveld Complex adapted from VanTongeren & Mathez (2015). Solid black lines indicate the two traverses which are the focus on this study. (c) Generalized stratigraphic column of the Rustenburg Layered Suite of the Eastern limb of the Bushveld Complex adapted from VanTongeren *et al.* (2010). Main Zone and UUMZ thicknesses at Roossenekal are discussed in the text, while thicknesses for the Critical and Lower Zones are estimates from Molyneux (2008).

Figure 2

Illustration of the mixing interval below the Pyroxenite Marker, adapted from VanTongeren & Mathez (2013). Stratigraphic thicknesses are for the Roossenekal traverse and discussed in the text. Grey dashed line through the stratigraphy shows general change in plagioclase An content and pyroxene Mg# through the stratigraphy.

Figure 3

(a) Snapshot of sample locations (black circles) for the Roossenekal traverse, from Google Earth, overlain with adapted geologic map of Molyneux (2008). Below, elevation profile of the Roossenekal traverse, perpendicular to strike, with the sample locations and other markers noted. Note slightly different scale in Google Earth image.

Vertical exaggeration is 10. Horizontal distance (0) is the mapped Upper Zone/Main Zone boundary based on appearance of cumulus magnetite. Image and elevation from Google Earth. (b) Constructed stratigraphic column on the Main Zone within the Eastern Limb at Roossenekal using a dip angle of 10°.

Figure 4

Average Cr concentrations measured in cores of low-Ca pyroxene (open triangles) and clinopyroxene (open diamonds) throughout the entire Roossekenal traverse. Error bars denote 1σ standard deviation of the average Cr concentration for each sample. Dashed line denotes the level of the Pyroxenite Marker (PM). Shaded region is graphic representation of the Zone of Magma Mixing from Table 8, Fig. 2. Data from Table 7.

Figure 5

(a) Average plagioclase An content (closed circles) and pyroxene Mg # (clinopyroxene – open diamonds; low-Ca pyroxene – open triangles) for the Roossenekal traverse, plotted against stratigraphic height (m above the Merensky Reef). Error bars denote 1σ standard deviation of the average major element composition for each sample. Record of plagioclase An content is extended (open circles) using data from Harney *et al.* (1996). Dashed line denotes the level of the Pyroxenite Marker. Shaded region is graphic representation of the Zone of Magma Mixing from Table 8, Fig. 2. (b) Entire dataset of single plagioclase analyses. (c) Entire dataset of single low-Ca pyroxene and clinopyroxene analyses.

Figure 6

Select trace element concentrations, for which equilibrium liquid compositions are calculated, measured in cores of (a) plagioclase and (b) low-Ca pyroxene. Error bars denote 1σ standard deviation of the average trace element composition for each sample. Dashed line denotes the level of the Pyroxenite Marker (PM). Shaded region is graphic representation of the Zone of Magma Mixing from Table 8, Fig. 2. Data from Table 7. Note varying scale on x-axis.

Figure 7

REE compositions from each mineral phase for each sample throughout the Roossenekal traverse. Samples are normalized to primitive mantle values of Sun & McDonough (1989). Dashed black line with open squares represents the most evolved sample below the Zone of Magma Mixing (B14-021). Solid black line with open circles represents samples that are within the Zone of Magma Mixing. Dashed black line with open triangles represents samples above the Zone of Magma Mixing. All grey lines denote samples below the mixing interval. Data from Table 7.

Figure 8

Representative photomicrographs of samples from the Roossenekal traverse. Samples shown are from the base of the Zone of Magma Mixing (the most evolved sample) (g-i), within the Zone of Magma Mixing (d-f) and above the Zone of Magma Mixing (a-c). The first two photomicrographs show internal textures of mineral phases as well as spots from laser ablation analyses (note larger spots for plagioclase and smaller spots for pyroxene).

In general, laser ablation analyses were conducted at the center of individual grains while microprobe analyses were conducted immediately adjacent to laser ablation spots.

Figure 9

Comparison of *in-situ* major element compositions between the Roossenekal and Leolo traverses. The grey profile for each mineral phase represents the northern Leolo traverse and the black profile represents the southern Roossenekal. The grey and black horizontal dashed lines represent the level of the Pyroxenite Marker for the Leolo and Roosenekal traverses, respectively. (a) Measured average An content of plagioclase cores. (b) Measured average Mg# of low-Ca pyroxene cores. (c) Measured average Mg# of clinopyroxene cores.

Figure 10

Stratigraphic comparison of the UUMZ interval for both the combined Leolo/Magnet Heights and Roossenekal areas. Y-axis is height (m) above the Pyroxenite Marker. Stratigraphic thicknesses for the Roosenekal Traverse in the Main Zone are from this study and in the Upper Zone from Scoon & Mitchell (2012). Stratigraphic thicknesses for the Leolo Mountain Traverse are from Molyneux (1974). Red numerals denote magnetitite seams that are traceable throughout the Eastern limb of the RLS.

Figure 11

Stratigraphic comparison of calculated crystallization temperatures for the Roossenkal (solid black circles) and Leolo (open grey circles) traverses plotted versus stratigraphic

height (m above the Merensky Reef). Temperatures are estimates of the co-crystallization temperatures (or equilibrium temperatures) of plagioclase and clinopyroxene, See text for full discussion. Temperatures for the Leolo traverse are from Sun & Liang (2017). Uncertainties are 1σ.

Figure 12

Comparison of calculated resident and incoming magma compositions, assuming a 0% magma loss scenario, normalized to primitive mantle values of Sun and McDonough (1989) between the Leolo and Roossenekal traverses. Primitive mantle values for Sc from McDonough & Sun (1995). (a) Resident magma compositions. Leolo resident magma composition from VanTongeren & Mathez (2013). (b) Incoming magma compositions. Leolo incoming magma composition recalculated from VanTongeren & Mathez (2013) using the updated crystallization temperatures of Sun & Liang (2017). Data from Table 10.

Figure 13

(a) Average plagioclase core An content versus average low-Ca pyroxene core Mg#. (b-e) Whole rock Mg# versus select whole rock incompatible trace element concentration (P, Ba, Zr, Rb) for both the Leolo Mountain and Roossenekal traverses. Only samples from below the Zone of Magma Mixing are shown. The offset between the two traverses supports the conclusion of Lundgaard *et al*. (2006) of a slight increase in the trapped liquid fraction within the lower Main Zone from north (Leolo) to south (Roossenekal).

Figure 14

(a) Average plagioclase core An content versus average low-Ca pyroxene core Mg#. (b-e) Whole rock Mg# versus select incompatible trace element concentrations (P, Ba, Zr, Rb) for both the Leolo Mountain and Roossenekal traverses. Only samples within, and immediately above, the Zone of Magma Mixing are shown. There is no noticeable difference between two traverses above the input of new primitive magma, suggesting no increase in trapped liquid fraction within these samples from north (Leolo) to south (Roossenekal).

Figure 15

Schematic illustration depicting the new emplacement model of the UUMZ. Dotted texture represents the cumulate pile. At t_0, new primitive magma is injected (represented by darker shading) in the northern part of the Eastern limb and becomes fully mixed to the roof. The resident magma (represented by lighter shading), at the time of input, is crystallizing plagioclase of higher An content at higher temperatures in the north. Crystallization front at chamber floor is evolving by *in situ* crystallization of a <4 m thick mush layer (e.g. Holness *et al.*, 2017). At t_1, incoming pulses of new primitive magma continue from the north while the mixed magma spreads to the south, with lower proportions of incoming versus resident magma from north to south. The resident magma at t_1 has more time to fractionate and crystallize which, combined with changing proportions of incoming magma, is reflected in the lateral changes in plagioclase An content and crystallization temperature. At t_2, magma replenishment ceases and the mixed magma has spread completely to the south, with decreasing proportions of

incoming versus resident magma. Again, the resident magma in the south has had more time to fractionate and crystallize, resulting in lower plagioclase An content, crystallization temperatures and the more negative Eu anomaly recorded in the incoming magma composition at Roossenekal.

Figure 1

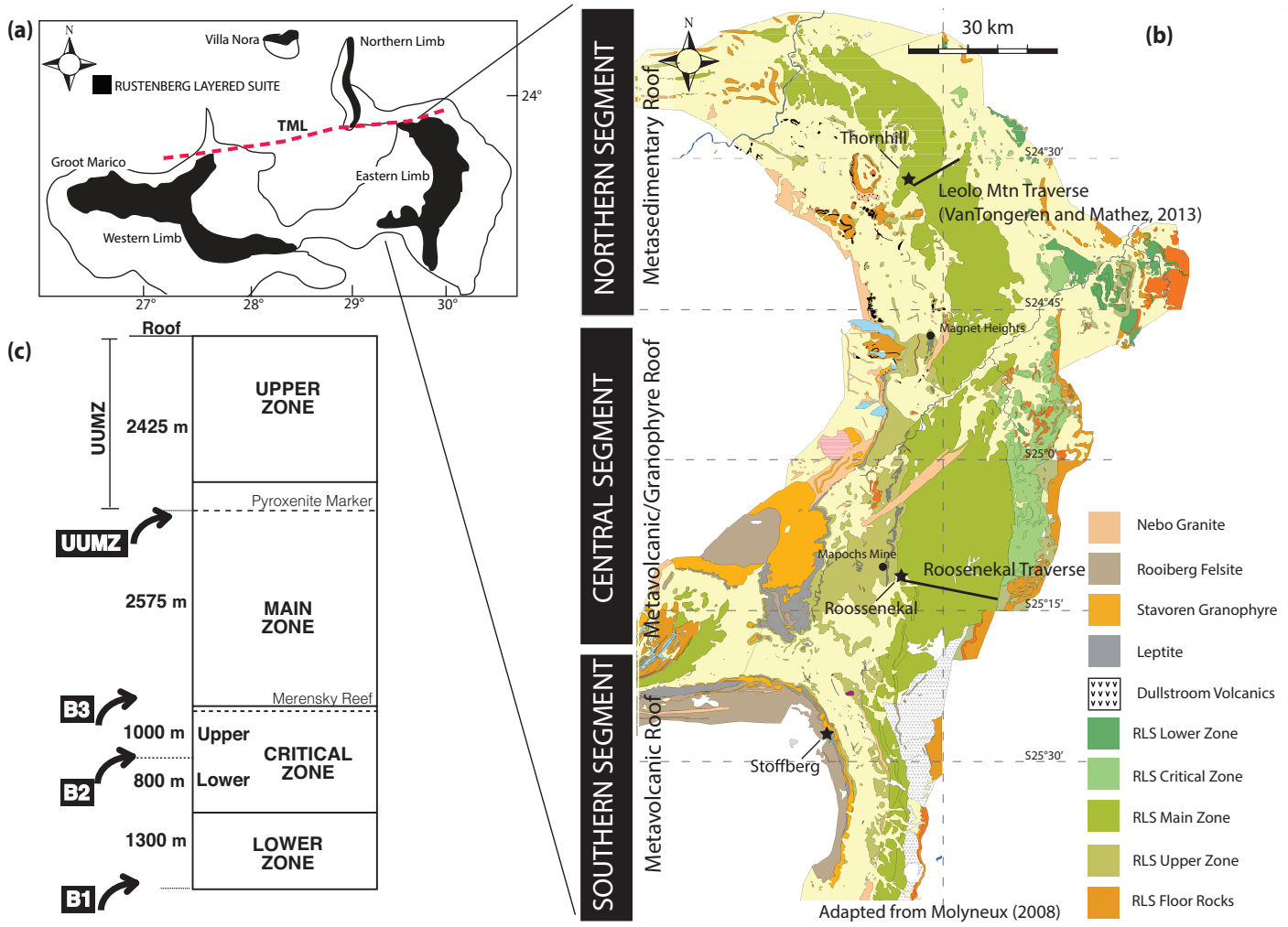
(a)
N
Villa Nora
Northern Limb
RUSTENBERG LAYERED SUITE
24°
TML
Groot Marico
Eastern Limb
Western Limb
27°
28°
29°
30°
(c)
Roof
UUMZ
2425 m
UPPER ZONE
Pyroxenite Marker
UUMZ
2575 m
MAIN ZONE
Merensky Reef
B3
1000 m
Upper
CRITICAL ZONE
B2
800 m
Lower
1300 m
LOWER ZONE
B1
NORTHERN SEGMENT
Metasedimentary Roof
CENTRAL SEGMENT
Metavolcanic/Granophyre Roof
SOUTHERN SEGMENT
Metavolcanic Roof
N
30 km
(b)
Thornhill
S24°30′
Leolo Mtn Traverse
(VanTongeren and Mathez, 2013)
S24°45′
Magnet Heights
S25°0′
Mapochs Mine
Roosenekal Traverse
Roossenekal
S25°15′
Stoffberg
S25°30′
Nebo Granite
Rooiberg Felsite
Stavoren Granophyre
Leptite
Dullstroom Volcanics
RLS Lower Zone
RLS Critical Zone
RLS Main Zone
RLS Upper Zone
RLS Floor Rocks
Adapted from Molyneux (2008)

Figure 2

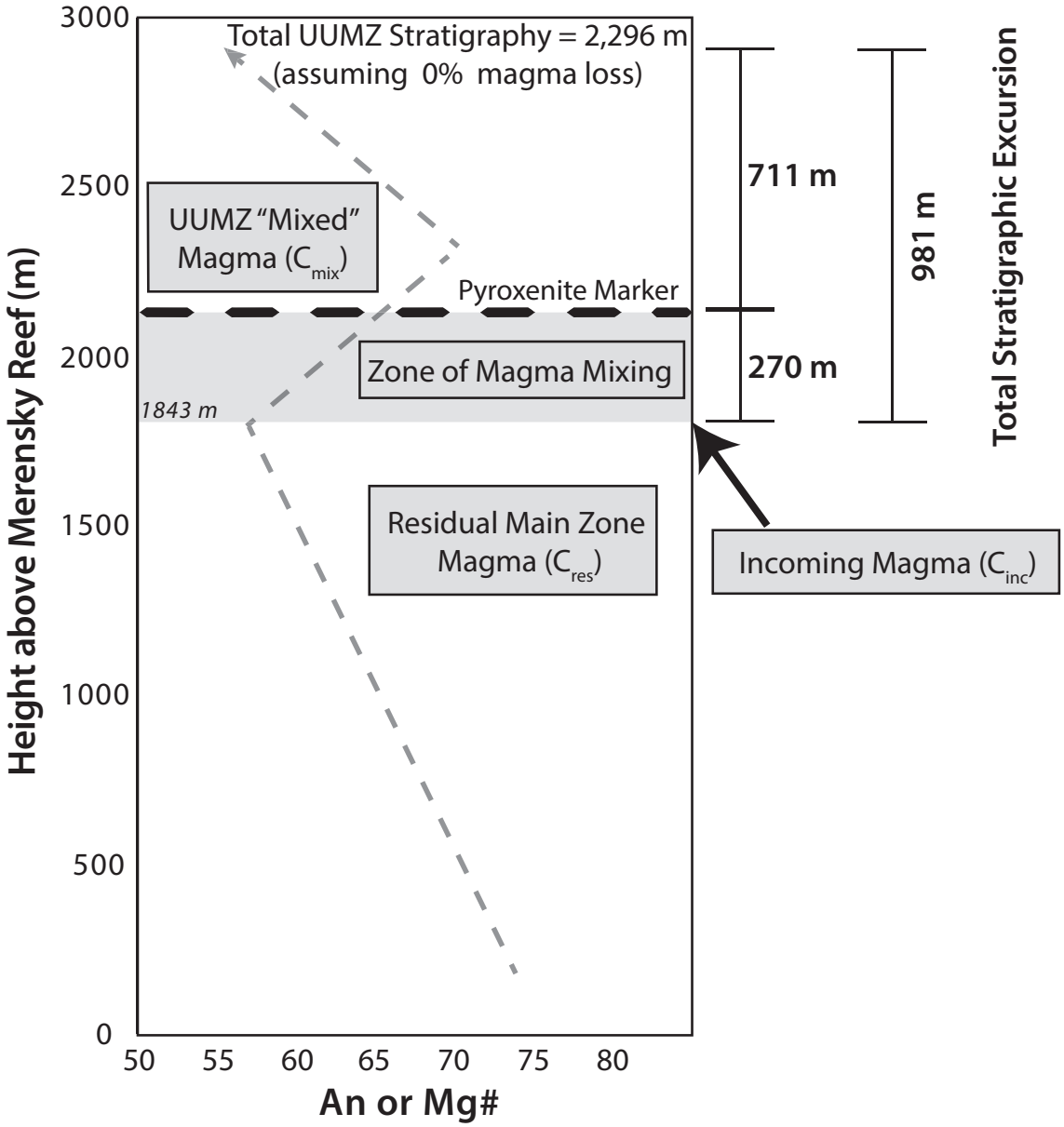
Total UUMZ Stratigraphy = 2,296 m
(assuming 0% magma loss)
UUMZ "Mixed" Magma (C_{mix})
Pyroxenite Marker
Zone of Magma Mixing
1843 m
Residual Main Zone Magma (C_{res})
Incoming Magma (C_{inc})
711 m
270 m
981 m
Total Stratigraphic Excursion
Height above Merensky Reef (m)
3000
2500
2000
1500
1000
500
0
50
55
60
65
70
75
80
An or Mg#

Figure 3

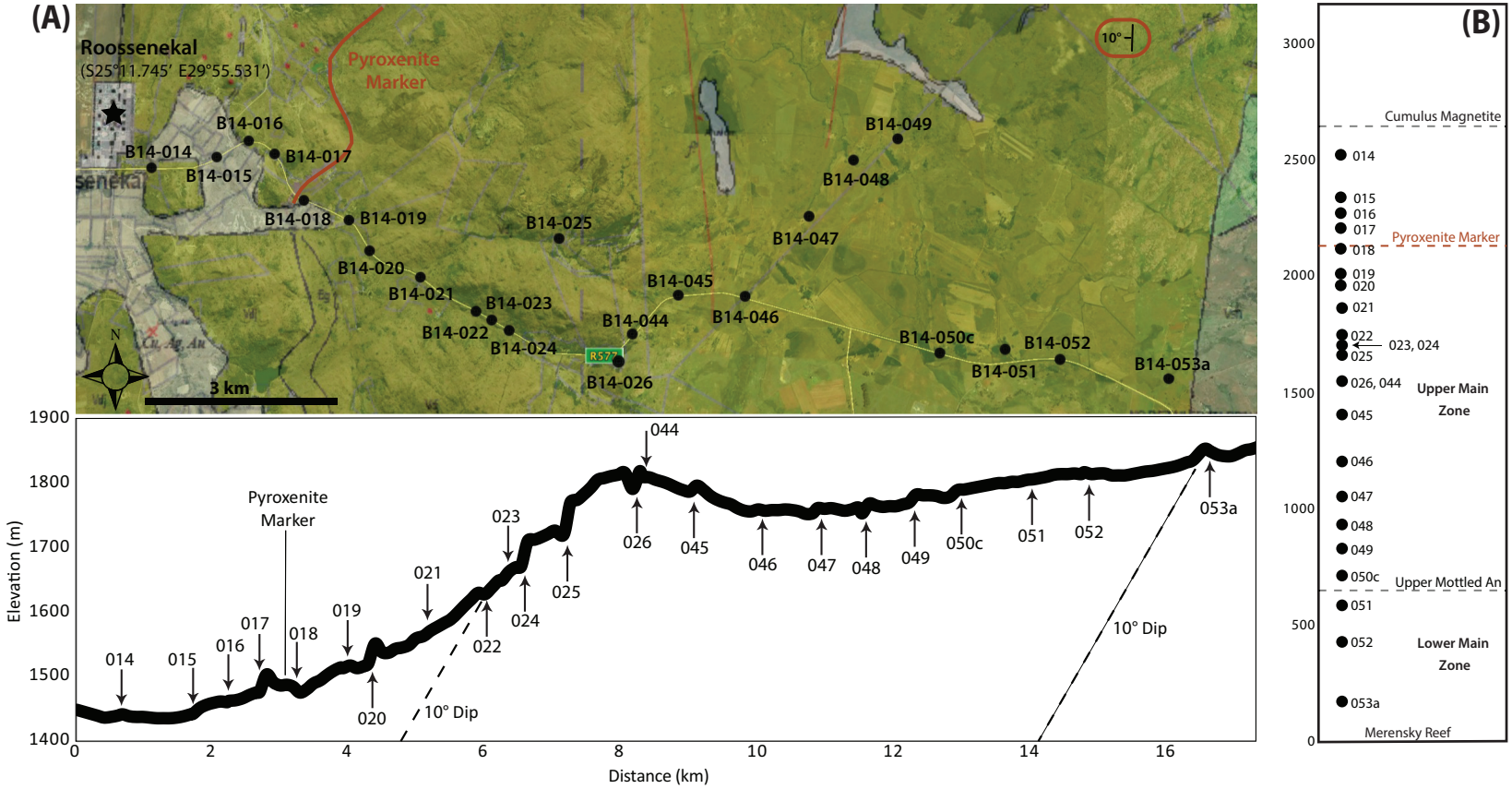
(A)
Roossenekal
(S25°11.745′ E29°55.531′)
Pyroxenite Marker
B14-014
B14-015
B14-016
B14-017
B14-018
B14-019
B14-020
B14-021
B14-022
B14-023
B14-024
B14-025
B14-026
B14-044
B14-045
B14-046
B14-047
B14-048
B14-049
B14-050c
B14-051
B14-052
B14-053a
R577
3 km
N
10°
Elevation (m)
Distance (km)
Pyroxenite Marker
10° Dip
(B)
Cumulus Magnetite
Pyroxenite Marker
Upper Main Zone
Upper Mottled An
Lower Main Zone
Merensky Reef
023, 024
026, 044

Figure 4

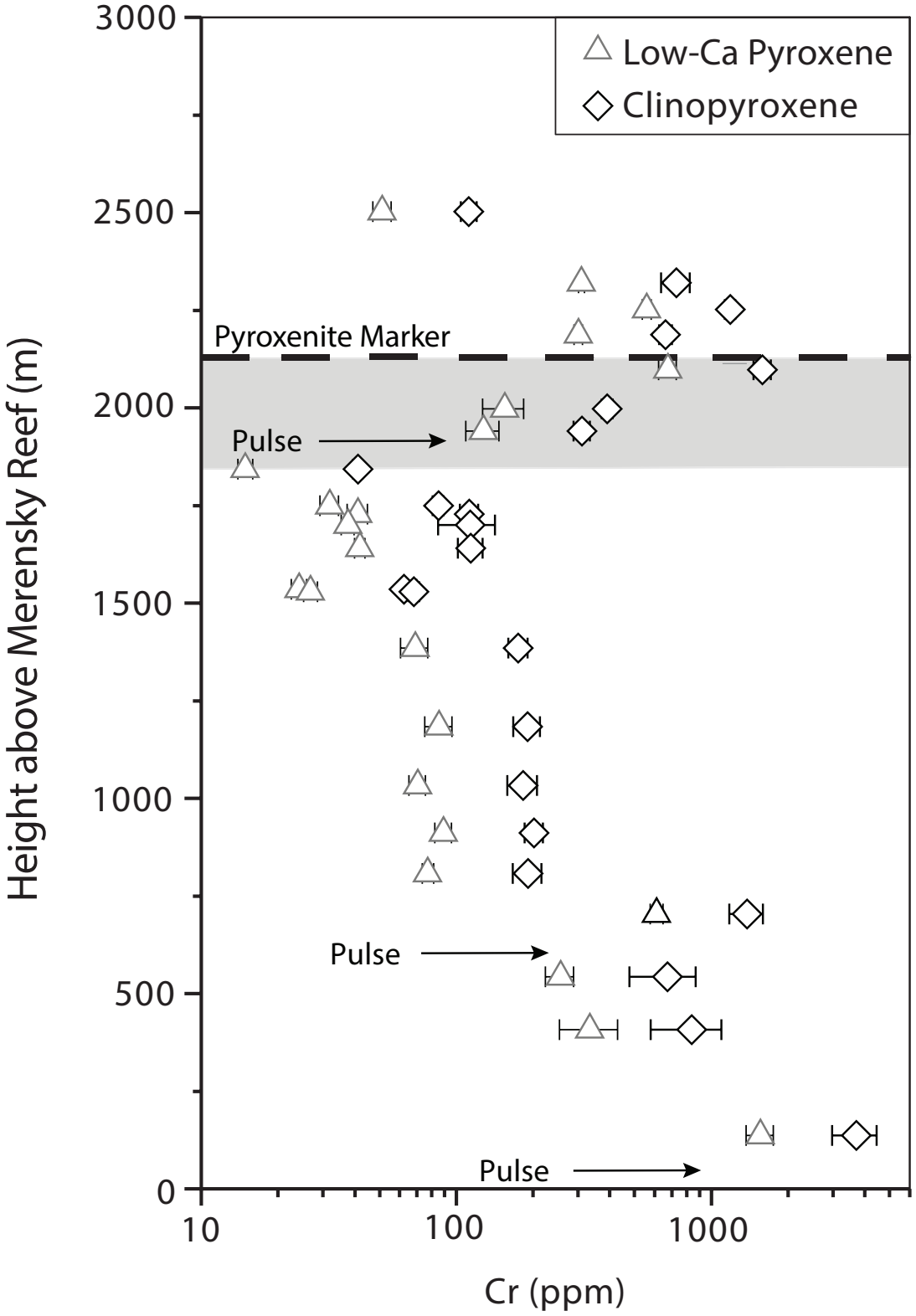
Low-Ca Pyroxene
Clinopyroxene
Pyroxenite Marker
Pulse
Pulse
Pulse
Height above Merensky Reef (m)
Cr (ppm)
3000
2500
2000
1500
1000
500
0
10
100
1000

Figure 5

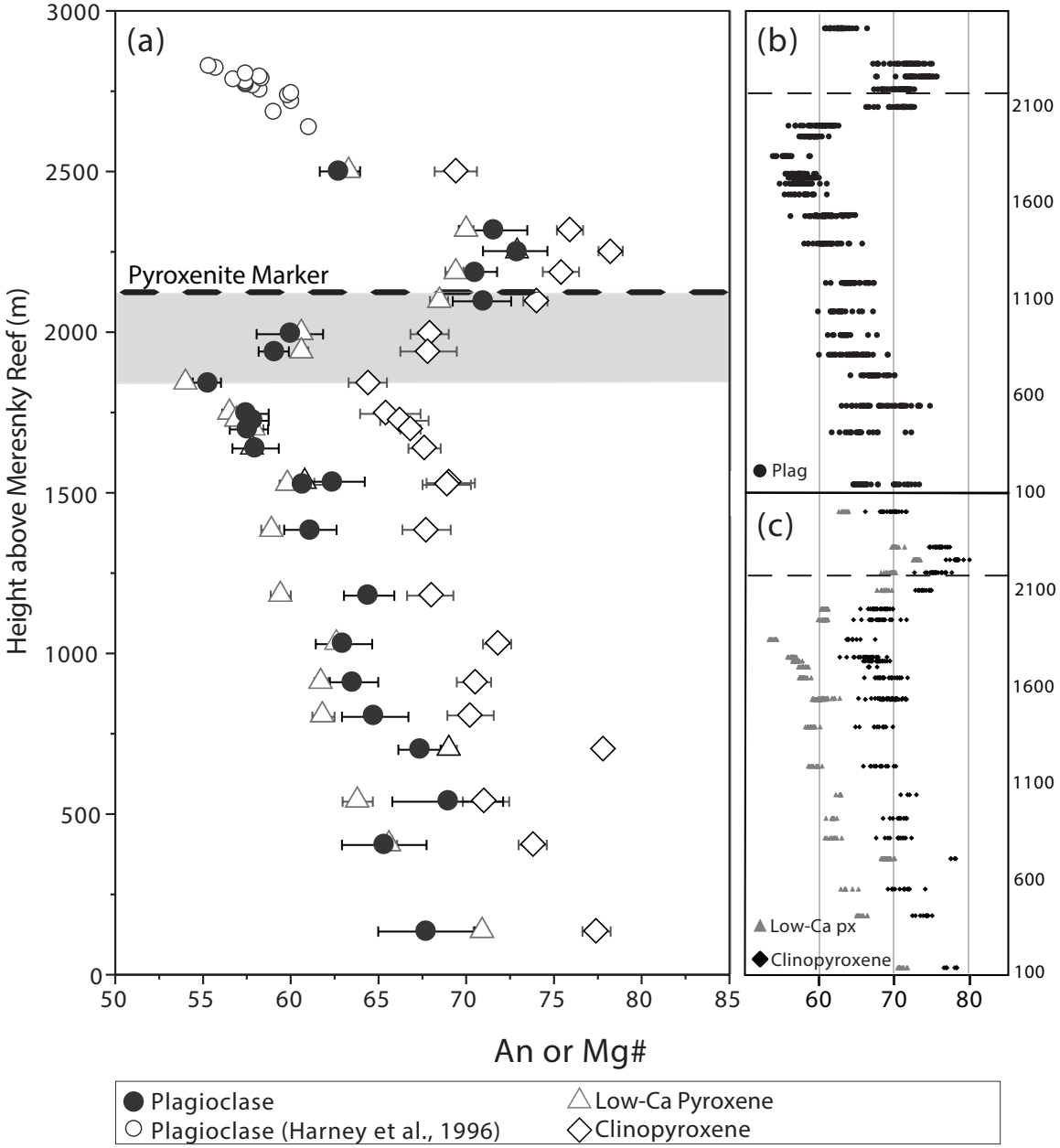
(a)
(b)
(c)
Pyroxenite Marker
Height above Meresnky Reef (m)
3000
2500
2000
1500
1000
500
0
50
55
60
65
70
75
80
85
60
70
80
2100
1600
1100
600
100
Plag
Low-Ca px
Clinopyroxene
An or Mg#
Plagioclase
Plagioclase (Harney et al., 1996)
Low-Ca Pyroxene
Clinopyroxene

Figure 6

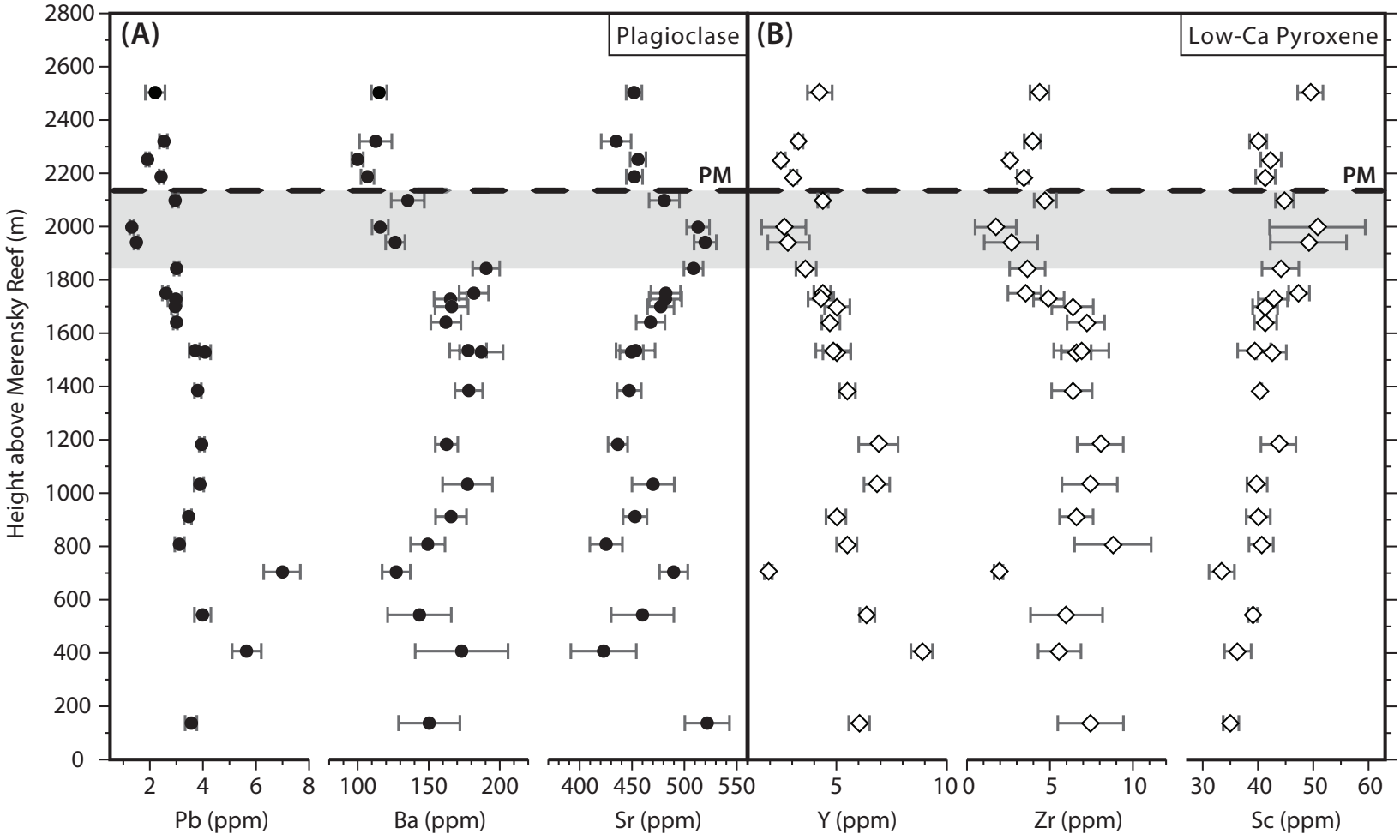
(A)
Plagioclase
(B)
Low-Ca Pyroxene
PM
PM
Height above Merensky Reef (m)
Pb (ppm)
Ba (ppm)
Sr (ppm)
Y (ppm)
Zr (ppm)
Sc (ppm)

Figure 7

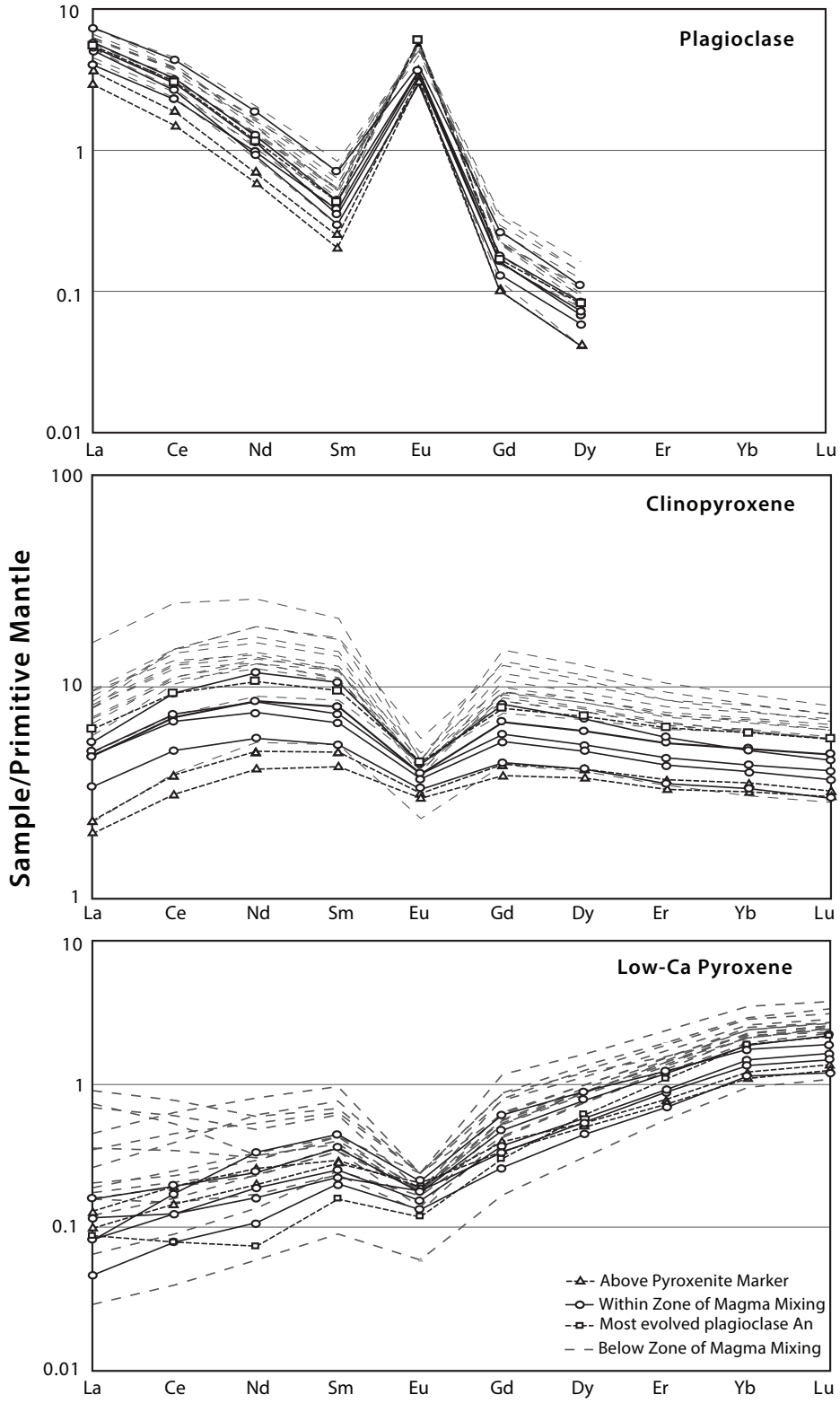
Plagioclase
Clinopyroxene
Low-Ca Pyroxene
Sample/Primitive Mantle
10
1
0.1
0.01
100
La
Ce
Nd
Sm
Eu
Gd
Dy
Er
Yb
Lu
Above Pyroxenite Marker
Within Zone of Magma Mixing
Most evolved plagioclase An
Below Zone of Magma Mixing

Figure 8

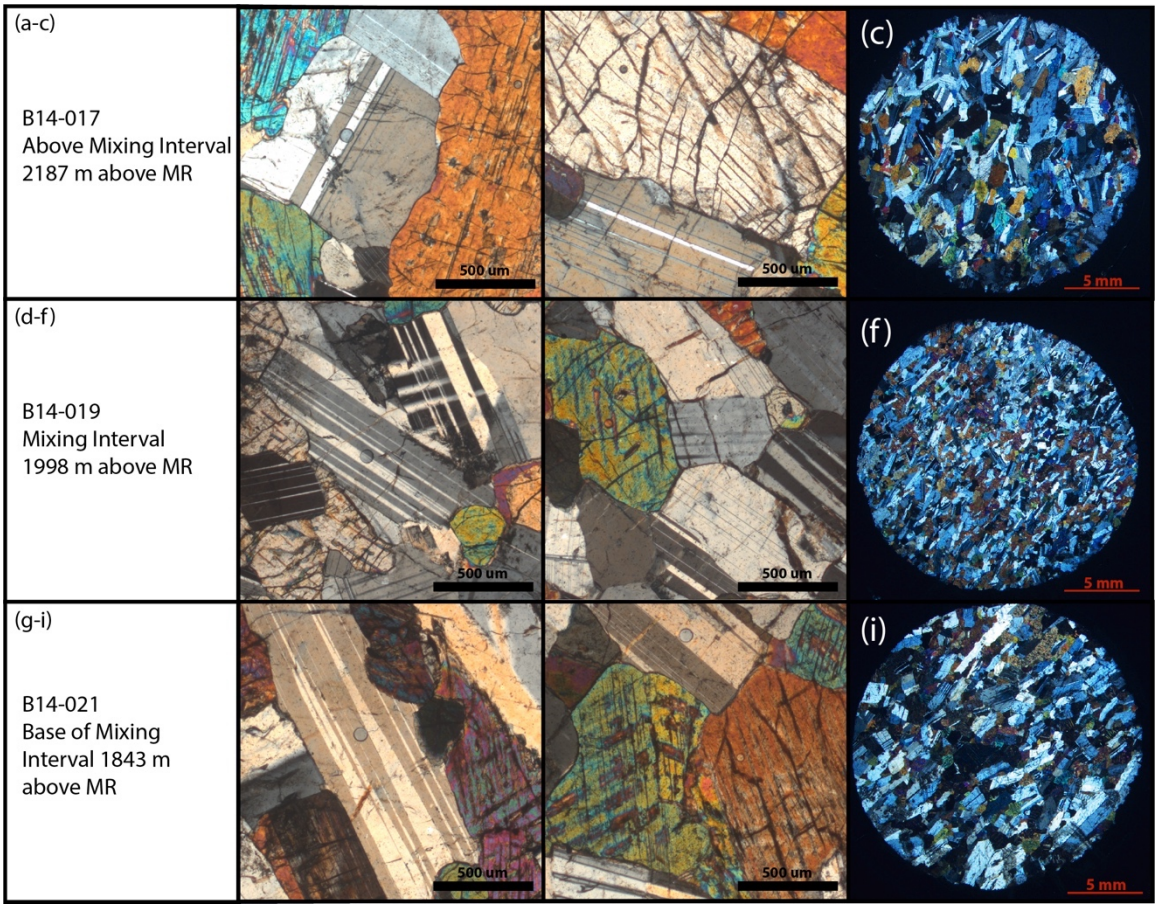
(a-c)
B14-017
Above Mixing Interval
2187 m above MR
500 um
500 um
(c)
5 mm
(d-f)
B14-019
Mixing Interval
1998 m above MR
500 um
500 um
(f)
5 mm
(g-i)
B14-021
Base of Mixing
Interval 1843 m
above MR
500 um
500 um
(i)
5 mm

Figure 8

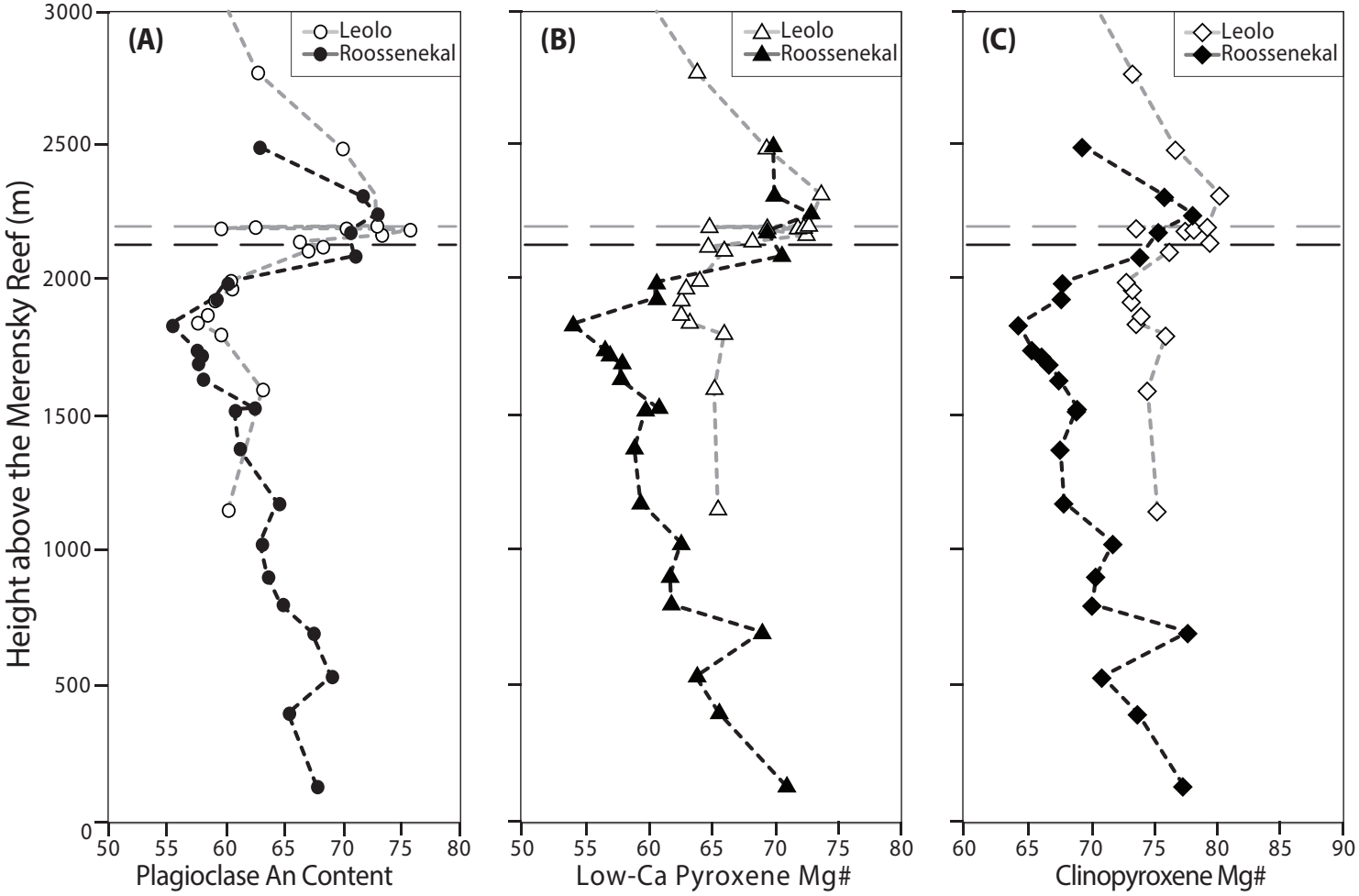
(A)
Leolo
Roossenekal
(B)
Leolo
Roossenekal
(C)
Leolo
Roossenekal
Height above the Merensky Reef (m)
3000
2500
2000
1500
1000
500
0
50 55 60 65 70 75 80
Plagioclase An Content
50 55 60 65 70 75 80
Low-Ca Pyroxene Mg#
60 65 70 75 80 85 90
Clinopyroxene Mg#

Figure 9

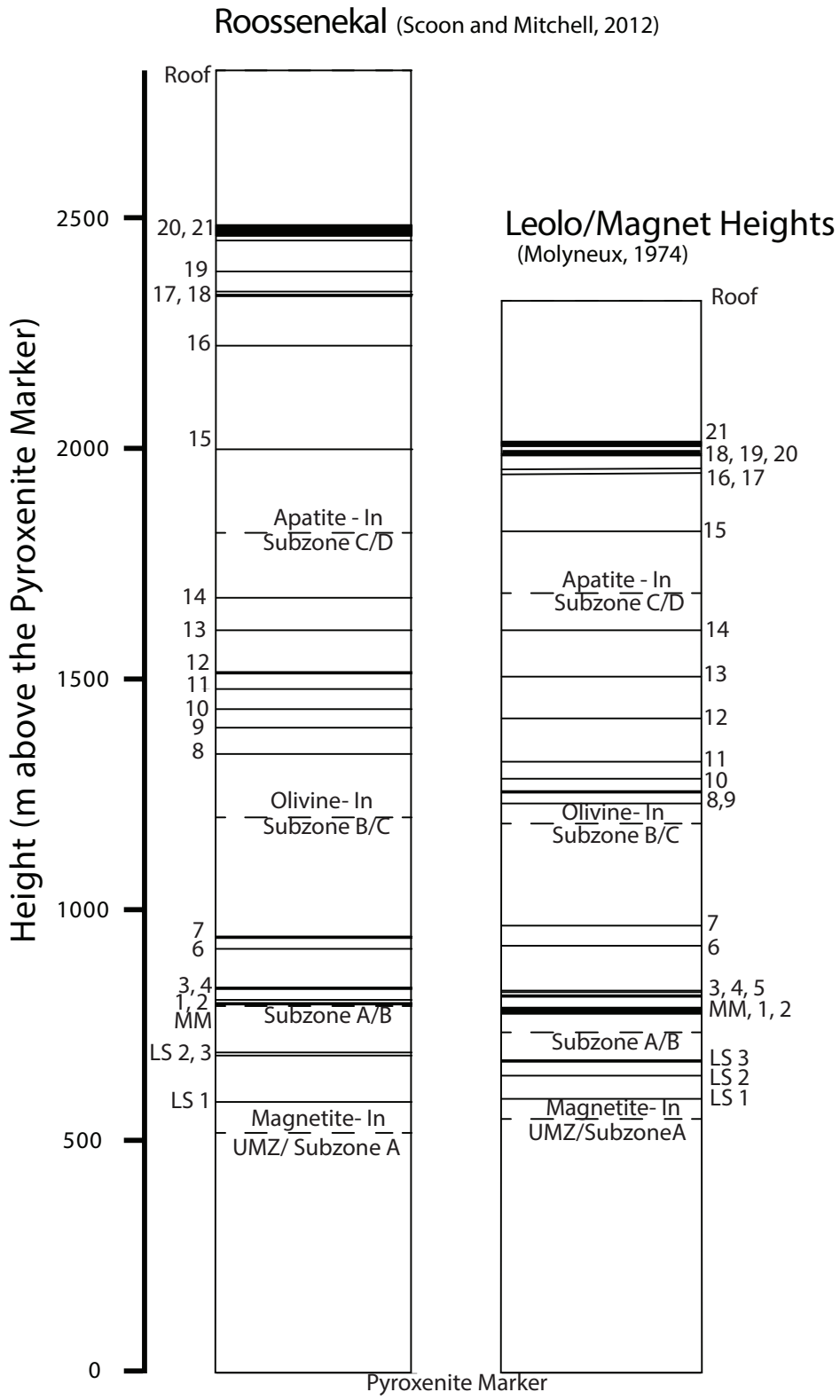
Roossenekal (Scoon and Mitchell, 2012)
Leolo/Magnet Heights
(Molyneux, 1974)
Height (m above the Pyroxenite Marker)
2500
2000
1500
1000
500
0
Roof
20, 21
19
17, 18
16
15
Apatite - In
Subzone C/D
14
13
12
11
10
9
8
Olivine- In
Subzone B/C
7
6
3, 4
1, 2
MM
Subzone A/B
LS 2, 3
LS 1
Magnetite- In
UMZ/ Subzone A
Pyroxenite Marker
Roof
21
18, 19, 20
16, 17
15
Apatite - In
Subzone C/D
14
13
12
11
10
8,9
Olivine- In
Subzone B/C
7
6
3, 4, 5
MM, 1, 2
Subzone A/B
LS 3
LS 2
LS 1
Magnetite- In
UMZ/SubzoneA

Figure 10

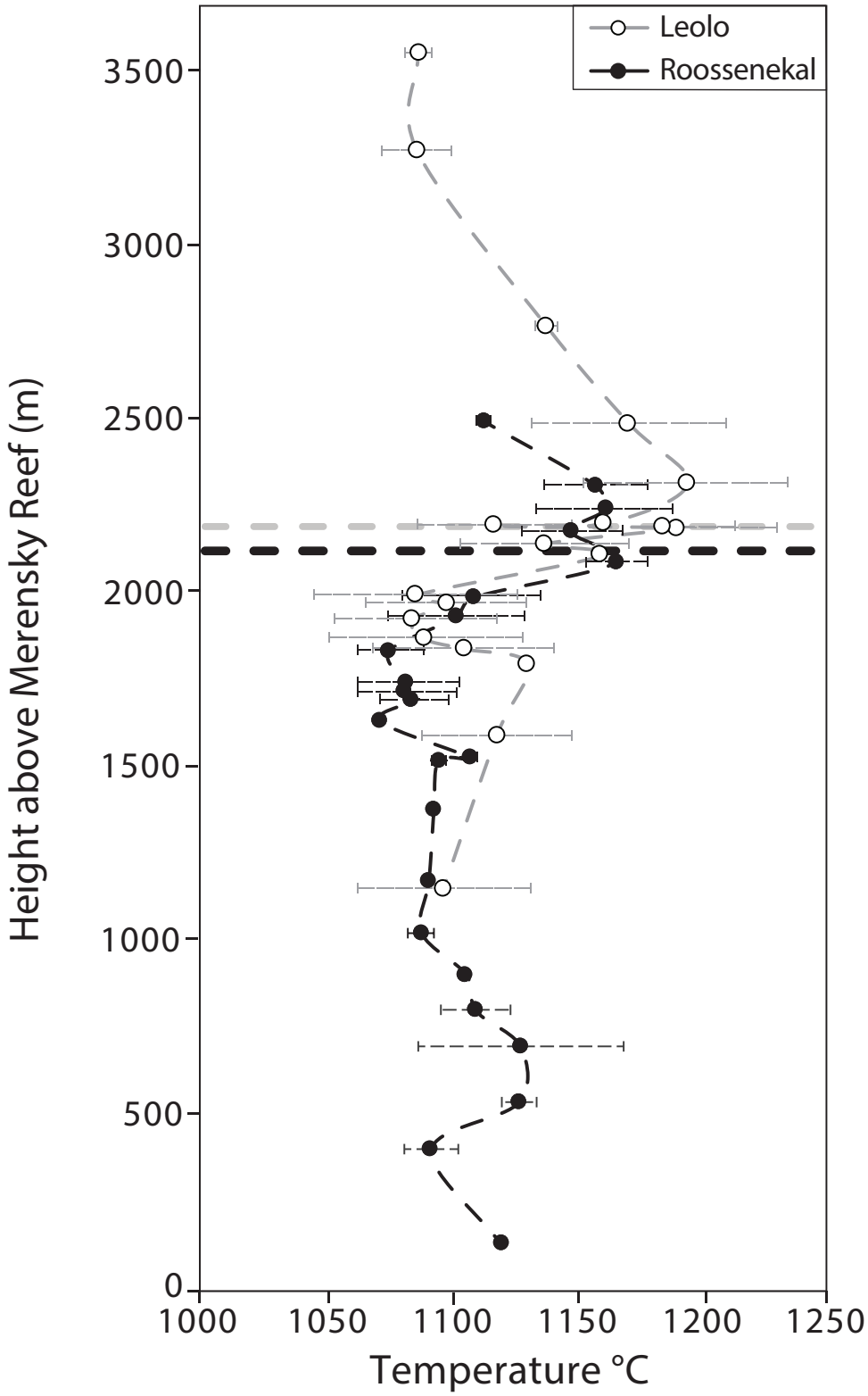
Leolo
Roossenekal
Height above Merensky Reef (m)
0
500
1000
1500
2000
2500
3000
3500
1000
1050
1100
1150
1200
1250
Temperature °C

Figure 11

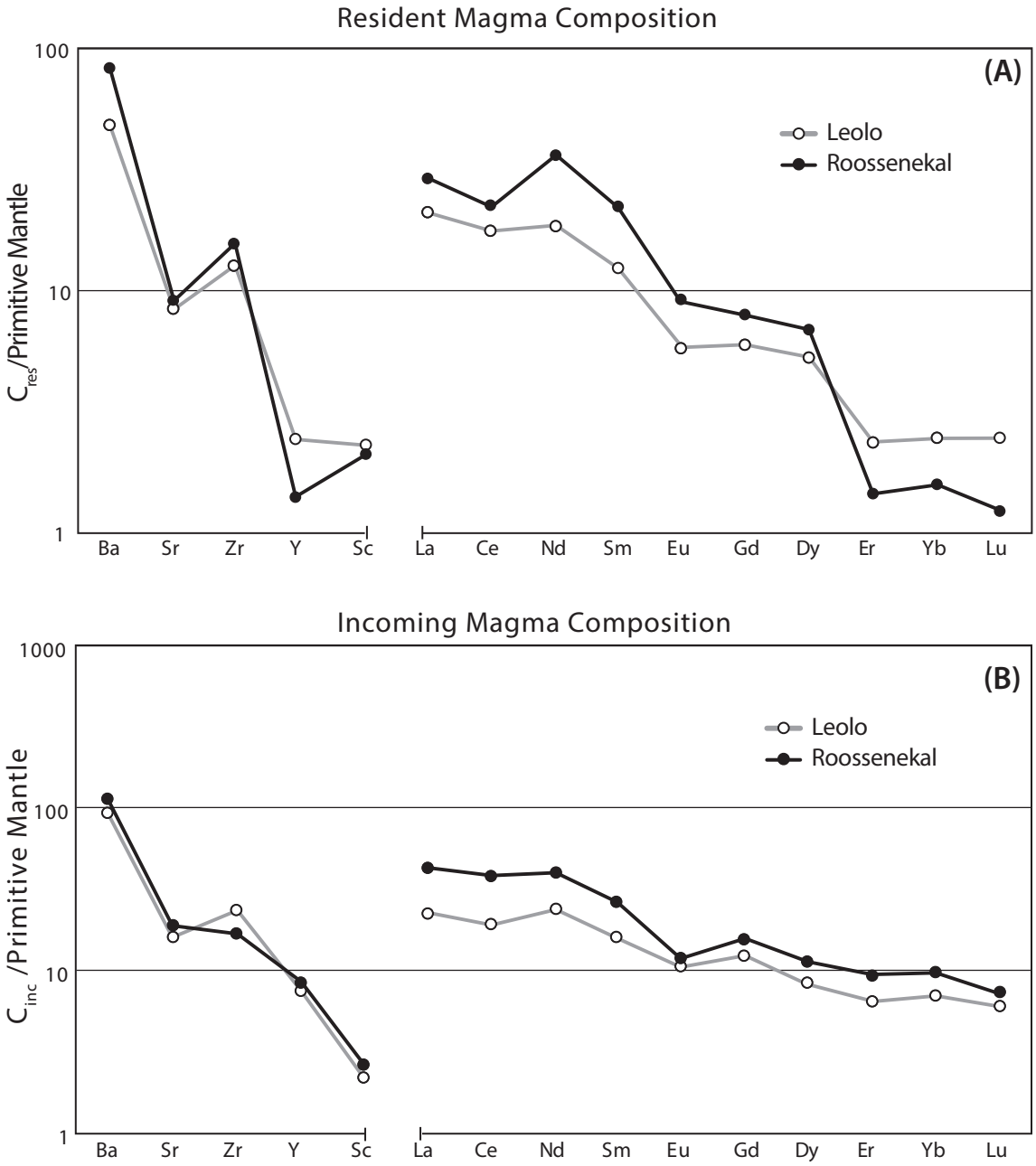
Resident Magma Composition
(A)
Leolo
Roossenekal
C_{res}/Primitive Mantle
100
10
1
Ba
Sr
Zr
Y
Sc
La
Ce
Nd
Sm
Eu
Gd
Dy
Er
Yb
Lu
Incoming Magma Composition
(B)
Leolo
Roossenekal
C_{inc} /Primitive Mantle
1000
100
10
1
Ba
Sr
Zr
Y
Sc
La
Ce
Nd
Sm
Eu
Gd
Dy
Er
Yb
Lu

Figure 12

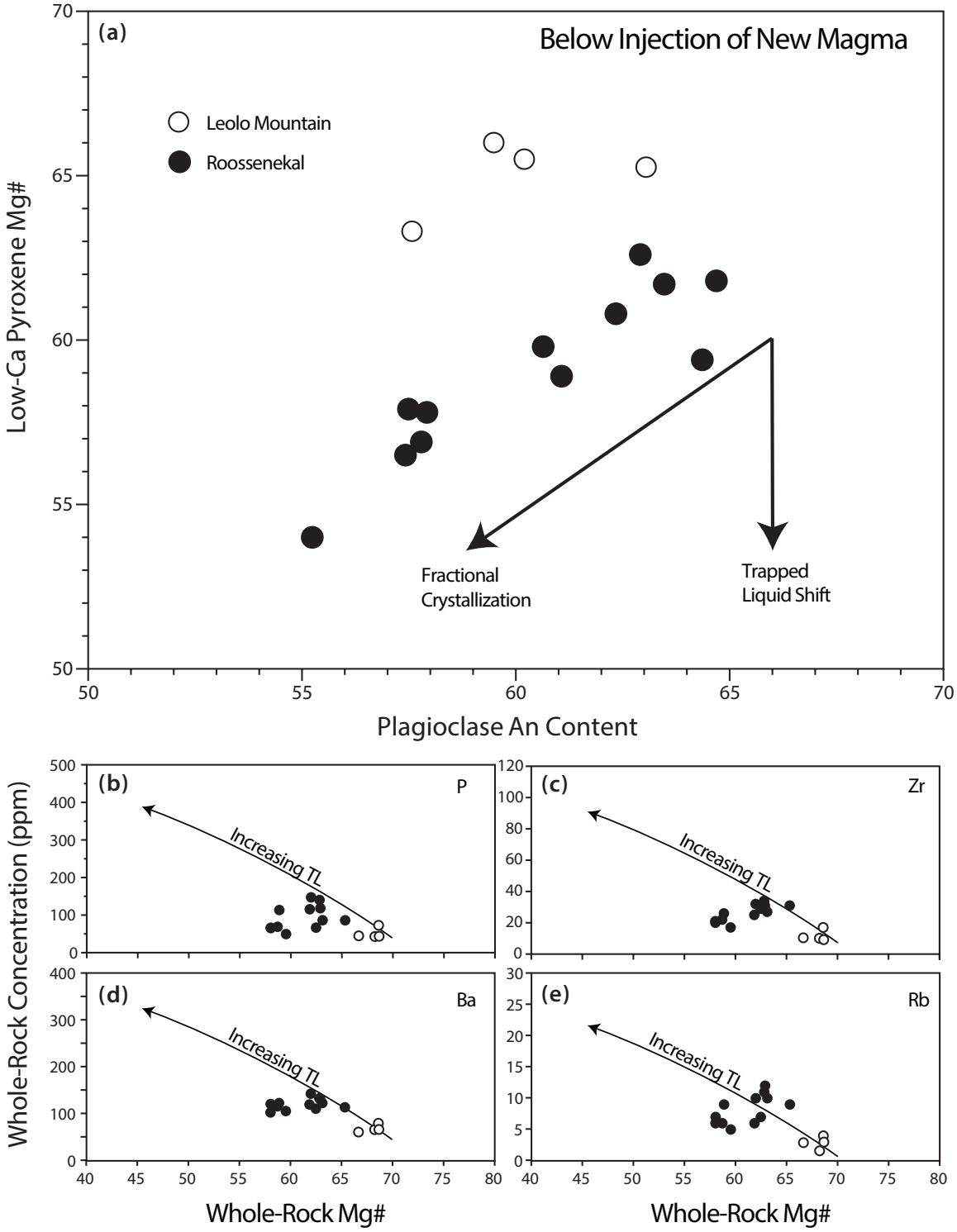
(a)
Below Injection of New Magma
Leolo Mountain
Roossenekal
Low-Ca Pyroxene Mg#
Plagioclase An Content
Fractional Crystallization
Trapped Liquid Shift
(b)
P
(c)
Zr
(d)
Ba
(e)
Rb
Increasing TL
Whole-Rock Concentration (ppm)
Whole-Rock Mg#

Figure 13

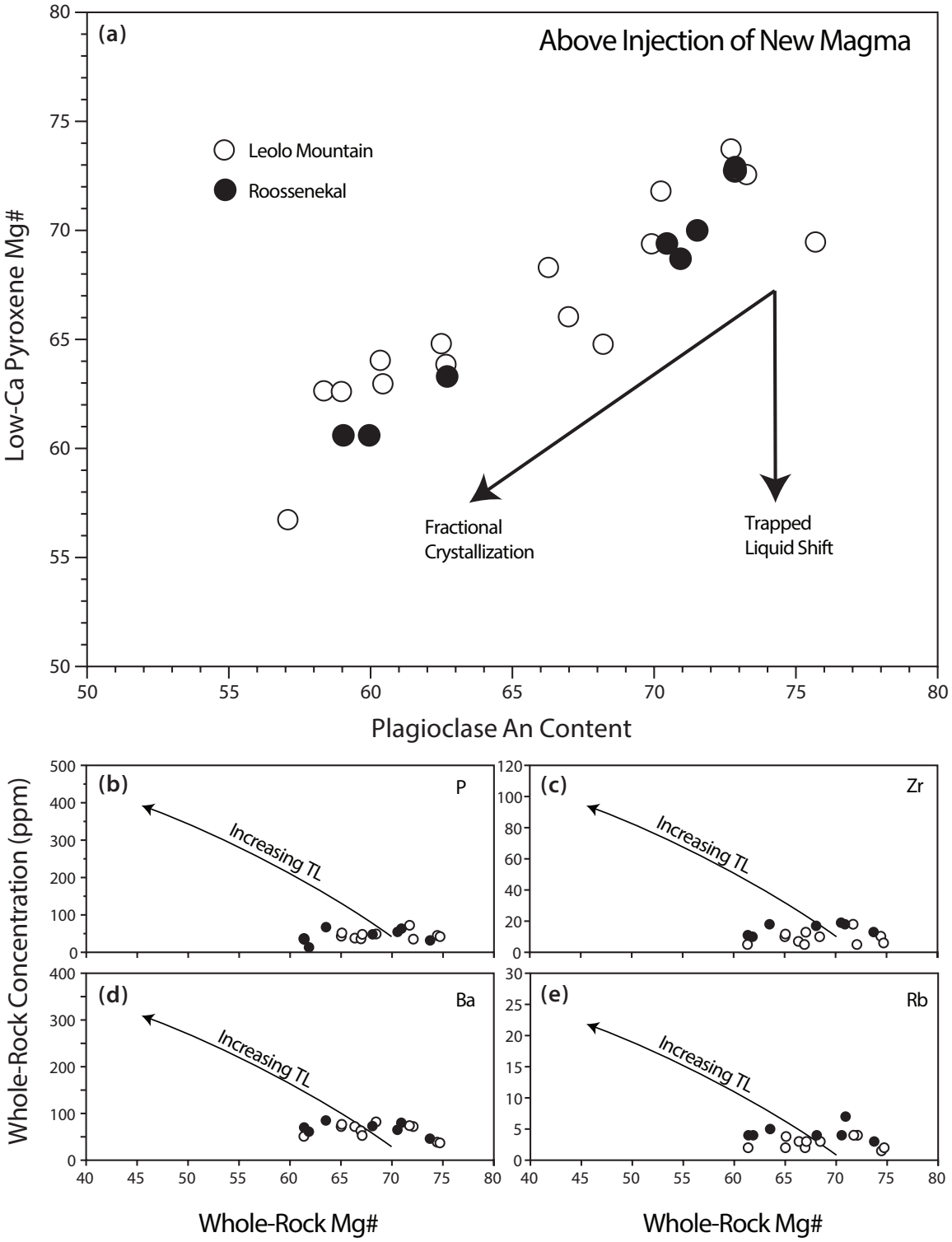
(a)
Above Injection of New Magma
Leolo Mountain
Roossenekal
Low-Ca Pyroxene Mg#
Plagioclase An Content
Fractional Crystallization
Trapped Liquid Shift
(b)
P
(c)
Zr
(d)
Ba
(e)
Rb
Increasing TL
Whole-Rock Concentration (ppm)
Whole-Rock Mg#

Figure 14

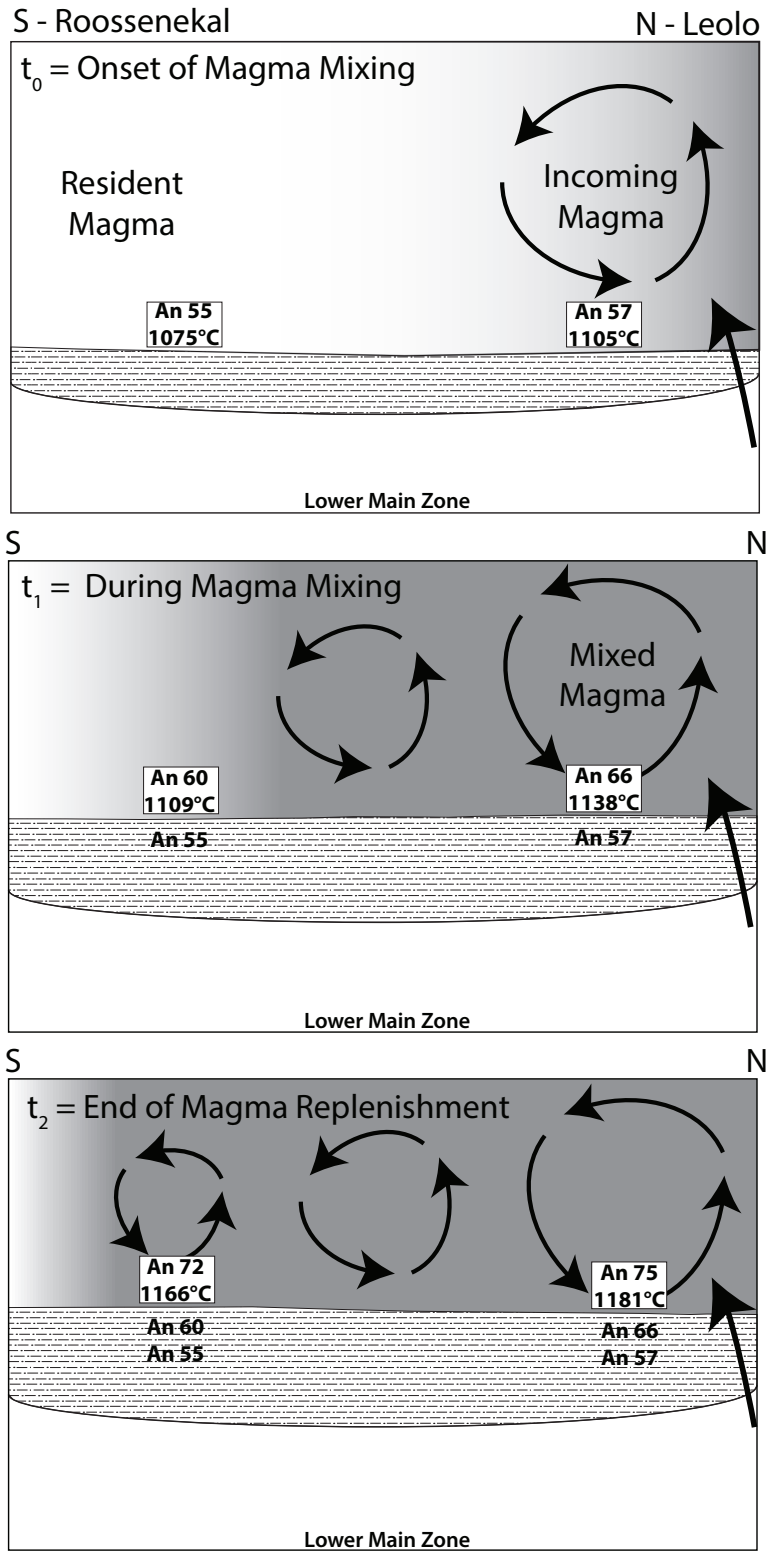
S - Roossenekal
N - Leolo
t0 = Onset of Magma Mixing
Resident Magma
Incoming Magma
An 55
1075°C
An 57
1105°C
Lower Main Zone
S
N
t1 = During Magma Mixing
Mixed Magma
An 60
1109°C
An 66
1138°C
An 55
An 57
Lower Main Zone
S
N
t2 = End of Magma Replenishment
An 72
1166°C
An 75
1181°C
An 60
An 55
An 66
An 57
Lower Main Zone

Table 1
Sample locations and stratigraphic depth (m above Merensky Reef)

Sample no.	Depth (m)	Latitude (S)	Longitude (E)
B14-053a	137	25°13.849’	30°05.374’
B14-052	407	25°13.692’	30°04.392’
B14-051	543	25°13.610’	30°03.892’
B14-050c	704	25°13.642’	30°03.294’
B14-049	808	25°11.863’	30°02.932’
B14-048	912	25°12.641’	30°02.521’
B14-047	1033	25°12.511’	30°02.104’
B14-046	1183	25°13.176’	30°01.509’
B14-045	1385	25°13.164’	30°00.893’
B14-044	1529	25°13.482’	30°00.471’
B14-026	1535	25°13.553’	30°00.397’
B14-025	1641	25°13.637’	29°59.707’
B14-024	1700	25°13.462’	29°59.328’
B14-023	1728	25°13.376’	29°59.165’
B14-022	1750	25°13.306’	29°59.016’
B14-021	1843	25°13.024’	29°58.485’
B14-020	1941	25°12.803’	29°57.999’
B14-019	1998	25°12.544’	29°57.800’
B14-018	2098	25°12.376’	29°57.366’
B14-017	2187	25°11.981’	29°57.082’
B14-016	2252	25°11.668’	29°56.828’
B14-015	2320	25°12.006’	29°56.524’
B14-014	2503	25°12.098’	29°55.907’

Table 2
Analyses of secondary standards for microprobe and laser ablation sessions

Microprobe session 1 (plagioclase): Cameca SX100 American Museum of Natural History

Summary	**Diopside**			**Clinopyroxene**			**Jadeite**			**Augite**			**Orthopyroxene**		
	Avg. (N=33)	1 Sig	Pub	Avg. (N=40)	1 Sig	Pub	Avg. (N=38)	1 Sig	Pub	Avg. (N=42)	1 Sig	Pub	Avg. (N=37)	1 Sig	Pub
SiO2	55.41	0.27	55.47	53.65	0.58	53.93	59.34	0.40	59.52	50.34	0.21	50.48	54.61	0.50	54.32
TiO2	0.00	0.00	0.00	0.24	0.01	0.27	0.05	0.03	0.03	0.50	0.01	0.52	0.13	0.01	0.17
Al2O3	0.02	0.01	0.00	0.64	0.13	0.66	24.78	0.46	24.98	7.38	0.04	7.54	4.67	0.71	4.36
Cr2O3	0.00	0.00	0.00	0.15	0.05	0.20	0.00	0.01	0.01	0.91	0.02	0.90	0.37	0.02	0.31
FeO	0.02	0.02	0.00	3.09	0.25	2.93	0.19	0.23	0.06	4.73	0.06	4.70	6.41	0.19	6.36
MnO	0.01	0.01	0.00	0.07	0.02	0.06	0.02	0.02	0.01	0.12	0.02	0.12	0.15	0.02	0.15
MgO	18.57	0.09	18.62	16.80	0.40	16.93	0.03	0.04	0.02	17.37	0.09	17.32	32.81	0.32	33.31
CaO	25.68	0.87	25.90	24.71	0.26	24.56	0.13	0.12	0.10	17.36	0.14	17.30	0.80	0.03	0.84
Na2O	0.01	0.01	0.00	0.23	0.05	0.24	14.99	0.20	15.08	0.85	0.03	0.85	0.11	0.02	0.08
Total	99.72	0.85		99.59	0.55		99.54	0.49		100.14			100.14		

Primary standards: Si, Mg, Ca (Diopside) Al, Na (Jadeite) Ti (TiO2) Cr (MgCrO4) Fe (Fayalite) Mn (Rhodonite)

Table 2 (Continued)
Microprobe session 2 (plagioclase): JEOL JXA 8200 Rutgers University

Summary	**Lk. County Plag**			**An 50 Glass**			**Anorthite**			**An 96**		
	Avg. (N=75)	1 Sig	Pub	Avg. (N=68)	1 Sig	Pub	Avg. (N=121)	1 Sig	Pub	Avg. (N=18)	1 Sig	Pub
SiO2	51.39	0.31	51.25	55.10	0.36	56.29	43.95	0.32	44.00	43.81	0.16	44.09
TiO2	0.04	0.02	0.05	0.01	0.01		0.01	0.01	0.03	0.01	0.01	0.02
Al2O3	30.95	0.12	30.91	28.56	0.19	27.95	35.91	0.18	36.03	35.97	0.11	35.47
Cr2O3	0.00	0.01		0.01	0.01		0.01	0.01		0.01	0.01	
FeO	0.42	0.03	0.46	0.02	0.02		0.47	0.03	0.62	0.41	0.02	0.46
MnO	0.01	0.01	0.01	0.01	0.01		0.01	0.02		0.01	0.01	
MgO	0.13	0.02	0.14	0.04	0.01	0.05	0.04	0.01	0.02	0.08	0.01	0.08
CaO	13.60	0.10	13.64	10.28	0.04	9.88	19.21	0.09	19.09	19.42	0.05	19.45
Na2O	3.63	0.09	3.45	5.71	0.16	5.94	0.51	0.04	0.53	0.43	0.04	0.40
K2O	0.11	0.01	0.18	0.01	0.01	0.01	0.01	0.00	0.03			
Total	100.28	0.33		99.74	0.51		100.12	0.70		100.14		

Primary standards: Si, Al, Ca (Lake County Plagioclase) Ti (TiO2) Cr (MgCrO4) Fe (Fayalite) Mn (Tephroite) Mg (Forsterite) Na (Jadeite) K (Orthoclase)

Table 2 (Continued)
Microprobe session 3 (plagioclase): JEOL JXA 8200 Rutgers University

Summary	**Lk. County Plag**			**Anorthite**			**An 96**		
	Avg. (N=12)	1 Sig	Pub	Avg. (N=12)	1 Sig	Pub	Avg. (N=12)	1 Sig	Pub
SiO2	51.98	0.80	51.25	44.30	0.79	44.00	44.97	0.93	44.09
Al2O3	30.62	0.13	30.91	36.01	0.06	36.03	36.01	0.15	35.47
Cr2O3	0.00	0.01		0.00	0.01		0.01	0.02	
FeO	0.41	0.05	0.46	0.49	0.05	0.62	0.43	0.07	0.46
MnO	0.00	0.01	0.01	0.01	0.01		0.00	0.01	
MgO	0.12	0.01	0.14	0.03	0.01	0.02	0.07	0.01	0.08
CaO	13.19	0.02	13.64	19.09	0.04	19.09	19.23	0.05	19.45
Na2O	3.89	0.11	3.45	0.52	0.02	0.53	0.45	0.03	0.40
K2O	0.12	0.01	0.18	0.01	0.00	0.03	0.00	0.00	
Total	100.34	0.91		100.45	0.81		101.16	1.02	

Primary standards: Si, Na (Albite) Al, Ca (Anorthite) Cr (Chromite) Fe (Fayalite) Mn (Rhodonite) Mg (Forsterite) K (Orthoclase)

Table 2 (Continued)
Microprobe session 3 (pyroxene): JEOL JXA 8200 Rutgers University

Summary	**Diopside**			**Enstatite**			**Jadeite**			**Augite**			**Orthopyroxene**		
	Avg. (N=16)	1 Sig	Pub	Avg. (N=16)	1 Sig	Pub	Avg. (N=16)	1 Sig	Pub	Avg. (N=16)	1 Sig	Pub	Avg. (N=16)	1 Sig	Pub
SiO2	56.53	0.35	54.87	60.94	0.40	59.10	59.52	0.13	59.52	51.08	0.36	50.73	55.60	0.13	54.70
TiO2	0.00	0.00	0.00	0.03	0.07		0.04	0.10	0.03	0.81	0.07	0.74	0.06	0.07	
Al2O3	0.26	0.05	0.11	0.15	0.05	0.07	24.99	0.16	24.98	8.06	0.13	8.73	0.47	0.02	0.53
Cr2O3	0.00	0.00	0.00	0.01	0.01		0.00	0.01	0.01	0.15	0.01	0.00	0.65	0.02	
FeO	0.18	0.08	0.24	0.03	0.06	0.07	0.20	0.24	0.06	6.57	0.20	5.37	15.59	0.34	15.20
MnO	0.03	0.02	0.00	0.03	0.01		0.03	0.03	0.01	0.14	0.02	0.13	0.15	0.02	
MgO	18.27	0.06	18.30	40.07	0.38	39.60	0.00	0.02	0.02	16.31	0.11	16.65	27.44	0.18	27.60
CaO	25.64	0.05	25.63	0.40	0.02	0.64	0.17	0.12	0.10	15.93	0.05	15.82	0.74	0.01	0.71
Na2O	0.20	0.04	0.34	0.01	0.02		15.11	0.13	15.08	1.30	0.07	1.27	0.00	0.01	
Total	101.14	0.40		101.68	0.72		100.23	0.56		100.29	0.41		101.06	0.75	

Primary standards: Si, Al, Na (Jadeite) Ti (TiO2) Cr (MgCrO4) Fe (Fayalite) Mn (Rhodonite) Mg, Ca (Diopside)

Table 2 (Continued)
LA-ICP-MS session: Thermo iCapQc Rutgers University

Summary	**BCR**				**BIR**			
	Avg. (N=65)	1 Sig	Pub	1 Sig	Avg. (N=65)	1 Sig	Pub	1 Sig
Sc	36.06	1.90	33	2	45.49	1.79	44	1
TiO2%	2.07	0.05	2.26	0.05	0.89	0.02	0.96	0.01
V	421.1	12.7	416	14	333.5	11.1	310	11
Cr	16.93	0.60	18	2	406.0	11.0	370	8
Mn	1500	100	1520	60	1400	100		
Cu	19.87	0.87	19	2	131.7	5.9	125	4
Zn	145.3	6.3	127	9	86.78	3.93	70	9
Rb	49.64	2.58	48	2	0.22	0.03		
Sr	336.1	7.1	346	14	111.6	4.5	110	2
Y	31.10	1.25	37	2	13.62	0.49	16	1
Zr	166.4	5.9	188	16	13.11	0.44	18	1
Nb	10.58	0.24			0.46	0.03		
Ba	676.9	17.8	683	28	6.68	0.32	7	
La	25.49	1.05	25	1	0.62	0.04	0.63	0.07
Ce	51.72	1.44	53	2	1.88	0.07	1.9	0.4
Pr	6.26	0.24	6.8	0.3	0.35	0.02		
Nd	27.26	0.9	28	2	2.3	0.12	2.5	0.7
Sm	6.3	0.24	6.8	0.3	1.07	0.08	1.1	
Eu	2.06	0.08	2	0.1	0.53	0.03	0.55	0.05
Gd	5.88	0.23	6.8	0.3	1.72	0.10	1.8	0.4
Dy	5.87	0.21			2.34	0.11	4	1.00
Er	3.24	0.12			1.49	0.08		
Yb	3.24	0.14	3.5	0.2	1.61	0.08	1.7	0.1
Lu	0.46	0.03	0.51	0.02	0.23	0.01	0.26	
Hf	4.43	0.19	4.8	0.2	0.53	0.04	0.6	0.08
Pb	10.56	0.75	11	2	3.98	0.18	3	
Th	5.68	0.2	6.2	0.7	0.03	0.01		
U	1.83	0.08	1.69	0.19	0.02	0.00		

Primary standards: NIST 612, NIST610

Table 3
Orthopyroxene major element composition by EPMA (ox wt.%) and trace element composition by LA-ICP-MS (ppm)

Sample	B14-014		B14-015		B14-016		B14-017		B14-018	
Depth (m)	2503		2320		2252		2187		2098	
Mg#	63.3		70.0		72.9		69.4		68.7	
SiO2	51.82	*0.10*	53.08	*0.40*	53.72	*0.24*	53.23	*0.42*	53.23	*0.18*
TiO2	0.32	*0.02*	0.27	*0.03*	0.18	*0.03*	0.22	*0.04*	0.24	*0.04*
Al2O3	0.82	*0.03*	0.79	*0.03*	0.86	*0.08*	0.83	*0.06*	0.90	*0.06*
Cr2O3	0.01	*0.01*	0.06	*0.01*	0.09	*0.01*	0.05	*0.01*	0.12	*0.02*
FeO	22.56	*0.24*	18.82	*0.46*	17.21	*0.22*	19.13	*0.48*	19.56	*0.52*
MnO	0.49	*0.01*	0.41	*0.02*	0.39	*0.03*	0.42	*0.03*	0.40	*0.03*
MgO	21.81	*0.19*	24.68	*0.25*	25.99	*0.19*	24.34	*0.21*	24.09	*0.26*
CaO	1.59	*0.30*	1.60	*0.58*	1.40	*0.27*	1.63	*0.41*	1.59	*0.64*
Na2O	0.02	*0.01*	0.01	*0.01*	0.02	*0.01*	0.02	*0.01*	0.02	*0.02*
Total	99.43	*0.10*	99.71	*0.42*	99.86	*0.33*	99.88	*0.37*	100.15	*0.29*
n	8		18		29		17		17	
Sc	49.46	*2.29*	40.03	*1.56*	42.35	*1.85*	41.35	*1.77*	45.44	*1.64*
Ti	1023.13	*65.41*	1443.36	*169.81*	575.67	*69.70*	676.15	*127.53*	769.83	*146.39*
V	171.27	*7.53*	141.56	*5.29*	130.12	*5.37*	138.53	*5.45*	185.94	*6.44*
Cr	51.31	*4.27*	310.14	*8.02*	557.83	*22.44*	300.91	*11.10*	675.42	*52.93*
Mn	2938.74	*117.64*	1420.39	*47.12*	2303.70	*36.97*	2493.41	*66.89*	2489.35	*40.75*
Cu	0.62	*0.09*	0.52	*0.15*	0.81	*0.94*	0.60	*0.11*	0.64	*0.07*
Zn	231.10	*8.44*	187.41	*3.62*	158.40	*2.51*	174.11	*4.20*	192.94	*3.30*
Sr	0.16	*0.04*	0.15	*0.12*	0.26	*0.44*	0.15	*0.05*	0.21	*0.07*
Y	4.25	*0.56*	3.30	*0.19*	2.51	*0.18*	3.07	*0.15*	4.63	*0.24*
Zr	4.37	*0.57*	3.95	*0.50*	2.55	*0.21*	3.37	*0.34*	4.93	*0.67*
Nb	0.02	*0.01*	0.02	*0.02*	0.02	*0.01*	0.02	*0.01*	0.02	*0.01*
Ba	0.01	*0.01*	0.01	*0.01*	0.04	*0.11*	0.01	*0.01*	0.02	*0.02*
La	0.11	*0.13*	0.06	*0.03*	0.03	*0.01*	0.08	*0.07*	0.06	*0.04*
Ce	0.35	*0.26*	0.22	*0.13*	0.14	*0.05*	0.22	*0.11*	0.31	*0.12*
Pr	0.05	*0.02*	0.04	*0.02*	0.03	*0.01*	0.04	*0.01*	0.06	*0.02*
Nd	0.33	*0.10*	0.26	*0.12*	0.15	*0.04*	0.22	*0.06*	0.45	*0.11*
Sm	0.16	*0.04*	0.11	*0.03*	0.09	*0.03*	0.10	*0.03*	0.20	*0.05*
Eu	0.03	*0.01*	0.03	*0.01*	0.02	*0.01*	0.03	*0.01*	0.04	*0.00*
Gd	0.28	*0.06*	0.22	*0.05*	0.16	*0.03*	0.20	*0.02*	0.36	*0.05*
Dy	0.57	*0.10*	0.43	*0.05*	0.33	*0.04*	0.40	*0.04*	0.65	*0.05*
Er	0.57	*0.07*	0.44	*0.05*	0.33	*0.06*	0.42	*0.04*	0.59	*0.04*
Yb	0.92	*0.10*	0.73	*0.06*	0.56	*0.05*	0.67	*0.05*	0.86	*0.05*
Lu	0.16	*0.01*	0.12	*0.01*	0.09	*0.01*	0.11	*0.01*	0.14	*0.01*
Hf	0.17	*0.02*	0.14	*0.02*	0.09	*0.02*	0.10	*0.01*	0.15	*0.04*
Pb	b.d.	*b.d.*	b.d.	*b.d.*	0.05	*0.05*	b.d.	*b.d.*	b.d.	*b.d.*
Th	0.06	*0.04*	0.04	*0.03*	0.04	*0.02*	0.04	*0.03*	0.05	*0.02*
U	0.03	*0.06*	0.01	*0.01*	0.00	*0.00*	0.02	*0.03*	0.01	*0.01*

Table 3 (Continued)

Sample	B14-019		B14-020		B14-021		B14-022		B14-023	
Depth (m)	1998		1941		1843		1750		1728	
Mg#	60.6		60.6		54.0		56.5		56.9	
SiO2	51.62	*0.37*	51.83	*0.27*	52.55	*0.27*	51.05	*0.35*	51.45	*0.19*
TiO2	0.23	*0.02*	0.21	*0.03*	0.18	*0.12*	0.25	*0.04*	0.29	*0.02*
Al2O3	0.73	*0.12*	0.66	*0.07*	0.57	*0.05*	0.61	*0.06*	0.63	*0.04*
Cr2O3	0.03	*0.01*	0.02	*0.01*	0.00	*0.01*	0.01	*0.01*	0.01	*0.01*
FeO	24.23	*0.25*	24.40	*0.23*	28.25	*0.23*	26.52	*0.25*	26.28	*0.36*
MnO	0.52	*0.03*	0.53	*0.03*	0.57	*0.03*	0.56	*0.03*	0.55	*0.03*
MgO	20.94	*0.18*	21.03	*0.12*	18.61	*0.1*	19.29	*0.15*	19.46	*0.12*
CaO	1.21	*0.28*	0.95	*0.17*	1.01	*0.13*	1.13	*0.28*	1.21	*0.32*
Na2O	0.01	*0.01*	0.01	*0.01*	0.01	*0.01*	0.01	*0.01*	0.01	*0.01*
Total	99.51	*0.38*	99.64	*0.32*	101.75	*0.41*	99.44	*0.36*	99.89	*0.24*
n	18		18		11		12		17	
Sc	50.75	*8.65*	49.12	*6.89*	44.05	*3.33*	47.43	*1.88*	42.70	*2.64*
Ti	736.03	*71.72*	694.13	*78.37*	606.61	*113.72*	816.71	*136.23*	852.13	*147.67*
V	197.45	*38.86*	194.18	*29.97*	223.75	*15.59*	245.81	*18.95*	214.37	*16.99*
Cr	155.17	*28.45*	127.73	*18.91*	14.91	*1*	31.87	*2.62*	41.08	*3.75*
Mn	3099.89	*148.40*	3053.68	*156.53*	3531.25	*87.58*	3397.98	*85.06*	3356.50	*79.76*
Cu	0.65	*0.23*	0.55	*0.26*	0.49	*0.08*	0.52	*0.17*	0.49	*0.07*
Zn	209.29	*12.80*	212.10	*13.74*	260.17	*6.71*	265.60	*5.77*	270.87	*6.70*
Sr	0.56	*0.95*	0.69	*0.68*	0.30	*0.52*	0.14	*0.09*	0.11	*0.05*
Y	2.62	*1.00*	2.84	*0.94*	3.63	*0.46*	4.36	*0.38*	4.30	*0.58*
Zr	1.73	*1.24*	2.65	*1.61*	3.64	*1.07*	3.47	*1.00*	4.93	*0.92*
Nb	0.03	*0.02*	0.07	*0.08*	0.01	*0.01*	0.01	*0.00*	0.01	*0.01*
Ba	0.08	*0.20*	0.05	*0.06*	0.09	*0.17*	0.27	*0.47*	0.04	*0.04*
La	0.07	*0.11*	0.09	*0.10*	0.06	*0.03*	0.04	*0.04*	0.11	*0.09*
Ce	0.26	*0.40*	0.34	*0.40*	0.14	*0.06*	0.16	*0.09*	0.27	*0.16*
Pr	0.05	*0.07*	0.06	*0.07*	0.02	*0.01*	0.03	*0.01*	0.04	*0.02*
Nd	0.27	*0.41*	0.35	*0.40*	0.10	*0.05*	0.18	*0.05*	0.23	*0.09*
Sm	0.12	*0.16*	0.13	*0.13*	0.07	*0.03*	0.11	*0.03*	0.10	*0.03*
Eu	0.03	*0.04*	0.03	*0.03*	0.02	*0.01*	0.03	*0.01*	0.02	*0.01*
Gd	0.20	*0.18*	0.24	*0.17*	0.18	*0.05*	0.26	*0.06*	0.25	*0.04*
Dy	0.37	*0.19*	0.39	*0.16*	0.45	*0.09*	0.56	*0.08*	0.55	*0.09*
Er	0.35	*0.11*	0.37	*0.09*	0.52	*0.07*	0.61	*0.06*	0.59	*0.07*
Yb	0.54	*0.10*	0.60	*0.08*	0.93	*0.09*	1.07	*0.06*	0.96	*0.12*
Lu	0.09	*0.01*	0.10	*0.01*	0.16	*0.01*	0.19	*0.01*	0.17	*0.01*
Hf	0.08	*0.05*	0.10	*0.06*	0.12	*0.04*	0.12	*0.03*	0.16	*0.03*
Pb	b.d.	*b.d.*	0.05	*0.06*	0.05	*0.03*	0.04	*0.06*	0.04	*0.04*
Th	0.06	*0.08*	0.22	*0.28*	0.15	*0.12*	0.07	*0.07*	0.10	*0.05*
U	0.01	*0.01*	0.03	*0.04*	0.05	*0.04*	0.02	*0.02*	0.06	*0.07*

Table 3 (Continued)

Sample	B14-024		B14-025		B14-026		B14-044		B14-045	
Depth (m)	1700		1641		1535		1529		1385	
Mg#	57.9		57.8		60.8		59.8		58.9	
SiO2	51.51	*0.37*	51.69	*0.25*	52.31	*0.37*	52.06	*0.29*	52.40	*0.27*
TiO2	0.28	*0.06*	0.28	*0.03*	0.30	*0.05*	0.36	*0.21*	0.25	*0.08*
Al2O3	0.65	*0.17*	0.61	*0.05*	0.64	*0.04*	0.62	*0.05*	0.68	*0.06*
Cr2O3	0.01	*0.01*	0.01	*0.01*	0.01	*0.01*	0.01	*0.01*	0.01	*0.01*
FeO	25.72	*0.38*	25.76	*0.40*	23.83	*0.97*	24.53	*0.42*	25.20	*0.52*
MnO	0.55	*0.03*	0.55	*0.03*	0.50	*0.03*	0.51	*0.03*	0.51	*0.02*
MgO	19.85	*0.19*	19.81	*0.15*	20.73	*0.36*	20.48	*0.19*	20.27	*0.28*
CaO	1.40	*0.35*	1.28	*0.31*	1.82	*1.18*	1.45	*0.45*	1.25	*0.62*
Na2O	0.02	*0.01*	0.02	*0.01*	0.02	*0.02*	0.02	*0.02*	0.01	*0.01*
Total	99.99	*0.39*	100.00	*0.27*	100.17	*0.35*	100.02	*0.26*	100.57	*0.6*
n	20		18		18		13		13	
Sc	41.29	*2.26*	41.36	*2.02*	39.31	*2.99*	42.43	*2.69*	40.51	*0.17*
Ti	887.13	*149.87*	907.72	*94.06*	977.37	*162.67*	996.49	*94.98*	1006.76	*25.4*
V	208.55	*14.45*	213.65	*10.77*	203.99	*17.27*	205.56	*14.96*	211.31	*14.3*
Cr	37.59	*2.16*	41.85	*1.89*	24.19	*1.65*	26.86	*1.72*	68.95	*8.46*
Mn	3149.58	*68.12*	3237.17	*63.49*	2998.85	*80.05*	3042.90	*129.94*	2944.17	*30.32*
Cu	0.50	*0.08*	0.50	*0.11*	0.81	*0.80*	0.52	*0.06*	0.52	*0.11*
Zn	252.99	*6.80*	238.55	*4.42*	251.79	*5.81*	270.26	*7.81*	255.27	*6.58*
Sr	0.16	*0.23*	0.14	*0.11*	0.24	*0.13*	0.16	*0.08*	0.16	*0.07*
Y	5.04	*0.57*	4.75	*0.41*	4.86	*0.79*	5.02	*0.63*	5.50	*0.36*
Zr	6.36	*1.25*	7.16	*1.13*	6.89	*1.66*	6.58	*0.90*	6.32	*1.22*
Nb	0.01	*0.01*	0.02	*0.02*	0.03	*0.02*	0.02	*0.01*	0.02	*0.02*
Ba	0.06	*0.20*	0.06	*0.11*	0.14	*0.23*	0.04	*0.05*	0.03	*0.07*
La	0.08	*0.08*	0.11	*0.08*	0.50	*0.50*	0.25	*0.26*	0.13	*0.1*
Ce	0.28	*0.29*	0.34	*0.16*	0.94	*0.81*	0.61	*0.48*	0.44	*0.23*
Pr	0.05	*0.05*	0.05	*0.02*	0.10	*0.07*	0.08	*0.05*	0.07	*0.02*
Nd	0.31	*0.27*	0.31	*0.09*	0.43	*0.22*	0.42	*0.16*	0.45	*0.13*
Sm	0.15	*0.09*	0.15	*0.04*	0.17	*0.06*	0.18	*0.05*	0.19	*0.05*
Eu	0.02	*0.01*	0.03	*0.01*	0.03	*0.01*	0.03	*0.01*	0.04	*0.01*
Gd	0.32	*0.09*	0.31	*0.04*	0.31	*0.08*	0.34	*0.07*	0.37	*0.05*
Dy	0.65	*0.11*	0.62	*0.05*	0.64	*0.14*	0.69	*0.11*	0.73	*0.09*
Er	0.68	*0.06*	0.64	*0.05*	0.68	*0.12*	0.70	*0.09*	0.74	*0.06*
Yb	1.11	*0.08*	1.03	*0.07*	1.04	*0.13*	1.18	*0.13*	1.18	*0.1*
Lu	0.19	*0.01*	0.18	*0.02*	0.18	*0.02*	0.20	*0.02*	0.20	*0.01*
Hf	0.22	*0.06*	0.23	*0.04*	0.22	*0.04*	0.21	*0.02*	0.21	*0.04*
Pb	0.04	*0.04*	0.07	*0.08*	0.10	*0.06*	0.04	*0.04*	0.05	*0.07*
Th	0.10	*0.10*	0.10	*0.07*	0.28	*0.20*	0.10	*0.07*	0.11	*0.08*
U	0.03	*0.03*	0.05	*0.06*	0.15	*0.13*	0.05	*0.05*	0.02	*0.02*

Table 3 (Continued)

Sample	B14-046		B14-047		B14-048		B14-049		B14-050c	
Depth (m)	1183		1033		912		808		704	
Mg#	59.4		62.6		61.7		61.8		69	
SiO2	52.32	*0.17*	53.36	*0.19*	53.21	*0.17*	52.99	*0.19*	53.74	*0.52*
TiO2	0.26	*0.08*	0.29	*0.11*	0.34	*0.12*	0.26	*0.07*	0.16	*0.07*
Al2O3	0.72	*0.06*	0.6	*0.07*	0.63	*0.05*	0.65	*0.08*	0.62	*0.04*
Cr2O3	0.02	*0.02*	0.01	*0.02*	0.01	*0.01*	0.01	*0.01*	0.1	*0.02*
FeO	24.87	*0.45*	23.06	*0.3*	23.74	*0.37*	23.6	*0.79*	19.58	*0.28*
MnO	0.49	*0.02*	0.46	*0.02*	0.48	*0.01*	0.47	*0.02*	0.46	*0.02*
MgO	20.38	*0.23*	21.72	*0.23*	21.49	*0.2*	21.39	*0.36*	24.42	*0.32*
CaO	1.15	*0.28*	1.22	*0.38*	1.18	*0.39*	1.48	*0.8*	0.94	*0.09*
Na2O	0	*0.01*	0	*0.01*	0.02	*0.02*	0.02	*0.02*	0.01	*0.01*
Total	100.21	*0.44*	100.72	*0.37*	101.09	*0.31*	100.88	*0.36*	100.03	*0.8*
n	6		15		16		16		30	
Sc	43.69	*3.16*	39.84	*1.83*	40.05	*2.18*	40.57	*2.2*	33.44	*2.3*
Ti	1023.74	*47.23*	982.06	*13.69*	1049.6	*19.81*	1000.31	*13.59*	529.12	*2.22*
V	206.23	*9.41*	191.14	*11.98*	202.04	*9.91*	204.64	*12.86*	108.35	*6.37*
Cr	85.54	*10.46*	70.69	*5.63*	89.01	*6.53*	77.4	*4*	611.55	*35.74*
Mn	2847.21	*17.86*	2805.82	*23.12*	2831.66	*20.27*	2827.57	*24.01*	2682.95	*17.84*
Cu	1.58	*2.16*	0.54	*0.06*	0.72	*0.42*	0.53	*0.13*	0.7	*0.29*
Zn	262.3	*8.1*	234.85	*5.79*	235.29	*5.16*	239.47	*6.35*	284.83	*6.27*
Sr	0.37	*0.17*	0.23	*0.16*	0.19	*0.2*	0.2	*0.07*	0.66	*1.52*
Y	6.9	*0.89*	6.83	*0.58*	4.98	*0.45*	5.47	*0.46*	1.92	*0.18*
Zr	8.03	*1.39*	7.39	*1.67*	6.59	*1.01*	8.79	*2.31*	1.9	*0.27*
Nb	0.02	*0.01*	0.04	*0.05*	0.02	*0.02*	0.03	*0.02*	0.04	*0.05*
Ba	0.17	*0.27*	0.05	*0.07*	0.08	*0.14*	0.1	*0.25*	0.31	*0.47*
La	0.62	*0.68*	0.47	*0.7*	0.12	*0.14*	0.14	*0.21*	0.02	*0.02*
Ce	1.37	*1.02*	1.07	*1.16*	0.37	*0.33*	0.41	*0.4*	0.07	*0.07*
Pr	0.17	*0.08*	0.13	*0.09*	0.06	*0.03*	0.07	*0.03*	0.01	*0.01*
Nd	0.8	*0.33*	0.65	*0.24*	0.33	*0.13*	0.4	*0.14*	0.08	*0.05*
Sm	0.3	*0.1*	0.27	*0.07*	0.16	*0.03*	0.19	*0.05*	0.04	*0.02*
Eu	0.04	*0.01*	0.03	*0.01*	0.03	*0.01*	0.03	*0.01*	0.01	*0.01*
Gd	0.52	*0.13*	0.47	*0.08*	0.33	*0.05*	0.38	*0.06*	0.1	*0.03*
Dy	0.99	*0.18*	0.92	*0.1*	0.66	*0.07*	0.73	*0.09*	0.23	*0.03*
Er	0.93	*0.11*	0.9	*0.09*	0.66	*0.06*	0.73	*0.05*	0.27	*0.04*
Yb	1.43	*0.1*	1.39	*0.11*	1.12	*0.08*	1.22	*0.09*	0.47	*0.06*
Lu	0.25	*0.01*	0.23	*0.02*	0.19	*0.02*	0.2	*0.01*	0.08	*0.01*
Hf	0.27	*0.03*	0.26	*0.05*	0.23	*0.03*	0.25	*0.04*	0.07	*0.02*
Pb	0.09	*0.04*	0.07	*0.07*	b.d.	*b.d.*	0.06	*0.03*	0.1	*0.1*
Th	0.19	*0.08*	0.22	*0.2*	0.1	*0.09*	0.16	*0.11*	0.04	*0.06*
U	0.1	*0.12*	0.11	*0.17*	0.03	*0.04*	0.04	*0.05*	0.01	*0.01*

Table 3 (Continued)

Sample	B14-051		B14-052		B14-053a	
Depth (m)	543		407		137	
Mg#	63.8		65.6		70.9	
SiO2	53.03	*0.23*	53.5	*0.59*	54.24	*0.45*
TiO2	0.13	*0.05*	0.13	*0.1*	0.2	*0.11*
Al2O3	0.8	*0.07*	0.77	*0.13*	0.87	*0.06*
Cr2O3	0.04	*0.01*	0.06	*0.02*	0.24	*0.05*
FeO	22.28	*0.88*	21.53	*0.39*	18.24	*0.48*
MnO	0.44	*0.04*	0.42	*0.02*	0.35	*0.02*
MgO	22.03	*0.42*	23.02	*0.2*	24.91	*0.41*
CaO	1.46	*0.86*	1.11	*0.24*	1.5	*0.74*
Na2O	0.01	*0.01*	0	*0.01*	0.01	*0.01*
Total	100.21	*0.68*	100.54	*0.74*	100.57	*0.6*
n	7		26		26	
Sc	39.06	*0.84*	36.34	*2.42*	35.12	*1.41*
Ti	596.93	*18.33*	529.41	*9.43*	653.16	*16.48*
V	165.36	*8.35*	177.36	*20.98*	175.41	*8.97*
Cr	256.16	*32.76*	334.07	*94.03*	1560.01	*191*
Mn	2532.98	*32.22*	2497.66	*32.78*	2052.58	*17.44*
Cu	5.42	*13.12*	0.53	*0.09*	0.68	*0.47*
Zn	235.96	*5.83*	217.34	*6.28*	184.12	*6.5*
Sr	0.58	*0.6*	0.26	*0.14*	0.36	*0.09*
Y	6.4	*0.34*	8.86	*0.49*	6.03	*0.47*
Zr	6	*2.17*	5.58	*1.29*	7.45	*1.98*
Nb	0.02	*0.01*	0.01	*0.01*	0.03	*0.03*
Ba	0.39	*0.66*	0.03	*0.05*	0.02	*0.01*
La	0.24	*0.13*	0.31	*0.17*	0.18	*0.21*
Ce	0.8	*0.28*	1.13	*0.35*	0.7	*0.39*
Pr	0.13	*0.04*	0.19	*0.05*	0.14	*0.04*
Nd	0.73	*0.2*	1.08	*0.28*	0.83	*0.19*
Sm	0.28	*0.09*	0.43	*0.1*	0.34	*0.07*
Eu	0.04	*0.01*	0.04	*0.01*	0.04	*0.01*
Gd	0.46	*0.06*	0.7	*0.09*	0.51	*0.09*
Dy	0.83	*0.08*	1.19	*0.09*	0.88	*0.1*
Er	0.82	*0.04*	1.14	*0.07*	0.75	*0.08*
Yb	1.27	*0.06*	1.72	*0.13*	1.08	*0.07*
Lu	0.21	*0.01*	0.28	*0.02*	0.17	*0.01*
Hf	0.17	*0.1*	0.17	*0.07*	0.21	*0.09*
Pb	0.1	*0.18*	0.05	*0.02*	0.05	*0.02*
Th	0.1	*0.08*	0.12	*0.05*	0.15	*0.06*
U	0.04	*0.05*	0.04	*0.06*	0.01	*0.01*

Table 4
Clinopyroxene major element composition by EPMA (ox wt.%) and trace element composition by LA-ICP-MS (ppm)

Sample	B14-014		B14-015		B14-016		B14-017		B14-018	
Depth (m)	2503		2320		2252		2187		2098	
Mg#	69.4		75.9		78.2		75.4		74.0	
SiO2	50.99	*0.23*	51.58	*0.65*	52.00	*0.26*	51.79	*0.49*	51.58	*0.40*
TiO2	0.54	*0.06*	0.47	*0.04*	0.36	*0.03*	0.46	*0.06*	0.52	*0.04*
Al2O3	1.78	*0.08*	1.70	*0.19*	1.58	*0.13*	1.69	*0.25*	1.73	*0.10*
Cr2O3	0.02	*0.01*	0.12	*0.02*	0.18	*0.02*	0.11	*0.01*	0.24	*0.02*
FeO	10.87	*0.83*	8.51	*0.45*	7.70	*0.43*	8.71	*0.66*	9.33	*0.62*
MnO	0.28	*0.02*	0.24	*0.02*	0.21	*0.03*	0.24	*0.02*	0.24	*0.03*
MgO	13.86	*0.31*	15.04	*0.23*	15.50	*0.29*	15.01	*0.35*	14.89	*0.55*
CaO	20.63	*1.00*	21.19	*0.85*	21.47	*0.69*	21.19	*1.06*	20.54	*1.13*
Na2O	0.27	*0.03*	0.28	*0.03*	0.27	*0.02*	0.29	*0.03*	0.30	*0.03*
Total	99.25	*0.31*	99.12	*0.75*	99.26	*0.32*	99.49	*0.52*	99.37	*0.53*
n	22		18		13		22		12	
Sc	114.52	*2.49*	103.70	*2.13*	103.54	*3.79*	105.91	*2.43*	108.17	*4.08*
Ti	1701.63	*154.50*	1515.09	*163.93*	1080.01	*61.48*	1424.77	*170.97*	1592.73	*121.97*
V	451.34	*16.96*	363.96	*16.14*	323.07	*9.09*	362.49	*10.54*	463.42	*19.11*
Cr	112.12	*7.91*	729.45	*95.30*	1185.09	*56.76*	662.80	*37.80*	1587.41	*122.39*
Mn	1772.78	*92.67*	1494.92	*99.97*	1387.22	*57.33*	1523.73	*129.89*	1468.92	*75.43*
Cu	7.40	*14.90*	3.58	*7.51*	0.95	*0.26*	0.93	*0.36*	0.82	*0.08*
Zn	73.83	*6.10*	57.31	*6.39*	43.58	*3.95*	56.27	*7.52*	56.65	*4.85*
Sr	11.86	*0.62*	12.67	*0.56*	12.95	*0.85*	12.51	*0.89*	12.13	*0.48*
Y	23.78	*1.21*	20.70	*0.72*	15.78	*0.40*	19.24	*1.02*	26.66	*1.92*
Zr	34.44	*5.84*	30.59	*4.83*	22.77	*2.96*	30.54	*5.67*	41.02	*10.24*
Nb	0.07	*0.03*	0.14	*0.02*	0.15	*0.04*	0.10	*0.03*	0.09	*0.05*
Ba	0.22	*0.18*	0.40	*0.50*	0.51	*0.78*	0.24	*0.23*	0.15	*0.10*
La	3.22	*0.17*	3.37	*0.25*	2.30	*0.11*	3.24	*0.37*	3.75	*0.29*
Ce	12.72	*0.68*	13.23	*0.56*	8.83	*0.26*	12.16	*0.97*	16.55	*1.21*
Pr	2.17	*0.12*	2.19	*0.11*	1.44	*0.05*	1.97	*0.14*	2.90	*0.24*
Nd	11.55	*0.64*	11.49	*0.55*	7.72	*0.16*	10.22	*0.67*	15.80	*1.30*
Sm	3.56	*0.18*	3.29	*0.20*	2.35	*0.09*	2.99	*0.19*	4.67	*0.42*
Eu	0.65	*0.04*	0.65	*0.04*	0.55	*0.02*	0.62	*0.03*	0.72	*0.04*
Gd	4.06	*0.27*	3.54	*0.21*	2.60	*0.09*	3.29	*0.20*	4.92	*0.39*
Dy	4.54	*0.28*	3.90	*0.18*	3.01	*0.13*	3.66	*0.23*	5.22	*0.42*
Er	2.60	*0.18*	2.22	*0.12*	1.67	*0.07*	2.04	*0.13*	2.76	*0.20*
Yb	2.52	*0.14*	2.10	*0.11*	1.63	*0.08*	1.97	*0.13*	2.47	*0.17*
Lu	0.35	*0.03*	0.30	*0.02*	0.22	*0.01*	0.27	*0.02*	0.33	*0.03*
Hf	1.15	*0.21*	0.90	*0.19*	0.72	*0.14*	0.94	*0.22*	1.16	*0.38*
Pb	0.29	*0.21*	0.25	*0.08*	0.36	*0.34*	0.23	*0.05*	0.20	*0.03*
Th	0.22	*0.14*	0.22	*0.08*	0.19	*0.05*	0.23	*0.09*	0.19	*0.06*
U	0.06	*0.06*	0.03	*0.02*	0.05	*0.02*	0.07	*0.06*	0.03	*0.03*

Table 4 (Continued)

Sample	B14-019		B14-020		B14-021		B14-022		B14-023	
Depth (m)	1998		1941		1843		1750		1728	
Mg#	67.9		67.8		64.4		65.4		66.2	
SiO2	51.04	*0.22*	51.08	*0.57*	52.69	*0.28*	50.99	*0.47*	51.05	*0.30*
TiO2	0.43	*0.04*	0.41	*0.02*	0.40	*0.13*	0.42	*0.08*	0.45	*0.08*
Al2O3	1.60	*0.11*	1.52	*0.13*	1.36	*0.07*	1.46	*0.23*	1.40	*0.08*
Cr2O3	0.07	*0.01*	0.06	*0.01*	0.01	*0.02*	0.02	*0.01*	0.03	*0.01*
FeO	11.42	*0.73*	11.53	*0.97*	12.36	*0.5*	12.25	*1.35*	11.84	*0.93*
MnO	0.29	*0.04*	0.29	*0.03*	0.30	*0.02*	0.30	*0.03*	0.31	*0.03*
MgO	13.58	*0.25*	13.59	*0.33*	12.54	*0.21*	13.01	*0.66*	13.00	*0.31*
CaO	20.66	*0.82*	20.40	*1.18*	21.33	*0.35*	20.40	*1.76*	20.91	*1.17*
Na2O	0.27	*0.03*	0.27	*0.03*	0.26	*0.03*	0.25	*0.03*	0.26	*0.02*
Total	99.36	*0.38*	99.14	*0.87*	101.24	*0.5*	99.10	*0.59*	99.25	*0.43*
n	20		15		15		21		17	
Sc	129.75	*5.09*	121.54	*4.18*	140.09	*6.67*	131.72	*3.65*	127.78	*6.13*
Ti	1373.08	*60.71*	1311.61	*86.52*	1403.10	*194.25*	1349.95	*165.41*	1429.14	*338.00*
V	600.94	*23.74*	586.78	*35.56*	779.50	*31.91*	740.06	*35.58*	674.73	*51.95*
Cr	390.78	*19.14*	310.85	*23.00*	41.13	*1.8*	85.10	*4.14*	112.51	*9.14*
Mn	1945.61	*141.97*	1880.07	*104.90*	2151.45	*213.64*	2008.50	*243.35*	1992.82	*279.86*
Cu	0.95	*0.38*	0.73	*0.12*	2.50	*3.62*	1.18	*0.72*	0.66	*0.17*
Zn	74.52	*8.68*	72.39	*6.48*	91.51	*15.67*	83.01	*16.06*	90.43	*20.96*
Sr	11.95	*0.39*	11.67	*0.59*	12.00	*0.56*	11.53	*0.76*	15.35	*17.01*
Y	14.54	*0.59*	15.86	*0.48*	28.65	*1.34*	28.04	*1.14*	29.96	*2.10*
Zr	15.80	*0.78*	23.52	*1.28*	51.66	*4.39*	36.65	*4.52*	56.26	*2.25*
Nb	0.13	*0.02*	0.21	*0.02*	0.05	*0.03*	0.04	*0.05*	0.04	*0.03*
Ba	0.29	*0.35*	0.17	*0.15*	0.77	*0.85*	0.43	*0.45*	11.31	*45.49*
La	1.38	*0.07*	1.60	*0.10*	4.32	*0.29*	3.33	*0.19*	4.84	*0.38*
Ce	5.50	*0.23*	6.80	*0.30*	16.59	*0.88*	13.02	*0.57*	19.17	*1.36*
Pr	0.96	*0.03*	1.20	*0.04*	2.72	*0.12*	2.21	*0.09*	3.18	*0.24*
Nd	5.52	*0.25*	6.69	*0.34*	14.35	*0.59*	12.18	*0.61*	16.44	*1.23*
Sm	1.85	*0.12*	2.18	*0.09*	4.25	*0.21*	3.84	*0.19*	4.74	*0.29*
Eu	0.50	*0.03*	0.53	*0.03*	0.74	*0.05*	0.74	*0.06*	0.71	*0.06*
Gd	2.27	*0.08*	2.56	*0.11*	4.73	*0.24*	4.45	*0.19*	5.10	*0.38*
Dy	2.73	*0.11*	3.02	*0.14*	5.35	*0.2*	5.17	*0.23*	5.64	*0.33*
Er	1.57	*0.08*	1.75	*0.09*	3.08	*0.13*	3.02	*0.11*	3.14	*0.21*
Yb	1.57	*0.08*	1.72	*0.07*	2.99	*0.15*	3.02	*0.16*	3.05	*0.24*
Lu	0.22	*0.02*	0.24	*0.01*	0.42	*0.02*	0.42	*0.02*	0.42	*0.04*
Hf	0.60	*0.05*	0.80	*0.07*	1.64	*0.13*	1.23	*0.11*	1.72	*0.08*
Pb	0.11	*0.05*	0.14	*0.03*	0.45	*0.32*	0.28	*0.11*	0.28	*0.11*
Th	0.13	*0.08*	0.23	*0.06*	0.79	*0.82*	0.40	*0.20*	0.80	*1.27*
U	0.04	*0.01*	0.06	*0.02*	0.14	*0.05*	0.09	*0.03*	0.12	*0.05*

Table 4 (Continued)

Sample	B14-024		B14-025		B14-026		B14-044		B14-045	
Depth (m)	1700		1641		1535		1529		1385	
Mg#	66.8		67.6		69.0		68.9		67.7	
SiO2	50.93	*0.37*	51.53	*0.25*	51.75	*0.31*	51.57	*0.33*	52.14	*0.28*
TiO2	0.44	*0.06*	0.43	*0.06*	0.46	*0.07*	0.46	*0.08*	0.45	*0.09*
Al2O3	1.34	*0.06*	1.32	*0.11*	1.40	*0.17*	1.34	*0.10*	1.47	*0.07*
Cr2O3	0.03	*0.01*	0.03	*0.01*	0.02	*0.01*	0.02	*0.01*	0.02	*0.02*
FeO	11.73	*0.53*	11.32	*0.54*	10.99	*0.91*	10.94	*0.95*	11.19	*0.79*
MnO	0.30	*0.02*	0.28	*0.03*	0.27	*0.03*	0.27	*0.03*	0.26	*0.02*
MgO	13.25	*0.31*	13.23	*0.15*	13.73	*0.25*	13.62	*0.33*	13.16	*0.19*
CaO	20.68	*0.58*	21.28	*0.73*	20.92	*1.09*	21.13	*1.07*	21.12	*0.68*
Na2O	0.28	*0.03*	0.27	*0.02*	0.25	*0.03*	0.25	*0.02*	0.27	*0.03*
Total	98.99	*0.47*	99.69	*0.42*	99.79	*0.50*	99.61	*0.32*	100.09	*0.36*
n	2		13		15		20		18	
Sc	122.49	*9.30*	123.55	*4.98*	114.84	*3.36*	121.62	*4.13*	111.56	*2.91*
Ti	1438.12	*58.81*	1344.68	*249.23*	1487.58	*332.49*	1594.63	*252.99*	1549.66	*33.26*
V	672.81	*52.19*	677.11	*37.65*	616.47	*36.16*	636.14	*19.01*	612.03	*17.76*
Cr	113.23	*28.55*	114.16	*12.57*	62.38	*7.35*	68.20	*3.40*	175.13	*15.29*
Mn	1988.21	*153.56*	1858.60	*104.29*	1846.02	*282.40*	1851.92	*177.00*	1779.43	*24.82*
Cu	0.71	*0.17*	0.67	*0.15*	4.25	*4.46*	0.88	*0.16*	1.96	*2.71*
Zn	94.95	*12.98*	78.53	*7.18*	87.60	*20.60*	87.43	*15.69*	84.65	*9.45*
Sr	11.00	*0.21*	11.21	*0.53*	11.10	*0.82*	11.64	*1.03*	11.49	*0.63*
Y	34.15	*0.59*	31.09	*1.62*	29.73	*1.24*	32.40	*1.15*	34.21	*1.86*
Zr	70.24	*7.29*	74.78	*9.70*	60.37	*8.54*	60.56	*9.23*	62.13	*9.21*
Nb	0.03	*0.01*	0.06	*0.04*	0.08	*0.08*	0.11	*0.30*	0.04	*0.02*
Ba	0.51	*0.07*	0.30	*0.24*	0.42	*0.35*	0.32	*0.39*	0.47	*0.53*
La	4.04	*0.12*	5.44	*0.38*	5.48	*0.27*	6.53	*0.79*	5.64	*0.59*
Ce	18.26	*0.07*	22.34	*1.41*	21.67	*0.90*	23.69	*1.20*	22.85	*1.16*
Pr	3.26	*0.08*	3.68	*0.21*	3.52	*0.17*	3.75	*0.17*	3.84	*0.18*
Nd	17.41	*0.54*	18.64	*1.08*	17.52	*0.75*	19.08	*0.77*	19.64	*0.88*
Sm	5.34	*0.01*	5.20	*0.28*	4.84	*0.21*	5.32	*0.26*	5.54	*0.28*
Eu	0.69	*0.01*	0.72	*0.06*	0.72	*0.05*	0.75	*0.04*	0.82	*0.04*
Gd	5.63	*0.11*	5.47	*0.26*	5.10	*0.23*	5.60	*0.20*	5.91	*0.34*
Dy	6.48	*0.05*	5.90	*0.37*	5.62	*0.23*	6.22	*0.26*	6.41	*0.41*
Er	3.54	*0.11*	3.27	*0.15*	3.16	*0.16*	3.50	*0.15*	3.64	*0.22*
Yb	3.39	*0.21*	3.04	*0.21*	3.02	*0.16*	3.43	*0.14*	3.52	*0.17*
Lu	0.46	*0.01*	0.42	*0.04*	0.42	*0.03*	0.47	*0.02*	0.49	*0.03*
Hf	2.14	*0.35*	2.18	*0.38*	1.86	*0.37*	1.83	*0.31*	1.92	*0.33*
Pb	0.33	*0.05*	0.27	*0.06*	0.38	*0.22*	0.34	*0.12*	0.49	*0.49*
Th	0.54	*0.17*	0.34	*0.07*	0.36	*0.12*	0.53	*0.43*	0.42	*0.24*
U	0.09	*0.04*	0.09	*0.04*	0.07	*0.05*	0.19	*0.25*	0.12	*0.15*

Table 4 (Continued)

Sample	B14-046		B14-047		B14-048		B14-049		B14-050c	
Depth (m)	1183		1033		912		808		704	
Mg#	68.0		71.8		70.5		70.2		77.8	
SiO2	52.15	*0.25*	52.86	*0.23*	52.77	*0.3*	52.41	*0.23*	52.87	*1.02*
TiO2	0.43	*0.1*	0.51	*0.17*	0.46	*0.09*	0.44	*0.14*	0.31	*0.09*
Al2O3	1.46	*0.11*	1.4	*0.05*	1.42	*0.09*	1.44	*0.09*	1.03	*0.06*
Cr2O3	0.03	*0.01*	0.04	*0.02*	0.03	*0.01*	0.02	*0.02*	0.2	*0.04*
FeO	11.15	*0.77*	9.7	*0.4*	10.34	*0.68*	10.44	*0.76*	7.63	*0.24*
MnO	0.27	*0.02*	0.23	*0.01*	0.25	*0.02*	0.25	*0.02*	0.22	*0.01*
MgO	13.31	*0.36*	13.88	*0.19*	13.84	*0.26*	13.82	*0.22*	14.93	*0.28*
CaO	21.19	*0.82*	21.6	*0.28*	21.33	*0.69*	21.22	*0.69*	21.97	*0.31*
Na2O	0.26	*0.02*	0.26	*0.02*	0.25	*0.02*	0.26	*0.03*	0.23	*0.02*
Total	100.26	*0.37*	100.46	*0.08*	100.67	*0.48*	100.31	*0.39*	99.37	*1.49*
n	19		4		23		18		4	
Sc	107.83	*4.08*	111.14	*1.65*	107.22	*2.5*	108.53	*2.8*	110.43	
Ti	1573.18	*188.80*	1648.12	*20.41*	1520.03	*62.77*	1555.24	*79.68*	957.66	*3.08*
V	551.12	*25.33*	574.61	*8.13*	543.69	*28.95*	564.44	*35.78*	319.1	*28.22*
Cr	190.33	*22.93*	182.86	*24.26*	201.9	*16.82*	191.35	*24.7*	1383.57	*24.96*
Mn	1725.92	*211.05*	1684.22	*12.36*	1607.81	*24.1*	1662.18	*22.24*	1627.42	*208.21*
Cu	4.01	*6.22*	1.44	*1.19*	1.16	*1.38*	2.74	*2.69*	1.64	*68.77*
Zn	87.21	*18.55*	77.2	*5.54*	71.29	*7.24*	74.42	*7.25*	94.44	*1.83*
Sr	11.44	*0.92*	11.52	*0.33*	11.46	*0.66*	11.18	*0.8*	12.22	*40.2*
Y	39.27	*1.7*	43.01	*0.93*	30.41	*0.95*	32.81	*1.71*	*15.45*	*0.87*
Zr	66.42	*9.28*	69.35	*8.16*	55.27	*8.73*	64.83	*14.3*	31.47	*0.17*
Nb	0.07	*0.05*	0.07	*0.04*	0.06	*0.03*	0.1	*0.11*	0.47	*5.26*
Ba	0.65	*0.73*	0.25	*0.07*	0.54	*1.03*	0.39	*0.32*	7.07	*0.5*
La	6.61	*0.42*	5.84	*0.46*	4.91	*0.39*	4.59	*0.9*	1.56	*13.83*
Ce	26.8	*1.46*	26.78	*1.13*	19.81	*0.88*	19.59	*1.7*	6.92	*0.23*
Pr	4.49	*0.22*	4.83	*0.08*	3.34	*0.11*	3.46	*0.19*	1.29	*0.68*
Nd	23.35	*1.14*	26.1	*0.21*	17.4	*0.65*	18.27	*0.89*	7.42	*0.12*
Sm	6.51	*0.37*	7.46	*0.15*	4.92	*0.2*	5.35	*0.24*	2.36	*0.4*
Eu	0.72	*0.04*	0.76	*0.03*	0.68	*0.04*	0.64	*0.04*	0.4	*0.21*
Gd	6.89	*0.26*	7.83	*0.19*	5.27	*0.23*	5.56	*0.26*	2.54	*0.04*
Dy	7.45	*0.32*	8.39	*0.16*	5.76	*0.24*	6.17	*0.26*	2.93	*0.06*
Er	4.15	*0.2*	4.54	*0.11*	3.22	*0.11*	3.43	*0.19*	1.64	*0.1*
Yb	4.04	*0.2*	4.08	*0.08*	3.11	*0.14*	3.31	*0.21*	1.5	*0.06*
Lu	0.55	*0.03*	0.55	*0.03*	0.43	*0.02*	0.46	*0.03*	0.21	*0.08*
Hf	1.93	*0.43*	1.88	*0.24*	1.54	*0.34*	1.94	*0.6*	0.07	*0.01*
Pb	0.38	*0.18*	0.4	*0.22*	0.28	*0.06*	0.33	*0.12*	0.1	*0.02*
Th	0.39	*0.22*	0.32	*0.14*	0.42	*0.21*	0.41	*0.34*	0.25	*0.11*
U	0.08	*0.05*	0.06	*0.01*	0.09	*0.1*	0.18	*0.14*	0.07	*0.23*

Table 4 (Continued)

Sample	B14-051		B14-052		B14-053a	
Depth (m)	543		407		137	
Mg#	71.0		73.8		77.4	
SiO2	52.19	*0.33*	52.82	*0.53*	53.14	*0.3*
TiO2	0.43	*0.15*	0.52	*0.14*	0.49	*0.11*
Al2O3	1.59	*0.16*	1.44	*0.16*	1.69	*0.07*
Cr2O3	0.11	*0.03*	0.11	*0.03*	0.42	*0.06*
FeO	9.96	*0.64*	9.02	*0.45*	7.68	*0.39*
MnO	0.23	*0.03*	0.23	*0.01*	0.19	*0.02*
MgO	13.71	*0.18*	14.28	*0.26*	14.77	*0.1*
CaO	21.44	*0.52*	21.67	*0.46*	21.78	*0.5*
Na2O	0.27	*0.02*	0.27	*0.03*	0.31	*0.01*
Total	99.94	*0.47*	100.35	*0.61*	100.48	*0.55*
n	22		10		6	
Sc	94.29	*4.28*	99.49	*5.65*	107.12	*3.83*
Ti	1454.21	*55.14*	1397.06	*67.42*	1716.46	*29.7*
V	429.03	*44.67*	485.07	*37.63*	522.87	*32.5*
Cr	671.93	*194.91*	837.97	*258.57*	3712.07	*740.75*
Mn	1654.13	*40.27*	1663.77	*44.51*	1543.35	*37.99*
Cu	8.1	*10.73*	2.92	*2.72*	1.39	*0.82*
Zn	85.65	*18.34*	85.77	*18.39*	72.7	*16.56*
Sr	12.13	*0.93*	11.85	*2.39*	16.46	*1.08*
Y	36.38	*2.44*	47.68	*5.55*	40.81	*3.75*
Zr	64.32	*15.02*	54.67	*13.46*	53.6	*13.58*
Nb	0.07	*0.06*	0.07	*0.02*	0.1	*0.03*
Ba	0.98	*1.44*	0.81	*1.42*	0.34	*0.27*
La	6.22	*0.44*	11.09	*0.85*	5.45	*0.54*
Ce	25.65	*1.33*	44.17	*2.82*	26.79	*1.72*
Pr	4.29	*0.23*	7.17	*0.62*	4.96	*0.45*
Nd	21.91	*1.29*	35.28	*3.72*	26.09	*3.17*
Sm	6.15	*0.56*	9.32	*1.31*	7.57	*0.92*
Eu	0.66	*0.05*	0.75	*0.05*	0.96	*0.05*
Gd	6.34	*0.45*	8.93	*1.27*	7.5	*0.97*
Dy	6.87	*0.51*	9.29	*1.29*	7.9	*0.97*
Er	3.85	*0.31*	4.98	*0.55*	4.15	*0.39*
Yb	3.72	*0.29*	4.51	*0.4*	3.79	*0.34*
Lu	0.52	*0.03*	0.6	*0.06*	0.51	*0.05*
Hf	1.54	*0.74*	1.71	*1.06*	1.17	*0.3*
Pb	0.53	*0.36*	0.57	*0.29*	0.38	*0.1*
Th	0.5	*0.32*	0.57	*0.31*	0.64	*0.32*
U	0.14	*0.14*	0.16	*0.22*	0.06	*0.05*

Table 5
Plagioclase major element composition by EPMA (ox wt.%) and trace element composition by LA-ICP-MS (ppm)

Sample	B14-014		B14-015		B14-016		B14-017		B14-018	
Depth (m)	2503		2320		2252		2187		2098	
An	62.7		71.52		72.86		70.45		70.93	
SiO2	52.47	*0.32*	50.13	*0.56*	49.97	*0.50*	50.82	*0.29*	49.89	*0.41*
TiO2	0.03	*0.02*	0.04	*0.02*	0.02	*0.02*	0.03	*0.02*	0.03	*0.02*
Al2O3	29.90	*0.21*	31.39	*0.39*	31.80	*0.35*	31.54	*0.21*	31.49	*0.27*
Cr2O3	0.00	*0.01*	0.01	*0.01*	0.00	*0.01*	0.01	*0.01*	0.01	*0.01*
FeO	0.48	*0.05*	0.48	*0.05*	0.43	*0.05*	0.46	*0.05*	0.50	*0.04*
MnO	0.01	*0.02*	0.01	*0.01*	0.01	*0.01*	0.01	*0.01*	0.01	*0.01*
MgO	0.02	*0.01*	0.02	*0.01*	0.02	*0.01*	0.02	*0.01*	0.02	*0.01*
CaO	12.76	*0.20*	14.50	*0.40*	14.69	*0.36*	14.38	*0.23*	14.40	*0.24*
Na2O	4.01	*0.15*	3.05	*0.22*	2.89	*0.20*	3.20	*0.17*	3.13	*0.15*
K2O	0.28	*0.03*	0.22	*0.03*	0.20	*0.04*	0.20	*0.02*	0.21	*0.03*
Total	99.97	*0.32*	99.86	*0.27*	100.04	*0.30*	100.66	*0.30*	99.65	*0.30*
Molar Ca/Na	7.03		10.53		11.24		9.93		10.17	
n	19		20		16		20		19	
Sc	4.57	*0.14*	6.45	*0.31*	4.10	*0.12*	4.07	*0.13*	4.06	*0.15*
V	2.75	*0.45*	2.80	*0.29*	2.03	*0.44*	2.56	*0.44*	3.86	*0.61*
Cr	1.86	*0.33*	1.25	*0.31*	1.87	*0.82*	1.78	*0.27*	1.77	*0.40*
Ti	124.53	*9.57*	112.47	*18.71*	94.78	*6.25*	101.58	*12.29*	128.29	*18.05*
Mn	14.54	*1.13*	14.56	*1.34*	12.94	*1.92*	15.52	*3.05*	14.23	*1.76*
Cu	1.07	*1.94*	b.d.	*b.d.*	1.07	*3.11*	0.80	*1.84*	b.d.	*b.d.*
Zn	6.63	*0.38*	4.61	*0.51*	3.76	*0.67*	4.42	*0.78*	4.53	*0.51*
Rb	0.67	*0.28*	1.00	*0.62*	0.83	*0.28*	0.46	*0.13*	0.58	*0.42*
Sr	451.88	*7.49*	434.84	*14.26*	455.72	*7.53*	452.27	*7.75*	480.76	*14.51*
Y	0.24	*0.01*	0.27	*0.02*	0.19	*0.02*	0.24	*0.02*	0.37	*0.04*
Zr	0.02	*0.01*	0.05	*0.05*	0.02	*0.01*	0.02	*0.02*	0.06	*0.05*
Ba	115.09	*5.40*	112.67	*11.37*	99.90	*4.05*	106.91	*4.56*	138.96	*11.64*
La	2.76	*0.65*	4.01	*0.70*	3.53	*0.21*	3.72	*0.68*	5.09	*0.69*
Ce	4.06	*0.82*	5.74	*0.83*	4.67	*0.20*	5.29	*0.67*	7.74	*0.89*
Pr	0.39	*0.06*	0.51	*0.06*	0.40	*0.02*	0.48	*0.04*	0.75	*0.08*
Nd	1.31	*0.19*	1.71	*0.18*	1.22	*0.07*	1.54	*0.10*	2.54	*0.28*
Sm	0.17	*0.03*	0.19	*0.03*	0.13	*0.02*	0.15	*0.02*	0.31	*0.04*
Eu	0.61	*0.03*	0.61	*0.04*	0.49	*0.02*	0.57	*0.03*	0.67	*0.03*
Gd	0.10	*0.02*	0.11	*0.01*	0.08	*0.01*	0.09	*0.02*	0.16	*0.02*
Dy	0.05	*0.01*	0.06	*0.01*	0.04	*0.01*	0.05	*0.01*	0.08	*0.02*
Pb	2.20	*0.37*	2.51	*0.15*	1.91	*0.07*	2.44	*0.09*	2.96	*0.12*

Table 5 (Continued)

Sample	B14-019		B14-020		B14-021		B14-022		B14-023	
Depth (m)	1998		1941		1843		1750		1728	
An	59.95		59.04		55.24		57.42		57.79	
SiO2	52.93	*0.57*	53.66	*0.29*	53.62	*0.48*	53.38	*0.43*	53.84	*0.39*
TiO2	0.04	*0.02*	0.04	*0.02*	-	-	0.04	*0.02*	0.04	*0.02*
Al2O3	29.25	*0.34*	29.17	*0.14*	28.73	*0.30*	29.00	*0.24*	29.12	*0.16*
Cr2O3	0.01	*0.01*	0.00	*0.01*	0.00	*0.01*	0.00	*0.01*	0.00	*0.01*
FeO	0.50	*0.06*	0.47	*0.05*	0.38	*0.06*	0.39	*0.05*	0.38	*0.08*
MnO	0.01	*0.01*	0.01	*0.01*	0.00	*0.01*	0.01	*0.01*	0.01	*0.01*
MgO	0.03	*0.01*	0.02	*0.01*	0.01	*0.01*	0.02	*0.01*	0.02	*0.02*
CaO	11.99	*0.38*	11.82	*0.14*	11.27	*0.23*	11.58	*0.24*	11.61	*0.15*
Na2O	4.22	*0.22*	4.31	*0.12*	4.71	*0.16*	4.49	*0.17*	4.43	*0.13*
K2O	0.31	*0.03*	0.33	*0.02*	0.42	*0.13*	0.39	*0.04*	0.39	*0.06*
Total	99.29	*0.34*	99.85	*0.35*	99.14	*0.70*	99.29	*0.46*	99.84	*0.49*
Molar Ca/Na	6.28		6.06		5.29		5.70		5.79	
n	18		18		18		18		19	
Sc	4.09	*0.17*	4.03	*0.11*	4.10	*0.1*	7.76	*0.39*	7.12	*0.18*
V	4.13	*0.92*	3.73	*0.53*	4.78	*0.54*	4.35	*0.85*	4.75	*0.96*
Cr	2.02	*0.30*	1.63	*0.39*	1.68	*0.38*	1.38	*0.26*	1.53	*0.40*
Ti	149.13	*15.38*	143.11	*9.01*	149.06	*9.84*	141.49	*3.44*	142.89	*11.85*
Mn	12.66	*3.18*	11.47	*3.05*	11.69	*0.98*	12.44	*2.08*	14.80	*7.27*
Cu	b.d.	*b.d.*	b.d.	*b.d.*	b.d.	*b.d.*	b.d.	*b.d.*	b.d.	*b.d.*
Zn	6.98	*0.80*	6.98	*0.79*	7.88	*0.44*	7.77	*0.74*	8.32	*1.32*
Rb	2.48	*0.37*	2.47	*102.00*	1.58	*0.47*	1.32	*0.42*	1.52	*1.35*
Sr	513.04	*10.89*	519.86	*10.62*	508.67	*9.13*	482.17	*14.11*	481.90	*15.54*
Y	0.16	*0.04*	0.17	*0.03*	0.27	*0.04*	0.25	*0.03*	0.27	*0.03*
Zr	0.05	*0.04*	0.09	*0.21*	0.02	*0.02*	0.02	*0.02*	0.03	*0.02*
Ba	115.85	*5.71*	126.46	*6.78*	190.41	*9.5*	181.76	*10.32*	165.25	*11.52*
La	2.02	*0.08*	2.48	*0.13*	3.79	*0.77*	3.61	*0.79*	4.04	*0.97*
Ce	2.65	*0.11*	3.32	*0.17*	5.40	*0.92*	4.79	*0.84*	5.74	*1.24*
Pr	0.24	*0.01*	0.29	*0.02*	0.48	*0.07*	0.43	*0.06*	0.52	*0.09*
Nd	0.79	*0.06*	0.93	*0.09*	1.57	*0.22*	1.39	*0.17*	1.68	*0.25*
Sm	0.09	*0.02*	0.11	*0.03*	0.19	*0.03*	0.17	*0.04*	0.20	*0.03*
Eu	0.51	*0.03*	0.55	*0.02*	1.01	*0.05*	1.03	*0.05*	0.97	*0.04*
Gd	0.06	*0.02*	0.06	*0.02*	0.10	*0.02*	0.09	*0.02*	0.11	*0.02*
Dy	0.03	*0.01*	0.03	*0.01*	0.06	*0.01*	0.06	*0.01*	0.06	*0.01*
Pb	1.32	*0.08*	1.48	*0.08*	3.01	*0.1*	2.58	*0.11*	2.94	*0.26*

Table 5 (Continued)

Sample	B14-024		B14-025		B14-026		B14-044		B14-045	
Depth (m)	1700		1641		1535		1529		1385	
An	57.49		57.92		62.34		60.64		61.07	
SiO2	53.94	*0.51*	53.48	*0.32*	52.43	*0.49*	52.70	*0.38*	52.42	*0.43*
TiO2	0.04	*0.02*	0.04	*0.02*	0.03	*0.02*	0.04	*0.02*	0.04	*0.02*
Al2O3	29.22	*0.20*	29.02	*0.21*	29.96	*0.35*	29.50	*0.27*	29.52	*0.29*
Cr2O3	0.00	*0.01*	0.01	*0.01*	0.00	*0.00*	0.00	*0.01*	0.00	*0.00*
FeO	0.40	*0.06*	0.43	*0.04*	0.37	*0.04*	0.39	*0.05*	0.44	*0.06*
MnO	0.01	*0.01*	0.01	*0.02*	0.01	*0.01*	0.01	*0.01*	0.01	*0.01*
MgO	0.02	*0.01*	0.02	*0.01*	0.01	*0.01*	0.01	*0.01*	0.02	*0.01*
CaO	11.68	*0.20*	11.72	*0.18*	12.63	*0.37*	12.19	*0.28*	12.35	*0.29*
Na2O	4.53	*0.16*	4.45	*0.20*	4.01	*0.21*	4.15	*0.17*	4.14	*0.17*
K2O	0.37	*0.03*	0.39	*0.04*	0.31	*0.03*	0.33	*0.05*	0.32	*0.04*
Total	100.21	*0.53*	99.56	*0.32*	99.76	*0.19*	99.33	*0.29*	99.25	*0.28*
Molar Ca/Na	5.70		5.82		6.96		6.49		6.59	
n	20		18		16		20		20	
Sc	6.38	*0.22*	6.60	*0.24*	6.33	*0.30*	5.89	*0.24*	5.78	*0.21*
V	4.70	*0.80*	5.09	*0.45*	4.58	*1.11*	4.57	*0.59*	4.58	*0.67*
Cr	1.22	*0.28*	1.54	*0.32*	1.52	*0.27*	1.49	*0.42*	1.19	*0.33*
Ti	142.99	*7.01*	140.07	*7.84*	123.95	*13.53*	129.56	*11.01*	124.27	*7.56*
Mn	12.62	*2.83*	15.11	*4.96*	12.58	*1.08*	12.76	*1.14*	13.48	*2.04*
Cu	b.d.	*b.d.*	b.d.	*b.d.*	b.d.	*b.d.*	b.d.	*b.d.*	0.70	*1.69*
Zn	7.47	*0.71*	8.04	*0.94*	6.88	*0.85*	7.18	*0.60*	7.55	*0.43*
Rb	1.06	*0.36*	1.32	*0.48*	0.89	*0.37*	0.95	*0.46*	0.96	*0.47*
Sr	477.40	*12.63*	467.68	*13.70*	453.35	*18.62*	449.56	*11.16*	447.25	*11.54*
Y	0.31	*0.03*	0.27	*0.02*	0.32	*0.06*	0.31	*0.05*	0.33	*0.04*
Zr	0.02	*0.02*	0.04	*0.03*	0.03	*0.01*	0.03	*0.03*	0.03	*0.05*
Ba	166.10	*11.63*	162.06	*10.57*	177.70	*12.95*	187.01	*15.27*	178.20	*9.76*
La	3.88	*1.13*	3.11	*0.64*	5.11	*1.38*	4.50	*1.63*	4.35	*1.39*
Ce	5.72	*1.45*	4.58	*0.97*	7.21	*1.73*	6.48	*2.09*	6.51	*1.95*
Pr	0.53	*0.11*	0.43	*0.08*	0.63	*0.12*	0.59	*0.18*	0.59	*0.15*
Nd	1.76	*0.32*	1.46	*0.26*	1.99	*0.35*	1.86	*0.46*	1.95	*0.48*
Sm	0.22	*0.03*	0.19	*0.05*	0.23	*0.03*	0.23	*0.05*	0.24	*0.06*
Eu	0.98	*0.04*	0.98	*0.05*	0.99	*0.05*	0.98	*0.04*	1.02	*0.04*
Gd	0.13	*0.02*	0.11	*0.01*	0.13	*0.03*	0.12	*0.03*	0.13	*0.02*
Dy	0.06	*0.01*	0.06	*0.01*	0.07	*0.01*	0.06	*0.01*	0.07	*0.02*
Pb	2.93	*0.12*	2.96	*0.08*	3.68	*0.20*	4.09	*0.20*	3.81	*0.13*

Table 5 (Continued)

Sample	B14-046		B14-047		B14-048		B14-049		B14-050c	
Depth (m)	1183		1033		912		808		704	
An	64.36		62.91		63.47		64.69		67.34	
SiO2	51.72	*0.39*	52.28	*0.49*	52.08	*0.99*	51.63	*0.52*	51.23	*0.40*
TiO2	0.03	*0.02*	0.03	*0.02*	-	-	0.03	*0.02*	0.01	*0.01*
Al2O3	30.11	*0.26*	30.00	*0.34*	30.43	*0.33*	30.07	*0.35*	30.90	*0.23*
Cr2O3	0.01	*0.01*	0.00	*0.01*	0.00	*0.01*	0.00	*0.01*	0.00	*0.01*
FeO	0.42	*0.05*	0.37	*0.04*	0.37	*0.05*	0.37	*0.04*	0.29	*0.04*
MnO	0.01	*0.01*	0.01	*0.01*	0.00	*0.01*	0.01	*0.01*	0.01	*0.01*
MgO	0.02	*0.01*	0.01	*0.01*	0.01	*0.01*	0.01	*0.01*	0.01	*0.01*
CaO	12.96	*0.27*	12.71	*0.37*	12.91	*0.31*	12.97	*0.40*	13.62	*0.27*
Na2O	3.78	*0.16*	3.95	*0.19*	3.89	*0.15*	3.73	*0.22*	3.50	*0.15*
K2O	0.28	*0.04*	0.30	*0.03*	0.30	*0.03*	0.28	*0.02*	0.22	*0.02*
Total	99.34	*0.28*	99.67	*0.26*	100.00	*0.91*	99.09	*0.38*	99.80	*0.28*
Molar Ca/Na	7.58		7.12		7.34		7.69		8.59	
n	17		19		20		20		20	
Sc	5.60	*0.22*	5.35	*0.27*	5.07	*0.16*	5.54	*0.24*	4.72	*0.18*
V	4.45	*0.57*	4.57	*0.69*	4.63	*0.78*	4.32	*0.71*	1.18	*0.31*
Cr	1.67	*0.27*	1.81	*0.34*	1.82	*0.5*	1.40	*0.33*	1.85	*0.64*
Ti	112.67	*10.82*	120.42	*12.39*	110.88	*17.32*	114.55	*17.40*	71.88	*8.11*
Mn	14.47	*1.04*	12.91	*0.69*	13.00	*1.36*	12.40	*0.97*	12.74	*5*
Cu	b.d.	*b.d.*	b.d.	*b.d.*	b.d.	*b.d.*	b.d.	*b.d.*	1.42	*1.49*
Zn	7.66	*0.74*	6.17	*0.93*	5.97	*0.39*	6.20	*0.42*	7.23	*1.1*
Rb	0.66	*0.25*	0.53	*0.28*	1.25	*0.43*	0.69	*0.23*	3.12	*3.24*
Sr	436.42	*9.33*	470.12	*20.18*	452.82	*11.39*	425.24	*15.56*	489.72	*13.51*
Y	0.36	*0.03*	0.43	*0.06*	0.36	*0.07*	0.35	*0.03*	0.15	*0.03*
Zr	0.03	*0.02*	0.04	*0.05*	0.12	*0.21*	0.02	*0.01*	0.04	*0.1*
Ba	162.53	*7.91*	177.29	*17.53*	165.69	*10.88*	149.34	*12.10*	127.14	*9.92*
La	3.62	*1.47*	4.28	*1.62*	3.59	*1.16*	4.55	*1.16*	2.95	*0.16*
Ce	5.49	*2.05*	6.76	*2.39*	5.63	*1.72*	6.87	*1.58*	4.15	*0.22*
Pr	0.54	*0.18*	0.66	*0.21*	0.55	*0.14*	0.64	*0.13*	0.37	*0.03*
Nd	1.74	*0.53*	2.23	*0.62*	1.79	*0.4*	2.06	*0.34*	1.18	*0.08*
Sm	0.23	*0.06*	0.28	*0.06*	0.24	*0.04*	0.25	*0.04*	0.13	*0.04*
Eu	0.91	*0.04*	0.94	*0.05*	0.90	*0.04*	0.88	*0.05*	0.51	*0.04*
Gd	0.13	*0.03*	0.16	*0.03*	0.13	*0.02*	0.14	*0.02*	0.07	*0.02*
Dy	0.08	*0.02*	0.09	*0.02*	0.08	*0.02*	0.07	*0.01*	0.03	*0.02*
Pb	3.96	*0.10*	3.85	*0.18*	3.43	*0.14*	3.12	*0.18*	6.98	*0.69*

Table 5 (Continued)

Sample	B14-051		B14-052		B14-053a	
Depth (m)	543		407		137	
An	68.94		65.29		67.69	
SiO2	50.54	*0.83*	50.80	*0.79*	51.7	*0.82*
TiO2	0.04	*0.02*	-	-	-	-
Al2O3	30.94	*0.56*	30.67	*0.47*	31.15	*0.53*
Cr2O3	0.00	*0.01*	0.00	*0.01*	0.00	*0.01*
FeO	0.41	*0.04*	0.36	*0.06*	0.34	*0.06*
MnO	0.01	*0.01*	0.00	*0.01*	0.00	*0.01*
MgO	0.01	*0.01*	0.01	*0.01*	0.01	*0.01*
CaO	13.92	*0.61*	13.25	*0.51*	13.64	*0.61*
Na2O	3.33	*0.34*	3.66	*0.28*	3.47	*0.35*
K2O	0.20	*0.04*	0.23	*0.04*	0.23	*0.04*
Total	99.41	*0.24*	98.99	*0.46*	100.55	*0.39*
Molar Ca/Na	9.24		8.00		8.69	
n	20		18		21	
Sc	5.32	*0.29*	5.21	*0.34*	4.63	*0.21*
V	3.69	*0.60*	4.59	*0.56*	3.42	*0.62*
Cr	1.39	*0.34*	1.66	*0.33*	1.58	*0.58*
Ti	120.63	*25.32*	132.89	*43.91*	114.36	*18.95*
Mn	16.57	*3.36*	14.34	*0.9*	10.54	*1.01*
Cu	2.16	*4.63*	b.d.	*b.d.*	0.79	*1.87*
Zn	7.28	*1.40*	5.27	*0.17*	3.66	*0.72*
Rb	0.78	*0.47*	0.51	*0.18*	0.54	*0.19*
Sr	459.98	*29.93*	422.83	*31.26*	521.74	*21.32*
Y	0.46	*0.09*	0.59	*0.09*	0.43	*0.05*
Zr	0.09	*0.11*	0.05	*0.07*	0.12	*0.39*
Ba	143.49	*22.39*	173.15	*32.67*	150.37	*21.57*
La	4.16	*1.45*	3.73	*1.18*	5.05	*1.19*
Ce	6.67	*2.06*	6.01	*1.78*	8.11	*1.8*
Pr	0.66	*0.18*	0.61	*0.17*	0.81	*0.15*
Nd	2.28	*0.56*	2.16	*0.59*	2.78	*0.54*
Sm	0.32	*0.07*	0.32	*0.06*	0.37	*0.06*
Eu	0.78	*0.07*	0.92	*0.07*	0.85	*0.04*
Gd	0.18	*0.03*	0.21	*0.05*	0.2	*0.03*
Dy	0.10	*0.02*	0.12	*0.03*	0.1	*0.02*
Pb	3.99	*0.31*	5.65	*0.55*	3.55	*0.22*

Table 6

Whole rock XRF major element (oxide wt. %) and trace element (ppm) compositions.

Sample	B14-014	B14-015	B14-016	B14-017	B14-018	B14-019	B14-020	B14-021	B14-022	B14-023
Depth (m)	2503	2320	2252	2187	2098	1998	1941	1843	1750	1728
					Unnormalized Major Elements (Weight %)					
SiO2	51.57	51.13	51.21	51.21	51.57	51.90	52.52	52.71	52.42	52.89
TiO2	0.229	0.216	0.168	0.221	0.199	0.181	0.167	0.240	0.237	0.234
Al2O3	19.38	16.76	13.24	14.47	15.57	15.20	17.19	15.74	14.98	16.97
FeO*	5.74	6.53	7.85	7.78	9.44	9.40	8.18	9.10	9.32	8.58
MnO	0.126	0.144	0.182	0.174	0.188	0.199	0.173	0.194	0.203	0.187
MgO	5.61	8.93	12.36	10.46	11.31	8.56	7.30	7.06	7.69	6.84
CaO	13.15	12.74	11.62	12.08	8.37	10.94	11.10	11.16	11.53	10.89
Na2O	2.47	1.67	1.20	1.51	1.61	2.10	2.45	2.39	2.20	2.51
K2O	0.24	0.24	0.12	0.16	0.17	0.16	0.18	0.32	0.26	0.29
P2O5	0.015	0.014	0.007	0.012	0.011	0.003	0.008	0.015	0.011	0.016
Sum	98.54	98.38	97.96	98.08	98.44	98.64	99.27	98.93	98.86	99.41
					Normalized Major Elements (Weight %)					
SiO2	52.34	51.97	52.27	52.21	52.39	52.62	52.91	53.28	53.02	53.20
TiO2	0.232	0.220	0.171	0.225	0.202	0.183	0.169	0.242	0.239	0.235
Al2O3	19.67	17.04	13.52	14.75	15.82	15.41	17.31	15.91	15.15	17.07
FeO*	5.83	6.63	8.01	7.93	9.59	9.53	8.24	9.20	9.43	8.63
MnO	0.128	0.146	0.185	0.178	0.191	0.202	0.174	0.196	0.205	0.188
MgO	5.70	9.08	12.62	10.66	11.49	8.67	7.36	7.14	7.78	6.88
CaO	13.34	12.95	11.86	12.32	8.50	11.09	11.18	11.28	11.66	10.96
Na2O	2.51	1.70	1.22	1.54	1.64	2.13	2.47	2.41	2.23	2.52
K2O	0.25	0.24	0.13	0.16	0.18	0.17	0.19	0.33	0.26	0.29
P2O5	0.015	0.015	0.007	0.013	0.011	0.003	0.008	0.015	0.011	0.016
Sum	100.00	100.00	100.00	100.00	100.00	100.00	100.00	100.00	100.00	100.00
					Unnormalized Trace Elements (ppm)					
Ni	124	162	237	193	220	139	113	104	120	111
Cr	33	248	470	257	358	133	94	18	28	30
Sc	34	36	41	41	24	41	36	44	46	35
V	140	132	128	141	112	198	174	233	252	184
Ba	85	80	46	65	73	61	70	103	106	116
Rb	5	7	3	4	4	4	4	6	5	6
Sr	285	222	173	202	222	241	282	265	239	273
Zr	18	18	13	19	17	10	11	21	17	22
Y	7	7	6	7	5	4	5	13	10	8
Nb	0.0	1.1	0.0	0.3	0.0	0.0	0.0	0.1	0.0	0.0
Ga	17	14	10	13	14	14	16	16	16	16
Cu	216	29	12	18	19	5	5	14	16	20
Zn	38	47	54	56	72	61	57	66	69	67
Pb	2	2	1	2	1	0	0	2	2	2
La	1	0	1	0	0	0	0	3	1	3
Ce	9	10	7	11	5	6	6	11	9	11
Th	1	1	1	0	0	1	0	0	1	1
Nd	4	6	3	3	1	3	4	5	6	3
U	0	0	1	2	1	2	1	1	1	0
sum tr.	1020	1020	1206	1033	1146	923	878	925	941	908
in %	0.10	0.10	0.12	0.10	0.11	0.09	0.09	0.09	0.09	0.09
sum m+tr	98.64	98.48	98.08	98.18	98.55	98.73	99.36	99.02	98.95	99.50
M+Toxides	98.67	98.52	97.96	98.08	98.44		99.27	99.05	98.98	99.52

Table 6 (Continued)

Sample	B14-024	B14-025	B14-026	B14-044	B14-045	B14-046	B14-047	B14-048	B14-049	B14-050c
Depth (m)	1700	1641	1535	1529	1385	1183	1033	912	808	704
				Unnormalized Major Elements (Weight %)						
SiO2	53.05	53.52	52.95	52.64	52.42	52.89	53.53	52.61	52.51	51.97
TiO2	0.194	0.241	0.274	0.288	0.255	0.260	0.224	0.239	0.199	0.089
Al2O3	18.36	17.42	15.30	16.34	17.08	20.87	20.05	18.23	20.64	18.13
FeO*	8.55	8.73	8.91	7.26	7.84	5.22	6.43	6.17	5.45	7.04
MnO	0.177	0.182	0.188	0.154	0.162	0.105	0.127	0.129	0.111	0.169
MgO	6.64	7.02	8.32	6.88	7.13	4.77	6.12	6.52	5.23	9.60
CaO	9.63	9.92	11.32	12.28	11.60	12.51	10.34	13.10	11.95	10.24
Na2O	2.67	2.59	2.03	2.29	2.24	2.60	2.57	2.21	2.56	1.89
K2O	0.33	0.38	0.30	0.43	0.30	0.42	0.44	0.33	0.39	0.14
P2O5	0.015	0.026	0.015	0.032	0.026	0.034	0.027	0.020	0.020	0.005
Sum	99.62	100.02	99.62	98.60	99.05	99.68	99.86	99.58	99.06	99.28
				Normalized Major Elements (Weight %)						
SiO2	53.26	53.50	53.15	53.39	52.92	53.06	53.60	52.84	53.01	52.35
TiO2	0.195	0.241	0.275	0.292	0.258	0.261	0.225	0.240	0.201	0.090
Al2O3	18.43	17.42	15.36	16.58	17.24	20.94	20.07	18.31	20.83	18.26
FeO*	8.58	8.73	8.94	7.36	7.91	5.24	6.44	6.20	5.50	7.10
MnO	0.178	0.182	0.189	0.156	0.163	0.105	0.128	0.130	0.112	0.170
MgO	6.66	7.01	8.35	6.98	7.20	4.79	6.13	6.55	5.28	9.67
CaO	9.67	9.91	11.36	12.46	11.71	12.55	10.36	13.16	12.07	10.32
Na2O	2.68	2.59	2.04	2.32	2.26	2.61	2.58	2.22	2.58	1.90
K2O	0.34	0.38	0.30	0.43	0.30	0.42	0.44	0.34	0.39	0.14
P2O5	0.015	0.026	0.015	0.032	0.026	0.034	0.027	0.020	0.020	0.005
Sum	100.00	100.00	100.00	100.00	100.00	100.00	100.00	100.00	100.00	100.00
				Unnormalized Trace Elements (ppm)						
Ni	107	111	146	120	131	91	117	125	101	151
Cr	22	25	20	21	55	39	29	61	38	315
Sc	24	29	38	39	33	25	18	35	21	22
V	132	157	206	209	181	130	100	177	123	69
Ba	121	123	111	133	120	143	132	114	123	72
Rb	7	9	7	11	6	10	12	9	10	3
Sr	292	284	227	248	254	299	290	257	289	259
Zr	20	26	29	34	25	32	31	31	27	8
Y	6	6	9	11	10	10	6	10	8	3
Nb	1.0	0.6	0.7	1.0	0.8	1.5	0.9	0.6	0.5	0.0
Ga	18	16	15	16	16	17	16	15	17	14
Cu	24	10	31	28	29	29	24	23	19	6
Zn	68	67	66	54	61	44	54	44	40	87
Pb	3	2	3	2	10	3	4	2	2	3
La	5	5	7	10	3	5	8	7	3	1
Ce	7	10	13	16	14	17	9	15	10	0
Th	2	2	1	1	1	2	2	2	2	1
Nd	4	6	7	9	7	8	6	7	8	1
U	1	2	1	1	1	1	0	0	1	0
sum tr.	863	891	939	963	956	906	860	934	843	1015
in %	0.09	0.09	0.09	0.10	0.10	0.09	0.09	0.09	0.08	0.10
sum m+tr	99.71	100.11	99.71	98.70	99.15	99.77	99.94	99.67	99.14	99.38
M+Toxides	99.73	100.13	99.74	98.72	99.18	99.79	99.97	99.70	99.16	99.42

Table 6 (Continued)

Sample	B14-051	B14-052	B14-053a	B14-015 (Rep)	B14-052 (Rep)
Depth (m)	543	407	137	2320	137
	Unnormalized Major Element (Weight %)				
SiO2	52.60	53.63	51.97	51.10	53.50
TiO2	0.225	0.359	0.205	0.214	0.354
Al2O3	21.13	17.07	18.12	16.76	17.00
FeO*	5.33	7.17	6.84	6.54	7.14
MnO	0.101	0.142	0.129	0.144	0.141
MgO	5.37	8.01	9.26	8.93	8.02
CaO	12.24	9.88	9.72	12.74	9.86
Na2O	2.34	2.07	1.91	1.66	2.12
K2O	0.43	0.60	0.31	0.24	0.61
P2O5	0.026	0.053	0.021	0.013	0.058
Sum	99.80	98.97	98.48	98.35	98.79
	Normalized Major Elements (Weight %)				
SiO2	52.71	54.18	52.77	51.96	54.15
TiO2	0.225	0.363	0.208	0.218	0.359
Al2O3	21.17	17.25	18.40	17.05	17.20
FeO*	5.35	7.25	6.94	6.65	7.22
MnO	0.101	0.144	0.131	0.146	0.143
MgO	5.38	8.09	9.40	9.08	8.12
CaO	12.27	9.98	9.87	12.96	9.98
Na2O	2.35	2.09	1.94	1.69	2.15
K2O	0.43	0.60	0.31	0.24	0.61
P2O5	0.026	0.054	0.022	0.014	0.059
Sum	100.00	100.00	100.00	100.00	100.00
	Unnormalized Trace Elements (ppm)				
Ni	115	169	201	163	168
Cr	108	166	662	249	165
Sc	20	23	19	35	23
V	98	128	98	127	129
Ba	128	153	123	80	153
Rb	11	19	8	7	19
Sr	299	225	296	223	226
Zr	32	52	24	18	49
Y	8	11	7	7	11
Nb	1.6	2.2	0.7	0.1	2.5
Ga	17	14	14	13	15
Cu	29	38	30	28	39
Zn	43	60	63	43	62
Pb	3	4	2	3	5
La	4	12	3	6	9
Ce	16	22	9	7	24
Th	2	3	1	1	3
Nd	10	12	6	3	8
U	1	1	0	2	0
sum tr.	945	1113	1566	1017	1112
in %	0.09	0.11	0.16	0.10	0.11
sum m+tr	99.89	99.08	98.64	98.45	98.90
M+Toxides	99.92	99.11	98.69	98.48	98.94

Table 7
Measured selected trace element compositions in plagioclase, clinopyroxene and low-Ca pyroxene.

Sample	B14-014	B14-015	B14-016	B14-017	B14-018	B14-019	B14-020	B14-021	B14-022
Depth (m)	2503	2320	2252	2187	2098	1998	1941	1843	1750
Measured in plagioclase									
An Content	62.70	71.52	72.86	70.45	70.93	59.95	59.04	55.24	57.42
Rb	0.67	1.00	0.83	0.46	0.58	2.48	2.47	1.58	1.32
Sr	451.88	434.84	455.72	452.27	480.76	513.04	519.86	508.67	482.17
Ba	115.09	112.67	99.90	106.61	138.96	115.85	126.46	190.41	181.76
Pb	2.20	2.51	1.91	2.44	2.96	1.32	1.48	3.01	2.58
La	2.76	4.01	3.53	3.72	5.09	2.02	2.48	3.79	3.61
Ce	4.06	5.74	4.67	5.29	7.74	2.65	3.32	5.40	4.79
Measured in clinopyroxene									
Mg#	69.4	75.9	78.2	75.4	74.0	67.9	67.8	64.4	65.4
La	3.22	3.37	2.30	3.24	3.75	1.38	1.60	4.32	3.33
Ce	12.72	13.23	8.83	12.16	16.55	5.50	6.80	16.59	13.02
Nd	11.55	11.49	7.72	10.22	15.80	5.52	6.69	14.35	12.18
Sm	3.56	3.29	2.35	2.99	4.67	1.85	2.18	4.25	3.84
Eu	0.65	0.65	0.55	0.62	0.72	0.50	0.53	0.74	0.74
Gd	4.06	3.54	2.60	3.29	4.92	2.27	2.56	4.73	4.45
Dy	4.54	3.90	3.01	3.66	5.22	2.73	3.02	5.35	5.17
Er	2.60	2.22	1.67	2.04	2.76	1.57	1.75	3.08	3.02
Yb	2.52	2.10	1.63	1.97	2.47	1.57	1.72	2.99	3.02
Lu	0.35	0.30	0.22	0.27	0.33	0.22	0.24	0.42	0.42
Measured in low-Ca pyroxene									
Mg#	56.9	57.9	57.8	60.8	59.8	58.9	59.4	62.6	61.7
Sc	49.46	40.03	42.35	41.35	45.44	50.75	49.12	44.05	47.43
Cr	51.31	310.14	557.83	300.91	675.42	155.17	127.73	14.91	31.87
Y	4.25	3.30	2.51	3.07	4.63	2.62	2.84	3.63	4.36
Zr	4.37	3.95	2.55	3.37	4.93	1.73	2.65	3.64	3.47
Gd	0.28	0.22	0.16	0.20	0.36	0.20	0.24	0.18	0.26
Dy	0.57	0.43	0.33	0.40	0.65	0.37	0.39	0.45	0.56
Er	0.57	0.44	0.33	0.42	0.59	0.35	0.37	0.52	0.61
Yb	0.92	0.73	0.56	0.67	0.86	0.54	0.60	0.93	1.07
Lu	0.16	0.12	0.09	0.11	0.14	0.09	0.10	0.16	0.19

Table 7 (Continued)

Sample	B14-023	B14-024	B14-025	B14-026	B14-044	B14-045	B14-046	B14-047	B14-048
Depth (m)	1728	1700	1641	1535	1529	1385	1183	1033	912
Measured in plagioclase									
An Content	57.79	57.49	57.92	62.34	60.64	61.07	64.36	62.91	63.47
Rb	1.52	1.06	1.32	0.89	0.95	0.96	0.66	0.53	1.25
Sr	481.90	477.40	467.68	453.35	449.56	447.25	436.42	470.12	452.82
Ba	165.25	166.10	162.06	177.70	187.01	178.02	162.53	177.29	165.69
Pb	2.94	2.93	2.96	3.68	4.09	3.81	3.96	3.85	3.43
La	4.04	3.88	3.11	5.11	4.50	4.35	3.62	4.28	3.59
Ce	5.74	5.72	4.58	7.21	6.48	6.51	4.49	6.76	5.63
Measured in clinopyroxene									
Mg#	66.2	66.8	67.6	69.0	68.9	67.7	68.0	71.8	70.5
La	4.84	4.04	5.44	5.48	6.53	5.64	6.61	5.84	4.91
Ce	19.17	18.26	22.34	21.67	23.69	22.85	26.80	26.78	19.81
Nd	16.44	17.41	18.64	17.52	19.08	19.64	23.35	26.10	17.40
Sm	4.74	5.34	5.20	4.84	5.32	5.54	6.51	7.46	4.92
Eu	0.71	0.69	0.72	0.72	0.75	0.82	0.72	0.76	0.68
Gd	5.10	5.63	5.47	5.10	5.60	5.91	6.89	7.83	5.27
Dy	5.64	6.48	5.90	5.62	6.22	6.41	7.45	8.39	5.76
Er	3.14	3.54	3.27	3.16	3.50	3.64	4.15	4.54	3.22
Yb	3.05	3.39	3.04	3.02	3.43	3.52	4.04	4.08	3.11
Lu	0.42	0.46	0.42	0.42	0.47	0.49	0.55	0.55	0.43
Measured in low Ca-pyroxene									
Mg#	56.9	57.9	57.8	60.8	59.8	58.9	59.4	62.6	61.7
Sc	42.70	41.29	41.36	39.31	42.43	40.51	43.69	39.84	40.05
Cr	41.08	37.59	41.85	24.19	26.86	68.95	85.54	70.69	89.01
Y	4.30	5.04	4.75	4.86	5.02	5.50	6.90	6.83	4.98
Zr	4.93	6.36	7.16	6.89	6.58	6.32	8.03	7.39	6.59
Gd	0.25	0.32	0.31	0.31	0.34	0.37	0.52	0.47	0.33
Dy	0.55	0.65	0.62	0.64	0.69	0.73	0.99	0.92	0.66
Er	0.59	0.68	0.64	0.68	0.70	0.74	0.93	0.90	0.66
Yb	0.96	1.11	1.03	1.04	1.18	1.18	1.43	1.39	1.12
Lu	0.17	0.19	0.18	0.18	0.20	0.20	0.25	0.23	0.19

Table 7 (Continued)

Sample	B14-049	B14-050c	B14-051	B14-052	B14-053a
Depth (m)	808	704	543	407	137
Measured in plagioclase					
An Content	64.69	67.34	68.94	65.29	67.69
Rb	0.69	3.12	0.78	0.51	0.54
Sr	425.24	489.72	459.98	422.83	521.74
Ba	149.34	127.14	143.39	173.15	150.37
Pb	3.12	6.98	3.99	5.65	3.55
La	4.55	2.95	4.16	3.73	5.05
Ce	6.87	4.15	6.67	6.01	8.11
Measured in clinopyroxene					
Mg#	70.2	77.8	71.0	73.8	77.4
La	4.59	1.56	6.22	11.09	5.45
Ce	19.59	6.92	25.65	44.17	26.79
Nd	18.27	7.42	21.91	35.28	26.09
Sm	5.35	2.36	6.15	9.32	7.57
Eu	0.64	0.40	0.66	0.75	0.96
Gd	5.56	2.54	6.34	8.93	7.50
Dy	6.17	2.93	6.87	9.29	7.90
Er	3.43	1.64	3.85	4.98	4.15
Yb	3.31	1.50	3.72	4.51	3.79
Lu	0.46	0.21	0.52	0.60	0.51
Measured in low-Ca pyroxene					
Mg#	61.8	69.0	63.8	65.6	70.9
Sc	52.99	33.44	39.06	36.34	35.12
Cr	77.40	611.55	256.16	334.07	1560.01
Y	5.47	1.92	6.40	8.86	6.03
Zr	8.79	1.90	6.00	5.58	7.45
Gd	0.38	0.10	0.46	0.70	0.51
Dy	0.73	0.23	0.83	1.19	0.88
Er	0.73	0.27	0.82	1.14	0.75
Yb	1.22	0.47	1.27	1.72	1.08
Lu	0.20	0.08	0.21	0.28	0.17

Table 8
Stratigraphic thicknesses and calculated proportions of incoming magma below the Pyroxenite Marker (PM) for both the Leolo and Roossenekal traverses

Transect	**Leolo Mountains**			**Roossenekal**		
% UUMZ Magma Loss*	0%	15%	25%	0%	15%	25%
Zone of Magma Mixing (m)		350			270	
PM to return to pre-mixing An content (m)		850			711	
Total Excursion Thickness (m)		1,200			981	
PM to Roof (m)	2,425	2,850	3,230	2,296	2,640	2,870
Total Magma Thickness (m)	2,775	3,200	3,580	2,566	2,910	3,140
$\mathbf{X_{inc}}$	43%	38%	34%	38%	34%	31%

*UUMZ magma loss scenarios based on results of VanTongeren *et al.* (2010). Leolo Mountain values from VanTongeren & Mathez (2013).

Table 9
Calculated crystallization temperature and equilibrium liquid composition for each sample as calculated per listed mineral phase.

Sample	**B14-014**	**B14-015**	**B14-016**	**B14-017**	**B14-018**	**B14-019**	**B14-020**	**B14-021**	**B14-022**
Depth (m)	2503	2320	2252	2187	2098	1998	1941	1843	1750
T (1σ)	1114 (4)	1158 (25)	1162 (33)	1148 (27)	1166 (17)	1109 (30)	1102 (31)	1075 (14)	1082 (23)
Calculated from plagioclase									
Rb	21.75	39.39	33.84	17.84	21.94	74.36	72.99	46.46	38.72
Sr	199.34	246.42	267.65	248.35	269.24	209.81	206.58	190.73	180.92
Ba	436.89	617.11	579.29	563.82	733.79	387.40	407.26	576.93	550.26
Pb	6.58	11.36	9.22	10.55	12.89	3.43	3.68	6.96	5.97
La	14.56	18.82	19.28	20.22	27.21	10.44	12.81	19.78	18.80
Ce	30.81	35.15	38.41	42.88	61.56	19.42	24.24	39.66	35.10
Calculated from clinopyroxene									
La	36.15	38.41	25.10	36.14	47.68	15.61	17.87	44.79	35.85
Ce	93.65	100.61	64.50	89.98	140.08	40.74	49.52	111.15	90.65
Nd	44.16	46.80	30.34	40.24	71.07	21.23	25.08	48.93	43.18
Sm	9.35	9.39	6.49	8.21	14.59	4.90	5.59	9.85	9.24
Eu	1.54	1.68	1.38	1.53	2.03	1.19	1.21	1.54	1.60
Gd	8.92	8.53	6.09	7.60	12.91	5.02	5.45	9.12	8.90
Dy	9.48	9.00	6.76	8.09	12.98	5.74	6.10	9.80	9.80
Er	5.75	5.43	3.99	4.78	7.22	3.52	3.74	6.00	6.07
Yb	6.26	5.78	4.37	5.18	7.23	3.95	4.15	6.58	6.84
Lu	0.94	0.87	0.63	0.76	1.04	0.60	0.61	0.99	1.02
Calculated from low-Ca pyroxene									
Sc	41.57	33.66	36.15	34.66	37.95	40.64	39.33	34.08	37.18
Cr	4.46	26.97	48.51	26.17	58.73	13.49	11.11	1.30	2.77
Y	21.42	16.75	15.47	14.96	21.52	7.06	7.67	6.29	8.94
Zr	207.99	187.95	121.43	160.48	234.83	82.52	126.40	173.33	165.20
Gd	3.44	2.75	2.90	2.28	3.76	0.71	0.83	0.26	0.53
Dy	2.91	2.21	2.50	1.91	2.84	0.55	0.59	0.28	0.48
Er	2.50	1.95	1.83	1.79	2.39	0.76	0.82	0.69	0.98
Yb	2.80	2.24	2.19	1.96	2.39	0.77	0.85	0.77	1.08
Lu	0.35	0.27	0.25	0.23	0.27	0.09	0.10	0.09	0.13

Table 9 (Continued)

Sample	B14-023	B14-024	B14-025	B14-026	B14-044	B14-045	B14-046	B14-047	B14-048
Depth (m)	1728	1700	1641	1535	1529	1385	1183	1033	912
T (1σ)	1081 (20)	1084 (15)	1071 (2)	1108 (3)	1095 (4)	1093 (3)	1091 (1)	1088 (5)	1106 (1)
Calculated from plagioclase									
Rb	45.32	30.89	40.44	28.96	30.26	31.32	24.09	18.59	42.69
Sr	182.51	179.74	176.47	197.39	185.57	186.51	198.52	205.32	202.90
Ba	509.82	503.76	507.43	666.89	654.60	638.05	683.91	697.45	657.70
Pb	6.94	6.78	7.07	10.84	11.13	10.62	13.18	11.89	10.75
La	21.14	20.21	16.49	27.05	23.80	23.18	19.93	23.34	19.25
Ce	42.41	41.86	34.39	54.92	48.99	49.72	44.21	53.49	43.73
Calculated from clinopyroxene									
La	49.20	41.57	50.52	59.95	66.46	59.66	68.09	53.92	51.30
Ce	126.33	122.19	134.63	155.31	157.55	157.32	179.60	160.84	135.25
Nd	55.71	59.85	57.64	65.18	65.83	69.58	80.48	80.66	61.50
Sm	11.02	12.55	11.01	12.39	12.64	13.42	15.34	15.78	1.93
Eu	1.48	1.47	1.37	1.66	1.62	1.78	1.52	1.44	1.48
Gd	9.91	11.08	9.71	10.92	11.16	11.94	13.56	12.90	10.67
Dy	10.52	12.16	10.03	11.47	11.85	12.32	13.95	14.14	11.10
Er	6.27	7.07	5.95	6.84	7.11	7.42	8.26	8.14	6.58
Yb	6.94	7.66	6.28	7.37	7.90	8.09	9.08	8.27	7.16
Lu	1.03	1.11	0.94	1.09	1.17	1.21	1.32	1.20	1.06
Calculated from low-Ca pyroxene									
Sc	33.54	32.60	32.64	31.51	33.84	32.15	34.77	32.24	32.26
Cr	3.57	3.27	3.64	2.10	2.34	6.00	7.44	6.15	7.74
Y	9.06	11.35	10.63	13.29	12.85	13.25	17.19	21.09	14.48
Zr	234.52	302.98	340.95	328.03	313.14	300.95	382.38	351.90	313.81
Gd	0.55	0.79	0.75	1.14	1.07	1.04	1.55	2.16	1.35
Dy	0.50	0.68	0.64	0.98	0.93	0.87	1.26	1.79	1.14
Er	0.97	1.21	1.13	1.52	1.44	1.42	1.86	2.29	1.57
Yb	1.01	1.26	1.16	1.50	1.57	1.45	1.84	2.32	1.74
Lu	0.12	0.15	0.14	0.18	0.18	0.17	0.22	0.27	0.21

Table 9 (Continued)

Sample	**B14-049**	**B14-050c**	**B14-051**	**B14-052**	**B14-053a**
Depth (m)	808	704	543	407	137
T (1σ)	1110 (14)	1128 (41)	1127 (7)	1092 (11)	1120 (2)
Calculated from Plagioclase					
Rb	24.44	115.14	30.51	19.26	20.59
Sr	197.25	245.84	240.64	197.30	263.28
Ba	625.92	592.87	722.40	761.36	719.27
Pb	10.38	26.27	16.33	19.74	13.71
La	24.58	15.97	22.88	20.70	27.69
Ce	54.08	33.08	54.59	49.03	65.78
Calculated from clinopyroxene					
La	49.17	14.51	69.21	99.24	44.73
Ce	137.38	42.79	188.42	257.70	144.56
Nd	66.53	24.41	84.73	106.32	73.59
Sm	13.39	5.44	16.49	19.27	14.73
Eu	1.44	0.84	1.60	1.40	1.68
Gd	11.64	4.95	14.30	15.46	12.23
Dy	12.30	5.51	14.80	15.35	12.29
Er	7.25	3.30	8.81	8.77	6.85
Yb	7.88	3.41	1.86	8.98	7.05
Lu	1.17	0.52	1.43	1.28	1.01
Calculated from low-Ca pyroxene					
Sc	32.69	27.97	31.80	29.87	29.67
Cr	6.73	53.18	22.27	29.05	135.65
Y	16.01	9.11	21.42	33.46	32.50
Zr	418.57	90.48	285.71	265.71	354.76
Gd	1.57	1.08	2.46	4.80	7.09
Dy	1.28	1.04	1.89	3.44	5.12
Er	1.75	1.12	2.29	3.64	3.58
Yb	1.91	1.33	2.34	3.68	3.58
Lu	0.22	0.16	0.27	0.42	0.40

Figure 10
Calculated incoming magma composition below the Pyroxenite Marker for the Leolo Mountain and Roossenekal traverses.

	Leolo Mountains*					**Roossenekal**				
	C_{UUMZ}	C_{res}		C_{inc}		C_{UUMZ}	C_{res}		C_{inc}	
			0%	**15%**	**25%**			**0%**	**15%**	**25%**
Sc^{opx}	36	37	35	34	34	37	34	42	43	44
Cr^{opx}	108	5	245	283	317	54	1	139	155	170
Rb^{plag}	24	33	13	10	7	-	-	-	-	-
Sr^{plag}	245	176	335	361	384	268	191	395	419	441
Y^{opx}	21	11	34	38	41	19	6	38	42	46
Zr^{opx}	192	141	260	279	296	178	173	186	187	189
Ba^{plag}	468	334	644	695	738	657	577	786	811	834
La^{plag}	14.68	14.32	15.17	15.30	15.42	23.25	19.78	28.90	29.97	30.96
Ce^{plag}	32.19	30.93	33.87	34.35	34.77	49.99	39.66	66.83	70.03	72.97
Nd^{cpx}	27.97	24.81	32.17	33.37	34.40	50.71	48.93	53.60	54.15	54.66
Sm^{cpx}	6.13	5.43	7.06	7.32	7.55	10.54	9.85	11.67	11.88	12.08
Eu^{cpx}	1.31	0.96	1.77	1.90	2.02	1.71	1.54	1.97	2.03	2.07
$Gd^{cpx,opx}$	5.13	3.52	7.26	7.87	8.40	6.42	4.69	9.23	9.76	10.26
$Dy^{cpx,opx}$	4.87	3.88	6.19	6.56	6.88	6.27	5.04	8.28	8.66	9.01
Er^{opx}	1.96	1.12	3.07	3.39	3.67	2.11	0.69	4.43	4.87	5.28
Yb^{opx}	2.17	1.21	3.44	3.80	4.12	2.29	0.77	4.76	5.23	5.67
Lu^{opx}	0.29	0.18	0.44	0.48	0.51	0.26	0.09	0.54	0.60	0.65

*Values for the Leolo Mountain traverse are recalculated from VanTongeren & Mathez (2013) utilizing the calculated plagioclase crystallization temperatures of Sun & Liang (2017).

Chapter 2

The mid-high temperature subsolidus thermal evolution of the Rustenburg Layered Suite

This chapter resulted in one submitted paper:

Setera, J. B., VanTongeren, J. A., Turrin, B. D., & Swisher, C. C. (2019). Rapid Cooling of the Rustenburg Layered Suite of the Bushveld Complex: Insights from biotite $^{40}Ar/^{39}Ar$ geochronology. **Geology**.

Abstract

Despite their importance to understanding magma chamber processes and the formation of economically viable precious metal deposits, the cooling histories of layered mafic intrusions remain enigmatic due to limited geochronologic constraints. We provide a comprehensive $^{40}Ar/^{39}Ar$ study of biotite throughout the Rustenburg Layered Suite (RLS) of the Bushveld Complex (South Africa). Analysis of individual biotite grains from 10 samples, encompassing ~5.5 km of RLS stratigraphy, yield weighted mean plateau ages that all overlap at 2σ (α-95 percent confidence level) and range from 2052.0 ± 7.6 Ma to 2056.3 ± 3.2 Ma (2σ). A weighted mean of all biotite plateau ages yields an age of 2054.47 ± 0.84 Ma (2σ, n=30, MSWD = 0.23, P = 1.00). The overlap between our $^{40}Ar/^{39}Ar$ biotite and published U-Pb zircon ages suggests that the RLS cooled rapidly to the closure temperature of biotite, with cooling rates on the order of 1000 °C Ma^{-1}

throughout the stratigraphy. Thermal modelling requires enhanced heat loss, due to the hydrothermal system associated with the emplacement of the RLS, to produce the inferred rapid cooling rates. Previously reported young $^{40}Ar/^{39}Ar$ biotite ages from the UG-2, MG-1, and Merensky Reef are likely a product of the late-stage circulation of hydrothermal fluids. The lack of similarly young $^{40}Ar/^{39}Ar$ biotite ages from the remainder of the stratigraphy suggests that late-stage hydrothermal events are potentially localized to chromitites and the Merensky Reef.

1. Introduction

The study of layered mafic intrusions is crucial for observing and understanding the geochemical and lithologic evolution of igneous bodies within the shallow crust. As is the case with the world's largest layered mafic intrusion, the Bushveld Complex in South Africa, these intrusive bodies also contain much of the world's largest known sources of precious metals. Despite their importance and a long history of research on their formation, understanding the cooling histories of layered mafic intrusions is hindered by a lack of widespread geochronologic data.

The large grain sizes and distinct layered stratigraphy of large mafic intrusions, such as the Bushveld Complex, were originally thought to be a product of very slow cooling [e.g. Grove et al. (1984); Hattingh (1995); Hess (1960); McCallum et al. (1980)]. Indeed, using available paleomagnetic pole positions, Hattingh (1995) provided an initial estimate of at least 50 Myr for the emplacement and cooling of the entire Rustenburg Layered Suite (RLS), the predominately mafic to ultramafic portion of the Bushveld Complex, to the Curie temperature (~580°C). However, recent geochronologic data in

some portions of from the Bushveld Complex has suggested the contrary, with high-precision U-Pb ages of zircon and baddeleyite [2056.45-2054.89 Ma (Mungall et al., 2016; Nomade et al., 2004; Scoates and Wall, 2015; Zeh et al., 2015)] combined with $^{40}Ar/^{39}Ar$ ages of biotite (Cassata et al., 2009; Nomade et al., 2004) indicating rapid cooling. With recent advances in U-Pb chronology of zircon, high temperature [~950-670°C; Ver Hoeve et al. (2018); Zeh et al. (2015)] estimates of the thermal history are well constrained throughout the stratigraphy. However, revealing the mid-temperature thermal history (~350-500°C) of the RLS is difficult, as precise mid-temperature geochronology (e.g. $^{40}Ar/^{39}Ar$ dating of biotite) is only available for 3 individual horizons thus far.

At present, published $^{40}Ar/^{39}Ar$ ages of biotite only exist from the UG-2 (Nomade et al., 2004) and MG-1 (Cassata et al., 2009) chromitite veins, and the Merensky Reef pyroxenite (Scoates and Wall, 2015). Although biotite $^{40}Ar/^{39}Ar$ ages from the two chromitites produce potential cooling ages, biotite from the Merensky Reef indicates a later hydrothermal event ~2 Ga (Scoates and Wall, 2015). Whether this late-stage hydrothermal event affected the entire complex or is limited to certain portions of the stratigraphy has yet to be determined, as current $^{40}Ar/^{39}Ar$ geochronology has not been conducted on the majority of the cumulate rocks of the ~8 km thick RLS.

To elucidate the mid-temperature thermal evolution of the Bushveld Complex, we provide $^{40}Ar/^{39}Ar$ ages of biotite from 10 samples throughout the RLS stratigraphy. Our results show evidence that the RLS cooled rapidly from the crystallization temperature of zircon to the closure temperature of the $^{40}Ar/^{39}Ar$ system in biotite. Our biotite plateau ages for the RLS are not reset by a late-stage hydrothermal event and we conclude that

rapid cooling must be due to advective heat loss from a hydrothermal system associated with initial the emplacement of the RLS.

2. Samples and Methods

2.1 Samples

Argon isotopes and major element compositions were analyzed for individual biotite grains from 10 samples of the RLS encompassing ~5.5 km of stratigraphy (Table 1). Geographic and stratigraphic positions for the Upper Zone samples are from VanTongeren et al. (2010) and VanTongeren and Mathez (2013), while Main Zone samples are from Setera and VanTongeren (2018). The Critical Zone samples are placed in their stratigraphic position relative to the Merensky Reef using the detailed map of Molyneux (2008).

2.2 Argon Isotope Analyses

For argon isotopic analyses, biotite separates along with the reference standard, Fish Canyon (FC) sanidine [28.201 Ma; Kuiper et al. (2008)] were placed in Al-disks for neutron irradiation, which was carried out at the US Geological Survey TRIGA reactor for 80 hours without Cd-shielding. Samples were incrementally step-heated using a New Wave 40-watt CO_2 laser and argon isotopes were analyzed using a Mass Analyzer Products (MAP) 215-50 noble gas mass spectrometer upgraded by Turrin et al. (2010). A typical ten-minute static system 'cold' blank, (10^{-18} mol) is: $^{40}Ar = 420 \pm 13$; $^{39}Ar = 12.0 \pm 3.6$; $^{38}Ar=1.0\pm0.4$; $^{37}Ar=22.4\pm1.4$; $^{36}Ar=3.3\pm0.3$.

Instrumental mass fractionation was monitored by analyzing a known volume of atmospheric Ar after every eighth sample and blank measurement. For the data reduction we assumed an initial value of $^{38}Ar/^{36}Ar = 0.1885 \pm 0.0003$ (Lee et al., 2006). As mentioned in the main text, we do not assume an initial $^{40}Ar/^{36}Ar = 298.56 \pm 0.31$ (Lee et al., 2006), but rather use the intercept value from inverse isochron correlations to calculate plateau ages. Signals for reactor produced ^{37}Ar and ^{39}Ar were corrected using the decay constants of 0.0198 day^{-1} and 7.07×10^{-6} day^{-1}, respectively. ^{37}Ar was not used because most of it had decayed by the time of measurement. Instead, a fixed $^{37}Ar/^{39}Ar$ value of 0.001 ± 0.001 was used in age calculations, a value that is supported by the electron microbe data collected on biotite from the RLS (Table DR2). Automated laser heating, gas extraction, mass spectroscopy measurements, and data reduction were implemented using automated software written by A. Deino of the Berkeley Geochronology Center. The age calculations incorporate the decay constants of Steiger and Jäger, (1977) and the following ratios ($/10^{-4}$), which are necessary for making reactor corrections: [$(^{36}Ar/^{37}Ar)_{Ca} = 2.75 \pm 0.003$); $(^{39}Ar/^{37}Ar)_{Ca} = 6.62 \pm 0.01$; $(^{38}Ar/^{37}Ar)_{Ca} = 0.210 \pm 0.1$; $(^{40}Ar_K/^{39}Ar)_K = 98.1 \pm 0.18$; $(^{38}Ar_K/^{39}Ar)_K = 13200 \pm 10$; $(^{37}Ar_K/^{39}Ar)_K = 2.20 \pm 0.007$; $(^{36}Ar_{Cl}/^{38}Ar)_{Cl} = 65000 \pm 3000$].

We define an age plateau as a sequence of three or more consecutive steps with apparent ages that agree within the 95% confidence interval and for which the sum of $^{39}Ar_K$ released is 50% or more of the total $^{39}Ar_K$ released on completion of the heating experiment (Dalrymple and Lanphere, 1969, 1974; Fleck et al., 1977). The plateau ages and their errors are calculated using the variance-weighted mean of the plateau steps (Taylor, 1997). Some authors have adopted the most recent determinations for the ^{40}K

decay constants and age of the Fish Canyon sanidine (Renne et al. 2011) in the calculation of $^{40}Ar/^{39}Ar$ ages. The values of Renne et al. (2011) can be used with the current dataset by recalculating the $^{40}Ar/^{39}Ar$ ages using the equation the following equation from Mercer and Hodges (2016):

$$t = \frac{1}{\lambda}\log_e\left[\frac{exp[\lambda t_m]-1}{exp[\lambda_o t_{m_o}]-1}(exp[\lambda_o t_o]-1)+1\right] \quad (1)$$

where, t is the new age of measured sample, t_m is the new age of the monitor mineral, t_{m_o} is the original age of the monitor mineral, t_o is the original age of the measured sample, λ is the new decay constant, and λ_o is the original decay constant. When our data is recalculated using the values of Renne et al. (2011), the weighted mean plateau age for all biotites increases from 2054.51 Ma to an implausible age of 2060.40 Ma, older than the U-Pb zircon ages. As such, we use the decay constants adopted by the IUGS Subcommission on Geochronology (Steiger and Jäger, 1977) and the reported age (28.201 Ma) of Fish Canyon sanidine of Kuiper et al. (2008).

As a secondary standard, the Hb3gr hornblende was irradiated alongside the samples and treated as an unknown. The runs of Hb3gr result in a weighted mean age of 1082.9 ± 3.6 Ma (1σ), well within the error limits of published values for Hb3gr, when adjusted for our age of FC sanidine [1080 ± 4 Ma (Schwarz and Trieloff, 2007); 1079 ± 8 (Jourdan et al., 2006)]. The runs Hb3gr result in a weighted mean R_{FCs}^{Hb3gr} value of 52.24 ± 0.17 (1σ).

2.3 Discordant Age Spectra (Chloritization)

In the $^{40}Ar/^{39}Ar$ dating of biotite from the UG-2 chromitite layer in the upper Critical Zone, Nomade et al. (2004) noted that ~50% of individual biotite grains yielded

concordant age spectra, while the rest yielded strongly discordant age spectra. Strongly discordant age spectra are characterized by young apparent ages in early heating steps, followed by anomalously old ages due to the various amount of interlayered chlorite within the grains. During irradiation, ^{39}Ar is recoiled into interlayered K_2O-poor chlorite from K_2O-rich biotite and results in low apparent ages in early heating steps (Hess et al., 1987; Min et al., 2001; Nomade et al., 2004). As step-heating progresses, biotite (now depleted in ^{39}Ar) becomes the main Ar releasing reservoir, resulting in anomalously old apparent ages.

Eight individual biotite grains from the Main Zone in this study also exhibit discordance accompanied by anomalously old ages (as calculated when using an initial $^{40}Ar/^{36}Ar = 298.56 \pm 0.31$), consistent with the interlayered chlorite found within these samples (Fig. 5). After concluding little to no Ar-loss from the UG-2 biotite, Nomade et al. (2004) use the total fusion age of each discordant sample as a comparison to the plateau ages yielded from concordant age spectra. Some samples in our study, however, show evidence of Ar-loss from a reheating event and we therefore cannot use the total fusion age as a direct comparison to other individual analyses. Instead, we use the isochron and inverse isochron regressions to deduce an age, trapped component and finally, a re-calculated plateau age for these discordant samples.

For the eight discordant biotite samples, isochron and inverse isochron relationships for heating-steps dominated by Ar release from biotite yield ages similar to the plateau ages of concordant analyses (~2055 Ma) but also indicate excess ^{40}Ar. Individual age spectra can be corrected for this trapped component by re-calculating the age spectra using the $^{40}Ar/^{36}Ar$ intercept value from an inverse isochron regression. This

results in the elimination the chlorite-dominated portion of the age spectra (low apparent ages at early gas release steps) and results in a plateau age for the biotite dominated portion of gas release that is indistinguishable from the isochron ages (Fig. 4). No isochrons were originally reported in the study of Nomade et al. (2004), however despite low precision in ^{36}Ar measurements, a similar general relationship can be found by re-analyzing the data of Nomade et al. (2004) (Fig. 6).

2.4 Electron Microprobe Analyses

In situ major element compositions for biotite were determined using the JEOL JXA 8200 electron microprobe at Rutgers University. All analyses used an acceleration potential of 15 kV, beam current of 15 nA, and a beam diameter of 5 µm. Count times consisted of 15 s on background for each element, while peak count times and primary standard varied per element (Si - Biotite Kristiansand = 20 s, Mg - F-phlogopite stoichiometric = 20 s, Al - Biotite Kristiansand = 20 s, Na - Jadeite = 10 s, F - F-phlogopite stoichiometric = 10 s, Fe - Biotite Kristiansand = 10 s, Mn - Rhodonite = 40 s, Ba - Benitoite = 45 s, Cl - Cl-Apatite Kragero = 10 s, Cr - Mg_2CrO_4 chromite = 40 s, Ca - Apatite Wilberforce = 40 s, K - F-phlogopite stoichiometric = 10 s, Ti - TiO_2 Synthetic = 40 s). H_2O calculated based on Cl + F + OH = 2.0 per formula unit.

3. Results

Weighted mean plateau ages, comprising ages of 2-5 individual biotite grains per single sample, for 10 stratigraphic horizons of the RLS range from 2052.0 ± 7.6 Ma to

2056.3 ± 3.2 Ma (2σ), with weighted means from individual samples indistinguishable at 2σ (α-95 percent confidence level; Fig. 7, Table 1).

Plateau ages were calculated using the $^{40}Ar/^{36}Ar$ intercept value from inverse isochron regressions (Figs. 2-4) rather than the modern atmospheric $^{40}Ar/^{36}Ar$ value of 298.56 (Lee et al., 2006) in order to account for the different atmospheric composition during the Paleoproterozoic (Pujol et al., 2013; Stuart et al., 2016), as well as any excess ^{40}Ar component. Individual analyses yield initial $^{40}Ar/^{36}Ar$ values ranging from 191 ± 63 to 630 ± 660 (1σ, Table DR3). A weighted mean of all plateau ages from this study yields an age of 2054.47 ± 0.84 Ma (2σ, n=30, MSWD = 0.23, P = 1.00). Biotite from the Upper Zone samples, as well as sample B14-086 from the Critical Zone, yield concordant plateaus, comprised of at least 95% of the total ^{39}Ar released (Fig. 4). Biotite from the Main Zone, as well as sample B14-080 from the Upper Critical Zone, yield young apparent ages during early heating steps followed by plateaus comprised of ~50-90% of the total ^{39}Ar released (Fig. 4). Young apparent ages during early heating steps are consistent with a potential late re-heating event above the $^{40}Ar/^{39}Ar$ closure temperature of biotite.

4. Rapid Cooling of the RLS

4.1 Geochronology, Cooling Rate, and Closure Temperature

Two noticeable observations from the biotite $^{40}Ar/^{39}Ar$ results are (1) the overlap between the ages of individual stratigraphic levels from $^{40}Ar/^{39}Ar$ ages of biotite and previously published zircon U-Pb ages (Mungall et al., 2016; Scoates and Wall, 2015; Zeh et al., 2015), as well as the proximity between their respective weighted means and

(2) the weighted mean plateau ages of biotite throughout the RLS all overlap at 2σ and indicate that the entire body cooled to roughly the same temperature (i.e. the closure temperature of the $^{40}Ar/^{39}Ar$ system in biotite) during the same time interval (Fig. 7).

The overlap between zircon U-Pb ages and biotite $^{40}Ar/^{39}Ar$ ages requires a rapid cooling rate. Ti-in-zircon thermometry of zircon indicates crystallization at ~788-713°C in the Upper Zone and 875-766°C for the Main and Critical Zones (Ver Hoeve et al., 2018; Zeh et al., 2015). The nominal closure temperature of the $^{40}Ar/^{39}Ar$ system in biotite is ~350°C (McDougall and Harrison, 1999), though this value may vary depending on the diffusive length scale, the chemical composition of biotite, and the cooling rate. For biotite from the RLS (Table 1), a closure temperature of 429°C is estimated using the equation of Dodson (1973) and assuming a cylindrical geometry, if the diffusion parameters of Grove and Harrison (1996) for Fe-rich biotite (Mg# = 29) are used in combination with the average biotite grain radius from this study (~350 μm) and a 1000°C Ma^{-1} cooling rate (416°C for 500°C Ma^{-1}). Given the elevated and variable Mg content of biotite from this study (Table 1), we consider a range of ~450-350°C to be an appropriate estimate of the closure temperature of biotite in our samples (Fig. 8) and infer average cooling rates upwards of 1000°C Ma^{-1} for the RLS to the closure of biotite.

4.2 Numerical Heat-loss Modelling

Some authors have used one dimensional (1-D) conductive cooling models to place constraints on the crystallization (Cawthorn and Walraven, 1998) and post-crystallization cooling duration of the RLS (Cawthorn and Webb, 2013; Zeh et al., 2015). For example, previous thermal modelling of the Bushveld Complex by Zeh et al. (2015),

which produced a cooling model that matched observed U-Pb zircon ages, assumed no additional heat was produced (e.g. radiogenic or latent heat), that no advection took place and that the magma body was an infinite sheet. The 1-D models assume the RLS is an infinite sheet and that heat is not lost through the sides, but rather only through the top and bottom.

With these assumptions in place, the cooling profile for the magma body can be solved using the following heat flow equation (Carslaw and Jaeger, 1959):

$$\frac{T-T_s}{T_o-T_s} = \frac{1}{2}\left(erf\left(\frac{a-x}{2\sqrt{kt}}\right) + erf\left(\frac{a+x}{2\sqrt{kt}}\right)\right) \tag{2}$$

Where:
T = actual temperature at position x (°C)
T_s = initial temperature of host rock (°C)
T_o = initial temperature of the magma body (°C)
a = half thickness of the magma body (m)
x = distance from center of magma body (m)
k = thermal conductivity (m^2/s)
t = time (s)

Also, where the initial temperature of the host rock (T_s) is calculated for a given depth within the intrusion assuming a local geothermal gradient of 20°C km^{-1} and an average surface temperature of 15°C.

Whereas the samples from this study do not come from the exact center of an infinite sheet, but rather from closer to the contact with the host rocks, we also solve the heat flow equation while allowing heat loss through the sides of the intrusion (a 2-D model). This cooling profile can be solved using a modification of equation (1) of Carslaw and Jaeger (1959):

$$\frac{T-T_s}{T_o-T_s} = \left[\frac{1}{2}\left(\mathrm{erf}\left(\frac{a-x}{2\sqrt{kt}}\right) + \mathrm{erf}\left(\frac{a+x}{2\sqrt{kt}}\right)\right)\right]\left[\frac{1}{2}\left(\mathrm{erf}\left(\frac{b-y}{2\sqrt{kt}}\right) + \mathrm{erf}\left(\frac{b+y}{2\sqrt{kt}}\right)\right)\right]\left[\frac{1}{2}\left(\mathrm{erf}\left(\frac{c-z}{2\sqrt{kt}}\right) + \mathrm{erf}\left(\frac{c+z}{2\sqrt{kt}}\right)\right)\right] \tag{3}$$

Where the following new variables are introduced:
b = half thickness of the magma body in horizontal direction “b” (i.e. East-West)
y = distance from center of magma body (b - direction)
c = half thickness of the magma body in horizontal direction “c” (i.e. North-South)
z = distance from center of magma body (c - direction)

The cooling models are solved using an initial temperature (T_o) of 1250°C for an 8 km sheet of magma. The choice of initial temperature has little effect on the final cooling model, as the model is built to pass through the observed U-Pb zircon ages and estimated temperatures. Both models are solved for a point at the center of the intrusion (i.e. 4 km from the roof contact), with an estimated 4 km of roof rocks on top of the intrusion (in terms of depth). A 4 km thick roof is consistent with the roof being composed of 2 km Rooiberg Group Lavas (Schweitzer et al., 1997) with 2 km of the coeval and related Bushveld Granite on top. In the case of the 2-D model, the point being solved for is still located at the center of the intrusion in terms of depth (x = 0 m), as well as at the center of the intrusion in terms of its North-South dimension (z = 0 m). However, the point is now placed at 30 km from the Eastern edge of the Bushveld Complex, while assuming a 450 km-wide intrusion (b = 225,000 m; y = 195,000 m). This placement allows for a significant amount of heat loss through the sides of the intrusion and provides a likely more realistic estimate of the cooling profile of the solidified body.

Our 2-D model is preferable in that it can estimate cooling rates for samples near the sides of the intrusion, such as our samples from the Eastern Limb. Although 1-D and 2-D conductive cooling models are indistinguishable at high temperatures, faster cooling rates in the 2-D model produce significantly lower temperatures as cooling progresses (Fig. 8).

4.3 Implications of modelling and observed cooling rate

Modelling results show that even with the accelerated cooling of the 2-D model, cooling of the intrusion via conductive-only heat loss results in average cooling rates on the order of ~100°C Ma^{-1}, inconsistent with our ages and closure temperatures. The average cooling rate of the RLS stratigraphy is upwards of ~1000°C Ma^{-1} when calculated to match the observed ages; a cooling rate similar to cooling rates experienced in the lower oceanic crust due to high temperature hydrothermal circulation [e.g. Hasenclever et al. (2014), VanTongeren et al. (2008)]. Similar rates were also calculated for the Skaergaard layered mafic intrusion (Norton and Taylor (1979) and attributed to hydrothermal circulation.

In fact, ample evidence exists for hydrothermal circulation within the RLS rocks at the high, mid and low temperature stages (Schiffries and Skinner, 1987), in addition to the contact aureole of the Bushveld Complex (e.g. Harris et al., 2003). Within the RLS, Schiffries and Skinner (1987) characterized three major post-magmatic hydrothermal stages encompassing the entire stratigraphy, with the most abundant of the hydrothermal stages being the upper amphibolite (>600°C) and greenschist facies (300-600°C) equivalent mineral assemblages. Additionally, Harris et al. (2003) found that the thermal structure of the contact aureole of the Bushveld Complex had been modified by fluid advection. This modification is contrary to a conductive-only heat-loss model, a model which results in greatly overestimated timescales (Harris et al., 2003), similar to the conductive heat-loss results in this study.

5. Long-lived, Localized Hydrothermal Activity

Our results for the gabbroic sections of the RLS stratigraphy are considerably different than those found for the mineralized horizons of the Merensky Reef and the UG-2 and MG-1 chromitites.

Scoates and Wall (2015) calculated a cooling rate of 125°C Ma^{-1} for the Merensky Reef, based on age differences between U-Pb ages of zircon and rutile [closure temperature ~400-450°C (Schmitz and Bowring 2003)]. Previous biotite $^{40}Ar/^{39}Ar$ ages from the RLS have yielded younger ages than those in this study (Fig. 7). These ages [Fig. 7, re-calculated for FC = 28.201 Ma; (Kuiper et al., 2008)] are limited to a weighted mean plateau age of 2050.3 ± 3.1 Ma from the UG-2 chromitite in the Western Limb (Nomade et al., 2004), a 2050 ± 4 Ma plateau age for a single biotite from near the MG-1 chromitite in the Western Limb (Cassata et al., 2009), and plateau ages of 2010 ± 10 Ma and 1999 ± 10 Ma for two biotites from the Merensky Reef (Scoates and Wall, 2015). The ages of Nomade et al. (2004) and Cassata et al. (2009) are reported as cooling ages, however they are reported without isotope correlation diagrams (i.e. an excess ^{40}Ar component cannot be resolved) and the true age may be slightly different than the reported plateau ages. Scoates and Wall (2015) suggest the ~2000 Ma biotite ages are a product of a late-stage hydrothermal event that locally affected the Merensky Reef.

The lack of young $^{40}Ar/^{39}Ar$ biotite ages throughout the RLS in this study, as well as the homogeneity of ages, suggests that previously reported ages from the UG-2 and MG-1 are potentially a product of localized late-stage hydrothermal fluids, similar to the ages of the Merensky Reef. While secondary mineralization due to hydrothermal alteration within the Merensky Reef and UG-2 is well characterized [e.g. Li et al. (2004)],

the resetting of $^{40}Ar/^{39}Ar$ biotite ages within the UG-2 by late-stage hydrothermal fluids is also supported by isotopic disequilibrium produced via post-magmatic circulating fluids (Mathez and Kent, 2007) as well as mineralogical variations due to interactions with fluids at intermediate temperatures (Penberthy and Merkle, 1999). As speculated by Scoates and Wall (2015), the source of these fluids may be related to the regional heat produced during the Limpopo Belt orogeny (2.0-2.4 Ga; Kramers and Mouri, 2011).

The observation of young apparent ages $^{40}Ar/^{39}Ar$ biotite ages and potential late-stage hydrothermal alteration of chromitites provides important context for interpreting small differences in precise geochronologic results from samples of or in contact with these chromitite veins. It is possible, as postulated by Mungall et al. (2016), that the Merensky Reef and other PGE-rich regions of the RLS experienced a different thermal history from the bulk of the stratigraphy.

6. Conclusions

Our data shows that biotite $^{40}Ar/^{39}Ar$ ages throughout the RLS stratigraphy all overlap at 2σ. The homogeneity of ages throughout the stratigraphy, along with overlapping ages between the $^{40}Ar/^{39}Ar$ and U-Pb systems, indicates that the RLS cooled rapidly through the closure temperature of biotite. Thermal modelling suggests that conductive heat loss alone cannot produce the observed ages and inferred cooling rates. We conclude that heat loss of the solidified body was enhanced by hydrothermal circulation associated with the emplacement of the RLS. This is supported by ample field evidence for hydrothermal circulation at intermediate temperatures within the RLS rocks (Schiffries and Skinner,

1987) as well as the conclusions of Harris et al. (2003) of enhanced heat-loss due to fluid advection within the contact aureole of the Bushveld Complex.

$^{40}Ar/^{39}Ar$ biotite ages from this study are considerably older than reported $^{40}Ar/^{39}Ar$ biotite ages of the Merensky Reef and chromitites (UG-2 and MG-1). The lack of similarly young ages throughout the RLS stratigraphy indicates that the young ages are likely a product of localized late-stage circulating hydrothermal fluids. This is consistent with the recent work of Schannor et al. (2018) suggesting that chromitites are fluid traps, not barriers.

7. References

Carslaw, H. S., and Jaeger, J. C., 1959, Conduction of heat in solids: Oxford: Clarendon Press, 1959, 2nd ed.

Cassata, W. S., Renne, P. R., and Shuster, D. L., 2009, Argon diffusion in plagioclase and implications for thermochronometry: a case study from the Bushveld Complex, South Africa: Geochimica et Cosmochimica Acta, v. 73, no. 21, p. 6600-6612.

Cawthorn, R. G., and Walraven, F., 1998, Emplacement and crystallization time for the Bushveld Complex: Journal of Petrology, v. 39, no. 9, p. 1669-1687.

Cawthorn, R. G., and Webb, S. J., 2013, Cooling of the Bushveld Complex, South Africa: implications for paleomagnetic reversals: Geology, v. 41, no. 6, p. 687-690.

Dalrymple, G. B., and Lanphere, M. A., 1969, Potassium-argon dating: Principles, techniques and applications to geochronology: San Francisco, California, Freeman, p. 258-258.

Dalrymple, G. B., and Lamphere, M. A., 1974, 40Ar/39Ar age spectra of some undisturbed terrestrial samples: Geochimica et Cosmochimica Acta, v. 38, no. 5, p. 715-738.

Dodson, M. H., 1973, Closure temperature in cooling geochronological and petrological systems: Contributions to Mineralogy and Petrology, v. 40, no. 3, p. 259-274.

Fleck, R. J., Sutter, J. F., and Elliot, D. H., 1977, Interpretation of discordant 40Ar/39Ar age-spectra of Mesozoic tholeiites from Antarctica: Geochimica et Cosmochimica Acta, v. 41, no. 1, p. 15-32.

Grove, M., and Harrison, T. M., 1996, 40Ar* diffusion in Fe-rich biotite.

Grove, T. L., Baker, M. B., and Kinzler, R. J., 1984, Coupled CaAl-NaSi diffusion in plagioclase feldspar: experiments and applications to cooling rate speedometry: Geochimica et Cosmochimica Acta, v. 48, no. 10, p. 2113-2121.

Harris, N., McMillan, A., Holness, M., Uken, R., Watkeys, M., Rogers, N., and Fallick, A., 2003, Melt Generation and Fluid Flow in the Thermal Aureole of the Bushveld Complex: Journal of Petrology, v. 44, no. 6, p. 1031-1054.

Hasenclever, J., Theissen-Krah, S., Rüpke, L. H., Morgan, J. P., Iyer, K., Petersen, S., and Devey, C. W., 2014, Hybrid shallow on-axis and deep-axid hydrothermal circulation at fast-spreading ridges: Nature, v. 508, no. 7497, p. 508.

Hattingh, P. J., 1995, Palaeomagnetic constraints on the emplacement of the Bushveld Complex: Journal of African Earth Sciences, v. 21, no. 4, p. 549-551.

Hess, H. H., 1960, Stillwater Igneous Complex, Montana a Quantitative Mineralogical Study: Geological Society of America Memoirs, v. 80, p. 1-240.

Hess, J. C., Lippolt, H. J., and Wirth, R., 1987, Interpretation of 40Ar/39Ar biotites: Evidence from hydrothermal degassing experiments and TEM studies: Chemical Geology: Isotope Geoscience section, v. 66, no. 1-2, p. 137-149.

Jourdan, F., Verati, C., and Féraud, G., 2006, Intercalibration of the Hb3gr 40Ar/39Ar dating standard: Chemical Geology, v. 231, no. 3, p. 177-189.

Kramers, J. D., and Mouri, H., 2011, The geochronology of the Limpopo Complex: a controversy solved: Geological Society of America Memoirs, v. 207, no. 11, p. 85.

Kuiper, K., Deino, A., Hilgen, F., Krijgsman, W., Renne, P., and Wijbrans, J., 2008, Synchronizing rock clocks of Earth history: Science, v. 320, no. 5875, p. 500-504.

Lee, J.-Y., Marti, K., Severinghaus, J. P., Kawamura, K., Yoo, H.-S., Lee, J. B., and Kim, J. S., 2006, A redetermination of the isotopic abundances of atmospheric Ar: Geochimica et Cosmochimica Acta, v. 70, no. 17, p. 4507-4512.

Li, C., Ripley, E. M., Merino, E., and Maier, W. D., 2004, Replacement of base metal sulfides by actinolite, epidote, calcite and magnetite in the UG2 and Merensky Reef of the Bushveld Complex, South Africa: Economic Geology, v. 99, no. 1, p. 0173-0184.

Ludwig, K. R., 2003, *ISOPLOT a plotting and regression program for radiogenic isotope data*, Version Ex./3.00.

Mathez, E., and Kent, A., 2007, Variable initial Pb isotopic compositions of rocks associated with the UG2 chromitite, eastern Bushveld Complex: Geochimica et Cosmochimica Acta, v. 71, no. 22, p. 5514-5527.

McCallum, I., Raedeke, L., and Mathez, E., 1980, Investigations of the Stillwater Complex: Part I. Stratigraphy and structure of the banded zone: American Journal of Science, v. 280, no. 1, p. 59-87.

McDougall, I., and Harrison, T. M., 1999, Geochronology and Thermochronology by the 40Ar/39Ar Method, Oxford University Press on Demand.

Mercer, C. M., and Hodges, K. V., 2016, ArAR - A software tool to promote the robust comparison of K-Ar and 40Ar/39Ar dates published using different decay, isotopic, and monitor-age parameters: Chemical Geology, v. 440, p. 148-163.

Min, K., Renne, P. R., and Huff, W. D., 2011, 40Ar/39Ar dating of Ordovician K-bentonites in Laurentia and Baltoscandia: Earth and Planetary Science Letters, v. 185, no. 1-2, p. 121-134.

Molyneux, T., 2008, Compilation on a scale of 1: 50000 of the geology of the eastern compartment of the Bushveld Complex: Special Publication, v. 1.

Mungall, J. E., Kamo, S. L., and McQuade, S., 2016, U–Pb geochronology documents out-of-sequence emplacement of ultramafic layers in the Bushveld Igneous Complex of South Africa: Nature Communications, v. 7.

Nomade, S., Renne, P. R., and Merkle, R. K., 2004, 40Ar/39Ar age constraints on ore deposition and cooling of the Bushveld Complex, South Africa: Journal of the Geological Society, v. 161, no. 3, p. 411-420.

Norton, D., and Taylor Jr, H. P., 1979, Quantitative simulation of the hydrothermal systems of crystallizing magmas on the basis of transport theory and oxygen isotope data: An analysis of the Skaergaard intrustion: Journal of Petrology, v. 20, no. 3, p. 421-486.

Penberthy, C. J., and Merkle, R. K. W., 1999, Lateral variations in the platinum-group element content and mineralogy of the UG2 chromitite layer, Bushveld Complex: South African Journal of Geology, v. 102, no. 3, p. 240-250.

Pujol, M., Marty, B., Burgess, R., Turner, G., and Philippot, P., 2013, Argon isotopic composition of Archaean atmosphere probes early Earth geodynamics: Nature, v. 498, no. 7452, p. 87-90.

Renne, P. R., Balco, G., Ludwig, K. R., Mundil, R., and Min, K., 2011, Response to thecomment by WH Schwarz et al. on "Joint determination of 40K decay constants and 40Ar*/40K for the Fish Canyon sanidine standard, and improved accuracy for 40Ar/39Ar geochronology" by PR Renne et al. (2010): Geochimica et Cosmochimica Acta, v. 75, no. 17, p. 5097-5100.

Schannor, M., Veksler, I. V., Hecht, L., Harris, C., Romer, R. L., and Manyeruke, T. D., 2018, Small-scale Sr and O isotope variations through the UG2 in the eastern Bushveld Complex: The role of crustal fluids: Chemical Geology, v. 485, p. 100-112.

Schiffries, C. M., and Skinner, B. J., 1987, The Bushveld hydrothermal system; field and petrologic evidence: American Journal of Science, v. 287, no. 6, p. 566-595.

Schmitz, M. D., and Bowring, S. A., 2003, Constraints on the thermal evolution of continental lithosphere from U-Pb accessory mineral thermochronometry of lower crustal xenoliths, southern Africa: Contributions to Mineralogy and Petrology, v. 144, no. 5, p. 592-618.

Schwarz, W. H., Winfried, H., and Mario, T. 2007, Intercalibration of 40Ar-39Ar age standards NL-25, HB3gr hornblende, GA1550, SB-3, HD-B1 biotite and BMus/2 muscovite: Chemical Geology, v. 242, no. 1-2, p. 218-231.

Scoates, J. S., and Wall, C. J., 2015, Geochronology of layered intrusions, Layered Intrusions, Springer, p. 3-74.

Schweitzer, J. K., Hatton, C. J., and De Waal, S. A., 1997, Link between the granitic and volcanic rocks of the Bushveld Complex, South Africa: Journal of African Earth Sciences, v. 24, no. 1-2, 95-104.

Setera, J. B., and VanTongeren, J. A., 2018, Lateral Variability in the Upper Main Zone, Bushveld Complex, owing to Directional Magma Recharge and Emplacement from North to South: Journal of Petrology, v. 59, no. 9, p. 1763-1786.

Steiger, R. H., and Jäger, E., 1977, Subcommission on geochronology: convention on the use of decay constants in geo-and cosmochronology: Earth and planetary science letters, v. 36, no. 3, p. 359-362.

Stuart, F. M., Mark, D. F., Gandanger, P., and McConville, P., 2016, Earth-atmosphere evolution based on new determination of Devonian atmosphere Ar isotopic composition: Earth and Planetary Science Letters, v. 446, p. 21-26.

Taylor, J., 1997, Introduction to error analysis, the study of uncertainties in physical measurements.

Turrin, B. D., Swisher, C. C., and Deino, A. L., 2010, Mass discrimination monitoring and intercalibration of dual collectors in noble gas mass spectrometer systems: Geochemistry, Geophysics, Geosystems, v. 11, no. 8.

VanTongeren, J., and Mathez, E., 2013, Incoming magma composition and style of recharge below the pyroxenite marker, eastern Bushveld complex, South Africa: Journal of Petrology, v. 54, no. 8, p. 1585-1605.

VanTongeren, J. A., Kelemen, P. B., and Hanghøj, K., 2008, Cooling rates in the lower crust of the Oman ophiolite: Ca in olivine, revisited: Earth and planetary science letters, v. 267, no. 1-2, p. 69-82.

VanTongeren, J. A., Mathez, E. A., and Kelemen, P. B., 2010, A felsic end to Bushveld differentiation: Journal of Petrology, v. 51, no. 9, p. 1891-1912.

Ver Hoeve, T. J., Scoates, J. S., Wall, C. J., Weis, D., and Amini, M., 2018, A Temperature-Composition Framework for Crystallization of Fractionated Interstitial Melt in the Bushveld Complex from Trace Element Systematics of Zircon and Rutile: Journal of Petrology, v. 59, no. 7, p. 1383-1416.

Zeh, A., Ovtcharova, M., Wilson, A. H., and Schaltegger, U., 2015, The Bushveld Complex was emplaced and cooled in less than one million years–results of zirconology, and geotectonic implications: Earth and Planetary Science Letters, v. 418, p. 103-114.

Figure Captions

Figure 1

Generalized geologic map of the Eastern Limb of the Bushveld Complex (after (VanTongeren et al., 2010). Stars indicate locations for sample analyzed for biotite $^{40}Ar/^{39}Ar$ geochronology. Inset: Sketch of the geologic map of the entire Bushveld Complex. Box indicates detailed map and the focus of this study, the Eastern Limb.

Figure 2

All Isochrons. Error ellipses, calculated ages, and $^{40}Ar/^{36}Ar$ Int. values are displayed with 1σ uncertainties.

Figure 3

All Inverse Isochrons. Error ellipses, calculated ages, and $^{40}Ar/^{36}Ar$ Int. values are displayed with 1σ uncertainties.

Figure 4

All Release Spectra. Data and calculated ages are presented with 1σ uncertainties.

Figure 5

Backscatter electron image of interlayered chlorite from B14-024. Arrows denote biotite (B) grain and areas of interlayered chlorite (C).

Figure 6

Inverse Isochron from sample UG2-02 of Nomade et al. (2004). UG2-01 of Nomade et al. (2004) is an example of a discordant age spectra dominated by interlayered chlorite. The inverse isochron was constructed for steps 4.5 W (watts) through 10 W using Isoplot (Ludwig, 2003). The original reported plateau age for the sample was 2102 Ma, recalculated to 2110 Ma to match the FC age of this study.

Figure 7

Compilation of available high-precision chronology (2σ uncertainties) plotted against the generalized stratigraphic column of the Eastern Limb of the RLS. $^{40}Ar/^{39}Ar$ biotite ages are weighted mean plateau ages (this study - filled blue squares) of multiple analyses from a single sample. The vertical blue shaded region is the weighted mean of all $^{40}Ar/^{39}Ar$ biotite plateau ages from this study. Previously reported U-Pb zircon ages are reported with a - grey closed circles (Zeh et al., 2015), b - open black circles with vertical dash (Mungall et al., 2016), and c - open grey circles (Scoates and Wall, 2015). A weighted mean of published U-Pb zircon ages from the listed studies is denoted by the vertical grey region. Previously reported Ar-Ar biotite ages are reported with d and e - open grey squares (Cassata et al., 2009; Nomade et al., 2004). References for previously reported U-Pb ages of baddeleyite (open black triangles) and rutile (open black diamonds) are denoted by b and c, respectively.

Figure 8

Conductive cooling models (Carslaw and Jager, 1959) solving for the center (at 4 km depth below the top) of an 8 km thick RLS. The solid grey line is a 1-D conductive

cooling model that allows for heat loss only through the top and bottom of the mafic body. The solid black line is a 2-D conductive cooling model that allows for heat loss through the sides of the mafic body. The 2-D model again solves for the center of the RLS, however 30 km away from the lateral contact with host rocks. The range of published mean U-Pb zircon ages as well as their measured Ti-in-zircon temperatures are represented by the orange shaded area, while the weighted mean age of biotite $^{40}Ar/^{39}Ar$ plateau ages (this study) as well as their assumed closure temperature are represented by the blue shaded region.

Figure 1

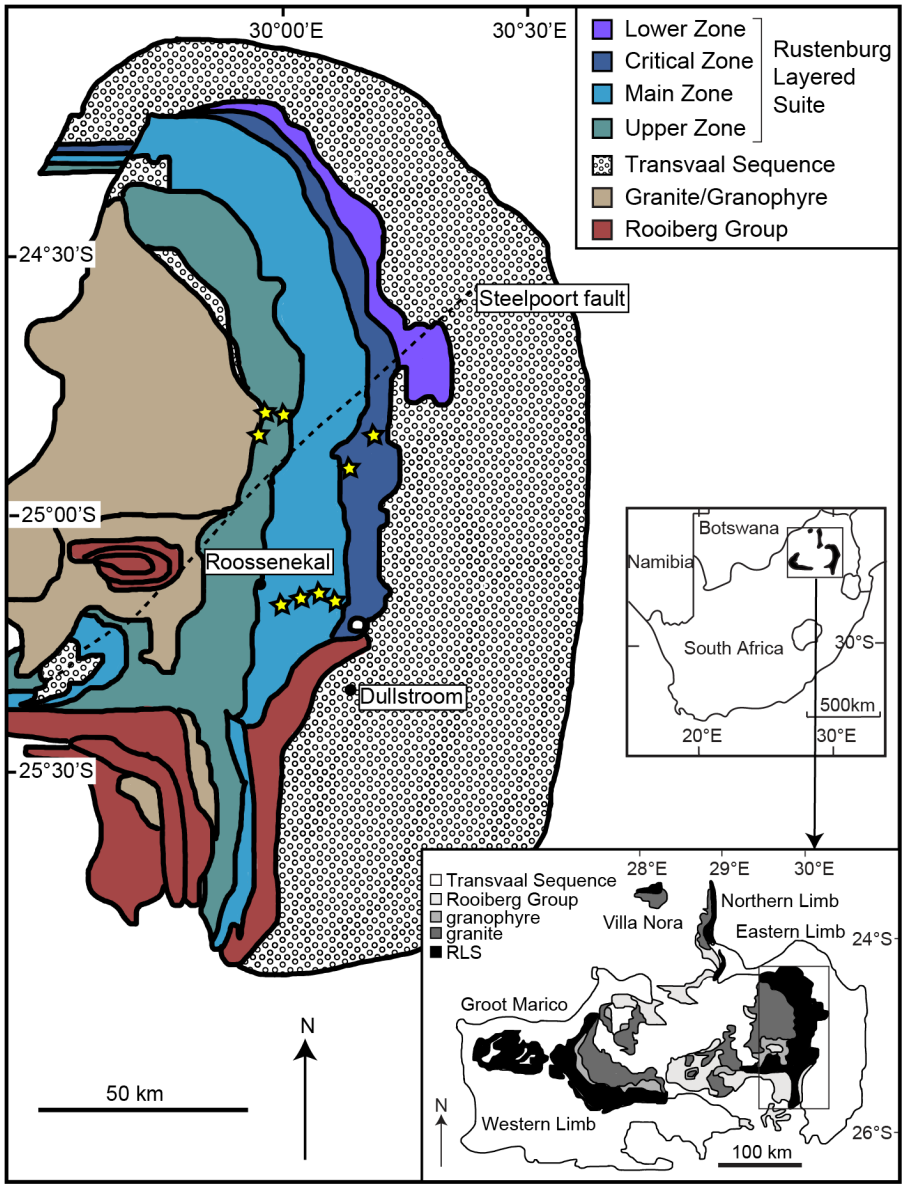
30°00'E
30°30'E
Lower Zone
Critical Zone
Main Zone
Upper Zone
Rustenburg Layered Suite
Transvaal Sequence
Granite/Granophyre
Rooiberg Group
24°30'S
Steelpoort fault
25°00'S
Roossenekal
Dullstroom
25°30'S
Botswana
Namibia
South Africa
30°S
500km
20°E
30°E
50 km
N
Transvaal Sequence
Rooiberg Group
granophyre
granite
RLS
28°E
29°E
30°E
Villa Nora
Northern Limb
Eastern Limb
24°S
Groot Marico
Western Limb
26°S
100 km

Figure 2

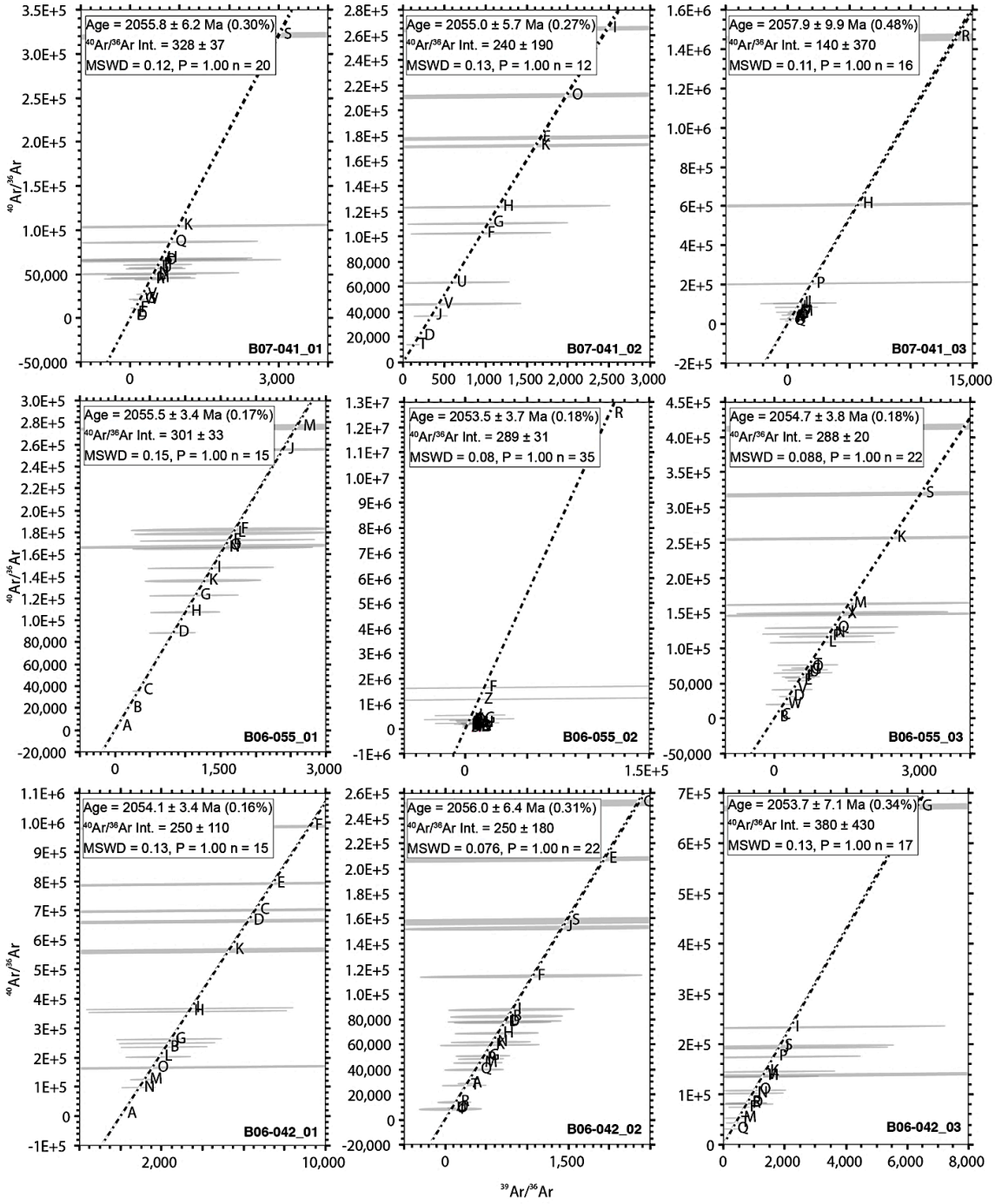
Age = 2055.8 ± 6.2 Ma (0.30%)
40Ar/36Ar Int. = 328 ± 37
MSWD = 0.12, P = 1.00 n = 20
B07-041_01
Age = 2055.0 ± 5.7 Ma (0.27%)
40Ar/36Ar Int. = 240 ± 190
MSWD = 0.13, P = 1.00 n = 12
B07-041_02
Age = 2057.9 ± 9.9 Ma (0.48%)
40Ar/36Ar Int. = 140 ± 370
MSWD = 0.11, P = 1.00 n = 16
B07-041_03
Age = 2055.5 ± 3.4 Ma (0.17%)
40Ar/36Ar Int. = 301 ± 33
MSWD = 0.15, P = 1.00 n = 15
B06-055_01
Age = 2053.5 ± 3.7 Ma (0.18%)
40Ar/36Ar Int. = 289 ± 31
MSWD = 0.08, P = 1.00 n = 35
B06-055_02
Age = 2054.7 ± 3.8 Ma (0.18%)
40Ar/36Ar Int. = 288 ± 20
MSWD = 0.088, P = 1.00 n = 22
B06-055_03
Age = 2054.1 ± 3.4 Ma (0.16%)
40Ar/36Ar Int. = 250 ± 110
MSWD = 0.13, P = 1.00 n = 15
B06-042_01
Age = 2056.0 ± 6.4 Ma (0.31%)
40Ar/36Ar Int. = 250 ± 180
MSWD = 0.076, P = 1.00 n = 22
B06-042_02
Age = 2053.7 ± 7.1 Ma (0.34%)
40Ar/36Ar Int. = 380 ± 430
MSWD = 0.13, P = 1.00 n = 17
B06-042_03
40Ar/36Ar
39Ar/36Ar

Figure 2 (Continued)

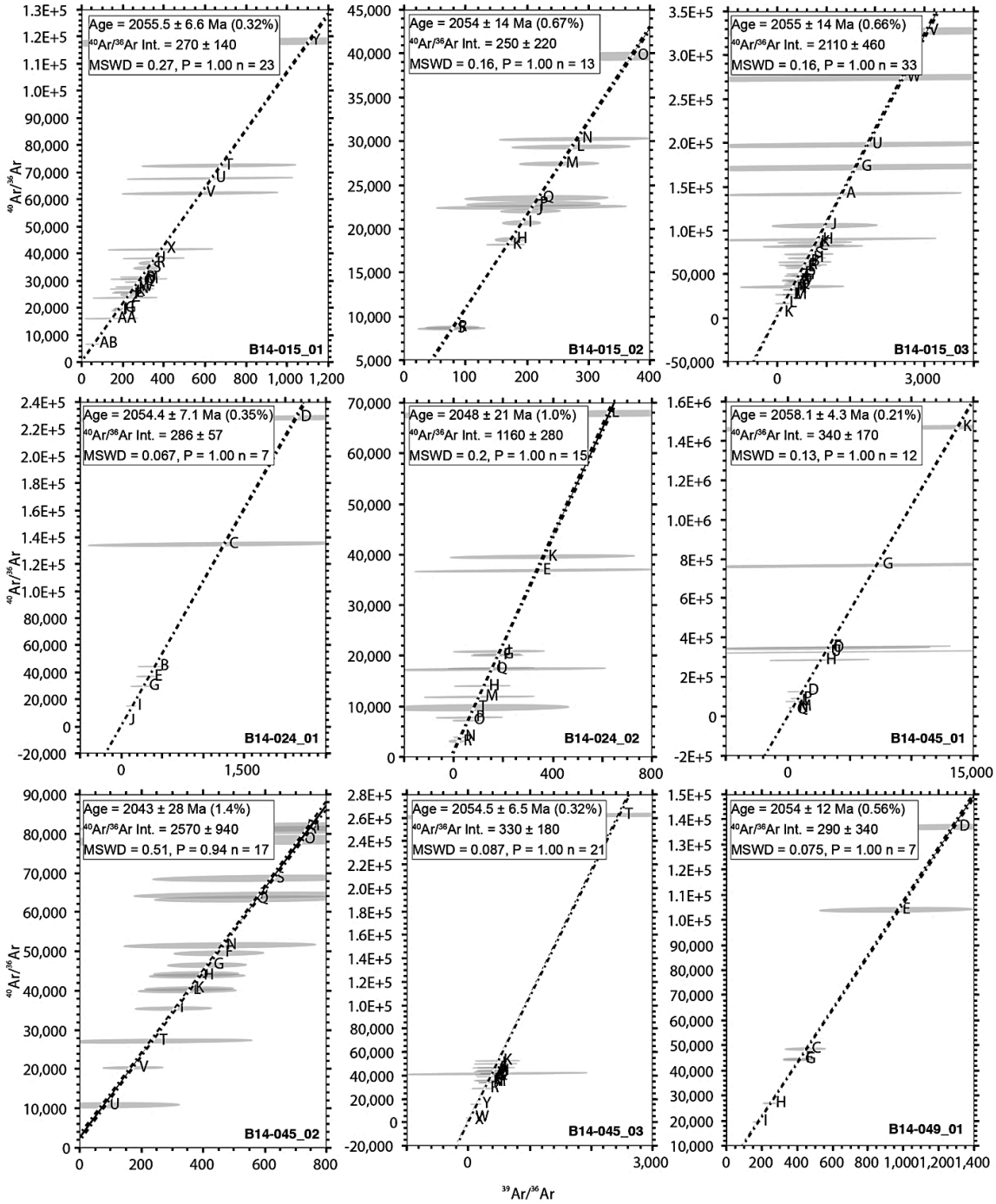

Figure 2 (Continued)

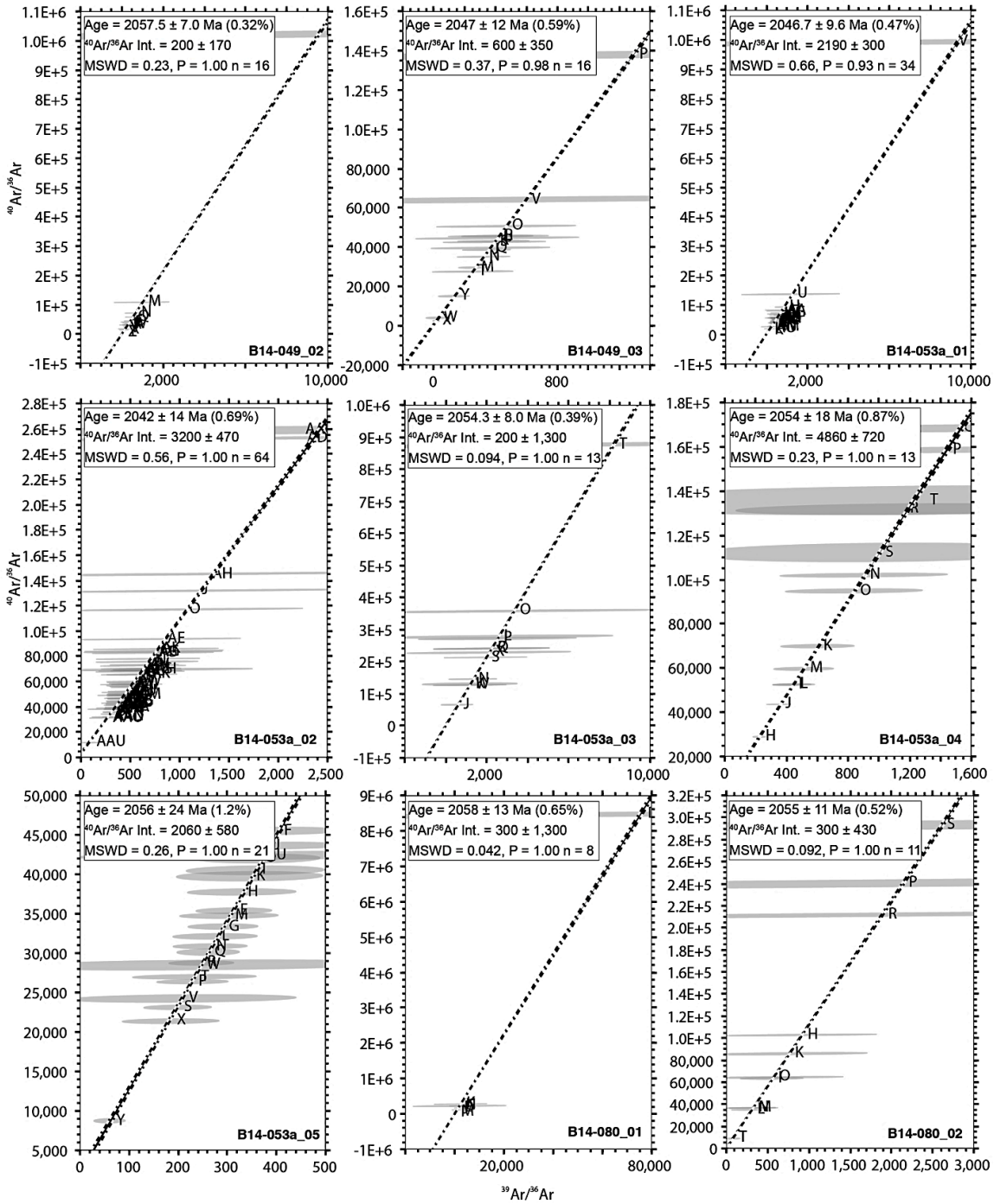

Figure 2 (Continued)

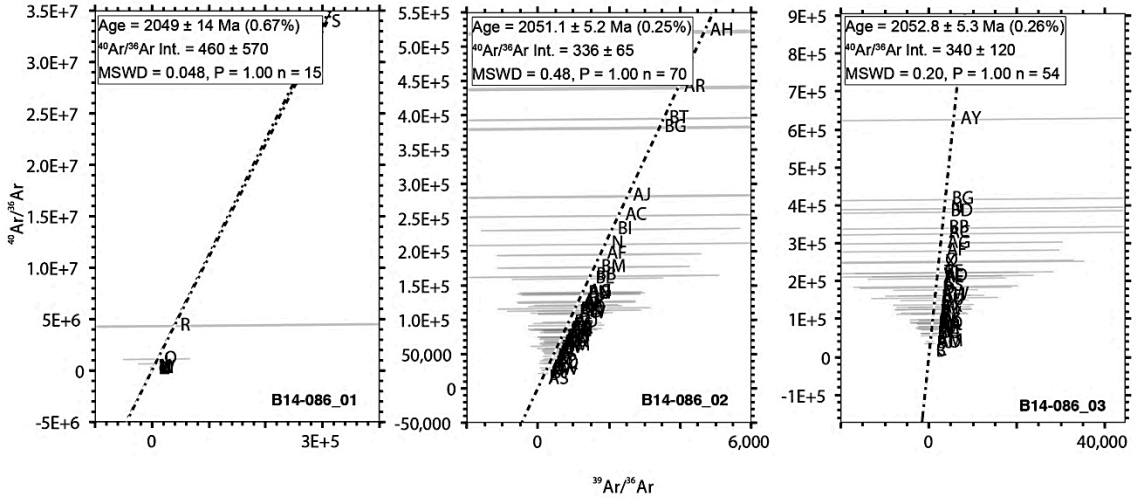

Figure 3

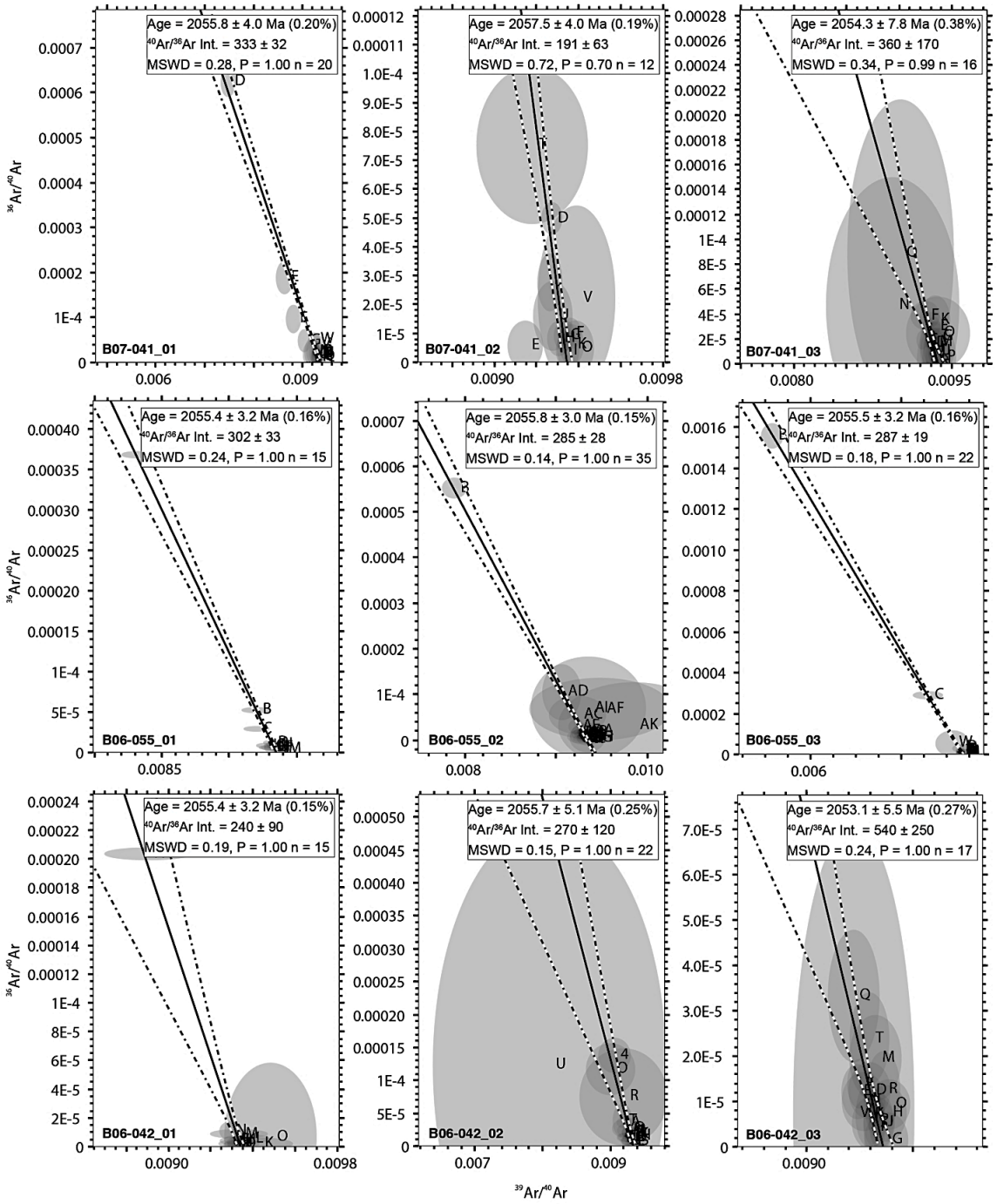
Age = 2055.8 ± 4.0 Ma (0.20%)
40Ar/36Ar Int. = 333 ± 32
MSWD = 0.28, P = 1.00 n = 20
B07-041_01
Age = 2057.5 ± 4.0 Ma (0.19%)
40Ar/36Ar Int. = 191 ± 63
MSWD = 0.72, P = 0.70 n = 12
B07-041_02
Age = 2054.3 ± 7.8 Ma (0.38%)
40Ar/36Ar Int. = 360 ± 170
MSWD = 0.34, P = 0.99 n = 16
B07-041_03
Age = 2055.4 ± 3.2 Ma (0.16%)
40Ar/36Ar Int. = 302 ± 33
MSWD = 0.24, P = 1.00 n = 15
B06-055_01
Age = 2055.8 ± 3.0 Ma (0.15%)
40Ar/36Ar Int. = 285 ± 28
MSWD = 0.14, P = 1.00 n = 35
B06-055_02
Age = 2055.5 ± 3.2 Ma (0.16%)
40Ar/36Ar Int. = 287 ± 19
MSWD = 0.18, P = 1.00 n = 22
B06-055_03
Age = 2055.4 ± 3.2 Ma (0.15%)
40Ar/36Ar Int. = 240 ± 90
MSWD = 0.19, P = 1.00 n = 15
B06-042_01
Age = 2055.7 ± 5.1 Ma (0.25%)
40Ar/36Ar Int. = 270 ± 120
MSWD = 0.15, P = 1.00 n = 22
B06-042_02
Age = 2053.1 ± 5.5 Ma (0.27%)
40Ar/36Ar Int. = 540 ± 250
MSWD = 0.24, P = 1.00 n = 17
B06-042_03
36Ar/40Ar
39Ar/40Ar

Figure 3 (Continued)

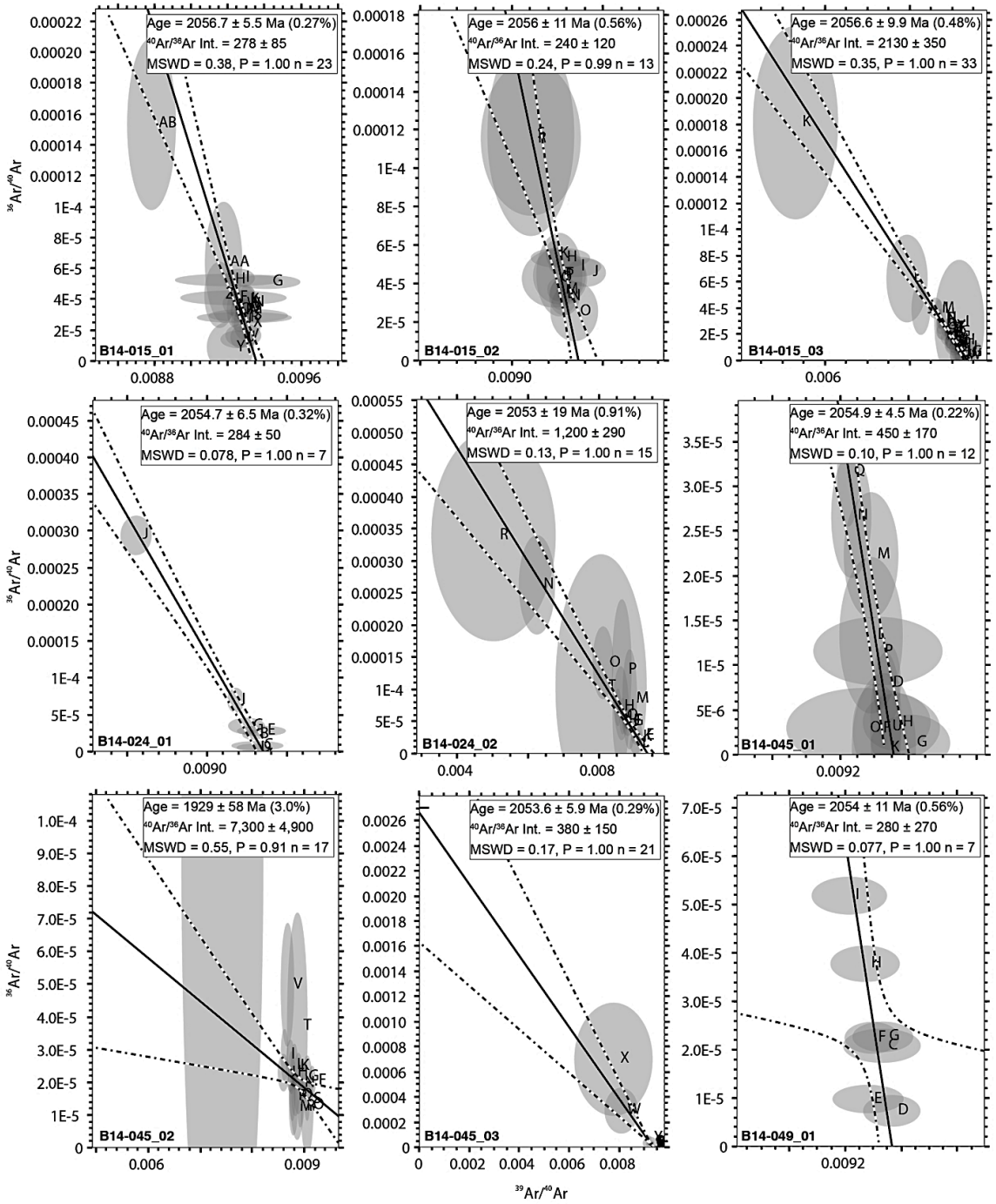

Figure 3 (Continued)

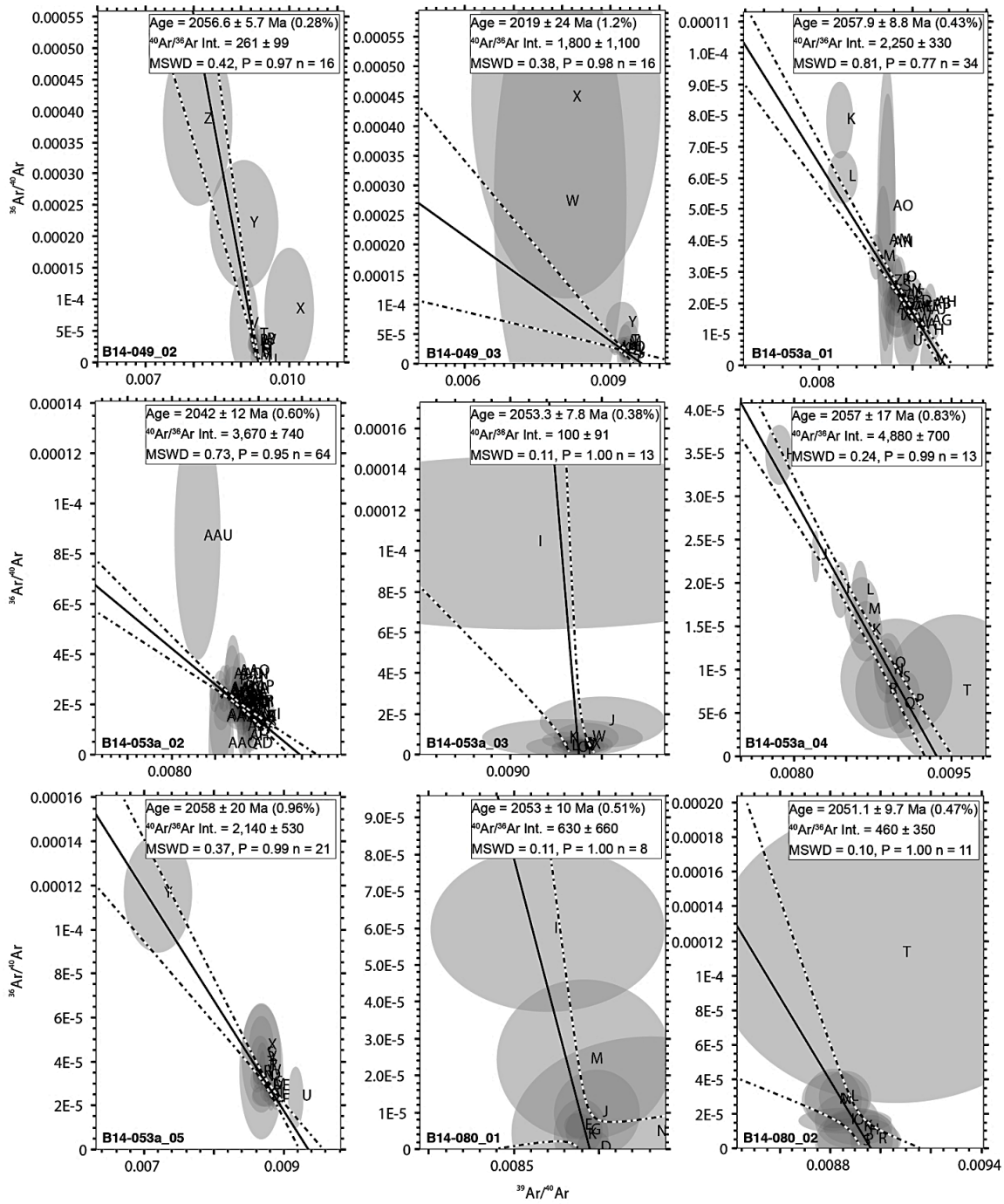

Figure 3 (Continued)

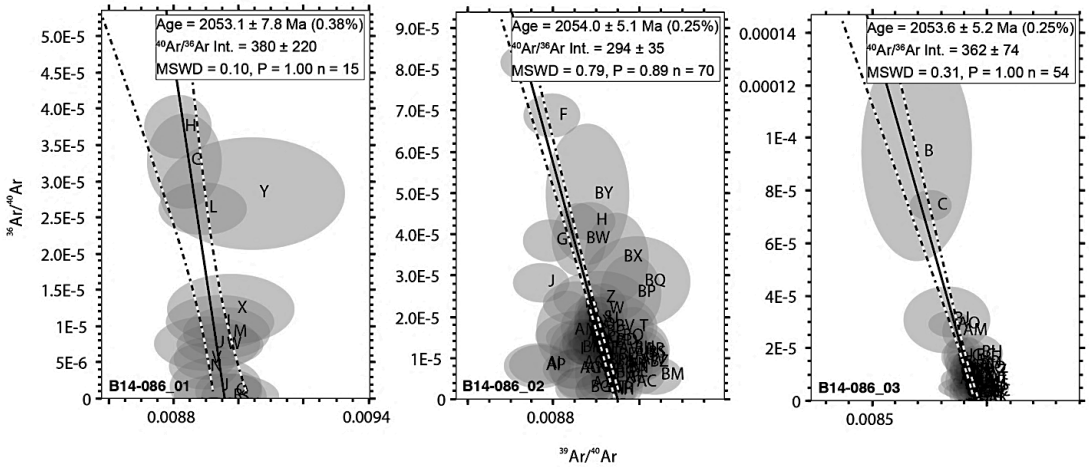

Figure 4

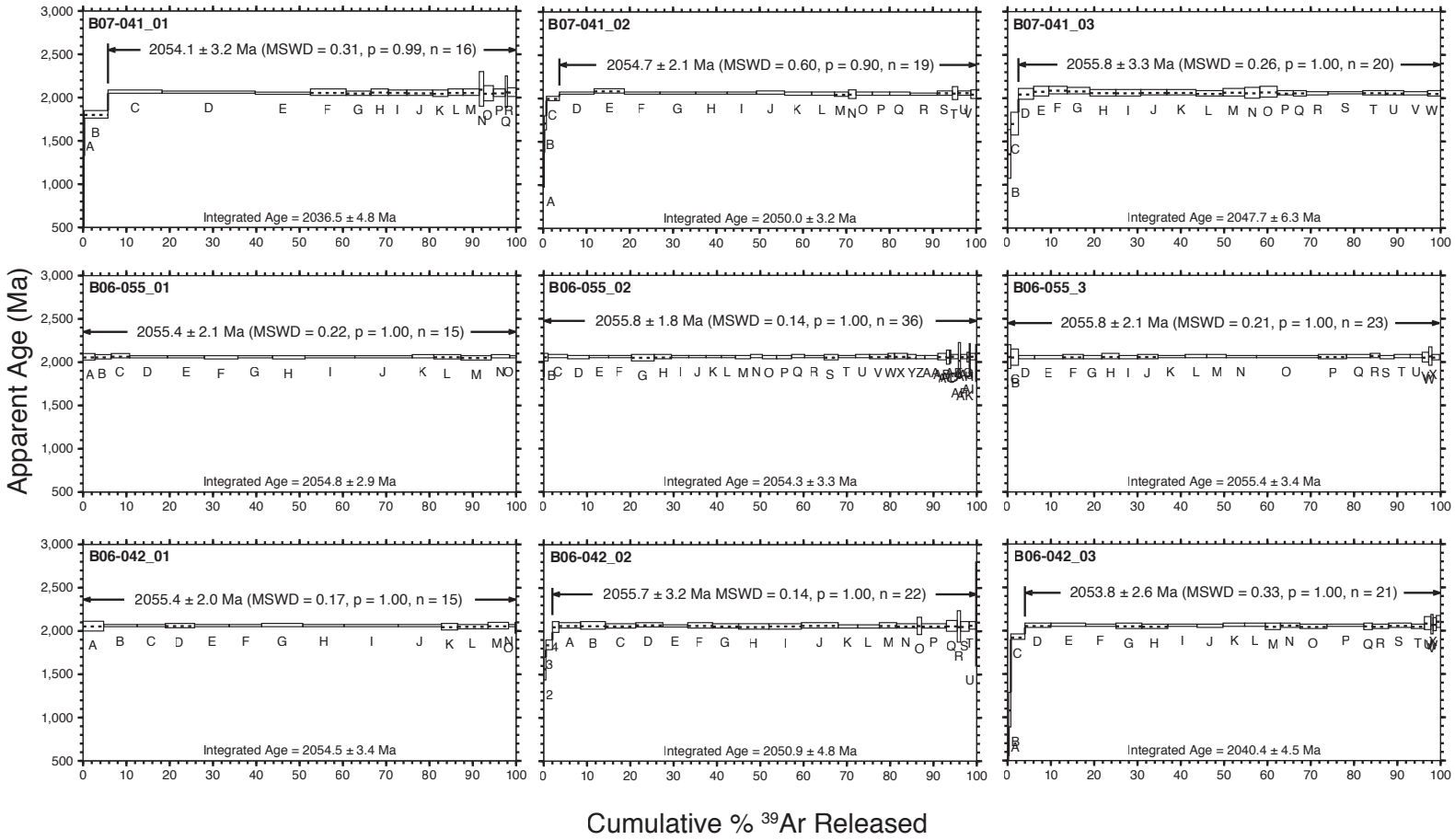
B07-041_01
2054.1 ± 3.2 Ma (MSWD = 0.31, p = 0.99, n = 16)
Integrated Age = 2036.5 ± 4.8 Ma
B07-041_02
2054.7 ± 2.1 Ma (MSWD = 0.60, p = 0.90, n = 19)
Integrated Age = 2050.0 ± 3.2 Ma
B07-041_03
2055.8 ± 3.3 Ma (MSWD = 0.26, p = 1.00, n = 20)
Integrated Age = 2047.7 ± 6.3 Ma
B06-055_01
2055.4 ± 2.1 Ma (MSWD = 0.22, p = 1.00, n = 15)
Integrated Age = 2054.8 ± 2.9 Ma
B06-055_02
2055.8 ± 1.8 Ma (MSWD = 0.14, p = 1.00, n = 36)
Integrated Age = 2054.3 ± 3.3 Ma
B06-055_3
2055.8 ± 2.1 Ma (MSWD = 0.21, p = 1.00, n = 23)
Integrated Age = 2055.4 ± 3.4 Ma
B06-042_01
2055.4 ± 2.0 Ma (MSWD = 0.17, p = 1.00, n = 15)
Integrated Age = 2054.5 ± 3.4 Ma
B06-042_02
2055.7 ± 3.2 Ma MSWD = 0.14, p = 1.00, n = 22)
Integrated Age = 2050.9 ± 4.8 Ma
B06-042_03
2053.8 ± 2.6 Ma (MSWD = 0.33, p = 1.00, n = 21)
Integrated Age = 2040.4 ± 4.5 Ma
Apparent Age (Ma)
Cumulative % 39Ar Released

Figure 4 (Continued)

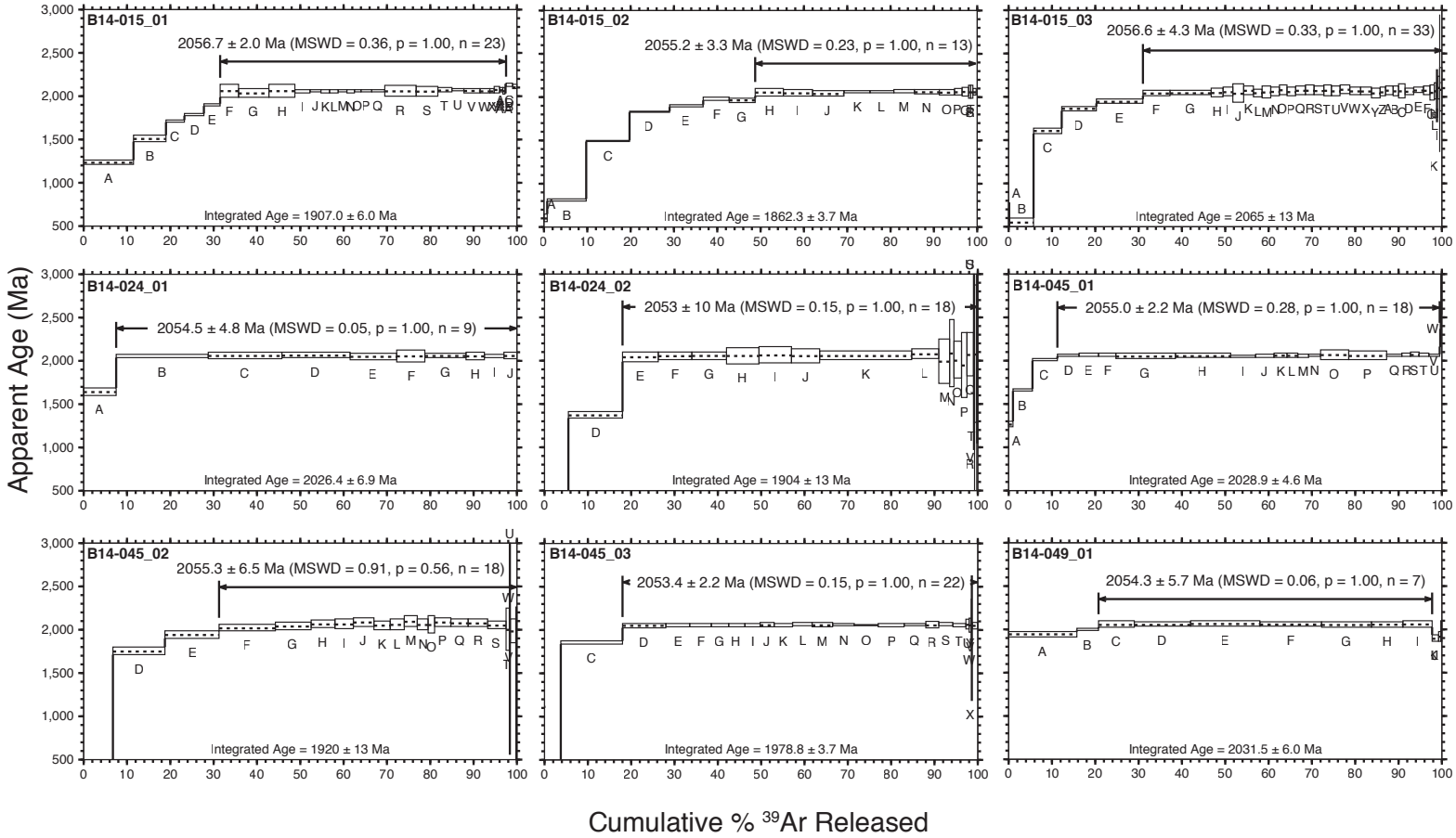

Figure 4 (Continued)

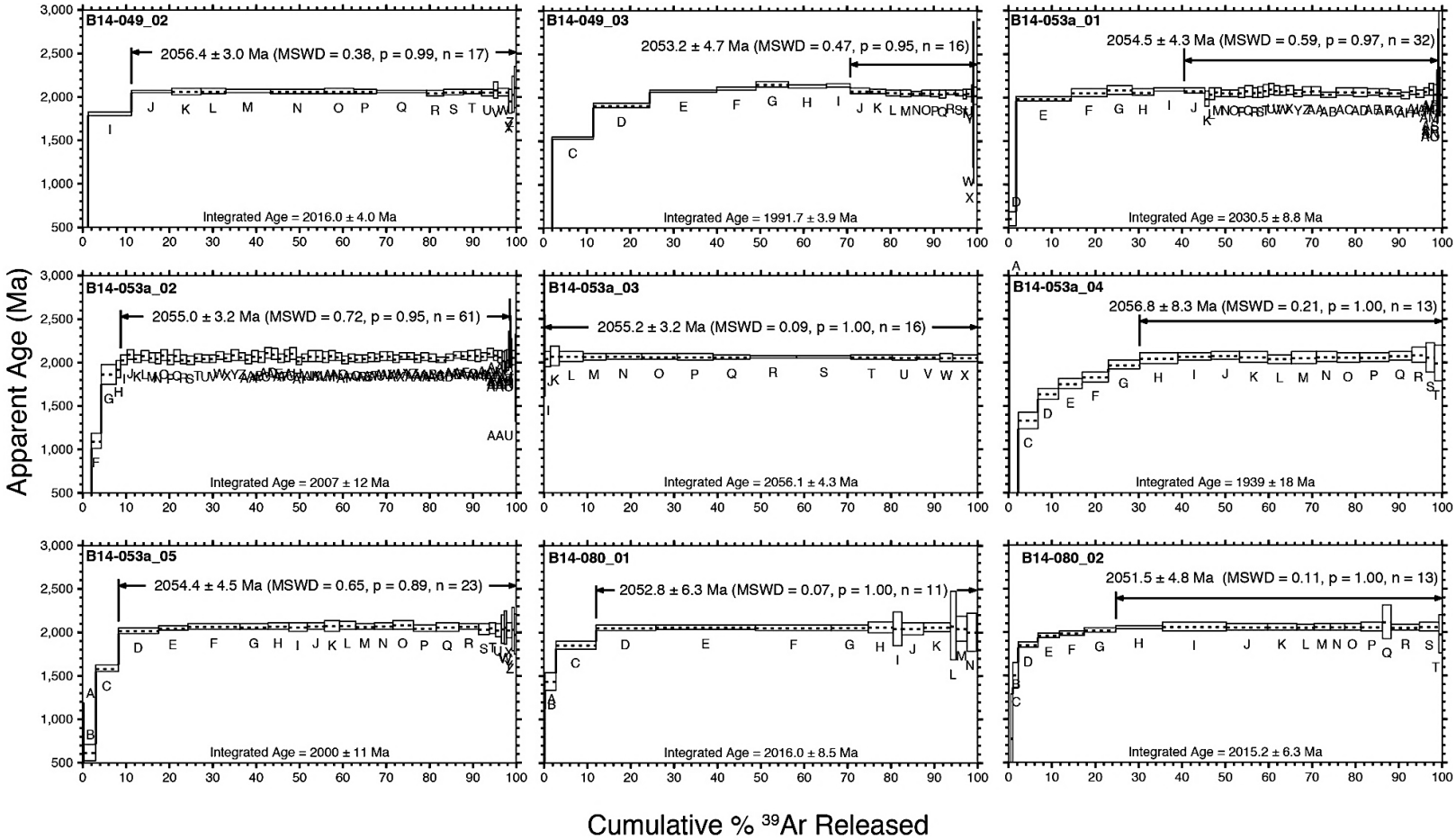

Figure 4 (Continued)

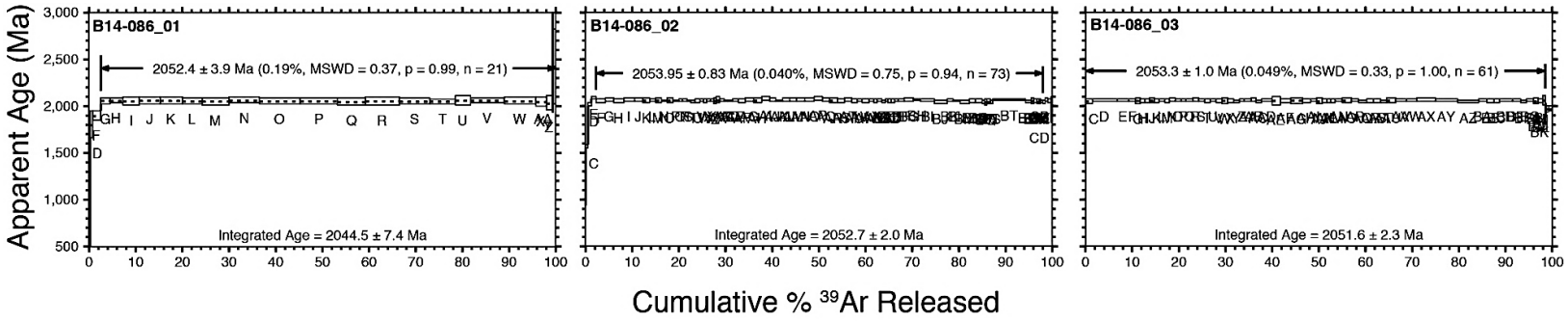

Figure 5

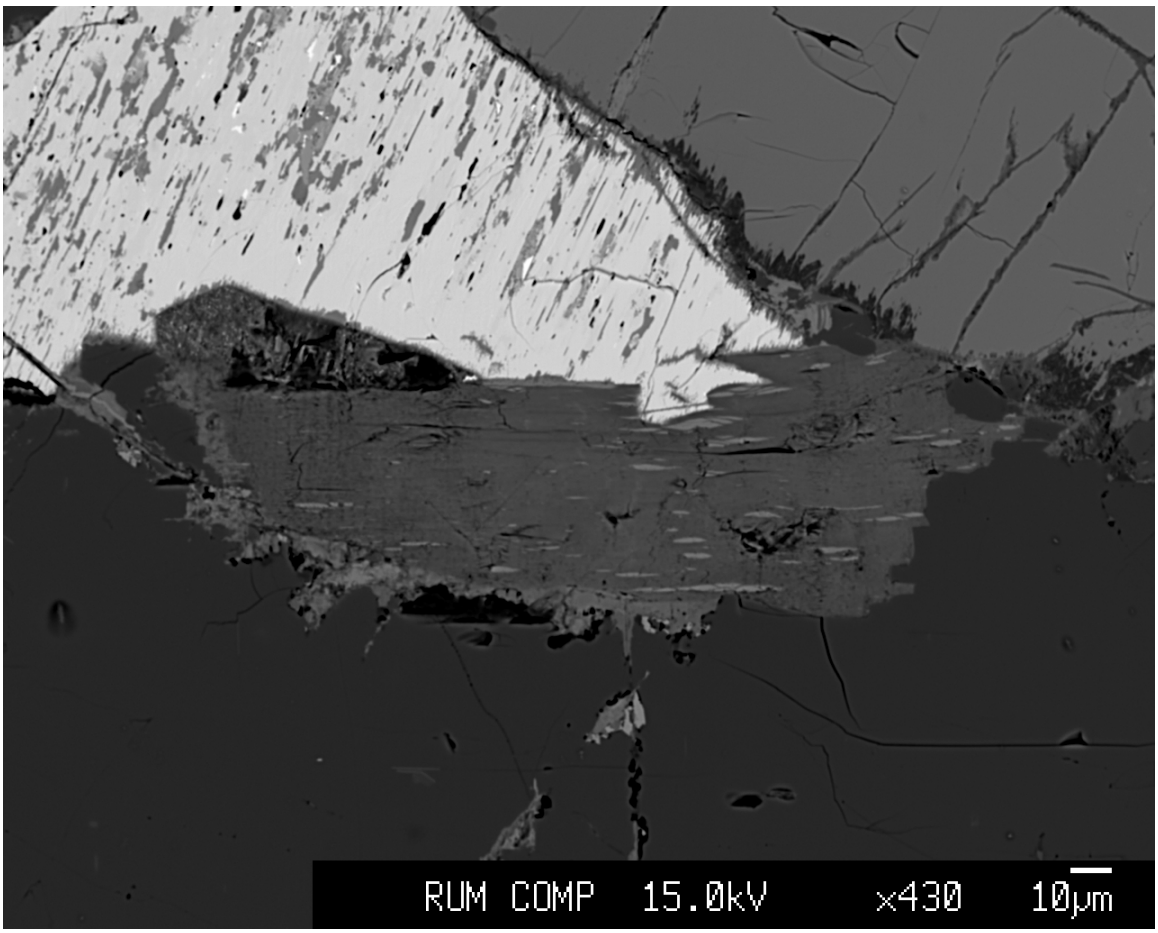

Figure 6

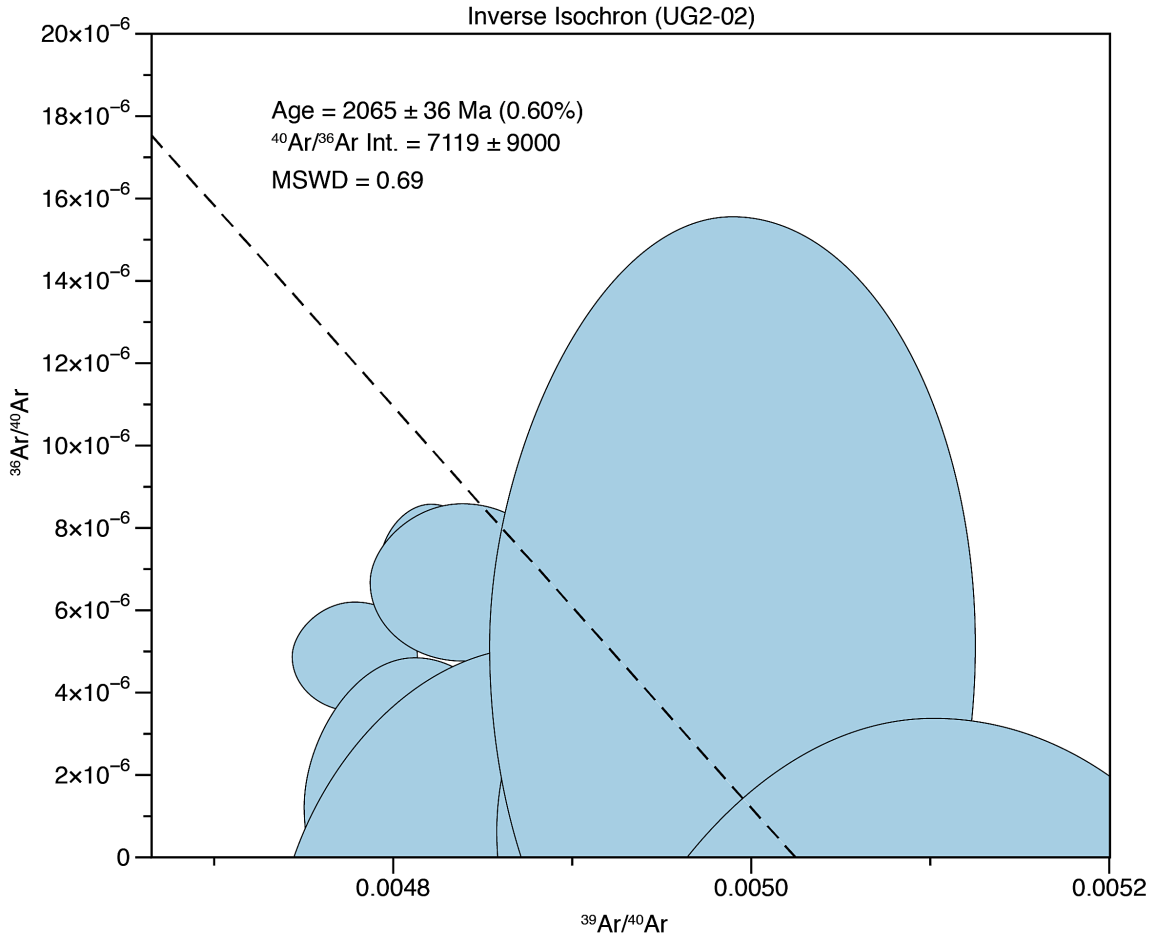
Inverse Isochron (UG2-02)
Age = 2065 ± 36 Ma (0.60%)
40Ar/36Ar Int. = 7119 ± 9000
MSWD = 0.69
20×10−6
18×10−6
16×10−6
14×10−6
12×10−6
10×10−6
8×10−6
6×10−6
4×10−6
2×10−6
0
36Ar/40Ar
0.0048
0.0050
0.0052
39Ar/40Ar

Figure 7

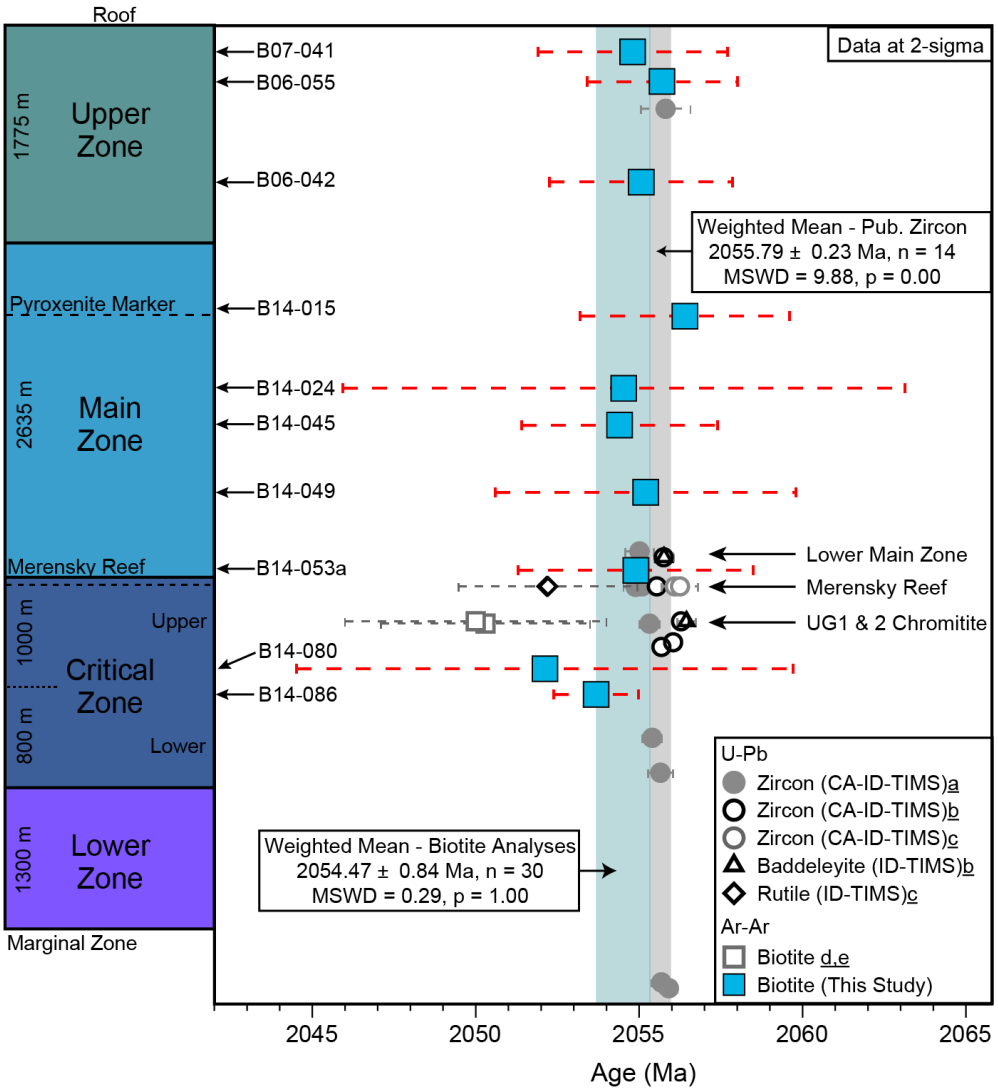
Roof
1775 m
Upper Zone
Pyroxenite Marker
2635 m
Main Zone
Merensky Reef
1000 m
Upper
Critical Zone
800 m
Lower
1300 m
Lower Zone
Marginal Zone
B07-041
B06-055
B06-042
B14-015
B14-024
B14-045
B14-049
B14-053a
B14-080
B14-086
Data at 2-sigma
Weighted Mean - Pub. Zircon
2055.79 ± 0.23 Ma, n = 14
MSWD = 9.88, p = 0.00
Lower Main Zone
Merensky Reef
UG1 & 2 Chromitite
Weighted Mean - Biotite Analyses
2054.47 ± 0.84 Ma, n = 30
MSWD = 0.29, p = 1.00
U-Pb
Zircon (CA-ID-TIMS)a
Zircon (CA-ID-TIMS)b
Zircon (CA-ID-TIMS)c
Baddeleyite (ID-TIMS)b
Rutile (ID-TIMS)c
Ar-Ar
Biotite d,e
Biotite (This Study)
2045
2050
2055
2060
2065
Age (Ma)

Figure 8

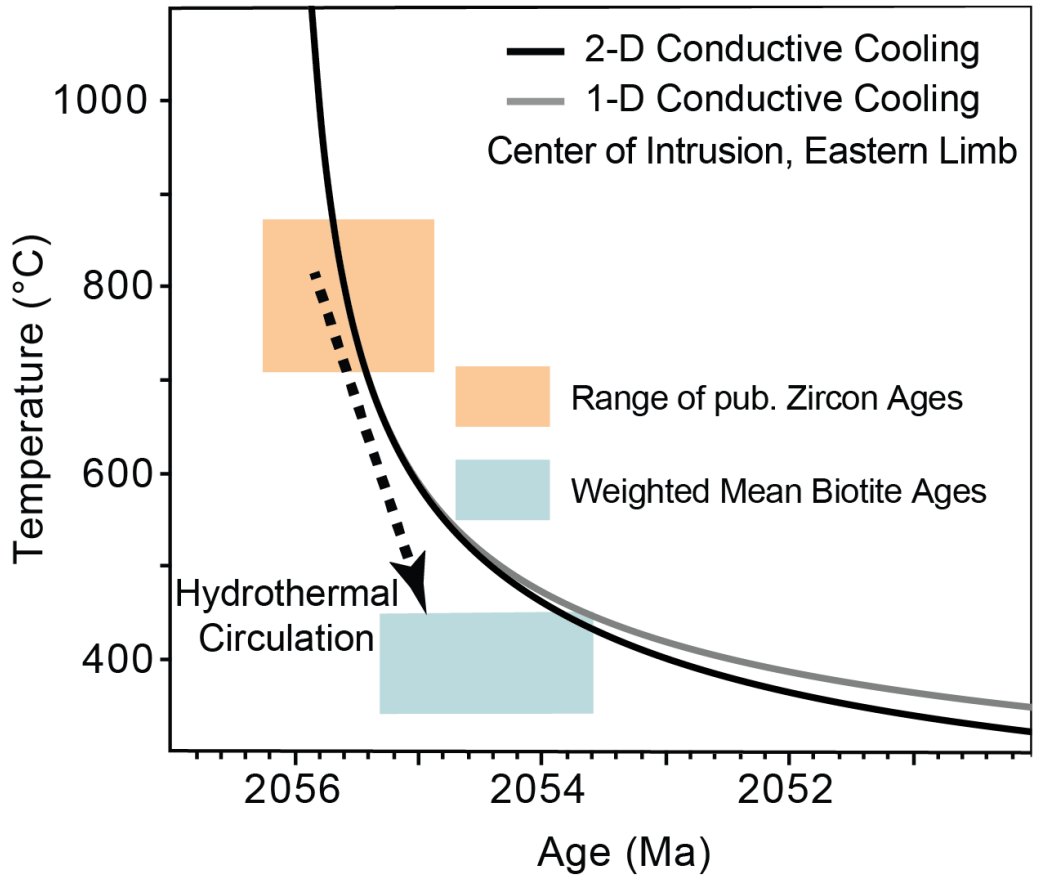
2-D Conductive Cooling
1-D Conductive Cooling
Center of Intrusion, Eastern Limb
Range of pub. Zircon Ages
Weighted Mean Biotite Ages
Hydrothermal
Circulation
Temperature (°C)
1000
800
600
400
2056
2054
2052
Age (Ma)

Table 1

Age, composition, and location summary of biotite from the Rustenburg Layered Suite of the Bushveld Complex.

Sample	Latitude (S)	Longitude (E)	Zone	Stratigraphic Height (m)[8]	Rock Type[†]	Weighted mean $^{40}Ar/^{39}Ar$ age (Ma)	n	MSWD	P	X_{annite}
B07-041	24° 51.829’	29° 54.430’	Upper Zone	4590	Ol-Mt gabbro	2054.8 ± 3.1	3	0.07	0.93	0.77 ± 0.02
B06-055	24° 51.874’	29° 54.756’	Upper Zone	4335	Ol-Mt gabbro	2055.7 ± 2.3	3	0.01	0.99	0.54 ± 0.01
B06-042	24° 48.776’	29° 57.036’	Upper Zone	3471	Mt gabbro	2055.0 ± 2.8	3	0.15	0.86	0.47 ± 0.08
B14-015	25° 12.006’	29° 56.524’	Main Zone	2320	Mt gabbro	2056.3 ± 3.2	3	0.08	0.93	0.30 ± 0.02
B14-024	25° 13.462’	29° 59.328’	Main Zone	1700	Gabbronorite	2054.2 ± 8.7	2	0.02	0.89	0.38 ± 0.03
B14-045	25° 13.164’	30° 00.893’	Main Zone	1385	Gabbronorite	2054.3 ± 3.0	3	0.15	0.86	0.35 ± 0.05
B14-049	25° 11.863’	30° 02.932’	Main Zone	808	Gabbronorite	2055.3 ± 4.6	3	0.19	0.83	0.34 ± 0.02
B14-053a	25° 13.849’	30° 05.374’	Main Zone	137	Gabbronorite	2055.0 ± 3.6	5	0.02	1.00	0.27 ± 0.02
B14-080	25° 00.181’	30° 07.035’	Critical Zone	-522	Gabbro	2052.0 ± 7.6	2	0.03	0.87	0.19 ± 0.01
B14-086	24° 56.880’	30° 09.099’	Critical Zone	-760	Pyroxenite	2053.7 ± 1.3	3	0.18	0.84	0.16 ± 0.01
Weighted Mean	N.A.	N.A.	N.A.	N.A.	N.A.	2054.47 ± 0.84	30	0.23	1.00	N.A.

Note: Weighted mean $^{40}Ar/^{39}Ar$ ages are reported at 2σ (95 percent confidence level). Biotite composition is reported at 1σ (68 percent confidence level).

[*]Stratigraphic depth is measured relative to the Merensky Reef pyroxenite in the Eastern Limb of the RLS.

[†]Ol - olivine, Mt - magnetite

Table 2

Stepwise Heating Results: moles (10^{-17} for $^{36, 38, 39}Ar$, 10^{-15} for ^{40}Ar and $^{40}Ar^*$) of each isotope for each heating step. J is the measure of the neutron flus in the reactor. All uncertainties reported at 1σ. Blank cells represent negative values.

Sample	Run ID	Power	36Ar	38Ar	39Ar	40Ar	40Ar*	Age (Ma)	Used in Plateau Age
B07-041_01	22486-01A	1.5	1.54±0.23	0.89±0.10	2.69±1.07	6.62±1.11	1.51±0.79	1350±630	
J = 1.98874e-2	22486-01B	3	3.66±0.24	2.85±0.14	12.47±1.13	19.18±1.14	7.00±0.82	1350±140	
± 3.18272e-5	22486-01C	5	6.60±0.25	3.31±0.15	26.29±1.04	42.70±1.17	20.74±0.84	1702±64	
	22486-01D	7	4.65±0.25	4.65±0.18	55.86±1.17	74.51±1.18	59.03±0.84	2042±30	x
	22486-01E	8	1.22±0.23	3.52±0.15	56.10±1.17	64.91±1.11	60.85±0.80	2074±29	x
	22486-01F	9	0.73±0.23	4.31±0.19	67.16±1.22	76.02±1.11	73.59±0.79	2087±24	x
	22486-01G	10	0.45±0.23	4.79±0.17	84.88±1.32	93.78±1.10	92.30±0.79	2077±20	x
	22486-01H	11	0.15±0.23	5.37±0.19	92.98±1.25	100.01±1.11	99.51±0.81	2058±17	x
	22486-01I	12	0.15±0.23	5.25±0.19	93.01±1.25	99.92±1.10	99.41±0.79	2056±17	x
	22486-01J	13	0.23±0.23	7.84±0.20	98.12±1.28	105.97±1.09	105.20±0.78	2060±16	x
	22486-01K	14	0.11±0.23	8.59±0.20	107.40±1.32	115.57±1.09	115.20±0.78	2060±15	x
	22486-01L	15	0.22±0.23	5.82±0.18	99.26±1.26	106.23±1.09	105.50±0.78	2049±15	x
	22486-01M	16	0.19±0.22	4.81±0.21	79.38±1.27	85.97±1.07	85.33±0.76	2063±21	x
	22486-01N	17	0.12±0.22	2.81±0.17	53.93±1.37	58.03±1.07	57.65±0.76	2056±34	x
	22486-01O	18	0.11±0.22	3.78±0.17	63.36±1.45	68.64±1.06	68.29±0.76	2066±30	x
	22486-01P	19	0.11±0.07	3.60±0.15	62.38±0.76	66.81±0.35	66.44±0.25	2052±12	x
	22486-01Q	20	0.06±0.07	2.67±0.13	46.51±0.66	49.86±0.36	49.67±0.27	2055±16	x
	22486-01R	22	0.19±0.08	5.09±0.18	77.86±0.86	83.51±0.37	82.86±0.27	2051±10	x
	22486-01S	24	0.04±0.08	8.70±0.22	130.30±1.36	139.45±0.42	139.30±0.31	2055.7±8.6	x
	22486-01T	26	0.16±0.08	4.97±0.17	82.37±0.96	88.65±0.39	88.13±0.28	2057±11	x
	22486-01U	28	0.13±0.08	4.26±0.16	67.29±0.80	72.17±0.37	71.74±0.27	2053±12	x
	22486-01V	30	0.36±0.08	4.68±0.17	88.75±1.00	95.67±0.40	94.45±0.30	2051±10	x
	22486-01W	32	0.24±0.07	2.72±0.12	45.01±0.64	48.63±0.36	47.82±0.26	2049±16	x

B07-041_02	22486-02A	1.5	1.37±0.08	0.25±0.08	5.32±0.45	5.73±0.33	1.72±0.24	890±110	
J = 1.98874e-2	22486-02B	3	2.86±0.09	0.87±0.10	12.91±0.41	17.13±0.37	8.78±0.26	1543±46	
± 3.18272e-5	22486-02C	5	5.29±0.12	2.18±0.14	58.36±0.57	71.99±0.49	56.56±0.35	1938±13	
	22486-02D	7	0.82±0.09	2.89±0.15	152.70±0.95	164.69±0.39	162.30±0.29	2049.0±6.6	x
	22486-02E	8	0.09±0.13	2.77±0.16	139.90±1.34	152.95±0.55	152.70±0.40	2081±11	x
	22486-02F	9	0.17±0.09	3.01±0.17	158.00±0.99	168.78±0.40	168.30±0.31	2051.6±6.8	x
	22486-02G	10	0.16±0.09	2.72±0.16	161.60±1.02	173.16±0.40	172.70±0.30	2055.6±6.8	x
	22486-02H	11	0.12±0.09	2.75±0.15	139.80±0.92	150.16±0.40	149.80±0.30	2059.6±7.4	x
	22486-02I	12	0.05±0.09	2.39±0.17	133.80±0.89	143.16±0.40	143.00±0.30	2055.5±7.5	x
	22486-02J	13	0.38±0.14	2.07±0.16	126.60±0.89	136.70±0.57	135.60±0.41	2058.1±8.5	x
	22486-02K	14	0.08±0.09	1.94±0.17	121.10±0.81	129.32±0.45	129.10±0.37	2052.2±7.9	x
	22486-02L	15		1.72±0.13	102.10±0.79	108.56±0.57	109.00±0.42	2053.8±9.8	x
	22486-02M	16		1.24±0.12	63.07±0.62	66.27±0.50	66.75±0.38	2044±13	x
	22486-02N	17		0.54±0.10	31.83±0.54	33.05±0.46	33.87±0.34	2050±24	x
	22486-02O	19	0.04±0.07	1.20±0.12	72.63±0.70	77.37±0.32	77.26±0.23	2050±12	x
	22486-02P	21		1.33±0.14	80.60±0.61	85.39±0.49	86.13±0.36	2055.8±9.7	x
	22486-02Q	23		1.64±0.12	90.69±0.73	96.05±0.43	96.68±0.31	2052.8±9.7	x
	22486-02R	25		2.00±0.15	122.70±0.86	129.83±0.35	130.00±0.27	2045.4±7.8	x
	22486-02S	27		1.12±0.10	69.94±0.67	74.99±0.33	75.03±0.24	2061±12	x
	22486-02T	29	0.20±0.07	0.56±0.10	24.05±0.69	26.18±0.30	25.61±0.21	2052±36	x
	22486-02U	31	0.10±0.07	1.13±0.12	56.29±0.59	60.66±0.31	60.38±0.23	2060±13	x
	22486-02V	33	0.05±0.08	0.20±0.10	22.68±0.44	24.14±0.32	23.99±0.23	2043±26	x
B07-041_03	22486-03A	1.5	2.10±0.14	0.63±0.10	4.55±0.42	8.83±0.71	1.26±0.50	790±260	
J = 1.98874e-2	22486-03B	3	2.43±0.10	1.67±0.12	53.92±0.91	55.15±0.50	46.39±0.36	1799±20	
± 3.18272e-5	22486-03C	5	0.25±0.10	3.02±0.15	126.10±0.95	136.61±0.51	135.70±0.37	2064.9±7.6	x
	22486-03D	7	0.37±0.11	5.16±0.21	214.40±1.43	230.54±0.57	229.20±0.42	2056.4±5.9	x
	22486-03E	8	0.41±0.10	3.32±0.16	129.90±1.01	139.08±0.53	137.60±0.38	2045.3±8.1	x
	22486-03F	9	0.34±0.10	2.27±0.14	81.70±1.24	88.31±0.54	87.10±0.40	2053±19	x

	22486-03G	10	0.13±0.07	1.28±0.11	56.45±0.61	60.32±0.37	59.85±0.27	2046±13	x
	22486-03H	11	0.01±0.10	0.92±0.11	42.37±0.52	45.37±0.54	45.34±0.39	2057±17	x
	22486-03I	12	0.05±0.07	1.01±0.09	41.83±0.47	44.80±0.36	44.61±0.26	2053±14	x
	22486-03J	14	0.06±0.07	1.25±0.11	59.09±0.67	62.98±0.43	62.77±0.33	2049±14	x
	22486-03K	16	0.14±0.07	0.73±0.10	36.42±0.55	38.99±0.41	38.50±0.31	2042±20	x
	22486-03L	18	0.04±0.07	0.73±0.09	34.01±0.52	36.38±0.36	36.25±0.26	2053±20	x
	22486-03M	20	0.07±0.10	0.83±0.10	39.17±0.52	41.99±0.53	41.74±0.39	2052±19	x
	22486-03N	22	0.04±0.09	0.24±0.07	8.11±0.57	9.06±0.48	8.91±0.34	2091±99	x
	22486-03O	24	0.06±0.07	0.58±0.09	22.59±0.73	24.11±0.36	23.90±0.25	2043±41	x
	22486-03P	26	0.01±0.07	0.85±0.10	28.39±0.44	30.18±0.36	30.13±0.25	2048±21	x
	22486-03Q	28	0.05±0.07	0.04±0.07	5.05±0.28	5.60±0.35	5.42±0.25	2061±88	x
	22486-03R	33	0.00±0.07	0.46±0.08	18.76±0.33	20.09±0.33	20.08±0.24	2058±25	x
B06-055_01	22485-01A	7	18.00±0.19	34.75±0.28	407.58±5.54	489.96±0.86	435.62±0.65	2054±17	x
J = 1.98616e-2	22485-01B	9	2.70±0.16	35.32±0.33	478.87±5.54	520.25±0.84	512.08±0.68	2055±14	x
± 3.84630e-5	22485-01C	11	1.78±0.18	44.46±0.35	578.45±5.55	628.49±1.85	623.15±1.77	2064±12	x
	22485-01D	14	1.46±0.34	88.20±0.52	1197.31±6.67	1285.11±3.34	1280.74±3.17	2055.2±7.6	x
	22485-01E	16	0.74±0.34	85.30±0.50	1177.16±5.21	1264.65±1.77	1262.38±1.42	2058.3±5.7	x
	22485-01F	18	0.61±0.31	74.84±0.45	1037.90±7.75	1107.52±1.92	1105.63±1.65	2050.2±6.6	x
	22485-01G	20	0.96±0.32	79.21±0.45	1093.31±5.18	1175.00±1.54	1172.06±1.20	2058.0±6.1	x
	22485-01H	22	1.01±0.30	73.51±0.45	1011.71±7.72	1082.20±1.67	1079.17±1.41	2051.8±9.6	x
	22485-01I	24	1.15±0.45	116.75±0.61	1582.39±8.12	1694.58±2.02	1691.02±1.47	2054.0±6.5	x
	22485-01J	26	0.76±0.51	131.40±0.66	1809.79±8.63	1932.19±3.64	1929.87±3.30	2051.4±6.3	x
	22485-01K	28	0.53±0.21	47.40±0.38	666.33±6.28	717.94±0.98	716.36±0.77	2061.4±9.6	x
	22485-01L	30	0.52±0.25	63.24±0.40	858.07±8.74	920.62±1.60	919.05±1.40	2057±13	x
	22485-01M	32	0.37±0.28	69.72±0.47	960.86±10.31	1022.71±2.48	1021.58±2.33	2048±12	x
	22485-01N	35	0.37±0.18	40.45±0.33	576.62±4.47	618.91±0.88	617.79±0.69	2057.2±9.7	x
	22485-01O	35	0.12±0.12	12.67±0.24	185.35±1.41	199.00±0.67	198.64±0.57	2057.6±7.1	x

B06-055-02	22485-02A	1.5	1.07±0.08	0.62±0.09	6.21±0.32	7.78±0.32	4.73±0.23	1663±77	x
J = 1.98616e-2	22485-02B	3	2.44±0.10	3.22±0.14	34.97±0.59	44.34±0.40	37.38±0.29	2054±22	x
± 3.84630e-5	22485-02C	5	0.22±0.13	11.19±0.18	152.80±1.12	164.62±0.53	164.00±0.38	2059.4±8.2	x
	22485-02D	6	0.06±0.09	12.18±0.21	169.90±1.20	181.57±0.40	181.40±0.30	2052.5±7.6	x
	22485-02E	7	0.10±0.11	14.72±0.19	158.70±0.99	170.58±0.59	170.30±0.50	2059.7±7.1	x
	22485-02F	8	0.01±0.10	15.99±0.21	176.67±1.15	188.98±0.54	188.94±0.40	2055.1±7.1	x
	22485-02G	8.5	0.14±0.14	12.31±0.22	180.30±2.76	192.20±0.71	191.80±0.58	2048±19	x
	22485-02H	9	0.15±0.13	9.70±0.19	138.80±1.43	148.43±0.53	148.00±0.39	2051±12	x
	22485-02I	9.5	0.23±0.11	9.61±0.23	132.90±0.88	143.05±0.46	142.40±0.34	2057.2±7.4	x
	22485-02J	10	0.03±0.08	9.81±0.20	136.20±0.92	145.98±0.42	145.90±0.35	2056.9±7.7	x
	22485-02K	10.5	0.06±0.08	8.58±0.20	123.20±0.89	131.99±0.32	131.80±0.24	2055.2±8.1	x
	22485-02L	11	0.15±0.08	7.89±0.17	115.80±0.79	124.14±0.37	123.70±0.28	2053.5±7.7	x
	22485-02M	11.5	0.18±0.09	8.10±0.20	113.10±0.93	121.30±0.37	120.80±0.27	2054.1±9.5	x
	22485-02N	12	0.13±0.08	6.61±0.21	100.20±0.84	107.86±0.38	107.50±0.30	2059±10	x
	22485-02O	12.5	0.14±0.08	7.73±0.17	108.50±0.88	116.39±0.35	116.00±0.26	2054.5±9.4	x
	22485-02P	13	0.05±0.08	9.20±0.21	124.40±0.94	133.04±0.41	132.90±0.34	2054.3±8.8	x
	22485-02Q	13.5		7.10±0.18	99.66±0.79	106.52±0.34	106.70±0.26	2056.5±9.3	x
	22485-02R	14	0.00±0.13	10.95±0.23	151.10±1.00	161.40±0.66	161.40±0.55	2053.8±8.1	x
	22485-02S	14.5	0.05±0.08	7.87±0.19	113.00±1.32	120.64±0.38	120.50±0.30	2051±14	x
	22485-02T	15	0.19±0.09	9.63±0.22	141.80±0.91	152.53±0.37	152.00±0.27	2058.7±7.0	x
	22485-02U	15.5	0.17±0.08	7.70±0.20	107.60±0.80	116.27±0.40	115.80±0.33	2062.0±8.8	x
	22485-02V	16	0.08±0.08	9.88±0.20	142.70±1.59	153.02±0.35	152.80±0.26	2056±13	x
	22485-02W	16.5	0.04±0.08	3.76±0.16	54.37±0.68	58.78±0.43	58.66±0.36	2066±17	x
	22485-02X	17	0.03±0.08	6.53±0.19	100.30±1.24	107.69±0.38	107.60±0.31	2060±15	x
	22485-02Y	17.5	0.10±0.07	4.82±0.16	70.60±0.70	75.49±0.37	75.20±0.31	2050±12	x
	22485-02Z	18	0.01±0.08	4.79±0.15	72.71±0.68	77.48±0.36	77.46±0.29	2050±12	x
	22485-02AA	18.5	0.20±0.11	6.98±0.17	99.87±0.81	106.76±0.45	106.20±0.33	2048.0±9.7	x
	22485-02AB	19	0.12±0.13	4.67±0.17	69.14±0.97	74.32±0.57	73.99±0.42	2056±18	x
	22485-02AC	19.5	0.13±0.10	1.35±0.10	22.25±0.74	24.07±0.41	23.70±0.30	2050±43	x

	22485-02AD	18.5	0.16±0.09	1.06±0.10	14.21±0.32	15.68±0.39	15.21±0.28	2056±36	x
	22485-02AE	20	0.18±0.10	3.90±0.15	58.14±0.56	63.02±0.39	62.50±0.28	2061±12	x
	22485-02AF	20.5	0.10±0.10	0.86±0.09	13.93±1.13	14.68±0.41	14.40±0.29	2010±100	x
	22485-02AG	22	0.02±0.08	3.38±0.10	50.83±0.55	54.45±0.33	54.41±0.25	2056±14	x
	22485-02AH	24	0.01±0.07	1.69±0.10	22.37±0.46	23.92±0.31	23.89±0.22	2054±27	x
	22485-02AI	26	0.06±0.10	0.51±0.08	8.68±0.58	9.27±0.42	9.09±0.30	2030±91	x
	22485-02AJ	30	0.02±0.07	2.51±0.14	38.58±0.55	41.52±0.29	41.45±0.22	2061±18	x
	22485-02AK	33	0.02±0.07	0.55±0.08	7.41±0.62	7.52±0.29	7.45±0.21	1980±110	x
B06-055_03	22485-04A	1.5	1.80±0.09	0.58±0.10	5.43±0.42	9.50±0.37	4.35±0.26	1720±110	
J = 1.98616e-2	22485-04B	3	4.43±0.17	1.74±0.11	14.72±0.66	28.50±0.69	15.82±0.50	2061±68	x
± 3.84630e-5	22485-04C	5	1.43±0.09	3.62±0.17	42.78±1.59	49.75±0.37	45.67±0.28	2053±46	x
	22485-04D	7	0.32±0.11	6.44±0.18	90.76±0.73	97.58±0.46	96.66±0.33	2045.0±9.8	x
	22485-04E	9	0.32±0.09	11.72±0.24	159.60±1.12	171.02±0.43	170.10±0.35	2051.3±7.8	x
	22485-04F	10	0.22±0.08	8.55±0.21	117.60±1.15	126.33±0.36	125.70±0.29	2054±12	x
	22485-04G	11	0.16±0.08	7.42±0.20	103.00±0.83	110.57±0.34	110.10±0.26	2054.3±9.3	x
	22485-04H	12	0.03±0.08	7.72±0.18	99.37±1.22	106.57±0.36	106.50±0.29	2058±15	x
	22485-04I	13	0.19±0.08	7.46±0.18	103.30±0.79	110.64±0.35	110.10±0.26	2050.4±8.7	x
	22485-04J	14	0.08±0.08	8.60±0.23	115.90±1.42	124.34±0.38	124.10±0.30	2057±15	x
	22485-04K	15	0.06±0.11	11.31±0.27	148.60±0.97	158.78±0.50	158.60±0.38	2052.5±7.2	x
	22485-04L	16	0.13±0.09	9.67±0.21	125.60±0.87	135.46±0.39	135.10±0.30	2062.0±7.7	x
	22485-04M	17	0.07±0.09	8.41±0.18	109.30±0.86	117.31±0.41	117.10±0.33	2057.4±9.2	x
	22485-04N	18	0.15±0.12	12.88±0.24	171.80±1.08	183.64±0.50	183.20±0.37	2051.3±6.6	x
	22485-04O	19	0.52±0.15	33.43±0.28	347.10±2.41	373.99±0.82	372.50±0.71	2059.3±7.4	x
	22485-04P	20	0.15±0.08	12.54±0.25	156.80±1.53	168.32±0.35	167.90±0.26	2057±11	x
	22485-04Q	21	0.11±0.08	9.35±0.26	131.70±0.95	141.92±0.38	141.60±0.30	2061.2±7.8	x
	22485-04R	22		3.92±0.15	56.73±0.67	61.30±0.30	61.43±0.22	2071±14	x
	22485-04S	23	0.03±0.07	5.88±0.16	76.87±0.69	82.23±0.30	82.16±0.23	2054±10	x
	22485-04T	24	0.13±0.08	6.77±0.17	92.48±0.66	99.62±0.32	99.24±0.24	2059.2±9.3	x

	22485-04U	25	0.11±0.07	5.03±0.16	67.76±0.47	72.98±0.34	72.66±0.27	2058.5±9.8	x
	22485-04V	27	0.10±0.07	2.67±0.13	38.45±0.79	41.26±0.30	40.97±0.21	2050±26	x
	22485-04W	29	0.09±0.10	1.29±0.10	15.14±0.60	16.57±0.42	16.32±0.30	2064±54	x
	22485-04X	31	0.03±0.07	3.66±0.15	47.82±0.53	51.08±0.32	50.98±0.24	2051±15	x
B06-042_01	22484-01A	7	13.86±0.28	80.07±0.58	608.09±13.98	682.68±1.18	649.43±0.97	2052±28	x
J = 1.98464e-2	22484-01B	10	0.45±0.29	119.09±0.60	978.95±4.82	1051.07±1.06	1050.02±0.83	2057.8±6.2	x
± 3.84784e-5	22484-01C	12	0.12±0.24	96.11±0.45	801.71±5.17	858.24±0.84	857.99±0.68	2055.0±8.0	x
	22484-01D	14	0.14±0.25	103.31±0.53	832.19±8.44	891.41±0.97	891.06±0.70	2056±13	x
	22484-01E	16	0.14±0.29	125.85±0.66	996.38±5.53	1069.39±1.15	1069.07±0.93	2058.2±7.0	x
	22484-01F	18	0.10±0.28	115.64±0.58	928.92±5.17	995.24±0.89	995.04±0.70	2056.1±7.0	x
	22484-01G	20	0.50±0.35	151.16±0.68	1210.54±8.43	1299.81±1.40	1298.64±1.15	2058.0±8.7	x
	22484-01H	22	0.36±0.34	148.56±0.66	1179.18±5.17	1264.98±1.21	1264.10±0.88	2057.2±5.6	x
	22484-01I	24	0.46±0.44	194.56±0.68	1548.21±5.57	1655.62±1.57	1654.46±1.11	2053.3±4.6	x
	22484-01J	26	0.55±0.36	153.94±0.71	1257.00±5.54	1343.22±2.35	1341.88±2.17	2052.0±5.9	x
	22484-01K	28	0.09±0.19	55.55±0.43	453.24±7.67	480.74±0.68	480.54±0.53	2044±21	x
	22484-01L	30	0.48±0.26	109.73±0.63	890.60±8.42	948.89±2.42	947.75±2.34	2048±12	x
	22484-01M	32	0.50±0.18	71.41±0.50	569.77±8.10	610.30±1.49	609.08±1.42	2054±18	x
	22484-01N	35	0.22±0.13	23.13±0.28	193.10±0.89	207.83±0.67	207.30±0.59	2058.7±6.7	x
	22484-01O	35	0.01±0.09	2.13±0.13	16.60±0.37	17.50±0.31	17.47±0.22	2035±32	x
B06-042_02	22484-02	1.5	1.16±0.08	1.96±0.11	11.40±0.62	11.04±0.32	7.90±0.23	1561±64	
J = 1.98464e-2	22484-03	3	4.53±0.11	4.46±0.16	29.53±0.64	38.59±0.44	26.35±0.31	1839±28	
± 3.84784e-5	22484-04	4	0.42±0.08	3.94±0.15	27.63±0.72	30.49±0.31	29.36±0.23	2046±33	x
	22484-05A	6	0.37±0.08	12.36±0.22	95.48±1.23	103.59±0.40	102.60±0.33	2060±15	x
	22484-05B	7.5	0.15±0.08	14.18±0.26	111.50±2.06	120.00±0.33	119.60±0.25	2058±22	x
	22484-05C	9	0.06±0.08	17.32±0.25	134.60±1.67	144.36±0.36	144.20±0.28	2056±14	x
	22484-05D	10	0.17±0.08	15.38±0.27	119.10±1.34	129.25±0.85	128.80±0.82	2068±14	x
	22484-05E	11	0.06±0.08	14.80±0.26	111.20±0.94	119.46±0.36	119.30±0.29	2057.3±8.6	x

	22484-05F	12	0.10±0.08	13.98±0.22	109.50±1.33	118.08±0.34	117.80±0.26	2061±14	x
	22484-05G	13	0.24±0.10	14.66±0.25	111.40±1.30	119.85±0.58	119.20±0.52	2055±14	x
	22484-05H	14	0.21±0.10	16.19±0.27	133.90±1.83	143.07±0.49	142.50±0.41	2048±16	x
	22484-05I	15	0.18±0.10	18.15±0.31	146.50±1.83	157.39±0.86	156.90±0.81	2055±15	x
	22484-05J	16	0.11±0.10	26.75±0.26	162.22±1.34	174.90±1.77	174.59±1.75	2062±15	x
	22484-05K	17	0.15±0.10	10.85±0.23	85.19±0.80	91.13±0.45	90.71±0.36	2049±11	x
	22484-05L	18	0.13±0.08	12.44±0.19	96.09±0.89	102.66±0.35	102.30±0.28	2049±10	x
	22484-05M	19	0.19±0.08	10.13±0.19	77.53±1.16	83.83±0.33	83.32±0.24	2060±18	x
	22484-05N	20	0.16±0.08	11.54±0.23	90.56±0.91	97.33±0.33	96.90±0.25	2055±11	x
	22484-05O	21	0.24±0.08	2.43±0.11	18.34±0.73	20.34±0.31	19.70±0.23	2060±51	x
	22484-05P	22	0.25±0.09	13.97±0.22	109.60±1.40	117.96±0.37	117.30±0.27	2055±14	x
	22484-05Q	23	0.14±0.08	5.77±0.19	49.79±1.28	53.71±0.32	53.34±0.23	2056±31	x
	22484-05R	24	0.08±0.08	1.23±0.10	10.18±0.71	11.06±0.31	10.84±0.22	2048±89	x
	22484-05S	26	0.03±0.08	5.06±0.17	40.59±0.84	43.31±0.31	43.24±0.23	2050±25	x
	22484-05T	28	0.12±0.08	3.39±0.12	28.66±0.46	31.19±0.30	30.87±0.21	2063±20	x
	22484-05U	30	0.04±0.11	0.42±0.10	2.34±0.49	2.88±0.41	2.79±0.29	2200±300	x
B06-042_03	22484-06A	1.5	0.50±0.12	1.08±0.11	11.19±0.68	3.25±0.54	1.66±0.38	465±97	
J = 1.98464e-2	22484-06B	3	1.02±0.09	1.13±0.11	10.60±0.50	9.87±0.42	6.61±0.30	1453±65	
± 3.84784e-5	22484-06C	5	1.79±0.09	8.35±0.19	69.32±0.82	75.98±0.42	70.24±0.31	1989±14	
	22484-06D	7	0.18±0.09	14.72±0.23	137.20±1.62	147.58±0.43	147.00±0.32	2056±13	x
	22484-06E	9	0.23±0.12	24.70±0.20	178.05±1.74	192.65±0.56	191.90±0.42	2064±10	x
	22484-06F	10	0.24±0.09	18.02±0.23	162.00±1.17	175.07±0.46	174.30±0.34	2061.9±7.8	x
	22484-06G	11	0.02±0.09	14.83±0.24	133.90±1.54	142.77±0.41	142.70±0.30	2051±13	x
	22484-06H	12	0.11±0.09	14.43±0.26	135.80±1.44	144.74±0.47	144.40±0.38	2048±13	x
	22484-06I	13	0.07±0.09	16.06±0.28	149.80±0.99	160.72±0.43	160.50±0.32	2056.6±7.0	x
	22484-06J	14	0.08±0.09	14.13±0.25	134.30±0.95	143.54±0.46	143.30±0.37	2051.7±7.9	x
	22484-06K	15	0.08±0.08	12.41±0.20	112.80±0.84	121.37±0.39	121.10±0.28	2059.0±8.3	x
	22484-06L	16		11.82±0.22	109.30±0.89	117.18±0.39	117.20±0.28	2057.5±9.3	x

	22484-06M	17	0.16±0.08	7.81±0.17	75.31±1.02	80.74±0.35	80.24±0.25	2050±16	x
	22484-06N	18	0.11±0.07	11.58±0.22	105.40±1.21	113.66±0.35	113.30±0.27	2061±14	x
	22484-06O	19	0.14±0.08	14.13±0.24	139.00±1.54	148.04±0.39	147.60±0.30	2045±13	x
	22484-06P	20	0.12±0.12	25.91±0.25	191.17±1.26	205.14±0.64	204.78±0.52	2056.1±7.1	x
	22484-06Q	21	0.16±0.07	4.98±0.15	45.66±0.61	49.52±0.35	48.99±0.26	2058±17	x
	22484-06R	22	0.11±0.07	8.35±0.21	83.03±0.77	88.71±0.35	88.35±0.25	2048±11	x
	22484-06S	23	0.07±0.08	12.45±0.25	121.50±1.38	130.41±0.38	130.20±0.28	2056±13	x
	22484-06T	24	0.17±0.07	6.98±0.18	67.76±0.72	72.88±0.34	72.33±0.24	2052±13	x
	22484-06U	25		3.25±0.14	30.46±0.74	32.44±0.46	32.97±0.33	2069±32	x
	22484-06V	27	0.01±0.08	1.22±0.10	11.19±0.34	12.14±0.35	12.11±0.25	2068±45	x
	22484-06W	29		1.86±0.12	18.62±0.40	19.33±0.34	19.80±0.24	2047±30	x
	22484-06X	31		1.97±0.11	19.39±0.40	21.14±0.34	21.40±0.25	2093±29	x
B14-015_01	22487-01A	6	5.13±0.23	64.70±0.37	726.92±12.35	371.98±0.96	357.73±0.72	1232±15	
J = 1.98979e-2	22487-01B	8	2.83±0.19	33.95±0.30	467.01±9.75	313.98±0.83	306.13±0.63	1506±21	
± 3.10646e-5	22487-01C	9	1.52±0.15	19.93±0.26	261.30±1.04	211.92±0.99	207.70±0.90	1711.1±6.5	
	22487-01D	10	1.45±0.14	20.39±0.23	268.60±0.94	231.83±0.70	227.80±0.57	1783.6±4.9	
	22487-01E	11	0.98±0.14	18.18±0.24	242.00±0.90	229.13±0.67	226.40±0.55	1896.8±5.2	
	22487-01F	12	1.13±0.12	21.54±0.22	256.68±7.96	277.90±0.75	274.76±0.67	2059±38	x
	22487-01G	13	2.37±0.19	35.28±0.35	438.70±8.33	465.96±0.97	459.39±0.81	2032±23	x
	22487-01H	14	2.09±0.15	29.43±0.28	369.12±11.57	400.82±0.87	395.01±0.77	2058±39	x
	22487-01I	14.5	1.29±0.14	16.90±0.25	224.50±1.64	242.30±1.33	238.70±1.27	2050±11	x
	22487-01J	15	0.41±0.12	10.83±0.23	143.80±0.72	155.14±0.51	154.00±0.39	2059.0±6.9	x
	22487-01K	15.5	0.53±0.12	8.84±0.20	126.00±0.64	135.58±0.68	134.10±0.60	2051.6±8.2	x
	22487-01L	16	0.53±0.13	9.41±0.18	124.40±0.74	133.88±0.72	132.40±0.63	2051.1±9.3	x
	22487-01M	16.5	0.46±0.10	9.00±0.17	128.70±0.45	138.57±0.59	137.30±0.52	2054.3±6.3	x
	22487-01N	17	0.42±0.12	7.58±0.16	103.30±0.39	110.86±0.66	109.70±0.56	2049.7±7.7	x
	22487-01O	17.5	0.37±0.12	7.32±0.20	102.90±0.41	111.42±0.53	110.40±0.40	2060.7±6.6	x
	22487-01P	18	0.54±0.12	11.36±0.20	154.40±0.68	166.60±0.62	165.10±0.52	2057.2±6.6	x

	22487-01Q	18.5	0.64±0.10	12.50±0.22	175.80±0.74	189.18±0.52	187.40±0.43	2054.0±5.9	x
	22487-01R	19	1.38±0.16	31.48±0.28	463.15±12.73	498.41±0.73	494.57±0.57	2056±34	x
	22487-01S	20	0.95±0.13	19.88±0.23	303.30±6.91	325.67±0.95	323.03±0.87	2052±28	x
	22487-01T	21	0.29±0.12	12.96±0.25	197.00±1.51	212.72±1.53	211.90±1.49	2064±13	x
	22487-01U	22	0.29±0.13	11.35±0.23	181.30±0.68	195.71±0.86	194.90±0.78	2063.7±6.7	x
	22487-01V	23	0.38±0.18	14.73±0.24	221.00±2.25	237.86±0.78	236.80±0.61	2060±13	x
	22487-01W	23.5	0.55±0.13	7.76±0.18	138.70±1.31	149.62±0.76	148.10±0.67	2055±13	x
	22487-01X	24	0.20±0.09	4.46±0.14	75.79±0.55	81.43±0.43	80.88±0.35	2055±10	x
	22487-01Y	24.5	0.06±0.12	3.32±0.14	65.04±0.89	70.57±0.47	70.40±0.34	2072±18	x
	22487-01Z	25	0.24±0.12	2.73±0.13	50.91±0.45	55.60±0.47	54.94±0.34	2069±13	x
	22487-01AA	26	0.19±0.11	1.54±0.10	27.14±0.26	29.56±0.48	29.04±0.35	2058±19	x
	22487-01AB	28	0.32±0.12	1.22±0.11	18.44±0.27	20.97±0.46	20.08±0.33	2080±27	x
	22487-01AC	31	0.29±0.12	5.67±0.16	91.98±0.58	104.60±0.59	103.80±0.49	2123.6±9.7	
	22487-01AD	35	1.52±0.13	3.68±0.15	58.43±0.43	69.01±0.59	64.78±0.45	2102±13	
B14-015_02	22487-02A	1.5	0.23±0.07	2.74±0.12	24.87±0.55	5.48±0.25	4.92±0.18	599±22	
J = 1.98979e-2	22487-02B	3	2.07±0.11	21.61±0.25	254.70±1.70	76.85±0.43	71.87±0.34	803.9±4.5	
± 3.10646e-5	22487-02C	5	1.93±0.11	23.06±0.31	281.00±1.69	185.04±0.43	180.40±0.33	1484.8±4.4	
	22487-02D	7	2.16±0.15	27.70±0.24	263.45±1.45	237.08±0.55	231.91±0.43	1826.0±4.1	
	22487-02E	9	1.71±0.14	22.48±0.22	216.48±1.27	206.65±0.48	202.54±0.35	1896.8±4.7	
	22487-02F	10	1.13±0.09	14.31±0.21	165.70±1.69	168.41±0.37	165.70±0.30	1976±11	
	22487-02G	11	1.03±0.13	14.88±0.23	171.90±1.90	172.48±0.61	170.00±0.52	1962±13	
	22487-02H	12	1.05±0.10	15.81±0.28	182.80±3.24	197.23±0.58	194.70±0.53	2052±21	x
	22487-02I	13	0.99±0.10	16.58±0.28	191.20±3.00	204.48±0.45	202.10±0.37	2044±18	x
	22487-02J	14	0.98±0.15	17.53±0.22	201.70±2.47	214.34±0.60	212.00±0.48	2036±14	x
	22487-02K	15	1.01±0.12	18.09±0.22	168.00±0.67	182.02±0.47	179.60±0.37	2056.8±5.6	x
	22487-02L	16	0.59±0.14	12.41±0.25	160.60±1.25	173.32±0.54	171.90±0.43	2057.8±7.7	x
	22487-02M	17	0.50±0.08	9.64±0.24	127.40±1.11	137.51±0.32	136.30±0.25	2058.4±8.8	x
	22487-02N	18	0.59±0.17	16.40±0.19	166.31±1.38	179.07±0.77	177.66±0.65	2056±11	x

	22487-02O	19	0.26±0.16	7.11±0.18	96.87±1.44	103.73±0.55	103.10±0.40	2051±17	x
	22487-02P	20	0.23±0.08	3.33±0.14	48.17±0.72	52.02±0.45	51.47±0.41	2056±19	x
	22487-02Q	22	0.20±0.07	2.69±0.14	42.50±0.80	46.02±0.26	45.55±0.20	2060±24	x
	22487-02R	25	0.18±0.06	1.01±0.09	14.37±0.43	15.78±0.22	15.34±0.16	2055±38	x
	22487-02S	28	0.15±0.07	0.57±0.09	11.65±0.30	12.80±0.23	12.44±0.16	2055±35	x
	22487-02T	31	0.14±0.07	1.82±0.10	28.17±0.37	30.42±0.22	30.09±0.16	2056±18	x
B14-015_03	22487-03A	1.5	0.16±0.09	2.33±0.21	18.75±0.43	3.52±2.74	0.21±1.94	40±360	
J = 1.98979e-2	22487-03B	3	2.20±0.15	29.78±0.48	363.70±3.47	111.50±4.43	64.75±3.13	547±24	
± 3.10646e-5	22487-03C	5	2.44±0.18	39.32±0.24	430.14±3.97	362.04±5.58	310.08±3.96	1605±15	
	22487-03D	7	2.36±0.20	47.45±0.28	524.58±4.83	526.34±5.96	476.13±4.26	1861±12	
	22487-03E	9	3.06±0.24	50.40±0.28	710.68±6.78	755.59±7.33	690.53±5.23	1941±11	
	22487-03F	10	1.12±0.19	35.64±0.28	409.78±4.61	455.02±5.73	431.22±4.07	2038±15	x
	22487-03G	10.5	1.47±0.22	54.52±0.40	631.68±6.05	697.42±6.71	666.17±4.88	2040±11	x
	22487-03H	11	0.30±0.09	11.47±0.31	187.30±3.73	204.42±2.84	198.00±2.01	2043±26	x
	22487-03I	11.5	0.20±0.08	9.51±0.23	147.80±2.83	161.70±2.47	157.50±1.75	2053±25	x
	22487-03J	12	0.16±0.09	9.91±0.27	157.00±6.48	168.32±2.78	164.90±1.98	2035±52	x
	22487-03K	12.5	0.19±0.09	9.40±0.30	148.80±2.77	164.70±2.84	160.60±2.01	2069±26	x
	22487-03L	13	0.61±0.11	9.40±0.30	135.90±1.52	156.30±3.18	143.40±2.25	2041±22	x
	22487-03M	13.5	0.57±0.11	8.61±0.30	126.60±2.61	146.74±3.36	134.50±2.38	2050±32	x
	22487-03N	14	0.47±0.10	8.69±0.27	128.50±1.42	147.21±3.12	137.30±2.22	2056±22	x
	22487-03O	14.5	0.34±0.11	8.24±0.28	126.40±1.82	144.40±3.32	137.20±2.35	2075±26	x
	22487-03P	15	0.46±0.11	8.50±0.29	129.50±1.80	147.97±3.32	138.20±2.35	2054±25	x
	22487-03Q	15.5	0.42±0.11	8.65±0.30	140.20±1.96	160.42±3.26	151.40±2.31	2069±24	x
	22487-03R	16	0.25±0.08	8.38±0.25	130.00±2.66	145.64±2.51	140.40±1.78	2070±28	x
	22487-03S	16.5	0.24±0.09	10.15±0.30	154.80±2.75	171.86±2.71	166.80±1.92	2067±24	x
	22487-03T	17	0.26±0.08	7.01±0.25	109.70±2.48	124.01±2.32	118.40±1.64	2069±31	x
	22487-03U	17.5	0.08±0.09	8.62±0.25	141.60±2.82	153.76±2.80	152.10±1.98	2062±28	x
	22487-03V	18	0.05±0.09	9.13±0.28	144.50±2.52	158.64±2.81	157.60±1.99	2081±25	x

	22487-03W	18.5	0.07±0.10	10.09±0.30	169.00±2.89	182.83±2.90	181.40±2.05	2062±23	x
	22487-03X	19	0.42±0.09	10.05±0.30	156.90±2.08	177.29±2.82	168.30±2.00	2061±20	x
	22487-03Y	19.5	0.36±0.09	8.30±0.24	129.10±2.72	143.74±2.71	136.00±1.92	2039±30	x
	22487-03Z	20	0.25±0.08	6.02±0.25	93.69±1.14	105.00±2.57	99.71±1.83	2051±25	x
	22487-04A	20.5	0.08±0.08	6.55±0.23	104.60±1.56	114.84±2.43	113.10±1.72	2071±24	x
	22487-04B	21	0.16±0.08	6.07±0.22	93.23±1.48	103.57±2.30	100.10±1.64	2063±26	x
	22487-04C	21.5	0.11±0.08	5.46±0.22	84.80±2.20	93.57±2.40	91.12±1.70	2063±38	x
	22487-04D	22	0.30±0.08	8.93±0.23	134.80±1.73	150.69±2.46	144.30±1.74	2058±19	x
	22487-04E	23	0.30±0.09	9.26±0.26	149.90±1.60	168.61±2.58	162.30±1.83	2072±16	x
	22487-04F	24	0.18±0.08	5.88±0.24	95.98±1.11	107.56±2.46	103.70±1.74	2069±23	x
	22487-04G	25	0.04±0.08	3.84±0.20	64.81±1.82	69.51±2.31	68.65±1.64	2046±44	x
	22487-04H	26	0.05±0.08	2.57±0.18	39.90±0.66	43.94±2.27	42.89±1.61	2064±49	x
	22487-04I	27	0.06±0.10	1.39±0.22	19.90±1.27	21.68±3.12	20.36±2.21	2000±150	x
	22487-04J	28	0.15±0.07	2.14±0.19	31.85±0.80	38.47±2.23	35.32±1.58	2102±64	x
	22487-04K	29	0.18±0.07	0.53±0.16	5.32±0.99	9.99±2.21	6.14±1.56	2150±400	x
	22487-04L	31	0.13±0.07	1.13±0.16	16.65±0.99	20.92±2.08	18.14±1.47	2080±120	x
B14-024_01	22489-01A	7	1.56±0.12	12.50±0.27	105.70±1.99	83.27±0.82	78.81±0.74	1639±22	
J = 1.98570e-2	22489-01B	10	0.73±0.19	24.48±0.25	296.75±1.86	319.34±1.34	317.26±1.23	2054.3±9.1	x
± 3.99183e-5	22489-01C	12	0.19±0.14	17.65±0.23	235.91±4.02	253.22±0.61	252.69±0.46	2057±21	x
	22489-01D	14	0.10±0.11	15.98±0.20	221.69±2.56	238.52±0.54	238.21±0.43	2060±14	x
	22489-01E	16	0.44±0.10	11.59±0.20	149.69±2.38	160.26±0.50	158.99±0.41	2046±20	x
	22489-01F	18		5.87±0.12	89.89±2.51	95.69±0.80	95.93±0.73	2052±36	x
	22489-01G	22	0.49±0.15	9.98±0.22	133.30±1.02	144.10±1.60	142.70±1.54	2056±15	x
	22489-01H	25		3.92±0.16	58.05±1.10	60.96±0.50	61.94±0.38	2052±24	x
	22489-01I	30	0.48±0.11	4.92±0.17	64.26±0.39	70.00±0.50	68.62±0.38	2053.0±8.9	x
	22489-01J	35	1.32±0.12	3.16±0.14	38.43±0.28	44.89±0.63	41.12±0.54	2055±18	x
B14-024_02	22489-02A	1.5	0.05±0.11	0.01±0.15		0.14±1.77	-0.49±1.25	3900±7900	

J = 1.98570e-2	22489-02B	3	0.35±0.08	0.40±0.13	1.37±0.51	0.83±1.36		N/A	
± 3.99183e-5	22489-02C	5	0.65±0.10	5.83±0.20	53.01±0.62	7.57±1.55	0.17±1.10	11±74	
	22489-02D	7	2.45±0.11	10.07±0.24	117.30±0.99	96.38±1.80	68.47±1.28	1389±20	
	22489-02E	8	0.23±0.15	6.32±0.25	75.70±0.71	82.65±2.37	80.08±1.68	2041±27	x
	22489-02F	9	0.41±0.10	6.10±0.22	72.56±0.78	82.35±1.67	77.65±1.18	2056±22	x
	22489-02G	10	0.43±0.10	6.16±0.24	76.15±0.79	86.58±1.61	81.68±1.15	2059±21	x
	22489-02H	11	0.59±0.23	5.58±0.30	70.04±0.73	81.97±3.76	75.23±2.66	2060±45	x
	22489-02I	12	0.47±0.23	5.63±0.28	70.93±0.75	81.82±3.63	76.50±2.57	2065±43	x
	22489-02J	13	0.33±0.14	4.68±0.21	59.86±1.07	67.84±2.29	64.11±1.63	2057±38	x
	22489-02K	14	0.55±0.25	14.17±0.38	198.20±3.26	218.41±4.11	212.10±2.91	2055±26	x
	22489-02L	15	0.10±0.10	4.01±0.19	59.61±1.03	65.89±1.58	64.78±1.12	2075±29	x
	22489-02M	16	0.22±0.20	1.63±0.25	23.46±0.53	26.44±3.29	23.89±2.32	2000±120	x
	22489-02N	17	0.40±0.12	0.93±0.16	9.46±0.75	15.09±1.87	10.58±1.32	2110±180	x
	22489-02O	18	0.29±0.11	1.09±0.16	16.58±0.57	20.38±1.84	17.12±1.30	2010±100	x
	22489-02P	19	0.17±0.15	0.77±0.19	11.58±0.35	13.38±2.35	11.41±1.66	1960±180	x
	22489-02Q	21	0.10±0.13	0.91±0.17	14.19±0.37	16.47±2.04	15.38±1.45	2070±120	x
	22489-02R	23	0.17±0.08	0.16±0.13	2.54±0.87	5.03±1.33	3.09±0.94	2220±590	x
	22489-02S	25	0.19±0.08	0.02±0.12		1.43±1.30	-0.73±0.92	5200±9100	x
	22489-02T	27	0.04±0.09	0.22±0.13	3.50±0.55	4.33±1.43	3.82±1.01	2080±380	x
	22489-02U	29	0.03±0.08	0.07±0.12		0.05±1.30	-0.25±0.92	4000±14000	x
	22489-02V	33		0.13±0.16	1.45±0.39	1.50±2.00	2.64±1.42	2760±850	x
B14-045_01	22490-02A	3	0.50±0.09	3.35±0.13	45.23±0.42	25.32±0.55	23.16±0.39	1266±18	
J = 1.98722e-2	22490-02B	5	0.45±0.10	10.43±0.19	162.40±0.69	124.76±0.62	122.80±0.44	1654.5±6.2	
± 2.50624e-5	22490-02C	6.5		14.44±0.24	206.30±1.00	211.15±0.75	211.20±0.54	2002.8±6.8	
	22490-02D	7	0.15±0.09	13.00±0.20	180.30±0.76	193.17±0.53	192.50±0.38	2053.2±5.9	x
	22490-02E	7.5		11.68±0.19	165.10±1.25	177.33±0.51	177.40±0.37	2061.5±9.8	x
	22490-02F	8	0.05±0.08	10.83±0.18	152.20±1.14	163.50±0.52	163.30±0.38	2059.8±9.7	x
	22490-02G	11	0.07±0.16	33.80±0.29	500.94±6.09	532.46±1.07	532.14±0.75	2048±15	x

	22490-02H	13	0.18±0.16	31.40±0.26	467.89±4.88	499.58±0.97	498.83±0.70	2052±13	x
	22490-02I	13.5		15.26±0.20	212.40±0.91	223.48±0.84	225.40±0.65	2046.0±6.5	x
	22490-02J	14		9.81±0.17	150.80±1.06	160.66±0.59	160.90±0.44	2053.1±9.4	x
	22490-02K	14.5	0.01±0.09	7.06±0.16	105.60±1.04	113.23±0.58	113.20±0.42	2058±13	x
	22490-02L	15	0.13±0.09	6.30±0.17	92.66±0.91	99.71±0.54	99.14±0.38	2056±13	x
	22490-02M	16	0.24±0.07	6.99±0.16	99.01±0.83	106.53±0.48	105.50±0.36	2052±11	x
	22490-02N	17.5	0.29±0.07	6.60±0.15	100.20±0.62	108.45±0.47	107.20±0.34	2056.9±8.6	x
	22490-02O	20.5	0.07±0.11	17.54±0.23	233.82±5.63	252.25±0.71	251.92±0.50	2065±30	x
	22490-02P	22.5	0.39±0.13	22.03±0.23	317.25±6.39	340.65±0.80	338.95±0.57	2055±25	x
	22490-02Q	23.5	0.45±0.09	9.03±0.17	132.10±0.43	143.26±0.56	141.30±0.41	2055.6±5.5	x
	22490-02R	24.5		4.91±0.16	73.63±0.35	78.64±0.60	78.95±0.44	2059.0±9.1	x
	22490-02S	26		4.82±0.14	73.23±0.69	77.15±0.49	78.89±0.35	2065±13	x
	22490-02T	29		5.23±0.15	79.55±0.65	83.87±0.49	85.59±0.36	2063±11	x
	22490-02U	32	0.03±0.08	6.58±0.16	92.16±0.41	98.72±0.53	98.59±0.39	2056.2±7.5	x
	22490-02V	35		0.80±0.10	10.71±0.24	12.07±0.57	13.34±0.40	2248±48	
B14-045_02	22490-03A	1.5	0.77±0.09	1.43±0.23	10.68±0.47	2.86±3.30		N/A	
J = 1.98722e-2	22490-03B	3	3.32±0.11	10.04±0.32	115.70±1.22	25.32±3.96		N/A	
± 2.50624e-5	22490-03C	5	4.67±0.21	12.97±0.54	184.60±1.79	132.70±7.63	12.60±5.40	229±96	
	22490-03D	7	2.59±0.18	0.00±0.00	327.84±3.66	336.44±6.55	269.76±4.67	1748±22	
	22490-03E	9	1.36±0.15	0.00±0.00	337.88±5.25	362.97±5.55	328.05±3.93	1939±22	
	22490-03F	11	0.78±0.18	0.00±0.00	355.35±3.72	388.04±6.66	367.90±4.77	2016±18	x
	22490-03G	12	0.55±0.12	14.91±0.37	227.30±2.81	253.35±4.30	239.30±3.05	2037±19	x
	22490-03H	12.5	0.39±0.11	10.13±0.33	149.20±1.62	170.32±3.94	160.30±2.79	2061±23	x
	22490-03I	13	0.37±0.10	7.40±0.31	113.00±1.27	130.91±3.69	121.40±2.62	2061±28	x
	22490-03J	14	0.35±0.09	8.28±0.29	131.60±1.93	152.91±3.10	144.00±2.20	2083±24	x
	22490-03K	14.5	0.29±0.08	6.69±0.28	102.40±1.15	116.09±2.91	108.70±2.06	2047±25	x
	22490-03L	15	0.25±0.08	5.43±0.23	88.40±1.11	101.07±2.87	94.56±2.03	2056±29	x
	22490-03M	15.5	0.11±0.07	5.18±0.23	77.71±0.95	88.32±2.72	85.54±1.93	2091±30	x

	22490-03N	16	0.15±0.07	4.60±0.23	69.38±0.90	78.04±2.62	74.14±1.85	2055±33	x
	22490-03O	17	0.06±0.07	2.91±0.20	43.71±0.66	48.26±2.64	46.68±1.87	2054±51	x
	22490-03P	19	0.17±0.08	6.74±0.24	98.35±1.00	112.08±3.00	107.60±2.12	2083±26	x
	22490-03Q	21	0.19±0.07	6.97±0.26	107.30±1.23	121.34±2.73	116.40±1.93	2074±23	x
	22490-03R	23	0.17±0.08	7.62±0.26	122.60±1.19	137.27±3.01	132.90±2.13	2072±21	x
	22490-03S	25	0.20±0.09	6.88±0.27	121.60±1.19	134.14±3.12	129.10±2.21	2047±22	x
	22490-03T	27	0.08±0.07	1.09±0.20	18.17±0.41	20.49±2.57	18.54±1.82	2000±120	x
	22490-03U	29	0.06±0.11	0.37±0.26	4.58±0.48	6.16±3.88	4.66±2.75	2000±720	x
	22490-03V	31	0.19±0.07	2.24±0.20	33.20±0.53	38.25±2.61	33.37±1.85	1980±69	x
	22490-03W	33	0.14±0.06	0.41±0.17	5.65±0.48	6.00±2.36	2.33±1.67	1080±590	x
B14-045_03	22490-04A	1.5	0.23±0.07	0.03±0.06	0.25±0.23	0.97±0.37	0.13±0.26	1300±2000	
J = 1.98722e-2	22490-04B	3	10.60±0.13	11.36±0.27	102.20±0.73	45.60±0.68	6.36±0.48	210±17	
± 2.50624e-5	22490-04C	5	12.01±0.26	24.44±0.24	370.70±2.55	379.44±1.57	335.00±1.24	1855.0±8.3	
	22490-04D	6	0.70±0.14	15.60±0.24	267.60±2.89	287.20±0.82	284.60±0.63	2049±13	x
	22490-04E	6.5	0.43±0.14	8.48±0.18	142.20±0.98	153.10±0.77	151.50±0.58	2051.0±8.6	x
	22490-04F	7	0.39±0.10	8.17±0.19	127.60±0.97	137.43±0.56	136.00±0.42	2051.1±9.0	x
	22490-04G	7.5	0.30±0.08	6.46±0.19	107.00±0.83	114.90±0.54	113.80±0.44	2049.6±9.7	x
	22490-04H	8	0.25±0.08	6.10±0.17	101.40±0.80	109.13±0.50	108.20±0.40	2053.1±9.7	x
	22490-04I	8.5	0.20±0.07	5.68±0.18	91.87±0.74	98.57±0.39	97.83±0.28	2050.5±9.5	x
	22490-04J	9	0.20±0.07	4.85±0.16	80.07±0.76	86.32±0.38	85.57±0.28	2055±11	x
	22490-04K	10	0.23±0.08	6.73±0.22	111.70±0.83	120.36±0.57	119.50±0.47	2055.5±9.3	x
	22490-04L	11	0.28±0.08	7.65±0.22	120.60±0.91	130.35±0.46	129.30±0.33	2058.2±8.7	x
	22490-04M	12	0.40±0.08	8.02±0.20	123.50±1.42	133.36±0.44	131.90±0.33	2054±14	x
	22490-04N	13	0.43±0.08	8.50±0.19	134.80±0.93	145.69±0.43	144.10±0.31	2054.8±7.7	x
	22490-04O	14	0.37±0.09	8.86±0.20	143.30±0.74	154.18±0.49	152.80±0.36	2051.9±5.4	x
	22490-04P	15	0.39±0.11	9.86±0.22	158.80±1.54	170.76±0.62	169.30±0.46	2052±12	x
	22490-04Q	16	0.34±0.11	7.19±0.17	124.90±0.66	134.84±0.66	133.60±0.52	2056.0±6.8	x
	22490-04R	17	0.30±0.10	4.82±0.18	78.56±1.14	84.91±0.58	83.81±0.43	2053±18	x

	22490-04S	18	0.21±0.08	5.03±0.17	87.45±0.68	95.03±0.42	94.27±0.31	2065.6±9.4	x
	22490-04T	19	0.03±0.07	4.59±0.16	79.53±0.73	84.88±0.38	84.76±0.28	2051±11	x
	22490-04U	20		1.10±0.10	18.47±0.38	19.77±0.35	19.82±0.25	2060±29	x
	22490-04V	23	0.03±0.07	0.89±0.08	13.35±0.38	14.39±0.36	14.26±0.26	2054±41	x
	22490-04W	26	0.12±0.07	0.19±0.07	3.24±0.26	3.99±0.37	3.56±0.27	2090±140	x
	22490-04X	29	0.11±0.07	0.03±0.07	1.25±0.25	1.59±0.37	1.18±0.27	1910±350	x
	22490-04Y	32	0.24±0.07	1.89±0.11	32.65±0.44	35.61±0.39	34.72±0.29	2049±19	x
B14-049_01	22488-01A	7	3.75±0.24	68.09±0.48	772.06±9.94	762.30±1.04	751.78±0.80	1943±15	
J = 1.98827e-2	22488-01B	8	0.66±0.14	18.18±0.25	233.20±3.40	238.45±0.82	236.60±0.73	1992.5±8.4	
± 2.50624e-5	22488-01C	10	0.89±0.15	34.10±0.32	402.15±5.89	430.93±0.63	428.43±0.48	2052±18	x
	22488-01D	12	0.49±0.21	40.38±0.36	631.56±6.73	674.33±1.19	672.98±1.04	2052±13	x
	22488-01E	14	0.80±0.23	47.50±0.32	768.29±10.32	827.79±1.20	825.56±1.00	2062±17	x
	22488-01F	16	1.68±0.24	43.63±0.39	695.83±7.18	748.45±0.98	743.74±0.72	2056±13	x
	22488-01G	18	1.33±0.18	35.80±0.39	548.10±6.25	587.08±0.77	583.38±0.58	2050±14	x
	22488-01H	20	1.45±0.14	28.23±0.27	355.87±4.67	383.84±0.66	379.81±0.53	2054±16	x
	22488-01I	23	1.83±0.13	25.58±0.29	325.10±4.67	352.81±0.63	347.70±0.51	2056±18	x
	22488-01J	26	5.13±0.11	5.95±0.17	67.00±1.31	76.82±0.47	62.46±0.35	1892±20	
	22488-01K	30	1.31±0.13	2.24±0.11	25.08±0.52	27.51±0.50	23.84±0.35	1915±26	
	22488-01L	35	0.87±0.10	1.17±0.09	10.81±0.49	13.26±0.39	10.83±0.28	1976±61	
B14-049_02	22488-02A	1.5	0.70±0.13	0.17±0.10	0.43±0.38	2.47±0.51	0.61±0.36	2400±1400	
J = 1.98827e-2	22488-02B	3	0.08±0.13	0.01±0.10	0.51±0.38	0.48±0.49	0.25±0.35	1200±1400	
± 2.50624e-5	22488-02C	5	0.14±0.09	0.01±0.10	0.56±0.37	0.62±0.34	0.26±0.24	1170±980	
	22488-02D	7	0.26±0.09	0.10±0.10	1.10±0.25	0.29±0.34		N/A	
	22488-02E	1.5				0.23±0.31	0.59±0.22	N/A	
	22488-02F	3				0.19±0.31	0.36±0.22	N/A	
	22488-02G	7		0.16±0.10	0.22±0.41	0.15±0.34	0.44±0.24	2900±2800	
	22488-02H	9	0.62±0.13	2.11±0.15	15.92±0.40	3.21±0.48	1.57±0.34	322±65	

	22488-02I	11	0.85±0.17	12.39±0.23	125.10±0.79	110.07±0.65	107.80±0.46	1800.3±8.4	
	22488-02J	12	0.40±0.13	11.03±0.22	118.90±0.78	128.17±0.50	127.10±0.36	2056.1±8.5	x
	22488-02K	13		7.29±0.20	84.38±1.25	89.89±0.38	90.12±0.28	2055±18	x
	22488-02L	14	0.22±0.10	6.31±0.20	73.67±0.96	79.44±0.39	78.86±0.28	2058±16	x
	22488-02M	16	0.13±0.11	11.81±0.24	129.20±0.85	139.35±0.44	139.00±0.32	2064.3±8.2	x
	22488-02N	18	0.24±0.11	13.69±0.28	158.50±1.55	170.25±0.49	169.60±0.39	2057±12	x
	22488-02O	19	0.22±0.10	6.98±0.22	86.90±1.08	93.53±0.39	92.94±0.28	2056±16	x
	22488-02P	20	0.24±0.10	5.43±0.17	66.61±0.63	71.97±0.38	71.34±0.28	2058±12	x
	22488-02Q	21	0.28±0.11	11.64±0.26	145.10±0.60	156.06±0.45	155.30±0.34	2057.5±5.2	x
	22488-02R	22	0.19±0.09	4.31±0.16	51.41±0.58	54.67±0.37	54.16±0.27	2038±15	x
	22488-02S	23	0.15±0.10	4.05±0.14	54.80±0.60	58.74±0.40	58.33±0.29	2051±15	x
	22488-02T	24	0.26±0.09	4.46±0.16	56.33±0.55	60.79±0.35	60.10±0.25	2053±13	x
	22488-02U	25	0.00±0.10	2.85±0.14	34.41±0.49	36.54±0.38	36.53±0.27	2047±19	x
	22488-02V	26	0.07±0.09	1.01±0.11	10.74±0.34	11.86±0.35	11.67±0.25	2076±47	x
	22488-02W	27	0.12±0.09	2.52±0.14	32.88±0.47	35.26±0.35	34.95±0.25	2049±20	x
	22488-02X	29	0.07±0.08	0.47±0.11	8.20±0.41	8.19±0.31	8.01±0.22	1946±68	x
	22488-02Y	31	0.18±0.08	0.53±0.11	7.35±0.57	8.12±0.31	7.64±0.22	2020±100	x
	22488-02Z	33	0.24±0.08	0.43±0.11	4.95±0.43	6.11±0.32	5.49±0.23	2100±120	x
B14-049_03	22488-03A	1.5	0.29±0.08	0.67±0.11	4.80±0.23	0.93±0.67	-0.83±0.47	N/A	
J = 1.98827e-2	22488-03B	3	0.61±0.09	8.28±0.19	63.40±0.46	10.78±0.75	7.09±0.53	362±25	
± 2.50624e-5	22488-03C	5	1.56±0.15	33.08±0.34	317.80±1.10	221.85±1.32	212.50±0.95	1525.7±6.0	
	22488-03D	7	6.27±0.52	50.13±0.30	436.89±2.14	449.45±4.49	411.88±3.21	1905±11	
	22488-03E	9	0.77±0.22	50.86±0.34	512.33±2.17	556.14±1.94	551.52±1.40	2064.5±6.2	
	22488-03F	10	0.26±0.17	28.30±0.25	303.91±2.09	338.62±1.42	337.06±1.01	2101.3±9.4	
	22488-03G	11	0.34±0.13	24.65±0.29	252.30±2.75	292.67±1.21	290.60±0.93	2148±14	
	22488-03H	12	0.19±0.19	27.73±0.28	294.60±2.09	333.84±1.60	332.70±1.15	2123.6±9.9	
	22488-03I	12.5	0.19±0.14	16.85±0.30	178.80±0.89	205.36±1.17	204.20±0.84	2137.5±8.1	
	22488-03J	13	0.43±0.14	13.88±0.29	148.00±1.60	162.96±1.16	160.40±0.83	2073±15	x

	22488-03K	13.5	0.33±0.14	11.75±0.24	128.80±1.06	141.58±1.18	139.60±0.84	2073±13	x
	22488-03L	14	0.26±0.10	9.23±0.24	106.80±1.23	115.73±0.87	114.20±0.62	2055±16	x
	22488-03M	14.5	0.32±0.09	7.26±0.22	87.62±1.44	94.65±0.77	92.71±0.55	2043±21	x
	22488-03N	15	0.25±0.10	7.01±0.21	81.20±0.64	87.75±0.82	86.24±0.58	2047±13	x
	22488-03O	15.5	0.13±0.09	5.02±0.17	63.53±0.61	68.35±0.80	67.54±0.57	2049±16	x
	22488-03P	16	0.06±0.10	5.48±0.19	73.23±1.13	77.81±0.85	77.47±0.60	2043±21	x
	22488-03Q	17	0.12±0.10	3.37±0.17	45.50±0.57	48.58±0.81	47.84±0.57	2036±21	x
	22488-03R	18	0.17±0.10	5.83±0.18	72.77±0.56	78.57±0.82	77.53±0.58	2052±13	x
	22488-03S	19	0.15±0.09	4.90±0.19	57.52±0.53	61.91±0.77	61.03±0.54	2047±16	x
	22488-03T	20	0.12±0.09	2.23±0.17	31.70±0.45	34.08±0.79	33.33±0.56	2035±27	x
	22488-03U	22	0.09±0.08	2.78±0.15	35.94±0.40	38.66±0.69	38.14±0.49	2047±21	x
	22488-03V	24	0.02±0.08	0.88±0.13	13.94±0.35	14.86±0.69	14.72±0.49	2041±51	x
	22488-03W	26	0.05±0.08	0.19±0.11	1.59±0.27	1.99±0.70	1.67±0.50	2040±420	x
	22488-03X	28	0.11±0.08	0.21±0.10	2.03±0.49	2.51±0.72	1.84±0.51	1860±420	x
	22488-03Y	32	0.17±0.09	1.87±0.13	22.74±0.80	24.60±0.74	23.61±0.52	2020±50	x
B14-053a_01	22477-01A	0.5	0.41±0.07	0.24±0.15	0.33±0.05	0.74±2.30	-8.48±1.63	N/A	
J = 1.99143e-2	22477-01B	1	0.23±0.08	0.53±0.16	1.83±0.06	0.73±2.42	-4.31±1.71	N/A	
± 2.87347e-5	22477-01C	2	0.32±0.07	0.96±0.16	6.70±0.09	1.75±2.30	-5.49±1.63	N/A	
	22477-01D	5	1.07±0.09	11.00±0.22	123.60±0.82	48.73±2.77	24.78±1.97	606±41	
	22477-01E	9	1.70±0.24	57.79±0.28	800.40±2.98	840.78±8.57	802.95±6.76	1981±11	
	22477-01F	10	0.64±0.17	34.61±0.22	523.70±7.70	569.55±5.95	555.31±4.65	2048±21	
	22477-01G	10.5	0.44±0.13	25.10±0.20	367.13±5.77	409.79±4.54	399.99±3.50	2081±22	
	22477-01H	11	0.38±0.12	21.45±0.17	320.03±3.86	348.97±4.10	340.52±3.13	2052±19	
	22477-01I	11	0.79±0.15	30.33±0.24	445.10±2.17	505.12±5.23	487.59±4.05	2088±12	
	22477-01J	11	0.71±0.12	20.52±0.17	297.79±2.43	337.47±3.98	321.68±3.02	2071±16	x
	22477-01K	9	0.53±0.08	4.06±0.19	55.78±0.93	67.77±2.59	55.94±1.84	1980±45	x
	22477-01L	10	0.59±0.08	6.09±0.20	81.60±1.54	98.88±2.59	85.65±1.84	2036±35	x
	22477-01M	10.5	0.41±0.09	7.30±0.20	103.50±0.84	120.12±2.70	110.90±1.92	2060±24	x

22477-01N	11	0.34±0.08	8.79±0.23	127.10±0.74	142.33±2.66	134.80±1.89	2048±19	x
22477-01O	11.2	0.36±0.08	8.08±0.21	114.30±0.76	128.80±2.68	120.80±1.90	2044±21	x
22477-01P	11.3	0.26±0.08	7.05±0.21	106.50±1.92	118.79±2.65	113.10±1.89	2050±30	x
22477-01Q	11.4	0.21±0.08	6.68±0.21	97.93±2.06	110.54±2.47	105.80±1.77	2071±33	x
22477-01R	11.5	0.26±0.08	5.61±0.19	84.09±0.67	95.25±2.47	89.55±1.76	2053±26	x
22477-01S	11.6	0.22±0.08	5.26±0.19	77.41±0.64	87.58±2.51	82.74±1.78	2058±29	x
22477-01T	11.8	0.15±0.08	5.20±0.18	77.56±1.37	87.48±2.45	84.03±1.77	2074±34	x
22477-01U	12.1	0.07±0.08	5.51±0.19	80.27±1.16	89.76±2.53	88.29±1.80	2093±31	x
22477-01V	12.4	0.01±0.08	5.65±0.20	83.29±0.91	90.56±2.47	90.36±1.75	2076±28	x
22477-01W	12.8	0.14±0.08	6.37±0.19	88.90±0.62	98.80±2.49	95.61±1.77	2065±24	x
22477-01X	13.5	0.21±0.09	8.51±0.22	118.50±1.38	134.21±2.76	129.60±1.96	2085±24	x
22477-01Y	14	0.33±0.09	9.02±0.21	124.20±0.66	138.86±2.77	131.60±1.97	2047±20	x
22477-01Z	14.5	0.40±0.12	9.26±0.26	130.30±0.74	149.16±3.67	140.30±2.62	2066±24	x
22477-01AA	15	0.20±0.12	10.25±0.29	144.70±1.41	160.97±3.83	156.40±2.72	2071±25	x
22477-01AB	16	0.44±0.10	14.97±0.25	211.20±1.57	230.55±3.13	220.70±2.26	2030±16	x
22477-01AC	17	0.63±0.11	17.89±0.16	253.56±1.14	285.89±5.25	271.76±4.68	2061±22	x
22477-01AD	17.5	0.49±0.10	14.43±0.15	218.46±1.97	244.70±4.71	233.71±4.18	2059±25	x
22477-01AE	18	0.34±0.09	11.12±0.22	164.80±0.92	183.71±2.90	176.20±2.08	2058±16	x
22477-01AF	18.5	0.30±0.09	9.86±0.23	144.60±1.50	159.79±2.85	153.20±2.03	2047±21	x
22477-01AG	19	0.28±0.12	11.87±0.28	182.00±1.08	198.85±3.67	192.70±2.60	2047±18	x
22477-01AH	19.5	0.26±0.08	7.80±0.20	123.00±0.79	133.71±2.59	127.80±1.83	2023±19	x
22477-01AI	20	0.13±0.08	6.20±0.19	93.04±0.57	103.64±2.56	100.80±1.82	2075±14	x
22477-01AJ	20.5	0.20±0.08	6.68±0.20	106.20±0.79	116.30±2.60	111.80±1.85	2039±22	x
22477-01AK	21	0.18±0.08	5.95±0.19	88.47±0.65	98.92±2.48	94.96±1.76	2063±25	x
22477-01AL	21.5	0.12±0.08	3.96±0.18	59.95±0.28	68.35±2.42	65.63±1.72	2087±33	x
22477-01AM	22	0.17±0.08	2.48±0.17	38.18±0.28	43.95±2.45	40.06±1.74	2035±54	x
22477-01AN	22.5	0.06±0.08	0.91±0.16	14.04±0.07	16.07±2.42	14.68±1.72	2030±140	x
22477-01AO	23	0.08±0.07	1.00±0.16	14.16±0.08	16.23±2.36	14.40±1.67	2000±140	x
22477-01AP	24		0.53±0.16	9.00±0.20	9.26±2.36	12.79±1.67	2420±180	

	22477-01AQ	25		0.35±0.15	5.89±0.09	6.00±2.30	9.09±1.63	2540±250	
	22477-01AR	30	0.02±0.07	0.91±0.16	14.03±0.14	15.61±2.36	15.06±1.67	2060±140	
	22477-01AS	35	0.05±0.08	1.41±0.17	21.31±0.30	23.35±2.43	22.27±1.72	2030±96	
B14-053a_02	22477-02A	1	0.06±0.05	0.26±0.16		0.46±2.48	-1.41±1.75	6900±9500	
J = 1.99143e-2	22477-02B	2	0.10±0.06	0.34±0.18	0.74±0.34	0.84±2.70	-2.30±1.91	N/A	
± 2.87347e-5	22477-02C	3	0.13±0.06	0.30±0.18	1.86±0.36	0.95±2.70	-3.17±1.91	N/A	
	22477-02D	4	0.24±0.07	3.51±0.21	35.98±0.30	7.53±3.05	-0.02±2.16	N/A	
	22477-02E	5	0.70±0.07	7.48±0.23	86.19±0.44	24.74±2.99	2.42±2.11	98±83	
	22477-02F	6	1.00±0.08	10.59±0.28	124.40±0.42	83.86±3.81	51.81±2.70	1090±43	
	22477-02G	7	1.09±0.08	16.88±0.28	208.70±3.07	224.24±9.09	189.30±8.72	1861±56	
	22477-02H	6.5	0.17±0.07	4.33±0.22	53.74±0.36	56.73±3.05	51.15±2.16	1918±51	
	22477-02I	7	0.16±0.07	7.56±0.24	94.03±0.42	102.88±3.31	97.80±2.34	2024±30	x
	22477-02J	7.2	0.07±0.07	6.94±0.23	86.12±0.42	96.71±2.97	94.35±2.10	2088±29	x
	22477-02K	7.5	0.15±0.05	7.35±0.20	92.45±0.48	102.32±2.41	97.49±1.71	2041±23	x
	22477-02L	7.8	0.16±0.07	7.81±0.25	97.34±0.85	110.38±3.24	105.30±2.29	2073±29	x
	22477-02M	8	0.15±0.07	6.93±0.23	89.06±0.42	99.30±3.18	94.62±2.25	2050±30	x
	22477-02N	8.2	0.16±0.07	6.08±0.22	81.26±0.42	90.78±3.04	85.69±2.15	2041±32	x
	22477-02O	8.5	0.08±0.07	6.68±0.23	87.23±0.45	97.55±3.07	94.87±2.17	2079±29	x
	22477-02P	8.8	0.28±0.05	6.59±0.20	84.59±0.82	97.08±2.48	87.99±1.76	2024±27	x
	22477-02Q	9	0.11±0.07	6.65±0.25	85.15±0.42	95.92±3.38	92.26±2.39	2074±32	x
	22477-02R	9.2	0.26±0.05	6.74±0.19	87.22±0.50	99.37±2.40	90.93±1.70	2027±24	x
	22477-02S	9.5	0.29±0.05	7.17±0.22	90.03±0.86	102.41±2.42	93.15±1.71	2018±25	x
	22477-02T	9.8	0.22±0.05	8.51±0.21	104.00±0.48	117.59±2.42	110.70±1.71	2052±20	x
	22477-02U	10	0.25±0.05	7.84±0.21	101.40±0.83	115.00±2.49	106.90±1.76	2041±23	x
	22477-02V	10.2	0.26±0.05	7.62±0.21	95.71±0.43	108.90±2.45	100.70±1.74	2038±22	x
	22477-02W	10.5	0.20±0.05	8.03±0.19	98.78±0.46	113.28±2.38	106.80±1.69	2072±21	x
	22477-02X	10.8	0.23±0.06	7.90±0.21	99.05±0.45	112.54±2.57	105.30±1.82	2051±22	x
	22477-02Y	11	0.14±0.07	7.43±0.24	95.84±0.40	108.91±3.36	104.40±2.38	2082±29	x

22477-02Z	11.2	0.17±0.05	6.95±0.19	87.21±0.40	98.74±2.32	93.28±1.64	2059±23	x
22477-02AA	11.5	0.24±0.05	6.84±0.19	87.89±0.42	99.78±2.41	91.96±1.71	2032±24	x
22477-02AB	11.8	0.12±0.07	6.62±0.23	86.74±0.45	97.14±3.11	93.36±2.20	2066±30	x
22477-02AC	12	0.14±0.07	6.50±0.24	85.38±0.47	95.79±3.32	91.24±2.35	2057±33	x
22477-02AD	12.2	0.04±0.07	6.76±0.23	85.46±0.40	96.42±3.16	95.19±2.24	2109±30	x
22477-02AE	12.5	0.11±0.07	7.14±0.24	87.71±0.37	99.64±3.28	96.21±2.32	2090±31	x
22477-02AF	12.8	0.20±0.05	6.59±0.19	82.91±0.42	94.15±2.47	87.67±1.75	2044±25	x
22477-02AG	13	0.11±0.07	6.10±0.24	80.21±0.42	90.39±3.25	86.90±2.30	2074±33	x
22477-02AH	13.3	0.06±0.07	6.17±0.23	77.75±0.45	88.09±3.13	86.13±2.22	2102±33	x
22477-02AI	13.7	0.26±0.05	6.30±0.18	81.84±0.42	92.63±2.30	84.24±1.63	2012±25	x
22477-02AJ	14	0.21±0.05	6.95±0.20	87.84±0.47	99.79±2.34	93.23±1.65	2049±23	x
22477-02AK	14.3	0.12±0.07	7.17±0.22	87.65±0.44	98.23±3.01	94.54±2.13	2069±29	x
22477-02AL	14.7	0.14±0.07	7.23±0.25	93.53±0.79	105.06±3.36	100.60±2.38	2065±31	x
22477-02AM	15	0.19±0.07	6.91±0.22	85.10±0.82	96.54±3.02	90.45±2.14	2051±32	x
22477-02AN	15.3	0.14±0.06	6.68±0.23	87.67±0.42	99.22±2.91	94.80±2.06	2072±28	x
22477-02AO	15.7	0.20±0.05	6.89±0.19	87.87±0.42	100.67±2.18	94.22±1.55	2062±21	x
22477-02AP	16	0.26±0.05	6.86±0.18	85.91±0.40	97.73±2.17	89.48±1.53	2026±22	x
22477-02AQ	16.3	0.21±0.05	7.19±0.18	87.82±0.40	99.74±2.27	93.13±1.61	2048±22	x
22477-02AR	16.7	0.21±0.05	7.15±0.21	91.88±0.40	103.25±2.29	96.43±1.62	2035±22	x
22477-02AS	17	0.21±0.05	6.46±0.19	83.79±0.45	94.79±2.16	88.20±1.53	2039±22	x
22477-02AT	17.3	0.15±0.05	6.42±0.18	79.05±0.40	89.42±2.28	84.57±1.62	2059±25	x
22477-02AU	17.7	0.18±0.05	6.02±0.17	77.37±0.37	87.77±2.10	82.10±1.49	2049±23	x
22477-02AV	18	0.14±0.05	7.02±0.19	90.31±0.42	101.93±2.35	97.44±1.66	2069±22	x
22477-02AW	18.3	0.15±0.05	6.27±0.18	77.49±0.42	88.39±2.27	83.63±1.61	2070±25	x
22477-02AX	18.7	0.24±0.05	6.82±0.18	87.40±0.37	99.48±2.24	91.72±1.59	2035±22	x
22477-02AY	19	0.20±0.05	7.90±0.19	100.60±0.45	114.71±2.33	108.30±1.65	2067±20	x
22477-02AZ	19.3	0.24±0.05	7.76±0.19	96.35±0.41	111.22±2.25	103.60±1.60	2065±20	x
22477-02AAA	19.7	0.29±0.05	7.75±0.19	98.13±0.44	112.46±2.18	103.20±1.55	2038±20	x
22477-02AAB	20	0.24±0.05	7.62±0.19	91.04±0.41	105.11±2.22	97.52±1.57	2060±21	x

	22477-02AAC	20.4	0.29±0.06	9.12±0.21	108.90±0.46	124.80±2.51	115.50±1.78	2049±20	x
	22477-02AAD	20.7	0.44±0.05	10.22±0.21	119.50±0.49	138.27±2.42	124.30±1.71	2024±18	x
	22477-02AAE	21	0.29±0.05	8.59±0.21	100.20±0.39	116.48±2.45	107.10±1.74	2058±21	x
	22477-02AAF	21.4	0.30±0.05	9.11±0.21	106.30±0.40	125.24±2.40	115.60±1.70	2080±19	x
	22477-02AAG	21.7	0.24±0.05	7.32±0.19	90.24±0.37	105.26±2.21	97.60±1.56	2072±21	x
	22477-02AAH	22	0.16±0.05	7.45±0.19	98.21±1.62	111.68±2.26	106.50±1.60	2076±28	x
	22477-02AAI	22.4	0.15±0.05	6.13±0.18	75.70±1.68	86.98±2.12	82.03±1.51	2075±36	x
	22477-02AAJ	22.7	0.18±0.05	6.56±0.18	83.05±0.39	95.27±2.16	89.38±1.53	2066±22	x
	22477-02AAK	23	0.15±0.05	6.32±0.20	82.32±0.74	95.98±2.34	91.28±1.66	2103±26	x
	22477-02AAL	23.4	0.18±0.05	5.01±0.18	64.58±0.37	75.99±2.20	70.28±1.56	2080±28	x
	22477-02AAM	23.7	0.12±0.05	4.07±0.16	51.56±0.30	59.02±2.14	55.17±1.52	2059±35	x
	22477-02AAN	24	0.11±0.04	2.51±0.15	31.97±0.30	36.73±1.99	33.05±1.41	2017±53	x
	22477-02AAO	24.4	0.11±0.05	2.19±0.16	28.99±0.26	33.27±2.17	29.77±1.53	2009±64	x
	22477-02AAP	24.7	0.09±0.04	2.25±0.15	28.11±0.29	31.98±1.99	29.25±1.40	2025±60	x
	22477-02AAQ	25.4	0.01±0.04	1.09±0.14	14.76±0.24	17.21±1.88	17.00±1.33	2150±100	x
	22477-02AAR	26		1.00±0.13	12.70±0.22	15.22±1.87	16.65±1.33	2320±110	
	22477-02AAS	27	0.03±0.04	1.35±0.13	18.04±0.25	21.07±1.79	20.09±1.27	2109±80	
	22477-02AAT	35	0.12±0.04	3.12±0.15	40.65±0.30	47.23±1.94	43.29±1.37	2053±40	
	22477-02AAU	45	0.07±0.04	0.53±0.13	7.03±0.22	8.47±1.87	6.13±1.32	1820±250	
B15-053a_03	22477-03A	3			0.00±0.00	0.00±0.23	0.21±0.16	10000±1600	
J = 1.99143e-2	22477-03B	5				0.00±0.21	0.38±0.15	N/A	
± 2.87347e-5	22477-03C	6				0.00±0.22	0.07±0.15	N/A	
	22477-03D	6.5				0.00±0.21	0.17±0.15	N/A	
	22477-03E	7	0.09±0.05			0.00±0.17	-0.23±0.12	12300±2600	
	22477-03F	9	0.20±0.05		0.00±0.00	0.00±0.17	-0.49±0.12	N/A	
	22477-03G	10	0.07±0.05		0.00±0.00	0.00±0.17	-0.17±0.12	N/A	
	22477-03H	4	0.08±0.05		0.00±0.00	0.00±0.17	-0.21±0.12	N/A	
	22477-03I	7	0.13±0.05	0.44±0.02	11.15±2.12	12.23±0.19	11.91±0.14	2060±230	x

	22477-03J	9	0.08±0.06	1.34±0.04	48.36±1.73	50.90±0.23	50.69±0.17	2033±44	x
	22477-03K	9.5	0.06±0.06	0.81±0.06	65.78±3.08	70.84±0.25	70.70±0.19	2064±58	x
	22477-03L	11	0.07±0.10	12.39±0.12	190.47±4.33	204.80±0.35	204.62±0.25	2064±28	x
	22477-03M	11.5		11.55±0.11	180.17±2.60	192.99±0.41	193.01±0.25	2060±18	x
	22477-03N	13	0.22±0.11	17.28±0.19	289.48±3.37	311.75±0.42	311.19±0.30	2064±14	x
	22477-03O	14.2	0.08±0.11	18.64±0.11	282.21±3.18	302.35±0.41	302.14±0.31	2059±14	x
	22477-03P	15.4	0.11±0.10	18.30±0.12	285.00±4.62	303.78±0.37	303.50±0.27	2053±20	x
	22477-03Q	16.6	0.13±0.10	17.75±0.16	299.87±3.37	320.16±0.36	319.84±0.26	2055±14	x
	22477-03R	18.1	0.16±0.12	23.54±0.17	371.08±2.32	396.16±0.46	395.76±0.35	2054.6±7.8	x
	22477-03S	19.6	0.22±0.13	25.87±0.22	429.23±1.85	457.83±0.51	457.28±0.39	2053.3±5.5	x
	22477-03T	21.1	0.04±0.12	23.49±0.12	331.18±3.09	353.24±0.46	353.14±0.33	2054±12	x
	22477-03U	22.6		14.24±0.09	200.69±2.12	213.21±0.34	213.38±0.24	2051±13	x
	22477-03V	25		12.71±0.12	181.26±2.22	193.49±0.29	193.51±0.23	2056±15	x
	22477-03W	28	0.09±0.08	7.80±0.08	108.92±2.02	115.72±0.30	115.49±0.22	2047±23	x
	22477-03X	31	0.09±0.10	13.76±0.09	190.87±2.89	202.80±0.37	202.58±0.27	2049±19	x
	22477-03Y	34	0.12±0.06	2.360.04	0.01±0.00	0.01±0.22	-0.30±0.16	N/A	
B14-053a_04	22477-04A	2.5	0.25±0.07	0.00±0.00	17.14±3.08	4.28±4.74	-7.95±3.35	N/A	
J = 1.99143e-2	22477-04B	4.5	1.13±0.06	0.00±0.00	76.64±3.08	49.95±4.07	-5.36±2.88	N/A	
± 2.87347e-5	22477-04C	6	1.29±0.10	0.00±0.00	185.51±3.28	164.28±6.58	101.40±4.65	1329±47	
	22477-04D	7	1.13±0.08	0.00±0.00	190.14±2.99	195.51±5.34	140.41±3.78	1632±34	
	22477-04E	8	1.13±0.09	0.00±0.00	232.99±2.99	246.30±6.05	191.16±4.28	1747±29	
	22477-04F	9	1.03±0.09	0.00±0.00	244.89±3.08	265.46±6.21	215.18±4.39	1825±28	
	22477-04G	10.2	1.26±0.11	0.00±0.00	291.58±2.70	350.30±7.66	289.00±5.41	1966±26	
	22477-04H	11.4	1.57±0.15	0.00±0.00	355.43±5.78	451.49±10.59	375.09±7.49	2042±32	x
	22477-04I	12.6	0.71±0.12	0.00±0.00	314.33±2.99	372.20±8.14	337.36±5.76	2063±25	x
	22477-04J	13.8	0.77±0.10	19.32±0.48	273.10±1.07	332.50±6.69	295.10±4.73	2071±21	x
	22477-04K	15	0.44±0.11	18.45±0.51	266.80±4.62	306.97±7.26	285.40±5.14	2059±31	x
	22477-04L	16.2	0.48±0.09	0.00±0.00	217.08±1.76	251.27±5.92	227.88±4.19	2036±25	x

	22477-04M	17.7	0.46±0.10	0.00±0.00	235.65±4.39	272.32±7.14	250.01±5.05	2049±34	x
	22477-04N	19.5	0.22±0.08	0.00±0.00	194.82±2.44	219.08±5.52	208.56±3.91	2060±28	x
	22477-04O	21.3	0.26±0.08	0.00±0.00	216.09±3.31	242.51±5.80	229.97±4.10	2052±29	x
	22477-04P	23.5	0.19±0.10	0.00±0.00	275.31±3.12	302.24±6.74	292.93±4.77	2052±25	x
	22477-04Q	26	0.14±0.08	17.97±0.38	218.50±3.12	242.85±5.53	235.80±3.91	2069±27	x
	22477-04R	28.5	0.11±0.06	0.00±0.00	128.69±3.70	145.41±4.40	140.02±3.11	2080±45	x
	22477-04S	31	0.08±0.06	0.00±0.00	83.09±4.87	92.48±4.37	88.44±3.09	2053±84	x
	22477-04T	34	0.05±0.06	0.00±0.00	63.94±4.48	66.90±4.12	64.49±2.91	1990±100	x
B14-053a_05	22477-05A	1.5	0.12±0.07	1.22±0.17	10.94±0.35	3.37±2.26	0.90±1.60	270±450	
J = 1.99143e-2	22477-05B	3	0.55±0.09	8.37±0.26	97.80±1.21	31.60±2.59	19.83±1.83	612±48	
± 2.87347e-5	22477-05C	5	1.09±0.10	15.40±0.31	189.10±2.17	156.00±2.90	132.60±2.07	1577±19	
	22477-05D	7	1.27±0.15	0.00±0.00	335.01±4.04	373.04±4.72	345.84±3.40	2015±16	x
	22477-05E	8	0.78±0.11	20.46±0.39	243.80±2.96	274.23±3.19	257.60±2.26	2044±15	x
	22477-05F	9.5	1.06±0.20	0.00±0.00	429.16±4.83	482.67±6.19	459.89±4.55	2061±15	x
	22477-05G	10	0.83±0.11	19.98±0.40	240.40±3.00	274.36±3.32	256.70±2.35	2057±16	x
	22477-05H	10.5	0.52±0.09	13.53±0.32	171.80±2.29	196.15±2.88	185.00±2.04	2067±18	x
	22477-05I	11	0.41±0.09	11.65±0.32	148.20±3.04	166.83±2.70	158.00±1.92	2055±27	x
	22477-05J	11.5	0.37±0.09	11.99±0.28	142.40±1.53	161.44±2.63	153.50±1.88	2068±17	x
	22477-05K	12	0.37±0.09	10.55±0.28	129.20±3.05	147.57±2.64	139.60±1.87	2071±31	x
	22477-05L	12.5	0.51±0.08	11.35±0.30	139.60±2.04	161.81±2.54	151.00±1.80	2072±20	x
	22477-05M	13	0.49±0.09	12.42±0.32	148.00±1.61	168.92±2.64	158.50±1.87	2060±16	x
	22477-05N	13.5	0.58±0.09	12.39±0.31	153.80±1.81	178.20±2.67	165.80±1.89	2068±17	x
	22477-05O	14	0.47±0.09	14.78±0.29	173.50±3.54	199.26±2.66	189.10±1.89	2082±26	x
	22477-05P	14.5	0.83±0.14	16.16±0.38	189.20±2.02	217.38±4.28	199.70±3.03	2042±20	x
	22477-05Q	15	0.72±0.09	16.69±0.34	188.90±3.62	216.82±2.86	201.40±2.03	2054±24	x
	22477-05R	15.5	0.65±0.09	14.55±0.31	160.40±1.82	185.95±2.79	172.10±1.98	2062±17	x
	22477-05S	16	0.43±0.08	8.10±0.25	86.13±1.49	99.36±2.41	90.14±1.71	2032±29	x
	22477-05T	16.5	0.23±0.07	5.70±0.23	53.72±0.73	61.71±2.02	56.80±1.43	2044±33	x

	22477-05U	18	0.12±0.07	6.86±0.21	47.36±0.69	51.63±2.14	49.02±1.51	2019±40	x
	22477-05V	19	0.12±0.07	5.40±0.20	24.58±0.81	28.30±2.11	25.79±1.49	2035±81	x
	22477-05W	22	0.08±0.07	8.98±0.24	20.48±0.74	23.58±2.18	21.80±1.54	2053±97	x
	22477-05X	25	0.24±0.07	35.79±0.38	44.16±0.95	50.84±2.07	45.75±1.46	2020±46	x
	22477-05Y	28	0.28±0.07	20.19±0.30	17.65±1.19	24.51±1.97	18.43±1.40	2030±120	x
	22477-05Z	33	0.14±0.06	7.70±0.22	15.34±0.60	18.38±1.91	15.29±1.35	1970±116	x
B14-080_01	22637-01A	3	0.71±0.07	1.05±0.05	4.77±2.33	5.19±0.63	0.88±0.45	540±330	
J = 1.89733e-2	22637-01B	5	0.38±0.09	2.32±0.07	29.93±1.22	21.53±0.81	19.22±0.57	1437±50	
± 6.79989e-5	22637-01C	7	0.20±0.08	8.44±0.10	110.92±2.22	105.89±0.67	104.69±0.47	1851±24	
	22637-01D	9	0.00±0.09	13.51±0.13	164.24±1.78	183.02±0.87	183.00±0.53	2049±14	x
	22637-01E	11	0.20±0.10	21.62±0.15	276.83±2.45	311.73±0.94	310.54±0.70	2057±11	x
	22637-01F	13		16.73±0.15	208.73±2.67	232.34±0.83	232.90±0.59	2051±16	x
	22637-01G	14.5	0.06±0.07	8.50±0.10	103.26±1.22	115.81±0.60	115.46±0.42	2053±15	x
	22637-01H	16		5.61±0.09	67.79±1.67	75.30±0.64	76.02±0.45	2057±31	x
	22637-01I	17.5	0.16±0.06	2.02±0.09	23.98±1.89	27.56±0.54	26.56±0.38	2042±98	x
	22637-01J	20.5	0.06±0.08	4.83±0.08	60.07±1.67	66.84±0.67	66.44±0.47	2040±35	x
	22637-01K	23.5	0.03±0.08	5.80±0.09	75.20±1.34	84.49±0.71	84.31±0.51	2057±23	x
	22637-01L	26.5		1.19±0.06	15.52±2.44	17.46±0.64	17.61±0.45	2070±200	x
	22637-01M	29.5	0.08±0.08	2.28±0.07	31.03±1.78	34.80±0.65	34.29±0.46	2039±72	x
	22637-01N	35	0.01±0.08	2.01±0.06	27.83±2.45	29.90±0.67	29.82±0.47	2002±108	x
B14-080_02	22637-08A	1.5	0.53±0.09	0.92±0.11	5.97±0.47	2.03±0.52	-0.20±0.37	N/A	
J = 1.89733e-2	22637-08B	3	0.25±0.12	0.51±0.10	5.22±0.84	2.64±0.70	1.57±0.49	820±230	
± 6.79989e-5	22637-08C	5	0.34±0.11	1.62±0.11	13.98±0.63	11.14±0.64	9.69±0.46	1515±67	
	22637-08D	7	0.27±0.07	4.41±0.16	45.30±0.50	43.83±0.42	42.71±0.30	1850±15	
	22637-08E	8	0.19±0.07	4.96±0.17	52.96±0.45	55.60±0.40	54.80±0.28	1960±12	
	22637-08F	9	0.04±0.07	6.10±0.16	60.01±0.55	63.62±0.45	63.45±0.33	1986±12	
	22637-08G	10		7.43±0.22	74.91±0.62	81.01±0.67	81.30±0.48	2017±12	

	22637-08H	11	0.12±0.08	10.85±0.21	112.00±0.71	125.42±0.51	124.90±0.37	2050±8.1	x
	22637-08I	12	0.27±0.12	14.56±0.34	152.20±3.11	171.75±0.97	170.60±0.82	2057±26	x
	22637-08J	12.5		9.60±0.19	100.10±1.38	111.33±0.74	111.90±0.55	2053±18	x
	22637-08K	13	0.09±0.08	6.29±0.19	68.58±1.04	76.97±0.48	76.59±0.36	2052±19	x
	22637-08L	13.5	0.14±0.07	4.22±0.17	42.85±0.48	48.36±0.46	47.77±0.34	2050±16	x
	22637-08M	14	0.11±0.07	3.36±0.13	36.61±0.45	41.54±0.46	41.06±0.34	2057±18	x
	22637-08N	15	0.11±0.07	3.04±0.14	35.90±0.53	40.69±0.40	40.22±0.29	2056±20	x
	22637-08O	17	0.07±0.07	3.90±0.16	38.94±0.52	43.90±0.47	43.61±0.37	2056±19	x
	22637-08P	19	0.02±0.07	4.71±0.19	51.04±0.95	57.24±0.45	57.14±0.32	2055±24	x
	22637-08Q	21		1.86±0.12	19.77±1.30	23.12±1.08	23.18±1.04	2112±99	x
	22637-08R	24	0.04±0.10	6.09±0.17	67.69±0.63	75.48±0.65	75.33±0.47	2048±13	x
	22637-08S	28	0.02±0.10	4.35±0.15	46.96±0.87	52.73±0.62	52.65±0.45	2057±25	x
	22637-08T	33	0.08±0.07	0.61±0.09	6.83±0.55	7.53±0.39	7.18±0.27	1980±110	x
B14-086_01	22638-01A	3	68.76±0.28	11.48±0.12	9.62±1.62	216.75±2.44	-120.23±2.03	NaN	
J = 1.89937e-2	22638-01B	4	8.76±0.09	1.95±0.05	3.41±1.72	31.20±0.68	-11.72±0.51	NaN	
± 7.62159e-5	22638-01C	5	20.98±0.20	6.13±0.09	23.47±1.76	73.08±1.47	-29.75±1.11	NaN	
	22638-01D	6	3.72±0.10	5.18±0.07	27.70±1.67	39.06±0.78	20.81±0.59	1599±72	
	22638-01E	7	2.75±0.07	6.69±0.10		75.67±0.74	62.21±0.65	NaN	
	22638-01F	8	1.13±0.09	6.64±0.10	105.40±2.50	107.35±0.95	101.80±0.85	1879±26	
	22638-01G	9	0.42±0.08	7.34±0.09	113.36±1.86	128.34±1.03	126.29±0.95	2050±17	x
	22638-01H	10	0.67±0.08	9.87±0.12	157.66±2.42	178.89±1.31	175.62±1.25	2050±15	x
	22638-01I	11	0.25±0.09	13.47±0.15	216.20±4.54	241.84±1.72	240.60±1.67	2049±23	x
	22638-01J	12	0.05±0.12	15.20±0.13	260.44±4.84	291.67±2.07	291.44±1.99	2056±19	x
	22638-01K	13		15.47±0.14	267.71±5.20	299.27±2.10	299.36±2.02	2055±21	x
	22638-01L	14	0.74±0.10	14.52±0.16	249.68±4.51	280.91±1.96	277.31±1.90	2047±19	x
	22638-01M	15.5	0.35±0.13	20.36±0.19	344.70±6.12	384.60±2.64	382.90±2.56	2047±18	x
	22638-01N	16.8	0.18±0.13	23.04±0.18	373.27±5.76	419.78±2.84	418.90±2.77	2059±15	x
	22638-01O	18	0.06±0.17	30.05±0.23	520.90±7.80	580.67±3.93	580.40±3.84	2050±14	x

	22638-01P	19.3		26.77±0.17	462.29±7.24	516.01±3.44	516.11±3.39	2053±15	x
	22638-01Q	20		20.75±0.15	359.28±6.02	397.83±2.69	398.30±2.62	2044±17	x
	22638-01R	21	0.01±0.14	23.93±0.17	417.77±8.54	466.12±3.13	466.08±3.07	2052±22	x
	22638-01S	22	0.00±0.14	22.32±0.15	383.31±5.66	426.59±2.81	426.59±2.81	2049±14	x
	22638-01T	23		18.06±0.18	317.70±4.53	353.20±2.43	353.60±2.35	2049±13	x
	22638-01U	24	0.16±0.08	11.40±0.12	192.39±3.97	216.14±1.50	215.34±1.45	2056±22	x
	22638-01V	25.5	0.26±0.13	24.42±0.18	423.59±6.13	476.20±3.22	474.92±3.15	2058±13	x
	22638-01W	27	0.33±0.13	22.99±0.19	398.90±7.08	446.00±3.02	444.40±2.96	2050±18	x
	22638-01X	28.5	0.19±0.05	8.24±0.11	140.48±3.35	156.53±1.14	155.59±1.09	2043±27	x
	22638-01Y	30	0.21±0.10	3.76±0.07	66.46±2.18	73.49±0.63	72.47±0.57	2024±39	x
	22638-01Z	33	0.11±0.10	1.75±0.05	20.27±4.10	31.95±0.43	31.40±0.34	2470±270	x
	22638-01AA	35	0.07±0.06	1.15±0.05	15.96±2.39	24.02±0.49	23.66±0.37	2420±200	x
B14-086_02	22638-05A	1.5	0.60±0.08	1.09±0.10	9.60±0.25	4.71±0.32	2.94±0.23	828±55	
J = 1.89937e-2	22638-05B	3	0.45±0.07	1.89±0.11	19.99±0.33	16.15±0.30	14.84±0.21	1587±23	
± 7.62159e-5	22638-05C	5	1.70±0.09	4.45±0.16	53.65±0.44	43.89±0.38	38.92±0.27	1563±11	
	22638-05D	7	2.04±0.10	13.45±0.31	133.00±0.75	149.87±0.42	143.90±0.32	2014.9±7.4	
	22638-05E	8	3.47±0.11	17.80±0.27	174.40±0.94	209.06±0.52	198.90±0.41	2079.8±7.2	
	22638-05F	9	2.32±0.18	26.49±0.26	297.40±2.11	337.99±1.02	331.20±0.88	2050.0±9.3	x
	22638-05G	9.5	1.33±0.17	27.36±0.26	304.00±2.11	345.74±0.76	341.87±0.57	2061.9±8.8	x
	22638-05H	10	1.64±0.17	30.77±0.27	338.67±2.12	381.15±1.11	376.35±0.99	2047.3±8.3	x
	22638-05I	10.5	0.47±0.27	29.72±0.22	347.06±2.12	392.27±1.17	390.89±0.86	2063.9±8.0	x
	22638-05J	10.7	0.93±0.15	23.92±0.24	290.76±2.12	331.42±0.72	328.70±0.57	2068.3±9.2	x
	22638-05K	10.9	0.66±0.15	21.29±0.21	254.62±2.11	287.47±1.21	285.52±1.13	2058±11	x
	22638-05L	11	0.47±0.11	17.12±0.27	206.20±0.50	232.38±0.55	231.00±0.45	2056.9±3.9	x
	22638-05M	11.1	0.34±0.10	17.27±0.24	203.10±1.91	228.89±0.67	227.90±0.60	2059±12	x
	22638-05N	11.2	0.10±0.14	15.38±0.28	192.40±0.49	215.00±0.59	214.70±0.43	2052.2±4.0	x
	22638-05O	11.3	0.31±0.10	15.07±0.24	192.60±1.63	216.12±0.45	215.20±0.35	2054±11	x
	22638-05P	11.4	0.24±0.10	13.99±0.31	174.30±0.47	195.40±0.43	194.70±0.33	2053.9±4.0	x

22638-05Q	11.5	0.30±0.09	11.38±0.25	149.80±0.84	168.38±0.40	167.50±0.30	2054.3±7.3	x
22638-05R	11.6	0.21±0.09	10.47±0.25	135.80±0.73	152.60±0.40	152.00±0.29	2056.6±7.1	x
22638-05S	11.7	0.32±0.08	11.19±0.27	144.10±0.42	161.82±0.38	160.90±0.29	2053.4±4.3	x
22638-05T	11.8	0.31±0.08	12.96±0.26	161.00±0.84	179.11±0.40	178.20±0.32	2042.9±6.8	x
22638-05U	11.9	0.27±0.08	9.97±0.23	127.30±0.75	142.91±0.36	142.10±0.28	2052.3±7.7	x
22638-05V	12	0.20±0.08	10.29±0.24	128.50±0.73	144.78±0.39	144.20±0.32	2059.6±7.5	x
22638-05W	12.1	0.29±0.08	9.29±0.21	118.10±0.72	132.44±0.42	131.60±0.34	2050.9±8.2	x
22638-05X	12.2	0.20±0.08	8.98±0.20	118.20±0.67	133.00±0.38	132.40±0.29	2057.5±7.5	x
22638-05Y	12.3	0.24±0.08	9.19±0.24	115.40±0.64	129.70±0.36	129.00±0.26	2054.3±7.3	x
22638-05Z	12.4	0.30±0.08	8.43±0.23	111.30±1.32	124.99±0.37	124.10±0.28	2051±15	x
22638-05AA	12.6	0.21±0.08	9.35±0.24	122.80±1.41	138.52±0.43	137.90±0.36	2060±14	x
22638-05AB	12.9	0.19±0.08	9.77±0.22	125.10±0.73	140.56±0.36	140.00±0.27	2055.4±7.6	x
22638-05AC	13.2	0.07±0.09	11.82±0.25	149.40±0.46	166.39±0.46	166.20±0.38	2048.7±4.8	x
22638-05AD	13.5	0.16±0.09	12.62±0.22	160.10±0.42	178.88±0.42	178.40±0.33	2050.6±4.0	x
22638-05AE	14	0.16±0.10	15.91±0.26	196.60±0.85	220.17±0.46	219.70±0.35	2054.5±5.7	x
22638-05AF	14.5	0.14±0.10	18.56±0.31	240.10±1.75	268.20±0.48	267.80±0.37	2051.6±9.1	x
22638-05AG	15	0.22±0.14	21.78±0.22	278.06±2.11	314.34±0.71	313.68±0.57	2065.8±9.6	x
22638-05AH	15.5	0.06±0.14	20.38±0.20	270.43±2.11	303.07±0.64	302.89±0.46	2057.0±9.8	x
22638-05AI	16	0.25±0.14	20.20±0.21	261.07±2.11	297.72±0.60	297.01±0.45	2076±10	x
22638-05AJ	16.5	0.09±0.10	17.04±0.28	217.60±1.56	245.16±0.52	244.90±0.43	2062.9±9.1	x
22638-05AK	17	0.21±0.11	17.75±0.31	233.00±0.99	260.13±0.50	259.50±0.39	2050.2±5.6	x
22638-05AL	17.5	0.32±0.11	18.11±0.27	237.30±1.67	266.82±0.56	265.90±0.46	2057.4±8.9	x
22638-05AM	18	0.49±0.29	20.16±0.19	264.02±2.11	298.86±1.21	297.43±0.86	2064±10	x
22638-05AN	18.3	0.22±0.15	19.75±0.19	266.26±2.11	300.53±0.64	299.90±0.48	2064±10	x
22638-05AO	18.6	0.30±0.28	23.58±0.22	306.88±2.11	346.53±1.32	345.67±1.03	2063.9±9.3	x
22638-05AP	19	0.25±0.17	21.35±0.21	275.15±2.11	313.84±1.74	313.12±1.67	2077±12	x
22638-05AQ	19.2		19.44±0.21	262.31±2.11	294.46±0.62	294.87±0.47	2061±10	x
22638-05AR	19.3	0.07±0.13	20.57±0.18	270.29±2.11	302.84±0.91	302.63±0.81	2057±10	x
22638-05AS	19.4	2.11±0.12	19.55±0.34	226.30±1.74	258.68±0.60	252.50±0.50	2052.4±9.8	x

22638-05AT	19.5	0.33±0.11	18.62±0.26	246.20±1.89	276.76±0.51	275.80±0.40	2057.0±9.6	x
22638-05AU	19.6	0.24±0.09	15.00±0.23	209.50±1.75	233.41±0.63	232.70±0.57	2047±11	x
22638-05AV	19.7	0.23±0.10	12.79±0.26	174.10±0.91	194.78±0.43	194.10±0.32	2051.5±6.8	x
22638-05AW	19.8	0.22±0.10	15.06±0.28	214.30±1.66	238.44±0.58	237.80±0.51	2045.6±9.9	x
22638-05AX	19.9	0.23±0.09	11.31±0.26	152.50±0.79	171.87±0.42	171.20±0.34	2060.2±6.9	x
22638-05AY	20	0.12±0.08	10.40±0.25	136.40±0.71	152.16±0.38	151.80±0.29	2049.6±6.8	x
22638-05AZ	20.1		9.72±0.22	138.20±0.78	154.35±0.51	154.70±0.37	2056.0±7.6	x
22638-05BA	20.2	0.16±0.08	9.24±0.22	120.60±0.67	134.36±0.43	133.90±0.35	2046.6±7.6	x
22638-05BB	20.3	0.07±0.08	7.24±0.19	98.00±0.56	110.00±0.42	109.80±0.35	2057.5±8.1	x
22638-05BC	20.6	0.23±0.08	9.64±0.24	127.60±0.70	143.27±0.64	142.60±0.60	2053.9±8.5	x
22638-05BD	20.9	0.18±0.08	8.54±0.20	117.90±0.65	132.04±0.42	131.50±0.35	2051.5±7.5	x
22638-05BE	21.2	0.14±0.07	9.20±0.21	118.90±0.62	133.11±0.39	132.70±0.32	2052.2±7.1	x
22638-05BF	21.7	0.21±0.09	15.18±0.26	209.60±0.88	235.13±0.46	234.50±0.37	2055.8±5.6	x
22638-05BG	22.2	0.09±0.17	20.85±0.22	300.27±2.11	338.47±0.93	338.20±0.78	2063.9±9.1	x
22638-05BH	22.7	0.32±0.10	16.54±0.28	231.00±0.96	261.03±0.50	260.10±0.40	2063.1±5.5	x
22638-05BI	23.2	0.24±0.20	36.50±0.24	491.07±2.18	551.30±0.93	550.58±0.72	2058.3±5.7	x
22638-05BJ	23.7		31.62±0.24	427.42±2.17	472.71±3.16	472.71±3.16	2042±10	x
22638-05BK	24.2	0.22±0.10	16.06±0.26	223.70±0.91	250.45±0.45	249.80±0.34	2053.6±5.3	x
22638-05BL	24.5	0.15±0.11	15.76±0.25	220.80±0.66	246.35±0.48	245.90±0.36	2049.8±3.9	x
22638-05BM	24.8	0.20±0.15	22.13±0.17	310.28±2.18	343.41±0.82	342.83±0.68	2040.3±8.8	x
22638-05BN	25.1	0.16±0.10	14.54±0.27	203.30±1.64	226.98±0.57	226.50±0.49	2050±10	x
22638-05BO	25.4	0.42±0.12	17.87±0.25	250.70±2.05	280.34±0.57	279.10±0.44	2049±10	x
22638-05BP	25.7	0.27±0.10	6.74±0.16	94.53±0.74	105.29±0.43	104.50±0.32	2041±10	x
22638-05BQ	26	0.23±0.09	5.77±0.17	73.21±1.00	81.37±0.37	80.69±0.27	2037±17	x
22638-05BR	26.3	0.13±0.08	6.95±0.17	98.16±0.76	109.07±0.35	108.70±0.26	2043.0±9.9	x
22638-05BS	27	0.12±0.07	6.36±0.19	97.41±0.67	108.15±0.32	107.80±0.24	2042.5±8.8	x
22638-05BT	28	0.32±0.34	82.49±0.41	1124.53±2.76	343.71±1.16	342.83±0.68	2057.9±3.1	x
22638-05BU	28.1	0.24±0.09	13.58±0.23	176.00±0.82	196.10±0.44	195.40±0.35	2046.5±6.0	x
22638-05BV	28.3	0.18±0.08	6.69±0.16	92.97±1.16	104.13±0.36	103.60±0.27	2051±16	x

	22638-05BW	28.5	0.43±0.10	7.17±0.19	98.05±0.69	110.66±0.43	109.40±0.32	2052.3±9.2	x
	22638-05BX	28.7	0.30±0.09	5.80±0.17	77.33±0.63	86.42±0.41	85.55±0.31	2042±11	x
	22638-05BY	28.9	0.27±0.09	3.63±0.16	48.16±0.52	54.24±0.39	53.45±0.28	2046±15	x
	22638-05BZ	29.3	0.08±0.07	6.19±0.16	86.99±0.58	96.56±0.31	96.31±0.23	2042.7±8.6	x
	22638-05CA	29.7	0.03±0.08	5.64±0.16	77.69±0.55	85.66±0.33	85.58±0.25	2036.7±9.3	
	22638-05CB	30.1		6.38±0.20	88.18±0.56	98.90±0.33	98.92±0.24	2058.9±8.2	
	22638-05CC	31	0.17±0.08	9.59±0.18	128.90±0.75	143.89±0.35	143.40±0.26	2048.6±7.3	
	22638-05CD	33	0.11±0.07	0.77±0.09	8.28±0.42	8.87±0.28	8.54±0.20	1957±67	
B14-086_03	22638-09A	1.5	0.40±0.07	0.43±0.09	5.07±0.39	4.12±0.45	2.39±0.32	1150±130	
J = 1.89937e-2	22638-09B	3	0.17±0.07	0.98±0.10	15.32±0.42	17.61±0.45	16.88±0.32	2038±41	x
± 7.62159e-5	22638-09C	5	1.24±0.10	10.10±0.21	147.20±1.50	168.13±0.61	162.70±0.44	2041±13	x
	22638-09D	7	0.32±0.20	29.50±0.29	494.00±2.22	552.48±1.44	551.10±1.14	2052.1±6.1	x
	22638-09E	7.2	0.28±0.11	14.59±0.27	246.40±0.94	276.14±0.69	274.90±0.51	2052.2±5.2	x
	22638-09F	7.3	0.25±0.09	9.71±0.19	156.50±0.90	176.29±0.63	175.20±0.49	2056.8±7.9	x
	22638-09G	7.4	0.19±0.08	5.68±0.17	101.20±1.15	113.62±0.52	112.80±0.39	2051±15	x
	22638-09H	7.6	0.12±0.08	5.69±0.19	97.38±0.73	108.94±0.53	108.40±0.39	2050±10	x
	22638-09I	7.8	0.07±0.08	5.57±0.17	99.71±0.77	111.52±0.52	111.20±0.40	2051±10	x
	22638-09J	8	0.18±0.08	5.38±0.18	94.78±0.72	106.67±0.51	105.90±0.37	2054±10	x
	22638-09K	8.2	0.10±0.08	5.82±0.17	97.94±0.64	109.33±0.57	108.90±0.44	2047.7±9.4	x
	22638-09L	8.4	0.13±0.08	6.49±0.18	105.90±0.69	118.98±0.54	118.40±0.39	2054.5±9.0	x
	22638-09M	8.6	0.10±0.09	7.09±0.18	114.20±0.77	127.25±0.55	126.80±0.40	2046.7±9.1	x
	22638-09N	8.8	0.03±0.09	6.03±0.16	105.80±0.74	118.73±0.54	118.60±0.39	2058.9±9.4	x
	22638-09O	9	0.14±0.09	7.48±0.20	122.10±0.74	137.13±0.57	136.50±0.42	2054.9±8.4	x
	22638-09P	9.3		6.24±0.18	112.50±0.68	125.94±0.48	126.20±0.35	2058.4±8.2	x
	22638-09Q	9.6	0.06±0.08	7.78±0.21	131.20±0.77	147.06±0.55	146.80±0.42	2055.8±8.0	x
	22638-09R	9.9	0.11±0.08	7.52±0.20	128.80±0.74	145.19±0.53	144.70±0.38	2060.3±7.8	x
	22638-09S	10.2	0.08±0.09	7.53±0.19	129.60±0.71	145.65±0.55	145.30±0.40	2057.6±7.5	x
	22638-09T	10.5	0.06±0.09	6.72±0.23	122.90±0.72	136.97±0.57	136.70±0.42	2048.1±8.1	x

22638-09U	10.8	0.10±0.08	7.56±0.22	123.40±0.87	138.55±0.55	138.10±0.42	2055.7±9.4	x
22638-09V	11.1		7.19±0.18	129.40±0.77	143.87±0.51	144.00±0.39	2049.1±8.0	x
22638-09W	11.4	0.06±0.08	6.82±0.22	120.40±1.40	134.58±0.50	134.30±0.37	2052±15	x
22638-09X	11.7	0.05±0.08	6.44±0.21	115.20±0.68	128.43±0.52	128.20±0.38	2049.4±8.1	x
22638-09Y	12		6.38±0.26	112.00±0.66	123.47±0.39	124.10±0.28	2044.4±7.7	x
22638-09Z	12.3	0.11±0.08	6.01±0.19	107.90±0.70	121.06±0.50	120.60±0.37	2054.3±8.9	x
22638-09AA	12.6	0.19±0.08	7.71±0.17	132.20±0.76	148.71±0.51	147.90±0.38	2055.3±7.8	x
22638-09AB	12.9		6.08±0.16	99.03±0.68	111.00±0.47	111.00±0.33	2058.2±9.2	x
22638-09AC	13.4	0.05±0.08	7.53±0.18	135.50±0.69	150.90±0.52	150.70±0.40	2047.9±7.0	x
22638-09AD	14	0.11±0.09	12.57±0.25	211.80±0.78	237.70±0.60	237.20±0.44	2056.5±5.1	x
22638-09AE	14.5	0.10±0.09	10.43±0.21	182.80±3.08	204.33±0.68	203.90±0.56	2052±21	x
22638-09AF	15	0.09±0.10	12.06±0.27	216.00±1.71	240.58±0.64	240.20±0.47	2048.2±10	x
22638-09AG	15.5	0.09±0.10	14.04±0.25	245.10±3.09	274.30±0.65	273.90±0.48	2055±16	x
22638-09AH	15.8	0.11±0.09	8.95±0.22	155.70±0.78	173.68±0.56	173.20±0.41	2049.2±6.8	x
22638-09AI	16.1	0.18±0.08	8.46±0.23	144.90±0.87	162.91±0.53	162.10±0.39	2056.0±8.0	x
22638-09AJ	16.4	0.16±0.08	6.10±0.17	104.50±1.24	116.60±0.53	115.90±0.40	2045.1±15	x
22638-09AK	16.7	0.00±0.07	5.36±0.16	92.43±0.65	103.01±0.47	103.00±0.35	2050.4±9.6	x
22638-09AL	17		4.53±0.17	80.63±0.61	89.89±0.47	90.18±0.34	2055.3±10	x
22638-09AM	17.5	0.33±0.08	6.07±0.17	110.90±0.67	125.13±0.54	123.70±0.41	2051.4±8.4	x
22638-09AN	18		8.35±0.21	146.70±0.82	164.22±0.58	164.30±0.44	2057.1±7.6	x
22638-09AO	18.5	0.59±0.10	10.49±0.25	181.20±1.86	204.88±0.72	202.30±0.58	2053±13	x
22638-09AP	19	0.22±0.08	8.94±0.20	153.40±0.78	172.85±0.60	171.90±0.48	2057.6±7.1	x
22638-09AQ	19.5	0.21±0.09	9.35±0.20	159.70±0.88	178.33±0.60	177.40±0.45	2046.6±7.4	x
22638-09AR	20	0.24±0.10	8.47±0.24	152.40±0.77	170.45±0.66	169.40±0.48	2047.7±7.1	x
22638-09AS	20.5	0.09±0.10	7.80±0.21	145.70±0.94	162.18±0.69	161.80±0.52	2046.4±8.8	x
22638-09AT	21	0.12±0.10	7.89±0.23	135.10±0.78	150.53±0.61	150.00±0.45	2045.9±8.0	x
22638-09AU	21.5	0.15±0.09	10.94±0.20	194.50±1.62	218.35±0.71	217.70±0.59	2056±11	x
22638-09AV	22	0.21±0.10	11.39±0.25	202.40±1.06	227.20±0.64	226.30±0.47	2054.5±6.9	x
22638-09AW	22.5	0.17±0.10	13.68±0.28	240.80±0.89	270.13±0.77	269.40±0.64	2055.2±5.4	x

22638-09AX	23	0.32±0.17	21.99±0.21	369.58±2.18	417.45±1.12	416.03±0.85	2063.1±7.7	x
22638-09AY	23.5	0.09±0.17	27.52±0.23	483.02±2.22	538.77±1.19	538.39±0.91	2051.0±6.0	x
22638-09AZ	24	0.50±0.18	24.10±0.20	418.40±2.19	466.49±1.25	464.29±0.96	2045.6±6.9	x
22638-09BA	24.3	0.23±0.11	10.46±0.23	182.80±0.94	205.22±0.74	204.20±0.57	2053.8±7.2	x
22638-09BB	24.6	0.05±0.13	8.30±0.20	140.60±0.84	157.00±0.87	156.80±0.64	2051.4±8.9	x
22638-09BC	24.9	0.25±0.10	7.59±0.19	131.70±0.72	147.59±0.67	146.50±0.49	2048.4±7.9	x
22638-09BD	25.2	0.08±0.11	14.53±0.22	260.00±1.25	292.24±0.75	291.90±0.57	2059.9±6.4	x
22638-09BE	25.5	0.09±0.09	10.20±0.22	176.80±0.97	198.59±0.57	198.20±0.41	2057.8±7.2	x
22638-09BF	25.8		6.84±0.19	126.30±0.76	139.88±0.79	140.00±0.57	2043.9±8.9	x
22638-09BG	26.1	0.04±0.08	7.75±0.20	135.60±0.70	151.46±0.50	151.30±0.37	2052.4±7.1	x
22638-09BH	26.5	0.18±0.07	5.08±0.16	92.00±1.23	102.81±0.48	102.00±0.35	2045±17	x
22638-09BI	27	0.15±0.08	6.05±0.19	101.80±0.62	113.85±0.49	113.20±0.36	2047.8±8.4	x
22638-09BJ	28	0.17±0.07	3.24±0.14	49.36±1.04	55.92±0.44	55.17±0.31	2054±27	x
22638-09BK	29	0.17±0.07	1.64±0.12	28.81±0.81	30.25±0.43	29.51±0.31	1949±36	
22638-09BL	31	0.16±0.07	2.75±0.14	49.32±0.60	51.87±0.45	51.16±0.33	1964±16	
22638-09BM	33	0.07±0.07	3.31±0.13	63.29±0.54	65.92±0.49	65.61±0.37	1963±12	

Table 3

Average Microprobe Analyses of Biotite: H_2O calculated based on Cl + F + OH = 2.0 per formula unit.

	B07-041	B06-055	B06-042	B14-015	B14-024	B14-045	B14-049	B14-053a	B14-080	B14-086
SiO_2	34.23	36.18	36.93	37.09	36.34	37.50	36.92	38.16	39.52	39.87
TiO_2	4.14	4.52	4.12	3.88	3.79	3.26	3.08	3.95	2.54	3.13
Al_2O_3	13.70	14.11	14.34	14.06	13.94	13.73	14.00	13.46	13.86	13.81
MnO	0.08	0.06	0.04	0.10	0.07	0.08	0.06	0.03	0.02	0.01
FeO	27.93	21.34	18.51	13.30	16.33	15.21	15.38	11.62	8.53	6.83
MgO	4.82	9.86	12.31	16.89	14.52	15.44	16.28	16.88	20.16	19.98
K_2O	9.30	9.34	9.84	7.35	8.01	9.03	7.69	9.56	9.64	9.51
Na_2O	0.10	0.30	0.18	0.06	0.05	0.13	0.06	0.16	0.10	0.29
BaO	0.24	0.26	0.23	0.09	0.07	0.13	0.09	0.20	0.21	0.17
CaO	0.00	0.06	0.03	0.75	0.15	0.08	0.13	0.10	0.12	0.08
Cl	0.23	0.42	0.62	0.39	0.51	0.68	0.44	0.50	0.67	0.65
F	0.11	0.37	0.30	0.30	0.28	0.42	0.49	0.61	1.05	0.48
H_2O	3.59	3.62	3.68	3.77	3.66	3.61	3.62	3.61	3.46	3.75
O=F, Cl	0.10	0.25	0.27	0.22	0.23	0.33	0.31	0.37	0.60	0.35
Total	98.37	100.19	100.85	98.00	97.50	98.99	97.98	98.82	99.85	99.11

Table 4
Summary of Isochron Regressions: All uncertainties reported at 1σ.

RunID	Isochron						Inverse Isochron						Steps
	Age (Ma)	±	MSWD	p	$^{40}Ar/^{36}Ar$ Int.	±	Age (Ma)	±	MSWD	p	$^{40}Ar/^{36}Ar$ Int.	±	
B07-041													
22486-01	2055.8	6.2	0.10	1.00	328	37	2055.8	4.0	0.28	1.00	333	32	D-W
22486-02	2055.0	5.7	0.13	1.00	240	190	2057.5	4.0	0.72	0.70	191	63	D-V
22486-03	2057.9	9.9	0.11	1.00	140	370	2054.3	7.8	0.34	0.99	360	170	C-R
B06-055													
22485-01	2055.5	3.4	0.15	1.00	301	33	2055.4	3.2	0.24	1.00	302	33	A-O
22485-02	2053.5	3.7	0.08	1.00	289	31	2055.8	3.0	0.14	1.00	285	28	B-AK
22485-04	2054.7	3.8	0.09	1.00	288	20	2055.5	3.2	0.18	1.00	287	19	B-X
B06-042													
22484-01	2054.1	3.4	0.13	1.00	250	110	2055.4	3.2	0.19	1.00	240	90	A-O
22484-05	2056.0	6.4	0.08	1.00	250	180	2055.7	5.1	0.15	1.00	270	120	04,A-U
22484-06	2053.7	7.1	0.13	1.00	380	430	2053.1	5.5	0.24	1.00	540	250	D-X
B14-015													
22487-01	2055.5	6.6	0.27	1.00	270	140	2056.7	5.5	0.38	1.00	278	85	F-AB
22487-02	2054	14	0.16	1.00	250	220	2056	11	0.24	0.99	240	120	H-T
22487-03	2055	14	0.16	1.00	2110	460	2056.6	9.9	0.35	1.00	2130	350	03F-04L
B14-024													
22489-01	2054.4	7.1	0.07	1.00	286	57	2054.7	6.5	0.08	1.00	284	50	B-J
22489-02	2048	21	0.20	1.00	1160	280	2053	19	0.13	1.00	1200	290	E-V
B14-045													
22490-02	2058.1	4.3	0.13	1.00	340	170	2054.9	4.5	0.10	1.00	450	170	D-U
22490-03	2043	28	0.51	0.94	2570	940	1929	58	0.55	0.91	7300	4900	F-V
22490-04	2054.5	6.5	0.09	1.00	330	180	2053.6	5.9	0.17	1.00	380	150	D-Y
B14-049													

22488-01	2054	12	0.08	1.00	290	340	2054	11	0.08	1.00	280	270	C-I
22488-02	2057.5	7.0	0.23	1.00	200	170	2056.6	5.7	0.42	0.97	261	99	J-Z
22488-03	2047	12	0.37	0.98	600	350	2019	24	0.38	0.98	1800	1100	J-Y
B14-053a													
22477-01	2046.7	9.6	0.66	0.93	2190	300	2057.9	8.8	0.81	0.77	2250	330	H-AO
22477-02	2042	14	0.56	1.00	3200	470	2042	12	0.73	0.95	3670	740	I-AAU
22477-03	2054.2	8.0	0.09	1.00	200	1300	2055.3	7.8	0.11	1.00	100	91	I-X
22477-04	2054	18	0.23	1.00	4860	720	2057	17	0.24	0.99	4880	700	H-T
22477-05	2056	24	0.26	1.00	2060	580	2058	20	0.37	0.99	2140	530	E-Y
B14-080													
22637-01	2058	13	0.04	1.00	300	1300	2053	10	0.11	1.00	630	660	D-N
22637-08	2055	11	0.09	1.00	300	430	2051.1	9.7	0.10	1.00	460	350	H-T
B14-086													
22638-01	2049	14	0.05	1.00	460	570	2053.1	7.8	0.10	1.00	380	220	G-Y
22638-05	2051.1	5.2	0.48	1.00	336	65	2054.0	5.1	0.79	0.89	294	35	F-BZ
22638-09	2052.8	5.3	0.20	1.00	340	120	2053.6	5.2	0.31	1.00	362	74	B-BJ

Table 5
Summary of Ages from Plateau Diagrams: All uncertainties are reported at 1σ.

RunID	Plateau Age (Ma)	±	MSWD	p	Integrated Age (Ma)	±
B07-041						
22486-01	2055.8	3.3	0.26	1.00	2047.7	6.3
22486-02	2054.7	2.1	0.60	0.90	2050.0	3.2
22486-03	2054.1	3.2	0.31	0.99	2036.5	4.8
B06-055						
22485-01	2055.4	2.1	0.22	1.00	2054.8	2.9
22485-02	2055.8	1.8	0.14	1.00	2054.3	3.3
22485-04	2055.8	2.1	0.21	1.00	2055.4	3.4
B06-042						
22484-01	2055.4	2.0	0.17	1.00	2054.5	3.4
22484-05	2055.7	3.2	0.14	1.00	2050.9	4.8
22484-06	2053.8	2.6	0.33	1.00	2040.4	4.5
B14-015						
22487-01	2056.7	2.0	0.36	1.00	1907.0	6.0
22487-02	2055.2	3.3	0.23	1.00	1862.3	3.7
22487-03	2056.6	4.3	0.33	1.00	2065	13
B14-024						
22489-01	2054.5	4.8	0.05	1.00	2026.4	6.9
22489-02	2053	10	0.15	1.00	1904	13
B14-045						
22490-02	2055.0	2.2	0.28	1.00	2028.9	4.6
22490-03	2055.3	6.5	0.91	0.56	1920	13
22490-04	2053.4	2.2	0.15	1.00	1978.8	3.7
B14-049						
22488-01	2054.3	5.7	0.06	1.00	2031.5	6.0
22488-02	2056.4	3.0	0.38	0.99	2016.0	4.0
22488-03	2053.2	4.7	0.47	0.95	1991.7	3.9
B14-053a						
22477-01	2054.5	4.3	0.59	0.97	2030.5	8.8
22477-02	2055.0	3.2	0.72	0.95	2007	12
22477-03	2055.2	3.2	0.09	1.00	2056.1	4.3
22477-04	2056.8	8.3	0.21	1.00	1939	18
22477-05	2054.4	4.5	0.65	0.89	2000	11
B14-080						
22637-01	2052.8	6.3	0.07	1.00	2016.0	8.5
22637-08	2051.5	4.8	0.11	1.00	2015.2	6.3
B14-086						

22638-01	2052.4	3.9	0.37	0.99	2044.5	7.4
22638-05	2053.95	0.83	0.75	0.94	2052.7	2.0
22638-09	2053.3	1.0	0.33	1.00	2051.6	2.3

Chapter 3

A new method for $^{40}Ar/^{39}Ar$ thermochronology for sub-milligram and low K_2O samples

This chapter resulted in one submitted paper:

Setera, J. B., Turrin B. D., Herzog G. F., Delaney J. S., VanTongeren J. A., Lindsay F. N., Boesenberg J F., & Swisher C. C. (2019). $^{40}Ar/^{39}Ar$ thermochronology for sub-milligram samples with illustrations from the Bushveld Complex and howardite, MAC 02666. **Geochemistry, Geophysics, Geosystems**.

Abstract

We report new data on a 174 μg mafic clast from the howardite meteorite, MAC 02666. An age of 3.64 Ga and thermal modelling using measured diffusion parameters (activation energy of 138.8 kJ/mol and a diffusion coefficient at infinite temperature ($\ln[D_0/a^2]$) = 5.23) suggest that the $^{40}Ar/^{39}Ar$ age for the mafic clast is a result of an average or high velocity impact during bombardment on the HED parent body, assumed to be asteroid 4 Vesta. Thereafter, the sample remained closed to Ar loss, requiring that any subsequent impact heating of MAC 02666 was brief and/or did not raise the temperature enough to promote Ar loss. Low average impact velocities of 5 km/s and burial depths of *c*. 1 km can readily explain the retention of Ar by the mafic clast, and more generally, the scarcity of recorded ages from young impact events on Vesta, such as

the Rheasilvia basin forming event. We also present an alternative method for $^{40}Ar/^{39}Ar$ thermochronologic step-heating measurements on anhydrous K-bearing minerals. Samples placed in dimples on Ta-foil platforms are heated indirectly with a laser while temperatures are measured with a two-color pyrometer. The system provides a simple, inexpensive, and reliable means for the heating of samples as small as a few to tens of micrograms. Our method yields results for plagioclase separates from the Rustenburg Layered Suite of the *c.* 2.06 Ga Bushveld Complex that closely match previously published data.

1. Introduction

The $^{40}Ar/^{39}Ar$ method figures importantly in thermochronology (Baxter, 2010; McDougall and Harrison, 1999) due to its applicability to a wide range of K-bearing minerals. The measurements made in determining $^{40}Ar/^{39}Ar$ ages during step-heating experiments also allow for the calculation of diffusion parameters for the same sample, provided that the durations and temperatures of individual heating steps are recorded. The coupling of sample specific diffusion parameters with sample ages can be useful in understanding complicated $^{40}Ar/^{39}Ar$ ages, as the dating method is sensitive to the *cumulative* effects of heating at temperatures typical of metamorphic, hydrothermal, and impact-related processes. This sensitivity is exemplified in the variable and complex $^{40}Ar/^{39}Ar$ age record of the HED suite of meteorites. Many of the HED meteorites are breccias composed of sub-milligram clasts with distinct histories. In this work, we present $^{40}Ar/^{39}Ar$ results for one such clast and the methods developed to make the necessary measurements.

The howardite-eucrite-diogenite (HED) family of meteorites is thought to be derived from the differentiated parent body, asteroid 4 Vesta (Binzel and Xu, 1993; Consolmagno and Drake, 1977; McCord et al., 1970; McSween et al., 2011). Data from the NASA Dawn mission revealed on the southern hemisphere of Vesta two prominent, overlapping basins, Rheasilvia and Veneneia. These basins probably formed as a result of the major impact events that also produced the immediate precursors of HED meteorites, the Vestoid family of asteroids (Marchi et al., 2012). The proposed ages of these major impact events are variable. Crater counting of the surface of 4-Vesta has yielded discordant ages of the two-basin forming events: 1.0 or 3.6 Ga for Rheasilvia and 2.1 or 3.8 Ga for Veneneia (Marchi et al., 2012; Schmedemann et al., 2014). Published $^{40}Ar/^{39}Ar$ ages of HEDs are similarly variable, with the majority falling between 3.1 and 4.5 Ga, likely representing a complex metamorphic and impact history of the proposed parent body, Vesta (Bogard, 2011).

The variable $^{40}Ar/^{39}Ar$ ages of HEDs suggest a variety of thermal histories that warrant detailed study. The components of many meteorites including howardites, however, are breccias whose individual components may weigh only nanograms to a few micrograms. Analyses of such large, heterogeneous samples may not produce reliable information (Delaney et al., 2016). The enhanced sensitivity of today's noble gas mass spectrometers opens up the ability to measure the age and diffusion parameters of the smaller samples, a capability that is useful in determining the degree of homogeneity of larger ones (Delaney et al., 2016).

We present new thermochronologic results from a small, low K_2O, mafic clast of the relatively unstudied howardite MAC 02666. The results -- precise diffusion

parameters and undisturbed age spectra -- provide insights concerning temperature constraints on potential impacts and resetting events associated with the meteorite's assumed parent asteroid, Vesta. As a part of that analysis, we also present a new variation of laser step-heating methods for the precise determination of $^{40}Ar/^{39}Ar$ ages and diffusion parameters of microgram quantities of terrestrial or extraterrestrial materials. In our method, samples are placed on a shaped, open platform of pure tantalum metal while precise temperature measurements are made using a two-color optical pyrometer. To validate the method, we measured the diffusion parameters of plagioclase separates from the Bushveld Complex in South Africa. The new design is simple, reliable, easily implemented, and allows for the measurement of small sample sizes.

2. Experimental Procedures

2.1 Samples and Sample Preparation

2.1.1 Plagioclase from the Bushveld Complex

Sample B06-042 is a magnetite-bearing gabbro from the Upper Zone of the Rustenburg Layered Suite (RLS) of the Bushveld Complex in South Africa. The sample is located *c.* 3741 m above the Merensky Reef and was collected as part of a transect of the Upper Zone in the Eastern Limb of the RLS near Magnet Heights (VanTongeren et al., 2010). Sample B14-053a is a gabbronorite from the Main Zone of the RLS, *c.* 137 m above the Merensky Reef and was collected as part of a transect of the Main Zone in the Eastern Limb near Roossenekal (S 25°13.849', E 30°05.374'). Plagioclase within samples B06-042 and B14-053a are homogenous (An_{54} and An_{68}) and inclusion free with homogenous

K_2O concentrations of 0.38 ± 0.04 and 0.23 ± 0.04 wt%, respectively. (Table 1). There is no discernable zonation or enrichment toward of K_2O the margins of the grains.

During sample preparations, all weathered surfaces were removed from a small hand specimen from each sample. The cleaned material was crushed using a steel plated micro-jaw crusher. After sieving, the 1000-600 μm size fraction was washed with distilled water in an ultrasonic bath and dried in an oven at 40°C. Plagioclase mineral separates were handpicked under a binocular microscope. Each grain was visually inspected, and qualitatively analyzed using energy-dispersive spectroscopy (EDS) to ensure grains were inclusion free and compositionally representative of the overall sample. Each grain was weighed with a microbalance; the average grain mass was *c.* 375 μg for B06-042 and *c.* 550 μg for B14-053a.

2.1.2 Mafic Clast - MAC 02666

The howardite MacAlpine Hills 02666 (MAC 02666), collected by the Antarctic Search for Meteorites (ANSMET) in 2002, comprises both coarse- and fine-grained basaltic clasts (Russell et al., 2004) in a fine-grained groundmass of fragmented pyroxene (up to 1 mm) and plagioclase. Warren et al. (2009) presented major and trace element analyses for the bulk meteorite and suggested it might be a regolith howardite, but apart from these chemical data, little is known about the howardite.

A sample of, MAC 02666 (*c.* 6 x 7 x 4 mm; 432 mg; Fig. 1a) was provided by the Meteorite Working Group. A portion of a brecciated, but monomict mafic clast (MC001) with a mass of 174 μg was manually separated (Fig. 1b). A similar fragment of the same mafic clast with attached matrix, and contiguous with the dated sample in the bulk portion

of MAC 02666, was polished for textural characterization and electron microprobe major element analyses (Table 1). The clast is very friable, but is composed of *c.* 10-500 μm plagioclase grains (An_{89}), large (*c.* 200 μm) orthopyroxene grains ($En_{34}Wo_{6}$) and minor ilmenite and Ti-rich chromite. The observed ranges in the An content of the plagioclase and in the pyroxene composition are similar to those of the basaltic eucrites (Mittlefehldt, 2015). These data are provided graphically in Fig. 2.

A large-scale BSE image of the fragment separated for electron microprobe analyses reveals porphyritic to anhedral textures (Fig. 1c). Some areas display weak mosaicism in the plagioclase (Fig. 1c). A closer look at individual plagioclase grains shows irregular fractures (Fig. 1d). Pyroxenes are also fractured, but to a lesser degree than the plagioclase. The fractures and mosaicism indicate a moderate level of shock (Stöffler et al., 2018). There is no evidence for disequilibrium shock effects in the form of melt veins or glass. The dark areas within the clast in Figures 1c-d are voids where individual grains were plucked out during polishing of the sample. A full mosaic BSE image of the fragment used for microprobe analysis is provided in Fig. 3.

2.2 Electron Microprobe Analyses

The major element composition of plagioclase was determined *in situ* for a representative thin section of samples B06-042 and B14-053a using the JEOL JXA 8200 electron microprobe at Rutgers University (Table 1). An acceleration potential of 15 kV, beam current of 15 nA, count time of 30 s on peak and 15 s on background for each element, and a beam diameter of 5 μm were used. Standards of anorthite, Lake County plagioclase, and

An96 were repeatedly analyzed between measurements of unknowns and consistently yielded results within 2σ of published values.

Quantitative analysis for MAC 02666 (primarily for feldspar) was performed on the Brown University Cameca SX-100 electron microprobe (Table 1). Operating conditions of the instrument consisted of 15 kV voltage, 10 nA current and a 5 μm diameter, defocussed beam. Counting times were 30 seconds for on peak, and half that time for backgrounds, for all elements. The data were calculated using the PAP correction procedures (Pouchou and Pichoir, 1991). One-sigma standard deviations are <1% for major elements and 3–8% for minor elements. Standards used for analysis included Great Sitkin anorthite, NMNH 137041, (Al, Ca); synthetic Fo97 forsterite, University of Rhode Island (Mg); Rockport, Massachusetts fayalite, NMNH 85276 (Fe); Amelia albite, Purdue University (Na); synthetic orthoclase OR-1, AMNH (Si, K); and synthetic rutile, Brown University, (Ti). The electron microprobe is equipped with extra-large diffracting crystals (LTAP, LLIF, LPET) that generate roughly five times the count rate of standard-sized diffracting crystals. Extra-large crystals were used in the analysis of Si, Al, K, Fe and Ti. Standard-sized crystals were used for Na, Mg and Ca. Na and K were analyzed using a loss routine to account for any volatilization of the elements under the beam. Lake County plagioclase NMNH 115900 was used as reference standard.

2.3 Irradiation and Standards

Samples along with the reference standards Fish Canyon (FC) sanidine [28.201 Ma; Kuiper et al. (2008)] and Hb3Gr hornblende [1080 Ma; Jourdan and Renne (2007)] were loaded into pits drilled into a 1-cm diameter Al-disks for neutron irradiation. The pits are

arranged in a controlled geometry to facilitate the correction of any measurable gradients in the neutron-flux. Neutron irradiation was carried out at the US Geological Survey TRIGA reactor for 80 hours without Cd-shielding. After irradiation, samples were incrementally step-heated using a New Wave 40-watt CO_2 laser. The J-values for B14-053a and MAC 02666 are (1.9945 ± 0.0041 and 2.0122 ± 0.0046) × 10^{-2}, respectively.

2.4 Step-Heating

2.4.1 Platform Design

$^{40}Ar/^{39}Ar$ thermochronologic studies employing laser heating *in vacuo* are commonly accomplished by wrapping a sample in a refractory metal (e.g., platinum or tantalum) jacket and step-heating the whole packet with a CO_2 or diode laser while measuring or controlling the temperature with an infrared pyrometer. The localization of temperature-controlled laser heating to a small area solves two problems of traditional furnace heating. The low-mass, low-thermal-inertia metal packets (i.e. Pt or Ta foil) reach the required temperature rapidly (Fig. 4) and the limited extent of ancillary heating of the extraction system lowers system blanks.

Our method is a variation of current *in vacuo* laser heating approaches. We use a high purity (3N8), 0.008 mm thick Ta-foil platform rather than the packet design (Fig. 5). Tantalum couples efficiently with the CO_2 laser and can be heated rapidly, within a few seconds, to about 300 to 1350° C by setting the laser to a constant energy output (Fig. 4).

The Ta-platform is formed from by cutting a 5 x 5 mm Ta-foil square from a larger sheet of Ta-foil. After pressing a small *c*. 1 mm diameter by 200 μm deep dimple adjacent to one corner, the corners of the cut sheet are folded 90° to the foil surface, forming legs

that raise the platform *c.* 2 mm. This shape minimizes the contact, and hence the thermal conduction, between the tantalum and the stainless-steel sample chamber (Fig. 5a). For step-heating, the samples are placed in the dimpled area (Figs. 5b and 5c). With the majority of the sample surface contained within the dimple, the method provides a *c*. 240° (3π steradians) direct heating to the sample.

The temperature effects of 240° (3π steradians) direct heating, rather than 360° (4π steradians), were investigated using the heat transfer simulation software, Energy 2D (Xie, 2012). Thermal properties (Engineering Toolbox, 2019; Hemingway et al. 1981; Robie et al., 1978;) for the sample holder, Ta-platform, feldspar, and air (calculated at 1 x 10^{-10} mbar) were input into the modelling software and set to run at 3 different heating temperatures of 500°C, 800°C, and 1000°C. In all three scenarios, the feldspar grain (1mm x 0.5 mm) reaches maximum temperatures in less than 0.5 seconds (Fig. 6). The maximum temperature difference between the feldspar surface in contact with the Ta-platform and the surface in contact with air is 0.8°C, 1.2°C, and 1.5°C for heating temperatures of 500°C, 800°C, and 1000°C. The modelling confirms that the heating of the silicate sample is mainly via conduction, and any temperature gradient within the sample is negligible. Full details of modelling are available (section 2.4.2; Fig. 6).

Before loading samples, the Ta-platforms are degassed for 2-hours within a stainless-steel tube under vacuum ($<10^{-5}$ mbar) at temperatures *c*. 600°C, to reduce atmospheric Ar contamination. The laser (2 x 2 mm spot) is focused at the corner of the Ta-platform farthest from the dimple. The field of view of the pyrometer is narrowed so as to exclude the dimple and sample. With this method of heating, the sample (including

verification metals; see section 2.3.2) can be viewed at all times and in particular, at the moment of complete fusion (Fig. 5b).

2.4.2 Energy 2D Modelling

In addition to *in situ* heating experiments of known materials, the heating of silicates on Ta platforms was also modelled using the heat transfer simulation software, Energy2D (Xie, 2012). This modelling was conducted to investigate how rapidly and efficiently heat is transferred from the Ta platform to the silicate sample, as well whether there is a significant temperature gradient within the sample during heating. Model set-up (Supplementary Fig. S6a) consists of a Ta platform, measuring 5 mm wide and 0.2 mm thick. The platform rests within a stainless-steel pit (5 mm depth), with the bent corners of the platform forming legs of 2.5 mm in height. The silicate sample (feldspar), with a generic size 1 mm x 0.5 mm (aspect ratio: 2), is placed on top of the Ta platform. For this model, there is no dimple within the Ta platform, as this represents the "worst case" scenario of a sample moving out of the dimple during the transfer of samples into the mass spectrometer. Thermal properties for the stainless-steel sample holder and the Ta-platform (Engineering Toolbox, 2019) are listed below along with the thermal properties of feldspar and air. Hemingway et al. (1981) provide the thermal conductivity of potassium feldspar at various temperatures, while Robie et al. (1978) provide the specific heat of potassium felspar. The thermal properties and density of air were calculated for a pressure of 1 x 10^{-10} mbar.

<u>Thermal Conductivity [W/(m·°C)]</u>

Stainless Steel = 14.4
Tantalum = 59.4

Feldspar = 6.44 (500°C), 7.30 (800°C), 8.33 (1000°C)
Air = 7.5×10^{-9}

Specific Heat [J/(kg·°C)]
Stainless Steel = 490
Tantalum = 138
Feldspar = 866.8
Air = 1005

Density [kg/m^3]
Stainless Steel = 7850
Tantalum = 16400
Feldspar = 2560
Air = 1.15×10^{-13}

The model was run at 3 different target temperatures (500, 800, 1000°C), where only the horizontal part of the Tantalum platform is constantly heated (i.e. not the legs). Results from the model runs are presented Fig. 6c-e.

2.4.3 Temperature Measurements

Temperature measurements above 500°C were measured directly with a Mikron-M780 two-color pyrometer with a 1 μm spectral range. The field of view of the pyrometer and the area illuminated by the New Wave 45-watt CO_2 laser are aligned to the same focused spot through a multi-step approach. First, the laser target is aligned by imaging, on a target of thermal paper, the square, 2 mm x 2 mm, mark made by the beam from the CO_2 laser. The spot is then marked on the live camera feed broadcast to the laboratory computer. The optical pyrometer observes the target through an optical fiber. We illuminate the target through this optical fiber ensuring it is matched to the previously marked laser spot.

Most target materials, including tantalum, have a ratio of spectral emissivities that deviate from $\varepsilon(\lambda_2)/\varepsilon(\lambda_1) = 1$ within the temperature range of interest. The M780 pyrometer accounts for this deviation with a fixed slope or "relative emissivity" adjustment. For

tantalum, the recommended slope adjustment is 1.060 (Gruner, 2003). We confirmed the calibration of the pyrometer and the appropriate slope adjustment experimentally by observing the melting of three metals: Al (660°C), Cu (1084°C), and Au (1063°C). The temperatures indicated for all three melting points were accurate to within 0.3%, agreeing well with the 0.5% factory reported accuracy of the Mikron-M870 two-color pyrometer. Moreover, the temperature measurements for Cu and Au (Fig. 7a), which have true melting points differing by only *c*. 19°C, further demonstrate the ability of the two-color pyrometer to make accurate and precise temperature measurements. The errors observed without a slope adjustment and an adjustment of 1.030 ranged from ΔT *c*. +50°C to ΔT *c*. +25°C, respectively.

To account for potential differences in the conductive properties between the various tested metals and actual samples (i.e. silicates), we also observed the melting of Pyrex glass. Initially, small pieces of Pyrex glass (~ 1mm in diameter) were placed in a muffle furnace. The Pyrex pieces were heated gradually until all pieces were melted ~1080°C. Subsequently, two pieces of the same Pyrex glass were placed on Ta-platforms and heated as described above for the observed melting of various metals. Like the metals, the melting temperatures observed for the Pyrex glass was within 0.3% of the melting temperature observed in the muffle furnace (Fig. 7a). The experiment confirms that heat is transferred indistinguishably from the Ta-platforms to both metals and silicates alike and both materials are appropriate for checking the accuracy of the pyrometer.

The two-color pyrometer directly measures temperatures during step-heating experiments between 500 – 1400°C. At temperatures below 500°C we relied on an approximate empirical relationship between temperature and laser power. Specifically,

with the adjustment factor listed above, we fit a four-point plot of melting point against laser power (W) for Sn (232°C), Al (660 °C), Cu (1084 °C), and Au (1063°C) (Fig. 7b, equation 1):

$$\mathrm{T}[°\mathrm{C}] = (396.38 * W^{0.5}) - \left(49.30 * W^{0.5} * \ln(W)\right) - 67.13 \qquad (1)$$

For most applications, the loss of accuracy stemming from the use of this equation for temperatures below 500°C is not critical as these heating steps typically yield uncertain data that are excluded from Arrhenius regressions. Re-checks of Eqn. 1 have continued to show good stability over a period of 18 months. Estimated temperatures (<500°C) for a given wattage and their associated uncertainties are given in table 2. We demonstrated the absence of significant temperature gradients by holding the laser position constant and sweeping the field of view of the pyrometer across the surface of the Ta-platform. The temperatures observed matched those within 2°C those predicted by the off-target calibration (Fig. 5b).

Ta-platforms are cleaned by manually clearing the platform of the previously fused sample and/or any debris, followed by a thorough rinsing (first in DI water, followed by ethanol) in an ultrasonic bath. The cost-effective Ta-platforms prove reliable after repeated use, with the continued step-heating of Ta foil platforms up to *c*. 1300 °C yielding Ar isotopic values that are indistinguishable from normal background values during both the first and subsequent use (Table 3).

2.5 Argon Measurements and Ages

Argon isotopes were measured at Rutgers University on a noble gas mass spectrometer made by Mass Analyzer Products (MAP 215–50) and upgraded by Turrin et al. (2010). A

typical ten-minute static system 'cold' blank, (10^{-18} mol) is: $^{40}Ar = 420 \pm 13$; $^{39}Ar = 12.0 \pm 3.6$; $^{38}Ar=1.0\pm0.4$; $^{37}Ar=22.4\pm1.4$; $^{36}Ar=3.3\pm0.3$. Spectrometer sensitivity is ~7.60 x 10^{-12} nA/mol and is calculated by analyzing atmospheric Ar from a pipet system that delivers a known amount of ^{40}Ar.

Instrumental mass fractionation was monitored by analyzing a known volume of atmospheric Ar after every eighth sample and blank measurement. For the data reduction we assumed initial values of $^{40}Ar/^{36}Ar = 298.56 \pm 0.31$ and $^{38}Ar/^{36}Ar = 0.1885 \pm 0.0003$ (Lee et al., 2006). Signals for reactor produced ^{37}Ar and ^{39}Ar were corrected using the decay constants of 0.0198 day^{-1} and 7.07 x 10^{-6} day^{-1}, respectively. Automated laser heating, gas extraction, mass spectroscopy measurements, and data reduction were implemented using automated software written by A. Deino of the Berkeley Geochronology Center. The age calculations incorporate the decay constants of Steiger and Jäger, (1977) and the following ratios ($/10^{-4}$), which are necessary for making reactor corrections: [$(^{36}Ar/^{37}Ar)_{Ca} = 2.75 \pm 0.003$); $(^{39}Ar/^{37}Ar)_{Ca} = 6.62 \pm 0.01$; $(^{38}Ar/^{37}Ar)_{Ca} = 0.210 \pm 0.1$; $(^{40}Ar_K/^{39}Ar)_K = 98.1 \pm 0.18$; $(^{38}Ar_K/^{39}Ar)_K = 13200 \pm 10$; $(^{37}Ar_K/^{39}Ar)_K = 2.20 \pm 0.007$; $(^{36}Ar_{Cl}/^{38}Ar)_{Cl} = 65000 \pm 3000$].

We define an age plateau as a sequence of three or more consecutive steps with apparent ages that agree within the 95% confidence interval and for which the sum of $^{39}Ar_K$ released is 50% or more of the total $^{39}Ar_K$ released on completion of the heating experiment (Dalrymple and Lanphere, 1969, 1974; Fleck et al., 1977). The plateau ages and their errors are calculated using the variance-weighted mean of the plateau steps (Taylor, 1997).

We discuss the methods used to make cosmogenic corrections (see, e.g., Cassata and Borg, 2016; Garrison et al., 2000) for the mafic clast from the howardite, MAC 02666 below (section 2.7). For all of the ages reported here, uncertainties are expressed as 1σ unless otherwise specified.

2.6 Arrhenius Regression and Closure Temperature Calculation

Diffusion parameters are calculated using a weighted linear regression, as implemented by Thirumalai et al. (2011), of Arrhenius plots obtained from the step-heating data (e.g., Cassata and Renne, 2013; Cassata et al., 2009; Lovera et al., 1997; Parsons et al., 1999) and using the equations of Fechtig and Kalbitzer (1966). In carrying out regression analyses of Arrhenius plots, we include data for the maximum number of consecutive low-temperature steps before clear departures from linearity. Closure temperatures are determined from these parameters by assuming a Fickian volume diffusion model and using the equation of Dodson (1973).

2.6.1 Detailed Calculation Diffusion Parameter, Closure Temperature and Calculation of Diffusive Losses

The quantity Dt/a^2 (D=diffusion coefficient; a =characteristic length scale for diffusion; t = heating duration) for the first step in the step-heating experiment can be calculated from the approximate equation quoted by Fechtig and Kalbitzer (1966) for a spherical geometry:

$$\frac{Dt}{a^2} = \frac{1}{3}\left[\left(\frac{6}{\pi} - f\right) - \frac{6}{\pi}\sqrt{1 - \frac{\pi}{3}f}\right]; \text{ f} \leq 0.9 \qquad (2)$$

where f is the first fractional release $f = {}^{39}Ar \; / {}^{39}Ar_{Total}$ (3)

and ${}^{39}Ar_{Total}$ is the initial ^{39}Ar concentration of the sample (total ^{39}Ar released).

Equation (2) assumes an initially uniform distribution of ^{39}Ar in the sample analyzed and a ^{39}Ar concentration of zero in the (exterior) boundary layer of the grain.

For each heating step after the first, theory predicts a non-uniform gas distribution in the interior of the particle, requiring the use of Equation 4 (Fechtig and Kalbitzer, 1966) for the calculation Dt/a^2.

$$\frac{Dt}{a^2} = \frac{1}{3}\left[-(F_{\mathrm{i+1}} - \mathrm{F}) - \frac{6}{\pi}\left(\sqrt{1 - \frac{\pi}{3}F_{\mathrm{i+1}}} - \sqrt{1 - \frac{\pi}{3}F_{\mathrm{i}}}\right)\right] \quad (4)$$

where t is again the is the heating duration for the step, F_{i+1} is the cumulative fractional release at a given heating step, and F_i is the cumulative fractional release as calculated at the previous step. Uncertainties in diffusion coefficients are directly calculated from the analytical precision of gas concentrations measured for each step. As in previous studies, the uncertainty of the cumulative release fraction (F) is ignored, as the uncertainty for each step depends on all previous steps (Cassata et al., 2009; Lovera et al., 1991).

The quantity, D/a^2 calculated from equation (2) or (4) is assumed to obey an Arrhenius relationship:

$$D/a^2 = (D_o/a^2)e^{-E/RT} \quad (5)$$

where D_o is the diffusion coefficient at an infinite temperature, E is the activation energy, R is the gas constant, 8.314 kJ/mol-K, and T is the absolute temperature. If diffusion within the sample proceeds via volume diffusion from a single domain, then a plot of Ln(D/a^2) *vs.* 1/T should be linear with a slope of $-E/R$ and an intercept of $\ln(D_0/a^2)$.

We obtained the slopes and intercepts of Arrhenius plots using York-type fitting (York et al., 2004) as implemented by Thirumalai et al. (2011). The best-fit diffusion

parameters were used to calculated a "closure temperature", T_c, of the sample using the equation of Dodson (1973):

$$\frac{E}{RT_c} = ln\left[\frac{ART_c^2(D_0/a^2)}{EdT/dt}\right] \tag{6}$$

Equation (6) can be solved iteratively for the closure temperature given an assumed cooling rate, (d*T*/d*t*), at the given closure temperature. The uncertainty on calculated closure temperature is derived below (section 2.6.2).

In constructing Figure 8 and Figure 15 of the text, we used equation 4. Specifically, by setting the fractional release (*f*) equal to a fixed amount and substituting the diffusion coefficient at a temperature of interest (eq. 5) into (eq. 2), the duration of a single heating event required to produce that release can be calculated. Fig. 15 shows the time needed at a given temperature to degas the mafic clast of either 90% or 10% of its initial ^{40}Ar*. We chose reactor-produced ^{39}Ar for this exercise as it is not subject to uncertainties arising from the deconvolution of a trapped Ar component. The use of data for the other Ar isotopes gives similar results which are shown in Figure 8 and Table 13.

2.6.2 Derivation of Closure Temperature Uncertainty

<u>Formula for Closure Temperature</u>

Written as a modification to equation (6):

$$T_C = \frac{E_a}{R}/\ln\left(A\frac{-RT_C^2}{E_a(dT/dt)|_{T_C}}{D_0}/_{a^2}\right) \tag{7}$$

$$T_C = \frac{E_a}{R}/\ln\left(\frac{-RA}{(dT/dt)|_{T_C}}\frac{1}{E_a}\frac{D_0}{a^2}T_C^2\right) \tag{7a}$$

$$T_C = \frac{E_a}{R}/\left(c_1 + \ln\left(\frac{1}{E_a}\frac{D_0}{a^2}T_C^2\right)\right) \tag{7b}$$

Where $c_1 = \ln\left(\frac{-RA}{(dT/dt)|_{T_C}}\right)$

General Error Formula

Equation (8a) gives the general error formula for a function, $f(x,y)$, of two correlated, experimental variables, $x \pm \sigma_x$ and $y \pm \sigma_y$; ρ_{xy} is the correlation coefficient of x and y.

$$\sigma_f = \sqrt{\left(\frac{\partial f}{\partial x}\sigma_x\right)^2 + \left(\frac{\partial f}{\partial y}\sigma_y\right)^2 + \frac{\partial f}{\partial x}\frac{\partial f}{\partial y}\rho_{xy}\sigma_x\sigma_y} \tag{8a}$$

Equation (8a) can also be written in the form:

$$\sigma_f = \sqrt{\left(\frac{\partial f}{\partial x}\sigma_x\right)^2 + \left(\frac{\partial x}{\partial y}\sigma_y\right)^2 + 2\frac{\partial f}{\partial x}\frac{\partial f}{\partial y}\sigma_{xy}} \tag{8b}$$

where σ_{xy} is the covariance of x and y.

Calculation of Partial Derivatives

We identify x as E_a, y as D_0/a^2, and T_C as $f(x,y)$ and re-write equation (7b).

$$f(x,y) = \frac{x}{R}\Big/\left(c_1 + \ln\left(\frac{y}{x}f^2(x,y)\right)\right) \tag{7c}$$

The partial derivatives of $\frac{\partial f}{\partial x}$ and $\frac{\partial f}{\partial y}$ are calculated by using implicit differentiation.

Expression for $\frac{\partial f}{\partial x}$

$$\left(\frac{\partial f(x,y)}{\partial x}\right)_y = \frac{1}{R}\Big/\left(c_1 + \ln\left(\frac{y}{x}f^2(x,y)\right)\right) + \frac{x}{R}\left[\frac{\partial}{\partial x}\left(c_1 + \ln\frac{y}{x}f^2(x,y)\right)^{-1}\right]_y \tag{9}$$

Evaluate the derivative in the second term on the right, namely the term, $\frac{x}{R}\left[\frac{\partial}{\partial x}\left(c_1 + \ln\frac{y}{x}f^2(x,y)\right)^{-1}\right]_y$

$$\left[\frac{\partial}{\partial x}\left(c_1 + \ln\left(\frac{y}{x}f^2(x,y)\right)\right)^{-1}\right]_y = -1 \times \left(c_1 + \ln\left(\frac{y}{x}f^2(x,y)\right)\right)^{-2}\frac{\partial}{\partial x}\left(c_1 + \ln\left(\frac{y}{x}f^2(x,y)\right)\right)_y \tag{10}$$

$$\frac{\partial}{\partial y}\left(c_1 \ln\left(\frac{y}{x}f^2(x,y)\right)\right)_y = \frac{1}{\frac{x}{y}f^2(x,y)}\frac{\partial}{\partial x}\left(\frac{y}{x}f^2(x,y)\right)_y \tag{11}$$

$$\frac{\partial}{\partial x}\left(\frac{y}{x}f^2(x,y)\right)_y = -\frac{y}{x^2}f^2(x,y) + 2\frac{y}{x}f(x,y)\left(\frac{\partial f(x,y)}{\partial x}\right)_y \tag{12}$$

Substitute equation (12) into equation (11):

$$\frac{\partial}{\partial x}\left(c_1 + \ln\left(\frac{y}{x}f^2(x,y)\right)\right)_y = \frac{1}{\frac{y}{x}f^2(x,y)}\left[-\frac{y}{x^2}f^2(x,y) + 2\frac{y}{x}f(x,y)\left(\frac{\partial f(x,y)}{\partial x}\right)_y\right] \tag{11a}$$

Substitute equation (11a) into (10):

$$\left[\frac{\partial}{\partial x}\left(c_1+\ln\left(\frac{y}{x}f^2(x,y)\right)\right)^{-1}\right]_y = -1\times\left(c_1+\ln\left(\frac{y}{x}f^2(x,y)\right)\right)^2\times\frac{1}{\frac{y}{x}f^2(x,y)}\left[-\frac{y}{x^2}f^2(x,y)+2\frac{y}{x}f(x,y)\left(\frac{\partial f(x,y)}{\partial x}\right)_y\right] \quad (10a)$$

Multiply equation (10a) by $\frac{x}{R}$ and substitute into equation (9):

$$\left(\frac{\partial f(x,y)}{\partial x}\right)_y = \frac{1}{R}\Big/\left(c_1+\ln\frac{y}{x}f^2(x,y)\right)+ \frac{x}{R}\left[-1\times\left(c_1+\ln\left(\frac{y}{x}f^2(x,y)\right)\right)^{-2}\times\frac{1}{\frac{y}{x}f^2(x,y)}\left[-\frac{y}{x^2}f^2(x,y)\left(\frac{\partial f(x,y)}{\partial x}\right)_y\right]\right]_y \quad (9a)$$

Bring x inside and simplify second term:

$$\left(\frac{\partial f(x,y)}{\partial x}\right)_y = \frac{1}{R}\Big/\left(c_1+\ln\left(\frac{y}{x}f^2(x,y)\right)\right)+ \frac{1}{R}\left[-1\times\left(c_1+\ln\left(\frac{y}{x}f^2(x,y)\right)\right)^{-2}\times\left(-1+\frac{2x}{f(x,y)}\left(\frac{\partial f(x,y)}{\partial x}\right)_y\right)\right] \quad (9b)$$

Solve for $\left(\frac{\partial f(x,y)}{\partial x}\right)_y$ in two steps. Transpose the second term on right-hand side, then factor out $f(x,y)$.

$$\left(\frac{\partial f(x,y)}{\partial x}\right)_y - \frac{1}{R}\left[-1\times\left(c_1+\ln\left(\frac{y}{x}f^2(x,y)\right)\right)^{-2}\times\left(-1+\frac{2x}{f(x,y)}\left(\frac{\partial f(x,y)}{\partial x}\right)_y\right)\right] = \frac{1}{R}\Big/\left(c_1+\ln\left(\frac{y}{x}f^2(x,y)\right)\right) \quad (5c)$$

$$\left(\frac{\partial f(x,y)}{\partial x}\right)_y\left\{1-\frac{1}{R}\left[-1\times\left(c_1+\ln\left(\frac{y}{x}f^2(x,y)\right)\right)^{-2}\times\left(-1+\frac{2x}{f(x,y)}\right)\right]\right\} = \frac{1}{R}\Big/\left(c_1+\ln\left(\frac{y}{x}f^2(x,y)\right)\right) \quad (5d)$$

$$\left(\frac{\partial f(x,y)}{\partial x}\right)_y = \left\{R\left(c_1+\ln\left(\frac{y}{x}f^2(x,y)\right)\right)\right\}^{-1}\left\{1-\frac{1}{R}\left[-1\times\left(c_1+\ln\left(\frac{y}{x}f^2(x,y)\right)\right)^{-2}\times\left(-1+\frac{2x}{f(x,y)}\right)\right]\right\}^{-1} \quad (5e)$$

Expression for $\frac{\partial f}{\partial y}$

Starting from equation (7c):

$$f(x,y) = \frac{x}{R} / \left(c_1 + \ln\left(\frac{y}{x} f^2(x,y)\right)\right) \tag{7c}$$

Differentiate with respect to *y*:

$$\left(\frac{\partial f(x,y)}{\partial y}\right) = \frac{x}{R} \times (-1)\left(c_1 + \ln\left(\frac{y}{x} f^2(x,y)\right)\right)^{-2} \frac{\partial}{\partial y}\left(c_1 + \ln\left(\frac{y}{x} f^2(x,y)\right)\right)_x \tag{13}$$

Evaluate partial derivative on the left-hand side:

$$\frac{x}{R}\left(c_1 + \ln\left(\frac{y}{x} f^2(x,y)\right)\right)_x = \frac{1}{\frac{y}{x} f^2(x,y)}\left(\frac{1}{x} f^2(x,y) + \frac{y}{x} 2f(x,y)\left(\frac{\partial f(x,y)}{\partial y}\right)_x\right) \tag{14}$$

Substitute equation (14) into equation (13):

$$\left(\frac{\partial f(x,y)}{\partial y}\right)_x = \frac{x}{R} x(-1)\left(c_1 + \ln\left(\frac{y}{x} f^2(x,y)\right)\right)^{-2} \frac{1}{\frac{y}{x} f^2(x,y)}\left(\frac{1}{x} f^2(x,y) + \frac{y}{x} 2f(x,y)\left(\frac{\partial f(x,y)}{\partial y}\right)_x\right) \tag{15}$$

Simplify equation (15):

$$\left(\frac{\partial f(x,y)}{\partial y}\right)_x = -\frac{x}{R}\left(c_1 + \ln\left(\frac{y}{x} f^2(x,y)\right)\right)^{-2}\left(\frac{1}{y} + \frac{2}{f(x,y)}\left(\frac{\partial f(x,y)}{\partial y}\right)_x\right) \tag{16}$$

Solve equation (16) for $\left(\frac{\partial f(x,y)}{\partial y}\right)_x$:

$$\left(\frac{\partial f(x,y)}{\partial y}\right)_x \left(1 + \frac{x}{R}\left(c_1 + \ln\left(\frac{y}{x} f^2(x,y)\right)\right)^{-2}\right)\left(\frac{2}{f(x,y)}\right) = -\frac{x}{R}\left(c_1 + \ln\left(\frac{x}{y} f^2(x,y)\right)\right)^{-2}\left(\frac{1}{y}\right) \tag{17}$$

Rearrange for the final expression:

$$\left(\frac{\partial f(x,y)}{\partial y}\right)_x = \left\{\left(1 + \frac{x}{R}\left(c_1 + \ln\left(\frac{y}{x} f^2(x,y)\right)\right)^{-2}\left(\frac{2}{f(x,y)}\right)\right)\right\}^{-1}\left\{-\frac{x}{R}\left(c_1 + \ln\left(\frac{y}{x} f^2(x,y)\right)\right)^{-2}\left(\frac{1}{y}\right)\right\} \tag{17a}$$

2.7 Accounting for cosmogenic Ar in isochron calculations.

The construction of an isochron requires knowledge for each temperature step of how much of the ^{36}Ar released is 'trapped' (Tr), i.e., neither cosmogenic (*cos*) nor chlorine-

derived. We will argue (S5.2) that the amount of chlorine-derived ^{36}Ar in our samples is small so that we have

$$^{36}\boldsymbol{Ar_{Tr}} \approx {}^{36}Ar - {}^{36}Ar_{cos} \tag{18}$$

We show below (section 2.7.1) that >90% of the measured ^{36}Ar in MAC 02666 is cosmogenic and that the small calculated amounts of $^{36}Ar_{Tr}$ exert little influence on the ages or intercepts found in fits to the isochron.

2.7.1 Lever rule calculations

The amounts (moles) of $^{36}Ar_{Tr}$ in MAC 02666 were calculated from equation (18) with the aid of the standard subsidiary relation (19).

$$^{38}Ar_{cos} = \left(5.35 \times {}^{38}Ar - {}^{36}Ar\right)/(5.35 - 0.65) \tag{19}$$

which is derived by assuming that the argon consists only of trapped and cosmogenic argon with $^{36}Ar/^{38}Ar$ ratios, 5.35 and 0.65, respectively. The amounts of trapped $^{36}Ar_{Tr}$ calculated in this way range from -0.6 ±1.0 × 10^{-18} mol (Step A) to 1.7 × 10^{-18} mol. Five of the eighteen values are negative, a consequence of having measured $^{36}Ar/^{38}Ar$ ratios less than the presumed cosmogenic lower limit of 0.65. In none of these cases, however, does that low ratio differ from 0.65 by more than one standard deviation. We infer temporarily (see 2.7.2) that these negative results reflect experimental error and are consistent with the absence of trapped ^{36}Ar. All positive values of $^{36}Ar_{Tr}$ sum to (11.7 ± 3.7) × 10^{-18} mol, or about 8% of the total ^{36}Ar measured for all steps. The corresponding and less biased percentage that includes the negative values sums to (8.9 ± 4.0) × 10^{-18} mol, or about 6% of the total. Further, the amount of $^{36}Ar_{Tr}$ is not correlated with

$^{40}Ar/^{39}Ar_K$ suggesting that the trapped component has no large systematic influence on the age.

To ensure that the trapped component and isochron have appropriate uncertainties, correlations between the various errors must be accounted for. In our calculations of the uncertainty of $^{36}Ar_{Tr}$, we adopt the approximate value $\rho = 0.90$ for the correlation of the uncertainties ^{36}Ar and ^{38}Ar. This approximate value is obtained from the covariance of the uncertainties of ^{36}Ar and ^{38}Ar over all temperature release steps. The use of a lower value, $\rho = 0.50$, lowers the uncertainties $\Delta^{36}Ar_{Tr}$ slightly, but yields an isochron age, 3578 ± 66 Ma, that is indistinguishable from the isochron and plateau ages reported in the main text, namely 3603 ± 60 Ma and 3643 ± 28 Ma (Table 11).

The IsoplotR software of Vermeesch (2018) accounts for the correlation between the errors of $^{40}Ar/^{36}Ar_{Tr}$ and $^{39}Ar/^{36}Ar_{Tr}$. IsoplotR allows for the input of three ratios ($^{39}Ar/^{40}Ar$, $^{36}Ar_{Tr}/^{40}Ar$, and $^{39}Ar/^{36}Ar_{Tr}$) and their respective standard errors from which the covariance between the ratios is calculated and used during error propagation. (Fig. 11 and 12).

2.7.2 The role of chlorine

Garrison et al. (2000) introduced the 'minimum $^{36}Ar/^{37}Ar$ method' to make cosmogenic corrections to ^{36}Ar in samples containing appreciable concentrations of chlorine. The activation of chlorine in the nuclear reactor can lead to the production of ^{38}Ar, which complicates the identification of cosmogenic ^{38}Ar, and may lead to underestimates of the amounts of $^{36}Ar_{Tr}$ present. Measured $^{36}Ar/^{38}Ar$ ratios less than the cosmogenic ratio of 0.65 may signal interference from chlorine, rather than experimental

uncertainties alone, as assumed in 2.7.1. For the MAC 02666 clast, all eighteen of the measured $^{36}Ar/^{38}Ar$ ratios lie within one standard deviation of 0.65. This observation suggests, but does not prove that the effects of chlorine are small, as $^{36}Ar/^{38}Ar$ ratios greater than 0.65 do not guarantee the absence of interference from Cl. However, semi-quantitative EDS analyses of the mafic clast of MAC 02666 did not yield any measureable Cl or P, an element expected to accompany Cl in its most abundant host mineral, chlorapatite. We conclude that corrections for Cl are likely negligible, but are aware that a direct analysis of Cl would be desirable.

2.7.3 Calculation of $^{38}Ar_{Tr}$ from the cosmic ray exposure age

Cassata & Borg (2017) discuss two approaches to cosmogenic corrections that incorporate as an independent parameter the cosmic ray exposure (CRE) age of the sample. Cosmogenic argon production in silicaceous phases is dominated by nuclear reactions on the target element Ca, with smaller contributions from K and Fe and other transition metal elements from Sc to Ni. With all target elements but Ca and K neglected, the amount (moles) of cosmogenic ^{36}Ar released in any temperature step can be written in a form that is proportional to the amount of ^{37}Ar measured (section 2.7, Equation (21); or see Cassata and Borg (2016), equations 5 and 6) and to the cosmic-ray exposure age. Cassata and Borg (2016) obtained the CRE age in either of two ways. In following their general line of calculation, we ignore the uncertainties on measured ^{37}Ar. As described in the main text, the uncertainties on ^{37}Ar are large because most of it had decayed by the time of measurement.

1) Cassata and Borg (2016) calculated a cosmic-ray exposure age from independent analyses of the noble gases in unirradiated samples and the composition-dependent production rate equations of Eugster and Michel (1995). We did not analyze an unirradiated sample of MAC 02666 and therefore relied instead on the CRE age obtained from i) lever-rule calculations of the *total* $^{38}Ar_c$ in MAC 02666; and ii) the published $^{38}Ar_c$ production rate of Eugster and Michel (1995) (section 2.7). If applied to the bulk sample, this method of calculating $^{36}Ar_{Tr}$ must give results identical to those obtained with the lever rule; it may, however, yield some independent information when applied singly to each temperature step.

   With a CRE age of 6.5 Ma and utilizing the IsoplotR software of Vermeesch (2018), we obtain an isochron age of 3679 ± 47 Ma and a $^{40}Ar/^{36}Ar$ intercept value of -46 ± 33. The age and intercept value are indistinguishable from those calculated using the cosmogenic correction described above.

2) Cassata and Borg (2016) treated the CRE age as a variable parameter and, using the calculational framework outlined above, searched for a value that minimizes a statistical measure of the isochron's goodness of fit. Full isochron calculations for a sampling of CRE ages produced no significant variations in the fitting parameters. For example, a CRE age of 4.5 Ma yields an isochron age of 3678 ± 47 Ma and a $^{40}Ar/^{36}Ar$ intercept value of -33 ± 33, while a CRE age of 7.5 Ma yields an isochron age of 3666 ± 44 Ma and a $^{40}Ar/^{36}Ar$ intercept value of -64 ± 31.

In summary, the cosmogenic correction is not critical for the determination of the $^{40}Ar/^{39}Ar$ ages of mafic clast of MAC 02666.

2.8 Calculation of cosmic-ray exposure age.

A cosmic-ray exposure age, T_{38} is calculated for the mafic clast from howardite MAC 02666 using the isotopic composition of the total amount of Ar released during step-heating and assuming the relationship:

$$t_{38} = \frac{^{38}Ar_c}{P_{38}} \tag{20}$$

where P_{38} is the production rate of cosmogenic ^{38}Ar, $^{38}Ar_c$. The above relationship can be written in terms of the measured quantities:

$$\boldsymbol{t_{38} = \left\{\frac{^{38}Ar_c(\text{mol } ^{38}\text{Ar})}{^{37}Ar(\text{mol } ^{37}\text{Ar})}\right\}\left[k_1c_1 + k_2c_2\left\{\frac{^{39}Ar(\text{mol } ^{39}\text{Ar})}{^{37}Ar(\text{mol } ^{37}\text{Ar})}\right\}\right]^{-1} \times 2.24 \times 10^{12}} \tag{21}$$

where k_1 and k_2 respectively are the Ca and K elemental production coefficients of Eugster and Michel (1995), and c_1 and c_2 are constants relating the irradiated masses of Ca and K to the amount of ^{37}Ar and ^{39}Ar produced during irradiation. $^{38}Ar_c$ is the amount of cosmogenic ^{38}Ar. $^{38}Ar_c$ is calculated using the lever rule and assuming $^{36}Ar/^{38}Ar$ trapped and cosmogenic ratios of 5.35 and 0.65, respectively. The average measured ratio of $^{36}Ar/^{38}Ar$ for MAC 02666, 0.76 ± 0.26 is nearly indistinguishable from the cosmogenic ratio, indicating minimal trapped argon and interferences from reactor-produced Cl. Constants used in calculations are found in table 9. This method of calculating the production rate of cosmogenic ^{38}Ar effectively assumes 'average' shielding conditions

for the sample studied, i.e., that the parent meteoroid of MA 02666 was neither very large nor very small; for details see Eugster and Michel (1995).

3. Results

3.1 Plagioclase from the Bushveld Complex

Two plagioclase grains from a sample from the Upper Zone of the RLS (B06-042) yield plateau ages of 2037.8 ± 3.9 Ma (*c*. 78% of the total ^{39}Ar) and 2037.7 ± 5.8 Ma (*c*. 85% of the total ^{39}Ar), and total fusion ages of 2019.7 ± 4.5 Ma and 2086.8 ± 8.1 Ma (Fig. 9a-b, Table 10). A single plagioclase grain, from the Main Zone of the RLS (B14-053a), yields a plateau age of 2025.6 ± 3.9 Ma (*c*. 60% of the ^{39}Ar) and a total fusion age of 1989.4 ± 4.5 Ma (Fig. 9c, Table 10). The young apparent ages observed for each sample during early, low temperature, steps are similar to those reported from the analyses of Cassata et al. (2009) and indicate Ar loss potentially from re-heating or slow cooling.

Figure 10 shows Arrhenius plots for each sample using the release of ^{39}Ar from the monotonically increasing heating schedule used to create the age spectra shown in Figure 9. ^{37}Ar was not used because most of it had decayed by the time of measurement. To construct Figure 10, we assumed a spherical geometry. A plane slab geometry has often been assumed when modeling Ar diffusion in feldspars (Cassata et al., 2009; Lovera et al., 1997; Lovera et al., 1989, 1991), but spherical geometries have proven to be more appropriate for feldspars with aspect ratios *c*. 0.5-1.0 (Cassata and Renne, 2013; Huber et al., 2011). We prefer a spherical geometry for both B06-042 and B14-053a because most of the grains separated from the samples have aspect ratios *c*. 0.6 – 0.9.

Weighted linear regressions of the data for both aliquots of B06-042 (Fig. 10a-b) yield indistinguishable diffusion parameters, with activation energies of 167.1 ± 7.9 kJ/mol and 165.4 ± 4.7 kJ/mol, and $ln(D_0/a^2)$ values of 3.80 ± 0.98 and 2.45 ± 0.50 (Table 10). The similarity in diffusion parameters indicates an internal homogeneity within plagioclase from a single sample, as would be expected given the almost identical age spectra of the two plagioclase separates from B06-042. B14-053a (Fig. 10c) yields a similar activation energy of 165.3 ± 3.7 kJ/mol and a $\ln(D_0/a^2)$ value of 3.25 ± 0.41 (Table 10). The samples from this study are from stratigraphic horizons different from those reported in Cassata et al. (2009) and Cassata and Renne (2013) and therefore are may not be the same. The measured diffusion parameters, however, are well within the range of those calculated by Cassata and Renne (2013) and Cassata et al. (2009) for interstitial plagioclase separates from the Critical Zone of the RLS which are similar in composition; namely, values in the ranges, $155.3 \leq E_a$ (kJ/mol) ≤ 188 and $0.6 \leq \ln(D_0/a^2) \leq 6.29$, respectively (Table 10). The diffusion parameters are also similar to numerous values reported and compiled by Cassata and Renne (2013) for feldspars modelled with a spherical geometry and with similar anorthite compositions to those in this study. The sample B06-042_01 is the only with enough measurable ^{37}Ar to form an Arrhenius plot; it yielded diffusion parameters indistinguishable from those calculated using ^{39}Ar from the same sample ($E_a = 156 \pm 13$ and $\ln(D_0/a^2) = 3.9 \pm 1.7$; Table 8).

3.2 Mafic Clast (MC 001) - MAC 02666

The mafic clast from howardite MAC 02666, yields a plateau age of 3643 ± 28 Ma (100% of the ^{39}Ar) and a total fusion age of 3708 ± 36 Ma (Table 11). The plateau and total fusion

ages are not corrected for any trapped component as there is little indication that such a component is present (see discussion below). The step-heating age spectrum appears mostly to be undisturbed, indicating no detectable argon loss since closure (Fig. 11). After correcting ^{36}Ar for the presence of ^{36}Ar produced by cosmic rays, a $^{39}Ar/^{36}Ar$ vs. $^{40}Ar/^{36}Ar$ isotope correlation diagram was constructed using the IsoplotR software package (Vermeesch, 2018) and defines an isochron age for MC 001 of 3603 ± 60 Ma and an intercept corresponding to an initial $^{40}Ar/^{36}Ar$ value of 85 ± 282 (Fig. 12). The initial $^{40}Ar/^{36}Ar$ value of 85 ± 282 indicates no detectable addition of primordial, solar, or terrestrial atmospheric ^{40}Ar. We discuss the methods used to make cosmogenic corrections for the construction of the isotope correlation diagram of Figure 12 (see, e.g., Cassata and Borg, 2016; Garrison et al., 2000) above (section 2.7). All three ages, plateau, total fusion, and isochron are analytically indistinguishable - the statistical probability that the values differ is less than 5% - indicating that the ratio of $^{40}Ar^*/K$ (as indicated by the K proxy $^{39}Ar_K$) is homogeneously distributed throughout the sample.

Figures 13a-d show Arrhenius diagrams for the mafic clast from MAC 02666. In constructing an Arrhenius plot for the plagioclase separates from the Bushveld Complex, we considered only ^{39}Ar because $^{40}Ar^*$, and by implication ^{36}Ar, underwent some loss and/or redistribution as evidenced by the low apparent ages at low temperatures (Fig. 9). In contrast, the clast from MAC 02666 shows no signs of Ar loss and so we modeled the behavior of ^{36}Ar, ^{38}Ar, ^{39}Ar and ^{40}Ar (Fig. 13). In calculating closure temperatures, and as with plagioclase samples from the Bushveld Complex, ^{37}Ar was not used in Arrhenius regressions because of large measurement errors due to the long delay between the times of sample irradiation and isotopic analysis.

Studies of the behavior of argon in ordinary chondrites suggest that the diffusion parameters for all argon isotopes should be similar (see, e.g., Table 2 of Fechtig et al., 1963). Indeed, the Arrhenius plots for the MC 001 sample yield similar activation energies and diffusion coefficients for all four isotopes, $^{36, 38, 39, 40}$Ar (Table 11). Taken together, the ages and thermal parameters indicate a system that closed at *c*. 3.64 Ga. The calculated activation energies, *c*. 130-145 kJ/mol, are similar to the published values of the Millbillillie and EET90020 eucrites (Yamaguchi et al., 1993; Bogard, 2009) as well as whole rock and gabbroic samples of mesosiderites which bear textural similarities to cumulate eucrites (Bogard et al., 1990). The closure temperatures calculated assuming spherical geometry range from 127.7 ± 4.7 °C to 163.7 ± 8.6 °C for a cooling rate of 10 °C Ma^{-1}. For simplicity, we will use the diffusion parameters calculated solely from ^{39}Ar for further discussion of the mafic clast from MAC 02666.

The diffusion parameters discussed above should be regarded as "bulk" values for the sample. As described in section 2.1.2, the mafic clast is not a single phase, but rather composed of plagioclase, pyroxene and minor ilmenite and Ti-rich chromite. The calculated diffusion parameters are necessarily from a mixture of phases, each with its own individual activation energy and frequency factor. We have confidence, however, that our calculated diffusion parameters are accurate and able to be related to the age of the sample in deducing a thermal history. This is for two reasons:

1. The dated mafic clast (*c*. 450 ppm K) is estimated to contain *c*. 75% plagioclase, with plagioclase being the dominant K-bearing phase within the clast. This observation implies that the majority of the ^{39}Ar released throughout the step-heating comes from the plagioclase diffusion domains.

2. The linearity of the Arrhenius relationship for all 4 isotopes ($R^2 = 0.99$; Fig. 13) suggests that the degassing of the sample follows continuous Fickian diffusion and that the modelling of the clast as a single domain is acceptable. If other diffusive domains from different phases or resulting from varying grain size were present, we would expect a departure from linearity at temperatures below those needed to melt the sample.

It is possible a more detailed heating schedule (i.e. more heating steps and temperature cycling) would reveal more complex diffusive properties of the mafic clast. In deciding not to pursue this course, we were swayed by the possibility that retrograde heating steps might result in meaningless ages of poor precision (e.g. Forster et al., 2015). We instead decided to maximize the precision on both the measured age as well as the diffusion parameters, given the small sample size and low K_2O content.

A cosmic-ray exposure age (CRE) of 6.5 ± 0.7 Ma is calculated for the mafic clast from the total isotopic concentrations released during step-heating and the elemental production coefficients of Eugster and Michel (1995). Details are in above (sections 2.7-2.8). The CRE age of the mafic clast (6.5 Ma) lies at the younger end of the range of CRE ages reported for HED meteorites of *c*. 5 to 60 Ma (Herzog and Caffee, 2014).

4. Discussion

4.1 Benefits of Ta-Platform Heating

Argon thermochonrologic experiments, which attempt to measure the diffusion kinetics of a sample during step-heating, require precise temperature measurements at each heating step. To achieve this, $^{40}Ar/^{39}Ar$ studies often use either a resistance furnace or an

in vacuo laser heating system. The resistance furnace offers good temperature control and can be configured for accurate temperature measurements, but difficulties in producing and maintaining low blanks generally require larger sample masses. Appreciable thermal inertia in some systems can also lengthen the times needed to attain thermal equilibrium and to return to ambient temperatures at the end of each heating step (e.g. Reus et al., 1980; McDougall and Harrison, 1999). Laser heating of samples *in vacuo* has largely compensated for these limitations and is commonly accomplished by wrapping a sample in a metal (e.g. platinum or tantalum) packet and step-heating the whole packet with a CO_2 or diode laser.

Currently, there are two general approaches to measuring temperatures with a single-color optical pyrometer. Both require the optical pyrometer to be externally calibrated to account for the changing emissivity of the target material within the temperature range of step-heating experiments. One method is by calibrating the optical pyrometer with a high-quality thermocouple (e.g. Cassata et al., 2009). In this scenario, the pyrometer is not used to directly determine temperature, but rather to regulate the laser power to produce to a constant temperature. Temperatures are inferred using a calibration curve (true or thermocouple temperature vs. pyrometer temperature) constructed independently for the specific target material with the use of a high-quality thermocouple, thus eliminating any issues relating to the changing emissivity of the target material with temperature. The second approach uses the melting point of pure metals to deduce the correct emissivity settings needed to construct a calibration curve without the need for a high-quality thermocouple (e.g. Oze et al., 2017; Miller et al., 2017; Strauss et al., 2017).

Oze et al. (2017) note that a potential drawback with the previously described thermocouple calibration is that the thermocouple lead is often of enough mass that heat is conducted away from the target and into the thermocouple. This results in the need for more laser energy to reach higher temperatures and complicates the confirmation of the calibration curve at these higher temperatures (>1100 °C). While the thermocouple calibration may be a suitable approach for temperature measurements, like Oze et al. (2017), our method does not use a high-quality thermocouple. As such we focus the following discussion on the benefits of the new method versus other methods that also use an optical pyrometer without the aid of a high-quality thermocouple calibration.

As mentioned above, the use of *single*-color pyrometer without a thermocouple requires external calibration. The calibration is necessary because single-color pyrometers rely on target materials that have a well-known and consistent emissivity. Alloys commonly used include Pt, Pt-Ir (Cassata et al. 2009) or Ta (Oze et al., 2017). While these alloys have well known emissivities within the infrared spectrum of a single-color pyrometer, their emissivity is not constant over the entire temperature range of most step-heating experiments [e.g. Deemyad and Silvera (2008); Savitskii (2012)]. The changing emissivity of the target material with temperature adds the potential for erroneous temperature measurements (by up to 10%) using a single-color pyrometer and in the case of Oze et al. (2017), requires the correction of temperatures from a calibration curve constructed from the melting of pure Al followed by subsequent emissivity experiments.

Oze et al. (2017) calibrated their single-color pyrometer to within ± 20 °C (3%) of the true temperature by inferring the melting point of aluminum (660 °C) in the following way. Aluminum metal was wrapped in a Ta foil packet, was heated to constant

temperatures while measuring the ^{40}Ar released during heating; accelerated releases of ^{40}Ar were taken to indicate the onset of complete melting of aluminum. Once the melting point was observed, the emissivity setting of the pyrometer was then adjusted until the temperature reading was 660 °C. This approach assumes that large releases only occur at the moment of complete melting. The broad temperature range (*c.* 640-680 °C) at which ^{40}Ar was released during the pyrometer experiment indicates that this may not be the case. After acquiring this fixed point (a calibrated emissivity at 660 °C), the authors incrementally changed the emissivity setting of the pyrometer while at the constant laser power, thus relating emissivity to the deviation from true temperature. This deviation served as a calibration curve (or correction factor) by using compiled emissivity values of Ta at different temperatures, and was used for all temperatures above and below 660 °C.

We, too make temperature measurements on a tantalum metal target with an optical pyrometer without the use of a high-quality thermocouple. However, we use a *two-color* pyrometer which can account for the change in emissivity with temperature using a fixed "relative emissivity" or slope adjustment in combination with the original calibration of the pyrometer (see. Section 2.3). This method allows for accurate temperature measurements to be made throughout the temperature range of the step-heating experiments without the need for any corrections from an external calibration curve. Our experiment observing the melting of pure metals (Fig. 7a) is a verification of the slope adjustment in combination with the pyrometer's original calibration. Additionally, our use of a tantalum platform, rather than a packet, allows for the direct observation of the melting point of the pure metals during verification experiments confirming the pyrometer calibration (Fig. 7a) and eliminates the need to measure ^{40}Ar to infer melting. This results

in an improvement in inferred pyrometer accuracy from *c*. 3% in the study of Oze et al. (2017) to *c*. 0.5% in this study.

The use of a platform design (Fig. 5) also provides a second modest improvement to conventional laser step-heating methods. The platform allows for continuous sample viewing throughout sample preparation, step-heating, and in particular, at the moment of complete fusion (Fig. 5d). Without such observations, melting is inferred by large gas releases, potentially leading to temperature steps before sample melting being left out of Arrhenius regressions (e.g. Reynolds et al., 1998). Without this observation, temperature steps after sample melting can similarly be incorrectly included in Arrhenius regressions, as was discussed as a potential issue in Forster et al. (2015).

Lastly, the Ta-platforms are cost-effective and are easily cleaned and degassed for repeated use.

A drawback of the method described here is that although the temperature of each heating step is constant and attained rapidly, that temperature is not precisely known in advance. The temperature achieved is determined by the geometry of the target, which may vary slightly, and by the laser power setting. In practice, based on experience we can normally predict the temperature to within *c.* 20 °C. Future set-ups could include the heating of tantalum platforms using a controlled feedback loop for laser power, similar to ones implemented by Cassata et al. (2009) and Oze et al. (2017).

4.2 Application to howardite, MAC 02666

4.2.1 Thermal Resetting Events on Vesta

Figure 14 shows the distribution of published $^{40}Ar/^{39}Ar$ ages of HED meteorites (Bogard and Garrison, 2009; Bogard et al., 1995; Bogard et al., 1993; Bogard et al., 1985; Bogard, 2011; Bogard and Garrison, 2003; Caffee et al., 1985; Cohen, 2013; Kaneoka et al., 1979; Kennedy et al., 2013; Korochantseva et al., 2005; Kunz et al., 1997; Lindsay et al., 2015; Rajan et al., 1975, 1979; Shankar et al., 2008; Shukoliukov et al., 1984; Takeda et al., 1994). A large peak between 4.2 and 4.6 Ga has been interpreted as the result of an extended period of eucrite formation and of internal metamorphism (Bogard, 2011). A second prominent peak, possibly with substructure, appears between 3.4 and 4.1 Ga of Figure 14. Bogard and Garrison (2009) suggested that these younger ages result from impact resetting during a period of enhanced asteroidal bombardment that also affected the Moon. Cohen (2013) obtained $^{40}Ar/^{39}Ar$ ages ranging from 3.3 to 3.8 Ga for what were clearly impact melt clasts, as opposed to bulk samples or unaltered mafic clasts, separated from several howardites. Cohen (2013) suggested that the resetting of the Ar ages for these impact melt clasts was caused by high-velocity impacts on Vesta rather than by an overall increase in the flux of impactors.

The $^{40}Ar/^{39}Ar$ ages of feldspar and glassy veins within one howardite, Kapoeta have an even wider range, from <1 to 3.9 Ga (Lindsay et al., 2015), suggesting that thermal events on Vesta continued to occur throughout the last 3.3 Ga. The varied ages that populate this extended time interval, from <1 to 3.8 Ga, are likely the consequence of both impact resetting and the uneven cooling of various mineral phases.

Against this background we examine how our new data constrain the thermal history of MAC 02666. The plateau age of the clast measured here is 3.64 ± 0.28 Ga (Fig. 11), and falls in the middle of the 3.4-4.1 Ga peak for HED meteorites (Fig. 14). The

possibility that this age was reset by impact is supported by mineral textures. Plagioclase in the clast shows areas of mosaicism that are consistent with shock deformation, as are the irregular fractures seen within both plagioclase and pyroxene grains and along grain boundaries (Fig. 1c-d). The mafic clast, although thoroughly brecciated, shows *no* evidence for partial re-melting of mineral phases after crystallization, indicating that temperatures experienced by the sample during the shock producing event never rose above the solidus.

Age-resetting of the mafic clast due to impact is also supported by thermal modelling. Figure 15 shows the times required for either 90% or 10% of the radiogenic ^{40}Ar to be lost from the sample, as a function of temperature, modelled with the diffusion parameters determined for the mafic clast. Ar losses of 90% would effectively reset the argon clock without the physical melting of the sample, a scenario similar to the one necessary to account for the thermal resetting and closure of the Ar-Ar system of the mafic clast at 3.64 Ga. Even at sub-solidus temperatures, relatively short heating times are sufficient to reset the age: 140 yr at 300 °C or a few hours at 700 °C, perhaps within the regolith surrounding an impact crater. The temperature of ejecta from an impact and therefore the temperature its resultant ejecta pile is strongly dependent on the velocity of the impactor, while the depth of the crater and volume of ejecta scales with the size of the impactor (Marchi et al., 2013). According to the Hydrocode-based impact modelling of Marchi et al. (2013), a wide range of impactor velocities striking the surface of Vesta can achieve the temperatures necessary for resetting the age of the mafic clast. For example, an above average velocity impactor (*c*. 7 km s^{-1}) on the surface of Vesta, with a 10 km diameter, can produce ejecta temperatures up to *c*. 750 °C, while even an average velocity impactor (*c*. 5 km s^{-1}) can produce ejecta temperatures up to *c*. 450 °C (Marchi et al., 2013).

As noted above (Section 3.2), the mafic clast of MAC 02666 lost little or no Ar since it closed *c*. 3.64 Ga (Fig. 11). Interestingly, numerous $^{40}Ar/^{39}Ar$ ages of HEDs, although within the proposed enhanced bombardment interval of Vesta, are significantly younger than the age of the mafic clast (e.g. Lindsay et al. 2015). The flat release pattern during step-heating (Fig. 11) indicates that any thermal events after the 3.64 Ga resetting age must have been sufficiently cool or short to limit any fractional loss of ^{40}Ar. Diffusion parameters can be used to model, and therefore exclude, the conditions that would reset or partially reset the Ar-Ar system. Cohen (2013) took a similar approach, but in the absence of diffusion parameters for the samples analyzed, relied on published results for similar terrestrial materials. Here, utilizing the step-heating method described above, the diffusion parameters of the sample of interest were measured directly (Table 11).

The second scenario presented in Fig. 15, a 10% fractional loss of ^{40}Ar, constrains the duration of a heating event needed to produce younger ages at low temperature steps during step-heating. Fig. 15 shows that heating at elevated temperatures (i.e. >450°C) produces a 10% fractional loss in only a few days; such losses would produce young apparent ages that are not observed in the release spectra of Fig. 11. From the calculated scenarios displayed in Fig. 15, we conclude that within the last 3.64 Ga, the temperature of the MAC 02666 clast did not exceed temperatures of *c.* 450°C. Conversely, if the sample was exposed to higher temperatures, it necessarily was only for a brief duration (< *c.* 1 day), limiting Ar loss.

A simple but restrictive astrophysical scenario that prevents Ar loss assumes that only high-velocity impacts are likely to reset Ar ages and, accordingly, places the sample far from all craters produced by such impacts. Calculations of impact probabilities for

Vesta (O'Brien et al., 2011) coupled with the crater simulations of Marchi et al. (2013) suggest that about 20% of the surface area of Vesta meets this description, with the majority of these impacts occurring before 4.1 Ga. More broadly, if small impacts can reset the Ar clock as suggested by the diffusion parameters of the mafic clast from MAC 02666, then the sample must have been buried 1 km or so beneath the Vestan surface.

4.2.2 Howardite Age Evolution

Two prominent overlapping basins, Rheasilvia and Veneneia, dominate the southern hemisphere of Vesta. These basins probably formed as a result of the major impact events that also produced the immediate precursors of HED meteorites (see, Marchi et al., 2012; McSween et al., 2011, 2013). Crater counting of the surface of Vesta has yielded discordant ages of the two basin-forming events: 1.0 or 3.6 Ga for Rheasilvia and 2.1 or 3.8 Ga for Veneneia (Marchi et al., 2012; Schmedemann et al., 2014). From a consideration of Vesta's cratering record, Marchi et al. (2012) concluded that the Rheasilvia basin was formed by a large impact *c*. 1 Ga ago and, in the process, produced enough ejecta to account for the Vestoid family of asteroids. Based on dynamical considerations, Marchi et al. (2012) also argued that the Vestoids could not have survived as a recognizable astronomical family for more than 1 Ga, a limit consistent with the 1-Ga age estimated for Rheasilvia, but not with the generation of the Vestoids by an earlier event.

The thermal parameters for the clast from MAC 02666 show its sensitivity to heating and, by extension, suggest that similar material in other HED meteorites also should be susceptible to Ar losses. Consistent with these observations and reasoning, Lindsay et al. (2015) reported $^{40}Ar/^{39}Ar$ ages of about 1 Ga in isolated feldspars from the

Kapoeta howardite. They also noted that the Ar release spectra of several other brecciated eucrites and howardites show signs of disturbance (i.e., young ages at low laboratory release temperatures) within the last 2 Ga. If these low ages mark Ar closure after cooling of samples buried 3.6 Ga ago in ejecta blankets on Vesta, then cooling rates $\Delta T/\Delta t$, less than 0.3 °C/Ma are implied ($\Delta T \leq 450$ °C; $\Delta t \geq (3.6\text{-}2.0)$ Ga). In this burial scenario, it is difficult to understand how most components of howardites could have escaped resetting of $^{40}Ar/^{39}Ar$ ages. Independent estimates of post-impact cooling rates for HED meteorites, albeit imperfectly analogous and derived from various thermometers, are orders of magnitude faster: 3.5 x 10^5 °C/Ma for the Moore County cumulate eucrite (Miyamoto and Takeda, 1994); and 80 to 500 °C/Ma for diogenites, the D in HED meteorites (Zema et al., 1997). It seems simpler to suppose that proto HEDs 1) cooled rapidly after resetting 3.6 Ga ago; 2) escaped later disturbance on Vesta itself because of a declining flux of high-energy impactors (Marchi et al., 2013) or burial to modest depths; and 3) record in their low-temperature Ar release spectra the effects of rapid, inhomogeneous heating and cooling of Vestoids that occurred in the aftermath of the proposed Rheasilvia ejection event.

5. Conclusions

A tantalum platform allows simple and reproducible laser heating of microgram samples for $^{40}Ar/^{39}Ar$ thermochronology. The use of a two-color pyrometer and platform design results in an improved temperature measurement and verification of the optical pyrometer calibration without the need for a calibration curve from a high-quality thermocouple. Plagioclase diffusion parameters obtained from two samples from the Rustenburg Layered Suite of the Bushveld Complex (E_a = 165.3 ± 7.9 to 167.1 ± 3.8 kJ/mol

and $\ln(D_0/a^2)$ = 2.45 ± 0.50 to 3.80 ± 0.98), using the Ta-platform system, agree with previously published values, thus validating our method.

We made $^{40}Ar/^{39}Ar$ measurements of a low K_2O, 174-μg sample taken from a mafic clast in the howardite MAC 02666. The undisturbed age spectrum gives a plateau age of 3.64 ± 0.28 Ga. Calculated ^{39}Ar diffusion parameters (E_a = 138.2 ± 5.6 kJ/mol and $\ln(D_0/a^2)$ = 5.23 ± 0.60) indicate that this age may result from heating in an impact blanket at 1000 °C for about 10 minutes or at 200 °C for 6.63 x 10^4 y and resulted in complete resetting of the Ar clock. Subsequent burial of the clast on Vesta at depths of *c*. 1 km, along with decreasing average velocities for asteroidal impactors, may have protected the clast from further diffusive Ar loss until it was launched into orbit *c*. 6.5 Ma ago. By analogous reasoning, temperatures while the meteoroid was in transit to Earth and after the meteorite landed in the Antarctic, were too low to cause appreciable Ar loss.

Ages younger than *c*. 3.3 Ga are scarce in HED meteorites (Fig. 15), which is surprising considering the sensitivity of at least one of their components, which we believe to be plagioclase, to thermal resetting. The scarcity of younger ages can be understood partly as the consequence of the decreasing frequency over time of high-velocity impacts on Vesta and the sourcing of HEDs in smaller, rapidly cooled Vestoids launched in the Rheasilvia-producing event *c*. 1 Ga ago (Marchi et al., 2013). To some degree, however, the scarcity of younger ages likely reflects a historical lack of data for samples small enough to contain components with a single age. The heating method described in this study offers one relatively simple way to fill this gap and improve histories of thermal evolution.

6. References

Baxter E.F. (2010) Diffusion of noble gases in minerals. *Rev. Min. Geochem.* **72**, 509-557.Binzel R. P. and Xu S. (1993) Chips off of asteroid 4 Vesta: evidence for the parent body of balsaltic achondrite meteorites. *Science* **260**(5105), 186-192.

Binzel R. P. and Xu S. (1993) Chips off asteroid 4 Vesta: evidence for the parent body of baslatic achondrite meteorites. *Science* **260**(5105), 186-192.

Bogard D. D. (2009) K-Ar dating of rocks on Mars: Requirements from meteorite analyses and isochron modeling. *Meteoritics and Planetary Science* **44**(1), 3-14.

Bogard D. and Garrison D. (2009) Ar-Ar impact heating ages of eucrites and timing of the LHB.

Bogard D., Garrison D., and Mittlefehldt D. (1990) 39Ar-40Ar dating of mesosiderites: Evidence for major parent body disruption< 4 Ga ago. *Geochimica et Cosmochimica Acta* **54**(9), 2549-2564.

Bogard D., Garrison D., Norman M., Scott E., and Keil K. (1995) 39 Ar□ 40 Ar age and petrology of Chico: Large-scale impact melting on the L chondrite parent body. *Geochimica et Cosmochimica Acta* **59**(7), 1383-1399.

Bogard D., Nyquist L., Takeda H., Mori H., Aoyama T., Bansal B., Wiesmann H., and Shih C.-Y. (1993) Antarctic polymict eucrite Yamato 792769 and the cratering record on the HED parent body. *Geochimica et Cosmochimica Acta* **57**(9), 2111-2121.

Bogard D., Taylor G., Keil K., Smith M., and Schmitt R. (1985) Impact melting of the Cachari eucrite 3.0 Gy ago. *Geochimica et Cosmochimica Acta* **49**(4), 941-946.

Bogard D. D. (2011) K–Ar ages of meteorites: clues to parent-body thermal histories. *Chemie der Erde-Geochemistry* **71**(3), 207-226.

Bogard D. D. and Garrison D. H. (2003) 39Ar-40Ar ages of eucrites and thermal history of asteroid 4 Vesta. *Meteoritics & Planetary Science* **38**(5), 669-710.

Caffee M., Hohenberg C., Swindle T., and Goswami J. (1985) Pre-Compaction Irradiation of Kapoeta: 40Ar-39Ar Ages of Individual Grains. *Meteoritics* **20**, 620.

Cassata W. S. and Borg L. E. (2016) A new approach to cosmogenic corrections in 40Ar/39Ar chronometry: implications for the ages of Martian meteorites. *Geochimica et Cosmochimica Acta* **187**, 279-293.

Cassata W. S. and Renne P. R. (2013) Systematic variations of argon diffusion in feldspars and implications for thermochronometry. *Geochimica et Cosmochimica Acta* **112**, 251-287.

Cassata W. S., Renne P. R., and Shuster D. L. (2009) Argon diffusion in plagioclase and implications for thermochronometry: a case study from the Bushveld Complex, South Africa. *Geochimica et Cosmochimica Acta* **73**(21), 6600-6612.

Cohen B. A. (2013) The Vestan cataclysm: Impact-melt clasts in howardites and the bombardment history of 4 Vesta. *Meteoritics & Planetary Science* **48**(5), 771-785.

Consolmagno G. J. and Drake M. J. (1977) Composition and evolution of the eucrite parent body: Evidence from rare earth elements. *Geochimica et Cosmochimica Acta* **41**(9), 1271-1282.

Dalrymple G. B. and Lanphere M. A. (1969) Potassium-argon dating: Principles, techniques and applications to geochronology. In *(Freeman) San Francisco, California*, pp. 258.

Dalrymple G. B. and Lanphere M. A. (1974) 40Ar/39Ar age spectra of some undisturbed terrestrial samples. *Geochimica et Cosmochimica Acta* **38**(5), 715-738.

Deemyad S. and Silvera I. F. (2008) Temperature dependence of the emissivity of platinum in the IR. *Review of Scientific Instruments* **79**(8), 086105.

Delaney J., Turrin B., Lindsay F., Herzog G., Park J., and Swisher C. (2016) Accurate Ages of Individual Meteoritic Lithologies are Useful, PreciseAges' of Bulk Meteorites are Not! *LPI Contributions* **1921**.

Dodson M. H. (1973) Closure temperature in cooling geochronological and petrological systems. *Contributions to Mineralogy and Petrology* **40**(3), 259-274.

Engineering Toolbox (2019) Engineering Toolbox, 2019. Metals and Alloys - Densities <https://www.engineeringtoolbox.com/metal-alloys-densities-d_50.html> (accessed 30.09.19).

Engineering Toolbox (2019) Engineering Toolbox, 2019. Specific Heat of some common Substances < https://www.engineeringtoolbox.com/specific-heat-capacity-d_391.html> (accessed 30.09.19).

Engineering Toolbox (2019) Engineering Toolbox, 2019. Thermal Conductivity of Metals, Metallic Elements and Alloys < https://www.engineeringtoolbox.com/thermal-conductivity-metals-d_858.html> (accessed 30.09.19).

Eugster O. and Michel T. (1995) Common asteroid break-up events of eucrites, diogenites, and howardites and cosmic-ray production rates for noble gases in achondrites. *Geochimica et Cosmochimica Acta* **59**(1), 177-199.

Fechtig H., Gentner W., and Lämmerzahl P. (1963) Argonbestimmungen an Kaliummineralien—XII: Edelgasdiffusionsmessungen an Stein-und Eisenmeteoriten. *Geochimica et Cosmochimica Acta* **27**(11), 1149-1169.

Fechtig H. and Kalbitzer S. (1966) The diffusion of argon in potassium-bearing solids. *Potassium-Argon Dating*, 68-106.

Fleck R. J., Sutter J. F., and Elliot D. H. (1977) Interpretation of discordant $^{40}Ar/^{39}Ar$ age-spectra of Mesozoic tholeiites from Antarctica. *Geochimica et Cosmochimica Acta* **41**(1), 15-32.

Forster M. A., Armstrong R., Kohn B., Lister G. S., Cottam, M. A., and Suggate, S. (2015) Highly retentive core domains in K-feldspar and their implications for 40Ar/39Ar thermochronology illustrated by determining the cooling curve for the Capoas Granite, Palawan, The Phillippines. *Australian Journal of Earth Sciences* **62**(7), 883-902.

Garrison D., Hamlin S. and Bogard, D. (2000) Chlorine abundances in meteorites. *Meteoritics & Planetary Science* **35**(2), 419-429.

Gruner K.-D. (2003) Principles of non-contact temperature measurement. *Raytek Company*.

Hemingway B. S., Krupka K. M., and Robie R. A. (1981) Heat capacities of the alkali feldspars between 350 and 1000 K from differential scanning calorimetry, the thermodynamic functions of the alkali feldpsars from 298.15 to 1400 K, and the reaction quartz+ jadeite= analbite. *American Mineralogist* **66**(11-12), 1202-1215.

Herzog G.F. and Caffee M.W. (2014) Cosmic-ray exposure ages of meteorites. In: *Treatise on Geochemistry, Second Edition, Vol. 1* (Eds.: Holland H.D. and Turekian K.K.) Oxford: Elsevier. 419-453.Huber C., Cassata W. S., and Renne P. R. (2011) A lattice Boltzmann model for noble gas diffusion in solids: the importance of domain shape and diffusive anisotropy and implications for thermochronometry. *Geochimica et Cosmochimica Acta* **75**(8), 2170-2186.

Jourdan F. and Renne P. R. (2007) Age calibration of the Fish Canyon sanidine 40 Ar/39 Ar dating standard using primary K–Ar standards. *Geochimica et Cosmochimica Acta* **71**(2), 387-402.

Kaneoka I., Ozima M., and Yanagisawa M. (1979) 40Ar-39Ar age studies of four Yamato-74 meteorites. *Memoirs of National Institute of Polar Research. Special issue* **12**, 186-206.

Kennedy T., Jourdan F., Bevan A. W., Gee M. M., and Frew A. (2013) Impact history of the HED parent body (ies) clarified by new 40 Ar/39 Ar analyses of four HED meteorites and one anomalous basaltic achondrite. *Geochimica et Cosmochimica Acta* **115**, 162-182.

Korochantseva E. V., Trieloff M., Buikin A. I., Hopp J., and Meyer H. P. (2005) $^{40}Ar/^{39}Ar$ dating and cosmic-ray exposure time of desert meteorites: Dhofar 300 and Dhofar 007 eucrites and anomalous achondrite NWA 011. *Meteoritics & Planetary Science* **40**(9-10), 1433-1454.

Kuiper K., Deino A., Hilgen F., Krijgsman W., Renne P., and Wijbrans J. (2008) Synchronizing rock clocks of Earth history. *Science* **320**(5875), 500-504.

Kunz J., Falter M., and Jessberger E. K. (1997) Shocked meteorites: Argon-40-argon-39 evidence for multiple impacts. *Meteoritics & Planetary Science* **32**(5), 647-670.

Lee J.-Y., Marti K., Severinghaus J. P., Kawamura K., Yoo H.-S., Lee J. B., and Kim J. S. (2006) A redetermination of the isotopic abundances of atmospheric Ar. *Geochimica et Cosmochimica Acta* **70**(17), 4507-4512.

Lindsay F. N., Delaney J. S., Herzog G. F., Turrin B. D., Park J., and Swisher C. C. (2015) Rheasilvia provenance of the Kapoeta howardite inferred from~ 1 Ga $^{40}Ar/^{39}Ar$ feldspar ages. *Earth and Planetary Science Letters* **413**, 208-213.

Lovera O. M., Grove M., Harrison T. M., and Mahon K. (1997) Systematic analysis of K-feldspar 40Ar39Ar step heating results: I. Significance of activation energy determinations. *Geochimica et Cosmochimica Acta* **61**(15), 3171-3192.

Lovera O. M., Richter F. M., and Harrison T. M. (1989) The $^{40}Ar/^{39}Ar$ thermochronometry for slowly cooled samples having a distribution of diffusion domain sizes. *Journal of Geophysical Research: Solid Earth* **94**(B12), 17917-17935.

Lovera O. M., Richter F. M., and Harrison T. M. (1991) Diffusion domains determined by ^{39}Ar released during step heating. *Journal of Geophysical Research: Solid Earth* **96**(B2), 2057-2069.

Marchi S., Bottke W., Cohen B., Wünnemann K., Kring D., McSween H., De Sanctis M., O'brien D., Schenk P., and Raymond C. (2013) High-velocity collisions from the lunar cataclysm recorded in asteroidal meteorites. *Nature Geoscience* **6**(4), 303-307.

Marchi S., McSween H. Y., O'Brien D. P., Schenk P., De Sanctis M. C., Gaskell R., Jaumann R., Mottola S., Preusker F., and Raymond C. A. (2012) The violent collisional history of asteroid 4 Vesta. *Science* **336**(6082), 690-694.

McCord T. B., Adams J. B., and Johnson T. V. (1970) Asteroid Vesta: Spectral reflectivity and compositional implications. *Science* **336**(6082), 690-694.

McDougall I. and Harrison T. M. (1999) *Geochronology and Thermochronology by the $^{40}Ar/^{39}Ar$ Method*. Oxford University Press on Demand.

McSween H.Y., Binzel R.P., de Sanctis M.C., Ammannito E., Prettyman T.H., Beck A.W., Reddy V., Corre L., Gaffey M.J., McCord T.B., Raymond C.A., and Russell C.T. (2013) Dawn; the Vesta-HED connection; and the geologic context for eucrites, diogenites, and howardites. *Meteoritics Planet. Sci.*, **48**, 2090-2104.

McSween H. Y., Mittlefehldt D. W., Beck A. W., Mayne R. G., and McCoy T. J. (2011) HED meteorites and their relationship to the geology of Vesta and the Dawn mission. *Space Science Reviews* **163**(1), 141-174.

Miller E. L., Akinin V. V., Dumitru T. A., Gottlieb E. S., Grove M., Meisling, K., and Seward, G. (2017) Deformational history and thermochronology of Wrangel Island, East Siberian Shelf and coastal Chukotka, Arctic Russia. *Geological Society*, *London, Special Publications* **460**, 460-467.

Mittlefehldt D. (2015) Asteroid (4) Vesta: I. The howardite-eucrite-diogenite (HED) clan of meteorites. *Cehmie der Erde-Geochemistry* **75**(2), 155-183.

Miyamoto M. and Takeda H. (1994) Evidence for excavation of deep crustal material of a Vesta-like body from Ca compositional gradients in pyroxene. *Earth and Planetary Science Letter* **122**(3-4), 343-349.

O'Brien D., Sykes M., and Tricarico P. (2011) Collision probabilities and impact velocity distributions for Vesta and Ceres. In *Lunar and Planetary Science Conference*, 2665.pdf.

Oze C., Cattell H., and Grove M. (2017) $^{40}Ar/^{39}Ar$ dating and thermal modeling of adularia to constrain the timing of hydrothermal activity in magmatic settings. *Geology* **45**(1), 43-46.

Parsons I., Brown W., and Smith J. (1999) $^{40}Ar/^{39}Ar$ thermochronology using alkali feldspars: real thermal history or mathematical mirage of microtexture? *Contributions to Mineralogy and Petrology* **136**(1), 92-110.

Rajan R., Huneke J., Smith S., and Wasserburg G. (1975) ^{40}Ar-^{39}Ar chronology of isolated phases from Bununu and Malvern howardites. *Earth and Planetary Science Letters* **27**(2), 181-190.

Rajan R., Huneke J., Smith S., and Wasserburg G. (1979) Argon 40-argon 39 chronology of lithic clasts from the Kapoeta howardite. *Geochimica et Cosmochimica Acta* **43**(7), 957-971.

Reiners P. W., Ehlers T. A., and Zeitler P. K. (2005) Past, present, and future of thermochronology. *Reviews of Mineralogy and Geochemistry* **58**, 1-18.

Renne P. R., Swisher C. C., Deino A. L., Karner D. B., Owens T. L., and DePaolo D. J. (1998) Intercalibration of standards, absolute ages and uncertainties in $^{40}Ar/^{39}Ar$ dating. *Chemical Geology* **145**(1-2), 117-152.

Reus, K. W., Zwakhals, C. J., and Smit, J. A. (1980) Measurement of diffusion coefficients via diffusion in flowing gas: I. Method. *Physica B+C*, **100**(2), 221-230.

Reynolds P., Ravenhurst C., Zentilli M., and Linsay D. (1998) High-precision 40Ar/39Ar dating of two consecutive hydrothermal events in the Cuquicamata prphyry copper system, Chile. *Chemical Geology* **148**(1-2), 45-60.

Robie R. A., Hemingway B. S., and Wilson W. H. (1978) Low-temperature heat capacities and entropies of feldspar glasses and of anorthite. *American Mineralogist* **63**(1-2), 109-123.

Russell S. S., Folco L., Grady M. M., Zolensky M. E., Jones R., Righter K., Zipfel J., and Grossman J. N. (2004) The meteoritical bulletin, no. 88, 2004 July. *Meteoritics & Planetary Science* **39**(S8).

Savitskii E. M. (2012) *Physical metallurgy of refractory metals and alloys*. Springer Science & Business Media.

Schmedemann N., Kneissl T., Ivanov B., Michael G., Wagner R., Neukum G., Ruesch O., Hiesinger H., Krohn K., and Roatsch T. (2014) The cratering record, chronology and surface ages of (4) Vesta in comparison to smaller asteroids and the ages of HED meteorites. *Planetary and Space Science* **103**, 104-130.

Setera J., Turrin B., VanTongeren J., Lindsay F., Herzog G., Delaney J., and Swisher C. (2016) $^{40}Ar/^{39}Ar$ Thermochronology: A method for precise age dating and closure temperatures with implications for meteoritic and terrestrial samples. In *Lunar and Planetary Science Conference*, 3017.pdf .

Shankar N., Swisher C., Turrin B., and Herzog G. (2008) $^{40}Ar/^{39}Ar$-CO_2 Laser incremental heating release spectra for the Pasamonte eucrite and Martian meteorites ALHA77005, Shergotty, and Y000749. In *Lunar and Planetary Science Conference*, 1924.pdf.

Shukoliukov I. A., Fugzan M., Dang V., Kolesov G., and Skripnik A. I. (1984) (AR-40)-(AR-39) dating of the meteorite Vetluga. *Geokhimiia*, 291-301.

Steiger R. H. and Jäger E. (1977) Subcommission on geochronology: convention on the use of decay constants in geo-and cosmochronology. *Earth and planetary science letters* **36**(3), 359-362.

Stöffler D., Hamann C., and Metzler K. (2018) Shock metamorphism of planetary silicate rocks and sediments: Proposal for an updated classification system. *Meteoritics and Planetary Science* **53**(1), 5-49.

Strauss J. V., Hoiland, C. W., Ward W. P., Johnson B. G., Nelson L. L., and McClelland W. C. (2017) Orogen transplant: Taconic-Caledonian arc magmatism in the central Brooks Range of Alaska. *Geological Society of America Bulletin* **129**, 649-676.

Takeda H., Mori H., and Bogard D. D. (1994) Mineralogy and39Ar-40Ar age of an old pristine basalt: Thermal history of the HED parent body. *Earth and Planetary Science Letters* **122**(1-2), 183-194.

Taylor J. (1997) *Introduction to error analysis, the study of uncertainties in physical measurements*. University Science Books, 327 pp.

Thirumalai K., Singh A., and Ramesh R. (2011) A MATLAB™ code to perform weighted linear regression with (correlated or uncorrelated) errors in bivariate data. *Journal of the Geological Society of India* **77**(4), 377-380.

Turrin B. D., Swisher C. C., and Deino A. L. (2010) Mass discrimination monitoring and intercalibration of dual collectors in noble gas mass spectrometer systems. *Geochemistry, Geophysics, Geosystems* **11**(8).

Vermeesch P. (2018) IsoplotR: a free and open toolbox for geochronology. *Geoscience Frontiers*, doi: 10.1016/j.gsf/2018.04.001 (in press).

Villa I. M. (2010) Disequilibrium textures versus equilibrium modelling: geochronology at the crossroads. *Geological Society, London, Special Publications* **332**(1), 1-15.

Warren P. H., Kallemeyn G. W., Huber H., Ulff-Møller F., and Choe W. (2009) Siderophile and other geochemical constraints on mixing relationships among HED-meteoritic breccias. *Geochimica et Cosmochimica Acta* **73**(19), 5918-5943.

Williams C., Keil K., Taylor G., and Scott E. (2000) Cooling rates of equilibrated clasts in ordinary chondrite regolith breccias: implications for parent body histories. *Chemieder Erde-Geochemistry* **59**(4), 287-305.

Xie C. (2012) Interactive heat transfer simulations for everyone. *The Physics Teacher* **50**(4), 237-240.

Yamaguchi A., Takeda H., Bogard D. D., and Garrison, D. (1993) Textural variations and impact history of the Millbillillie eucrite. *Meteoritics* **29**(2), 237-245.

York D., Evensen N. M., Martínez M. L., and De Basabe Delgado J. (2004) Unified equations for the slope, intercept, and standard errors of the best straight line. *American Journal of Physics* **72**(3), 367-375.

Zema M., Domeneghetti M. C., Molin G., and Tazzoli V. (1997) A study of Fe^{2+}-Mg ordering in orthopyroxene by single-crystal x-ray diffraction. *Meteoritics & Planetary Science* **32**, 855-862.

Figure Captions

Figure 1

(a) Bulk portion of MAC02666. (b) *174* μg mafic clast (MC 001) from howardite MAC 02666 separated for $^{40}Ar/^{39}Ar$ thermochronology. (c) BSE image of a fragment of the mafic clast used for EMPA analyses. (d) Magnified BSE image of the same fragment showing plagioclase textures.

Figure 2

Compositional ranges of pyroxene and plagioclase from the mafic clast of howardite, MAC 02666. (a) Pyroxene quadrilateral diagram. (b) Normative anorthite (An), albite (Ab), orthoclase (Or) diagram.

Figure 3

Photomosaic of BSE images of the mafic clast of the howardite, MAC 02666. Annotated areas are where electron microprobe analyses were taken. The red dotted line denotes the contact between the mafic clast and the howardite matrix. Only analyses of the mafic clast are reported.

Figure 4

Example of the temperature of a Ta-platform during heating with the CO_2 laser. The Ta-platform reaches temperature in ~10s and takes ~10s to return to room temperature.

Figure 5

Images of Ta platforms used during heating experiments. (a) Schematic drawing (not to scale) of the tantalum platform design. The red circled points on the platform illustrate the areas in contact with the steel pit which are responsible for heat conduction away from the sample. (b) Example of Ta platform and sample heated to *c*. 1100°C. The image is heavily filtered by the camera and does not display true colors. In the initial calibration of the system and in subsequent recalibration checks, no temperature differences were noted with the pyrometer in the "dimpled" sample area" of the Ta-platform (indicated by the dotted red circle) and the point of focus of the laser (indicated by the solid red circle). (c) Images showing the true color of heated tantalum platforms. (d) Image demonstrating the dimensions of a Ta platform. Each side of the platform is approximately 5 mm in length. The glass ball in image provides visual of a fused sample within the augured dimple.

Figure 6

(a) Model set-up in Energy2D. Horizontal platform and folded legs are Ta, while sample holder is stainless-steel. A single feldspar grain is placed on top of the Ta-platform. (b) Model run at 1000°C, shown after 5 s. Open circles are locations of temperature measurements. (c) (d) (e) Temperature recordings for 500°C, 800°C and 1000°C heating steps, respectively.

Figure 7

(a) Experimental results, relating laser output (W) to pyrometer temperature (°C), verifying the calibration of the optical pyrometer. The data were fitted with with StataMP

statistical analysis software in order to estimate temperatures below 500°C. Measured melting points are labeled for Au (gold), Cu (copper) and Al (aluminum). The melting point of Sn (tin) was used to anchor temperatures below 500 °C. (b) Apparent pyrometer temperatures resulting from incorrect slope adjustment values. Each adjustment of 0.030 results in an *c*. 25°C offset of the apparent from the true temperature.

Figure 8

Modelled values of minimum duration of re-heating events required to result in 90% (solid line) and 10% (dashed line) fractional losses from the mafic clast of howardite, MAC 02666. Diffusion parameters used in modelling are from ^{39}Ar (black), ^{40}Ar* (dark grey) and ^{36}Ar (light grey).

Figure 9

Step-heating age spectrum and K/Ca ratios for plagioclase separates for samples B06-042 (Upper Zone) and B14-053a (Main Zone) from Rustenburg Layered Suite of the Bushveld Complex. The dashed line within individual steps represents the apparent age of the step.

Figure 10

Arrhenius plots for plagioclase separates from sample B06-042 of the Upper Zone and B14-053a of the Main Zone of the RLS. Activation energy = E_a (kJ/mol), diffusion constant = $\ln(D_0/a^2)$. Closed circles are used in Arrhenius regressions. Open circles are not used.

Figure 11

Step-heating age spectrum and K/Ca ratios for a 174-μg mafic clast (MC 001) from the howardite MAC 02666. The dashed line within individual steps represents the apparent age of the step.

Figure 12

Isochron for a 174-μg mafic clast (MC 001) from howardite MAC 02666 after applying cosmogenic correction to obtain $^{36}Ar_{Tr}$. $\rho(^{36}Ar,^{38}Ar)$ is the correlation of the uncertainties for ^{36}Ar and ^{38}Ar (see supplementary information). The isochron age and the plateau age are analytically indistinguishable (α=0.05). The intercept of the best fit line, $^{40}Ar/^{36}Ar_{Tr}$ Int., is analytically indistinguishable from zero (α=0.05), indicating negligible concentrations of trapped ^{40}Ar.

Figure 13

Arrhenius plots of (a) ^{40}Ar (b) ^{39}Ar (c) ^{38}Ar and (d) ^{36}Ar for the mafic clast (MC 001) from the howardite MAC 02666. Activation energy = E_a (kJ/mol), diffusion constant = $\ln(D_0/a^2)$, and closure temperature (T_c, °C). Closed circles are used in Arrhenius regression. Open circles are not used.

Figure 14

Cumulative Gaussian probability diagram and histogram for published $^{40}Ar/^{39}Ar$ ages of HEDs. Histogram bin size is 150 Myr. See text for full references.

Figure 15

Minimum duration of re-heating events required to result in 90% (solid line) and 10% (dashed line) fractional losses from the mafic clast of howardite MAC 02666. Diffusion parameters used in the calculations are from ^{39}Ar. The use of the other diffusion parameters listed in Table 11 yield similar results (Table 13, Fig. 8).

Figure 1

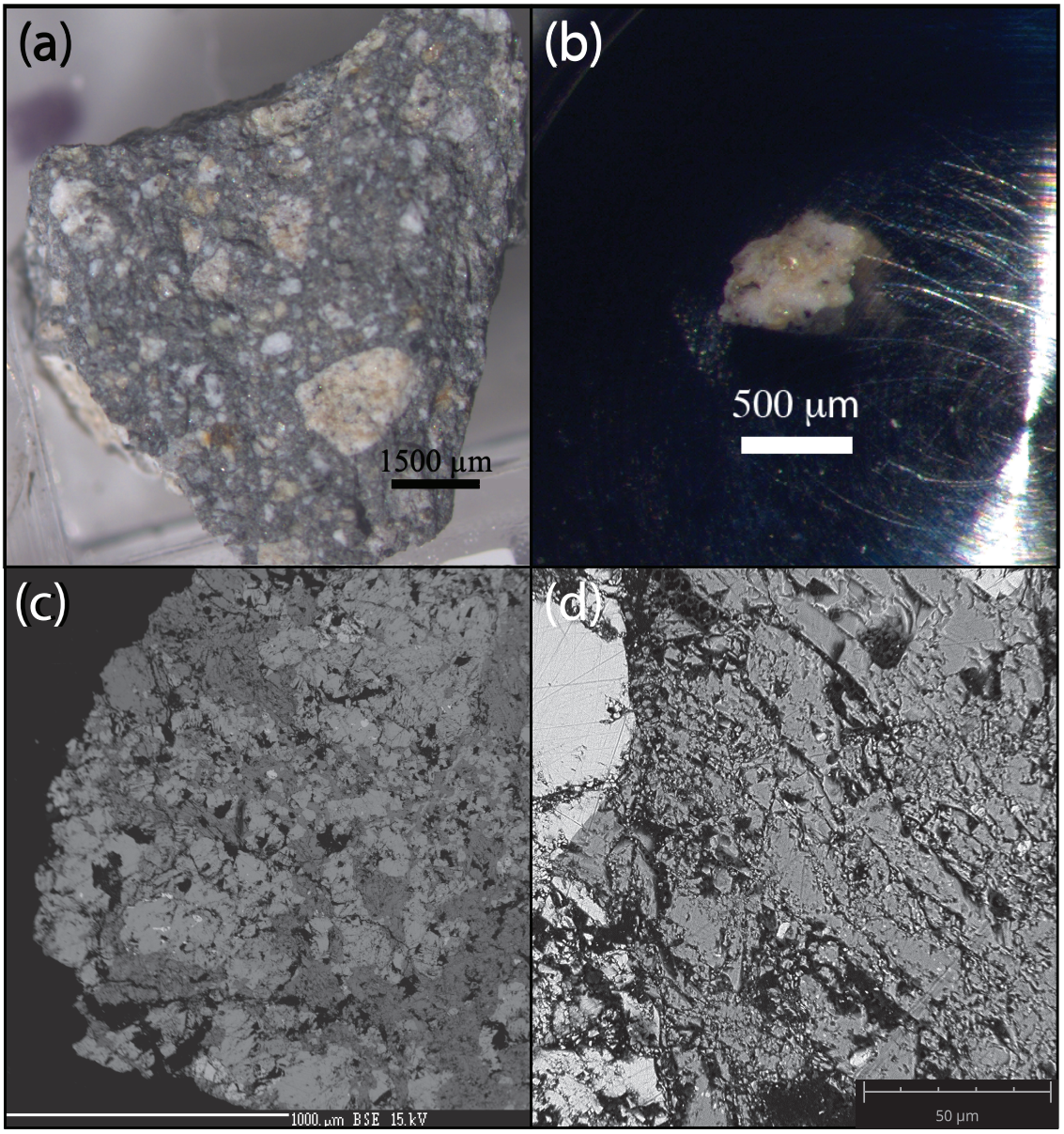

Figure 2

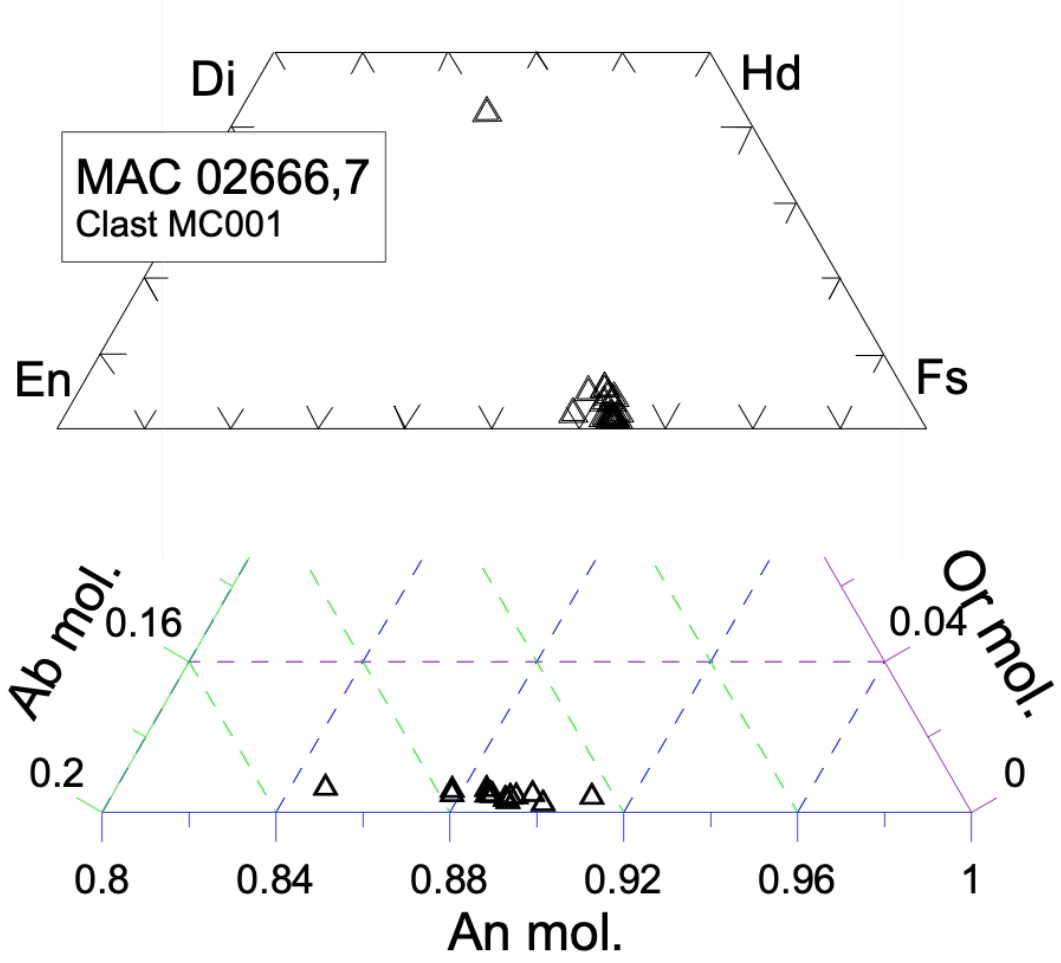
Di
Hd
MAC 02666,7
Clast MC001
En
Fs
Ab mol.
0.16
0.2
Or mol.
0.04
0
0.8
0.84
0.88
0.92
0.96
1
An mol.

Figure 3

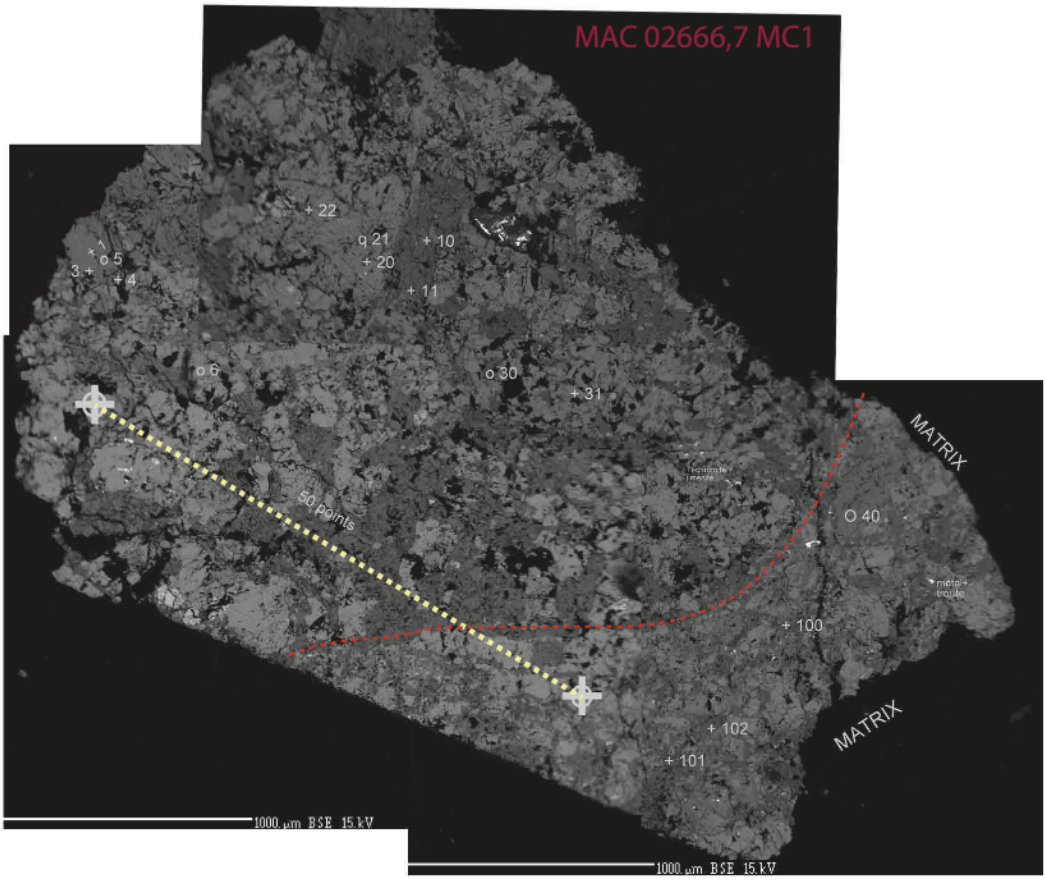
MAC 02666,7 MC1
+ 22
q 21
+ 10
+ 20
+ 11
+ 1
o 5
3 +
+ 4
o 6
o 30
+ 31
50 Points
MATRIX
O 40
+ 100
+ 102
+ 101
MATRIX
1000 µm BSE 15 kV
1000 µm BSE 15 kV

Figure 4

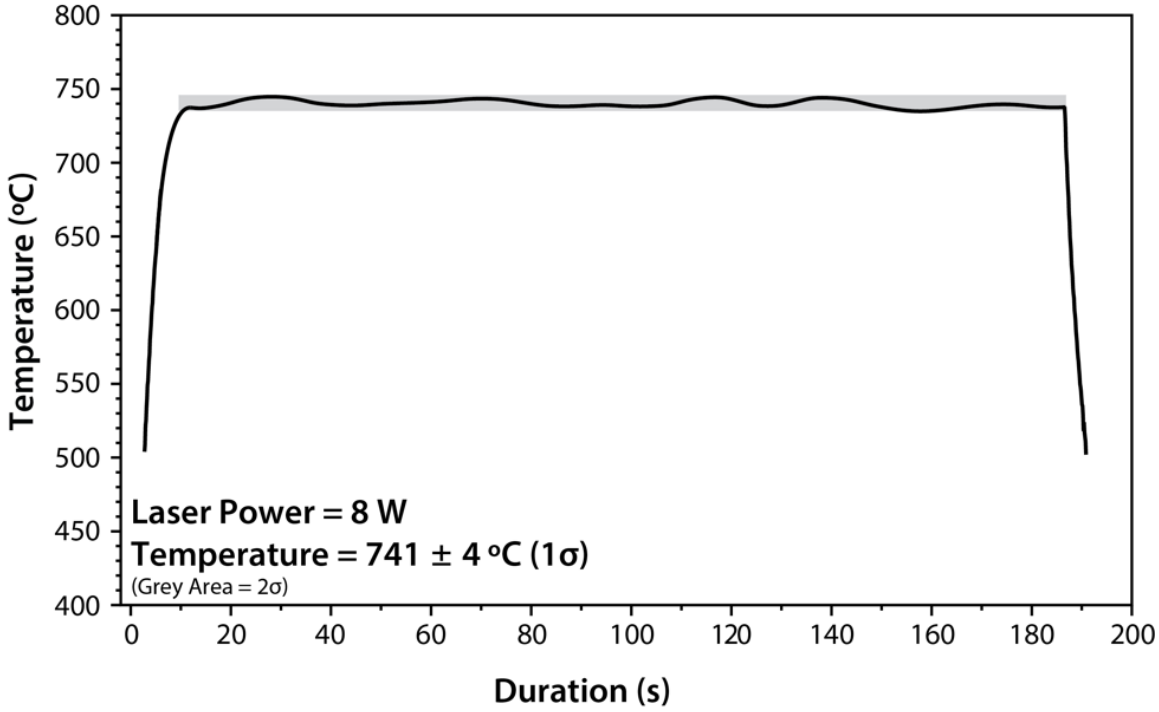
800
750
700
650
600
550
500
450
400
Temperature (°C)
Laser Power = 8 W
Temperature = 741 ± 4 °C (1σ)
(Grey Area = 2σ)
0
20
40
60
80
100
120
140
160
180
200
Duration (s)

Figure 5

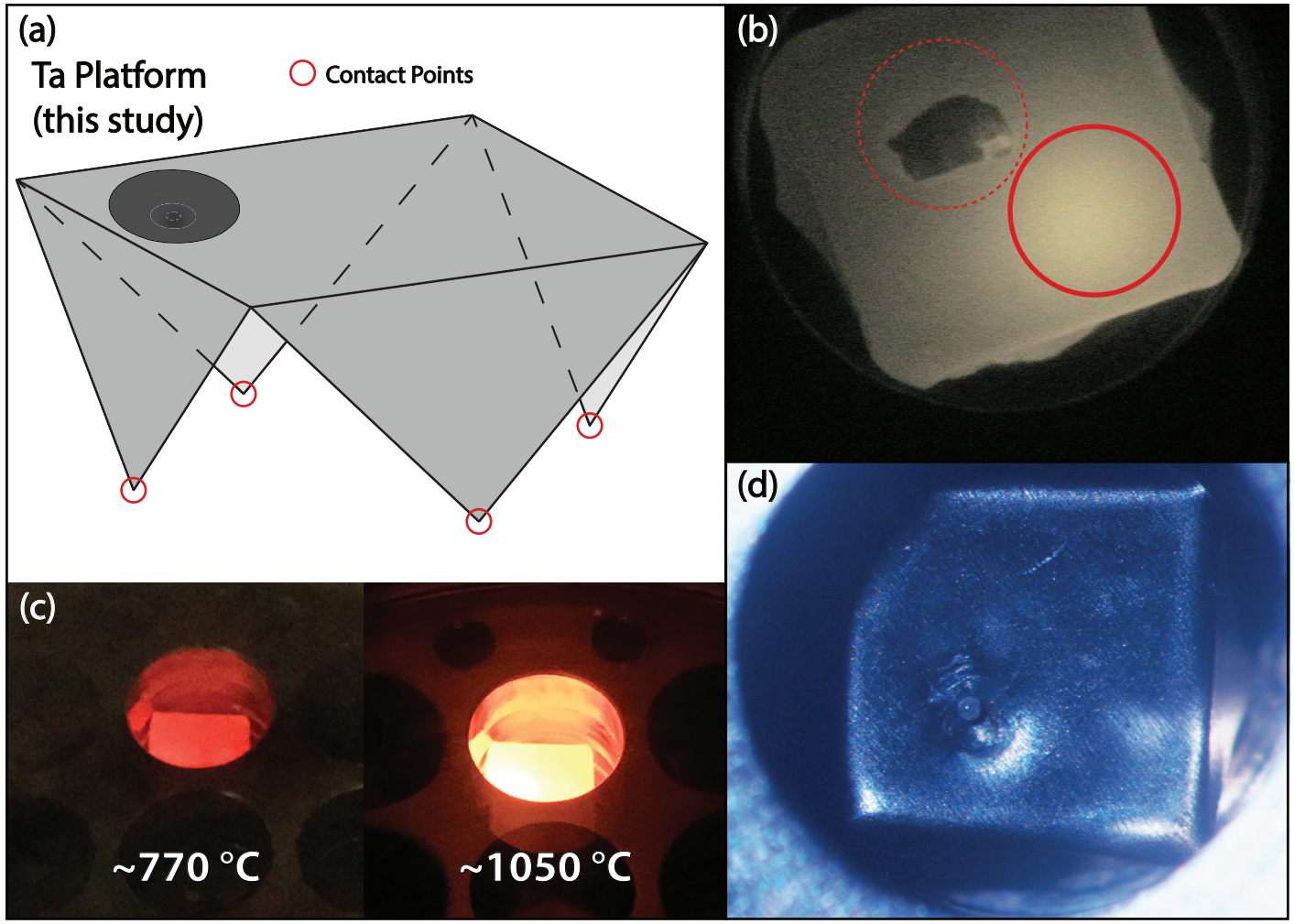

Figure 6

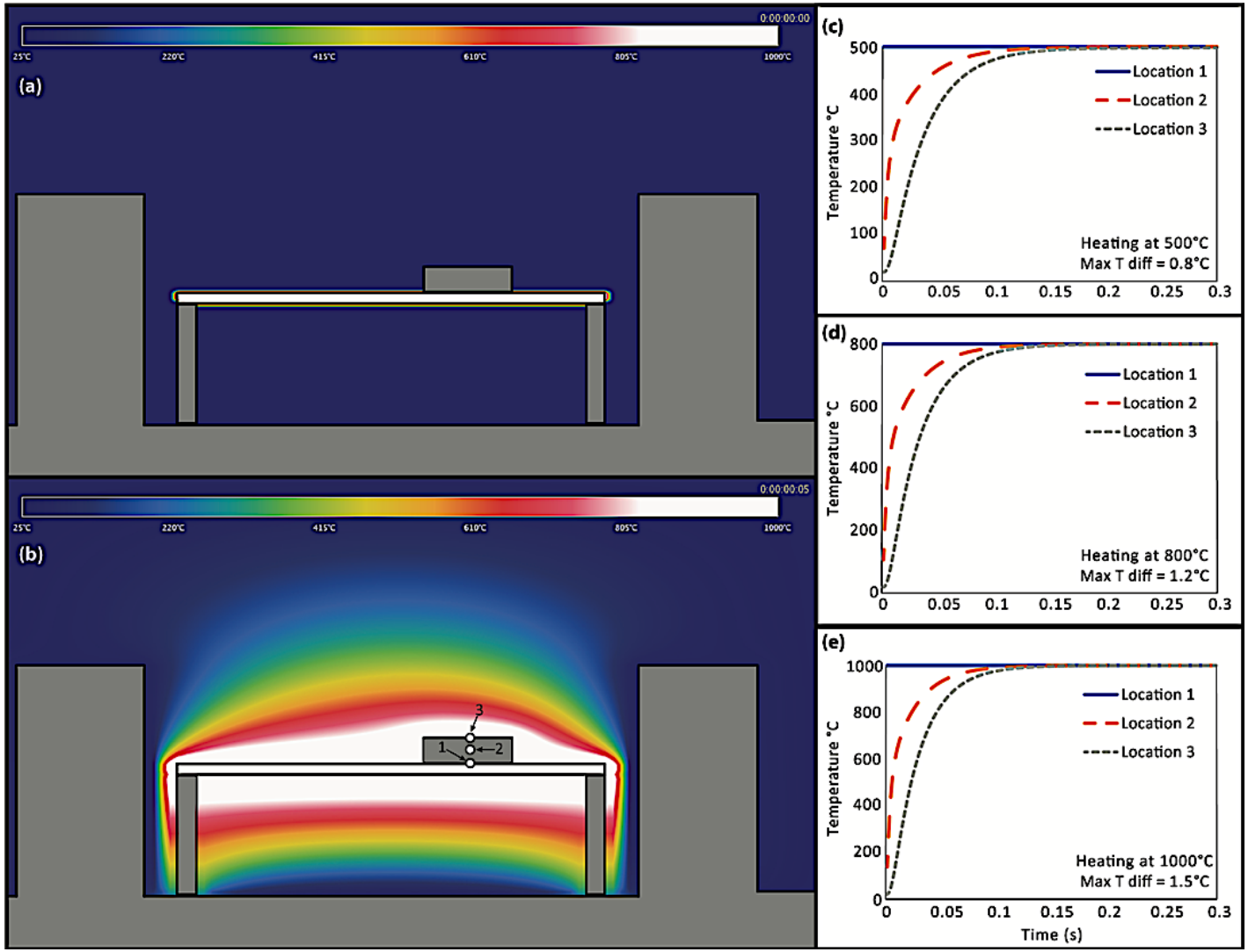
(a)
(b)
(c)
(d)
(e)
Temperature °C
Time (s)
Location 1
Location 2
Location 3
Heating at 500°C
Max T diff = 0.8°C
Heating at 800°C
Max T diff = 1.2°C
Heating at 1000°C
Max T diff = 1.5°C

Figure 7

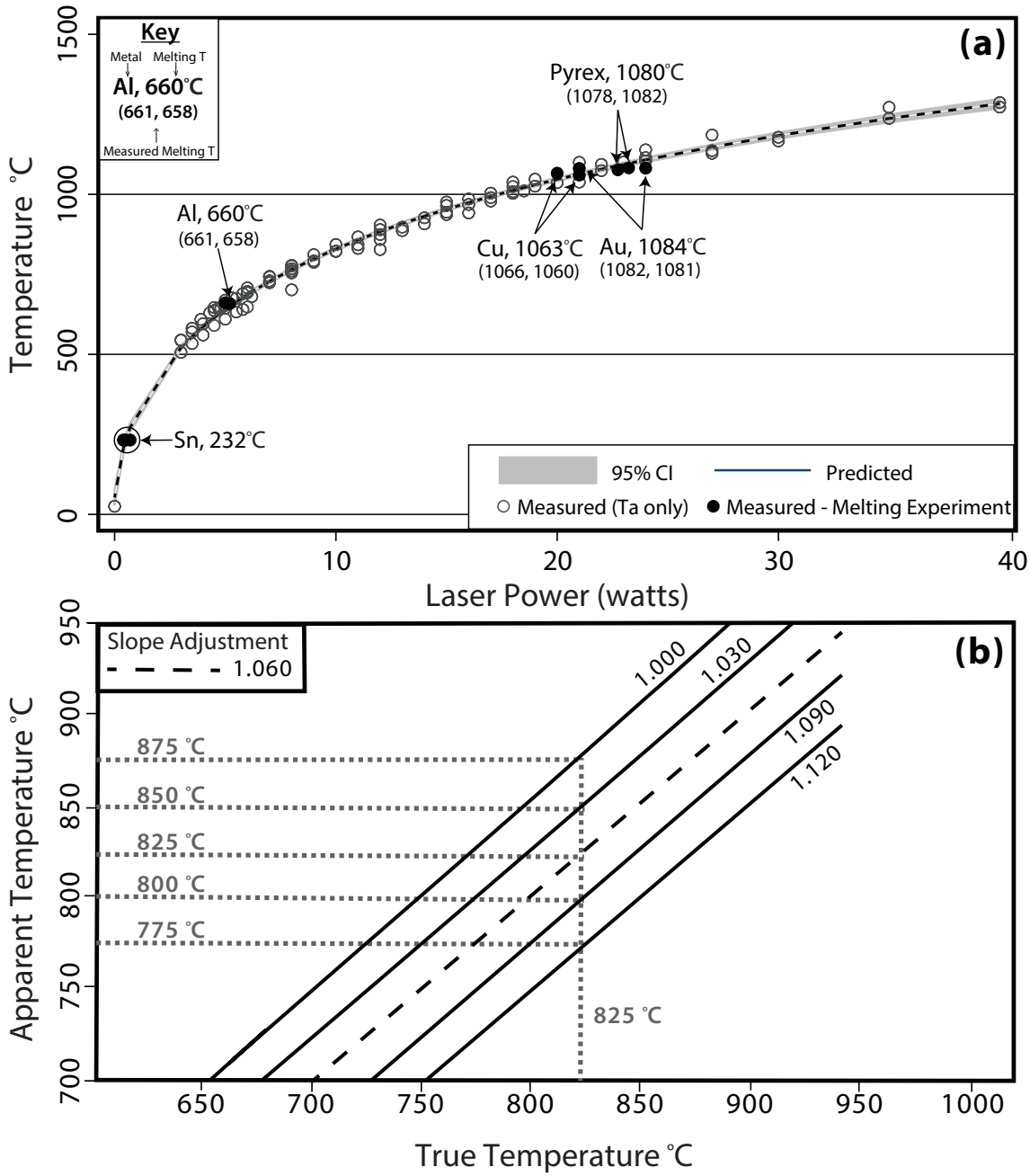
(a)
Key
Metal Melting T
Al, 660°C
(661, 658)
Measured Melting T
Pyrex, 1080°C
(1078, 1082)
Al, 660°C
(661, 658)
Cu, 1063°C
(1066, 1060)
Au, 1084°C
(1082, 1081)
Sn, 232°C
95% CI
Predicted
Measured (Ta only)
Measured - Melting Experiment
Temperature °C
Laser Power (watts)
(b)
Slope Adjustment
1.060
1.000
1.030
1.090
1.120
875 °C
850 °C
825 °C
800 °C
775 °C
825 °C
Apparent Temperature °C
True Temperature °C

Figure 8

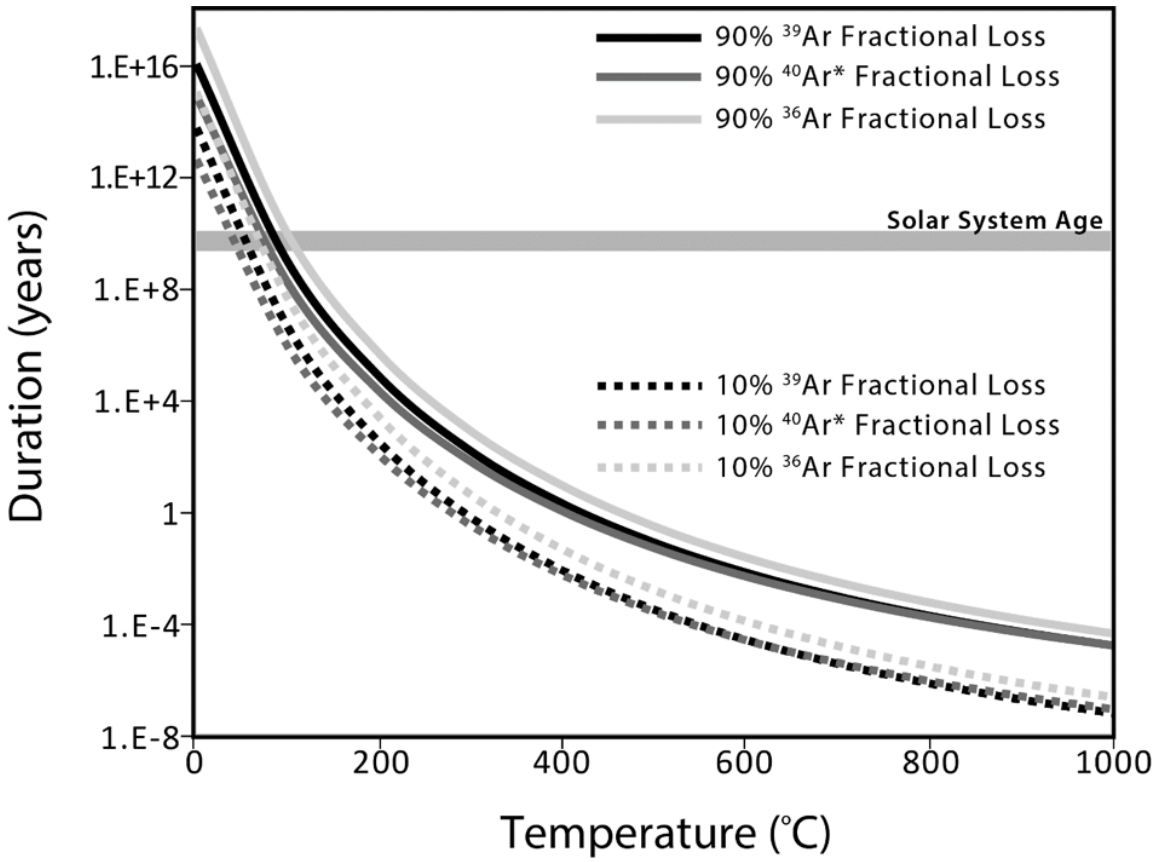
90% 39Ar Fractional Loss
90% 40Ar* Fractional Loss
90% 36Ar Fractional Loss
Solar System Age
10% 39Ar Fractional Loss
10% 40Ar* Fractional Loss
10% 36Ar Fractional Loss
Duration (years)
1.E+16
1.E+12
1.E+8
1.E+4
1
1.E-4
1.E-8
0
200
400
600
800
1000
Temperature (°C)

Figure 9

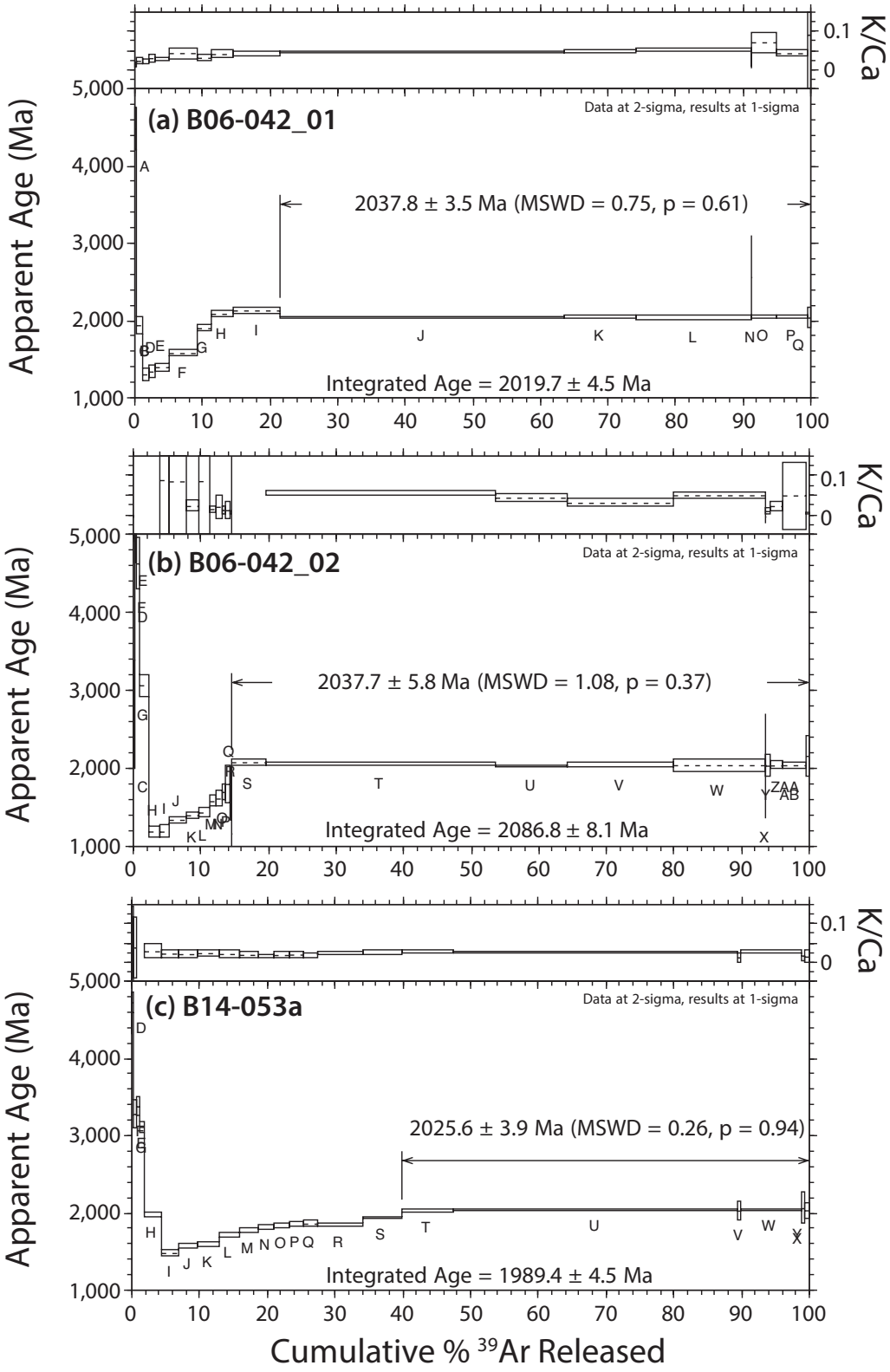
(a) B06-042_01
Data at 2-sigma, results at 1-sigma
2037.8 ± 3.5 Ma (MSWD = 0.75, p = 0.61)
Integrated Age = 2019.7 ± 4.5 Ma
(b) B06-042_02
Data at 2-sigma, results at 1-sigma
2037.7 ± 5.8 Ma (MSWD = 1.08, p = 0.37)
Integrated Age = 2086.8 ± 8.1 Ma
(c) B14-053a
Data at 2-sigma, results at 1-sigma
2025.6 ± 3.9 Ma (MSWD = 0.26, p = 0.94)
Integrated Age = 1989.4 ± 4.5 Ma
Apparent Age (Ma)
K/Ca
Cumulative % 39Ar Released

Figure 10

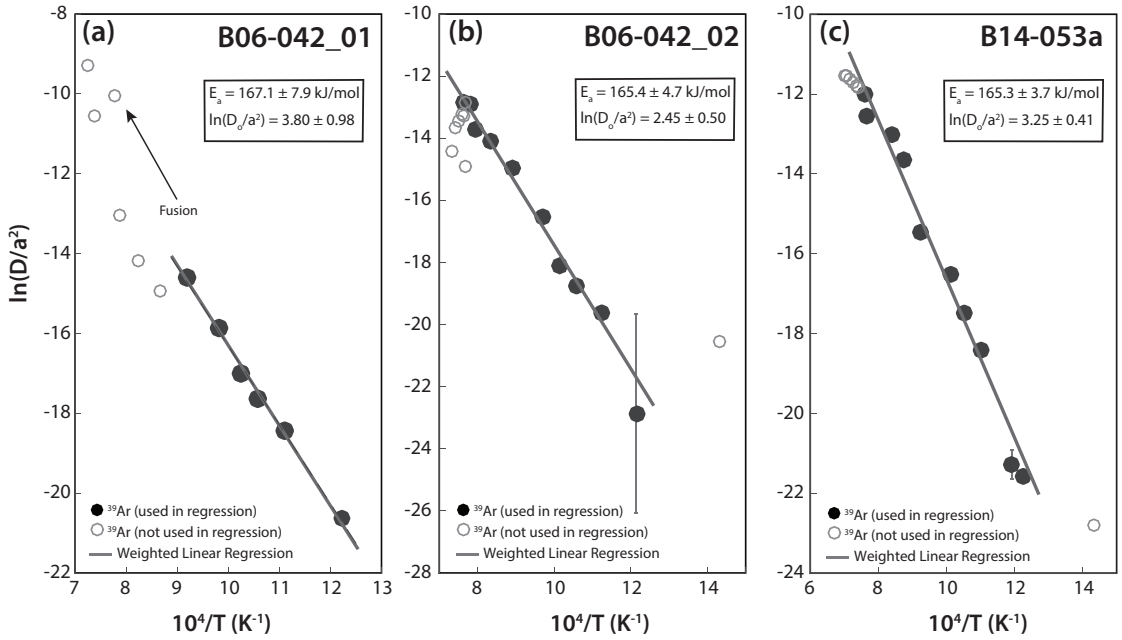
(a)
B06-042_01
E_a = 167.1 ± 7.9 kJ/mol
ln(D_o/a²) = 3.80 ± 0.98
Fusion
(b)
B06-042_02
E_a = 165.4 ± 4.7 kJ/mol
ln(D_o/a²) = 2.45 ± 0.50
(c)
B14-053a
E_a = 165.3 ± 3.7 kJ/mol
ln(D_o/a²) = 3.25 ± 0.41
ln(D/a²)
10^4/T (K^{-1})
^{39}Ar (used in regression)
^{39}Ar (not used in regression)
Weighted Linear Regression

Figure 11

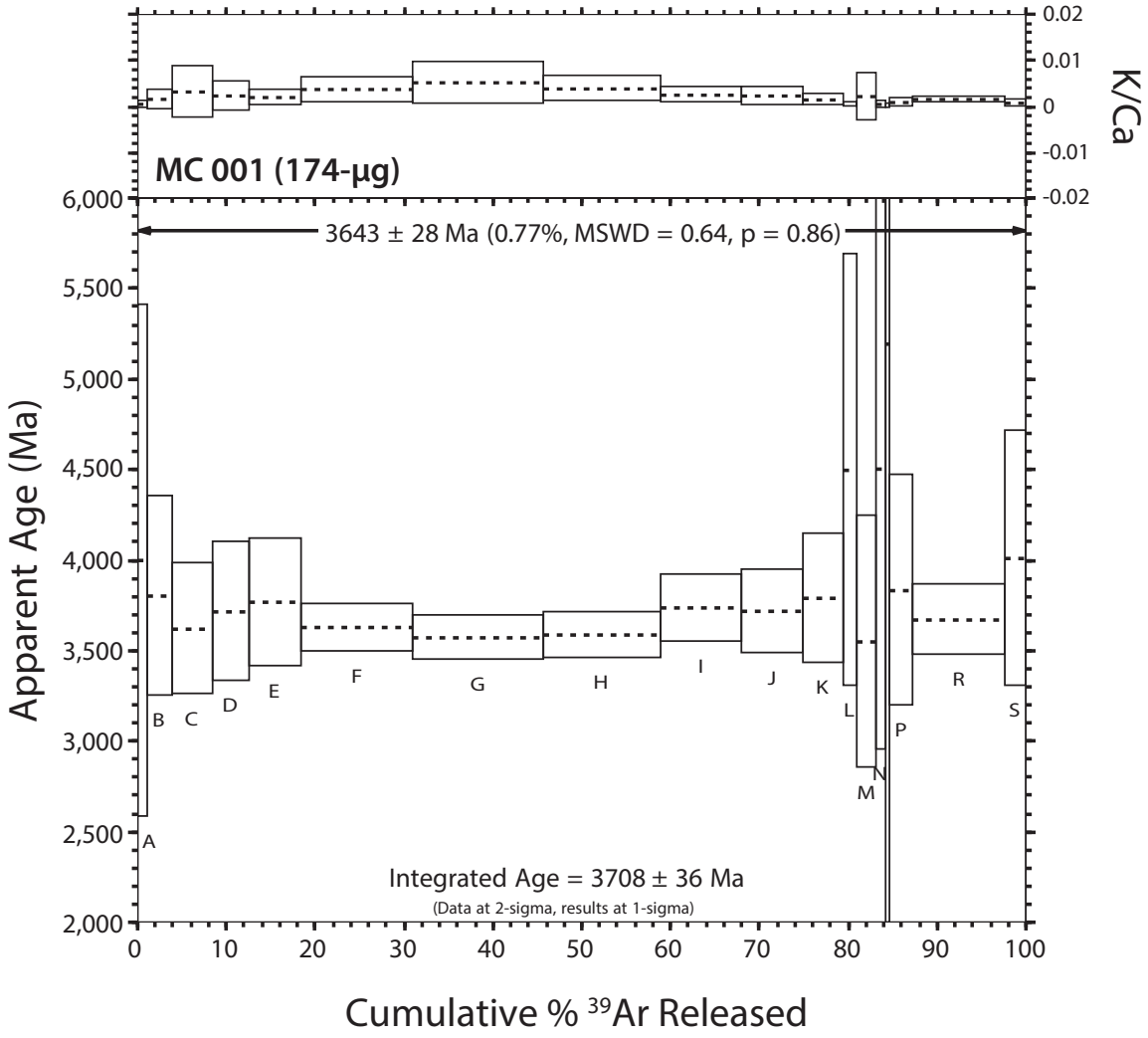
MC 001 (174-µg)
3643 ± 28 Ma (0.77%, MSWD = 0.64, p = 0.86)
Integrated Age = 3708 ± 36 Ma
(Data at 2-sigma, results at 1-sigma)
Apparent Age (Ma)
Cumulative % 39Ar Released
K/Ca
0.02
0.01
0
-0.01
-0.02
6,000
5,500
5,000
4,500
4,000
3,500
3,000
2,500
2,000
0
10
20
30
40
50
60
70
80
90
100
A
B
C
D
E
F
G
H
I
J
K
L
M
N
P
R
S

Figure 12

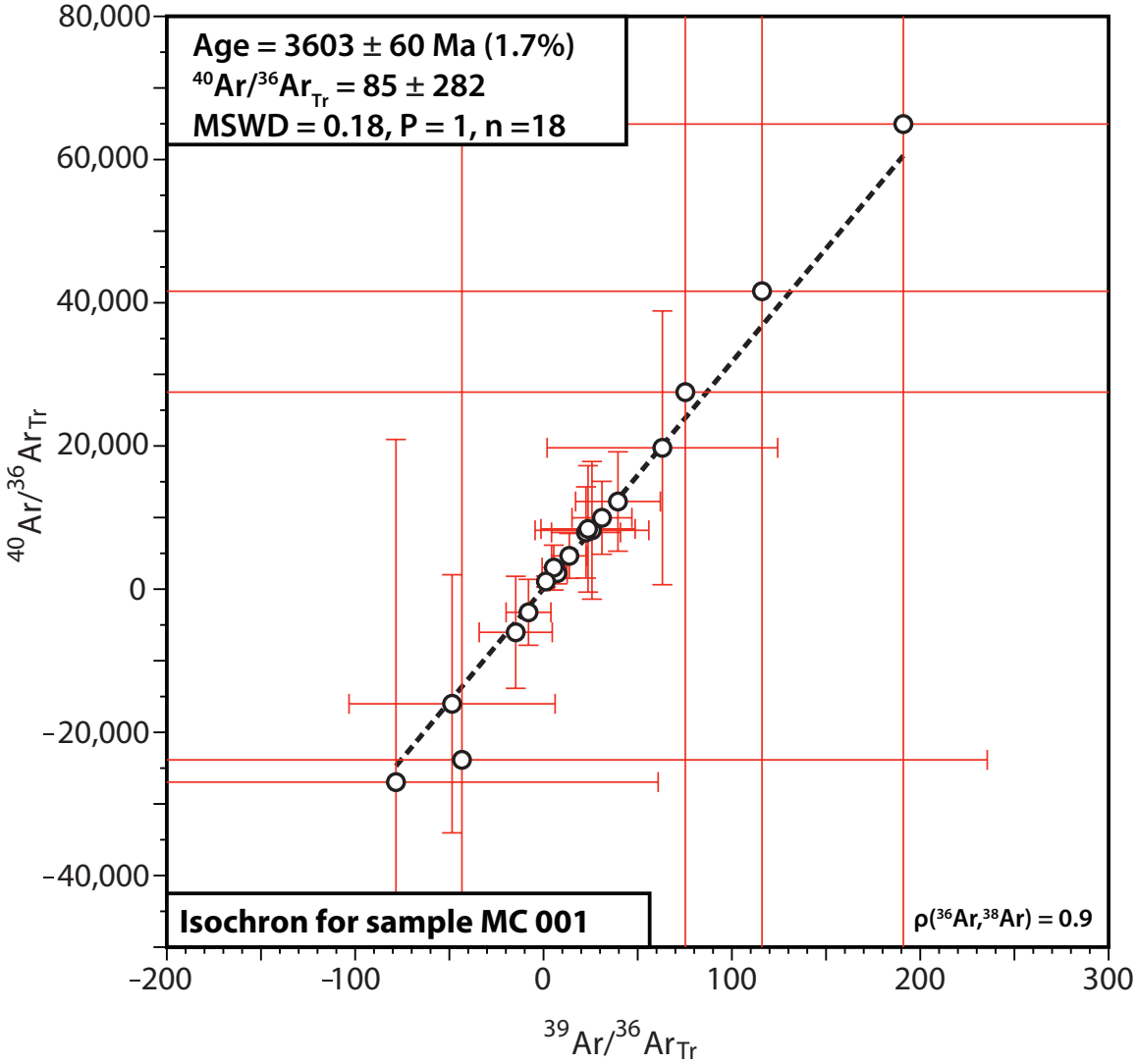
Age = 3603 ± 60 Ma (1.7%)
40Ar/36ArTr = 85 ± 282
MSWD = 0.18, P = 1, n =18
Isochron for sample MC 001
ρ(36Ar,38Ar) = 0.9
80,000
60,000
40,000
20,000
0
-20,000
-40,000
40Ar/36ArTr
-200
-100
0
100
200
300
39Ar/36ArTr

Figure 13

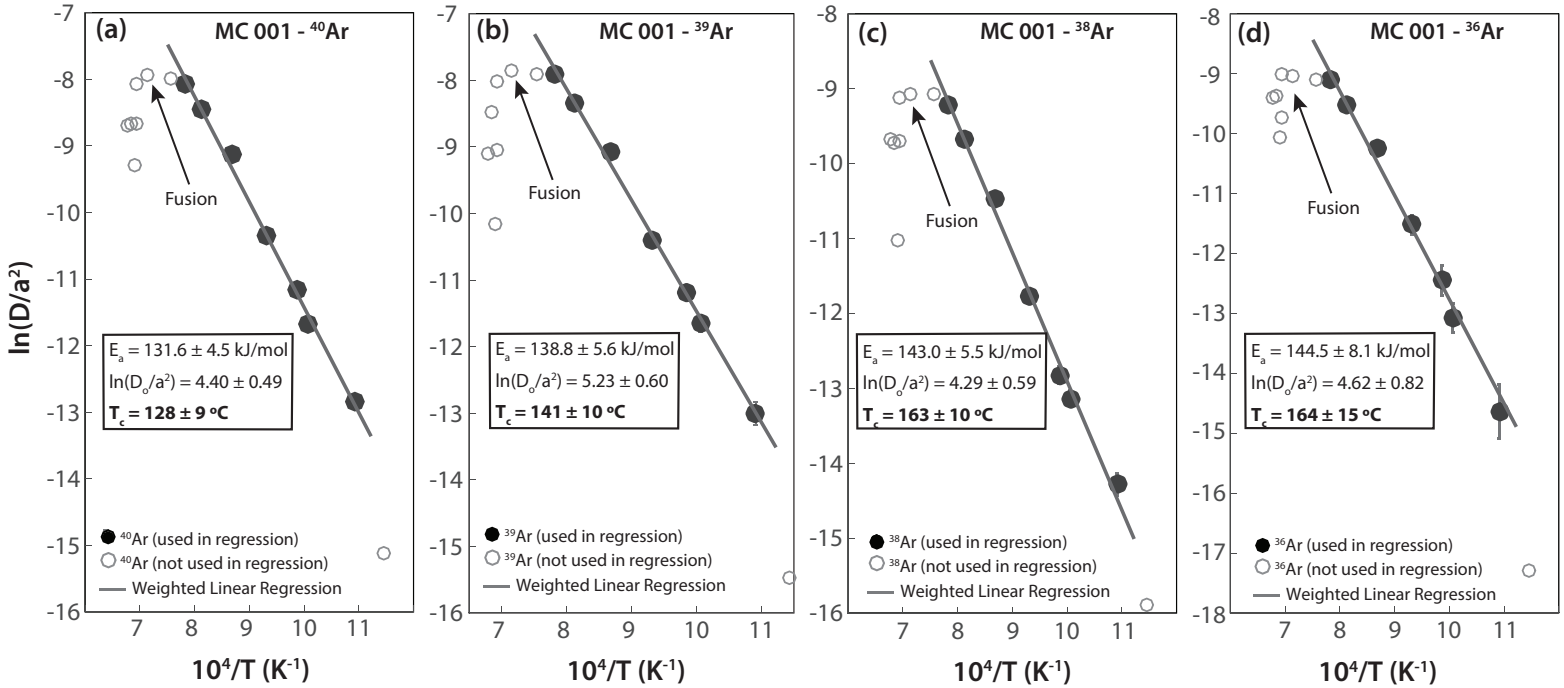
(a)
MC 001 - 40Ar
Fusion
Ea = 131.6 ± 4.5 kJ/mol
ln(Do/a2) = 4.40 ± 0.49
Tc = 128 ± 9 °C
40Ar (used in regression)
40Ar (not used in regression)
Weighted Linear Regression
(b)
MC 001 - 39Ar
Fusion
Ea = 138.8 ± 5.6 kJ/mol
ln(Do/a2) = 5.23 ± 0.60
Tc = 141 ± 10 °C
39Ar (used in regression)
39Ar (not used in regression)
Weighted Linear Regression
(c)
MC 001 - 38Ar
Fusion
Ea = 143.0 ± 5.5 kJ/mol
ln(Do/a2) = 4.29 ± 0.59
Tc = 163 ± 10 °C
38Ar (used in regression)
38Ar (not used in regression)
Weighted Linear Regression
(d)
MC 001 - 36Ar
Fusion
Ea = 144.5 ± 8.1 kJ/mol
ln(Do/a2) = 4.62 ± 0.82
Tc = 164 ± 15 °C
36Ar (used in regression)
36Ar (not used in regression)
Weighted Linear Regression
ln(D/a2)
10^4/T (K^-1)

Figure 14

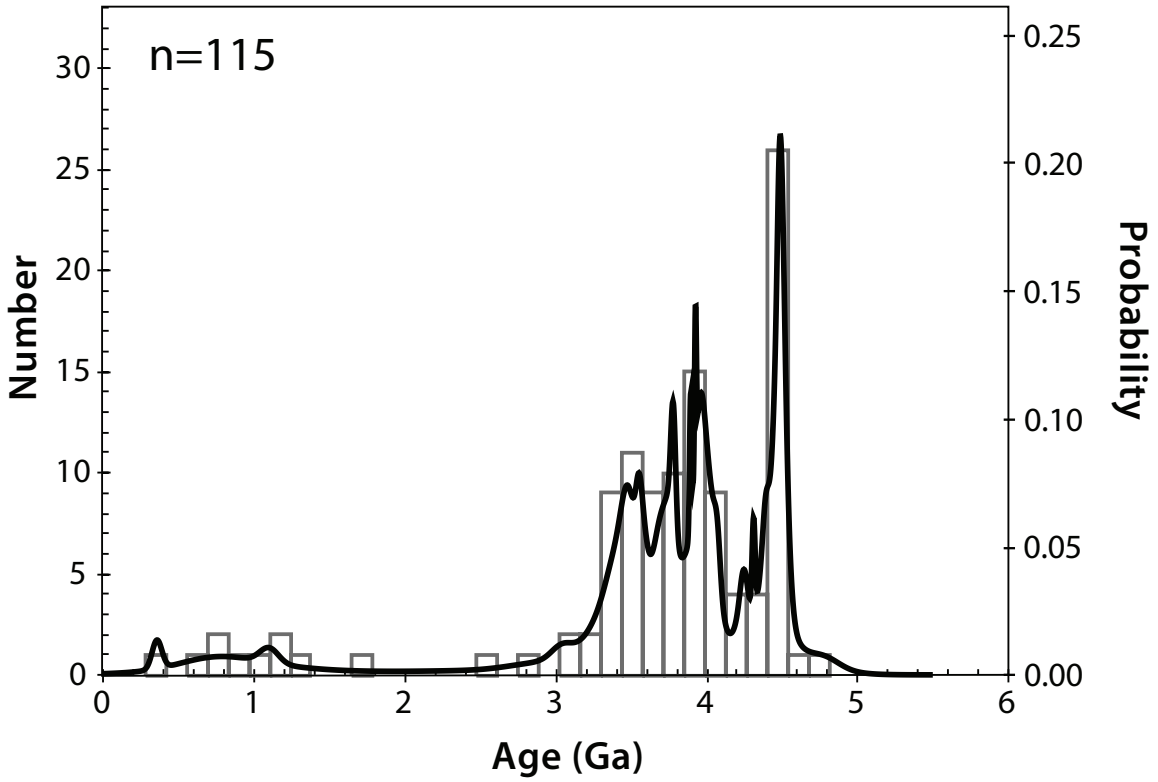
n=115
Number
Probability
Age (Ga)
0
5
10
15
20
25
30
0.00
0.05
0.10
0.15
0.20
0.25
0
1
2
3
4
5
6

Figure 15

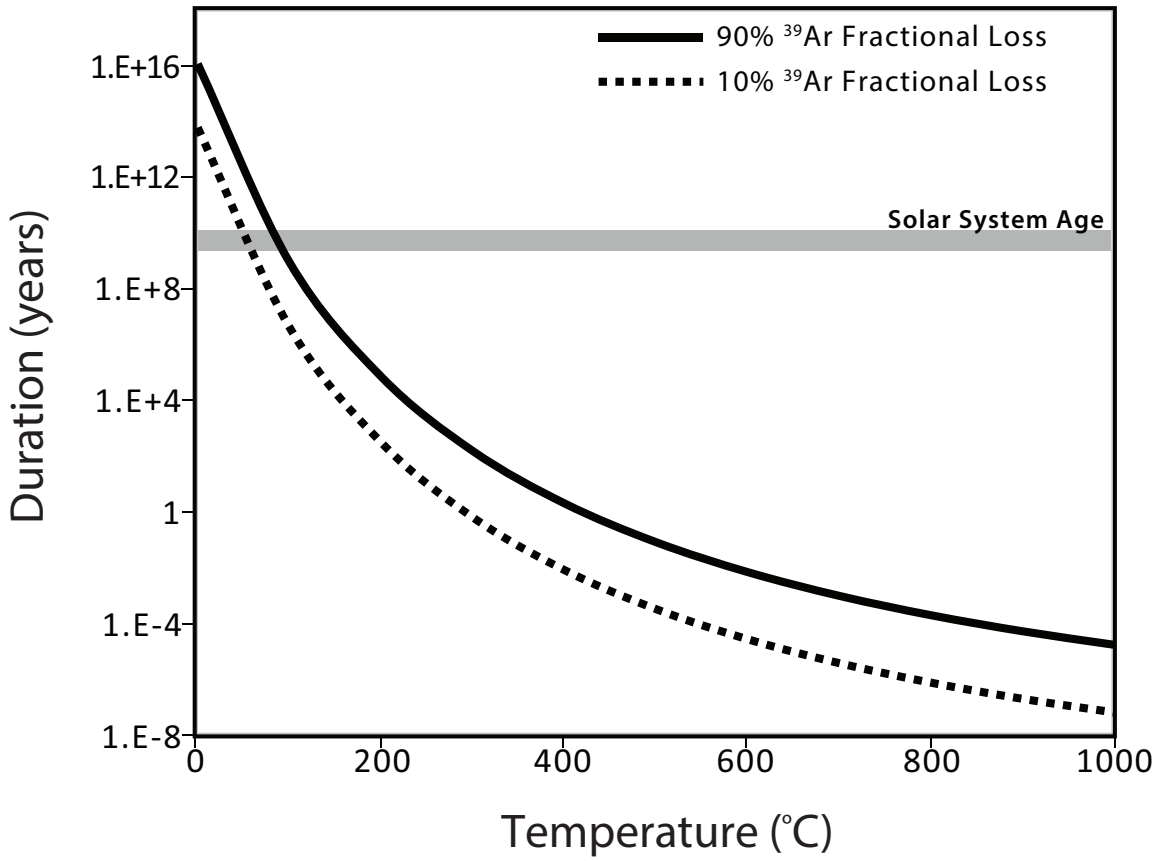
90% 39Ar Fractional Loss
10% 39Ar Fractional Loss
Solar System Age
Duration (years)
1.E+16
1.E+12
1.E+8
1.E+4
1
1.E-4
1.E-8
0
200
400
600
800
1000
Temperature (°C)

Table 1
Electron microprobe, major element compositions (wt. %) of the samples dated in this study.

Oxide	**MC 001 (Px)**	**MC 001 (Pl)**	**B06-042**	**B14-053a**
SiO_2	50.1	45.8	54.32	51.70
TiO	0.15	0.02	n.a.	n.a.
Al_2O_3	0.19	35.3	28.79	31.15
Cr_2O_3	n.a.	n.a.	b.d.	b.d.
FeO	34.4	0.42	0.24	0.34
MnO	n.a.	n.a.	b.d.	b.d.
MgO	11.4	0.02	b.d.	0.01
CaO	3.28	17.8	10.88	13.64
Na_2O	0.03	1.20	4.93	3.47
K_2O	0.02	0.08	0.38	0.23
Total	99.6	100.6	99.52	100.55
	Endmember Compositions			
% An or En	34.0	88.7	53.7	67.5
% Ab or Fs	59.0	10.8	44.0	31.1
% Or or Wo	7.0	0.5	2.2	1.4

Table 2
Estimated temperatures versus laser power for temperature steps below 500 °C, the lower limit of the pyrometer temperature measurements.

Laser Power (W)	Predicted Temperature (°C)
0.2	146±13
0.3	182±12
0.4	212±11
0.5	237±10
0.6	259±9
0.7	279±9
0.8	297±8
0.9	314±8
1.0	329±7
1.1	344±7
1.2	357±7
1.3	370±6
1.4	382±6
1.5	394±6
1.6	405±6
1.7	416±5
1.8	426±5
1.9	436±5
2.0	445±5
2.1	454±5
2.2	463±5
2.3	472±4
2.4	480±4
2.5	488±4
2.6	486±4

Table 3
Three separate hot blank measurements at varying heating durations and typical cold blank measurements.

RunID H22913	Power [W]	T [°C]	*t* [s]	^{40}Ar	^{39}Ar	^{38}Ar	^{37}Ar	^{36}Ar
01A	3.5	575	120	43.1	0.477	0.174	2.42	0.366
01B	10	797	120	42.0	0.752	0.181	2.44	0.351
01C	24	1054	120	45.8	0.852	0.076	2.31	0.390
02A	3.5	566	180	46.4	0.833	0.144	2.61	0.341
02B	10	795	180	44.1	0.439	0.176	2.54	0.346
02C	24	1047	180	40.6	0.155	0.077	2.64	0.308
03A	3.5	567	300	43.0	1.160	0.034	2.47	0.255
03B	10	802	300	38.9	0.130	0.127	2.36	0.269
03C	24	1048	300	47.9	0.505	0.074	2.74	0.364
Cold	-	20	-	43.6±8.2	0.90±0.49	0.11±0.03	2.39±0.15	0.32±0.03

Note. Power=laser power; T=temperature; *t*=duration of heating; Isotope measurements in moles x 10^{-17}; Spectrometer sensitivity is *c*. 7.60 x 10^{-12} mol/nA; n=7 for cold blank.

Table 4
Stepwise heating results of B06-042_01: moles of each isotope for each heating step. W is laser power in watts. J = 0.0199108 ± 0.0000394.

Run ID	W	^{36}Ar (±) 1E-18 mol	$^{37}Ar_{Ca}$ (±) 1E-15 mol	^{38}Ar (±) 1E-18 mol	$^{39}Ar_{K}$ (±) 1E-17 mol	^{40}Ar (±) 1E-15 mol	^{40}Ar* (±) 1E-15 mol	Age (Ma) (±)
22459-01A	3.5	16.36 (0.59)	3.15 (0.82)	26.33 (0.71)	6.30 (0.51)	39.59 (0.26)	34.71 (0.19)	4480 (130)
22459-01B	5.2	8.40 (0.53)	4.03 (0.88)	8.51 (0.53)	13.53 (0.62)	15.56 (0.23)	13.05 (0.16)	1933 (57)
22459-01C	6.5	5.58 (0.49)	4.45 (0.76)	1.08 (0.44)	14.68 (0.59)	9.42 (0.21)	7.75 (0.15)	1296 (42)
22459-01D	7.5	5.79 (0.49)	3.58 (0.79)	0.59 (0.44)	17.09 (0.67)	11.11 (0.21)	9.39 (0.15)	1333 (41)
22459-01E	9	5.72 (0.52)	7.66 (0.81)	0.06 (0.51)	33.15 (0.82)	21.03 (0.22)	19.32 (0.16)	1390 (25)
22459-01F	12	11.56 (0.54)	6.36 (0.83)	5.63 (0.65)	67.19 (1.14)	50.35 (0.24)	46.90 (0.17)	1572 (18)
22459-01G	15	7.83 (0.76)	5.71 (0.79)	2.81 (0.55)	32.82 (0.50)	32.95 (0.32)	30.61 (0.23)	1894 (20)
22459-01H	17.5	12.15 (0.56)	6.94 (0.79)	4.37 (0.59)	53.13 (0.94)	61.47 (0.24)	57.84 (0.17)	2080 (22)
22459-01I	20	13.41 (0.60)	14.20 (0.97)	8.66 (0.81)	114.70 (1.56)	133.20 (0.26)	129.20 (0.19)	2123 (17)
22459-01J	22	18.63 (0.89)	81.10 (1.74)	49.18 (1.29)	681.50 (4.34)	719.66 (0.47)	714.10 (0.38)	2033.2 (6.6)
22459-01K	29.5	16.15 (0.61)	18.68 (0.83)	9.60 (0.70)	170.80 (1.27)	184.62 (0.53)	179.80 (0.50)	2038.5 (8.8)
22459-01L	38	21.54 (0.72)	28.75 (0.92)	26.50 (1.15)	279.54 (3.29)	299.52 (0.32)	293.05 (0.24)	2034 (14)
22459-01M	1.5	-	-	-	-	-	-	-
22459-01N	3	5.70 (0.48)	1.54 (0.86)	0.32 (0.38)	0.90 (0.14)	3.10 (0.20)	1.40 (0.14)	2550 (270)
22459-01O	5	7.93 (0.49)	4.23 (0.79)	2.87 (0.53)	57.89 (0.41)	63.51 (0.25)	61.14 (0.20)	2042.8 (8.7)
22459-01P	6	7.64 (0.54)	9.61 (0.85)	5.88 (0.63)	77.76 (0.43)	84.18 (0.25)	81.90 (0.19)	2039.4 (6.1)
22459-01Q	6	6.04 (0.45)	0.23 (0.83)	1.13 (0.38)	3.96 (0.14)	5.95 (0.19)	4.14 (0.14)	2031 (65)

Table 5
Stepwise heating results of B06-042_02: moles of each isotope for each heating step. W is laser power in watts. J = 0.0199108 ± 0.0000394.

Run ID	W	^{36}Ar (±) 1E-18 mol	$^{37}Ar_{Ca}$ (±) 1E-15 mol	^{38}Ar (±) 1E-18 mol	$^{39}Ar_{K}$ (±) 1E-17 mol	^{40}Ar (±) 1E-15 mol	^{40}Ar* (±) 1E-15 mol	Age (Ma) (±)
22459-02A	1.8	18.65 (0.91)	-	41.18 (0.96)	2.08 (0.29)	63.99 (0.39)	58.42 (0.28)	7300 (250)
22459-02B	3.5	0.56 (0.82)	1.60 (2.32)	1.15 (0.44)	0.10 0.31)	0.23 (0.35)	0.06 (0.25)	1500 (6000)
22459-02C	5.2	4.39 (1.18)	-	8.03 (0.56)	1.77 (0.30)	4.36 (0.50)	3.05 (0.35)	2700 (350)
22459-02D	6.5	7.19 (1.07)	-	15.22 (0.65)	2.41 (0.30)	16.83 (0.45)	14.68 (0.32)	4600 (230)
22459-02E	7.5	10.86 (1.18)	-	18.56 (0.77)	3.02 (0.30)	26.05 (0.50)	22.81 (0.35)	5010 (190)
22459-02F	9	23.06 (2.87)	-	40.85 (1.09)	8.63 (0.70)	58.63 (1.21)	51.75 (0.86)	4620 (160)
22459-02G	12	13.95 (1.22)	-	30.79 (0.85)	19.71 (0.88)	48.19 (0.53)	44.02 (0.39)	3058 (69)
22459-02H	15	2.36 (1.28)	-	3.29 (0.62)	25.47 (0.35)	12.58 (0.54)	11.88 (0.38)	1185 (36)
22459-02I	17.5	0.08 (1.35)	1.48 (4.05)	1.13 (0.58)	25.33 (0.41)	11.81 (0.57)	11.79 (0.41)	1183 (39)
22459-02J	20	2.20 (1.00)	2.32 (2.46)	3.35 (0.62)	38.26 (0.40)	21.70 (0.42)	21.04 (0.30)	1334 (18)
22459-02K	22	-	7.49 (2.57)	0.87 (0.58)	30.72 (0.35)	17.81 (0.45)	17.95 (0.32)	1392 (23)
22459-02L	23.5	-	1.54 (2.73)	-	25.54 (0.36)	15.44 (0.45)	15.48 (0.32)	1428 (28)
22459-02M	25	-	5.83 (2.03)	0.22 (0.55)	14.77 (0.25)	10.07 (0.34)	10.32 (0.24)	1573 (35)
22459-02N	27	-	3.84 (3.05)	0.04 (0.55)	14.19 (0.30)	9.82 (0.47)	10.24 (0.33)	1607 (50)
22459-02O	29.2	-	4.90 (2.00)	1.32 (0.51)	10.35 (0.23)	7.72 (0.38)	8.07 (0.27)	1691 (51)
22459-02P	31	-	4.02 (4.64)	0.68 (0.56)	8.02 (0.44)	6.57 (0.61)	6.86 (0.43)	1790 (120)
22459-02Q	33.5	-	5.53 (2.88)	0.09 (0.44)	3.66 (0.27)	2.53 (0.40)	2.80 (0.28)	1670 (170)
22459-02R	38	0.28 (0.92)	-	0.42 (0.46)	2.20 (0.31)	1.07 (0.39)	0.99 (0.27)	1150 (300)
22459-02S	1.5	11.78 (2.27)	-	12.98 (0.88)	81.03 (0.74)	91.14 (0.96)	87.62 (0.68)	2072 (19)
22459-02T	1.8	16.56 (1.03)	50.40 (2.38)	32.12 (1.26)	546.06 (5.05)	585.83 (0.55)	580.91 (0.45)	2052 (10)
22459-02U	2	2.19 (0.91)	20.67 (2.33)	13.54 (0.80)	170.50 (1.39)	177.45 (0.41)	176.75 (0.31)	2020.5 (9.0)
22459-02V	2.2	-	44.26 (7.23)	11.32 (3.59)	252.73 (3.94)	264.59 (0.92)	265.84 (0.65)	2038 (19)
22459-02W	2.5	0.50 (1.50)	22.91 (1.97)	8.51 (10.36)	218.38 (7.36)	229.16 (0.34)	229.02 (0.26)	2034 (41)
22459-02X	2.7	1.50 (1.02)	-	0.11 (0.56)	2.84 (0.67)	3.39 (0.43)	2.94 (0.30)	2020 (340)
22459-02Y	3	-	5.62 (2.90)	1.37 (0.51)	8.64 (0.27)	9.01 (0.42)	9.02 (0.30)	2028 (70)
22459-02Z	4	0.87 (0.86)	7.64 (2.28)	3.21 (0.55)	31.09 (0.55)	32.78 (0.39)	32.52 (0.30)	2031 (25)

22459-02AA	5	2.40 (1.70)	6.00 (5.38)	2.23 (1.32)	56.35 (0.54)	59.79 (1.02)	59.07 (0.52)	2034 (19)
22459-02AB	6	-	7.45 (2.90)	0.17 (0.16)	4.37 (0.26)	4.91 (0.59)	5.05 (0.30)	2150 (130)

Table 6
Stepwise heating results of B14-053a: moles of each isotope for each heating step. W is laser power in watts. J = 0.0199458 ± 0.000040.

Run ID	W	^{36}Ar (±) 1E-18 mol	$^{37}Ar_{Ca}$ (±) 1E-15 mol	^{38}Ar (±) 1E-18 mol	$^{39}Ar_{K}$ (±) 1E-17 mol	^{40}Ar (±) 1E-15 mol	^{40}Ar* (±) 1E-15 mol	Age (Ma) (±)
22458-01A	3.5	4.13 (0.63)	-	19.12 (0.72)	1.17 (0.16)	15.75 (0.28)	14.52 (0.21)	5870 (240)
22458-01B	1.8	-	0.03 (0.82)	0.16 (0.60)	0.16 (0.41)	0.10 (0.35)	0.41 (0.25)	3300 (4000)
22458-01C	3.5	-	0.91 (0.76)	1.01 (0.62)	0.58 (0.21)	1.20 (0.34)	1.32 (0.25)	3090 (620)
22458-01D	5.2	5.10 (0.85)	-	24.48 (0.84)	4.14 (0.16)	27.84 (0.37)	26.32 (0.27)	4720 (69)
22458-01E	6.5	3.33 (0.85)	0.68 (0.74)	14.36 (0.66)	4.86 (0.27)	13.51 (0.36)	12.52 (0.26)	3274 (92)
22458-01F	7.5	7.70 (1.36)	-	14.21 (0.80)	7.43 (0.22)	22.72 (0.59)	20.42 (0.42)	3371 (57)
22458-01G	9	6.69 (0.82)	-	26.26 (0.90)	12.57 (0.26)	30.96 (0.36)	28.96 (0.26)	3106 (34)
22458-01H	12	2.18 (0.94)	7.28 (2.56)	21.57 (0.72)	37.82 (0.32)	37.96 (0.40)	37.31 (0.29)	1963 (15)
22458-01I	15	-	9.67 (2.62)	2.58 (0.51)	38.62 (0.34)	24.15 (0.40)	24.49 (0.28)	1475 (17)
22458-01J	17.5	-	11.36 (2.64)	1.88 (0.49)	42.37 (0.38)	28.55 (0.40)	29.13 (0.28)	1558 (16)
22458-01K	21	-	12.07 (2.61)	-	51.12 (0.58)	36.24 (0.40)	36.37 (0.29)	1594 (16)
22458-01L	22	-	12.12 (2.58)	0.40 (0.53)	45.92 (0.33)	35.98 (0.41)	36.13 (0.30)	1702 (14)
22458-01M	23.5	-	11.99 (2.61)	-	40.18 (0.33)	32.72 (0.41)	33.23 (0.29)	1758 (15)
22458-01N	25	-	13.74 (2.91)	0.91 (0.50)	36.07 (0.31)	30.78 (0.44)	31.21 (0.31)	1809 (18)
22458-01O	27	-	10.58 (2.60)	0.59 (0.51)	34.59 (0.33)	30.01 (0.40)	30.36 (0.28)	1826 (18)
22458-01P	29.2	-	9.92 (2.59)	0.25 (0.49)	34.57 (0.32)	31.05 (0.41)	31.09 (0.29)	1854 (18)
22458-01Q	31	-	10.84 (2.59)	0.87 (0.63)	30.59 (0.30)	27.42 (0.40)	27.52 (0.29)	1854 (19)
22458-01R	1.5	0.25 (1.03)	24.21 (2.70)	4.47 (0.63)	103.60 (0.60)	92.06 (0.46)	91.98 (0.34)	1838.9 (7.5)
22458-01S	1.7	-	19.03 (2.62)	7.14 (0.68)	88.67 (0.52)	84.71 (0.43)	84.77 (0.31)	1925.2 (7.9)
22458-01T	1.9	1.54 (1.02)	23.10 (2.61)	21.21 (0.80)	115.30 (0.63)	120.06 (0.44)	119.60 (0.32)	2022.8 (6.5)
22458-01U	2.1	8.57 (1.10)	134.04 (2.86)	14.65 (0.53)	643.67 (4.10)	670.43 (0.49)	667.88 (0.36)	2023.4 (6.3)
22458-01V	2.3	0.43 (0.96)	4.42 (2.53)	1.19 (0.49)	9.17 (0.24)	9.64 (0.41)	9.51 (0.29)	2023 (60)
22458-01W	3	3.43 (0.88)	27.81 (2.56)	13.95 (0.80)	137.60 (0.96)	144.92 (0.40)	143.90 (0.29)	2033.0 (7.9)
22458-01X	4	0.07 (0.85)	4.98 (2.53)	-	5.80 (0.33)	6.20 (0.36)	6.18 (0.26)	2060 (100)
22458-01Y	5	0.79 (0.83)	4.00 (2.53)	1.23 (0.45)	9.84 (0.24)	10.48 (0.35)	10.24 (0.25)	2027 (52)

Table 7
Stepwise heating results of the mafic clast from howardite, MAC 02666: moles of each isotope for each heating step. W is laser power in watts. J = 0.0020122 ± 0.0000463.

Run ID	W	^{36}Ar (±) 1E-18 mol	$^{37}Ar_{Ca}$ (±) 1E-15 mol	^{38}Ar (±) 1E-18 mol	$^{39}Ar_{K}$ (±) 1E-17 mol	^{40}Ar* (±) 1E-15 mol	Age (Ma) (±)
22413-01A	3.8	0.66 (0.85)	4.97 (2.63)	1.94 (0.42)	0.48 (0.21)	1.95 (0.02)	3996 (710)
22413-01B	5.2	1.93 (0.86)	3.99 (2.65)	2.82 (0.40)	1.22 (0.21)	4.39 (0.02)	3800 (280)
22413-01C	6.5	3.42 (0.85)	3.03 (2.59)	4.27 (0.45)	1.88 (0.22)	6.00 (0.02)	3620 (180)
22413-01D	7.5	3.48 (0.85)	3.85 (2.62)	3.64 (0.42)	1.73 (0.21)	5.87 (0.02)	3710 (190)
22413-01E	9	5.44 (0.87)	6.43 (2.64)	6.90 (0.43)	2.47 (0.27)	8.66 (0.03)	3770 (180)
22413-01F	12	11.00 (0.88)	7.29 (2.61)	14.62 (0.57)	5.29 (0.22)	16.98 (0.02)	3626 (65)
22413-01G	15	13.33 (0.89)	6.07 (2.61)	18.41 (0.63)	6.13 (0.24)	19.00 (0.03)	3569 (60)
22413-01H	17.5	12.94 (0.87)	7.47 (2.61)	18.71 (0.55)	5.59 (0.23)	17.49 (0.02)	3585 (63)
22413-01I	20	9.48 (0.87)	7.91 (2.63)	15.33 (0.52)	3.82 (0.22)	13.14 (0.02)	3734 (92)
22413-01J	22.5	8.05 (0.86)	6.54 (2.60)	12.18 (0.55)	2.94 (0.21)	9.98 (0.02)	3720 (120)
22413-01K	25	6.93 (0.85)	6.83 (2.63)	9.57 (0.45)	1.92 (0.22)	6.83 (0.02)	3790 (180)
22413-01L	25	2.96 (0.86)	6.70 (2.62)	4.76 (0.40)	0.59 (0.21)	3.22 (0.05)	4490 (600)
22413-01M	28	3.95 (0.85)	2.23 (2.59)	4.34 (0.40)	0.94 (0.21)	2.88 (0.05)	3550 (350)
22413-01N	31	3.45 (0.85)	4.97 (2.63)	4.20 (0.42)	0.45 (0.21)	2.47 (0.05)	4500 (780)
22413-01O	38	1.70 (0.84)	4.57 (2.61)	1.03 (0.38)	0.15 (0.21)	1.25 (0.05)	5200 (2400)
22413-01P	1	8.14 (0.86)	6.24 (2.62)	12.33 (0.55)	1.07 (0.21)	3.90 (0.05)	3830 (320)
22413-01R	3	43.47 (1.03)	14.58 (2.67)	68.27 (0.95)	4.40 (0.27)	14.50 (0.05)	3668 (97)
22413-01S	6	4.38 (0.85)	6.73 (2.64)	7.74 (0.50)	0.96 (0.21)	3.94 (0.05)	4010 (350)

Table 8
Values of (D/a^2) calculated during step-heating of plagioclase samples from the Bushveld Complex. D/a^2 is stripped of dimensions for taking the logarithm. Bold values indicate steps included in Arrhenius regression. At the conclusion of indirect heating steps, the sample was heated directly with the laser to an unknown temperature for 8 additional periods of 60 s. During direct heating, the pyrometer is focused on the sample and not the Ta-platform. As such, these temperatures are not measured. Laser power settings for additional direct heating steps are found in table 4.

Sample	Run ID	Temperature (°C)	Duration (s)	^{39}Ar $\ln(D/a^2)$	^{37}Ar $\ln(D/a^2)$
B06-042_01	**22459-01A**	544	1200	**-20.63±0.08**	**-19.14±0.26**
	22459-01B	628	1200	**-18.44±0.05**	**-16.85±0.22**
	22459-01C	672	1200	**-17.62±0.04**	**-15.74±0.17**
	22459-01D	603	1200	**-17.00±0.04**	**-15.61±0.22**
	22459-01E	745	1200	**-15.86±0.02**	**-14.52±0.11**
	22459-01F	815	1200	**-14.58±0.02**	-14.48±0.13
	22459-01G	883	1200	-14.92±0.02	-14.54±0.14
	22459-01H	941	1200	-14.19±0.02	-14.23±0.11
	22459-01I	996	1200	-13.03±0.01	-13.24±0.07
	22459-01J	1011	1200	-10.04±0.01	-10.40±0.02
	22459-01K	1083	1200	-10.54±0.01	-11.01±0.04
	22459-01L	1109	1200	-9.29±0.01	-9.85±0.03

Sample	Run ID	Temperature (°C)	Duration (s)	^{39}Ar $\ln(D/a^2)$
B06-042_02	**22459-02A**	425	120	-20.53±0.13
	22459-02B	548	120	**-22.9±3.2**
	22459-02C	617	120	**-19.61±0.17**
	22459-02D	673	120	**-18.78±0.13**
	22459-02E	714	120	**-18.13±0.10**
	22459-02F	758	120	**-16.52±0.08**
	22459-02G	848	120	**-14.98±0.04**
	22459-02H	923	120	**-14.11±0.01**
	22459-02I	985	120	**-13.70±0.02**
	22459-02J	1006	120	**-12.92±0.01**
	22459-02K	1037	120	-12.83±0.01
	22459-02L	1026	120	-13.26±0.02
	22459-02M	1037	120	-13.22±0.02
	22459-02N	1042	120	-13.47±0.02
	22459-02O	1061	120	-13.68±0.06
	22459-02P	1075	120	-14.43±0.07

	22459-02Q	1089	120	-14.93±0.14
Sample	**Run ID**	**Temperature (°C)**	**Duration (s)**	**^{39}Ar ln(D/a^2)**
B14-053a	**22458-01A**	543	120	**-21.59±0.14**
	22458-01B	425	120	-22.8±2.6
	22458-01C	565	120	**-21.27±0.36**
	22458-01D	634	120	**-18.40±0.04**
	22458-01E	675	120	**-17.48±0.06**
	22458-01F	713	120	**-16.51±0.03**
	22458-01G	812	120	**-15.46±0.02**
	22458-01H	869	120	**-13.64±0.01**
	22458-01I	917	120	**-13.03±0.01**
	22458-01J	1032	120	**-12.54±0.01**
	22458-01K	1042	120	**-12.01±0.01**
	22458-01L	1075	120	-11.85±0.01
	22458-01M	1090	120	-11.78±0.01
	22458-01N	1106	120	-11.73±0.01
	22458-01O	1121	120	-11.64±0.01
	22458-01P	1143	120	-11.52±0.01
	22458-01Q	1156	120	-11.54±0.01

Table 9
Diffusivities calculated during step-heating of MAC 02666. D/a^2 is stripped of dimensions for taking the logarithm. Bold values indicate steps included in Arrhenius regressions. At the conclusion of indirect heating step O, the sample was heated directly with the laser to an unknown temperature for 3 additional periods of 60 s. During direct heating, the pyrometer is focused on the sample and not the Ta-platform. Laser power settings for additional direct heating steps are found in table 5.

Run ID	Temperature (°C)	Duration (s)	^{39}Ar ln(D/a^2)	^{40}Ar ln(D/a^2)	^{36}Ar ln(D/a^2)
22413-01A	601	60	-15.47±0.44	-15.11±0.01	-16.44±1.00
22413-01B	643	60	**-13.01±0.17**	**-12.83±0.00**	**-14.35±0.50**
22413-01C	721	60	**-11.66±0.12**	**-11.68±0.00**	**-13.12±0.33**
22413-01D	741	60	**-11.19±0.12**	**-11.17±0.00**	**-12.59±0.33**
22413-01E	799	60	**-10.40±0.11**	**-10.35±0.00**	**-11.63±0.20**
22413-01F	879	60	**-9.08±0.04**	**-9.13±0.00**	**-10.26±0.09**
22413-01G	958	60	**-8.34±0.04**	**-8.46±0.00**	**-9.54±0.08**
22413-01H	1006	60	**-7.92±0.04**	**-8.07±0.00**	**-9.09±0.08**
22413-01I	1051	60	-7.90±0.06	-7.98±0.00	-9.15±0.11
22413-01J	1127	60	-7.85±0.07	-7.95±0.00	-9.05±0.13
22413-01K	1169	60	-8.02±0.11	-8.08±0.00	-8.99±0.14
22413-01L	1170	60	-9.05±0.36	-8.66±0.02	-9.71±0.33
22413-01M	1188	60	-8.48±0.22	-8.66±0.02	-9.34±0.25
22413-01N	1200	60	-9.11±0.47	-8.71±0.02	-9.54±0.33
22413-01O	1178	60	-10.16±1.40	-9.30±0.04	-9.88±0.50

Table 10
Comparison of sample ages and diffusion parameters for plagioclase from samples B06-042 and B14-053a with published data from plagioclase separates from the Critical Zone of the Rustenburg Layered Suite of the Bushveld Complex (BV-8 series).

Sample	Plateau Age (Ma)	Fusion Age (Ma)	G.	$E_a \pm 1\sigma$ (kJ/mol)	$\ln(D_0/a^2) \pm 1\sigma$
B06-042_01	2037.8 ± 3.5[c]	2019.7 ± 4.5[c]	S	167.1 ± 7.9[c]	3.80 ± 0.98[c]
B06-042_02	2037.7 ± 5.8[c]	2086.6 ± 8.1[c]	S	165.4 ± 4.7[c]	2.45 ± 0.50[c]
B14-053a	2025.6 ± 3.9[c]	1989.4 ± 4.5[c]	S	165.3 ± 3.7[c]	3.25 ± 0.41[c]
BV-8-1[a]	2000 ± 7	1949 ± 7	P	155.3 ± 3.1	3.95 ± 0.34
BV-8-2[a]	2030 ± 6	1988 ± 6	P	161.2 ± 2.5	4.75 ± 0.25
BV-8-3[a]	2053 ± 5	2021 ± 6	P	178.4 ± 2.1	5.58 ± 0.22
BV-8-4[a]	2042 ± 7	2009 ± 7	P	170.8 ± 2.1	6.29 ± 0.30
BV-8-5[a]	2046 ± 7	2014 ± 7	P	176.3 ± 3.7	3.60 ± 0.85
BV-8p-1[b]	No Age	No Age	S	183.6 ± 9.5	3.3 ± 1.4
BV-8p-2[b]	No Age	No Age	S	188 ± 19	3.3 ± 2.5
BV-8p-3[b]	No Age	No Age	S	160.4 ± 8.3	0.6 ± 1.2

Note. Abbreviations: G.=assumed grain geometry: S (spherical) or P (plane slab). E_a = activation energy; D_0= the diffusion coefficient at infinite temperature and a^2=the diffusion domain size. The quantity D_0/a^2 is stripped of dimensions for taking the logarithm. T_c = closure temperature.
Notes: [a]Cassata et al. (2009). Ages recalculated assuming an age of 28.201 Ma for Fish Canyon sanidine; [b]Cassata and Renne (2013).
[c]These values supersede those reported by Setera et al. (2016) due to refinement of *J* and correction of an arithmetic error in calculating diffusion parameters.

Table 11
Ages and diffusion parameters for a mafic clast (MC 001) from howardite, MAC 02666.

Plateau age (Ma)	Fusion age (Ma)	Isochron age (Ma)	CRE age (Ma)		$E_a \pm 1\sigma$ (kJ/mol)	$\ln(D_0/a^2) \pm 1\sigma$	$T_c^a \pm 1\sigma$ (°C)
3643 ± 28	3708 ± 36	3603 ± 60	6.5 ± 0.7	^{40}Ar	131.6 ± 4.5	4.40 ± 0.49	127.7 ± 4.7
				^{39}Ar	138.2 ± 5.6	5.23 ± 0.60	139.1 ± 5.8
				^{38}Ar	143.0 ± 5.5	4.29 ± 0.59	162.7 ± 6.2
				^{36}Ar	144.5 ± 8.1	4.62 ± 0.82	163.7 ± 8.6

Note. Abbreviations are the same as for Table 10.
[a]A geometric factor, A =55 for a sphere and a cooling rate of 10°C Ma^{-1} are assumed in calculating the closure temperature (see S4.1 equation S5).
All values reported here supersede those reported by Setera et al. (2016) due to refinement of *J* and correction of an arithmetic error in calculating diffusion parameters.

Table 12
Units for constants k_1 and k_2 are [10^{-8} cm^3 STP ^{38}Ar/(g sample)]/[g Ca-Ma] and [10^{-8} cm^3 STP ^{38}Ar/(g sample)]/[g Ca-Ma], respectively. Summary of isotopic data used to calculate the total cosmic-ray exposure age for the mafic clast from howardite MAC 02666. Production coefficients, k_1 and k_2, are from Eugster and Michel, 1995. The constants, c_1 and c_2, relate the mass of Ca and K in the irradiated sample to the amount of ^{37}Ar and ^{39}Ar produced during sample irradiation.

Cosmic-Ray Exposure Age – Mafic Clast from MAC02666	
Mass (μg)	174
$^{38}Ar_c$ (mol)	2.095×10^{-16}
±	2.612×10^{-18}
^{37}Ar (mol)	1.112×10^{-13}
±	1.143×10^{-14}
^{39}Ar (mol)	4.207×10^{-16}
±	9.695×10^{-18}
k_1 (Ca coefficient)	2.9
k_2 (K coefficient)	1.81
c_1 (Ca constant) g Ca/(mol ^{37}Ar)	3.58×10^{8}
c_2 (K constant) g K/(mol ^{39}Ar)	2.15×10^{8}
total t_{38} (Ma)	6.5
±	0.7

Table 13
Calculated, best-fit values of (D/a^2) for the temperature range 0 – 1000 °C for the mafic clast of howardite, MAC 02666. (D/a^2) values for each isotope are calculated based on the weighted linear regression of diffusion data from the step-heating experiment of the mafic clast (Table 11). Columns 3 and 4 show the times in years required to degas the sample of 90% and 10% of its initial $^{40}Ar^*$ at the given temperature.

T (°C)	^{39}Ar (D/a^2)	t (yr) (f = 0.9)	t (yr) (f = 0.1)
0	5.28E-25	1.11E+16	5.54E+13
100	6.87E-18	8.48E+08	4.25E+06
200	8.80E-14	6.63E+04	3.32E+02
300	4.16E-11	1.40E+02	7.03E-01
400	3.15E-09	1.85E+00	9.28E-03
500	7.79E-08	7.48E-02	3.75E-04
600	9.25E-07	6.31E-03	3.16E-05
700	6.60E-06	8.84E-04	4.43E-06
800	3.26E-05	1.79E-04	8.95E-07
900	1.23E-04	4.74E-05	2.38E-07
1000	3.76E-04	1.55E-05	7.77E-08
T (°C)	**$^{40}Ar^*$ (D/a^2)**	**t (yr) (f = 0.9)**	**t (yr) (f = 0.1)**
0	5.60E-24	1.04E+15	5.22E+12
100	3.08E-17	1.90E+08	9.50E+05
200	2.44E-13	2.39E+04	1.20E+02
300	8.24E-11	7.08E+01	3.55E-01
400	4.97E-09	1.17E+00	5.88E-03
500	1.05E-07	5.56E-02	2.79E-04
600	1.10E-06	5.30E-03	2.66E-05
700	7.00E-06	8.34E-04	4.18E-06
800	3.20E-05	1.82E-04	9.13E-07
900	1.13E-04	5.17E-05	2.59E-07
1000	3.29E-04	1.77E-05	8.89E-08
T (°C)	**^{36}Ar (D/a^2)**	**t (yr) (f = 0.9)**	**t (yr) (f = 0.1)**
0	2.55E-26	2.28E+17	1.14E+15
100	6.29E-19	9.27E+09	4.65E+07
200	1.17E-14	4.99E+05	2.50E+03
300	6.90E-12	8.46E+02	4.24E+00
400	6.15E-10	9.49E+00	4.75E-02
500	1.75E-08	3.33E-01	1.67E-03
600	2.27E-07	2.57E-02	1.29E-04
700	1.73E-06	3.38E-03	1.69E-05
800	9.17E-06	6.36E-04	3.19E-06
900	3.68E-05	1.58E-04	7.94E-07
1000	1.17E-04	4.97E-05	2.49E-07

Table 14
Values used in the cosmogenic corrections for the mafic clast of howardite, MAC 02666 to construct the isochron in Fig. 12. $^{38}Ar_c$ and $^{36}Ar_c$ are the cosmogenic derived amounts of ^{38}Ar and ^{36}Ar, respectfully. $^{36}Ar_{Tr}$ is the calculated amount of ^{36}Ar that is neither cosmogenic nor chlorine derived. Both ratios $^{40}Ar^*/^{36}Ar_{Tr}$ and $^{39}Ar/^{36}Ar_{Tr}$ are used in construction of the isochron in Fig. 12. The uncertainties in both ratios were calculated using the approximate value ρ = 0.90 for the correlation of the uncertainties ^{36}Ar and ^{38}Ar. See text S4 for full details.

Run ID	**$^{38}Ar_c$ (±)** 1E-18 mol	**$^{36}Ar_c$ (±)** 1E-18 mol	**$^{36}Ar_{Tr}$ (±)** 1E-18 mol	**$^{40}Ar^*/^{36}Ar_{Tr}$ (±)**	**$^{39}Ar/^{36}Ar_{Tr}$ (±)**
22413-01A	1.94 (0.52)	1.26 (0.34)	-0.60 (1.02)	-3237 (3758)	-8.0 (7.8)
22413-01B	2.80 (0.49)	1.82 (0.32)	0.11 (1.02)	41611 (283105)	116.0 (789.4)
22413-01C	4.14 (0.54)	2.69 (0.35)	0.73 (1.03)	8214 (7731)	25.7 (24.4)
22413-01D	3.41 (0.52)	2.21 (0.34)	1.26 (1.02)	4645 (2557)	13.7 (7.7)
22413-01E	6.69 (0.52)	4.35 (0.34)	1.09 (1.04)	7915 (5242)	22.5 (15.1)
22413-01F	14.30 (0.68)	9.30 (0.44)	1.70 (1.09)	9964 (3777)	31.0 (11.8)
22413-01G	18.12 (0.74)	11.78 (0.48)	1.55 (1.12)	12241 (4975)	39.5 (16.1)
22413-01H	18.54 (0.65)	12.05 (0.42)	0.89 (1.07)	19736 (14376)	63.1 (46.0)
22413-01I	15.33 (0.62)	9.96 (0.41)	-0.49 (1.06)	-26955 (36764)	-78.3 (106.9)
22413-01J	12.15 (0.65)	7.90 (0.42)	0.15 (1.06)	64956 (272128)	191.0 (800.4)
22413-01K	9.42 (0.54)	6.12 (0.35)	0.81 (1.02)	8414 (7096)	23.6 (20.1)
22413-01L	4.76 (0.49)	3.09 (0.32)	-0.14 (1.02)	-23844 (127512)	-43.3 (232.2)
22413-01M	4.10 (0.49)	2.66 (0.32)	1.29 (1.01)	2240 (1245)	7.3 (4.4)
22413-01N	4.04 (0.52)	2.63 (0.34)	0.82 (1.02)	3011 (2556)	5.4 (5.3)
22413-01O	8.12 (0.47)	5.28 (0.30)	1.18 (0.99)	1064 (644)	1.3 (1.9)
22413-01P	12.30 (0.65)	8.00 (0.42)	0.14 (1.06)	27516 (123467)	75.3 (338.1)
22413-01R	68.27 (1.10)	44.38 (0.71)	-0.91 (1.36)	-16015 (10952)	-48.6 (33.3)
22413-01S	7.74 (0.59)	5.03 (0.39)	-0.65 (1.04)	-6028 (6076)	-14.8 (15.2)

Chapter 4

An end to hydrothermal circulation: Low temperature plagioclase $^{40}Ar/^{39}Ar$ thermochronology of the Rustenburg Layered Suite

This chapter resulted in one prepared manuscript:

Setera, J. B., VanTongeren J. A., Turrin B. D., & Swisher C. C. (2020). A low-temperature hydrothermal cutoff: Plagioclase $^{40}Ar/^{39}Ar$ thermochronology of the Rustenburg Layered Suite., Bushveld Complex. **Earth & Planetary Science Letters**.

Abstract

The mid-low temperature thermal history of layered mafic intrusions is crucial to understanding the duration of hydrothermal systems and the formation of economically viable ore deposits within the large thermal anomaly of these magma bodies. Due to a lack of low-temperature chronometry, the mid-low temperature thermal evolution of the world's largest layered intrusion, the Bushveld Complex, remains relatively unknown. We provide the first comprehensive $^{40}Ar/^{39}Ar$ thermochronologic study of plagioclase throughout the Rustenburg Layered Suite (RLS) of the Bushveld Complex in South Africa. $^{40}Ar/^{39}Ar$ step-heating analysis of 20 individual plagioclase grains cover 12 stratigraphic levels and the entire ~7 km thickness of the RLS in the Eastern Limb of the Bushveld Complex. Individual plagioclase grains yield $^{40}Ar/^{39}Ar$ plateau ages ranging

from 1997.9 ± 5.0 Ma to 2051.4 ± 5.3 Ma, and diffusion parameters that correspond to closure temperatures of 151.1 ± 6.3°C to 309.5 ± 5.2°C (assuming a 10°C Ma^{-1} cooling rate). The combination of plagioclase $^{40}Ar/^{39}Ar$ ages and closure temperatures with reported $^{40}Ar/^{39}Ar$ biotite ages from the same samples, suggests that the cooling rates of the RLS decrease abruptly (from ~1000°C Ma^{-1} to ~10°C Ma^{-1}) near the $^{40}Ar/^{39}Ar$ closure temperature of biotite. The transition to slower observed cooling rates is a product of the cessation of hydrothermal circulation associated with the emplacement of the RLS. Numerical heat-loss simulations support the observations from $^{40}Ar/^{39}Ar$ thermochronology, with hydrothermal circulation needed at high-temperatures to produce the observed geochronology throughout the RLS. Cessation of the hydrothermal system occurs within ~1 Ma of zircon crystallization. This duration places precise age constraints on hydrothermal ore deposits within the host rocks (Transvaal and Witwatersrand Supergroups), as any ore deposits related to emplacement of the RLS must be at a minimum, coeval with $^{40}Ar/^{39}Ar$ biotite ages.

1. Introduction

Layered mafic intrusions provide the some of the best opportunities for observing and understanding the geochemical and lithologic evolution of igneous bodies within the shallow crust. With distinct layering, large grain sizes, and high-grade economic deposits, layered mafic intrusions are traditionally thought to have crystallized and cooled slowly after emplacement. For the world's largest layered intrusion, the Bushveld Complex in South Africa, this certainly could be expected, as it represents the rapid emplacement of on the order of 1 million km^3 of magma into the shallow crust. In addition to processes

within the intrusion itself, the massive thermal disturbance associated with the emplacement of the Bushveld Complex is also tied to economically viable hydrothermal ore deposits within the host rocks (e.g. Gleason et al., 2010; Rasmussen et al., 2007).

Recent chronologic data throughout the Rustenburg Layered Suite (RLS), the predominately mafic to ultramafic portion of the Bushveld Complex (Fig. 1), suggest that the intrusive body cooled rapidly at high to intermediate sub-solidus temperatures (~875-400°C; e.g. Cassata et al., 2009; Scoates & Wall, 2015; Setera et al., chapter 2). Zeh et al. (2015) reported high-precision U-Pb zircon ages from the marginal zone through the roof of the intrusion that indicated zircon crystallization over a period of ~1.02 ± 0.63 Ma. Ti-in-zircon thermometry places this crystallization at temperatues ranging from ~875-713°C (Ver Hoeve et al., 2018; Zeh et al., 2015). Additional U-Pb ages of zircon and baddeleyite are fairly homogenous throughout the RLS stratigraphy, ranging from 2056.45 Ma - 2054.89 Ma (Fig. 2; Mungall et al., 2016; Scoates & Wall, 2015), and indicate that zircon crystallized throughout the intrusion at roughly the same time interval.

At lower temperatures, the $^{40}Ar/^{39}Ar$ system in biotite produces ages associated with closure temperatures of ~350-450°C (McDougall & Harrison, 1999; Setera et al., chapter 2). Setera et al. (chapter 2) showed that weighted mean $^{40}Ar/^{39}Ar$ plateau ages of biotite are uniform throughout the stratigraphy of the RLS (Fig. 2), with a weighted mean of 2054.47 ± 0.84 Ma (2σ). Thermal modelling suggests that the lack of change in biotite ages with stratigraphic height in the RLS, as well as the overlap between the $^{40}Ar/^{39}Ar$ and U-Pb systems, is a product of rapid cooling rates (upwards of 1000°C Ma^{-1}) aided by hydrothermal circulation (Setera et al., chapter 2). This conclusion is supported by

abundant hydrothermal vein mineralization (>300°C) observed throughout the RLS (Schiffries & Skinner, 1987) and thought to be derived from saline fluids from the host Transvaal Supergroup sediments (Schiffries & Rye, 1990).

The cooling rate of the RLS to temperatures below 350-450°C is still largely unconstrained however. The only published thermochronologic data below the $^{40}Ar/^{39}Ar$ closure temperature of biotite for the RLS are $^{40}Ar/^{39}Ar$ plagioclase ages from a single sample within the Critical Zone, near the MG-1 chromitite (Cassata et al., 2009), which showed that this part of the RLS experienced protracted cooling from the $^{40}Ar/^{39}Ar$ closure temperature of biotite to ambient crustal temperatures. However, the biotite $^{40}Ar/^{39}Ar$ age from this sample is also younger than those elsewhere in the RLS and it is plausible that the MG-1 chromitite, as well as the Merensky Reef and UG-2 chromitite, experienced a different thermal history than the majority of the RLS (e.g. Setera et al., chapter 2).

Plagioclase is less commonly exploited in $^{40}Ar/^{39}Ar$ thermochronology than biotite and amphibole due to its low K_2O content. However, plagioclase is found throughout the RLS stratigraphy both as an interstitial phase in the Lower and Lower Critical Zones, and as a cumulus phase in the Upper Critical, Main and Upper Zones (Fig. 1). In addition to its abundance throughout the stratigraphy, the low closure temperature of the $^{40}Ar/^{39}Ar$ system in plagioclase (~175-300°C; Berger & York, 1981; Cassata & Renne, 2013) provides the best tool to investigate the low temperature evolution of the RLS magma chamber.

We present diffusion parameters, closure temperatures, and $^{40}Ar/^{39}Ar$ ages for individual plagioclase grains from 12 samples of the RLS. Together, the samples cover a

complete ~7 km stratigraphic profile of the Eastern Limb of the RLS. Combined with numerical modeling, our age and diffusion results show that between the $^{40}Ar/^{39}Ar$ closure temperatures of biotite (~400°C) and plagioclase (~200°C) there is a marked change in the cooling regime of the RLS from rapid cooling aided by hydrothermal circulation to primarily conductive cooling. This change in cooling regime provides age constraints to RLS-related economically viable mineral resources in the Transvaal Supergroup sedimentary rocks (e.g. Gleason et al., 2010; Gutzmer et al., 2007; Rasmussen et al., 2007).

2. Geologic Setting

The RLS represents the layered mafic to ultramafic sequence of the larger Bushveld Complex, which also includes the felsic Rooiberg Group, the Rashoop Granophyre Suite, and the Lebowa Granite Suite. The layered sequence is approximately 8-9 km thick, 450 km E-W, and 150-200 km N-S (Fig. 1) and predominately crops out gently inward dripping Eastern and Western limbs which are inferred to connect at depth (Cawthorn & Webb, 2001; Cole et al. 2014; Webb et al., 2004). The RLS was intruded ~2.06 Ga (Buick et al., 2001; Scoates & Friedman, 2008; Olsson et al., 2010; Scoates & Wall, 2015; Zeh et al., 2015; Mungall et al., 2016) into the Kaapvaal craton. The RLS is commonly thought to have intruded subparallel to layering of the Neoarchean to Paleoproterozoic Transvaal Supergroup sediments (Eriksson & Altermann, 1998), specifically between the shales and quartzites of the Pretoria Group and overlying Rooiberg lavas (Cheney & Twist, 1991). However, this is complicated by variability in

the rocks that constitute the immediate roof of the RLS, as described in the Eastern Limb (VanTongeren & Mathez, 2015).

The RLS is stratigraphically subdivided (SACS, 1980) into zones based on cumulus mineral assemblages. In stratigraphic order these are: the Lower Zone, Critical Zone, Main Zone, and Upper Zone. Although highly complex, the full RLS stratigraphy represents a progression of more lithologically and chemically evolved rocks upward through the stratigraphy, and was likely emplaced in a very short time span (e.g. Cawthorn & Walraven, 1998).

In general, the roof of the RLS intrusive rocks is comprised of 1-3 km of felsic lavas, called the Rooiberg Group, which are coeval with the intrusion (e.g. Schweitzer et al., 1997), and ~1.5-3.5 km (Ferré et al., 1999) of granitic material called the Lebowa Granite Suite, which is considered to be slightly younger than the mafic RLS (2054.4 ± 1.8; Walraven & Hattingh, 1993).

3. Samples and Methods

3.1 Samples & Stratigraphy

A total of 12 samples, encompassing ~7 km of RLS stratigraphy, were chosen for $^{40}Ar/^{39}Ar$ thermochronology (Table 1). Samples range from magnetite-bearing gabbro in the Upper Zone, gabbronorite in the Main Zone and Upper Critical Zone, to pyroxenite in the Upper Critical and Lower Zones. Plagioclase is a cumulus mineral phase within all of the samples with exception of the 3 pyroxenite samples within the Lower Critical and Lower Zones.

To compare depth-specific samples to any numerical cooling model, the stratigraphic placement of each sample is significant. As seen in Figure 1, the samples from this study are from various localities within the Eastern Limb of the RLS. Although the thickness of the intrusion varies by location, a careful combining of the samples from the different localities can provide an appropriate estimate of their stratigraphic relationship to one another.

Geographic and stratigraphic positions for the three Upper Zone samples are from the reconstruction of VanTongeren et al. (2010) for the combined Leolo Mountain and Magnet Heights traverse of Molyneux (1974). Geographic and stratigraphic positions for the five Main Zone samples are from the Roosenekal traverse of Setera & VanTongeren (2018). The stratigraphic position relative to the Merensky Reef for samples from the two traverses can be placed together, as the thicknesses of the Main Zone between these two traverses is remarkably similar, at ~2634 m at Roossenekal (Setera & VanTongeren, 2018) and ~2900 m near the Leolo Mountains (Molyneux, 1974).

The two Critical Zone samples are placed in their stratigraphic position relative to the Merensky Reef using a dip angle of 15° (Molyneux, 2008). The two Lower Zone samples are from Fraaiuitzicht Hill located in the Burgersfort bulge area of the eastern Bushveld Complex (Fig. 1). Here, stratigraphic positions are calculated using a dip angle of 45° (Molyneux (2008) and assuming the top of Fraaiuitzicht hill represents the contact between the Lower Zone and Lower Critical Zone (e.g. Williams et al., 2006). The Critical Zone thickness in the area of Burgersfort bulge is ~1700 m thick based on the map of Molyneux (2008). Therefore, the stratigraphic position of the Lower Zone samples relative to the Merensky Reef is estimated by adding 1700 m to their position

relative to the Lower Zone/Lower Critical Zone contact. For comparison to numerical model results, as described below, sample depths are also given relative to the contact with the roof (Table 1), which is located ~290 m above sample B06-055 (VanTongeren & Mathez, 2012).

3.2 Electron Microprobe

Major element compositions for plagioclase were determined using the JEOL JXA 8200 electron microprobe at Rutgers University. Analyses were carried out using an electron acceleration potential of 15kV, beam current of 15nA, count times of 30s on peak and 15s on background for each element, and a beam diameter of 5μm. Standards were analyzed between every ~50 unknowns and consistently yielded results within 2σ of published values. Complete major element analyses of plagioclase unknowns and standards are available in supplementary information (Table 2-3)

3.3 Irradiation & Standards

Cleaned mineral separates were hand-picked under a binocular microscope, with care to avoid grains with noticeable fractures for inclusions (both fluid and mineral). Grains with aspect ratios of ~0.6-0.9 were preferentially picked, supporting the use of a spherical geometry in Arrhenius regressions and closure temperature calculations. Samples along with the reference standards Fish Canyon (FC) sanidine [28.201 Ma; Kuiper et al. (2008)] and Hb3Gr hornblende [1080 Ma; Jourdan and Renne (2007)] were loaded into pits drilled into a 1-cm diameter Al-disks for neutron irradiation. The pits are arranged in a controlled geometry to facilitate the correction of any measurable gradients in the

neutron-flux. Neutron irradiation was carried out at the US Geological Survey TRIGA reactor for 80 hours without Cd-shielding.

3.4 Argon Measurements & Calculations

See chapter 3 of this dissertation (sections 2.5 and 2.6) for complete details on $^{40}Ar/^{39}Ar$ measurements as well as necessary equations for the calculation of diffusion parameters and closure temperatures.

4. Results

$^{40}Ar/^{39}Ar$ step-heating was undertaken on 17 individual plagioclase grains and combined with the dataset of Setera et al. (chapter 2), totaling 20 individual grains in 12 samples encompassing ~7 km of RLS stratigraphy (Fig. 3). Each grain produces a complete step-heating age spectrum as well as coupled, grain-specific diffusion parameters which allow for the calculation of a closure temperature (T_c) and cooling rate.

4.1 Plagioclase $^{40}Ar/^{39}Ar$ Plateau Ages

Age spectra for all plagioclase grains are characterized by a "staircase pattern" with low apparent ages during initial heating-steps followed by increasingly older ages that result in plateau ages ranging from 1997.9 ± 5.0 Ma to 2051.4 ± 5.3 Ma (Fig. 3a-4), with individual plateaus consisting of between 32 and 85% of the total ^{39}Ar released (Table 6). Despite evidence of Ar-loss (low ages in early heating steps), $^{40}Ar/^{39}Ar$ Plateau ages are a best estimate of when each grain passed through its given closure temperature. Plateau ages show a general stratigraphic trend of younging towards the center of the intrusion

(Fig. 4). Plagioclase grains from the uppermost stratigraphic sample within the Upper Zone (B06-055) yield plateau ages of 2051.3 ± 2.4 Ma and 2044.4 ± 3.7 Ma, while the lowest stratigraphic sample within the Lower Zone (B14-042) yields plateau ages of 2051.4 ± 5.3 Ma and 2046 ± 12 Ma. Near the center of the stratigraphy, younger plagioclase plateau ages cluster ~2025-2035 Ma, with a sample from the upper Main Zone (B14-015) yielding the youngest plateau age of 1997.9 ± 5.0 Ma.

While published biotite $^{40}Ar/^{39}Ar$ plateau ages of biotite overlap with U-Pb zircon ages (Fig. 2, 4), all plagioclase $^{40}Ar/^{39}Ar$ plateau ages are younger than those reported for biotite from the same samples. $^{40}Ar/^{39}Ar$ plateau ages for plagioclase are as few as ~3 Ma younger than their biotite counterpart near the upper and lower contacts of the intrusion. The large cluster of plateau ages near the center of the intrusion are ~20-30 Ma younger than biotite plateau ages, while the largest age difference is ~58 Ma for the youngest grain from sample B14-015.

Samples with duplicate analyses (Table 6) include examples of both samples that have indistinguishable plateau ages (e.g. B06-042) and samples that yield ages that differ by up to ~12 Ma (e.g. B14-015). Differing $^{40}Ar/^{39}Ar$ plateau ages for individual plagioclase grains are not uncommon (e.g. Cassata & Renne, 2013). For example, plagioclase grains from the single RLS sample of Cassata et al. (2009) yielded plateau ages ranging from 2000 ± 6 Ma to 2053 ± 5 Ma (recalculated for FC = 28.201 Ma). The low closure temperature of the $^{40}Ar/^{39}Ar$ system in plagioclase (~175-300°C; Berger & York, 1981; Cassata & Renne, 2013) can result in age differences due to varying closure temperatures between individual grains within a single sample. The varying closure temperatures, coupled with slow cooling, can produce grains within a single sample that

differ in age, but still fall along the same cooling profile (i.e. same thermal history). Varying closure temperatures for individual plagioclase grains can occur due to a number of factors including, but not limited to: composition, grain size and shape, shock or grain defects, and assumptions in temperature calculations (e.g. geometry, cooling rate). Therefore, the coupling of diffusion parameters with ages from the same grain is necessary to further elucidate the age differences displayed both within samples and compared to other chronometers (Fig. 4).

Full age details and plateau diagrams are given in table 7 and Fig. 5.

4.2 Diffusion Parameters

Grain specific diffusion parameters, to be coupled with individual ages, are calculated from Arrhenius regressions of ^{39}Ar released during step-heating (e.g. Fig 3b) according to the method of Setera et al. (chapter 2). In the constructing of Arrhenius regressions, we assume a spherical geometry as spherical geometries have proven to be more appropriate than a plane slab geometry for feldspars with aspect ratios of ~0.5-1.0 (Huber et al., 2011), similar to the plagioclase grains measured in this study. The individual analyses produce activation energies ranging from 143.5 ± 5.0 kJ/mol to 211.2 ± 3.7 kJ/mol and $ln(D_0/a^2)$ values of 2.45 ± 0.50 to 11.6 ± 0.4 (Table 6). Diffusion parameters yield closure temperatures (T_c) ranging from 151.1 ± 6.3°C to 309.5 ± 5.2°C, when calculated assuming a spherical geometry and a 10°C Ma^{-1} cooling rate. Diffusion parameters for all samples, excluding the significantly lower closure temperatures of sample B14-015, yield an average closure temperature of 249 ± 26°C. Both diffusion parameters and closure temperatures match well with previously published values for terrestrial plagioclase

samples (e.g. Harrison & McDougall, 1981; Onstott et al., 1989; Renne et al., 1990; Renne et al., 1996; Boven et al., 2001; Cassata et al., 2009; Garrick-Bethell et al., 2011; Cassata & Renne, 2013).

As mentioned above, individual replicate plagioclase grains from a single sample can produce highly variable ages and diffusion parameters (see Table 6). Because plagioclase is generally compositionally homogenous (Table 2) within each sample, replicate activation energies are indistinguishable in most samples. Values of $\ln(D_0/a^2)$ are can be variable within each sample, likely reflecting differences in the size and shape of each grain (Table 6). As expected, samples with replicate analyses yielding varying plagioclase plateau ages also yield varying closure temperatures (Table 6). In all cases, the older age of the sample is associated with a higher closure temperature, while the younger age is associated with a lower closure temperature. The trend with age and closure temperature within individual samples further supports the fact that varying diffusion parameters of individual grains is causing the observed age variations. In the end, the diffusion parameters for each individual grain can be combined with the observed age of that same grain and treated to its own thermal history. All Arrhenius regressions are provided in table 5 and Fig. 6.

4.3 Calculation of Cooling Rates & Closure Temperatures

Closure temperatures are often calculated assuming an appropriate cooling rate (e.g. 10°C Ma^{-1}). However, with both $^{40}Ar/^{39}Ar$ biotite ages and $^{40}Ar/^{39}Ar$ plagioclase ages available from the same samples, a more accurate closure temperature can be calculated by iteratively solving for cooling rate and closure temperature between the two ages.

Although the closure temperature of biotite is traditionally quoted to be ~350°C (McDougall and Harrison, 1999), the exact value is dependent on diffusion parameters that are affected by a number of factors such as composition, geometry and cooling rate. Based on composition and estimated cooling rates, Setera et al. (2019) estimated that $^{40}Ar/^{39}Ar$ ages of biotite from the RLS represented closure at ~350-450°C. As such, a closure temperature of 400°C was assumed for the $^{40}Ar/^{39}Ar$ system in biotite for this calculation (used throughout the rest of the study), and age differences were calculated between the biotite $^{40}Ar/^{39}Ar$ ages of Setera et al. (chapter 2) and the $^{40}Ar/^{39}Ar$ plateau ages of plagioclase. Samples that do not have a paired $^{40}Ar/^{39}Ar$ biotite age (B06-020, B14-029 and B14-042) are calculated using the weighted mean $^{40}Ar/^{39}Ar$ biotite age from Setera et al. (chapter 2) of 2054.47 Ma.

Calculated cooling rates below 400°C from samples near the top and floor contacts of the intrusion are as high as ~40-70°C Ma^{-1} for individual plagioclase grains, resulting in ages that are only ~ 3-4 Ma younger than the $^{40}Ar/^{39}Ar$ biotite ages. The majority of the RLS stratigraphy, however, records low temperature cooling rates of between 5-10°C Ma^{1}, resulting in plagioclase ages that are significantly younger than biotite from the same sample (Table 6, Fig.7a). A linear regression also shows a significant correlation ($\alpha = 0.05$) between plagioclase $^{40}Ar/^{39}Ar$ plateau ages versus iteratively calculated closure temperature ($R^2 = 0.55$).

4.4 Early, Young Apparent $^{40}Ar/^{39}Ar$ Ages

As mentioned above (section 4.1), all plagioclase age spectra (with the exception of sample B07-041) are characterized by young apparent ages during low-temperature

heating steps, similar to those observed by Cassata et al. (2009), indicative of diffusive Ar-loss (Fig. 3a). The youngest of these apparent ages during early heating steps range from ~1200 Ma to ~1400 Ma for all samples. These ages are similar to those reported for plagioclase from a single sample of the RLS (Cassata et al. 2009), as well as those reported for biotite grains from the Main Zone (Setera et al., chapter 2). The observed diffusive Ar-loss is potentially a product of later event causing elevated temperatures above or near the closure temperature of the $^{40}Ar/^{39}Ar$ system in plagioclase for an extended duration. Potential sources for the added heat include the Vredefort meteorite impact and/or heat related the intrusion of the nearby 1.4 Ga Pilanesberg Complex and related alkaline magmatism (Elburg & Cawthorn, 2017).

The ~2.02 Ga (Kamo et al., 1996; Moser et al., 2011; Spray et al., 1995) Vredefort meteorite impact formed an 80 km wide crater and produced an elevated thermal anomaly in the region (Gibson et al., 1997; Turtle et al., 2003). However, the impact pre-dates many of the plagioclase plateau ages from this study (Table 6). Therefore, it would necessarily need to produce enough heat to completely reset those younger plagioclase grains, while at the same time not producing enough heat to completely reset the older plagioclase grains. The Vredefort impact as the source of Ar-loss in our samples is also hindered by the work of Turtle et al. (2003) who modelled the heat produced from the impact and concluded that it was contained to within immediate crater vicinity. With the impact crater located ~160 km Southwest of the Bushveld Complex, it is unlikely that heat produced by the impact affected the rocks of the RLS.

The most well studied alkaline magmatism within the area of Bushveld Complex is the ~1.4 Ga (Elburg & Cawthorn, 2016) Pilanseberg alkaline complex. Located near

the Western Limb of the Bushveld Complex, the Pilanesburg Complex is in contact with both the mafic rocks of the RLS as well as the felsic rocks that constitute top sequence of the Bushveld Complex. The thermal anomaly associated with the alkaline complex is potentially widespread, as alkaline magmatism is seemingly laterally extensive during this time interval. In the Western Limb alone, the Pilanesberg Complex is also associated with many coeval smaller intrusions (forming the Pilanesberg Alkaline Province, Vaerwoerd (2006)) and dyke swarms (Cawthorn et al., 2012). There is also evidence for coeval alkaline magmatism in the Eastern Limb of the RLS, with the intrusion of the ~ 1.3 Ga Spitskop Complex, with a surface expression of least 50 km^2 (Harmer, 1999). While early $^{40}Ar/^{39}Ar$ heating steps yield imprecise ages, the ages of widespread alkaline magmatism match fairly well with the youngest apparent ages seen during $^{40}Ar/^{39}Ar$ step-heating (Cassata et al., 2009; Setera et al., 2019; Fig. 3a and Fig. 5). Age similarities, as well as the large lateral extent, make the ~1.3-1.4 Ga alkaline magmatism the likely source heat responsible for Ar-loss within samples of the Eastern Limb of the RLS.

5. Discussion

In their recent study on the mid temperature thermal evolution of the RLS, Setera et al. (chapter 2) measured $^{40}Ar/^{39}Ar$ ages in biotite throughout the RLS. They showed that biotite $^{40}Ar/^{39}Ar$ plateau ages (T_c = ~350-450°C) were uniform from the lower Critical Zone to the Upper Zone, with a weighted mean age of 2054.47 ± 0.84 Ma. The biotite $^{40}Ar/^{39}Ar$ plateau ages overlap with the range of high precision U-Pb zircon ages (zircon saturation temperature of 700-875°C) of 2054.40 - 2056.28 (Fig. 2). These two observations led Setera et al. (chapter 2) to conclude that rapid cooling rates, on the order

of 1000°C Ma^{-1} were caused by an active hydrothermal system associated with the emplacement of the RLS into the shallow crust.

Two main observations from the plagioclase $^{40}Ar/^{39}Ar$ age results point to a major shift in cooling regime of the RLS at low temperatures (e.g., below the closure temperature of biotite (~350-450°C; McDougall & Harrison, 1999; Setera et al., chapter 2):

(1) Plagioclase $^{40}Ar/^{39}Ar$ plateau ages are significantly younger than biotite $^{40}Ar/^{39}Ar$ plateau ages from the same samples (Fig.4). In contrast to the short timespan (~1.3 Myrs) between mean U-Pb zircon ages (700-875°C) and the $^{40}Ar/^{39}Ar$ biotite ages (350-450°C) observed by Setera et al. (chapter 2), the $^{40}Ar/^{39}Ar$ plagioclase ages (T_c = ~150-300°C) are between ~3 - 58 Ma younger than biotites from the same samples (Fig. 4). While the data presented in Setera et al. (chapter 2) show that the mid temperature cooling rate of the RLS was on the order of 1000°C Ma^{-1}, the data presented here show that the low temperature cooling rate of the RLS is between 4-56°C Ma^{-1} (see below section 5.1).

(2) Plagioclase $^{40}Ar/^{39}Ar$ plateau ages show a trend of younging considerably from the upper and lower contacts of the intrusion to the center (Fig.4). Individual plagioclase grains near the upper and lower contacts of the intrusion yield the oldest $^{40}Ar/^{39}Ar$ plateau ages of ~2051 Ma, while grains near the center of the intrusion cluster ~2025-2035 Ma. In contrast to the U-Pb zircon and $^{40}Ar/^{39}Ar$ biotite ages, which are both uniform with stratigraphic height, the trends in plagioclase suggest that intrusion must have cooled from the margins towards the center. Hydrothermal circulation and advective heat transport commonly result in both rapid cooling rates and homogenization of

temperature over large length scales (e.g. Norton and Taylor, 1979), inconsistent with our plagioclase dataset.

5.1 Low Temperature Cooling Rates

Calculated low temperature (e.g. biotite - plagioclase) cooling rates (see section 4.3) from the RLS are faster in samples near the margins of the intrusion, and slower near the center (Fig. 8, Table 6). Calculated cooling rate decreases rapidly from ~28-56°C Ma^{-1} at ~2051 Ma to below ~10°C Ma^{-1} by ~2037 Ma (Fig. 7a).

The trend towards slower cooling rates indicates a transition from rapid advective heat loss due to active hydrothermal circulation at high-mid temperatures to a primarily conductive cooling regime at low temperatures (<400°C). This transition is likely due to the cessation of hydrothermal circulation in the region. Data from our fastest cooling (56°C Ma^{-1}) sample shows that this transition must happen within 3 million years (Fig. 4).

5.2 Numerical Modeling of Heat Loss

Ages and corresponding crystallization (zircon) or closure temperatures (biotite and plagioclase) observed throughout the RLS can be compared with numerical models of heat loss in order to place better constraints on the nature of heat loss from the magma chamber. Two 2-dimensional Heat3D simulations of the emplacement and cooling of the RLS were run using the freely available code of Wohletz (1999). Initial conditions for both runs are similar (Fig. 9), with a modeled area of 1000 km x 30km. In both cases, the RLS was modeled as a 7 km thick, 450 km wide sheet of mafic magma with an initial

starting temperature of 1200°C. The nearly coeval 3 km thick Lebowa Granite Suite is modeled as the same width with an initial temperature of 1000°C, and the overlying Rooiberg Group lavas are modeled as a 2 km thick tuff with a porosity of 0.1 and a starting temperature equal to a geothermal gradient of 20°C/km with a surface temperature of 20°C. The remainder of the grid is modeled as Pretoria Group sediments with a porosity of 0.1 and a starting temperature at each node equivalent to the geothermal gradient of 20°C/km and surface temperature of 20°C. Each grid in the numerical solution is 1 km x 1 km, however specific stratigraphic depths can be solved using spline interpolation within MATLAB™. Full thermal properties used during Heat3D numerical modelling are provided in table 8.

The first model is run assuming purely conductive cooling of the RLS from 1200°C to the ambient crustal geotherm (Fig. 10). The second model incorporates hydrothermal circulation in the country rocks and RLS (Fig. 10). In order to place the country rocks at an appropriate temperature at the time of zircon crystalllization, the model is run with conductive-only heat loss for the first 600,000 years after emplacement of the RLS at 1200°C. After the initial 600,000 years, hydrothermal circulation is initiated and is able to penetrate the country rock as well as the now solidified magmatic rocks. Hydrothermal circulation is allowed to continue for 1 million years, before returning to conductive cooling only.

The duration of hydrothermal circulation for the RLS was chosen based on several observations from the RLS: (1) While there is no measured crystallization rate for the cumulus phases of the RLS (e.g. those crystallizing between 1250-900°C), Cawthorn and Walraven (1998) estimated that the crystallization of the cumulates over this

temperature interval would take approximately 210,000 years. (2) The range of zircon U-Pb ages seen in Zeh et al. (2015) is approximately 1 million years, indicating that different sections of the RLS passed through the zircon crystallization temperature (~700-875°C) at different times; (3) the U-Pb zircon (700-875°C) and $^{40}Ar/^{39}Ar$ ages from biotite (350-450°C) are overlapping, necessitating additional heat loss and (4) there is abundant field evidence from Schiffries and Skinner (1987) indicating high temperature (>600°C) hydrothermal vein mineralization both within the RLS and its contact aureole (Schiffries and Skinner, 1987).

Comparison of the numerical model results with our observations is done only for the temperature intervals in which we have measurements. Namely, the highest closure temperature observed from Ti-in-zircon thermometry (e.g. 875°C; Ver Hoeve et al., 2018; Zeh et al., 2015), to the ~150°C lower limit of closure temperatures for the $^{40}Ar/^{39}Ar$ system in plagioclase. Above 875°C, we do not have any direct observations on the crystallization rate of the cumulus phases in the RLS.

5.2.1 Confirmation of Hydrothermal Circulation

Figure 10 shows both heat loss simulations solved for a single point in the RLS, at a depth of 4 km below the roof and 30 km from the edge of the intrusion. The conduction-only simulation produces a cooling profile that cannot reproduce the observed U-Pb zircon and $^{40}Ar/^{39}Ar$ biotite ages reported for the RLS (Fig. 10). It takes approximately 1.2 Ma longer to reach the 400°C isotherm than what is recorded in the $^{40}Ar/^{39}Ar$ biotite ages of Setera et al. (2019).

The required additional heat loss can be produced by incorporating hydrothermal circulation throughout the host rocks immediately after emplacement as well as within RLS itself after crystallization. This necessary rapid cooling was produced in the heat loss simulation that included 1 million years of hydrothermal circulation, where the model reaches the 400°C isotherm ~1 Ma faster than the conduction-only model. The strong fit between the U-Pb zircon and $^{40}Ar/^{39}Ar$ biotite ages of the RLS, supports the need for a hydrothermal system associated with the emplacement of the RLS.

5.2.2 Comparison to $^{40}Ar/^{39}Ar$ Plagioclase Data

The numerical simulation from above (dashed curve in Fig. 8), including 1 million years of hydrothermal circulation, was extended to have the conductive-cooling portion last a duration of ~55 Ma. Average low temperature cooling rates (400-200°C) were then calculated from the numerical simulation for entirety of the RLS stratigraphy. Calculated cooling rates from the numerical simulation are similar to those calculated from $^{40}Ar/^{39}Ar$ data, but only for the lower portion of the stratigraphy (Fig. 8, solid line). All samples from the RLS that are stratigraphically above the Merensky Reef (e.g. the uppermost 4.5 km of RLS stratigraphy) have calculated cooling rates from the numerical simulations are higher than those calculated from the $^{40}Ar/^{39}Ar$ data. Near the top of the stratigraphy, for example, the numerical simulation produces a cooling rate of ~100°C Ma^{-1}, higher than that calculated for sample B06-055 (Upper Zone). The difference in calculated cooling rates dictates two plausible scenarios, either (1) there is a mechanism or source that allows heat to remain in the upper portion of the stratigraphy for a longer period than conductive cooling predicts, or (2) the samples in the upper portion of the stratigraphy are

actually at greater depths (i.e. higher temperatures) than currently predicted. The possibility of an extended duration of elevated temperature in the upper part of the stratigraphy is unlikely, as this part of the stratigraphy needs to cool rapidly to the closure temperature of the $^{40}Ar/^{39}Ar$ system in biotite (Fig. 2) and then not rise back above that temperature.

The potential for samples in the upper part of the stratigraphy being at greater depths can be potentially explained by a slight dip towards the center of the intrusion due to isostatic adjustment. Cawthorn & Webb (2001) used Bouguer gravity models combined with estimates of isostatic response to conclude that isostatic adjustment of the RLS would have depressed the base of the crust by up to 6 km, resulting in a shallow dipping of the Eastern and Western Limbs toward each other. Based on comparisons to glacial rebound (~1 cm yr^{-1}; Kearey and Vine, 1996) and hydro-isostatic deflection, while considering the much greater density of the mafic rocks of the RLS, Cawthorn & Webb (2001) concluded that this adjustment would take place rapidly.

Conductive cooling at low temperatures is dominated by heat loss through the top (i.e. Earth's surface), and thus the depth below the surface for each sample becomes imperative. The samples of this study are collected over a lateral distance, perpendicular to strike, of ~40 km (Fig. 1). A rudimentary estimate of the effect of tilting the RLS indicates that over this distance every degree of dip results in an ~9.5% vertical compression (relative to Earth's surface) of the stratigraphic thickness. When tilted about the relatively stationary lower and lateral contact (e.g. sample B14-042), samples higher in the stratigraphy move closer (increasing in depth) relative to samples lower in the stratigraphy. Figure 8 shows the effect on calculated cooling rates using shallow dips for

the intrusive body of 2°, 3.5°, and 5°. With increased tilting, calculated cooling rates from the numerical simulation for the samples in the upper part of the stratigraphy move closer to those calculated iteratively from $^{40}Ar/^{39}Ar$ data, with a 3.5-5° tilting towards the center of the intrusion producing the best results.

The estimated 6 km flexure of the crust below the RLS, calculated by Cawthorn & Webb (2001), would produce an average dip angle ~2° towards the center of the intrusion, with shallower dip angles near the center and steeper near the edges. With the samples from this study, and the Eastern Limb in general, being much closer to the edge of the intrusion than its center, a 3.5-5° tilt of the stratigraphic section due to isostatic adjustment is conceivable. It is important to note, however, that a number of factors will affect this calculation including: (1) the estimated thickness of the roof, as a thicker roof sequence would result in a slightly shallower dip needed to match the observed cooling rates; (2) how rapidly and homogenously the depressed area on the surface fills due to sedimentation; (3) when the present-day dip angles developed, as any added dip after initial isostatic adjustment combined with the widespread $^{40}Ar/^{39}Ar$ plagioclase ages would make it difficult to find a single solution for all samples.

Lower Zone sample B14-042 is not included in this comparison as (1) it does not have a paired biotite $^{40}Ar/^{39}Ar$ age (outlier in Fig. 8) and (2) it is located almost at the lowermost contact of the RLS and likely has a dynamic and complicated thermal history.

5.3 Physical Evidence of Hydrothermal Circulation at High-Mid Temperatures

The transition from hydrothermal advective heat loss to primarily conductive heat loss below ~350-450°C, as inferred from thermochronology, is also supported by ample field

evidence. Schiffries and Skinner (1987) characterized three major hydrothermal stages involving fluids derived from the Transvaal Supergroup sediments. The three hydrothermal stages are recorded as mineralized veins that occur within every stratigraphic zone of the RLS stratigraphy.

The two mid-high temperature vein assemblages, a 300-600°C greenschist facies equivalent and a >600°C amphibolite facies equivalent, are both equally abundant throughout the RLS. However, while the high temperature amphibolite facies is found both within the RLS and the rocks of the contact aureole, the mid temperature greenschist facies is confined to only RLS rocks themselves (Schiffries & Skinner, 1987). The localization to the RLS rocks themselves indicates that while temperatures were high enough to circulate some fluids, that circulation may not have been vigorous enough to effectively produce any additional heat loss from the RLS at this temperature interval. In either case, the combined cooling to ~400°C is rapid enough to produce the observed biotite $^{40}Ar/^{39}Ar$ ages (Fig. 2).

Finally, the observed low temperature (<300°C) prehnite, pumpellyite and quartz hydrothermal assemblages are significantly less abundant in the RLS (Schiffries & Skinner, 1987). The lack of an abundant low temperature (<300°C) hydrothermal mineralization of the RLS indicates the almost complete cessation of hydrothermal circulation at these temperatures, agreeing with our significantly slower cooling rates calculated from biotite and plagioclase $^{40}Ar/^{39}Ar$ plateau ages and closure temperatures down to the same general temperature interval. Together, field evidence along with thermochonrologic results confirm a rapid cessation of the hydrothermal system

responsible for rapid cooling rates down to the ~400°C $^{40}Ar/^{39}Ar$ closure temperature of biotite, which was followed by a primarily conductive-only cooling regime.

5.4 Implications for the Timing of Hydrothermal Ore Deposits

The transition between dominant heat loss mechanisms, and the cessation of hydrothermal circulation within the RLS, provides constraints on the formation of economically viable hydrothermal ore deposits that extend outward into the Transvaal Supergroup sediments and are thought to be associated with the emplacement of the Bushveld Complex.

Through the dating of authigenic monazite and xenotime, Rasmussen et al. (2007) suggested that the emplacement of the Bushveld was responsible for a wide range in phosphate ages (~2.06-2.03 Ga) of both gold-bearing reefs and unmineralized strata within the Witwatersrand basin, some ~100 km outward from the RLS into both the Transvaal and Witwatersrand Supergroups. Gleason et al. (2010) extended the radial transport of hydrothermal fluids from the RSL to ~700 km, via the dating of Mississippi Valley-type (MVT) deposits at ~2.05 Ga. With the connection of most deposits to the RLS based on geochronology, it is important to note that many of the chronological constraints of these deposits have large uncertainties of ~2-3%. For example, a "coeval" Sm-Nd isochron age of Gleason et al. (2010) for fluorites in the Zeerust MVT deposits yields an age of 2046 ± 42 Ma. The age uncertainties, as well as the overall range in ages (see above), makes it difficult to deduce what deposits are actually related to fluids that are circulate due to the emplacement of the RLS.

The thermal history elucidated by the $^{40}Ar/^{39}Ar$ plagioclase data from this study, in combination with published chronology of the RLS, indicates that the RLS had cooled to ~400°C within at least 3 Ma followed by slow conductive cooling to the ambient geotherm. Based on the localization of mid temperature (~300-600°C) hydrothermal mineralization to the RSL only, it is likely cessation of hydrothermal circulation within the host rocks occurred even slightly prior to that. With the RLS at 400°C, there is not enough heat to produce circulating fluids within the host rocks. Any hydrothermal ore deposits forming from fluids associated with the emplacement of the RLS must therefore be coeval with the $^{40}Ar/^{39}Ar$ biotite ages of the RLS. Any hydrothermal deposits within the Transvaal that are younger than the $^{40}Ar/^{39}Ar$ biotite ages of the RLS, while formed by circulation hydrothermal fluids, are not related to the emplacement of the RLS itself.

Hydrothermal fluids related to the emplacement of the Lebowa Granites have also been thought to account for some of this ore mineralization (e.g. Rozendaal et al., 1995; Robb et al., 2000). However, given the indistinguishable age (2054.4 ± 1.8; Walraven & Hattingh, 1993) and immediate emplacement of the Lebowa Granite, any heat associated with its intrusion would homogenize with that of the RLS. The two bodies, therefore can be treated as a single thermal anomaly producing the same circulating fluids within the host rocks.

6. Conclusions

Plagioclase $^{40}Ar/^{39}Ar$ plateau ages throughout the RLS stratigraphy are significantly younger than reported $^{40}Ar/^{39}Ar$ biotite ages. When combined with grain specific diffusion parameters, the $^{40}Ar/^{39}Ar$ plagioclase data produces cooling rates that strongly

correlate with age and are significantly slower than cooling rates inferred by Setera et al. (chapter 2) for the temperature interval between U-Pb zircon and $^{40}Ar/^{39}Ar$ biotite ages (~800-400°C). We conclude that age differences between biotite and plagioclase $^{40}Ar/^{39}Ar$ ages, in addition to slower calculated cooling rates, is a product of the RLS transitioning from rapid heat loss associated with hydrothermal circulation to primarily conductive heat loss. The rapid cessation of hydrothermal circulation suggests that hydrothermal ore deposits within the Transvaal Supergroup sediments, genetically related to the emplacement of the RLS, must have formation ages coeval with that of the $^{40}Ar/^{39}Ar$ biotite ages of the RLS (2054.47 ± 0.84 Ma). This suggests that not only is the RLS responsible for vast PGE ore deposits within the mafic rocks themselves, but it is also a trigger for regional hydrothermal ore deposits (e.g. Sn, F, Zn) all within ~3 Ma.

Numerical heat-loss simulations using the Heat3D code further confirm the need for additional heat-loss associated with hydrothermal circulation, as a conduction-only model cannot produce the reported U-Pb zircon and $^{40}Ar/^{39}Ar$ biotite ages of the RLS. Reported U-Pb zircon and $^{40}Ar/^{39}Ar$ biotite ages are, however, reproduced by using a numerical heat-loss simulation that includes hydrothermal circulation for 1 million years after the initial emplacement of the RLS. The same model also reproduces the calculated cooling rates for $^{40}Ar/^{39}Ar$ plagioclase samples for the lower part of the RLS stratigraphy. Calculated cooling rates for $^{40}Ar/^{39}Ar$ plagioclase samples for the entire stratigraphy are reproduced when the RLS is dipped shallowly at ~3.5-5° due to isostatic adjustment.

With the collective observations above, we present a full thermal model of the RLS (Fig. 11) where we propose that the RLS was initially emplaced and closely followed by the Lebowa Granite Suite. Cooling at high temperatures (Fig. 11, t=0) takes

place rapidly (within 1 million years), with a hydrothermal circulation first developing within the host Transvaal Supergroup sediments. At slightly lower temperatures (~900-600°C; Fig. 11, t=1), cooling rates are still rapid and aided by the circulating saline fluids from the Transvaal Supergroup Sediments that have penetrated the solidified RLS to form amphibolite facies (>600°C) hydrothermal vein assemblages throughout the stratigraphy and the contact aureole. At mid temperatures (~600-400°C; Fig. 11, t-2), the RLS has cooled to a point where hydrothermal circulation within the Transvaal Supergroup (associated with the original emplacement) ceases. Less vigorous hydrothermal circulation continues to form ~300-600°C greenschist facies vein assemblages throughout the stratigraphy, but is localized to the RLS rocks only. Upon reaching 400°C (~1-2 Ma after U-Pb zircon ages), the $^{40}Ar/^{39}Ar$ system in biotite is uniformly closed throughout the stratigraphy. At 400°C and below (Fig. 11, t=4), the hydrothermal system associated with the emplacement of the RLS is essentially finished, and any hydrothermal ore deposits within the host rocks that are directly linked to the heat produced from either the RLS or Lebowa Granite Suite have already formed (within ~1 Ma U-Pb zircon ages). Heat loss is now entirely conductive, producing scattered $^{40}Ar/^{39}Ar$ plagioclase ages dependent on their individual closure temperature.

Finally, the thermal perturbation responsible for Ar-loss from individual plagioclase grains is likely sourced, not from the Vredefort meteorite impact, but from widespread alkaline magmatism within the Bushveld Complex area at ~1.3-1.4 Ga.

7. References

Berger, G. W., and York, D., 1981, Geothermometry from 40Ar39Ar dating experiments: Geochimica et Cosmochimica Acta, v. 45, no. 6, p. 795-811.

Boven, A., Pasteels, P., Kelley, S. P., Punzalan, L., Bingen, B., and Demaiffe, D., 2001, 40Ar/39Ar study of plagioclases from the Rogaland anorthosite complex (SW Norway); an attempt to understand argon ages in plutonic plagioclase: Chemical Geology, v. 176, no. 1-4, p. 105-135.

Buick, I. S., Maas, R., and Gibson, R., 2001, Precise U–Pb titanite age constraints on the emplacement of the Bushveld Complex, South Africa: Journal of the Geological Society, v. 158, p. 3-6.

Cassata, W. S., and Renne, P. R., 2013, Systematic variations of argon diffusion in feldspars and implications for thermochronometry: Geochimica et Cosmochimica Acta, v. 112, p. 251- 287.

Cassata, W. S., Renne, P. R., and Shuster, D. L., 2009, Argon diffusion in plagioclase and implications for thermochronometry: a case study from the Bushveld Complex, South Africa: Geochimica et Cosmochimica Acta, v. 73, no. 21, p. 6600-6612.

Cawthorn, R. G., Ellam, R. M., Ashwal, L. D., and Webb, S. J., 2012, A clinopyroxenite intrusion from the Pilanesberg Alkaline Province, South Africa: Precambrian Research, v. 198, p. 25-36.

Cawthorn, R. G. and Walraven, F., 1998, Emplacement and crystallization time for the Bushveld Complex: Journal of Petrology, v. 39, p. 1669-1687.

Cawthorn, R. and Webb, S., 2001, Connectivity between the western and eastern limbs of the Bushveld Complex: Tectonophysics, v. 330, p. 195-209.

Cheney, E. S., and Twist, D., 1991, The conformable emplacement of the Bushveld mafic rocks along a regional unconformity in the Transvaal succession of South Africa: Precambrian Research, v. 52, no. 1-2, p. 115-132.

Cole, J., Webb, S. J., and Finn, C. A., 2014, Gravity models of the Bushveld Complex–Have we come full circle?: Journal of African Earth Sciences, v. 92, p. 97-118.

Eales, H. V., and Cawthorn, R. G., 1996, The bushveld complex, Developments in Petrology, v. 15, Elsevier, p. 181-229.

Elburg, M. A., and Cawthorn, R. G., 2017, Source and evolution of the alkaline Pilanesberg Complex, South Africa: Chemical Geology, v. 455, p. 148-165.

Eriksson, P. and Altermann, W., 1998, An overview of the geology of the Transvaal Supergroup dolomites (South Africa): Environmental geology, v. 36, p. 179-188.

Ferré, E. C., Wilson, J., and Gleizes, G., 1999, Magnetic susceptibility and AMS of the Bushveld alkaline granites, South Africa: Tectonophysics, v. 307, no. 1-2, p. 113-133.

Garrick-Bethell, I., Weiss, B. P., Shuster, D. L., and Buz, J., 2009, Early lunar magnetism: Science, v. 323, no. 5912, p. 356-359.

Gibson, R. L., Armstrong, R. A., and Reimold, W. U., 1997, The age and thermal evolution of the Vredefort impact structure: A single-grain U-Pb zircon study: Geochimica et Cosmochimica Acta, v. 61, no. 7, p. 1531-1540.

Gibson, R. L., and Jones, M. Q. W., 2002, Late Archaean to Palaeoproterozoic geotherms in the Kaapvaal Craton, South Africa: constraints on the thermal evolution of the Witwatersrand Basin: Basin Research, v. 14, no. 2, p. 169-181.

Gleason, J. D., Gutzmer, J., Kesler, S. E., and Zwingmann, H., 2011, 2.05-Ga Isotopic Ages for Transvaal Mississippi Valley–Type Deposits: Evidence for Large-Scale Hydrothermal Circulation around the Bushveld Igneous Complex, South Africa: The Journal of Geology, v. 119, no. 1, p. 69-80.

Harmer, R. E., 1999, The petrogenetic association of carbonatite and alkaline magmatism: constraints from the Spitskop Complex, South Africa: Journal of Petrology, v. 40, no. 4, p. 525-548.

Harrison, T. M., and McDougall, I., 1981, Excess 40Ar in metamorphic rocks from Broken Hill, New South Wales: implications for40Ar/39Ar age spectra and the thermal history of the region: Earth and Planetary Science Letters, v. 55, no. 1, p. 123-149.

Huber, C., Cassata, W. S., and Renne, P. R., 2011, A lattice Boltzmann model for noble gas diffusion in solids: the importance of domain shape and diffusive anisotropy and implications for thermochronometry: Geochimica et Cosmochimica Acta, v. 75, no. 8, p. 2170-2186.

Kamo, S. L., Reimold, W. U., Krogh, T. E., and Colliston, W. P., 1996, A 2.023 Ga age for the Vredefort impact event and a first report of shock metamorphosed zircons in pseudotachylitic breccias and granophyre: Earth and Planetary Science Letters, v. 144, no. 3-4, p. 369-387.

Kearey, P., Klepeis, K. A., and Vine, F. J., 2009, *Global tectonics*. John Wiley & Sons.

Kuiper, K., Deino, A., Hilgen, F., Krijgsman, W., Renne, P., and Wijbrans, J., 2008, Synchronizing rock clocks of Earth history: Science, v. 320, no. 5875, p. 500-504.

Jourdan, F., Verati, C., and Féraud, G., 2006, Intercalibration of the Hb3gr 40Ar/39Ar dating standard: Chemical Geology, v. 231, no. 3, p. 177-189.

McDougall, I., and Harrison, T. M., 1999, Geochronology and Thermochronology by the 40Ar/39Ar Method, Oxford University Press on Demand.

Molyneux, T. G., 1974, A geological investigation of the Bushveld Complex in Sekhukhuneland and part of the Steelpoort Valley: Transactions, Geological Society of South Africa, v. 77, p. 329-338.

Molyneux, T., 2008, Compilation on a scale of 1: 50000 of the geology of the eastern compartment of the Bushveld Complex: Special Publication, v. 1.

Mungall, J. E., Kamo, S. L., and McQuade, S., 2016, U–Pb geochronology documents out-of-sequence emplacement of ultramafic layers in the Bushveld Igneous Complex of South Africa: Nature Communications, v. 7.

Norton, D., and Taylor Jr, H. P., 1979, Quantitative simulation of the hydrothermal systems of crystallizing magmas on the basis of transport theory and oxygen isotope data: An analysis of the Skaergaard intrusion: Journal of Petrology, v. 20, no. 3, p. 421-486.

Olsson, J., Söderlund, U., Klausen, M., and Ernst, R., 2010, U–Pb baddeleyite ages linking major Archean dyke swarms to volcanic-rift forming events in the Kaapvaal craton (South Africa), and a precise age for the Bushveld Complex: Precambrian Research, v. 183, p. 490-500.

Onstott, T. C., Hall, C. M., and York, D., 1989, 40Ar/39Ar thermochronometry of the Imataca Complex, Venezuela: Precambrian Research, v. 42, no. 3-4, p. 255-291.

Rasmussen, B., Fletcher, I. R., Muhling, J. R., Mueller, A. G., and Hall, G. C., 2007, Bushveld-aged fluid flow, peak metamorphism, and gold mobilization in the Witwatersrand basin, South Africa: Constraints from in situ SHRIMP U-Pb dating of monazite and xenotime: Geology, v. 35 no. 10, p. 931-934.

Renne, P. R., Deckart, K., Ernesto, M., Fe, G., and Piccirillo, E. M., 1996, Age of the Ponta Grossa dike swarm (Brazil), and implications to Paraná flood volcanism: Earth and Planetary Science Letters, v. 144, no. 1-2, p. 199-211.

Renne, P. R., Onstott, T. C., D'Agrella-Filho, M. S., Pacca, I. G., and Teixeira, W., 1990, 40Ar/39Ar Dating of 1.0–1.1 Ga magnetizations from the Sa˜ o Francisco and Kalahari cratons: tectonic implications for Pan-African and Brasiliano mobile belts: Earth and Planetary Science Letters, v. 101, no. 2-4, p. 349-366.

Robb, L. J., Freeman, L. A., and Armstrong, R. A., 2000, Nature and longevity of hydrothermal fluid flow and mineralisation in granites of the Bushveld Complex, South Africa: Earth a nd Environmental Science Transactions of The Royal Society of Edinburgh, v. 91, no. 1-2, p. 269-281.

Rozendaal, A., Misiewicz, J. E., and Scheepers, R., 1995, The tin zone: sediment-hosted hydrothermal tin mineralization at Rooiberg, South Africa: Mineralium Deposita, v. 30, no. 2, p. 178-187.

SACS, 1980, *Lithostratigraphy of the Republic of South Africa, South West Africa/Namibia and the Republic of Botswana, Transkei, and Venda. South African Geological Survey Handbook*, v. 8, p. 690.

Schweitzer, J. K., Hatton, C. J., and De Waal, S. A., 1997, Link between the granitic and volcanic rocks of the Bushveld Complex, South Africa: Journal of African Earth Sciences, v. 24, no. 1-2, p. 95-104.

Scoates, J. S. and Friedman, R. M., 2008, Precise age of the platiniferous Merensky Reef, Bushveld Complex, South Africa, by the U-Pb zircon chemical abrasion ID-TIMS technique: Economic Geology, v. 103, p. 465-471.

Scoates, J. S., and Wall, C. J., 2015, Geochronology of layered intrusions, Layered Intrusions, Springer, p. 3-74.

Schiffries, C. M., and Rye, D. M., 1990, Stable isotopic systematics of the Bushveld Complex: II. Constraints on hydrothermal processes in layered intrusions: American Journal of Science, v. 290, no. 3, p. 209-245.

Schiffries, C. M., and Skinner, B. J., 1987, The Bushveld hydrothermal system; field and petrologic evidence: American Journal of Science, v. 287, no. 6, p. 566-595.

Setera, J. B., and VanTongeren, J. A., 2018, Lateral Variability in the Upper Main Zone, Bushveld Complex, owing to Directional Magma Recharge and Emplacement from North to South: Journal of Petrology, v. 59, no. 9, p. 1763-1786.

Turtle, E. P., Pierazzo, E., and O'Brien, D. P., 2003, Numerical modeling of impact heating and cooling of the Vredefort impact structure: Meteoritics & Planetary Science, v. 38, no. 2, p. 293-303.

VanTongeren, J. A., and Mathez, E. A., 2012, Large-scale liquid immiscibility at the top of the Bushveld Complex, South Africa: Geology, v. 40, no. 6, p. 491-494.

VanTongeren, J. and Mathez, E., 2015, On the relationship between the Bushveld Complex and its felsic roof rocks, part 2: the immediate roof: Contributions to Mineralogy and Petrology, v. 170, p. 56.

VanTongeren, J. A., Mathez, E. A., and Kelemen, P. B., 2010, A felsic end to Bushveld differentiation: Journal of Petrology, v. 51, no. 9, p. 1891-1912.

Walreaven, F. and Hattingh, E., 1993, Geochronology of the Nebo Granite, Bushveld Complex: South African Journal of Geology, v. 96, p. 21-41.

Webb, S. J., Cawthorn, R. G., Nguuri, T., and James, D., 2004, Gravity modeling of Bushveld Complex connectivity supported by Southern African seismic experiment results: South African Journal of Geology, v. 107, p. 207-218.

Williams, E., Boudreau, A. E., Boorman, S., and Kruger, F. J., 2006, Textures of orthopyroxenites from the Burgersfort bulge of the eastern Bushveld Complex, Republic of South Africa: Contributions to Mineralogy and Petrology, v. 151, no. 4, p. 480.

Wohletz, K., 1999, KWare HEAT3D software. *Los Alamos Nat. Lab., Open File Program LA-CC*, 99-27.

Verwoerd, W. J., 2006, The Pilanesberg alkaline province. *The Geology of South Africa*, p 381- 393.

Ver Hoeve, T. J., Scoates, J. S., Wall, C. J., Weis, D., and Amini, M., 2018, A Temperature-Composition Framework for Crystallization of Fractionated Interstitial Melt in the Bushveld Complex from Trace Element Systematics of Zircon and Rutile: Journal of Petrology, v. 59, no. 7, p. 1383-1416.

Zeh, A., Ovtcharova, M., Wilson, A. H., and Schaltegger, U., 2015, The Bushveld Complex was emplaced and cooled in less than one million years–results of zirconology, and geotectonic implications: Earth and Planetary Science Letters, v. 418, p. 103-114.

Figure Captions

Figure 1

(a) Generalized geologic map of the Eastern Limb of the Bushveld Complex modified after Setera et al. (2019) VanTongeren et al. (2010). Stars indicate sample locations for samples analyzed for plagioclase $^{40}Ar/^{39}Ar$ thermochronology. (b) Samples placed in generalized stratigraphic column of the Rustenburg Layered Suite of the Eastern Limb of the Bushveld Complex. Thicknesses discussed in text.

Figure 2

Compilation of published high-precision chronology plotted against the generalized stratigraphic column of the Eastern Limb of the RLS (2σ uncertainties reported). Weighted mean biotite age is from Setera et al. (2019). Data sources: 1 - Zeh et al. (2015), 2 - Mungall et al. (2016), 3 - Scoates & Wall (2015), 4 - Cassata et al. (2009), 5 - Nomade et al. (2004), 6 - Setera et al. (2019).

Figure 3

Example from sample B14-045_01 (Main Zone). (a) Step-heating age spectrum. The dashed line within individual steps represents the apparent age of the step. (b) Arrhenius plot. Activation energy = E_a (kJ/mol), diffusion constant = $\ln(D_0/a^2)$. Closed circles are used in Arrhenius regressions. Open circles are not used.

Figure 4

Compilation of high-precision chronology plotted against the generalized stratigraphic column of the Eastern Limb of the RLS. Data sources are the same as Fig. 2. Plagioclase $^{40}Ar/^{39}Ar$ ages are single-grain analyses with 1σ uncertainties.

Figure 5

All release spectra. Data and calculated ages are presented with 1σ uncertainties.

Figure 6

All Arrhenius regressions. Data and calculated diffusion parameters are presented with 1σ uncertainties. Activation energy = E_a (kJ/mol), diffusion constant = $\ln(D_0/a^2)$. Closed circles are used in Arrhenius regressions. Open circles are not used.

Figure 7

(a) Plagioclase $^{40}Ar/^{39}Ar$ plateau age versus iteratively calculated average cooling rate between biotite and plagioclase $^{40}Ar/^{39}Ar$ ages. (b) Plagioclase $^{40}Ar/^{39}Ar$ plateau age versus iteratively calculated closure temperature (blue closed circles). Simple linear regression (dashed line) do not incorporate sample B14-042 (open symbols).

Figure 8

A comparison of stratigraphic position within the RLS and cooling rate. Blue closed circles represent iteratively calculated cooling rates from biotite and plagioclase $^{40}Ar/^{39}Ar$ results (Table 2). Cooling curves are calculated from numerical simulations for dip angles of 0°, 2°, 3.5°, and 5°.

Figure 9

Initial conditions for both Heat3D numerical heat loss simulations, conductive-only and hydrothermally circulation.

Figure 10

After Setera et al. (2019), conductive-only (dashed line) and conductive-plus-convection (solid line) heat-loss simulations from Heat3D code. Models are solved for the depth center (3 km) of the RLS, 30 km away from the lateral contact with the host rocks. Orange shaded area denotes range of published U-Pb zircon ages as well as their measure Ti-in-zircon temperatures (see main text for full references). Blue shaded region denotes published weighted mean age of biotite $^{40}Ar/^{39}Ar$ plateau ages from Setera et al. (2019).

Figure 11

Schematic illustration depicting the post-emplacement thermal evolution of the RLS as inferred from thermochronology. White circular arrows denote active hydrothermal circulation, while non-circular arrows denote hydrothermal interaction between RLS and host rock. Black arrows denote conductive cooling. Size and length of arrow qualitatively represent magnitude. At t_0, cooling of the intrusion is rapid, but hydrothermal circulation first involves circulating fluids within the host Transvaal Supergroup (green lithology). At t_1, hydrothermal circulation now penetrates the entire RLS forming hydrothermal veins. As temperature lowers, hydrothermal circulation is less vigorous and limited to only the RLS (t_2) and conductive heat-loss begins to take over as the dominant heat-loss

mechanism. At t_4, as suggested from plagioclase $^{40}Ar/^{39}Ar$ ages, heat-loss from the RLS is now controlled via conduction only.

Figure 1

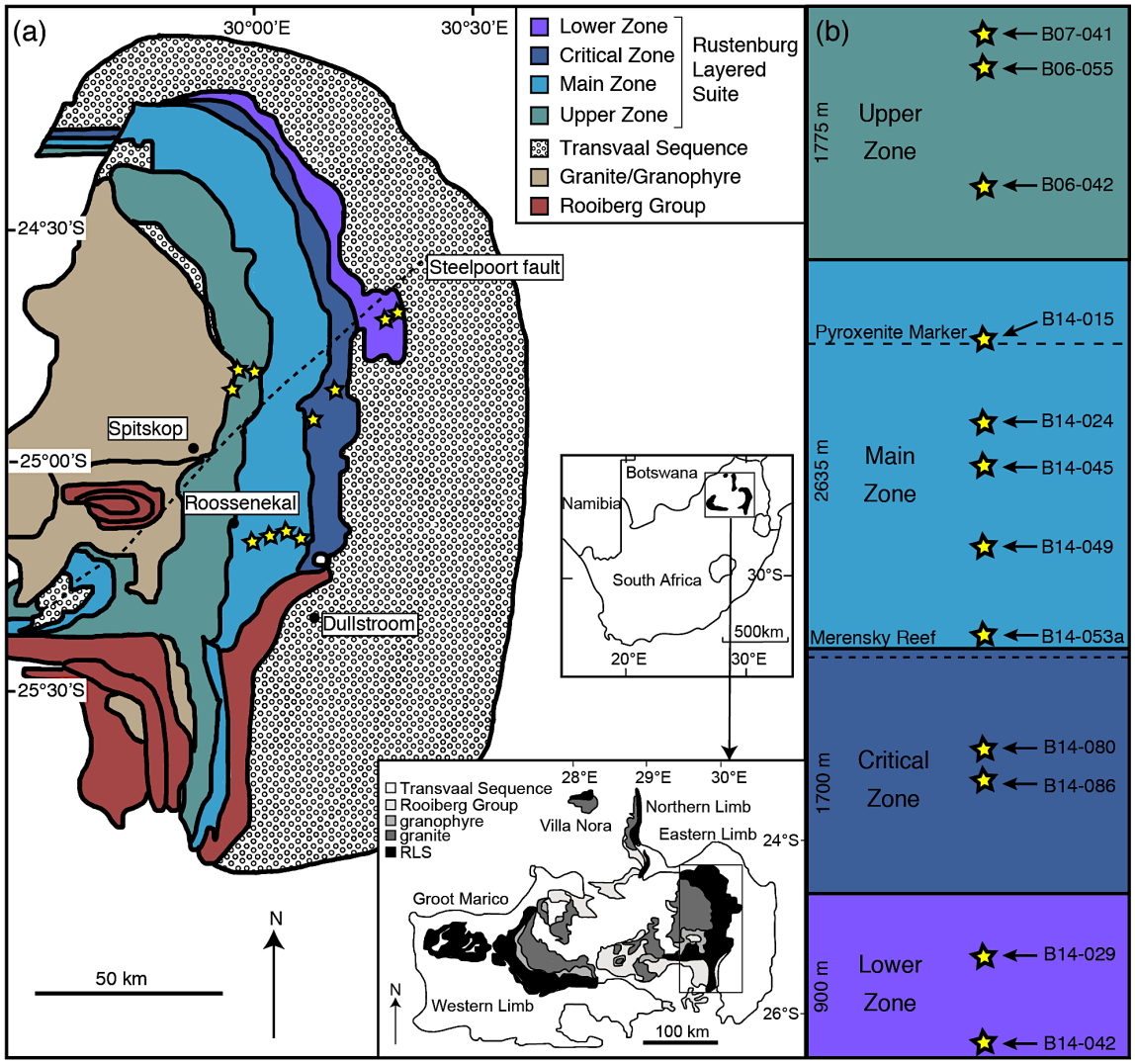
(a)
30°00'E
30°30'E
Lower Zone
Critical Zone
Main Zone
Upper Zone
Rustenburg Layered Suite
Transvaal Sequence
Granite/Granophyre
Rooiberg Group
24°30'S
Steelpoort fault
Spitskop
25°00'S
Roossenekal
Dullstroom
25°30'S
50 km
N
Botswana
Namibia
South Africa
30°S
500km
20°E
30°E
Transvaal Sequence
Rooiberg Group
granophyre
granite
RLS
28°E
29°E
30°E
Villa Nora
Northern Limb
Eastern Limb
24°S
Groot Marico
Western Limb
26°S
100 km
(b)
1775 m
Upper Zone
B07-041
B06-055
B06-042
Pyroxenite Marker
B14-015
2635 m
Main Zone
B14-024
B14-045
B14-049
Merensky Reef
B14-053a
1700 m
Critical Zone
B14-080
B14-086
900 m
Lower Zone
B14-029
B14-042

Figure 2

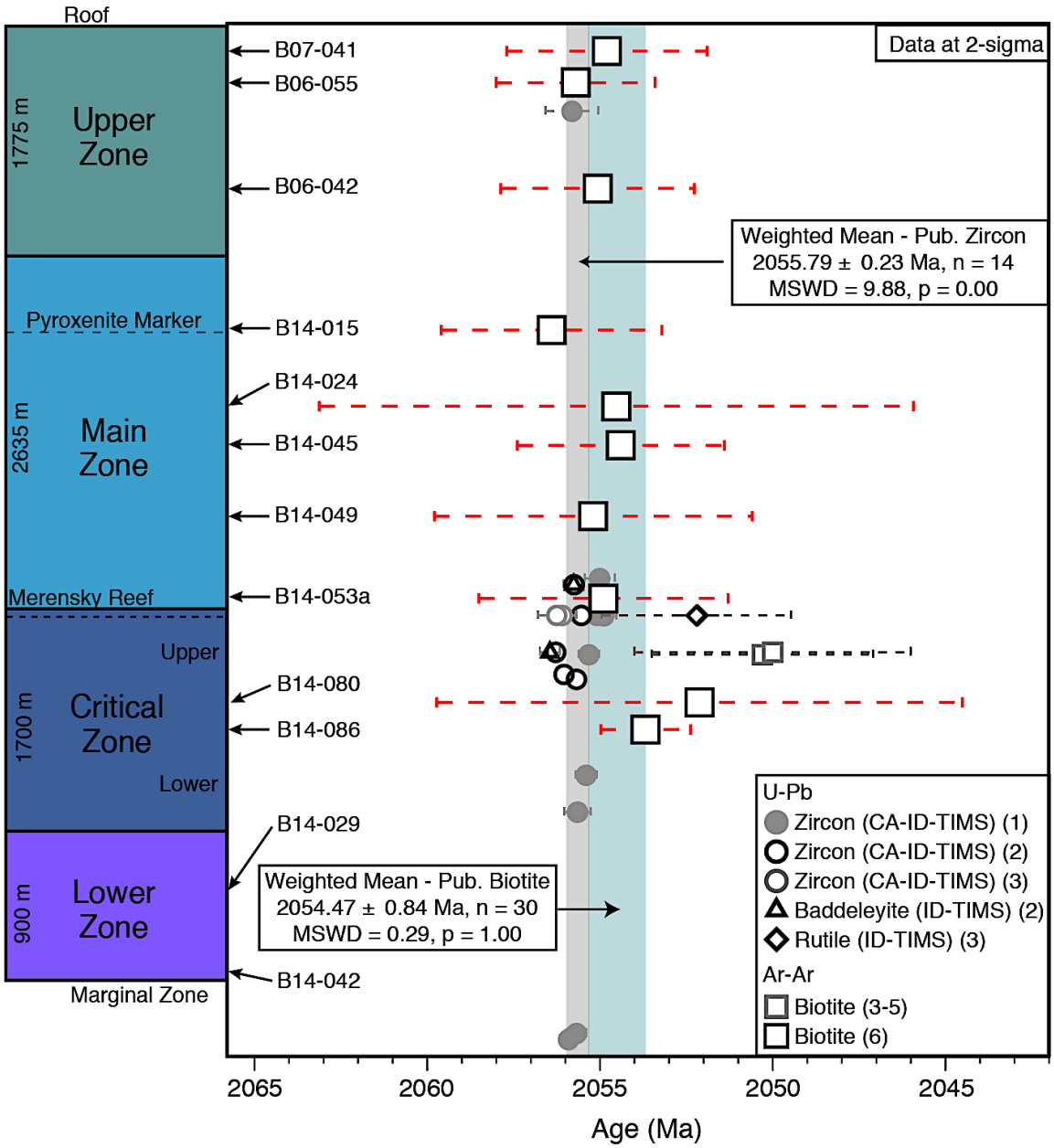
Roof
1775 m
Upper Zone
Pyroxenite Marker
2635 m
Main Zone
Merensky Reef
Upper
1700 m
Critical Zone
Lower
900 m
Lower Zone
Marginal Zone
B07-041
B06-055
B06-042
B14-015
B14-024
B14-045
B14-049
B14-053a
B14-080
B14-086
B14-029
B14-042
Data at 2-sigma
Weighted Mean - Pub. Zircon
2055.79 ± 0.23 Ma, n = 14
MSWD = 9.88, p = 0.00
Weighted Mean - Pub. Biotite
2054.47 ± 0.84 Ma, n = 30
MSWD = 0.29, p = 1.00
U-Pb
Zircon (CA-ID-TIMS) (1)
Zircon (CA-ID-TIMS) (2)
Zircon (CA-ID-TIMS) (3)
Baddeleyite (ID-TIMS) (2)
Rutile (ID-TIMS) (3)
Ar-Ar
Biotite (3-5)
Biotite (6)
2065
2060
2055
2050
2045
Age (Ma)

Figure 3

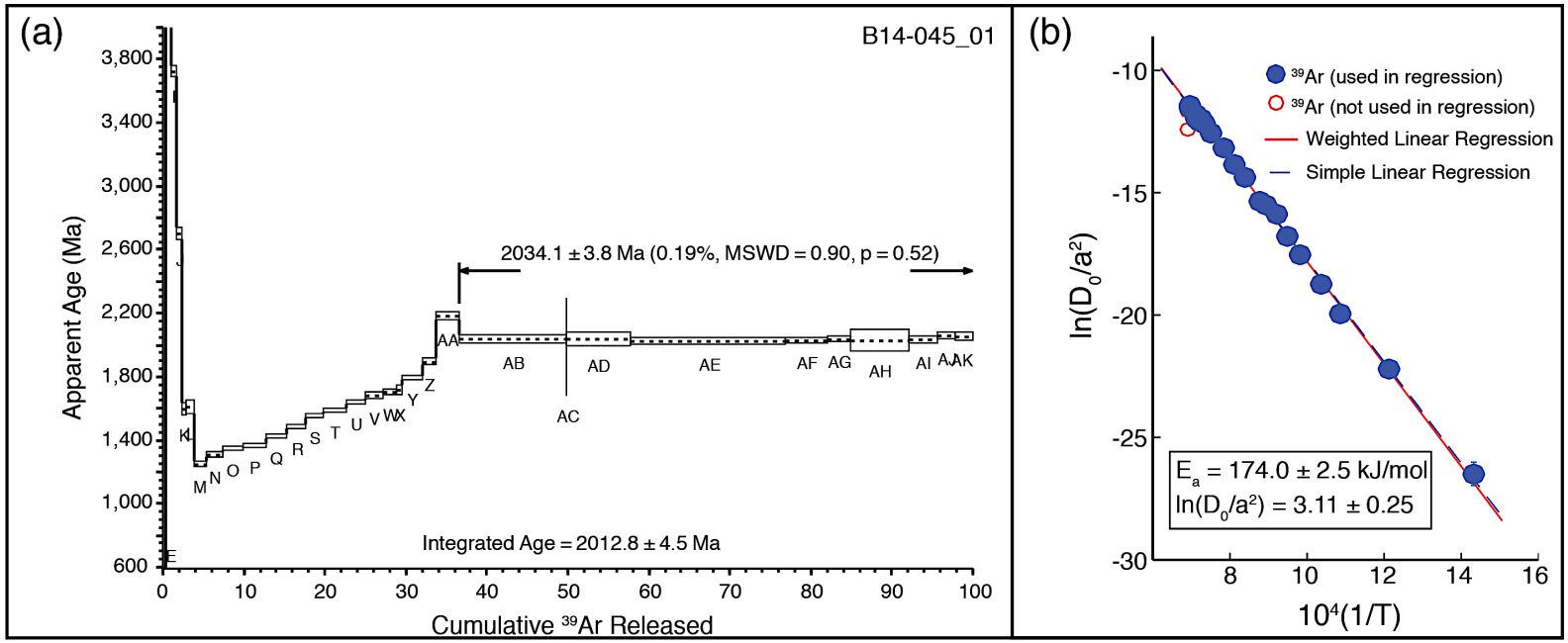
(a)
B14-045_01
Apparent Age (Ma)
3,800
3,400
3,000
2,600
2,200
1,800
1,400
1,000
600
2034.1 ± 3.8 Ma (0.19%, MSWD = 0.90, p = 0.52)
Integrated Age = 2012.8 ± 4.5 Ma
Cumulative ³⁹Ar Released
0
10
20
30
40
50
60
70
80
90
100
(b)
³⁹Ar (used in regression)
³⁹Ar (not used in regression)
Weighted Linear Regression
Simple Linear Regression
ln(D₀/a²)
-10
-15
-20
-25
-30
E_a = 174.0 ± 2.5 kJ/mol
ln(D₀/a²) = 3.11 ± 0.25
8
10
12
14
16
10⁴(1/T)

Figure 4

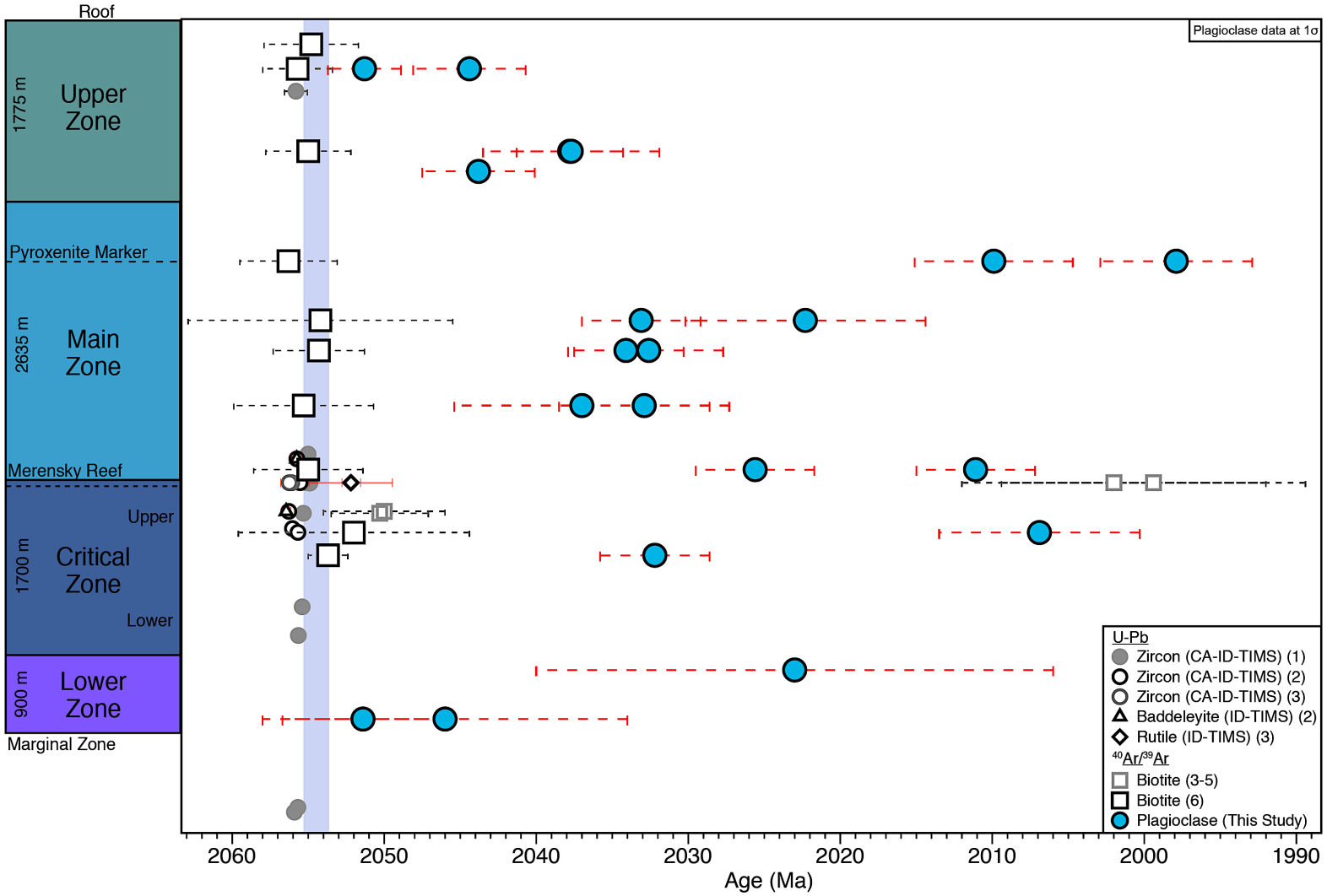
Roof
1775 m
Upper Zone
Pyroxenite Marker
2635 m
Main Zone
Merensky Reef
Upper
1700 m
Critical Zone
Lower
900 m
Lower Zone
Marginal Zone
Plagioclase data at 1σ
U-Pb
Zircon (CA-ID-TIMS) (1)
Zircon (CA-ID-TIMS) (2)
Zircon (CA-ID-TIMS) (3)
Baddeleyite (ID-TIMS) (2)
Rutile (ID-TIMS) (3)
40Ar/39Ar
Biotite (3-5)
Biotite (6)
Plagioclase (This Study)
2060
2050
2040
2030
2020
2010
2000
1990
Age (Ma)

Figure 5

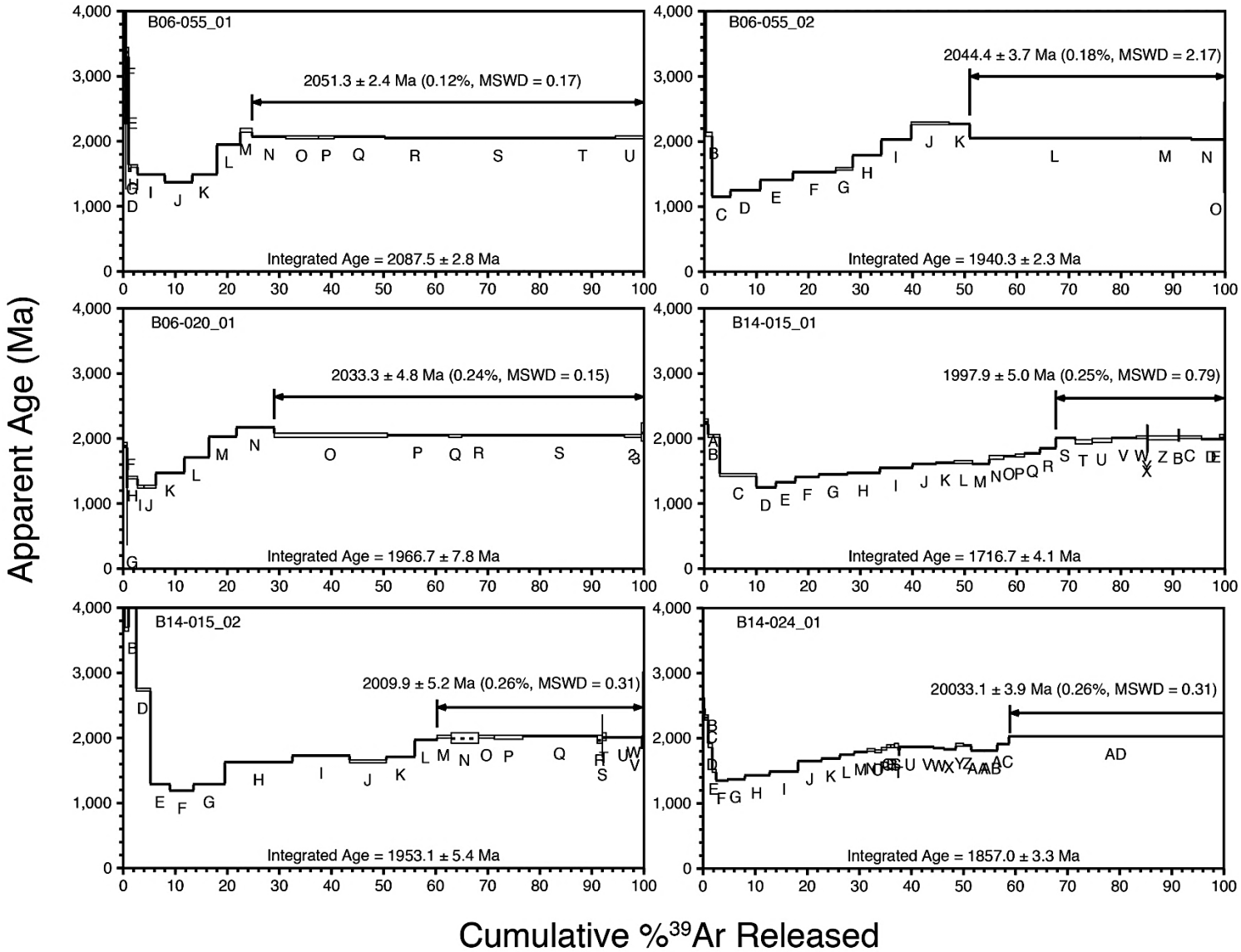
B06-055_01
2051.3 ± 2.4 Ma (0.12%, MSWD = 0.17)
Integrated Age = 2087.5 ± 2.8 Ma
B06-055_02
2044.4 ± 3.7 Ma (0.18%, MSWD = 2.17)
Integrated Age = 1940.3 ± 2.3 Ma
B06-020_01
2033.3 ± 4.8 Ma (0.24%, MSWD = 0.15)
Integrated Age = 1966.7 ± 7.8 Ma
B14-015_01
1997.9 ± 5.0 Ma (0.25%, MSWD = 0.79)
Integrated Age = 1716.7 ± 4.1 Ma
B14-015_02
2009.9 ± 5.2 Ma (0.26%, MSWD = 0.31)
Integrated Age = 1953.1 ± 5.4 Ma
B14-024_01
20033.1 ± 3.9 Ma (0.26%, MSWD = 0.31)
Integrated Age = 1857.0 ± 3.3 Ma
Apparent Age (Ma)
Cumulative %39Ar Released

Figure 5 (Continued)

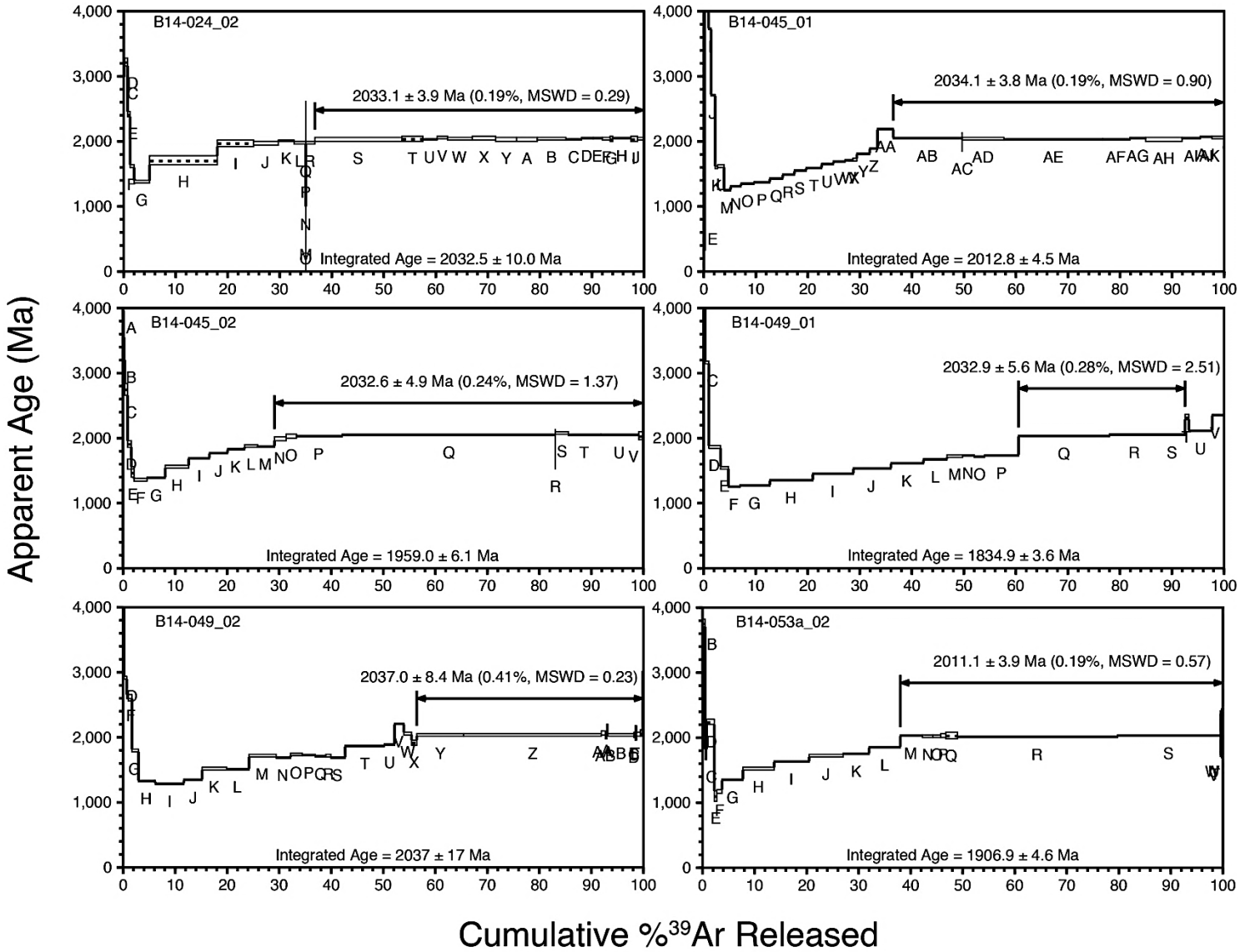

Figure 5 (Continued)

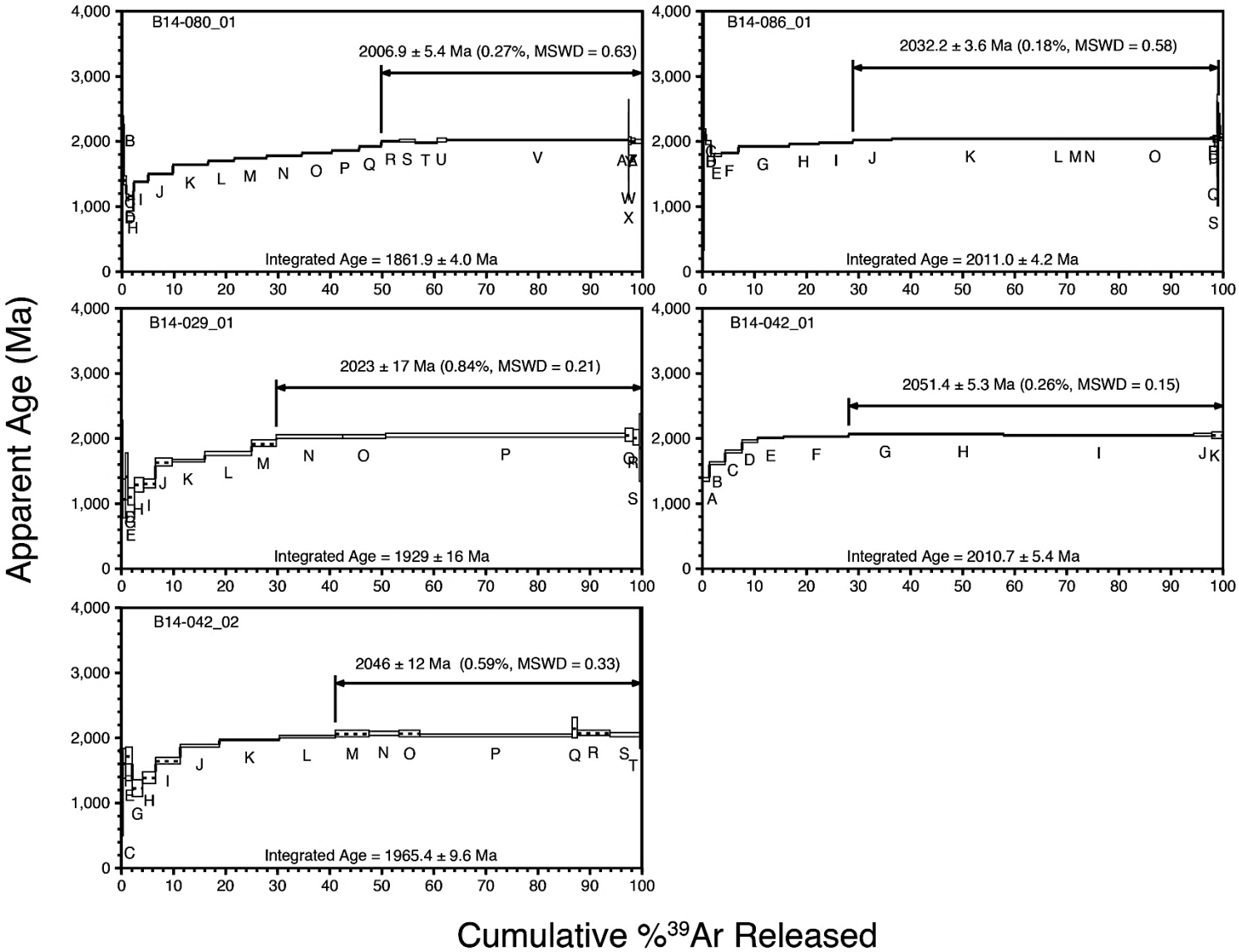

Figure 6

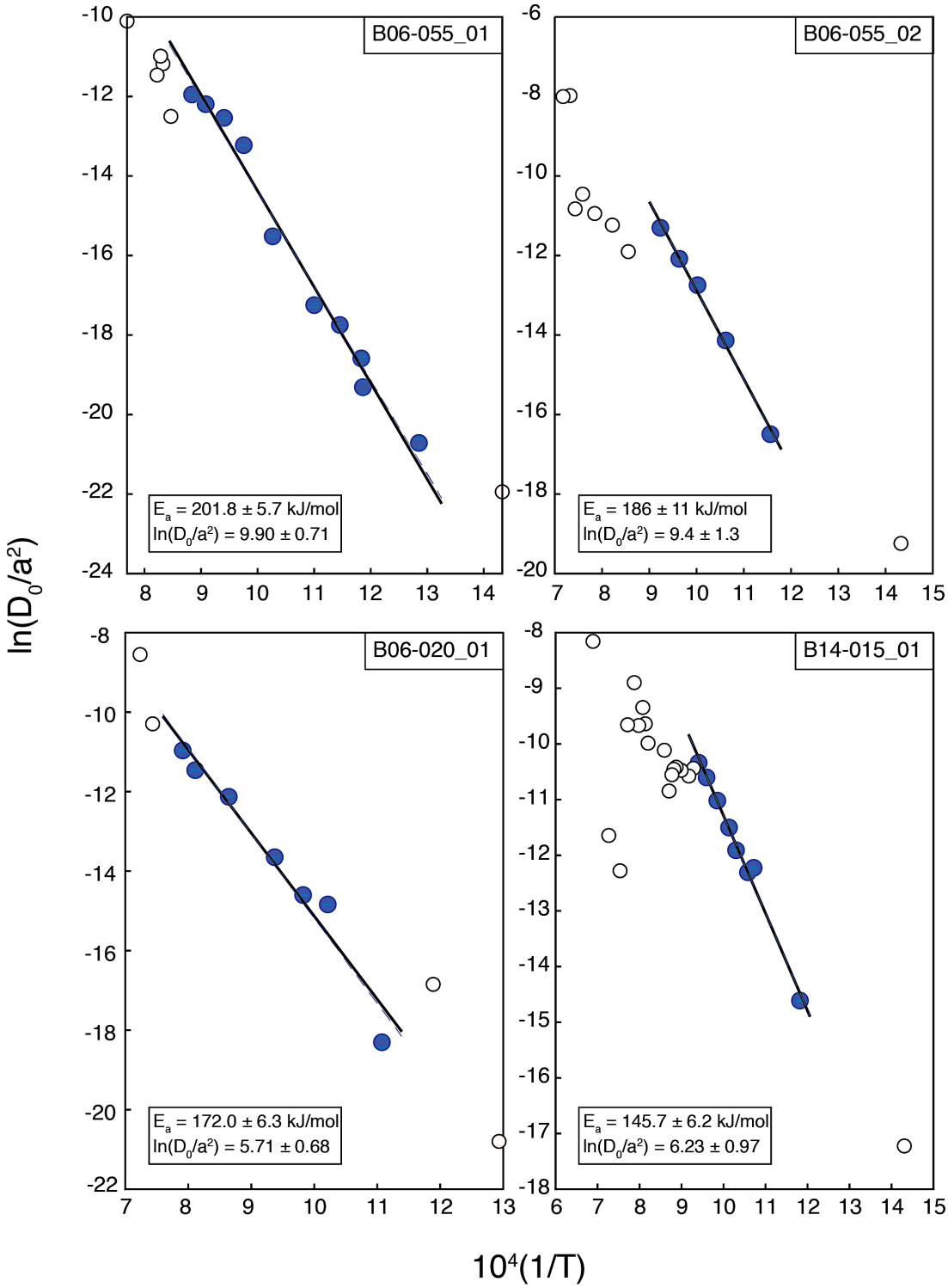
B06-055_01
E_a = 201.8 ± 5.7 kJ/mol
ln(D_0/a^2) = 9.90 ± 0.71
B06-055_02
E_a = 186 ± 11 kJ/mol
ln(D_0/a^2) = 9.4 ± 1.3
B06-020_01
E_a = 172.0 ± 6.3 kJ/mol
ln(D_0/a^2) = 5.71 ± 0.68
B14-015_01
E_a = 145.7 ± 6.2 kJ/mol
ln(D_0/a^2) = 6.23 ± 0.97
ln(D_0/a^2)
10^4(1/T)

Figure 6 (Continued)

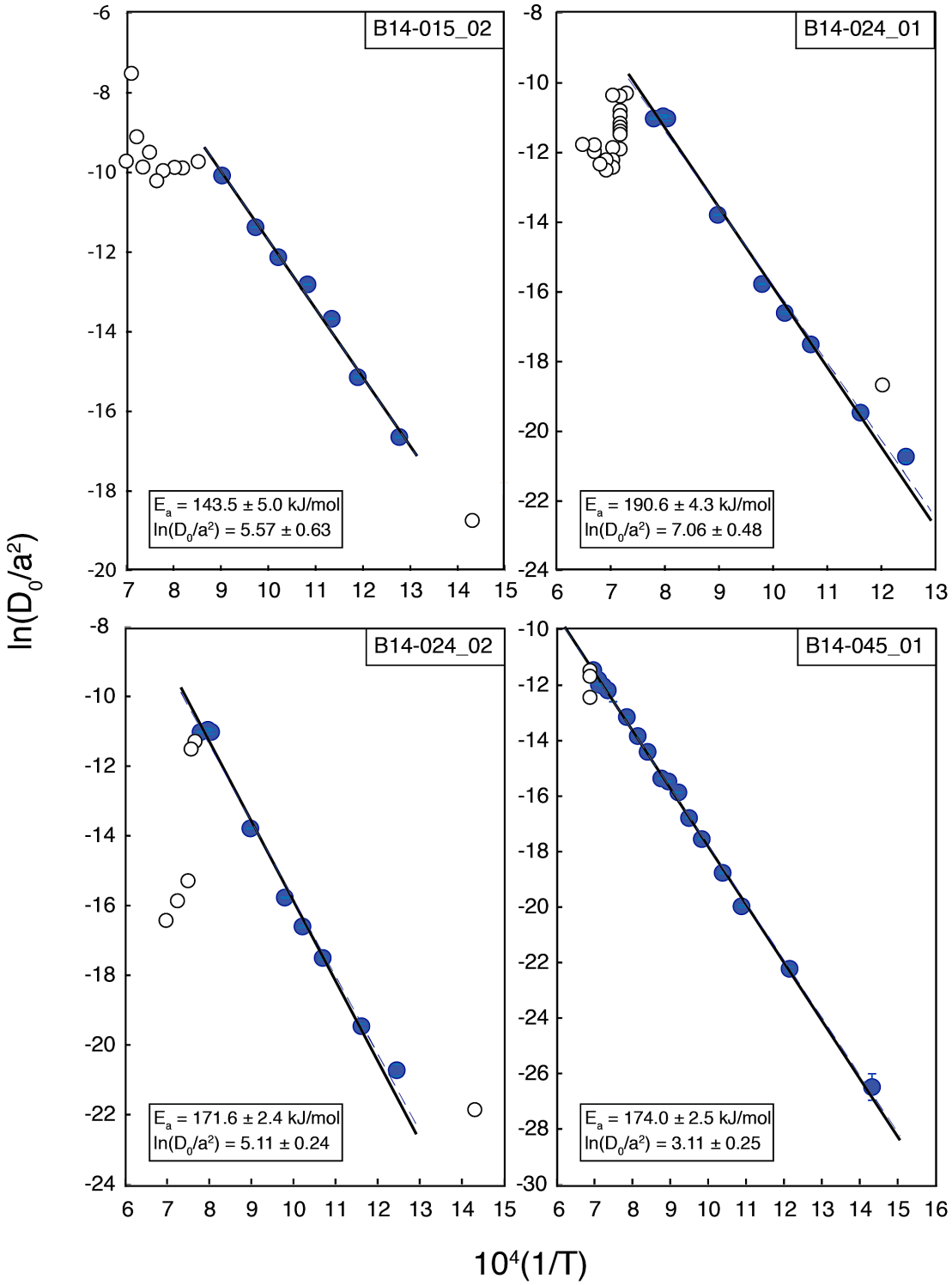

Figure 6 (Continued)

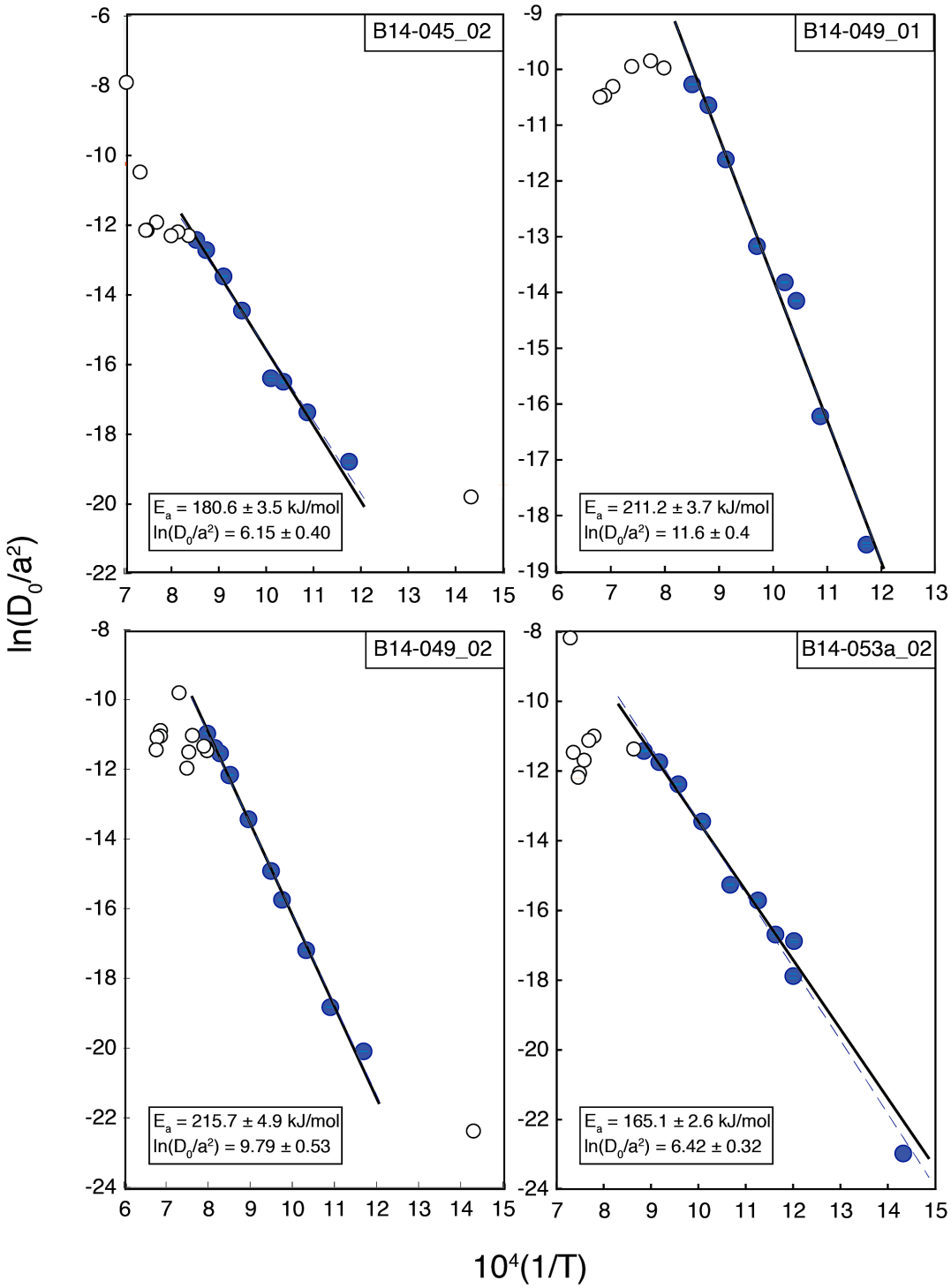

Figure 6 (Continued)

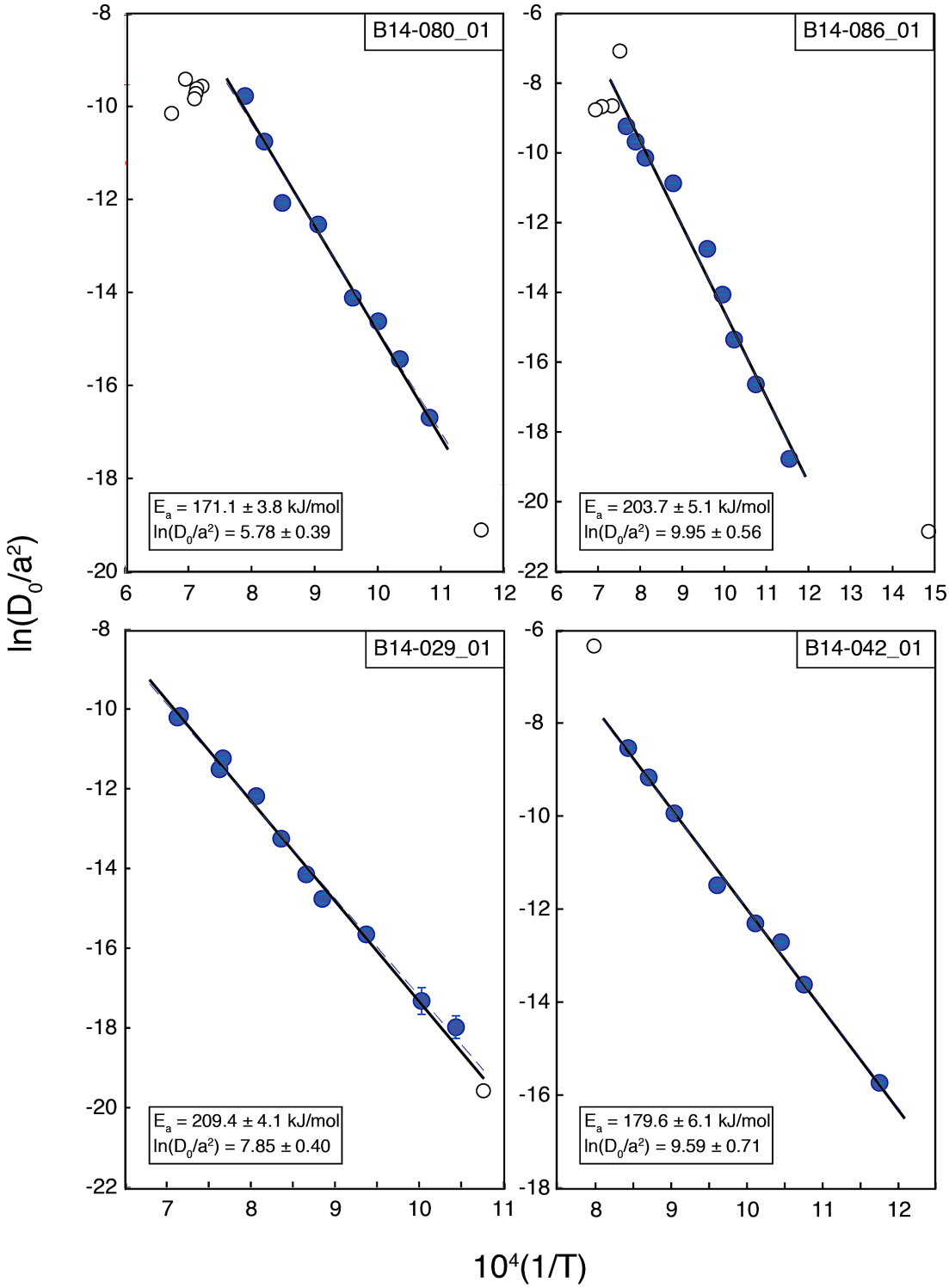

Figure 6 (Continued)

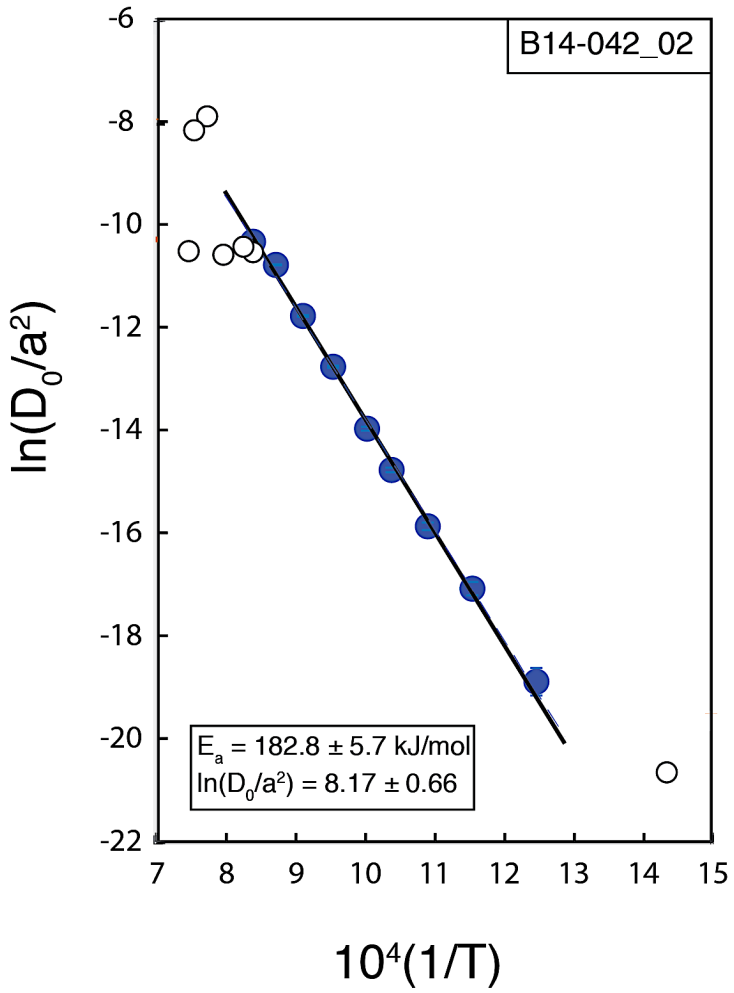

Figure 7

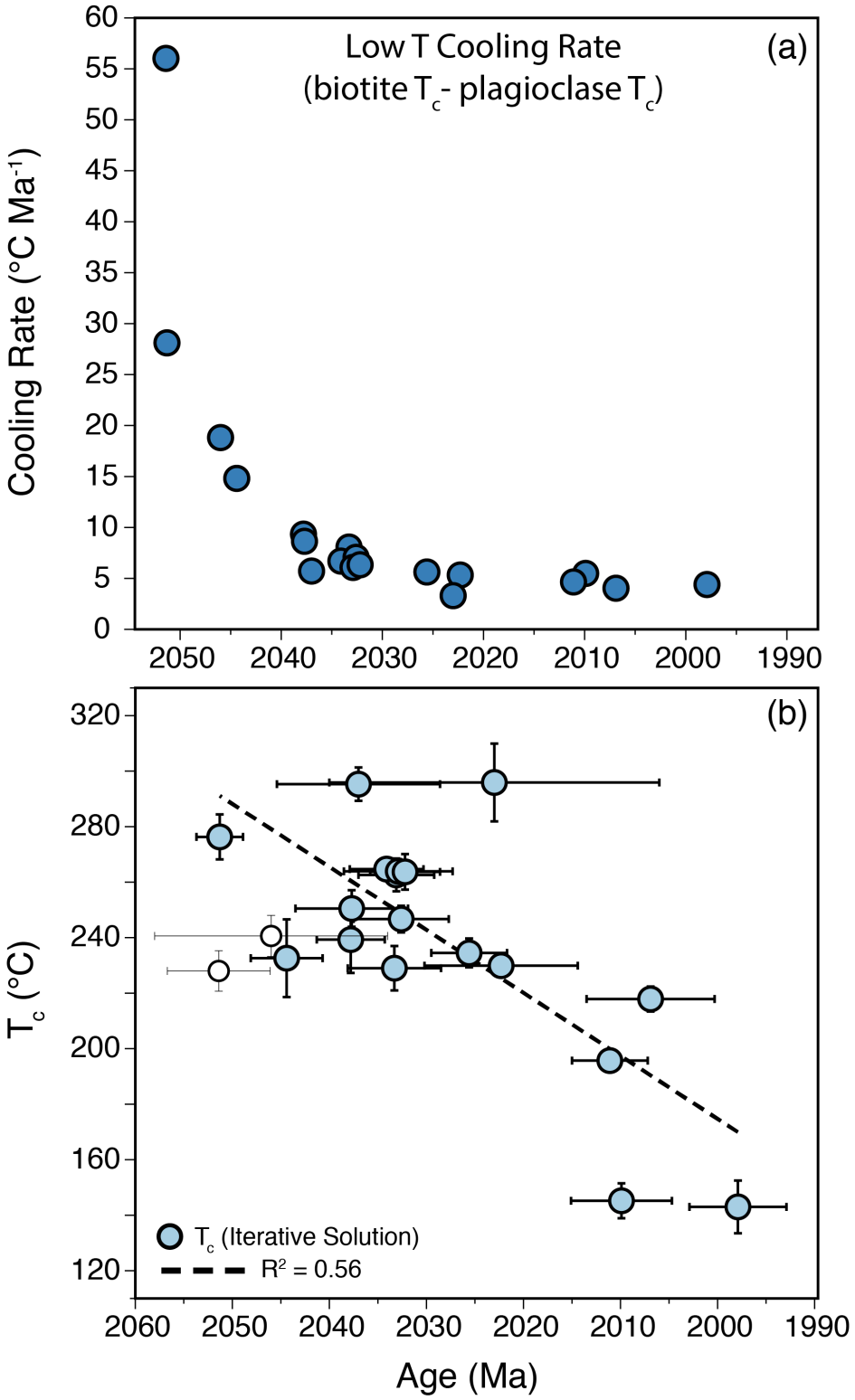
Low T Cooling Rate
(biotite T_c- plagioclase T_c)
(a)
Cooling Rate (°C Ma^{-1})
60
55
50
45
40
35
30
25
20
15
10
5
0
2050
2040
2030
2020
2010
2000
1990
(b)
T_c (°C)
320
280
240
200
160
120
T_c (Iterative Solution)
R^2 = 0.56
2060
2050
2040
2030
2020
2010
2000
1990
Age (Ma)

Figure 8

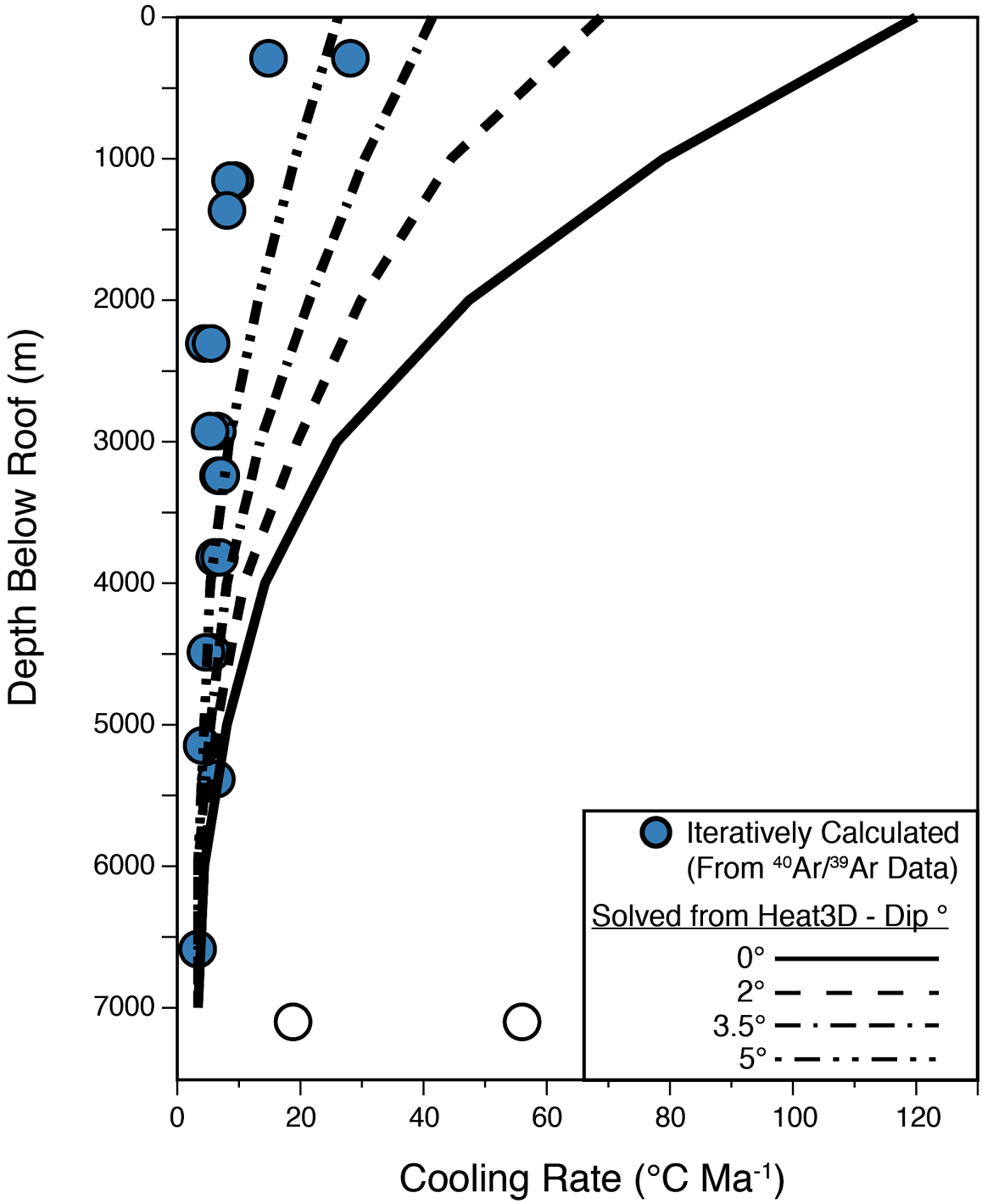
Depth Below Roof (m)
0
1000
2000
3000
4000
5000
6000
7000
0
20
40
60
80
100
120
Cooling Rate (°C Ma-1)
Iteratively Calculated
(From 40Ar/39Ar Data)
Solved from Heat3D - Dip °
0°
2°
3.5°
5°

Figure 9

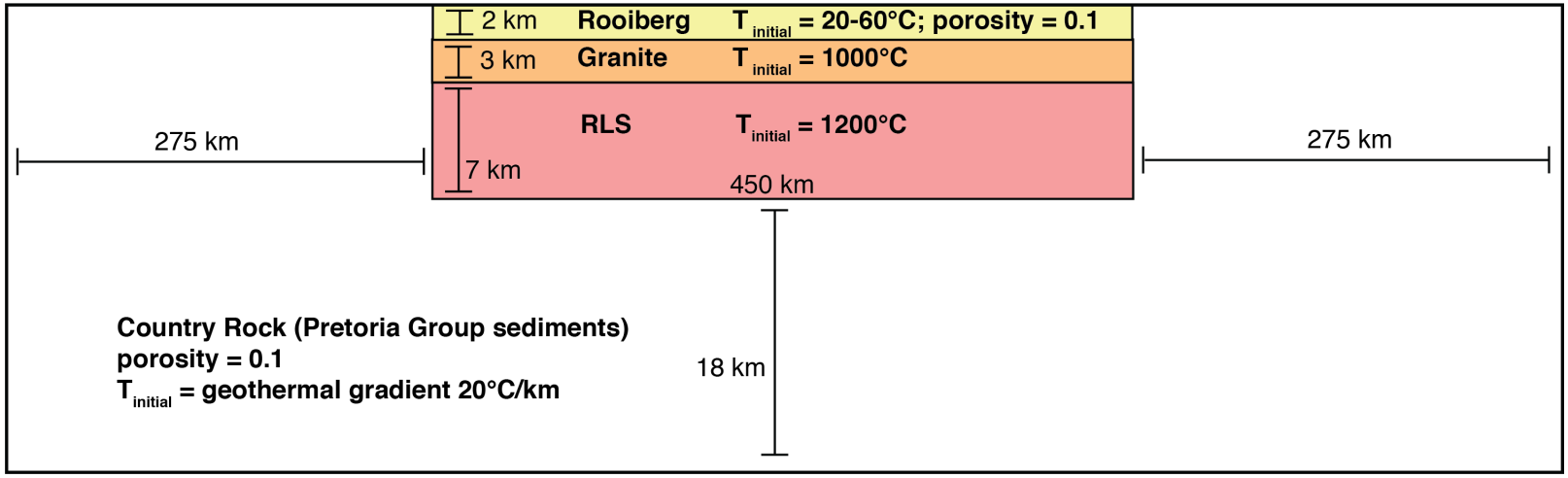
2 km
Rooiberg
T initial = 20-60°C; porosity = 0.1
3 km
Granite
T initial = 1000°C
RLS
T initial = 1200°C
7 km
275 km
275 km
450 km
18 km
Country Rock (Pretoria Group sediments)
porosity = 0.1
T initial = geothermal gradient 20°C/km

Figure 10

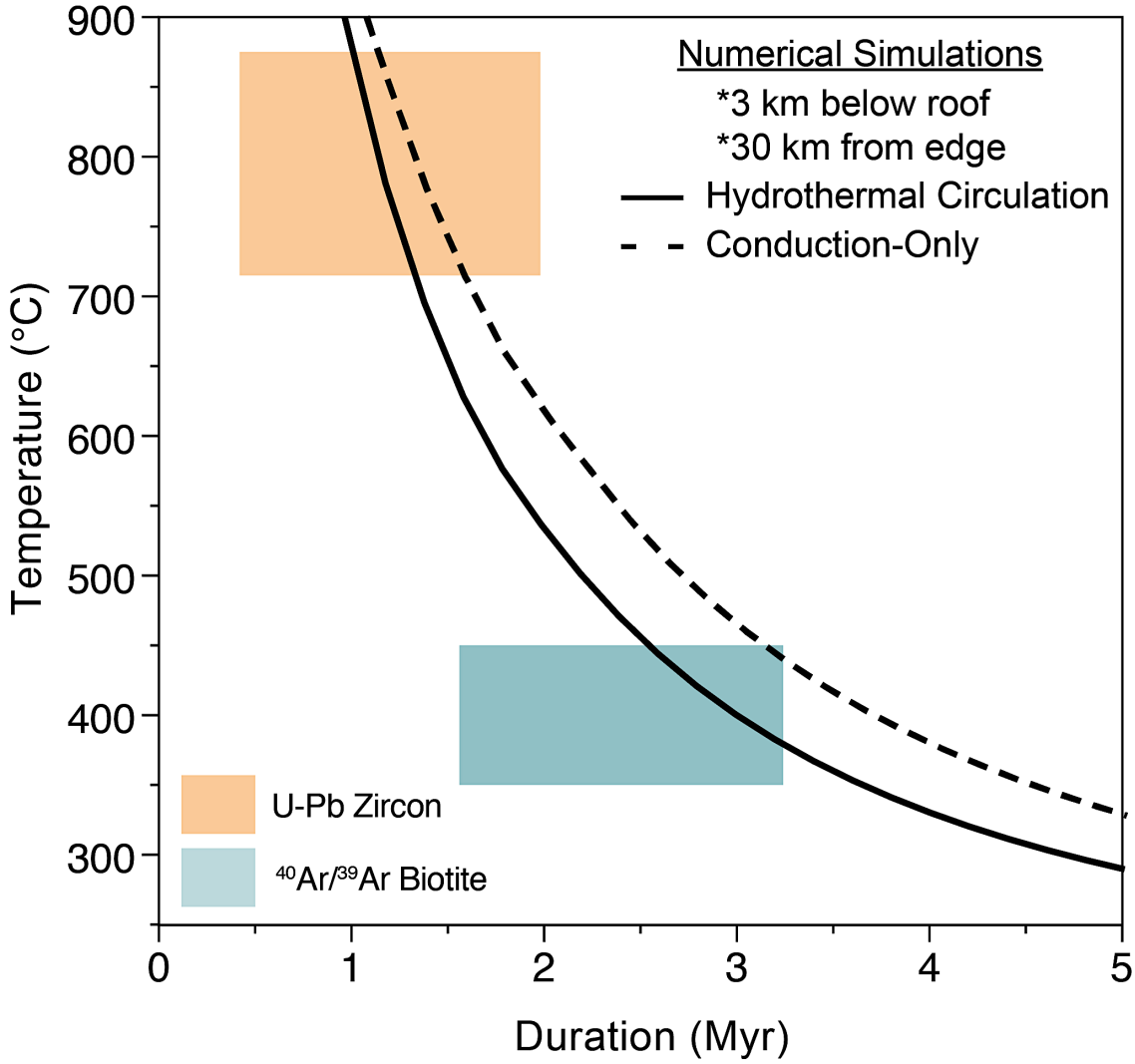
Numerical Simulations
*3 km below roof
*30 km from edge
Hydrothermal Circulation
Conduction-Only
U-Pb Zircon
40Ar/39Ar Biotite
Temperature (°C)
900
800
700
600
500
400
300
0
1
2
3
4
5
Duration (Myr)

Figure 11

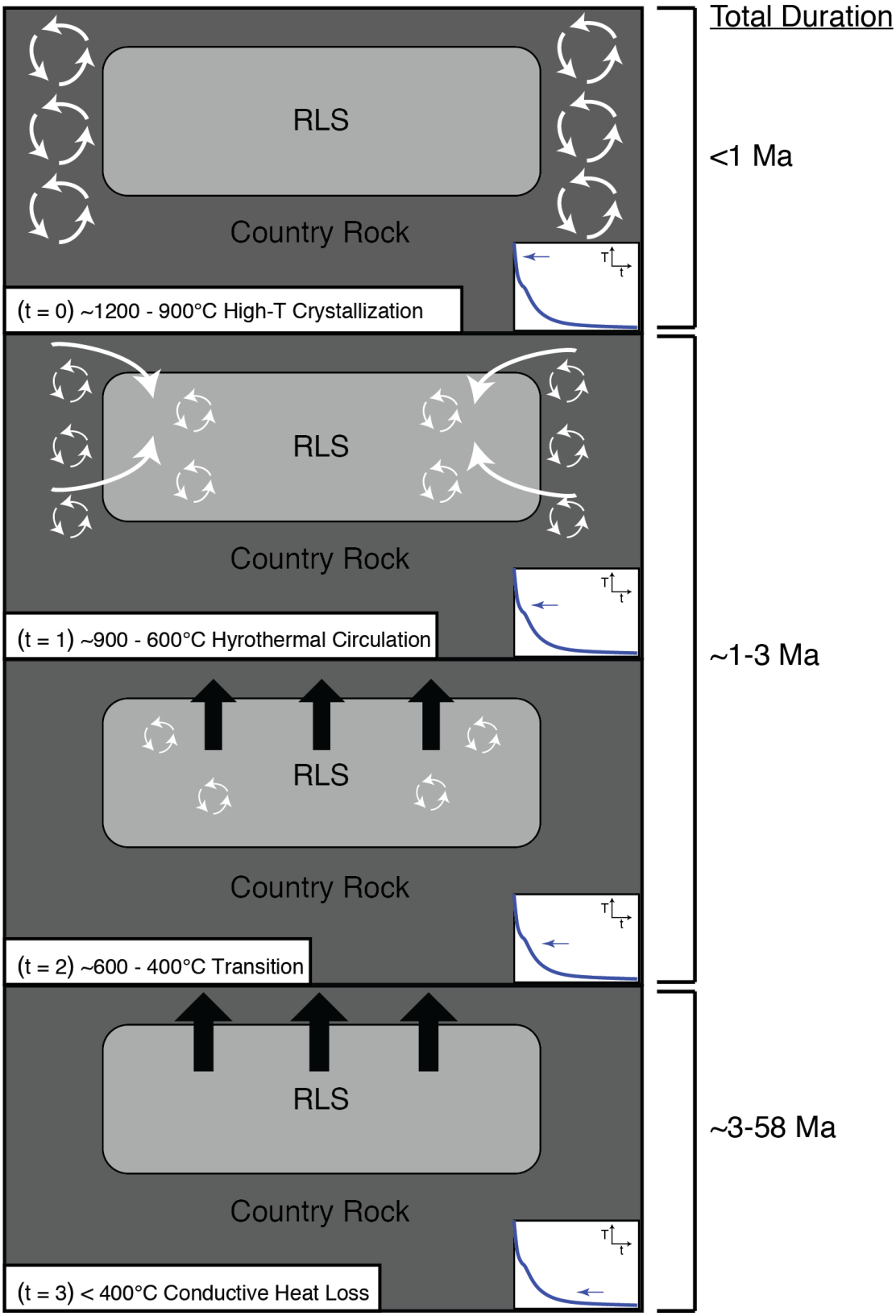
Total Duration
<1 Ma
~1-3 Ma
~3-58 Ma
RLS
Country Rock
(t = 0) ~1200 - 900°C High-T Crystallization
RLS
Country Rock
(t = 1) ~900 - 600°C Hyrothermal Circulation
RLS
Country Rock
(t = 2) ~600 - 400°C Transition
RLS
Country Rock
(t = 3) < 400°C Conductive Heat Loss
T
t

Table 1
Sample locations, descriptions, and stratigraphic depth (m above the Merensky Reef and below the roof contact)

Sample	Latitude	Longitude	Depth (m)[a]	Depth (m)[b]	Lithology	Plagioclase Texture
B06-055	24°, 51.874	029°, 54.756	4335	290	Ol-Mt Gabbro	Cumulus
B06-042	24°, 48.776	029°, 57.036	3741	884	Mt Gabbro	Cumulus
B06-020	24°, 48.974	029°, 58.149	3260	1365	Mt Gabbro	Cumulus
B14-015	25°, 12.006	029°, 56.524	2320	2305	Gabbronorite	Cumulus
B14-024	25°, 13.462	029°, 59.328	1700	2925	Gabbronorite	Cumulus
B14-045	25°, 13.164	030°, 00.893	1385	3240	Gabbronorite	Cumulus
B14-049	25°, 11.863	030°, 02.932	808	3817	Gabbronorite	Cumulus
B14-053a	25°, 13.849	030°, 05.374	137	4488	Gabbronorite	Cumulus
B14-080	25°, 00.181	030°, 07.035	-522	5147	Gabbronorite	Cumulus
B14-086	24°, 56.880	030°, 09.099	-760	5385	Pyroxenite	Interstitial
B14-029	24°, 41.431	030°, 16.504	-1961	6586	Pyroxenite	Interstitial
B14-042	24°, 41.409	030°, 16.820	-2475	7100	Pyroxenite	Interstitial

[a]Estimated sample depths reported relative to the Merensky Reef.
[b]Estimated sample depths reported relative to the contact between the Upper Zone and the roof.

Table 2
Major element composition (wt. %) for plagioclase from electron microprobe analyses.

Sample	SiO_2		Al_2O_3		FeO		CaO		Na_2O		K_2O		Total[1]	An#
B06-055[2]	55.81	(0.51)	22.79	(0.29)	0.18	(0.04)	9.76	(0.40)	5.68	(0.22)	0.30	(0.04)	99.51	47.9
B06-042[2]	54.32	(0.40)	28.79	(0.25)	0.24	(0.04)	10.88	(0.27)	4.93	(0.14)	0.38	(0.04)	99.52	53.7
B06-020[2]	53.75		29.98		0.31		11.95		4.66		0.34		101.07	57.5
B14-015[3]	50.13	(0.32)	31.39	(0.39)	0.48	(0.05)	14.50	(0.40)	3.05	(0.22)	0.22	(0.03)	99.86	71.5
B14-024[3]	53.94	(0.51)	29.22	(0.22)	0.40	(0.06)	11.68	(0.20)	4.53	(0.16)	0.37	(0.03)	100.21	57.5
B14-045[3]	53.42	(0.43)	29.52	(0.29)	0.44	(0.06)	12.35	(0.29)	4.14	(0.17)	0.32	(0.04)	99.25	61.1
B14-049[3]	51.63	(0.52)	30.07	(0.35)	0.37	(0.04)	12.97	(0.40)	3.73	(0.22)	0.28	(0.02)	99.09	64.7
B14-053a[3]	51.70	(0.82)	31.15	(0.53)	0.34	(0.06)	13.64	(0.61)	3.47	(0.35)	0.23	(0.04)	100.55	67.7
B14-080	49.58	(0.45)	31.92	(0.33)	0.29	(0.06)	14.83	(0.34)	2.84	(0.17)	0.21	(0.02)	99.68	73.3
B14-086	50.27	(2.65)	31.72	(1.80)	0.17	(0.04)	14.12	(2.00)	3.24	(1.09)	0.18	(0.09)	99.69	69.9
B14-029	52.86	(1.01)	29.91	(0.67)	0.17	(0.04)	12.41	(0.78)	4.23	(0.42)	0.32	(0.04)	99.91	60.7
B14-042	48.48	(0.36)	33.21	(0.29)	0.26	(0.04)	15.82	(0.27)	2.28	(0.13)	0.15	(0.02)	100.19	78.7

[1]Totals taken from previous studies include the measurement of additional major elements.
[2]Analyses from VanTongeren & Mathez (2013).
[3]Analyses from Setera & VanTongeren (2018).

Table 3
Secondary standards used during electron microprobe analyses listed in Table 2.

	Lake County Plag (N=17)			OR-1* (N=12)			Sanidine (N=8)		
Element	Avg.	1σ	Pub.	Avg.	1σ	Pub.	Avg.	1σ	Pub.
Si	51.22	0.20	51.25	64.34	0.19	64.39	64.64	0.12	64.67
Al	31.08	0.10	30.91	18.65	0.19	18.57	19.15	0.03	18.76
Fe	0.45	0.05	0.46	0.02	0.02	0.00	0.17	0.02	0.18
Ca	13.61	0.13	13.64	0.00	0.00	0.00	0.01	0.02	0.00
Na	3.58	0.06	3.45	1.13	0.04	1.15	3.02	0.01	3.01
K	0.11	0.005	0.18	14.96	0.04	14.93	12.12	0.01	12.11
Total	100.05	0.253	99.89	98.95	0.29	99.04	100.23	0.15	100.12
M-Site	1.00	0.008	1.00	0.99	0.01	0.99	0.99	0.00	0.99
T Sites	4.01	0.004	4.01	4.01	0.00	4.01	4.02	0.00	4.01
An	0.67	0.004	0.68	0.00	0.00	0.00	0.00	0.00	0.00
Ab	0.32	0.004	0.31	0.10	0.00	0.10	0.27	0.00	0.27
Or	0.01	0.000	0.01	0.90	0.00	0.90	0.72	0.00	0.73

	Tektite (N=8)			AGV-1 (N=8)		
Element	Avg.	1σ	Pub.	Avg.	1σ	Pub.
K	1.87	0.01	1.88	2.96	0.04	2.92

Table 4

Stepwise Heating Results: moles (10^{-17} for $^{36, 38, 39}Ar$, 10^{-15} for ^{37}Ar, ^{40}Ar and $^{40}Ar^*$) of each isotope for each heating step. J is the measure of the neutron flus in the reactor. All uncertainties reported at 1σ. Blank cells represent negative values.

Sample	Run ID	Power	36Ar	37Ar	38Ar	39Ar	40Ar	40Ar*	Age (Ma)	Used in Plateau Age
B06-055_01	22918-03A	1.8	0.67±0.09	1.39±0.73	3.09±0.13	2.86±0.35	110.53±0.42	108.52±0.33	7793±215	
J = 1.9511e-2	22918-03B	3.2	0.75±0.09	0.96±0.91	1.70±0.12	3.15±0.29	55.74±0.38	53.50±0.27	6372±164	
± 4.0873e-5	22918-03C	5	1.48±0.09	1.82±0.93	4.00±0.14	10.41±0.42	156.25±0.43	151.84±0.32	6103±71	
	22918-03D	3.5				1.19±0.44	0.81±0.33	0.99±0.24	1750±508	
	22918-03E	5	0.03±0.08		0.30±0.08	2.96±0.46	5.55±0.34	5.46±0.24	2756±233	
	22918-03F	6.5	0.25±0.08	0.42±0.86	1.19±0.11	10.44±0.45	30.01±0.36	29.26±0.26	3368±68	
	22918-03G	7.5	0.11±0.09	6.98±1.56	0.25±0.07	11.96±0.48	8.89±0.38	8.57±0.27	1578±56	
	22918-03H	9	0.06±0.09	11.86±1.61	0.47±0.09	39.46±0.54	29.10±0.40	28.92±0.28	1602±19	
	22918-03I	12	0.10±0.10	29.26±1.77	1.47±0.15	150.70±0.76	99.19±0.43	98.89±0.31	1487±6.2	
	22918-03J	14	0.15±0.08	21.10±1.27	0.50±0.11	147.40±0.81	86.25±0.37	85.80±0.27	1368.8±6.1	
	22918-03K	16	0.07±0.09	20.66±1.06	0.78±0.13	136.20±0.87	88.60±0.37	88.39±0.27	1476.3±7.2	
	22918-03L	18	0.18±0.09	20.48±1.30	2.35±0.13	128.20±0.71	127.33±0.42	126.78±0.31	1939.1±7.2	
	22918-03M	20	0.38±0.09	10.27±1.04	1.98±0.13	61.55±1.52	74.27±0.39	73.13±0.28	2164±31	
	22918-03N	23	0.47±0.11	30.01±1.16	8.42±0.17	186.40±1.44	204.26±0.56	202.85±0.46	2054±10	x
	22918-03O	26	0.49±0.09	25.50±1.21	10.32±0.26	171.80±2.79	188.72±0.48	187.25±0.40	2057±20	x
	22918-03P	28.5	0.11±0.09	14.72±1.05	9.72±0.22	89.18±0.95	97.02±0.44	96.70±0.35	2050±14	x
	22918-03Q	31	0.48±0.14	56.90±1.55	12.78±0.18	272.43±1.72	298.12±0.81	296.68±0.69	2055.6±8.2	x
	22918-03R	2	0.05±0.19	66.69±1.61	7.89±0.13	336.39±2.12	364.89±1.93	364.74±1.85	2050.1±9.9	x
	22918-03S	3		106.93±1.84	10.56±0.13	569.58±2.42	615.28±1.61	615.89±1.23	2046.7±5.7	x
	22918-03T	4.5	0.07±0.14	66.86±1.50	7.24±0.13	352.74±0.83	383.27±0.67	383.04±0.52	2052.0±3.2	x
	22918-03U	6	0.04±0.09	22.07±1.04	1.05±0.12	149.80±1.59	162.51±0.82	162.38±0.76	2050±14	x
B06-055_02	22918-04A	1.8	0.59±0.09	1.21±0.83	3.35±0.13	6.41±0.35	58.47±0.39	56.70±0.28	5241±93	

J = 1.9511e-2	22918-04B	3.5		1.96±0.82	2.10±0.13	19.62±0.42	22.15±0.35	22.27±0.25	2106±30	
± 4.0873e-5	22918-04C	5.2		9.05±0.86	0.71±0.09	59.20±0.57	26.45±0.38	26.60±0.27	1136±12	
	22918-04D	6.5	0.11±0.08	12.75±1.19	0.32±0.11	95.56±0.60	49.13±0.34	48.80±0.24	1247.3±7.4	
	22918-04E	7.5	0.05±0.08	15.06±0.96	0.38±0.11	101.20±0.70	61.34±0.33	61.20±0.24	1405.4±7.9	
	22918-04F	9		19.48±1.16	0.50±0.12	136.30±0.71	92.58±0.34	92.79±0.25	1525.0±6.1	
	22918-04G	11	0.01±0.09	7.47±1.02	0.28±0.11	55.46±0.57	39.56±0.37	39.53±0.26	1572±13	
	22918-04H	13		11.29±0.97	0.17±0.10	88.64±0.55	76.03±0.36	76.06±0.26	1774.6±8.1	
	22918-04I	16	0.07±0.09	13.09±0.99	0.42±0.10	94.41±0.65	100.30±0.38	100.10±0.28	2022.5±9.1	
	22918-04J	19	0.23±0.09	17.18±1.07	0.46±0.11	120.00±1.10	155.58±0.44	154.90±0.35	2270±12	
	22918-04K	21	0.06±0.08	11.03±1.00	0.69±0.11	67.67±0.53	86.99±0.36	86.81±0.27	2262±11	
	22918-04L	23	0.13±0.16	98.10±1.89	10.13±0.10	539.24±0.91	583.53±0.93	583.18±0.81	2046.8±2.7	x
	22918-04M	25		23.87±1.03	2.80±0.15	160.00±1.44	172.07±0.41	172.20±0.32	2041±11	x
	22918-04N	27	0.68±0.09	18.13±1.11	3.44±0.15	103.60±0.62	112.12±0.40	110.10±0.30	2025.3±8.1	x
	22918-04O	29	0.44±0.12	1.15±0.82	0.23±0.09	1.27±0.64	2.52±0.49	1.22±0.35	1907±690	x
B06-020_01	22472-01A	1.8								
J = 1.98874e-2	22472-01B	3.5								
± 3.18272e-5	22472-01C	5.2								
	22472-01D	6.5								
	22472-01E	3.5	0.78±0.90			1.50±0.16	1.51±0.39	1.28±0.28	1793±292	
	22472-01F	3.5	10.14±0.62		2.46±0.46	9.38±0.21	11.70±0.27	8.67±0.19	1884±39	
	22472-01G	5.2	1.25±0.65		0.03±0.34	1.18±0.17	0.70±0.28	0.33±0.20	794±434	
	22472-01H	6.5	10.62±0.71		3.08±0.53	25.74±0.37	18.09±0.30	14.92±0.22	1385±20	
	22472-01I	7.5	0.08±0.63	5.26±1.31	0.51±0.42	17.29±0.27	8.71±0.27	8.69±0.19	1251±25	
	22472-01J	9	1.22±0.59	5.90±1.17	0.83±0.46	29.37±0.38	15.16±0.25	14.79±0.18	1253±14	
	22472-01K	12	3.46±0.67	10.81±1.41	0.99±0.51	74.34±0.87	48.00±0.30	46.97±0.22	1470±8.0	
	22472-01L	15	3.73±0.63	7.76±1.21	1.54±0.54	59.78±0.72	48.26±0.29	47.15±0.22	1703.7±9.4	
	22472-01M	17.5	5.22±0.91	8.56±1.75	2.26±0.64	69.78±0.99	73.89±0.40	72.33±0.30	2021±14	
	22472-01N	20	10.92±0.70	9.30±1.50	3.45±0.60	96.25±1.28	114.86±0.31	111.60±0.23	2160±12	

	22472-01O	22	25.97±0.90	36.89±1.42	9.54±2.68	290.09±6.56	313.77±0.41	306.02±0.32	2042±25	x
	22472-01P	1.8	10.86±1.03	16.24±2.94	4.45±0.92	153.80±1.76	164.64±0.53	161.40±0.43	2035.0±7.6	x
	22472-01Q	2	0.36±0.63	7.23±1.32		33.54±0.47	35.05±0.27	34.94±0.19	2027±14	x
	22472-01R	3	1.34±0.91	16.72±1.50	0.75±0.65	88.45±1.21	93.10±0.39	92.70±0.28	2034±11	x
	22472-01S	4	4.79±0.64	49.95±1.19	9.49±3.65	327.00±4.66	344.71±0.30	343.26±0.22	2036±12	x
	22472-01T	6	1.97±0.98	5.28±2.95	0.70±0.58	43.98±0.62	46.33±0.43	45.74±0.32	2024±16	x
	22472-01U	6	0.73±0.93	1.09±2.79	0.75±0.47	3.89±0.24	4.47±0.39	4.25±0.28	2085±142	x
B14-015_01	22914-01A	1.8	0.72±0.07	0.76±0.07	2.26±0.11	25.03±0.86	34.01±0.31	31.85±0.22	2249±44	
J = 1.9470e-2	22914-01B	3.5	2.43±0.09	1.89±0.06	4.73±0.14	70.13±1.25	82.15±0.38	74.90±0.28	2029±21	
± 8.9489e-5	22914-01C	5	6.21±0.15	13.76±0.15	3.84±0.05	215.91±4.87	153.69±0.69	135.14±0.51	1438±22	
	22914-01D	6	0.29±0.06	12.81±0.16	0.98±0.12	106.60±1.00	55.15±0.28	54.29±0.20	1242.5±7.5	
	22914-01E	7	0.08±0.06	17.07±0.19	0.80±0.10	117.20±1.07	64.76±0.27	64.53±0.20	1314.2±7.3	
	22914-01F	8		22.08±0.47	0.81±0.13	134.10±1.08	80.09±0.40	80.26±0.29	1393.9±6.7	
	22914-01G	9	0.22±0.06	25.47±0.32	0.61±0.11	165.70±1.32	104.87±0.26	104.20±0.20	1442.0±6.1	
	22914-01H	10	0.43±0.06	26.79±0.28	0.45±0.12	190.60±1.38	124.68±0.27	123.40±0.20	1471.7±5.1	
	22914-01I	11	0.22±0.06	28.41±0.30	0.46±0.10	191.30±1.41	132.46±0.27	131.80±0.20	1534.8±5.4	
	22914-01J	11.5	0.16±0.07	22.54±0.23	0.29±0.11	140.60±1.08	104.48±0.30	104.00±0.23	1608.6±6.1	
	22914-01K	12	0.20±0.06	16.72±0.20	0.25±0.11	105.60±1.02	79.48±0.27	78.90±0.20	1619.7±8.9	
	22914-01L	13	0.16±0.09	15.42±0.27	0.19±0.09	103.50±1.38	78.54±0.38	78.06±0.28	1630±14	
	22914-01M	14	0.25±0.06	13.68±0.19	0.43±0.11	97.39±0.94	72.47±0.34	71.73±0.29	1604.9±9.4	
	22914-01N	15	0.22±0.06	12.30±0.17	0.72±0.10	84.41±2.00	68.39±0.33	67.73±0.28	1697±26	
	22914-01O	16	0.18±0.06	10.00±0.33	0.52±0.10	69.86±0.81	57.64±0.30	57.09±0.24	1718±12	
	22914-01P	17	0.20±0.06	7.96±0.15	0.48±0.08	48.62±0.97	41.00±0.24	40.39±0.17	1736±22	
	22914-01Q	18.5	0.25±0.06	14.97±0.16	1.40±0.12	92.85±0.87	80.01±0.28	79.25±0.21	1766.2±8.8	
	22914-01R	20	0.23±0.07	15.76±0.17	1.48±0.12	94.00±0.85	86.35±0.30	85.66±0.22	1840.8±8.6	
	22914-01S	21.5	0.28±0.06	22.05±0.45	2.13±0.12	116.00±1.46	121.24±0.28	120.40±0.21	1995±14	x
	22914-01T	22.5	0.31±0.09	16.67±0.18	2.61±0.14	97.26±2.37	97.88±0.39	96.96±0.28	1946±28	x
	22914-01U	24	0.25±0.10	25.37±0.39	2.60±0.15	114.60±2.47	116.56±0.45	115.80±0.35	1962±25	x

	22914-01V	25.5	0.14±0.11	36.24±0.27	2.45±0.13	143.50±1.21	150.31±0.49	149.90±0.36	2002.3±8.1	x
	22914-01W	27	0.18±0.06	16.50±0.21	0.83±0.09	55.33±0.75	58.80±0.26	58.26±0.18	2012±15	x
	22914-01X	29	0.03±0.05	0.93±0.06		3.76±0.69	3.97±0.23	3.87±0.16	1985±226	x
	22914-01Y	31		2.10±0.10	0.19±0.06	7.00±1.01	7.20±0.23	7.33±0.16	2005±176	x
	22914-01Z	33	0.61±0.10	50.98±0.24	2.00±0.04	173.88±3.91	184.01±0.47	182.18±0.35	2006±27	x
	22914-02A	0.5	0.22±0.05		0.01±0.06	0.21±0.51	0.08±0.20	-0.56±0.14	NaN	
	22914-02B	2	0.14±0.05	2.72±0.09	0.10±0.07	9.62±0.69	10.76±0.20	10.33±0.15	2036±89	x
	22914-02C	4	0.41±0.11	33.96±0.51	3.84±0.05	129.00±1.64	136.73±0.47	135.50±0.34	2009±14	x
	22914-02D	5	0.30±0.16	28.26±0.37	2.18±0.13	103.90±1.40	107.58±0.68	106.70±0.50	1982±15	x
	22914-02E	6	0.01±0.09	8.54±0.24	0.52±0.08	27.49±0.84	28.86±0.39	28.83±0.28	2007±38	x
B14-015_02	22914-03A	1.8	2.02±0.09	0.58±0.13	2.86±0.13	9.48±0.45	109.04±0.39	103.00±0.28	5590±81	
J = 1.9470e-2	22914-03B	3.2	1.93±0.08	0.62±0.13	2.76±0.12	19.08±0.41	70.69±0.36	64.93±0.26	3665±34	
± 8.9489e-5	22914-03C	4.2	7.20±0.12	1.69±0.15	3.84±0.17	35.05±0.87	182.98±0.59	161.50±0.48	4149±40	
	22914-03D	5	5.57±0.11	5.65±0.20	9.30±0.22	69.83±0.83	144.23±0.50	127.60±0.38	2736±17	
	22914-03E	6	1.07±0.08	8.84±0.22	2.56±0.12	89.20±0.86	50.95±0.34	47.74±0.24	1288.0±9.5	
	22914-03F	7.5	0.16±0.07	12.34±0.24	0.76±0.12	109.40±0.88	52.71±0.31	52.24±0.23	1185.5±7.2	
	22914-03G	9	0.07±0.07	20.46±0.31	0.45±0.13	150.60±0.98	79.85±0.31	79.65±0.23	1277.2±5.6	
	22914-03H	12	0.96±0.13	46.53±0.56	3.24±0.06	316.92±1.49	242.04±0.62	239.16±0.47	1630.8±3.8	
	22914-03I	15	0.86±0.12	51.06±0.59	2.66±0.07	269.63±1.60	222.74±0.54	220.18±0.40	1716.8±5.5	
	22914-03J	17.5	0.41±0.08	26.26±0.41	1.05±0.15	165.80±3.12	126.33±0.43	125.10±0.35	1630±20	
	22914-03K	19	0.47±0.13	21.04±0.40	1.36±0.14	135.20±1.07	110.49±0.59	109.10±0.45	1704.1±9.0	
	22914-03L	21.5	0.29±0.12	22.05±1.31	1.67±0.14	104.80±0.92	106.67±0.52	105.80±0.38	1961±11	
	22914-03M	23	0.31±0.12	14.85±0.30	1.23±0.14	71.36±0.76	75.99±0.53	75.06±0.39	2011±14	x
	22914-03N	25	0.67±0.09	22.06±0.61	3.07±0.17	125.60±8.24	132.01±0.45	130.00±0.37	1991±79	x
	22914-03O	27	0.03±0.11	16.93±0.37	1.02±0.13	73.85±1.31	77.40±0.49	77.30±0.35	2005±22	x
	22914-03P	29.2	0.23±0.12	30.75±0.48	2.04±0.15	131.80±2.82	138.29±0.56	137.60±0.43	2002±26	x
	22914-03Q	31	2.29±0.26	104.73±0.82	6.76±0.10	352.23±2.60	378.05±1.25	371.21±0.97	2013.0±8.2	x
	22914-03R	33	0.07±0.12	5.03±0.23	0.51±0.10	20.15±0.95	20.58±0.50	20.36±0.35	1962±60	x

	22914-03S	1.5	0.03±0.10	0.95±0.13	0.05±0.08	2.83±0.70	3.08±0.42	3.01±0.30	2023±324	x
	22914-03T	2.5		6.00±0.24		18.81±0.82	19.37±0.67	19.70±0.47	2005±60	x
	22914-03U	3.5		53.56±2.26	1.18±0.16	164.90±1.25	172.40±0.90	173.30±0.66	2009.9±8.9	x
	22914-03V	4		2.32±0.16	0.08±0.07	7.33±0.53	6.79±0.31	7.12±0.22	1916±93	x
	22914-03W	6		0.41±0.13	0.13±0.06	1.40±0.49	1.72±0.29	2.19±0.21	2523±491	x
B14-024_01	22471-01A	3.5	0.42±0.03		1.14±0.04	2.55±0.18	13.62±0.12	12.37±0.09	4271±116	
J = 1.9922e-2	22471-01B	5.2	0.17±0.03		0.52±0.03	2.96±0.16	5.03±0.11	4.54±0.08	2526±79	
± 3.9607e-5	22471-01C	6.5	0.30±0.03	0.48±0.34	0.90±0.04	6.01±0.17	8.78±0.11	7.88±0.08	2317±39	
	22471-01D	7.5	0.23±0.03	0.47±0.29	0.74±0.04	9.41±0.17	9.33±0.11	8.64±0.08	1877±24	
	22471-01E	9	0.10±0.02		0.36±0.03	10.34±0.17	6.94±0.10	6.63±0.08	1484±21	
	22471-01F	12	0.17±0.03	1.59±0.44	0.43±0.04	23.09±0.21	13.22±0.13	12.72±0.09	1336±11	
	22471-01G	15	0.11±0.03	4.75±0.46	0.20±0.03	37.98±0.22	21.69±0.12	21.36±0.09	1356.0±6.6	
	22471-01H	17.5	0.16±0.03	3.39±0.44	0.25±0.04	52.89±0.27	32.40±0.13	31.93±0.10	1424.7±5.6	
	22471-01I	20	0.12±0.03	4.78±0.45	0.23±0.04	63.16±0.29	40.71±0.13	40.35±0.10	1481.1±4.8	
	22471-01J	22	0.06±0.03	5.56±0.37	0.19±0.04	49.34±0.27	36.96±0.12	36.77±0.09	1642.1±6.0	
	22471-01K	23.5	0.05±0.03	5.39±0.35	0.04±0.03	40.33±0.25	31.57±0.12	31.43±0.09	1690.4±7.1	
	22471-01L	25	0.06±0.03	2.64±0.33	0.08±0.03	31.69±0.23	26.15±0.12	25.98±0.09	1746.7±8.9	
	22471-01M	27	0.08±0.03	2.73±0.32	0.08±0.04	28.84±0.21	24.66±0.12	24.41±0.09	1782.7±8.9	
	22471-01N	25	0.03±0.02	3.50±0.32	0.06±0.03	16.99±0.17	14.82±0.10	14.73±0.08	1810±13	
	22471-01O	25	0.03±0.02	3.05±0.33	0.02±0.03	13.89±0.17	11.90±0.10	11.81±0.08	1788±16	
	22471-01P	25		2.15±0.35	0.03±0.03	10.65±0.18	9.39±0.10	9.41±0.08	1832±22	
	22471-01Q	25	0.00±0.02	2.68±0.33	0.05±0.03	9.18±0.14	8.40±0.10	8.39±0.07	1871±21	
	22471-01R	25	0.01±0.03	0.91±0.34	0.04±0.03	7.95±0.14	7.30±0.11	7.26±0.08	1869±25	
	22471-01S	25	0.01±0.03	0.37±0.31		7.06±0.14	6.51±0.11	6.49±0.08	1878±28	
	22471-01T	25				4.54±0.11	3.26±0.10	3.78±0.07	1764±37	
	22471-01U	27	0.36±0.03	3.36±0.32	0.08±0.03	43.45±0.22	40.67±0.12	39.60±0.09	1867.7±6.1	
	22471-01V	27	0.34±0.03	1.35±0.30	0.06±0.03	27.11±0.17	25.63±0.12	24.63±0.09	1864.2±8.3	
	22471-01W	27	0.38±0.03	1.23±0.32	0.04±0.03	20.31±0.17	19.12±0.16	17.99±0.13	1835±13	

	22471-01X	29.2	0.36±0.03	1.59±0.32	0.07±0.03	23.38±0.17	21.37±0.12	20.30±0.09	1811.7±9.5	
	22471-01Y	29.2	0.24±0.03	0.31±0.31	0.12±0.03	16.36±0.15	15.94±0.11	15.23±0.08	1892±13	
	22471-01Z	31	0.27±0.03	0.67±0.31	0.13±0.03	18.42±0.17	17.66±0.11	16.86±0.08	1873±12	
	22471-01AA	33.5	0.33±0.03	1.26±0.30	0.16±0.03	24.56±0.17	22.00±0.11	21.00±0.08	1794.1±8.9	
	22471-01AB	35.5	0.41±0.03	1.76±0.33	0.21±0.03	27.36±0.18	24.75±0.12	23.53±0.09	1800.7±8.7	
	22471-01AC	38	0.25±0.04	1.84±0.34	0.20±0.03	25.43±0.16	24.67±0.16	23.93±0.12	1905.0±9.1	
	22471-01AD	5	0.50±0.04	57.37±0.52	24.16±0.18	442.33±2.86	462.55±0.20	461.07±0.15	2022.3±7.4	x
B14-024_02	22913-01A	1.8	0.44±0.06	0.22±0.05	3.78±0.14	3.22±0.54	56.51±0.25	55.21±0.18	6385±295	
J = 1.9487e-2	22913-01B	3.5	0.37±0.05	0.22±0.06	2.17±0.10	3.30±0.56	35.32±0.23	34.21±0.17	5511±291	
± 4.0758e-5	22913-01C	5	0.31±0.06	0.61±0.07	1.45±0.09	5.96±0.39	14.91±0.23	13.99±0.17	3098±99	
	22913-01D	6.5	0.58±0.06	1.69±0.09	3.68±0.14	18.45±0.71	48.39±0.26	46.66±0.19	3211±58	
	22913-01E	7.5	0.37±0.06	2.64±0.09	1.63±0.11	23.15±0.74	34.36±0.26	33.24±0.19	2407±43	
	22913-01F	9	0.19±0.08	3.30±0.11	0.67±0.08	32.01±0.54	24.21±0.34	23.63±0.24	1608±21	
	22913-01G	12	0.63±0.06	11.95±0.30	1.77±0.13	112.70±1.27	67.67±0.28	65.80±0.21	1370±11	
	22913-01H	15	0.25±0.12	63.20±0.32	3.50±0.47	517.40±33.07	416.35±0.57	415.60±0.45	1670±70	
	22913-01I	16	0.02±0.08	36.50±0.31	3.79±0.09	271.50±11.09	275.15±0.38	275.10±0.31	1966±49	
	22913-01J	17.5	0.05±0.08	21.64±0.22	2.57±0.08	188.95±4.30	190.46±0.39	190.31±0.32	1959±27	
	22913-01K	19		13.61±0.18	1.06±0.11	121.80±1.28	127.26±0.39	127.50±0.31	2006±13	
	22913-01L	20	0.16±0.09	9.47±0.13	0.72±0.08	87.10±1.15	88.72±0.37	88.25±0.27	1967±16	
	22913-01M	21		0.06±0.06		1.90±0.50	0.28±0.20	0.50±0.14	743±238	
	22913-01N	24	0.07±0.05	0.03±0.05		1.07±0.47	0.24±0.19	0.03±0.14	101±427	
	22913-01O	28	0.01±0.05			0.61±0.46	0.35±0.22	0.32±0.15	1279±823	
	22913-01P	0.2	0.09±0.07	0.14±0.05	0.05±0.06	1.47±0.47	0.59±0.28	0.33±0.20	650±374	
	22913-01Q	0.5	0.09±0.05	0.22±0.07		1.11±0.35	1.63±0.19	1.36±0.14	2201±416	
	22913-01R	1	0.16±0.05	6.74±0.12	0.35±0.10	65.24±0.95	66.45±0.23	65.97±0.18	1964±18	
	22913-01S	1.3	0.43±0.11	77.05±0.36	3.52±0.28	665.20±16.56	704.68±0.72	703.40±0.64	2018±30	x
	22913-01T	1.5	0.11±0.09	19.36±0.19	2.03±0.07	155.26±4.30	166.55±0.56	166.23±0.48	2033±34	x
	22913-01U	1.7	0.10±0.07	12.51±0.27	0.38±0.10	111.30±1.23	118.01±0.30	117.70±0.23	2018±14	x

	22913-01V	1.9	0.21±0.07	8.75±0.12	0.35±0.10	71.02±1.20	77.28±0.29	76.66±0.22	2043±21	x
	22913-01W	2.2	0.02±0.08	23.16±0.22	2.57±0.07	194.71±4.66	208.12±0.49	208.06±0.40	2031±29	x
	22913-01X	2.5		20.97±0.17	2.13±0.07	178.67±4.65	190.96±0.44	191.24±0.35	2033±32	x
	22913-01Y	3		17.15±0.17	0.52±0.10	148.60±4.30	157.39±0.59	157.70±0.45	2022±35	x
	22913-02A	3.3		18.63±0.22	1.95±0.06	163.28±4.30	173.19±0.34	173.23±0.28	2022±32	x
	22913-02B	3.6	0.05±0.07	26.17±0.21	2.17±0.05	221.42±4.30	237.30±0.39	237.16±0.33	2034±24	x
	22913-02C	4	0.07±0.09	13.31±0.18	0.34±0.10	113.10±0.84	120.71±0.39	120.50±0.29	2027±9.4	x
	22913-02D	4.2	0.05±0.06	11.45±0.15	0.29±0.11	93.90±0.86	101.96±0.26	101.80±0.20	2048±11	x
	22913-02E	4.4	0.05±0.06	7.90±0.14	0.30±0.08	60.87±0.76	65.87±0.24	65.71±0.17	2043±16	x
	22913-02F	4.6	0.05±0.05	7.13±0.11	0.08±0.09	62.37±0.70	66.85±0.24	66.70±0.18	2032±14	x
	22913-02G	4.8		2.60±0.08	0.08±0.07	21.53±0.62	22.93±0.22	22.95±0.16	2028±36	x
	22913-02H	5.2	0.10±0.06	16.26±0.20	0.56±0.12	135.50±0.84	145.51±0.27	145.20±0.20	2034.2±7.6	x
	22913-02I	5.4	0.09±0.05	5.58±0.12	0.19±0.09	48.09±1.57	51.50±0.23	51.22±0.17	2027±40	x
	22913-02J	5.4		5.99±0.10	3.79±0.09	47.27±0.87	50.60±0.33	50.76±0.25	2037±23	x
B14-045_01	22473-01A	1.8	0.18±0.05	0.51±1.29	0.34±0.04	0.27±0.13	20.63±0.23	20.10±0.17	9001±861	
J = 1.9912e-2	22473-01B	3.5	0.86±0.05	2.19±1.15	1.40±0.07	1.75±0.13	57.20±0.23	54.64±0.17	7480±138	
± 4.1054e-5	22473-01C	5.2	0.72±0.06	3.78±1.23	2.29±0.06	3.42±0.15	52.46±0.24	50.32±0.17	6156±76	
	22473-01D	6.5	0.65±0.05	1.92±1.29	1.79±0.06	5.27±0.16	41.95±0.23	40.01±0.17	5015±53	
	22473-01E	7.5	-	-	-	-	-	-	-	
	22473-01F	0	-	-	-	-	-	-	-	
	22473-01G	8	0.48±0.06	2.76±1.23	1.07±0.05	6.24±0.16	29.45±0.25	28.02±0.18	4144±45	
	22473-01H	9	1.05±0.06	2.59±1.14	2.84±0.08	13.03±0.19	65.32±0.26	62.17±0.19	4243±24	
	22473-01I	10	1.04±0.06	1.22±1.28	2.99±0.08	19.35±0.21	69.80±0.27	66.69±0.20	3720±17	
	22473-01J	11	0.59±0.06	1.39±1.17	1.64±0.07	19.18±0.23	35.13±0.24	33.36±0.17	2699±18	
	22473-01K	12	0.13±0.05	4.81±1.13	0.74±0.06	16.37±0.19	12.05±0.22	11.67±0.16	1594±20	
	22473-01L	14	0.42±0.08	7.01±1.88	1.53±0.15	32.23±0.51	24.53±0.32	23.27±0.23	1608±21	
	22473-01M	16	0.19±0.05	2.08±0.95	0.98±0.06	41.33±0.33	21.17±0.21	20.60±0.15	1243.8±9.0	
	22473-01N	18	0.09±0.05	7.89±1.22	0.83±0.06	59.23±0.42	31.86±0.23	31.58±0.17	1305.3±7.2	

	22473-01O	20	0.17±0.06	11.15±1.38	0.54±0.05	74.50±0.55	41.96±0.25	41.45±0.18	1345.3±6.8	
	22473-01P	22	0.17±0.06	10.76±1.36	0.35±0.06	83.67±0.61	47.97±0.25	47.46±0.18	1363.6±6.3	
	22473-01Q	23.5	0.17±0.06	10.72±1.29	0.22±0.06	76.81±0.56	46.85±0.24	46.35±0.17	1423.8±6.5	
	22473-01R	25	0.12±0.06	8.68±1.27	0.25±0.05	67.60±0.49	43.47±0.24	43.10±0.17	1478.7±6.8	
	22473-01S	27	0.15±0.06	11.03±1.28	0.10±0.06	68.80±0.50	47.37±0.24	46.91±0.17	1547.5±6.6	
	22473-01T	29.2	0.12±0.05	12.07±1.26	0.49±0.06	83.79±0.62	59.60±0.22	59.23±0.16	1585.0±6.2	
	22473-01U	31	0.20±0.06	11.41±1.33	0.26±0.05	69.94±0.51	52.51±0.24	51.92±0.17	1637.2±6.7	
	22473-01V	33.5	0.24±0.08	6.90±1.33	0.15±0.06	64.09±0.51	50.14±0.35	49.42±0.26	1678.4±8.9	
	22473-01W	35	0.21±0.06	7.16±1.29	0.18±0.05	47.60±0.39	38.12±0.25	37.50±0.18	1701.8±9.2	
	22473-01X	38	0.22±0.05	0.94±1.18	0.02±0.04	21.06±0.23	17.45±0.22	16.78±0.16	1714±16	
	22473-01Y	1.5	0.25±0.05	9.44±1.18	0.39±0.06	72.65±0.50	62.90±0.24	62.15±0.17	1794.1±6.4	
	22473-01Z	1.6	0.13±0.09	6.84±1.29	0.33±0.07	48.34±0.40	45.28±0.36	44.90±0.26	1889±11	
	22473-01AA	1.8	0.38±0.06	11.29±1.26	1.16±0.08	85.80±0.88	102.34±0.28	101.20±0.20	2180±12	
	22473-01AB	1.8	0.85±0.08	53.26±1.60	0.00±0.00	392.29±4.77	414.61±0.41	412.08±0.34	2036±14	x
	22473-01AC	0		1.23±1.21		1.90±0.14	1.51±0.22	1.90±0.16	1981±154	x
	22473-01AD	2	0.41±0.06	30.73±1.22	0.00±0.00	234.09±4.18	246.90±0.29	245.67±0.21	2035±21	x
	22473-01AE	2.2	0.02±0.11	83.12±1.88	0.00±0.00	565.40±5.73	586.97±0.52	586.91±0.35	2022±11	x
	22473-01AF	2.2	0.19±0.09	24.80±1.39	1.85±0.10	153.40±1.23	160.17±0.43	159.60±0.34	2024.5±8.6	x
	22473-01AG	2.4	0.09±0.08	16.40±1.39	1.27±0.08	85.70±0.58	90.05±0.36	89.78±0.27	2032.9±7.6	x
	22473-01AH	2.7	0.16±0.06	36.37±1.28	2.37±0.11	209.50±5.75	218.47±0.27	218.00±0.20	2025±33	x
	22473-01AI	3.5		17.95±1.50	0.83±0.08	103.80±0.95	108.69±0.42	108.70±0.35	2032±11	x
	22473-01AJ	5	0.01±0.07	14.45±1.26	0.66±0.07	68.47±0.64	73.13±0.32	73.10±0.23	2056±11	x
	22473-01AK	5	0.15±0.07	9.71±1.26	0.72±0.06	60.26±0.62	64.44±0.34	64.00±0.26	2050±13	x
B14-045_02	23000-01A	1.8	0.29±0.14	0.12±0.06	0.23±0.09	4.59±0.50	19.69±0.58	18.81±0.41	4123±179	
J = 2.1531e-2	23000-01B	3.5	0.56±0.11	0.48±0.11	0.20±0.08	4.29±0.45	12.50±0.49	10.83±0.34	3360±166	
± 2.3094e-4	23000-01C	5.2	0.52±0.12	0.73±0.11	0.15±0.08	8.89±0.50	16.30±0.49	14.74±0.35	2742±86	
	23000-01D	6.5	0.26±0.10	0.96±0.08	0.09±0.09	11.93±0.36	11.16±0.44	10.39±0.32	1905±50	
	23000-01E	7.5	0.15±0.11	1.04±0.09	0.03±0.08	9.10±0.48	5.73±0.45	5.28±0.32	1463±80	

	23000-01F	10	0.28±0.11	3.93±0.14		37.31±0.51	20.31±0.45	19.46±0.32	1358±19	
	23000-01G	12	0.45±0.11	5.99±0.15		53.99±0.71	30.19±0.45	28.86±0.32	1382±15	
	23000-01H	14	0.25±0.11	7.19±0.16		69.44±0.81	44.65±0.46	43.90±0.33	1550±12	
	23000-01I	16	0.28±0.11	6.53±0.16		63.71±0.76	46.29±0.46	45.45±0.33	1679±13	
	23000-01J	18	0.10±0.08	5.48±0.26	0.14±0.09	55.43±0.70	42.85±0.32	42.55±0.23	1760±13	
	23000-01K	20	0.10±0.07	5.04±0.12	0.00±0.00	50.40±0.65	41.00±0.32	40.69±0.23	1817±14	
	23000-01L	22		4.14±0.13	0.02±0.09	38.88±0.60	32.33±0.40	32.90±0.28	1872±18	
	23000-01M	24	0.13±0.07	5.10±0.12		49.84±0.67	42.03±0.31	41.64±0.22	1857±14	
	23000-01N	26	0.14±0.08	3.52±0.11		35.14±0.83	32.90±0.33	32.47±0.23	1976±28	x
	23000-01O	28	0.20±0.07	3.69±0.23	0.02±0.08	31.86±0.83	31.04±0.30	30.43±0.22	2015±31	x
	23000-01P	30	0.65±0.11	15.09±0.22	0.14±0.11	135.90±1.34	132.43±0.48	130.50±0.34	2021.9±8.1	x
	23000-01Q	33	1.45±0.14	67.95±1.73		635.40±7.57	620.74±0.95	616.40±0.85	2035±11	x
	23000-01R	2	0.27±0.11	0.45±0.08	0.07±0.08	2.32±0.49	2.68±0.46	1.87±0.33	1817±314	x
	23000-01S	4		3.75±0.08	0.07±0.09	35.82±0.50	35.43±0.34	35.61±0.24	2065±17	x
	23000-01T	5		11.69±0.19	0.02±0.10	98.47±0.89	95.65±0.39	95.68±0.28	2037±6.7	x
	23000-01U	6		12.95±0.21		112.10±1.47	109.03±0.39	109.10±0.28	2039±13	x
	23000-01V	6		1.19±0.13		10.20±0.48	9.81±0.30	9.80±0.21	2022±62	x
B14-049_01	22464-01A	1.6		0.30±0.79	0.07±0.05		1.89±0.23	2.17±0.16	NaN	
J = 1.9923e-2	22464-01B	3.5	0.75±0.06	0.83±0.77	4.53±0.08	5.57±0.16	75.65±0.25	73.41±0.19	5963±48	
± 2.7611e-5	22464-01C	5.2	0.69±0.06	0.56±0.82	3.02±0.08	12.85±0.19	32.48±0.25	30.42±0.18	3145±22	
	22464-01D	6.5	1.91±0.07	5.97±1.39	4.38±0.09	34.04±0.35	36.18±0.32	30.48±0.24	1847±14	
	22464-01E	7.5	0.17±0.06	7.48±1.43	1.34±0.06	25.41±0.30	17.54±0.27	17.02±0.20	1529±17	
	22464-01F	9		10.34±1.42	0.63±0.06	33.07±0.35	16.20±0.26	16.34±0.19	1236±14	
	22464-01G	12	0.15±0.06	16.85±1.49	1.24±0.08	91.18±0.73	46.52±0.28	46.06±0.20	1256.2±6.2	
	22464-01H	15	0.24±0.07	19.36±1.63	0.74±0.08	131.70±0.99	73.77±0.29	73.05±0.21	1342.7±4.8	
	22464-01I	17.5	0.04±0.07	18.30±1.56	0.56±0.07	120.50±0.92	74.20±0.29	74.08±0.21	1442.9±5.2	
	22464-01J	20	0.15±0.05	16.07±0.88	0.45±0.06	114.90±0.88	76.43±0.25	75.99±0.18	1516.7±4.9	
	22464-01K	22.5	0.28±0.06	9.49±0.83	0.48±0.07	99.56±1.43	72.26±0.28	71.41±0.22	1601±14	

	22464-01L	25	0.07±0.08	12.44±2.33	0.61±0.06	73.46±0.62	55.45±0.35	55.23±0.25	1651.5±8.7	
	22464-01M	27		6.61±1.54	0.22±0.06	44.84±0.41	35.55±0.29	35.59±0.23	1711±11	
	22464-01N	29.2	0.17±0.06	6.31±0.92	0.22±0.05	34.89±0.35	28.23±0.25	27.72±0.18	1712±12	
	22464-01O	31	0.13±0.05	3.41±0.94	0.35±0.05	31.42±0.32	24.95±0.23	24.56±0.17	1694±12	
	22464-01P	1.5	0.27±0.06	10.43±1.00	1.30±0.07	104.00±0.81	83.95±0.27	83.15±0.20	1718.8±5.7	
	22464-01Q	2	0.70±0.09	48.51±1.89	5.21±0.09	276.90±2.55	288.18±0.38	286.10±0.28	2016.8±8.0	x
	22464-01R	2.2	0.40±0.08	27.51±1.01	3.76±0.10	152.90±1.16	161.90±0.37	160.70±0.28	2037.2±5.2	x
	22464-01S	2.5	0.25±0.09	15.87±0.87	1.83±0.08	77.42±0.57	82.03±0.37	81.27±0.27	2036.1±6.0	x
	22464-01T	2.8	0.15±0.05	1.50±0.89	0.39±0.05	9.06±0.20	12.25±0.23	11.80±0.17	2309±35	
	22464-01U	5	0.22±0.06	19.82±0.93	2.28±0.08	74.07±0.56	83.36±0.27	82.72±0.19	2112.5±5.3	
	22464-01V	5	0.35±0.06	11.81±0.82	1.57±0.07	32.31±0.33	44.33±0.25	43.28±0.18	2345±12	
B14-049_02	22915-01A	1.8	0.72±0.06	0.11±0.05	1.52±0.10	3.11±0.53	86.07±0.27	83.93±0.20	7184±304	
J = 1.9478e-2	22915-01B	3.5	1.02±0.06	0.29±0.05	6.96±0.15	7.11±0.53	90.84±0.29	87.78±0.21	5810±130	
± 1.0791e-4	22915-01C	5	0.71±0.05	0.50±0.06	4.81±0.14	10.76±0.61	55.94±0.24	53.81±0.18	4283±93	
	22915-01D	6.5	2.15±0.07	0.99±0.06	6.27±0.18	25.48±0.49	58.96±0.30	52.55±0.22	2910±28	
	22915-01E	7.8	4.26±0.12	4.18±0.11	8.96±0.11		190.24±0.36	177.53±0.00	NaN	
	22915-01F	8.5	1.47±0.07	5.94±0.21	6.69±0.18	50.51±0.99	89.20±0.31	84.81±0.23	2619±27	
	22915-01G	9.5	0.93±0.07	7.72±0.12	3.33±0.14	63.68±0.69	58.30±0.29	55.52±0.21	1791±13	
	22915-01H	12	1.13±0.07		2.81±0.14	150.50±1.43	86.26±0.30	82.87±0.22	1315±9.1	
	22915-01I	15	1.47±0.07		2.07±0.15	273.60±1.13	149.30±0.32	144.90±0.24	1279±3.9	
	22915-01J	17	0.83±0.06		0.64±0.13	172.70±0.92	100.49±0.29	98.01±0.22	1343±5.3	
	22915-01K	19	0.26±0.09	32.67±0.24	2.50±0.06	238.99±4.69	160.69±0.42	159.90±0.32	1505±20	
	22915-01L	21	1.01±0.07		0.77±0.16	212.90±1.71	146.20±0.30	143.20±0.23	1510.4±8.2	
	22915-01M	22.5	0.47±0.10	35.31±0.27	2.64±0.07	252.61±5.39	207.24±0.49	205.85±0.39	1715±24	
	22915-01N	23		19.19±0.16	0.42±0.11	141.50±1.37	111.33±0.39	111.40±0.28	1677±11	
	22915-01O	24	0.16±0.06	16.52±0.33	0.41±0.10	115.70±1.42	96.06±0.27	95.58±0.20	1730±14	
	22915-01P	25	0.08±0.06	16.40±0.19	0.35±0.11	119.50±0.89	97.84±0.26	97.59±0.19	1718±8.4	
	22915-01Q	26	0.18±0.06	12.24±0.18	0.61±0.11	92.75±0.84	75.25±0.27	74.71±0.20	1702±10	

	22915-01R	27	0.03±0.06	7.66±0.23	0.30±0.09	55.14±0.68	44.87±0.24	44.79±0.18	1711±14	
	22915-01S	29.5	0.32±0.09	14.99±0.18	0.76±0.11	131.40±1.42	104.56±0.38	103.60±0.27	1678±12	
	22915-01T	32		42.10±0.31	5.57±0.09	370.07±3.96	344.94±0.58	342.39±0.47	1859±12	
	22915-01U	32	0.86±0.11	13.57±0.18	1.18±0.11	105.80±0.73	101.30±0.28	99.98±0.21	1884.0±8.3	
	22915-01V	33	0.38±0.06	13.43±0.18	1.43±0.12	84.47±0.70	104.84±0.27	103.70±0.21	2203±11	
	22915-01W	34	0.43±0.06	11.69±0.14	1.95±0.11	76.43±0.79	84.20±0.27	82.92±0.21	2049±13	
	22915-01X	35	0.27±0.13	7.80±0.15	1.30±0.11	51.34±1.82	50.59±0.56	49.79±0.40	1914±43	
	22915-01Y	1	1.86±0.13	78.82±0.67	8.63±0.10	440.78±5.39	476.71±0.59	471.27±0.46	2031±15	x
	22915-01Z	1.5	1.84±0.17	265.17±0.76	27.37±0.18	1308.47±17.59	1405.56±0.89	1400.22±0.75	2032±16	x
	22915-01AA	1	0.06±0.06	8.15±0.08	0.66±0.09	39.40±1.00	43.01±0.25	42.84±0.19	2052±31	x
	22915-01AB	1.2	0.01±0.07	2.72±0.21	0.29±0.08	15.01±0.63	15.95±0.31	15.92±0.22	2021±54	x
	22915-02A	1.5	0.04±0.05	1.47±0.05	0.20±0.07	6.10±0.34	7.13±0.22	7.00±0.16	2118±75	x
	22915-02B	2	0.39±0.16	51.59±0.29	4.27±0.16	248.00±4.30	266.46±0.73	265.30±0.56	2031±21	x
	22915-02C	2.2		3.37±0.12	0.12±0.07	16.42±0.45	17.51±0.22	17.56±0.16	2031±35	x
	22915-02D	2.8		1.85±0.09	0.14±0.08	9.29±0.77	10.10±0.23	10.18±0.16	2061±104	x
	22915-02E	4	0.01±0.06	8.51±0.14	0.48±0.11	39.99±1.01	43.37±0.26	43.34±0.19	2047±31	x
	22915-02F	6		4.04±0.10	0.37±0.09	19.25±0.79	20.81±0.23	20.95±0.17	2052±51	x
B14-053a_02	22998-01A	1.8	0.08±0.07	0.13±0.07	0.01±0.07	0.41±0.32	6.27±0.29	6.02±0.21	6228±1356	
J = 2.0928e-2	22998-01B	3.5	0.55±0.08	0.39±0.06	0.31±0.09	8.26±0.29	29.16±0.33	27.51±0.24	3745±55	
± 1.1911e-4	22998-01C	3.5	0.16±0.06	0.31±0.07	0.05±0.07	5.89±0.37	5.02±0.28	4.53±0.20	1729±85	
	22998-01D	5.2	0.52±0.11	1.82±0.09	0.46±0.10	22.87±0.69	28.30±0.45	26.73±0.32	2232±41	
	22998-01E	5.2	0.09±0.07	0.43±0.08	0.05±0.07	5.53±0.25	2.47±0.30	2.20±0.21	1092±88	
	22998-01F	6.5	0.15±0.07	1.97±0.10	0.09±0.08	17.74±0.35	8.07±0.29	7.63±0.21	1158±28	
	22998-01G	9	0.25±0.08	8.23±0.19		60.59±1.03	32.60±0.33	31.85±0.23	1339±16	
	22998-01H	11	0.81±0.08	13.50±0.15	0.02±0.11	92.04±1.36	60.00±0.36	57.58±0.26	1510±13	
	22998-01I	13	0.16±0.08	14.18±0.15		103.30±1.10	72.31±0.35	71.84±0.26	1620.2±8.1	
	22998-01J	15	0.01±0.08	12.92±0.19		96.92±1.91	72.62±0.34	72.58±0.25	1701±20	
	22998-01K	16.5	0.29±0.07	8.97±0.15	0.03±0.09	78.01±0.88	61.48±0.33	60.62±0.24	1741.9±9.4	

	22998-01L	18	0.13±0.08	7.91±0.30	0.17±0.10	89.31±1.01	75.68±0.34	75.28±0.25	1834.2±9.4	
	22998-01M	19	0.16±0.08	6.79±0.16	0.22±0.10	64.91±0.80	64.29±0.33	63.81±0.24	2016±12	x
	22998-01N	20		4.77±0.14	0.04±0.09	32.68±0.48	32.01±0.40	32.09±0.29	2015±18	x
	22998-01O	21	0.02±0.07	3.32±0.13	0.04±0.08	21.17±0.40	20.75±0.32	20.68±0.23	2008±24	x
	22998-01P	22	0.16±0.11	2.87±0.11	0.01±0.08	17.94±0.37	18.09±0.45	17.60±0.32	2014±32	x
	22998-01Q	23	0.01±0.13	5.44±0.13		34.49±1.21	34.10±0.56	34.06±0.40	2022±44	x
	22998-01R	24	0.47±0.28	68.08±0.91		470.50±4.40	458.50±1.33	457.10±1.04	2001.6±5.7	x
	22998-01S	24.5	0.40±0.17	55.73±0.47	0.25±0.17	299.20±2.84	296.70±1.00	295.50±0.86	2021.8±6.8	x
	22998-01T	25	0.15±0.12	0.35±0.07	0.06±0.08	2.05±0.46	2.53±0.52	2.07±0.37	2049±351	x
	22998-01U	26	0.11±0.14	0.34±0.07		2.36±0.44	2.69±0.57	2.36±0.41	2033±310	x
	22998-01V	28	0.18±0.07	0.20±0.08	0.13±0.07	1.04±0.23	1.60±0.32	1.05±0.23	2051±376	x
	22998-01W	30	0.14±0.08	0.36±0.07	0.00±0.07	1.24±0.26	1.69±0.33	1.28±0.23	2081±346	x
B14-080_01	22474-01A	1.8	0.24±0.08	3.93±1.65	0.93±0.06	3.32±0.16	5.21±0.03	4.49±0.25	2358±114	
J = 1.9906e-2	22474-01B	3.5	1.92±0.10	3.39±1.69	1.55±0.07	6.83±0.17	14.76±0.05	9.03±0.31	2328±63	
± 4.5366e-5	22474-01C	5.2	0.96±0.09	5.95±1.69	0.60±0.05	7.67±0.18	7.41±0.03	4.56±0.27	1409±69	
	22474-01D	6.5	0.90±0.09	5.78±1.69	0.60±0.06	10.41±0.20	7.31±0.03	4.61±0.28	1140±58	
	22474-01E	7.5	0.46±0.07	2.85±1.24	0.52±0.05	11.58±0.21	6.49±0.02	5.12±0.20	1140±38	
	22474-01F	9	-	-	-	-	-	-	NaN	
	22474-01G	12	-	-	-	-	-	-	NaN	
	22474-01H	9	0.11±0.09		0.03±0.04	3.93±0.20	1.96±0.03	1.62±0.26	1082±158	
	22474-01I	12	0.36±0.09	6.92±2.39	0.16±0.05	44.44±0.39	26.87±0.03	25.79±0.26	1386±14	
	22474-01J	14	0.40±0.11	21.28±2.52	0.29±0.06	80.18±0.57	53.25±0.10	52.05±0.35	1497±9.6	
	22474-01K	16		47.30±4.00	0.40±0.08	110.30±0.74	82.04±0.09	82.40±0.43	1644.1±8.8	
	22474-01L	18	0.02±0.03	10.52±0.58	0.08±0.02	26.77±0.18	21.06±0.03	21.01±0.10	1697.9±8.0	
	22474-01M	20		13.08±0.82	0.08±0.03	34.42±0.27	28.18±0.07	28.31±0.12	1749.9±8.9	
	22474-01N	22	0.03±0.02	13.05±0.54	0.10±0.02	36.67±0.23	31.04±0.03	30.94±0.08	1778.4±5.7	
	22474-01O	24	0.08±0.03	9.77±0.59	0.08±0.02	32.29±0.20	28.63±0.04	28.40±0.08	1826.0±6.2	
	22474-01P	26	0.00±0.00	9.45±0.57	0.09±0.02	27.53±0.29	24.72±0.03	24.80±0.10	1854±12	

	22474-01Q	28	0.02±0.03	8.02±0.59	0.07±0.02	23.63±0.17	22.53±0.04	22.47±0.10	1916.9±8.8	
	22474-01R	30	0.01±0.03	7.07±0.54	0.13±0.02	19.54±0.15	20.07±0.09	20.04±0.12	2007±11	x
	22474-01S	32		7.41±0.57	0.10±0.02	16.25±0.13	16.68±0.04	16.71±0.08	2010±11	x
	22474-01T	35		8.71±0.97	0.11±0.02	22.91±0.25	22.87±0.04	22.93±0.12	1978±14	x
	22474-01U	38		3.49±1.23	0.03±0.02	10.28±0.19	10.55±0.01	10.61±0.13	2015±31	x
	22474-01V	40	0.00±0.00	0.00±0.00	0.00±0.00	575.17±5.55	197.61±0.05	196.40±0.13	2019±10	x
	22474-01W	1.8		5.06±2.97	0.02±0.04	1.41±0.47	1.13±0.03	1.35±0.29	1921±536	x
	22474-01X	2.5	0.06±0.10			0.75±0.24	0.88±0.03	0.69±0.29	1873±781	x
	22474-01Y	4	0.14±0.08	1.60±1.92	0.04±0.04	6.81±0.23	7.41±0.04	7.00±0.23	2011±66	x
	22474-01Z	6	0.06±0.09	6.03±2.58	0.20±0.05	14.28±0.31	14.84±0.03	14.65±0.27	2008±39	x
	22474-01AA	8	0.01±0.09	7.98±2.23	0.13±0.05	17.63±0.35	18.09±0.03	18.06±0.28	2006±31	x
B14-086_01	22475-01A	1.8	0.09±0.03	2.60±0.55	0.58±0.02	0.80±0.05	2.20±0.12	1.94±0.09	3185±138	
J = 1.9909e-2	22475-01B	3.5	0.07±0.03	2.28±0.57	0.27±0.02	1.21±0.05	1.49±0.12	1.30±0.08	2062±112	
± 4.5276e-5	22475-01C	5.2	0.48±0.03	3.91±0.62	0.88±0.03	3.70±0.07	5.67±0.14	4.25±0.10	2146±42	
	22475-01D	6.5	0.52±0.03	6.03±0.58	0.55±0.03	5.91±0.07	7.48±0.14	5.92±0.10	1979±27	
	22475-01E	7.5	0.29±0.03	2.42±0.75	0.37±0.02	10.79±0.09	10.10±0.14	9.24±0.10	1795±18	
	22475-01F	9	0.24±0.03	3.62±0.71	0.35±0.02	20.43±0.11	18.68±0.14	17.95±0.10	1824.6±9.7	
	22475-01G	12	0.00±0.00	15.27±0.79	0.78±0.03	57.41±0.20	54.95±0.16	55.02±0.13	1925.8±5.0	
	22475-01H	14	0.05±0.03	8.39±0.86	0.53±0.03	34.06±0.15	33.89±0.13	33.73±0.09	1965.1±6.8	
	22475-01I	16	0.01±0.03	10.73±0.65	0.50±0.03	38.75±0.25	38.83±0.14	38.81±0.11	1978.3±8.5	
	22475-01J	18	0.05±0.03	9.06±0.62	1.17±0.03	43.89±0.17	45.80±0.16	45.65±0.12	2024.2±5.9	x
	22475-01K	20	0.26±0.03	49.52±0.85	1.37±0.27	179.05±1.70	190.05±0.18	189.29±0.15	2044±12	x
	22475-01L	22	0.18±0.02	5.60±0.64	0.06±0.02	20.97±0.11	22.58±0.13	22.04±0.11	2037.0±9.2	x
	22475-01M	25	0.08±0.02	4.48±0.60	0.08±0.02	17.95±0.20	19.28±0.12	19.03±0.09	2047±15	x
	22475-01N	28	0.08±0.02	3.36±0.66	0.07±0.02	14.54±0.11	15.68±0.11	15.44±0.08	2049±12	x
	22475-01O	32	0.14±0.03	45.99±0.74	1.18±0.44	133.43±0.95	142.28±0.14	141.88±0.10	2051.0±8.7	x
	22475-01P	38	0.05±0.02		0.04±0.02	3.81±0.11	4.17±0.10	4.03±0.07	2042±46	x
	22475-01Q	2	0.03±0.02		0.02±0.02	0.17±0.05	0.27±0.08	0.18±0.06	2042±586	x

	22475-01R	2.5		3.24±0.58	0.01±0.01	0.63±0.13	0.73±0.09	0.89±0.07	2416±306	x
	22475-01S	3.5	0.03±0.02		0.02±0.01	0.16±0.05	0.24±0.09	0.14±0.07	1800±799	x
	22475-01T	3.5		3.53±0.63	0.01±0.01	1.43±0.06	1.69±0.10	1.90±0.07	2338±87	x
	22475-01U	5		2.26±0.64	0.00±0.02	2.88±0.07	3.10±0.10	3.11±0.07	2068±50	x
B14-029_01	22919-01A	1.8	0.07±0.05	0.08±0.05	0.11±0.07		0.34±0.22	0.14±0.15	NaN	
J = 1.9494e-2	22919-01B	3.5	0.14±0.08	0.09±0.05	0.07±0.07		0.78±0.35	0.38±0.25	NaN	
± 5.5136e-5	22919-01C	5	0.06±0.05		0.09±0.07		0.55±0.20	0.38±0.14	NaN	
	22919-01D	6.5		0.04±0.05	0.04±0.07	1.11±0.55	0.61±0.29	0.86±0.21	1661±603	
	22919-01E	7.5		0.07±0.05		1.59±0.45	0.58±0.22	0.66±0.15	1066±297	
	22919-01F	9		0.22±0.08		1.65±0.55	0.88±0.22	1.00±0.15	1410±361	
	22919-01G	12	0.10±0.05	0.25±0.09	0.05±0.07	4.60±0.64	2.28±0.23	1.98±0.16	1098±132	
	22919-01H	15	0.11±0.05	0.36±0.07	0.06±0.07	6.13±0.68	3.59±0.23	3.27±0.17	1286±113	
	22919-01I	17.5	0.07±0.05	0.51±0.07	0.08±0.06	7.18±0.46	4.12±0.23	3.90±0.16	1303±71	
	22919-01J	21	0.05±0.05	1.10±0.07	0.14±0.07	11.44±0.61	8.77±0.23	8.60±0.16	1629±61	
	22919-01K	24	0.06±0.05	2.43±0.08	0.06±0.07	20.34±0.45	15.81±0.22	15.63±0.16	1652±26	
	22919-01L	28	0.09±0.05	4.39±0.09	0.24±0.08	30.83±0.84	26.45±0.23	26.17±0.17	1762±31	
	22919-01M	29.5	0.07±0.06	2.90±0.09	0.04±0.07	16.33±0.66	16.05±0.23	15.83±0.17	1914±49	
	22919-01N	32	0.01±0.06	7.28±0.20	0.02±0.08	42.53±0.64	44.79±0.77	44.76±0.75	2013±27	x
	22919-01O	35		4.68±0.11	0.11±0.08	27.77±0.59	29.11±0.53	29.20±0.40	2012±31	x
	22919-01P	1.5	0.17±0.09	25.53±0.19	0.06±0.04	155.62±3.87	169.00±0.45	168.48±0.35	2047±31	x
	22919-01Q	2	0.02±0.06	0.79±0.07	0.13±0.06	4.94±0.36	5.38±0.23	5.33±0.17	2044±98	x
	22919-01R	3		0.73±0.07	0.11±0.06	4.02±0.36	4.20±0.25	4.21±0.18	2006±119	x
	22919-01S	6		0.10±0.05		1.27±0.52	0.88±0.31	1.17±0.22	1857±522	x
B14-042_01	22463-01A	3.5	0.22±0.07	4.17±1.31	0.15±0.05	11.21±0.17	6.96±0.30	6.31±0.21	1359±39	
J = 1.9958e-2	22463-01B	5.2	0.25±0.07	8.54±0.49	0.22±0.05	22.65±0.24	16.99±0.28	16.26±0.20	1604±17	
± 4.0549e-5	22463-01C	6.5	0.27±0.07	9.10±0.47	0.21±0.05	26.38±0.23	23.25±0.29	22.44±0.21	1790±14	
	22463-01D	7.5	0.17±0.06	10.92±0.68	0.26±0.05	24.87±0.40	24.61±0.27	24.10±0.20	1942±21	

	22463-01E	9	0.00±0.08	18.44±0.81	0.15±0.06	38.05±0.29	38.76±0.33	38.75±0.24	2002±11	
	22463-01F	12	0.12±0.09	41.15±1.87	0.39±0.06	98.76±0.55	102.26±0.39	101.90±0.29	2017.7±6.7	
	22463-01G	15	0.31±0.06	41.76±1.14	0.41±0.07	114.00±0.82	122.72±0.31	121.80±0.26	2053.2±8.7	x
	22463-01H	17.5	0.43±0.09	39.46±1.74	0.76±0.08	122.60±0.93	131.58±0.41	130.30±0.30	2053.3±8.9	x
	22463-01I	20	0.80±0.02	114.99±1.49	1.09±0.01	290.23±2.73	306.22±0.07	306.22±0.07	2043±12	x
	22463-01J	22	0.21±0.05	11.96±0.79	0.11±0.05	26.64±0.41	28.98±0.23	28.35±0.17	2055±20	x
	22463-01K	25	22.07±0.18	10.22±0.76	4.19±0.09	17.47±0.43	84.33±0.76	18.45±0.54	2046±52	x
B14-042_02	23002-02A	1.8	0.03±0.07	0.11±0.07	0.11±0.07		0.36±0.31	0.10±0.22	NaN	
J = 2.0857e-2	23002-02B	3.5	0.21±0.08	0.11±0.08	0.10±0.07	0.48±0.20	1.34±0.32	0.63±0.22	2539±704	
± 2.6152e-4	23002-02C	5.2	0.27±0.08	0.35±0.07	0.08±0.07	0.78±0.21	1.13±0.32	0.81±0.22	1123±628	
	23002-02D	1.8	0.01±0.07		0.09±0.06		0.30±0.29	0.04±0.21	NaN	
	23002-02E	3.5	0.23±0.07	0.18±0.07	0.04±0.06	1.87±0.24	1.96±0.32	0.68±0.22	1606±232	
	23002-02F	5.2	0.02±0.07	0.57±0.07	0.03±0.06	2.97±0.22	2.32±0.30	0.06±0.21	1716±133	
	23002-02G	6.5	0.27±0.10	1.35±0.08	0.00±0.00	4.76±0.22	3.04±0.43	0.82±0.30	1226±127	
	23002-02H	7.5	0.30±0.10	1.85±0.09	0.05±0.08	6.31±0.24	4.39±0.43	0.90±0.30	1385±91	
	23002-02I	9	0.34±0.10	4.00±0.11		12.26±0.27	9.74±0.43	1.02±0.30	1641±44	
	23002-02J	11	0.14±0.07	6.59±0.15	0.02±0.07	18.71±0.30	16.74±0.30	0.42±0.21	1870±24	
	23002-02K	13	0.13±0.07	9.96±0.17	0.09±0.07	28.55±0.32	27.19±0.31	0.38±0.22	1957±17	
	23002-02L	15	0.06±0.07	9.43±0.17		27.35±0.35	26.86±0.32	0.19±0.22	2003±19	
	23002-02M	17	0.10±0.07	5.77±0.14		16.13±0.61	16.78±0.29	0.29±0.21	2060±49	x
	23002-02N	20	0.06±0.07	4.92±0.15	0.06±0.07	14.43±0.32	14.86±0.32	0.17±0.22	2055±33	x
	23002-02O	23	0.01±0.10	3.52±0.12	0.10±0.07	10.37±0.32	10.66±0.43	0.03±0.30	2064±52	x
	23002-02P	26	0.15±0.12	25.69±0.29	0.00±0.00	73.10±0.95	73.61±0.50	0.44±0.35	2034±17	x
	23002-02Q	29	0.00±0.07	0.78±0.09		2.53±0.25	2.77±0.29	0.01±0.21	2143±158	x
	23002-02R	32	0.12±0.07	5.66±0.15		16.04±0.36	16.91±0.32	0.37±0.22	2070±32	x
	23002-02S	2	0.13±0.07	4.92±0.14		14.35±0.27	14.84±0.30	0.40±0.21	2041±29	x
	23002-02T	4		0.41±0.10		0.25±0.19	0.36±0.38	-0.22±0.27	3144±1322	x
	23002-02U	6	0.13±0.07			0.00±0.00	0.06±0.29	0.40±0.21	4915±6648	x

Table 5
Diffusion coefficients for each heating step. Those used for Arrhenius regressions are noted for each sample. All uncertainties reported at 1σ. "--" indicates the laser not firing, while "-" indicates pyrometer software not recording temperature.

Sample ID	Run ID	Temperature (C)	Heating Duration (s)	39Ar $\ln(D_0/a^2)$	±	Used in Arrhenius
B06-055_01	22918-03A	425	300	-21.943	0.121	
	22918-03B	505	300	-20.714	0.093	x
	22918-03C	572	300	-18.586	0.040	x
	22918-03D	--	300	-20.341	0.375	
	22918-03E	570	300	-19.312	0.157	x
	22918-03F	600	300	-17.747	0.043	
	22918-03G	636	300	-17.247	0.040	x
	22918-03H	701	300	-15.517	0.014	x
	22918-03I	752	300	-13.224	0.005	x
	22918-03J	790	300	-12.538	0.005	x
	22918-03K	828	300	-12.192	0.006	x
	22918-03L	858	300	-11.951	0.006	x
	22918-03M	908	300	-12.500	0.025	
	22918-03N	928	300	-11.176	0.008	
	22918-03O	934	300	-10.984	0.016	
	22918-03P	943	300	-11.460	0.011	
	22918-03Q	1027	300	-10.102	0.006	
	22918-03R	Direct	60			
	22918-03S	Direct	60			
	22918-03T	Direct	60			
	22918-03U	Direct	60			
B06_055_02	22918-04A	425	300	-19.241	0.054	

	22918-04B	592	300	-16.493	0.021	x
	22918-04C	669	300	-14.136	0.010	x
	22918-04D	725	300	-12.745	0.006	x
	22918-04E	765	300	-12.083	0.007	x
	22918-04F	810	300	-11.302	0.005	x
	22918-04G	896	300	-11.902	0.010	
	22918-04H	944	300	-11.234	0.006	
	22918-04I	1002	300	-10.943	0.007	
	22918-04J	1045	300	-10.456	0.009	
	22918-04K	1073	300	-10.825	0.008	
	22918-04L	1093	300	-7.977	0.002	
	22918-04M	1121	300	-8.002	0.009	
	22918-04N	1148	300			
	22918-04O	1173	300			
B06-020_01	22472-01A	--	240			
	22472-01B	--	180			
	22472-01C	--	120			
	22472-01D	--	120			
	22472-01E	500	120	-20.798	0.108	
	22472-01F	586	120	-16.847	0.022	
	22472-01G	630	120	-18.304	0.141	x
	22472-01H	706	180	-14.837	0.014	x
	22472-01I	745	180	-14.601	0.016	x
	22472-01J	794	180	-13.649	0.013	x
	22472-01K	884	180	-12.130	0.012	x
	22472-01L	960	120	-11.460	0.012	x
	22472-01M	991	120	-10.964	0.014	x
	22472-01N	1101	120	-10.295	0.013	

	22472-01O	1134	120	-8.552	0.023	
	22472-01P	Direct	45			
	22472-01Q	Direct	45			
	22472-01R	Direct	45			
	22472-01S	Direct	45			
	22472-01T	Direct	45			
	22472-01U	Direct	45			
B14-015_01	22914-01A	426	180	-17.223	0.034	
	22914-01B	573	180	-14.611	0.018	x
	22914-01C	660	180	-12.226	0.023	x
	22914-01D	672	180	-12.306	0.009	x
	22914-01E	698	180	-11.910	0.009	x
	22914-01F	714	180	-11.502	0.008	x
	22914-01G	742	180	-11.018	0.008	x
	22914-01H	769	180	-10.602	0.007	x
	22914-01I	790	180	-10.338	0.007	x
	22914-01J	804	180	-10.438	0.008	
	22914-01K	817	180	-10.577	0.010	
	22914-01L	839	180	-10.474	0.013	
	22914-01M	854	180	-10.418	0.010	
	22914-01N	861	180	-10.455	0.024	
	22914-01O	867	180	-10.554	0.012	
	22914-01P	876	180	-10.846	0.020	
	22914-01Q	891	180	-10.113	0.009	
	22914-01R	946	180	-9.985	0.009	
	22914-01S	956	180	-9.639	0.013	
	22914-01T	980	180	-9.669	0.024	
	22914-01U	965	180	-9.345	0.022	

	22914-01V	997	180	-8.899	0.008	
	22914-01W	1023	180	-9.656	0.013	
	22914-01X	1054	180	-12.279	0.183	
	22914-01Y	1103	180	-11.644	0.144	
	22914-01Z	1178	180	-8.157	0.022	
	22914-02A	Direct	60	-13.466	2.414	
	22914-02B	Direct	60	-9.625	0.072	
	22914-02C	Direct	60			
	22914-02D	Direct	60			
	22914-02E	Direct	60			
B14-015_02	22914-03A	426	180	-18.736	0.047	
	22914-03B	510	180	-16.642	0.021	x
	22914-03C	568	180	-15.140	0.025	x
	22914-03D	609	180	-13.672	0.012	x
	22914-03E	650	180	-12.809	0.010	x
	22914-03F	706	180	-12.126	0.008	x
	22914-03G	755	180	-11.373	0.007	x
	22914-03H	835	180	-10.076	0.005	x
	22914-03I	900	180	-9.725	0.006	
	22914-03J	948	180	-9.885	0.019	
	22914-03K	973	180	-9.871	0.008	
	22914-03L	1012	180	-9.952	0.009	
	22914-03M	1035	180	-10.206	0.011	
	22914-03N	1061	180	-9.490	0.066	
	22914-03O	1087	180	-9.862	0.018	
	22914-03P	1112	180	-9.102	0.021	
	22914-03Q	1133	180	-7.509	0.007	
	22914-03R	1155	180	-9.714	0.047	

	22914-03S	Direct	45	-10.212	0.247	
	22914-03T	Direct	45	-8.231	0.043	
	22914-03U	Direct	45			
	22914-03V	Direct	45			
	22914-03W	Direct	45			
B14-024_01	22471-01A	559	60	-18.667	0.070	
	22471-01B	651	60	-17.366	0.055	x
	22471-01C	708	60	-15.905	0.028	x
	22471-01D	746	60	-14.806	0.018	x
	22471-01E	797	60	-14.229	0.017	x
	22471-01F	882	60	-12.918	0.009	x
	22471-01G	951	60	-11.858	0.006	x
	22471-01H	1000	60	-11.009	0.005	x
	22471-01I	1045	60	-10.386	0.005	x
	22471-01J	1077	60	-10.309	0.005	x
	22471-01K	1099	60	-10.294	0.006	
	22471-01L	1121	60	-10.378	0.007	
	22471-01M	1148	60	-10.350	0.007	
	22471-01N	1121	60	-10.791	0.010	
	22471-01O	1121	60	-10.935	0.012	
	22471-01P	1121	60	-11.156	0.017	
	22471-01Q	1121	60	-11.269	0.016	
	22471-01R	1121	60	-11.381	0.018	
	22471-01S	1121	60	-11.474	0.020	
	22471-01T	1121	60	-11.895	0.025	
	22471-01U	1148	600	-11.855	0.005	
	22471-01V	1148	600	-12.209	0.006	
	22471-01W	1148	600	-12.420	0.008	

	22471-01X	1173	600	-12.208	0.007	
	22471-01Y	1173	600	-12.501	0.009	
	22471-01Z	1197	600	-12.326	0.009	
	22471-01AA	1220	600	-11.969	0.007	
	22471-01AB	1220	600	-11.778	0.007	
	22471-01AC	1270	600	-11.765	0.006	
	22471-01AD	Direct	30			
B14-024_02	22913-01A	426	180	-21.857	0.169	
	22913-01B	530	180	-20.725	0.169	x
	22913-01C	588	180	-19.462	0.066	x
	22913-01D	662	180	-17.504	0.039	x
	22913-01E	706	180	-16.601	0.032	x
	22913-01F	748	180	-15.771	0.017	x
	22913-01G	841	180	-13.787	0.011	x
	22913-01H	970	180	-11.018	0.064	x
	22913-01I	982	180	-10.957	0.041	x
	22913-01J	1010	180	-11.022	0.023	x
	22913-01K	1032	180	-11.284	0.011	
	22913-01L	1048	180	-11.508	0.013	
	22913-01M	1061	180	-15.287	0.264	
	22913-01N	1107	180	-15.863	0.437	
	22913-01O	1161	180	-16.426	0.761	
	22913-01P	Direct	45	-14.156	0.323	
	22913-01Q	Direct	45	-14.433	0.311	
	22913-01R	Direct	45	-10.326	0.015	
	22913-01S	Direct	45	-7.642	0.025	
	22913-01T	Direct	45	-8.740	0.028	
	22913-01U	Direct	45	-8.953	0.011	

	22913-01V	Direct	45	-9.319	0.017	
	22913-01W	Direct	45	-8.184	0.024	
	22913-01X	Direct	45	-8.087	0.026	
	22913-01Y	Direct	45	-8.098	0.029	
	22913-02A	Direct	45	-7.819	0.026	
	22913-02B	Direct	45	-7.244	0.019	
	22913-02C	Direct	45	-7.624	0.007	
	22913-02D	Direct	45	-7.564	0.009	
	22913-02E	Direct	45	-7.751	0.012	
	22913-02F	Direct	45	-7.435	0.011	
	22913-02G	Direct	45	-8.211	0.029	
	22913-02H	Direct	45			
	22913-02I	Direct	45			
	22913-02J	Direct	45			
B14-045_01	22473-01A	425	240	-26.489	0.477	x
	22473-01B	550	180	-22.224	0.077	x
	22473-01C	646	120	-19.971	0.043	x
	22473-01D	690	120	-18.764	0.030	x
	22473-01E	--	120			
	22473-01F	--	120			
	22473-01G	744	120	-17.547	0.025	x
	22473-01H	780	120	-16.788	0.015	x
	22473-01I	812	120	-15.863	0.011	x
	22473-01J	844	120	-15.471	0.012	x
	22473-01K	868	120	-15.361	0.012	x
	22473-01L	917	120	-14.402	0.016	x
	22473-01M	955	120	-13.832	0.008	x
	22473-01N	1000	120	-13.147	0.007	x

	22473-01O	1061	120	-12.594	0.007	x
	22473-01P	1087	120	-12.185	0.007	x
	22473-01Q	1110	120	-12.031	0.007	x
	22473-01R	1132	120	-11.975	0.007	x
	22473-01S	1135	120	-11.805	0.007	x
	22473-01T	1162	120	-11.454	0.007	x
	22473-01U	1165	120	-11.493	0.007	x
	22473-01V	1180	120	-11.467	0.008	
	22473-01W	1180	120	-11.674	0.008	
	22473-01X	1180	120	-12.437	0.011	
	22473-01Y	Direct	60			
	22473-01Z	Direct	60			
	22473-01AA	Direct	60			
	22473-01AB	Direct	60			
	22473-01AC	Direct	60			
	22473-01AD	Direct	60			
	22473-01AE	Direct	60			
	22473-01AF	Direct	60			
	22473-01AG	Direct	60			
	22473-01AH	Direct	60			
	22473-01AI	Direct	60			
	22473-01AJ	Direct	45			
	22473-01AK	Direct	45			
B14-045_02	23000-01A	425	300	-19.793	0.109	
	23000-01B	578	300	-18.782	0.104	x
	23000-01C	647	300	-17.368	0.057	x
	23000-01D	692	300	-16.490	0.031	x
	23000-01E	717	300	-16.389	0.053	x

	23000-01F	781	300	-14.447	0.014	x
	23000-01G	826	300	-13.468	0.013	x
	23000-01H	872	300	-12.713	0.012	x
	23000-01I	900	300	-12.422	0.012	x
	23000-01J	923	300	-12.297	0.013	
	23000-01K	956	300	-12.192	0.013	
	23000-01L	978	300	-12.300	0.015	
	23000-01M	1028	300	-11.913	0.013	
	23000-01N	1063	300	-12.140	0.024	
	23000-01O	1068	300	-12.145	0.026	
	23000-01P	1090	300	-10.474	0.010	
	23000-01Q	1146	300	-7.901	0.012	
	23000-01R	Direct	60			
	23000-01S	Direct	60			
	23000-01T	Direct	60			
	23000-01U	Direct	60			
	23000-01V	Direct	60			
B14-049_01	22464-01A	404	120			
	22464-01B	580	120	-18.520	0.028	x
	22464-01C	647	120	-16.219	0.015	x
	22464-01D	686	120	-14.149	0.010	x
	22464-01E	706	120	-13.818	0.012	x
	22464-01F	758	120	-13.168	0.011	x
	22464-01G	823	120	-11.613	0.008	x
	22464-01H	863	120	-10.643	0.008	x
	22464-01I	903	120	-10.269	0.008	x
	22464-01J	980	120	-9.974	0.008	
	22464-01K	1020	120	-9.846	0.014	

	22464-01L	1081	120	-9.947	0.008	
	22464-01M	1148	120	-10.306	0.009	
	22464-01N	1179	120	-10.467	0.010	
	22464-01O	1197	120	-10.498	0.010	
	22464-01P	Direct	60			
	22464-01Q	Direct	60			
	22464-01R	Direct	60			
	22464-01S	Direct	60			
	22464-01T	Direct	60			
	22464-01U	Direct	45			
	22464-01V	Direct	45			
B14-049_02	22915-01A	426	180	-22.379	0.002	
	22915-01B	582	180	-20.093	0.002	x
	22915-01C	644	180	-18.827	0.003	x
	22915-01D	695	180	-17.191	0.004	x
	22915-01E	733	180			
	22915-01F	752	180	-15.746	0.003	x
	22915-01G	780	180	-14.919	0.004	x
	22915-01H	843	180	-13.435	0.003	x
	22915-01I	900	180	-12.159	0.002	x
	22915-01J	903	180	-12.177	0.002	x
	22915-01K	924	180	-11.546	0.002	x
	22915-01L	943	180	-11.388	0.002	x
	22915-01M	964	180	-10.977	0.002	x
	22915-01N	983	180	-11.376	0.003	
	22915-01O	981	180	-11.467	0.002	
	22915-01P	993	180	-11.338	0.002	
	22915-01Q	1053	180	-11.507	0.003	

	22915-01R	1061	180	-11.970	0.004	
	22915-01S	1038	180	-11.030	0.003	
	22915-01T	1095	180	-9.807	0.001	
	22915-01U	1183	180	-10.890	0.002	
	22915-01V	1183	180	-11.047	0.002	
	22915-01W	1200	180	-11.090	0.002	
	22915-01X	1205	180	-11.442	0.008	
	22915-01Y	Direct	60	-8.010	0.001	
	22915-01Z	Direct	60	-6.011	0.001	
	22915-01AA	Direct	60	-8.498	0.004	
	22915-01AB	Direct	60	-9.345	0.014	
	22915-02A	Direct	60	-10.192	0.023	
	22915-02B	Direct	60			
	22915-02C	Direct	60			
	22915-02D	Direct	60			
	22915-02E	Direct	60			
	22915-02F	Direct	60			
B14-053a_02	22998-01A	425	60	-22.970	0.776	
	22998-01B	559	60	-16.877	0.035	x
	22998-01C	560	300	-17.881	0.063	x
	22998-01D	615	300	-15.711	0.030	x
	22998-01E	587	300	-16.689	0.044	x
	22998-01F	664	300	-15.262	0.020	x
	22998-01G	719	300	-13.448	0.017	x
	22998-01H	771	300	-12.378	0.015	x
	22998-01I	817	300	-11.745	0.011	x
	22998-01J	857	300	-11.424	0.020	x
	22998-01K	885	300	-11.367	0.011	

	22998-01L	1010	300	-10.998	0.011	
	22998-01M	1028	300	-11.121	0.012	
	22998-01N	1045	300	-11.689	0.015	
	22998-01O	1062	300	-12.059	0.019	
	22998-01P	1067	300	-12.178	0.021	
	22998-01Q	1086	300	-11.463	0.035	
	22998-01R	1098	300	-8.180	0.009	
	22998-01S	1108	300			
	22998-01T	1121	300			
	22998-01U	1135	300			
	22998-01V	1161	300			
	22998-01W	1186	300			
B14-080_01	22474-01A	425	240	-19.108	0.049	
	22474-01B	570	180	-16.693	0.025	x
	22474-01C	647	120	-15.435	0.024	
	22474-01D	697	120	-14.622	0.019	x
	22474-01E	739	120	-14.115	0.018	x
	22474-01F	713	120			
	22474-01G	812	120			
	22474-01H	791	60	-12.540	0.052	x
	22474-01I	877	120	-12.076	0.009	x
	22474-01J	926	120	-10.757	0.007	x
	22474-01K	971	120	-9.777	0.007	x
	22474-01L	1027	60	-10.155	0.007	x
	22474-01M	1054	60	-9.763	0.008	x
	22474-01N	1097	60	-9.546	0.006	x
	22474-01O	1118	60	-9.529	0.006	x
	22474-01P	1123	60	-9.568	0.010	

	22474-01Q	1130	60	-9.619	0.007	
	22474-01R	1155	60	-9.723	0.008	
	22474-01S	1165	60	-9.837	0.008	
	22474-01T	1178	60	-9.415	0.011	
	22474-01U	-	60	-10.151	0.019	
	22474-01V	-	60	-5.464	0.017	
	22474-01W	Direct	45			
	22474-01X	Direct	45			
	22474-01Y	Direct	45			
	22474-01Z	Direct	45			
	22474-01AA	Direct	45			
B14-086_01	22475-01A	400	180	-20.852	0.067	
	22475-01B	593	120	-18.773	0.043	x
	22475-01C	657	120	-16.636	0.018	x
	22475-01D	704	120	-15.352	0.012	x
	22475-01E	731	120	-14.064	0.008	x
	22475-01F	769	120	-12.752	0.005	x
	22475-01G	865	120	-10.872	0.003	x
	22475-01H	958	60	-10.140	0.004	x
	22475-01I	994	60	-9.678	0.006	x
	22475-01J	1030	60	-9.238	0.004	x
	22475-01K	1057	60	-7.079	0.009	
	22475-01L	1090	60	-8.652	0.005	
	22475-01M	1137	60	-8.674	0.011	
	22475-01N	-	60	-8.765	0.007	
	22475-01O	-	60			
	22475-01P	-	60			
	22475-01Q	Direct	45			

	22475-01R	Direct	45			
	22475-01S	Direct	45			
	22475-01T	Direct	45			
	22475-01U	Direct	45			
B14-029_01	22919-01A	425	300			
	22919-01B	551	300			
	22919-01C	609	300			
	22919-01D	656	300	-19.578	0.499	
	22919-01E	685	300	-17.982	0.284	x
	22919-01F	724	300	-17.325	0.335	x
	22919-01G	794	300	-15.655	0.138	x
	22919-01H	857	300	-14.764	0.111	x
	22919-01I	882	300	-14.149	0.065	x
	22919-01J	923	300	-13.255	0.054	x
	22919-01K	967	300	-12.187	0.022	x
	22919-01L	1031	300	-11.238	0.027	x
	22919-01M	1038	300	-11.513	0.040	x
	22919-01N	1124	300	-10.175	0.015	x
	22919-01O	1130	300	-10.215	0.021	x
	22919-01P	Direct	60			
	22919-01Q	Direct	60			
	22919-01R	Direct	60			
	22919-01S	Direct	60			
B14-042_01	22463-01A	578	120	-15.737	0.016	x
	22463-01B	657	120	-13.625	0.011	x
	22463-01C	684	120	-12.711	0.009	x
	22463-01D	716	120	-12.309	0.016	x

	22463-01E	768	120	-11.488	0.008	x
	22463-01F	833	120	-9.942	0.006	x
	22463-01G	876	120	-9.171	0.007	x
	22463-01H	913	120	-8.539	0.008	x
	22463-01I	990	120	-6.344	0.009	
	22463-01J	1030	120			
	22463-01K	1091	120			
B14-042_02	23002-02A	425	300			
	23002-02B	530	300	-20.659	0.407	
	23002-02C	530	300	-18.895	0.267	x
	23002-02D	435	300			
	23002-02E	594	300	-17.086	0.131	x
	23002-02F	645	300	-15.873	0.074	x
	23002-02G	691	300	-14.777	0.046	x
	23002-02H	725	300	-13.974	0.037	x
	23002-02I	776	300	-12.769	0.022	x
	23002-02J	826	300	-11.781	0.016	x
	23002-02K	875	300	-10.788	0.011	x
	23002-02L	920	300	-10.337	0.013	x
	23002-02M	940	300	-10.540	0.038	
	23002-02N	984	300	-10.434	0.022	
	23002-02O	1022	300	-10.591	0.031	
	23002-02P	1068	300	-7.898	0.013	
	23002-02Q	1054	300	-10.520	0.100	
	23002-02R	1093	300	-8.170	0.022	
	23002-02S	Direct	60			
	23002-02T	Direct	60			
	23002-02U	Direct	60			

Table 6

Summary of plateau ages, diffusion parameters, and calculated cooling rates and closure temperatures. All uncertainties reported at 1σ.

Sample	Plateau Age (Ma)	Plateau $\%^{39}Ar$	E_a (kJ/mol)	$\ln(D_0/a^2)$	T_c (°C)[a]	dT/dt (°C Ma^{-1})[b]	T_c (°C)[c]
B06-055_01	2051.3 ± 2.4	75	201.8 ± 5.7	9.90 ± 0.71	264.4 ± 8.1	28.1	276.3 ± 8.1
B06-055_02	2044.4 ± 3.7	49	186 ± 11	9.4 ± 1.3	229 ± 14	14.8	233 ± 14
B06-042_01	2037.8 ± 3.5	78	167.1 ± 7.9	3.80 ± 0.98	240 ± 12	9.3	239 ± 12
B06-042_02	2037.7 ± 5.8	85	165.4 ± 4.7	2.45 ± 0.50	252.4 ± 6.6	8.6	250.5 ± 6.6
B06-020_01	2033.3 ± 4.8	71	172.0 ± 6.3	5.71 ± 0.68	231.5 ± 8.0	8.1	229.0 ± 8.0
B14-015_01	1997.9 ± 5.0	32	145.7 ± 6.2	6.23 ± 0.97	150.9 ± 9.5	4.4	143.0 ± 9.5
B14-015_02	2009.9 ± 5.2	40	143.5 ± 5.0	5.57 ± 0.63	151.1 ± 6.3	5.5	145.2 ± 6.3
B14-024_01	2033.1 ± 3.9	63	190.6 ± 4.3	7.06 ± 0.48	267.8 ± 5.9	6.5	262.6 ± 5.9
B14-024_02	2022.3 ± 7.9	41	171.6 ± 2.4	5.11 ± 0.24	237.5 ± 2.9	5.3	229.9 ± 2.9
B14-045_01	2034.1 ± 3.8	63	174.0 ± 2.5	3.11 ± 0.25	270.0 ± 3.4	6.7	264.7 ± 3.4
B14-045_02	2032.6 ± 4.9	71	180.6 ± 3.5	6.15 ± 0.40	250.8 ± 4.8	7.1	246.7 ± 4.8
B14-049_01	2032.9 ± 5.6	32	211.2 ± 3.7	11.6 ± 0.4	269.4 ± 4.4	6.1	263.9 ± 4.4
B14-049_02	2037.0 ± 8.4	43	215.7 ± 4.9	9.79 ± 0.53	302.0 ± 6.5	5.7	295.3 ± 6.5
B14-053a_01	2025.6 ± 3.9	60	165.3 ± 3.7	3.25 ± 0.41	241.7 ± 5.2	5.6	234.5 ± 5.2
B14-053a_02	2011.1 ± 3.9	62	165.1 ± 2.6	6.42 ± 0.32	203.8 ± 3.5	4.7	195.7 ± 3.5
B14-080_01	2006.9 ± 5.4	50	171.1 ± 3.8	5.78 ± 0.39	228.1 ± 4.5	4.0	217.9 ± 4.5
B14-086_01	2032.2 ± 3.6	70	203.7 ± 5.1	9.95 ± 0.56	268.8 ± 6.4	6.3	263.7 ± 6.4
B14-029_01	2023 ± 17	70	209.4 ± 4.1	7.85 ± 0.40	309.5 ± 5.2	3.3	295.9 ± 5.2
B14-042_01	2051.4 ± 5.3	72	179.6 ± 6.1	9.59 ± 0.71	209.7 ± 7.3	56.0	228.0 ± 7.3
B14-042_02	2046 ± 12	59	182.8 ± 5.7	8.17 ± 0.66	233.5 ± 7.4	18.8	240.6 ± 7.4

E_a = activation energy; D_0= the diffusion coefficient at infinite temperature and a^2=the diffusion domain size. The quantity D_0/a^2 is stripped of dimensions for taking the logarithm. T_c = closure temperature.

[a]Closure temperature calculated for a 10°C Ma^{-1} cooling rate. For comparison to previous datasets only.

[b]Cooling rate obtained from Δt between biotite and plagioclase, as described in text.

[c]Closure temperature calculated using the cooling rate obtained from dT/dt (°C Ma^{-1})[b].

Table 7

Detailed ages from all age-spectra. All uncertainties reported at 1σ.

Sample	Plateau							Integrated Age	
	Age (Ma)	±	% error	MSWD	p	n	$\%^{39}$Ar.	Age (Ma)	±
B06-055_01	2051.3	2.4	0.12	0.17	0.99	8	75	2087.5	2.8
B06-055_01	2044.4	3.7	0.18	2.17	0.09	4	49	1940.3	2.3
B06-020_01	2033.3	4.8	0.24	0.15	0.99	8	71	1966.7	7.8
B14-015_01	1997.9	5.0	0.25	0.79	0.66	12	32	1716.7	4.1
B14-015_02	2009.9	5.2	0.26	0.31	0.98	11	40	1953.1	5.4
B14-024_01	2033.1	3.9	0.19	0.29	1.00	17	63	2032.5	10
B14-024_02	2022.3	7.9	0.39	N.A.	N.A.	1*	41	1857.0	3.3
B14-045_01	2034.1	3.8	0.19	0.90	0.52	10	63	2012.8	4.5
B14_045_02	2032.6	4.9	0.24	1.37	0.21	9	71	1959.0	6.1
B14-049_01	2032.9	5.6	0.28	2.51	0.08	3	32	1834.9	3.6
B14-049_02	2037.0	8.4	0.41	0.23	0.99	10	43	2037	17
B14-053a_02	2011.1	3.9	0.19	0.57	0.84	11	62	1906.9	4.6
B14-080_01	2006.9	5.4	0.27	0.63	0.77	10	50	1861.9	4.0
B14-086_01	2032.2	3.6	0.18	0.58	0.82	10	70	2011.0	4.2
B14-029_01	2023	17	0.84	0.21	0.96	6	70	1929	16
B14-042_01	2051.4	5.3	0.26	0.15	0.97	5	72	2010.7	5.4
B14-042_02	2046	12	0.59	0.33	0.95	9	59	1965.4	9.6

Table 8
Rock and magma properties used in Heat3D numerical simulations.

Rock Type	**K (W/m K)**	**Cp (J/kg K)**	**Density (kg/m^3)**	**Porosity (%)**
Pretoria Group[1]	4.18	880	2757	0.1
Rooiberg[1]	3.43	790	2660	0.1
Magma Type	**K (W/m K)**	**Cp (J/kg K)**	**Density (kg/m^3)**	**T_0 (°C)**
Mafic (RLS)	1.80	1200	-	1200
Felsic (Lebowa)	1.50	1100	-	1000

[1]Thermal properties for Bushveld area rocks available from Gibson & Jones (2002).